INVESTIGATIONS ON DIRECT TORQUE AND FLUX CONTROL OF SPEED SENSORLESS INDUCTION MOTOR DRIVE

Dissertation submitted to the

National Institute of Technology Rourkela

in partial fulfillment of the requirements
of the degree of

Doctor of Philosophy

in

Electrical Engineering

by

Tejavathu Ramesh

(Roll Number: 511EE102)

Under the supervision of

Prof. Anup Kumar Panda

March, 2016

Department of Electrical Engineering

National Institute of Technology Rourkela

Electrical Engineering
National Institute of Technology Rourkela

August 26, 2016

Certificate of Examination

Roll Number: 511EE102
Name: Tejavathu Ramesh
Title of Dissertation: Investigations on direct torque and flux control of speed sensorless induction motor drive

We the below signed, after checking the dissertation mentioned above and the official record book (s) of the student, hereby state our approval of the dissertation submitted in partial fulfillment of the requirements of the degree of Doctor of Philosophy in Electrical Engineering at National Institute of Technology Rourkela. We are satisfied with the volume, quality, correctness, and originality of the work.

Anup Kumar Panda
Principal Supervisor

Kanungo Barada Mohanty
Member (DSC)

Somnath Maity
Member (DSC)

Sukadev Meher
Member (DSC)

Tapas Kumar Bhattacharya
Examiner

Bidyadhar Subudhi
Chairman (DSC)

Electrical Engineering
National Institute of Technology Rourkela

Prof./Dr. Anup Kumar Panda
Professor

March 16, 2016

Supervisor's Certificate

This is to certify that the work presented in this dissertation entitled *"Investigations on direct torque and flux control of speed sensorless Induction motor drive"* by "*Tejavathu Ramesh*", Roll Number 511EE102, is a record of original research carried out by him under my supervision and guidance in partial fulfilment of the requirements of the degree of *Doctor of Philosophy* in *Electrical Engineering*. Neither this dissertation nor any part of it has been submitted for any degree or diploma to any institute or university in India or abroad.

Anup Kumar Panda

Dedicated

To

All My Family Members

and

Well-Wishers

…Tejavathu Ramesh

Declaration of Originality

I, Tejavathu Ramesh, Roll Number 511EE102 hereby declare that this dissertation entitled *"Investigations on direct torque and flux control of speed sensorless Induction motor drive"* represents my original work carried out as a doctoral student of NIT Rourkela and, to the best of my knowledge, it contains no material previously published or written by another person, nor any material presented for the award of any other degree or diploma of NIT Rourkela or any other institution. Any contribution made to this research by others, with whom I have worked at NIT Rourkela or elsewhere, is explicitly acknowledged in the dissertation. Works of other authors cited in this dissertation have been duly acknowledged under the section "Bibliography". I have also submitted my original research records to the doctoral scrutiny committee for evaluation of my dissertation.

I am fully aware that in case of any non-compliance detected in future, the Senate of NIT Rourkela may withdraw the degree awarded to me on the basis of the present dissertation.

March 16, 2016
NIT Rourkela

Tejavathu Ramesh

Acknowledgement

It has been a pleasure for me to work on this dissertation. I hope the reader will find it not only interesting and useful, but also comfortable to read.

The research reported here has been carried out in the Department of Electrical Engineering, National Institute of Technology Rourkela at the Power Electronics and Drives Laboratory. I am greatly indebted to many persons for helping me complete this dissertation.

First and foremost, I would like to express my sense of gratitude and indebtedness to my supervisor Prof. Anup Kumar Panda, Professor, Department of Electrical Engineering, for his inspiring guidance, encouragement, and untiring effort throughout the course of this work. His timely help and painstaking efforts made it possible to present the work contained in this thesis. I consider myself fortunate to have worked under his guidance. Also, I am indebted to him for providing all official and laboratory facilities.

I am grateful to Director, Prof. S.K. Sarangi and Prof. Jitendriya Kumar Satpathy, Head of Electrical Engineering Department, National Institute of Technology, Rourkela, for their kind support and concern regarding my academic requirements.

I am grateful to my Doctoral Scrutiny Committee members, Prof. Bidyadhar Subudhi, Prof. Kanungo Barada Mohanty, Prof. Somnath Maity and Prof. Sukadev Meher, for their valuable suggestions and comments during this research period. I express my thankfulness to the faculty and staff members of the Electrical Engineering Department for their continuous encouragement and suggestions.

I express my heartfelt thanks to the International Journal Reviewers for giving their valuable comments on the published papers in different International Journals, which helps to carry the research work in a right direction. I also thank to the International Conference Organizers for intensely reviewing the published papers

I am especially indebted to my colleagues in the power electronics group. First, I would like to thank Dr. D Giribabu, Dr. Jayram Nakka and Mr. Aeidapu Mahesh, who helped me in my research work. We shared each other a lot of knowledge in the field of power electronics and drives. I would like to thank my seniors Dr. Y Suresh, Dr. Mikkili Suresh and Dr. N. Rajendra Prasad, for their help and support throughout my research work.

This section would remain incomplete if I don’t thank the lab assistant Mr. Rabindra Nayak without whom the work would have not progressed.

I would also like to thank my friends, Mr. Muralidhar Killi, Mr. D Koteswarao, Mr. Kishore Ragi, Mr. K. Vinay Sagar, Mr. S. Shiva Kumar, Mr. G. Kiran Kumar, Ms. Sushree Sangitha Patnaik, Mr. Aenugu Mastanaiah and Mr. Nishanth Patnaik for extending their technical and personal support.

I express my deep sense of gratitude and reverence to my beloved father Sri. Tejavath Bheemla, Mother Smt. Bikshani, brother Mr. Ravinder and sister Ms. Ratna Kumari who supported and encouraged me all the time, no matter what difficulties I encountered. I would like to express my greatest admiration to all my family members and relatives for their positive encouragement that they showered on me throughout this research work. Without my family's sacrifice and support, this research work would not have been possible. It is a great pleasure for me to acknowledge and express my appreciation to all my well-wishers for their understanding, relentless supports, and encouragement during my research work. Last but not the least, I wish to express my sincere thanks to all those who helped me directly or indirectly at various stages of this work.

Above all, I would like to thank The Almighty God for the wisdom and perseverance that he has been bestowed upon me during this research work, and indeed, throughout my life.

March 16, 2016
NIT Rourkela

Tejavathu Ramesh
Roll Number: 511EE102

Abstract

The Induction motors (IM) are used worldwide as the workhorse in most of the industrial applications due to their simplicity, high performance, robustness and capability of operating in hazardous as well as extreme environmental conditions. However, the speed control of IM is complex as compared to the DC motor due to the presence of coupling between torque and flux producing components. The speed of the IM can be controlled using scalar control and vector control techniques. The most commonly used technique for speed control of IM is scalar control method. In this method, only the magnitude and frequency of the stator voltage or current is regulated. This method is easy to implement, but suffers from the poor dynamic response. Therefore, the vector control or field oriented control (FOC) is used for IM drives to achieve improved dynamic performance. In this method, the IM is operated like a fully compensated and separately excited DC motor. However, it requires more coordinate transformations, current controllers and modulation schemes. In order to get quick dynamic performance, direct torque and flux controlled (DTFC) IM drive is used. The DTFC is achieved by direct and independent control of flux linkages and electromagnetic torque through the selection of optimal inverter switching which gives fast torque and flux response without the use of current controllers, more coordinate transformations and modulation schemes. Many industries have marked various forms of IM drives using DTFC since 1980.

The linear fixed-gain proportional-integral (PI) based speed controller is used in DTFC of an IM drive (IMD) under various operating modes. However, The PI controller (PIC) requires proper and accurate gain values to get high performance. The PIC gain values are tuned for a specific operating point and which may not be able to perform satisfactorily when the load torque and operating point changes. Therefore, the PIC is replaced by Type-1 fuzzy logic controller (T1FLC) to improve the dynamic performance over a wide speed range and also load torque disturbance rejections. The T1FLC is simple, easy to implement and effectively deals with the nonlinear control system without requiring complex mathematical equations using simple logical rules, which are decided by the expert. In order to further improve the controller performance, the T1FLC is replaced by Type-2 fuzzy logic controller (T2FLC). The T2FLC effectively handles the large footprint of uncertainties compared to the T1FLC due to the availability of three-dimensional control with type-reduction technique (i.e. Type-2 fuzzy sets and Type-2 reducer set) in the defuzzification process, whereas the T1FLC consists only a Type-1 fuzzy sets and single membership function. The training data for T1FLC and T2FLC is selected based on the PIC scheme.

The closed-loop control of direct torque and flux controlled IM drive requires accurate information of speed or position. This information can be obtained by the speed/position sensor. However, use of speed sensor has associated with many drawbacks, such as requirement of space, lower reliability, increased weight, size and cost and also difficulty of using in hazardous environments and submersible drives, etc. These drawbacks of sensors can be eliminated by using sensorless speed estimation techniques for DTFC method. In the last one decade, there has been considerable development of sensorless direct torque controlled IM drives for high performance industrial applications. Various techniques have been proposed to implement a sensorless drive such as model reference adaptive system (MRAS), signal injection and observer based methods. Among these methods, MRAS is simple to implement and require less computational effort compared to other methods. The MRAS is further classified into three types, such as rotor-flux, back-emf and reactive power based methods. The back-emf based MRAS speed estimator improves the low speed performance, but it has the stability problem and also it is more sensitive to stator resistance variation. The reactive power based MRAS speed estimation method suffers from the inherent instability in the low speed during regenerative mode and sensitive to rotor resistance variation. The rotor flux based MRAS (RFMRAS) is the most popular method and significant attempts have been made to enhance the performance of the sensorless IM drive over a wide range of speed.

The RFMRAS speed estimation method consists two models (reference model/adjustable model) and an adaptation mechanism (**AM**). The performance of RFMRAS speed estimation is highly dependent on the type of adaptation mechanism controller is used. Initially, the PIC based **AM** scheme is developed for DTFC of a speed sensorless IMD. In order to further improve the performance of the speed sensorless IM drive, the PIC is replaced by T1FLC and T2FLC, respectively.

The DTFC of a speed sensorless IMD is developed using switching-table (ST), flux and torque hysteresis controllers to get a quick dynamic response of the sensorless IMD. The torque and flux are controlled independently using hysteresis controllers. However, the hysteresis control produces considerable torque and flux ripples with variable switching frequency. Therefore, in order to overcome these drawbacks, the DTFC with space vector modulation (DTFC-SVM) technique is proposed for a speed sensorless IM drive using PIC, T1FLC and T2FLC schemes, respectively. The basic concept of SVM strategy is the adjustment of stator flux position by zero voltage vector insertion for controlling the generated torque. The ST based DTFC algorithm uses the instantaneous values and directly calculated switching pulses for the voltage source inverter (VSI), whereas the control algorithm in DTFC-SVM method is based on average values and switching pulses for the

VSI are calculated by SVM. Basically, DTFC-SVM control technique calculates the required stator voltage vector, averaged over a sampling period and then it is realized by the SVM technique. The overall performance of closed-loop controlled IMD is largely influenced by the type of controllers used in speed, torque, flux and adaptation mechanism. Usually, PICs are used due to its simplicity. To further improve the performance of the sensorless IMD, the PICs are replaced by T1FLC and T2FLC schemes, respectively.

The parameter sensitivity with the temperature variation is the major issue of a rotor-flux based MRAS speed estimation technique, especially at low speed operation. In the RFMRAS, the precise calculation of stator resistance is of crucial importance for accurate rotor speed estimation of a speed sensorless IM drive, since any mismatch between the actual value and the value used within speed estimator may not only lead to a substantial speed estimation error but also affects the stability. Therefore, in order to overcome this issue, a parallel rotor speed and stator resistance estimation algorithm using T1FLC and T2FLC schemes for DTFC-SVM of a speed sensorless IM drive is proposed to improve the performance of the sensorless drive under parameter variation at low speed operation.

Detailed simulations in the MATLAB/SIMULINK environment are first reported and are validated with the experimental results obtained from a laboratory experimental setup using dSPACE DS-1104 controller board. The simulation and experimental results show the improvement in the overall performance of the proposed MRAS speed estimation schemes for a speed sensorless IM drive over a wide speed range.

Keywords*: *Direct torque and flux control; Induction motor drive; Model reference adaptive system; PI controller; Space vector modulation; Type-1 fuzzy logic controller, Type-2 fuzzy logic controller.

List of Symbols

A	Ampere
B	Viscous friction coefficient
$e\omega_r$	Error speed between reference and actual speed
$E\omega_r$	Error speed between actual and estimated speed
f	Frequency
i	Current, absolute value
i_{ar}, i_{br}, i_{cr}	Instantaneous values of rotor phase currents
i_{As}, i_{Bs}, i_{Cs}	Instantaneous values of stator phase currents
$\vec{i}_r$	Rotor current space vector
$\vec{i}_s$	Stator current space vector
i_{dr}, i_{qr}	Rotor current space vector components in stationary d-q coordinate system
i_{ds}, i_{qs}	Stator current space vector components in stationary d-q coordinate system
i^e_{Dr}, i^e_{Qr}	Rotor current space vector components in rotating D^e-Q^e coordinate system
i^e_{Ds}, i^e_{Qs}	Stator current space vector components in rotating D^e-Q^e coordinate system
i^e_{dr}, i^e_{qr}	Rotor current space vector components in rotating d^e-q^e coordinate system
i^e_{ds}, i^e_{qs}	Stator current space vector components in rotating d^e-q^e coordinate system
j	Complex operator
J	Moment of inertia
K_p	Controller proportional gain
K_{pT}	Torque controller proportional gain
$K_{p\psi}$	Flux controller proportional gain
$K_{p\omega}$	Speed controller proportional gain
L	Inductance, absolute value
L_m	Mutual inductance
L_r	Rotor winding self-inductance
L_s	Stator winding self-inductance
Nm	Newton-meter
p	Differential operator

P	Number of poles
R	Resistance, absolute value
rpm	Revolution per minute
R_r	Rotor phase windings resistance
R_s	Stator phase windings resistance
s	second
S_a, S_b, S_c	switching states for the voltage source inverter
T	Torque, absolute value
T_e	Electromagnetic torque
T_L	Load torque
T_i	Controller integrating time
T_{iT}	Torque controller integrating time
$T_{i\psi}$	Flux controller integrating time
$T_{i\omega}$	Speed controller integrating time
T_r	Rotor time constant
T_s	sampling time
T_{sw}	switching time
V	Voltage, absolute value
V_{ar}, V_{br}, V_{cr}	Instantaneous values of rotor phase voltages
V_{As}, V_{Bs}, V_{Cs}	Instantaneous values of stator phase voltages
$\vec{V}_r$	Rotor voltage space vector
$\vec{V}_s$	Stator voltage space vector
V_{dr}, V_{qr}	Rotor voltage space vector components in stationary *d-q* coordinate system
V_{ds}, V_{qs}	Stator voltage space vector components in stationary *d-q* coordinate system
V_{Dr}^e, V_{Qr}^e	Rotor voltage space vector components in rotating D^e-Q^e coordinate system
V_{Ds}^e, V_{Qs}^e	Stator voltage space vector components in rotating D^e-Q^e coordinate system
V_{dr}^e, V_{qr}^e	Rotor voltage space vector components in rotating d^e-q^e coordinate system
V_{ds}^e, V_{qs}^e	Stator voltage space vector components in rotating d^e-q^e coordinate system
$\vec{V}_k$	Inverter output voltage space vectors, $k = 1, \ldots, 8$
V_{dc}	Inverter dc link voltage

V_{AB}, V_{BC}, V_{CA}	Line to line voltages
Wb	Weber
Ψ	Flux linkage, absolute value
$\Psi_{ar}, \Psi_{br}, \Psi_{cr}$	Flux linkages of the rotor phase windings
$\Psi_{As}, \Psi_{Bs}, \Psi_{Cs}$	Flux linkages of the stator phase windings
$\vec{\Psi}_r$	Space vector of the rotor flux linkage
$\vec{\Psi}_s$	Space vector of the stator flux linkage
Ψ_{dr}, Ψ_{qr}	Rotor flux linkage space vector components in stationary d-q coordinate system
Ψ_{ds}, Ψ_{qs}	Stator flux linkage space vector components in stationary d-q coordinate system
Ψ^e_{Dr}, Ψ^e_{Qr}	Rotor flux linkage space vector components in rotating D^e-Q^e coordinate system
Ψ^e_{Ds}, Ψ^e_{Qs}	Stator flux linkage space vector components in rotating D^e-Q^e coordinate system
Ψ^e_{dr}, Ψ^e_{qr}	Rotor flux linkage space vector components in rotating d^e-q^e coordinate system
Ψ^e_{ds}, Ψ^e_{qs}	Stator flux linkage space vector components in rotating d^e-q^e coordinate system
θ_r	Rotor electrical position
θ_m	Rotor mechanical position
θ_f	Rotor flux vector angle
θ_e	Stator flux vector angle
θ_T	Angle between rotor flux and stator current space vectors
θ_s	Angle between stator current space vector and stator
ϕ	Angle between stator current and stator voltage space vectors
δ	Difference between stator flux position and electrical rotor position
γ	Difference between stator flux position and rotor flux position
ω	Angular speed, absolute value
ω_a	Angular speed of the arbitrary coordinate system
ω_m	Angular speed of the motor shaft
ω_r	Electrical rotor speed
ω_e	Electrical synchronous speed
ω_{sl}	slip frequency
ξ	Speed tuning signal
σ	Total leakage factor

Superscript:

^	Estimated value
*	Reference value

Subscripts:

r	Rotor quantity
s	Stator quantity

Rectangular coordinate systems:

d-q	Stator oriented, stationary coordinate system
D-Q	Rotor oriented, rotated coordinate system
d^e-q^e	Stator flux oriented, rotated coordinate system
D^e-Q^e	Rotor flux oriented, rotated coordinate system
d^a-q^a	Arbitrarily rotated coordinate system

List of Abbreviations

AC	Alternating current
ADC	Analog to Digital Converter
AM	Adjustable model
AM	Adaptation mechanism
ANN	Artificial neural network
APIC	Adaptation proportional integral controller
AT1FLC	Adaptation type-1 fuzzy logic controller
AT1FLC	Adaptation type-2 fuzzy logic controller
BEMFMRAS	Back-emf based model reference adaptive system
CM	Current model
COA	Center of area
DC	Direct current
DFOC	Direct field oriented control
DTFC	Direct torque and flux control
DTFC-SVM	Direct torque and flux control with space vector modulation
DSC	Direct self-control
DSP	Digital signal processor
DOF	Degree of freedom
DOM	Degrees of membership
EKF	Extended kalman filter
ELO	Extended luenberger observer
EPS	Experimental prototype system
FLS	Fuzzy logic system
FLC	Fuzzy logic controller
FIS	Fuzzy inference system
FMG	Fuzzy membership grade
FOC	Field oriented control
FOU	Footprint of Uncertainty
FPIC	Flux PI controller
FT1FLC	Flux type-1 fuzzy logic controller
FT2FLC	Flux type-2 fuzzy logic controller
GA	Genetic algorithm
GUI	Graphical user interface
HE	Hall-effect
HPF	High pass filter
IFOC	Indirect field oriented control

IGBT	Insulated-gate bipolar transistor
IM	Induction motor
IMD	Induction motor drive
IPM	Intelligent power module
IT2FL	Interval type-2 fuzzy logic
KF	Kalman filter
LMF	Lower membership function
LMP	Left-most-point
LO	Luenberger observer
LPF	Low-pass filter
MISO	Multi input single output
MMC	Max-min composition
MPC	Max-prod composition
MF	Membership function
MMF	Magnetomotive Force
MRAS	Model reference adaptive system
NFC	Neuro-fuzzy control
NNC	Neural network control
OC	Over current
OT	Over temperature
OV	Over voltage
PC	Power circuit
PIC	Proportional integral controller
PM	Power module
PMF	Primary membership function
PMSM	Permanent magnet synchronous motor
PWM	Pulse width modulation
QEP	Quadrature encoder pulses
RFMRAS	Rotor flux based model reference adaptive system
RM	Reference model
RMP	Right-most-point
RPMRAS	Reactive power based model reference adaptive system
RTI	Real-Time Interface
RTW	Real-Time Workshop
SC	Short circuit
SIMD	Sensorless induction motor drive
SMC	Sliding mode controller
SMF	Secondary membership function
SSIMD	Speed sensorless Induction motor drive

ST-DTFC	Switching table based direct torque and flux control
STS	Speed tuning signal
SVM	Space vector modulation
SVPWM	Space Vector Pulse Width Modulation
T1FIS	Type-1 fuzzy inference system
T1FLC	Type-1 fuzzy logic controller
T1FS	Type-1 fuzzy sets
T2FLC	Type-2 fuzzy logic controller
T2FS	Type-2 fuzzy sets
TMF	Triangular membership function
TPIC	Torque proportional integral controller
TR	Type-reducer
TT1FLC	Torque type-1 fuzzy logic controller
TT2FLC	Torque type-2 fuzzy logic controller
UMF	Upper membership function
UV	Under voltage
VC	Vector control
VM	Voltage model
VS	Vertical slice
VSD	Variable speed drive
VSI	Voltage source inverter

Contents

Supervisor's Certificate……iii
Declaration of Originality……v
Acknowledgement……vi
Abstract……viii
List of Symbols……xi
List of Abbreviations……xv
Contents……xviii
List of Figures……xxii
List of Tables……xxvii

CHAPTER 1: INTRODUCTION **1**

1.1 Introduction……1
1.2 Literature Review……3
  1.2.1 Field Oriented Control of IMD……4
  1.2.2 Direct Torque and Flux Control of an IMD……4
  1.2.3 Soft Computing Techniques……6
  1.2.4 Speed Estimation Methods……8
  1.2.5 Stator and Rotor Resistance Estimation Methods……9
1.3 Scope of Work and Author Contribution……9
1.4 Thesis Organization……12

CHAPTER 2: DTFC OF AN INDUCTION MOTOR DRIVE **14**

2.1 Introduction……14
2.2 Modelling of Induction Motor……15
  2.2.1 Scalar control of the IM Drive……16
  2.2.2 Simulation Results……17
2.3 Field Oriented Control of Induction Motor Drive……18
  2.3.1 Principle of Field Oriented Control……18
  2.3.2 Indirect Field Oriented Control of IMD……20
  2.3.3 Design of Controllers……22
2.4 Simulation Model of Indirect field Oriented Controlled IM……28
  2.4.1 Simulation Results……28
2.5 Direct Torque and Flux Control of IMD……29
2.6 Principle of Direct Torque and Flux Control……29
  2.6.1 Stator Flux and Torque Estimation……32
  2.6.3 Two-level Voltage Source Inverter……34
  2.6.4 Optimum Voltage Vector Selection Table……34

2.7 Speed Controller ... 36
    2.7.1 PI Speed Controller ... 36
2.8 Simulation Results ... 36
    2.8.1 Performance under No-load Torque Condition ... 37
    2.8.2 Performance under Load Torque Condition ... 37
    2.8.3 Tracking Performance of the Speed Commands ... 38
2.9 Conclusion ... 41

CHAPTER 3: TYPE-1 AND TYPE-2 FUZZY LOGIC CONTROL BASED DIRECT TORQUE AND FLUX CONTROL OF AN INDUCTION MOTOR DRIVE 43

3.1 Introduction ... 44
3.2 Type-1 Fuzzy Logic Controller ... 44
    3.2.1 Fuzzification ... 45
    3.2.2 Rule Base ... 45
    3.2.3 Fuzzy Inference Systems ... 46
    3.2.4 Defuzzification ... 47
    3.2.5 Design of Control Rules ... 49
    3.2.6 Rule Base ... 50
    3.2.7 Construction of Type-1 Fuzzy Inference System ... 51
3.3 Introduction to Type-2 FLC ... 52
    3.3.1 Why Type-2 FLCs? ... 53
    3.3.2 The Structure of Type-2 FLC ... 54
3.4 Simulation Results ... 62
    3.4.1 Performance under Forward Motoring ... 64
    3.4.2 Loading Performance ... 65
    3.4.3 Performance under Reversal Speed Command ... 68
    3.4.4 Tracking Performance of the Speed Commands ... 68
    3.4.5 Performance under Forward Speed with Load Torque Operation ... 70
    3.4.6 Performance Indices ... 72
3.5 Conclusion ... 73

CHAPTER 4: DEVELOPMENT OF EXPERIMENTAL SYSTEM 74

4.1 Introduction ... 74
4.2 The Development of Experimental Setup ... 75
    4.2.1 Power Circuit ... 76
    4.2.2 The Induction Motor ... 77
    4.2.3 Power Module ... 77
    4.2.4 Measurement of Various Signals ... 78
    4.2.5 Signal Conditioner ... 81
    4.2.6 Protection Circuit ... 81

4.2.7 Optocouplers 83
4.2.8 System Software 83
4.2.9 Hardware Control Development 86
4.3 Experimental Results 88
4.3.1 Performance under Forward Motoring 88
4.3.2 Performance under Reversal Speed Command 91
4.3.3 Tracking Performance of the Speed Commands 92
4.3.4 Loading Performance 93
4.4 Conclusion 98

CHAPTER 5: MRAS SPEED ESTIMATOR FOR DTFC OF A SPEED SENSORLESS IMD 100

5.1 Introduction 101
5.1.1 Observers 102
5.1.2 Model Reference Adaptive System 106
5.2 Rotor-Flux based MRAS Speed Estimator 112
5.2.1 PIC based MRAS Speed Estimator 117
5.2.2 Type-1 Fuzzy Logic Controller based MRAS Speed Estimator 118
5.2.3 Type-2 Fuzzy Logic Controller based MRAS Speed Estimator 120
5.3 Simulation Results 122
5.3.1 Performance under Forward Motoring 122
5.3.2 Loading Performance 123
5.3.3 Performance under Reversal Speed Command 124
5.3.4 Tracking Performance of the Speed Commands 125
5.3.5 Performance under Forward Motoring with Load Torque Operation 129
5.3.6 Performance Indices 129
5.4 Experimental Results 129
5.4.1 Performance under Forward Motoring 129
5.4.2 Performance under Reversal Speed Command 130
5.4.3 Tracking Performance of Various Speed Commands 132
5.4.4 Loading Performance 134
5.4.5 Performance under Low Speed Operation 137
5.5 Conclusion 140

CHAPTER 6: MRAS SPEED ESTIMATOR FOR DTFC-SVM OF A SPEED SENSORLESS IMD 142

6.1 Introduction 143
6.1.1 DTFC-SVM Scheme with Closed-loop Flux Control 143
6.1.2 DTFC-SVM Scheme with Closed-loop Torque Control 144
6.1.3 DTFC-SVM Scheme with Closed-loop Torque and Flux Control 145

6.1.4 DTFC-SVM Scheme with Closed-loop Torque and Flux Control 146
6.2 Space Vector Modulation..148
6.3 DTFC-SVM of a Speed Sensorless IMD 151
6.3.1 PIC based DTFC-SVM of a Speed Sensorless IMD 152
6.3.2 T1FLC based DTFC-SVM of a Speed Sensorless IMD...152
6.3.3 T2FLC based DTFC-SVM of a Speed Sensorless IMD...154
6.4 Simulation Results 157
6.4.1 Performance under Forward Motoring 158
6.4.2 Loading Performance...158
6.4.3 Performance under Reversal Speed Command...159
6.4.4 Tracking Performance of the Speed Commands 161
6.4.5 Performance Indices 163
6.5 Experimental Results 164
6.5.1 Performance under Forward Motoring 164
6.5.2 Performance under Reversal Speed Command...165
6.5.3 Tracking Performance of Various Speed Commands...166
6.5.4 Loading Performance...168
6.5.5 Performance under Low Speed Operation..173
6.6 Conclusion 174

CHAPTER 7: STATOR RESISTANCE ESTIMATION 175

7.1 Introduction...175
7.2 Parallel Rotor Speed and Stator Resistance Estimation...176
7.2.1 Fuzzy Logic Controller based Stator Resistance Estimator..180
7.3 Simulation Results 182
7.3.1 Performance under Parameter Variation...182
7.4 Experimental Results 185
7.5 Conclusion 186

CHAPTER 8: CONCLUSIONS AND FUTURE SCOPE 187

8.1 Conclusion 187
8.2 Scope for Future Work...190
Bibliography……………………………………………………………………………….................192
Appendix A…………………………………………………………………………………………... 203
Appendix B…………………………………………………………………………………………... 215
Appendix C…………………………………………………………………………………………... 225
Dissemination ……………………………………………………………………………………… 228

List of Figures

1.1 Classification of IM control methods 2
2.1 Equivalent circuit representation of an IM in stationary (d, q) reference frame 15
2.2 Performance of the induction motor drive 17
2.3 Phasor diagram of field oriented control scheme....20
2.4 Phasor diagram of rotor flux based IFOC 23
2.5 Schematic model of PI current controller 23
2.6 Simplified block diagram of flux/torque current loop of IFOC 24
2.7 Schematic model of PI speed controller 25
2.8 The block diagram of closed loop speed with PI controller....26
2.9 Simplified block diagram of closed loop speed with PI controller 26
2.10 Root locus of the closed loop speed control system 27
2.11 Schematic model of indirect field oriented controlled induction motor drive 27
2.12 Simulation responses of indirect field oriented controlled IMD 29
2.13 Phasor diagram of DTFC strategy in stationary reference frame 30
2.14 Schematic model of direct torque controlled IMD 31
2.15 Two-level flux hysteresis controller 32
2.16 Three level torque hysteresis controller 33
2.17 Schematic model of two-level voltage source inverter 34
2.18 Eight possible switching states of the VSI 34
2.19 The voltage space vector influence on stator flux and torque in six sectors 35
2.20 Schematic model of PI speed controller 37
2.21 Performance of the IMD under no-load torque operating condition....38
2.22 Steady-state performance of the IMD under no-load torque operating condition 39
2.23 Performance of the IMD under load torque 40
2.24 Performance of the IMD under the command 40
2.25 Performance of the IMD under the command 41
3.1 Schematic model of DTFC of an IMD using FLC based speed controller 44
3.2 Schematic model of Type-1 FLC....46
3.3 Schematic model of T1FIS 47
3.4 The T1FIS using Mamdani max-min composition 47
3.5 The T1FIS using Mamdani max-prod composition 48
3.6 Defuzzification....49
3.7 Various types of defuzzification schemes....49
3.8 Schematic model of T1FLC with rule base 51
3.9 Membership functions of Type-1 FLC are 51
3.10 Type-1 fuzzy inference system using triangular membership functions 53

3.11 The schematic model of Type-2 FLC 54
3.12 Membership Functions of: (a) Type-1 FLC and (b) Type-2 FLC 55
3.13 Type-2 Fuzzy Inference System with TMF 7x7 57
3.14 The Mamdani T2FIS using MMC 58
3.15 Membership functions of Type-2 FLC 59
3.16 The flowchart of T2FLC for finding the crisp value 62
3.17 Performance of IMD under no-load torque operating condition 63
3.18 Steady-state performance under no-load torque operating condition 64
3.19 Loading performance at 1200 rpm using: (a) T1FLC and (b) T2FLC 65
3.20 Loading and unloading performance at 1200 rpm 66
3.21 Steady-state performance of the actual speed under various load torque conditions 67
3.22 Performance of IMD under reversal speed command 67
3.23 Transient performance of IMD under reversal speed command 68
3.24 Performance under sudden change in step speed command 69
3.25 Performance under sudden change in square speed command 70
3.26 Performance under forward motoring with starting load torque of 9 Nm 71
3.27 Dynamic responses of time domain specifications 71
3.28 Bar chart of performance indices under various starting load conditions 71
3.29 Performance indices under forward motoring with no-load torque operation 72
3.30 Performance indices under forward motoring with sudden load torque operation 73
4.1 Configuration of the experimental setup 76
4.2 Configuration of the power circuit 76
4.3 Schematic model of IPM based power module 77
4.4 Voltage and current sensing cards 78
4.5 Current measurement through LA-55P 79
4.6 Voltage measurement through LV-25P 80
4.7 (a) Signals from incremental encoder and (b) Frequency to voltage converter circuit 80
4.8 Speed sensing with incremental encoder 81
4.9 Current signals processing circuit, Here X=A, B, C 81
4.10 Various stages of protection circuit 82
4.11 Total development environment of dSPACE with MATLAB/SIMULINK 84
4.12 Digital signal processor (dSPACE DS-1104) circuit board interfacing 86
4.13 Schematic diagram of interfacing firing pulses from dSPACE controller board 86
4.14 Dead-band circuit for each switching device 87
4.15 Firing signals for the switches S_A and $\overline{S}_A$ with dead-band circuit 87
4.16 Performance of the IM under no-load torque operating condition 88
4.17 Performance of the IM under no-load torque operating condition 89
4.18 Steady-state performance of the IM under no-load torque operating condition 90
4.19 Performance of the IM under reversal speed command 90

4.20 Transient performance of the IM under reversal speed command 91

4.21 Performance of the IM under sudden change in step speed command 92

4.22 Performance of the IM under sudden change in square speed command 93

4.23 Performance of the IM under sudden load torque operation at 1200 rpm 94

4.24 Performance of the IM under sudden load and unload torque at 1200 rpm 95

4.25 Performance of the IM under sudden load and unload torque operation 96

4.26 Steady-state performance of the actual speed under various load torque conditions 96

4.27 THD performance of the stator current 97

5.1 Various types of speed estimation methods 101

5.2 Adaptive speed observer (Speed adaptive flux observer) 103

5.3 Extended Kalman filter based speed estimation 105

5.4 Flowchart diagram of EKF algorithm 105

5.5 The basic schematic model of MRAS speed estimator 107

5.6 Rotor-flux based MRAS speed estimation 108

5.7 The schematic model of back emf based MRAS speed estimator 109

5.8 Reactive power based MRAS speed estimator 110

5.9 Schematic model of RFMRAS speed estimator for DTFC of a speed sensorless IM drive 112

5.10 Nonlinear and time-varying feedback system 114

5.11 Equivalent model of the rotor flux-based MRAS 115

5.12 Adaptation mechanism for MRAS observer 116

5.13 Schematic model of RFMRAS speed estimator using PIC based adaptation mechanism 117

5.14 Schematic model of T1FLC based MRAS speed estimator 118

5.15 Type-1 FLC: (a) Input MFs (ξ_ω and $\Delta\xi_\omega$) and (b) output MF of $\hat{\omega}_r$ 118

5.16 Schematic model of T2FLC based MRAS speed estimator 119

5.17 Type-2 FLC: (a) Input MFs (ξ_ω and $\Delta\xi_\omega$) and (b) output MF of $\hat{\omega}_r$ 120

5.18 The flowchart of T2FLC for finding the crisp value of the estimated speed 121

5.19 Performance under no-load torque operating condition 123

5.20 Loading performance at 1200 rpm 124

5.21 Loading and unloading performance at 1200 rpm 125

5.22 Steady-state performance of the estimated speed under various load conditions 126

5.23 Performance under reversal speed command 126

5.24 Transient performance under reversal speed command 127

5.25 Performance under a step change in speed command 127

5.26 Performance under square change in speed command 128

5.27 Performance under no-load torque operating condition 130

5.28 Steady-state performance under no-load torque operating condition 131

5.29 Performance under reversal speed command 131

5.30 Transient performance under the reversal speed command 132

5.33 Performance under sudden load torque operation at 1200 rpm 134

5.34 Performance under loading and unloading torque at 1200 rpm....135
5.35 Performance under load torque operation at 1200 rpm....137
5.36 Steady-state performance of the estimated speed under various load torque conditions....137
5.37 Performance of the sensorless IMD under low speed operation....138
5.38 Performance of the sensorless IMD under the deceleration command at 1200 rpm....139
5.39 THD performance of the stator current....139
6.1 The schematic model of DTFC-SVM scheme with closed-loop flux control....144
6.2 The schematic model of DTFC-SVM scheme with closed-loop torque control....145
6.3 vector diagram of DTFC-SVM....145
6.4 The schematic model of DTFC-SVM scheme with closed-loop torque and flux control....146
6.5 The schematic model of DTFC-SVM scheme with closed-loop torque and flux control....147
6.6 vector diagram of DTFC-SVM with closed-loop torque and flux control operating....147
6.7 Space vector representation for two-level VSI....148
6.8 Typical seven-segment switching pattern of the VSI in all the six sectors....150
6.9 Schematic model of DTFC-SVM for a sensorless IMD....152
6.10 Membership functions of Type-1 fuzzy logic controllers....153
6.11 Membership functions of Type-2 fuzzy logic controllers....155
6.12 The flowchart of T2FLC for finding the crisp value of the estimated speed....156
6.13 Performance under no-load torque operating condition....158
6.14 Loading performance at 1200 rpm....159
6.15 Loading and unloading performance at 1200 rpm....160
6.16 Steady-state performance of the estimated speed under various sudden load torque....160
6.17 Performance under reversal speed command....161
6.18 Transient performance under reversal speed command....162
6.19 Performance under a step change in speed command....162
6.20 Performance under square change in speed command....163
6.21 Performance under no-load torque operating condition....164
6.22 Steady-state performance under no-load torque operating condition....165
6.23 Performance under reversal speed command....166
6.24 Transient performance under the reversal speed command....166
6.25 Performance under a step change in speed command....167
6.26 Performance under square change in speed command....167
6.27 Performance under sudden load torque operation at 1200 rpm....169
6.28 Performance under loading and unloading torque at 1200 rpm....169
6.29 Performance under load torque operation at 1200 rpm....170
6.30 Steady-state performance of the estimated speed under various load torque....171
6.31 Performance of the sensorless IMD under the step change in acceleration speed command 171
6.32 Performance of the sensorless IMD under the step change in deceleration speed command 172
6.33 THD performance of the stator current....172

7.1 Schematic model of parallel RFMRAS rotor speed and stator resistance estimation............176
7.2 Internal model of parallel rotor speed and stator resistance estimation................................177
7.3 MFs of FLC based stator resistance estimation: (a) T1FLC and (b) T2FLC........................181
7.4 Performance under stator resistance variation without stator resistance estimation.............183
7.5 Performance with stator resistance estimation..183
7.6 Performance under accelerating speed command with stator resistance estimation.............184
7.7 Performance under step variation of stator resistance with stator resistance estimation 184
7.8 Performance under ramp variation of stator resistance with stator resistance estimation......184
7.9 Performance under acceleration speed command 185
7.10 Performance under deceleration speed command...185
8.1 Neural network based MRAS speed observer 191
A. 1 Different types of reference frames 203
A. 2 Idealized three-phase induction motor...204
A. 3 Axes of two pole three-phase Induction motor..204
A. 4 Construction of space vector for three phase voltage variable 205
A. 5 Equivalence of induction motor stator and rotor windings..207
A. 6 Two axis components of stator voltage space vector...207
A. 7 Stator voltage space vector component in stationary and synchronous reference frame.......209
B. 1 Open loop transfer function of flux control loop 217
B. 2 Open loop transfer function of torque control loop. 218
B. 3 Block diagram of PI Controller..218
B. 4 Generalized feedback control system 218
B. 5 Desired (hatched) region of other closed loop poles..219
B. 6 Flux control loop with PI controller...220
B. 7 Root loci of the closed loop flux control system 221
B. 8 Torque control loop with PI controller 222
B. 9 Root loci of the closed loop torque control system..222
B. 10 Generalized block diagram of the speed control loop..223
B. 11 Speed control loop with PI controller 223
B. 12 Root locus of the closed loop speed control system 224
B. 13 Root locus of the closed loop speed control system 224
C. 1 Photographic view of the complete experimental setup 227

List of Tables

2.1 Switching logic of flux hysteresis controller 33
2.2 Switching logic for torque error 33
2.3 Optimum voltage vector selection table 35
3.1 Fuzzy logic controller rule base 52
3.2 Performance indices under forward motoring with different starting load torque conditions using three different controller schemes 72
4.1 Comparison of three controller schemes under different load torque conditions 97
4.2 Comparison of three controller schemes under various operating conditions 98
5.1 Rule base of fuzzy logic controller 120
5.2 Performance indices under forward motoring with different starting load torque conditions using three different controller schemes 128
5.3 Comparison of three control schemes under different load torque conditions at 1200 rpm 136
5.4 Comparison of three different controllers under various operating conditions 140
6.1 Switching states and the corresponding space vectors 149
6.2 Rule base of TT1FLC and TT2FLC 154
6.3 Rule base of FT1FLC and FT2FLC 155
6.4 Performance indices under forward motoring with different starting load torque conditions using three different controller schemes 163
6.5 Comparison of three control schemes under different load torque conditions at 1200 rpm 170
6.6 Comparison of three control schemes under various operating conditions 173
7.1 Rule base of T1FLC and T2FLC based stator resistance estimation 182
C.1 Parameters and ratings of induction motor 225
C.2 Specifications of the intelligent power module 225
C.3 Specification of the current sensor (LA-55P) 225
C.4 Specification of the voltage sensor (LV-25P) 226
C.5 Specification of the speed sensor 226
C.6 Gain values of PI speed controller 226
C.7 Gain values of PI torque controller 226
C.8 Gain values of PI flux controller 226
C.9 Gain values of PI adaptation controller 226
C.10 Gain values of PI resistance controller 226

Chapter 1

Introduction

CHAPTER 1: INTRODUCTION

1.1 Introduction

Variable speed drives (VSDs) are used to meet the speed and torque requirements of the load and also to improve the overall efficiency of the drive system. In contrast to the hydraulic and mechanical variable speed control methods, the electrical VSDs are easy to control, more efficient and accurate. The initial development of the VSDs were only for separately excited direct current (DC) motors because of their simplicity in the control of flux and torque by the inherently decoupled field and armature currents, respectively. But, the attractiveness of AC drives has rapidly increased because of the recent technological advancements in fabrication and design of semiconductor devices (especially insulated gate bipolar junction transistor) and digital signal processors (DSP). Overall, the AC drives are much superior to DC drives, and it appears that eventually DC drives will be totally obsolete. However, the speed control of AC motors is more complex than that of DC motors due to the presence of coupling effect between the flux and torque producing components [1-3]. The recent technological developments have made AC drives most popular for VSDs especially induction motor drives (IMD) due to its simple construction, low inertia, high efficiency, rugged and reliable nature with the absence of brushes and commutators and are also cheaper than DC motors [4-5].

The speed control techniques of IM drive are broadly classified into two major categories [6], such as, scalar control and vector control (VC) methods are shown in Figure 1.1. In scalar control [6-7], only magnitude and frequency of voltage, flux and current space vectors are controlled. Whereas, in VC not only the magnitude and frequency but also the instantaneous positions of voltage, flux and current space vectors are controlled. The VC method can provide high performance compared to the scalar control method. The invention of VC started in the beginning of 1970's brought a renaissance in the performance and control of IM drives [8-9]. The VC of an IM drive is operated like a fully compensated and separately excited DC motor drive, such that the torque producing currents and flux are decoupled from each other. This method is further divided into two types such as field oriented control (FOC) method [8] and direct torque and flux control (DTFC) method [10-29]. Depending upon how the field angle is obtained, the FOC is further classified into two types, such as direct FOC (DFOC) proposed by Blaschke [8] and indirect FOC (IFOC) proposed by Hasse. In these methods, the flux and torque producing components are indirectly controlled by controlling the dq-axes stator current components to enhance the dynamic performance of the IM like a separately excited DC motor [6], [9]. However, the FOC method has various drawbacks, such as the requirement of coordinate transformations, current controllers, rotor position information and also it is sensitive to rotor parameters. Moreover, the torque control is indirect, that creates a delay between the input references and the resulting stator voltage vector. These factors limit the ability of FOC to get rapid flux and torque control [6]. In order to overcome these drawbacks and also to get the fast dynamic performance of IM drive, direct self-control (DSC) and DTFC methods are used, which are proposed by Depenbrock [11] and Takahasi et al. [12] in mid of 1980. In these methods, the flux and torque are directly controlled using less number of transformations and sensors.

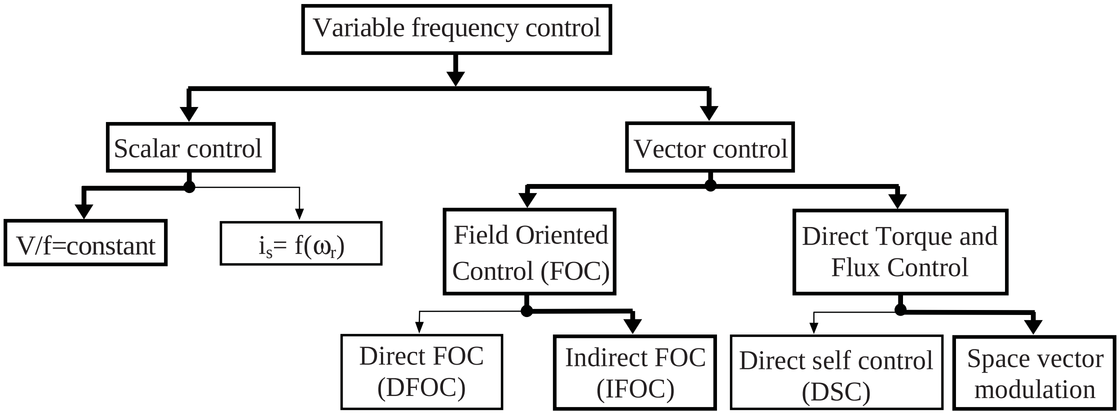

Figure 1.1: Classification of IM control methods

The fixed gain linear PIC, which is used in DTFC is designed using a mathematical model of the system [10-35]. The PIC gain values are tuned in a specific operating point, it does not work effectively when the operating point changes and also it shows poor load torque disturbance rejections. In order to overcome this problem the PIC is replaced by nonlinear soft-computing techniques, such as, Genetic Algorithm (GA) [36-37], sliding-mode controller (SMC) [38-40], model predictive control [41-43], Type-1 fuzzy logic controller (T1FLC) [44-63], Fuzzy-SMC [64-65] Artificial Neural Network (ANN) [66-69], Neuro-fuzzy (NF) [70-78] and Type-2 fuzzy logic controller (T2FLC) [79-92] to improve the performance of the IM drive over a wide range of speed operation and also robust to load torque disturbances.

In recent years, the use of IM drives with DTFC method have gradually increased due to its good dynamic performance, precise control of stator flux and electromagnetic torque, robust against variations in machine parameters, elimination of current control loops and simplicity of the control algorithm. However, this method requires accurate rotor speed or position information for speed control. This speed information can be measured by using an incremental encoder, which is the most common positioning transducer used in industrial applications. Use of speed sensor has several problems such as sensor-mounting, signal transmission, lower reliability, increased weight and size, and also difficult to operate in hazardous environment, etc. Moreover, the cost of the sensor reduces the economical benefits of the drive. Therefore, in order to overcome these drawbacks, the speed estimation from machine terminal quantities (i.e. voltage and current) is preferred than the speed sensing for high performance industrial applications [93-150].

The DTFC of a speed sensorless IM drive provides satisfactory performance over a wide range of speed operation and also simple to implement. However, it requires flux hysteresis and torque hysteresis comparators. The use of flux and torque hysteresis comparators causes a variable switching frequency and produces considerable ripple contents in flux and torque. Several solutions have been proposed by the researchers to reduce the ripple contents in flux and torque and also to maintain the constant switching frequency in DTFC of a sensorless IM drives [151-178]. Recently, a new control technique has been developed for maintaining constant switching frequency and reducing flux and torque ripple in DTFC method by using a space vector modulation (DTFC-SVM) technique. It implements closed-loop control for both torque and stator flux in a similar manner as in DTFC method, but the voltage is produced by SVM technique. Usually, the fixed gain linear PI controllers are used in DTFC-SVM of a sensorless IM drive [151-173]. In order to further improve the performance under various load torque disturbances and changes in speed operating conditions, the PI controllers are replaced by the soft-computing techniques [174-178].

1.2 Literature Review

Several solutions have been proposed by the researchers to improve the performance of the inverter-fed IM drive with sensor and sensorless operations. They are broadly discussed by classifying the literature into the following categories as:

- Field oriented control of an IMD [1-6], [8-9]
    - ➢ Direct field oriented control (DFOC) [6]
    - ➢ Indirect field oriented control (IFOC) [8]
- Direct torque and flux control (DTFC) of an IMD
    - ➢ Variable switching frequency based DTFC methods without modulation [10-21]
    - ➢ Constant switching frequency based DTFC methods without modulation [146-150]
    - ➢ Constant switching frequency based DTFC methods with modulation [151-178]
- Soft computing techniques
    - ➢ Genetic Algorithm (GA) [36-37]
    - ➢ Fuzzy logic controllers

    - Type-1 fuzzy logic controller (T1FLC) [44-65]
    - Type-2 fuzzy logic controller (T2FLC) [78-92]
  - Neural network control (NNC) [66-69]
  - Neuro-fuzzy control (NFC) [70-77]
- Speed estimation methods
  - Signal injection based method [93-94]
  - Observer based methods
    - Luenberger/Extended Luenberger [95-98]
    - Kalman filter/ Extended Kalman filter [99-105]
    - Sliding-Mode [106-111]
  - Model based methods
    - Back EMF [112-113]
    - Rotor-Flux [114-133], [140-145]
    - Active/Reactive power [134-139]
- Stator and rotor resistance estimation methods [179-200]

1.2.1 Field Oriented Control of IMD

The speed of an IM is controlled using various control techniques and they are explained in this literature. Blaschke et al. [8] and Leonhard et al. [5] have introduced a FOC method for IM. The basic goal of the FOC is to control the IM similar to DC motor by resolving the stator current vector into two components: one is used to control machine flux and the other to control the machine torque, thus, it allows the flux and torque to be controlled independently. This method guarantees decoupling of currents that produces flux and torque. However, the IM equations are still nonlinear and fully decoupled only for constant flux operation [6]. Moreover, it requires current controllers, coordinate transformations and modulation techniques and also sensitive to parameter variations.

1.2.2 Direct Torque and Flux Control of an IMD

Over the past few years, DTFC method for IM drives has gained massive attention in industrial motor drive applications. The main reason for its popularity is due to its simple structure, especially when compared to the FOC method [6], which was introduced a decade earlier. Several modifications were proposed by the researchers to its original structure to reduce the inherent drawbacks of the hysteresis based DTFC method [12]. In this method, the inverter switching frequency is not constant and also produces considerable torque and flux ripples [140-150] due to the use of hysteresis torque and flux controllers, respectively. Several solutions have been proposed by the researchers in the literature to improve the performance of IM drive using DTFC method. Marian et al. [14] has proposed the DTC method, in which a high frequency triangular wave is additionally introduced in the torque control loop to increase the inverter switching frequency. However, the switching frequency is still a function of the torque and flux hysteresis band and operating frequency. At the time of starting, the DTFC scheme selects more zero voltage vectors, which results in flux reduction owing to stator resistance drop. In order to overcome this shortcoming, Noguchi et al. [15] proposed a method in which switching frequency is increased by using the dithering technique. In this method, the switching frequency of the inverter is increased by mixing the high frequency dither signals with the error signals of torque and flux. Here, the switching frequency is uncontrolled and requires high sampling frequency to reach the desired performance. In [148] Toh et al. has proposed the DTFC method using field-programmable gate array and DSP to maintain a constant switching frequency with reduced flux and torque ripple contents using duty ratio control. Yen-Shin et al. [154] has presented a novel switching technique to reduce the ripple contents in torque and flux by inserting more active voltage vectors and/or zero-voltage vectors to the conventional switching table, for IM drives with DTFC method. But, the inverter switching frequency is a function of hysteresis controllers and operating frequency, which results in poor performance under low speed operation. Abdelli et al. [149] has presented a method to reduce the ripple contents in flux and torque by injecting dithering signal to the flux and torque reference values in a DTFC based IM drive. In this method performance is improved by reducing the ripple content in torque and flux without using any modulation technique. But, a high frequency triangular signal is required to improve the inverter switching frequency and a variable switching frequency problem remains unsolved. Masood et al. [143] has proposed a DTFC method with SM observer for detecting the rotor flux, motor speed and time constant simultaneously. Additionally, a fast and search based method has been introduced to maximize the motor efficiency.

In order to further improve the performance of the IM drive by reducing the ripple contents in torque and flux, Yongchang et al. [145] has proposed DTFC method with three-level inverter. Moreover, Type-1 fuzzy logic controller and speed adaptive flux observer are introduced to improve the performance of the system. But, the complexity of the system is increased and also the switching cost. Rumzi et al. [104] has proposed DTFC with low pass filter (LPF) and compensates the control scheme to improve the torque and flux performance under steady-state condition. In [146] Jun-Koo et al. has proposed a method to improve the performance by reducing the torque and flux ripples using constant switching frequency. However, its effectiveness is demonstrated only at low speed operation with no-load torque. In [150] Auzani et al. has proposed a method to minimize the torque and flux ripple in DTFC of an IMD and achieved constant switching frequency operation. In this method, the hysteresis controllers of the DTFC are replaced by PI controllers. But, it requires high sampling frequency and design of torque controller is complex.

In DTFC method using space vector modulation (SVM) technique, the switching frequency of the inverter can be maintained constant in order to minimize the ripple contents in flux and torque. Habetler et al. [152] has introduced a novel method based on SVM to achieve constant switching frequency and also reduce the ripple contents in flux and torque. Yen-Shin et al. [154] has investigated on DTFC-SVM and proved that the ripple contents in flux and torque have drastically reduced and also obtained constant switching frequency. But, this method requires high sampling frequency. Rodriquez et al. [155] presented a method based on load angle control to get the constant switching frequency. But, it suffers from nonlinear relationship between torque and load angle. Zhang et al. [164] has proposed a novel DTFC-SVM of IM with adaptive stator flux observer. Domenico et al. [153] has proposed the new DTFC method based on the discrete space vector modulation (DSVM) to achieve high performance IM drive. Kumsuwana et al. [158] has investigated on the modified DTFC of an IMD based on stator flux space vector control technique. The required reference stator flux angle is obtained from the integrator output, which is a function of the sum of controlled slip speed and measured rotor speed. But, the integrator suffers from saturation in real-time implementation.

1.2.3 Soft Computing Techniques

The fixed gain PI controllers are widely used in industrial control system applications due to its simple structure and it can provide a satisfactory performance over a wide range of speed operations. However, the PIC requires a precise mathematical model and accurate gain values. Due to the continuous changes in the plant parameters and the nonlinear operating conditions, the linear PI controllers may not offer the required control performance. Moreover, it requires continuous tuning whenever parameter changes in the system [60]. Therefore, in order to overcome these drawbacks and improve the performance of the AC drives under transient and steady-state conditions, the fixed gain linear PI controllers are replaced by the nonlinear controllers, such as SMC, self-tuning PI controllers and soft-computing based controllers such as, T1FLC and T2FLC, NNC, NF and GA. Genetic algorithms are adaptive search methods based on the fittest survival biological aspect. They have shown an effective way for optimization applications by searching global minimal without needing the derivative of the cost function [59]. However, their application in real-time implementation is limited due to random solutions and convergence. Gadoue et al. [60] has shown that the ripple contents in torque and flux can be reduced by using Type-1 FLC based DTFC of an IM drive. In [70] it is presented that the speed of the IM drive can be controlled by combining the T1FLC with NN, i.e. hybrid adaptive Neuro-fuzzy controller. Telford et al. [22] has shown that the ripple contents in flux and torque can be reduced at low speed by using duty cycle control. This method also effectively controls the mean of the output torque and limits the variation of switching frequency. The combination of fuzzy and sliding-mode controllers is used to improve the performance of the IM drive [64]. However, the robustness of the system is highly dependent on the boundary layer thickness. Luis et al. [180] has developed the training algorithms, the back propagation, Extended Kalman Filter (EKF), adaptive neuron model and parallel recursive prediction error. The results of the EKF and the parallel recursive prediction error offer the better torque performance of the IM.

Bird et al. [51] has shown that the amount of torque and flux ripples reduced using T1FLC in DTFC method especially under low speed operation. Arias et al. [54] has proposed the T1FLC based DTFC of IMD. In this method not only reduces the torque ripple but also reduces the reactive power taken from the mains by choosing the optimum reference flux value. Pawel et al. [76] has proposed adaptive Neuro-fuzzy inference system to achieve improved dynamic performance along with decoupled torque and flux control. Yuedou et al. [168] has investigated on T1FLC based DTFC-SVM for reducing the torque and flux ripples under various load torque disturbances. Jose et al. [174] has proposed self-tuning based PI-fuzzy controller for DTFC-SVM of an IMD to get the constant switching frequency as well as low ripple contents in torque and flux. The T1FLC provides satisfactory performance over a wide range of speed operation and reduced ripple contents in torque and flux compared to PI controller. However, it shows considerable ripple contents in flux and torque, because it has only a single membership function (MF) with two-dimensional control [176]. Therefore, in order to further enhance the performance of the DTFC of an IM drive Type-2 FLC is proposed in [175-178]. This controller offers satisfactory performance in terms of torque disturbance, overshoot, steady-state error and accuracy in tracking the reference speed. Moreover, it reduces the speed undershoot which occurs when a sudden load torque disturbance applied and also settled quickly compared to T1FLC. This controller provides satisfactory performance because it estimates the control variable accurately as close to the actual values compared to T1FLC.

The VC of IM drive requires the rotor speed information for accurate speed control. The rotor speed can be measured using an incremental encoder or a tacho-generator. The use of speed sensor is associated with some drawbacks, such as the requirement of shaft extension, reduction in mechanical robustness of the motor, unsuitability for hostile environment, difficulty in signal transmission, lower reliability, etc. Moreover, the cost of the speed sensor increases the economy of the drive. In order to overcome these drawbacks various speed estimation methods for eliminating the rotor speed or position sensors have been proposed.

1.2.4 Speed Estimation Methods

In the vector control algorithms, the rotor speed is estimated from the instantaneous values of voltages and currents of the IM. Several estimation methods for sensorless AC drives have been proposed in the literature over the past few years, such as signal injection based methods [93-94], observer based methods [95-111], and model reference adaptive system (MRAS) based methods [112-145]. The most recent research effort is focussed on speed sensorless drives for improving the speed estimation methods over a wide speed range [129]. The signal injection based methods are suitable for low and zero speed operations and also less sensitive to the variation of parameters [94]. However, it requires extra computations to inject the high frequency signals [96]. The observer based methods are mainly classified into mainly four types: (i) Luenberger/Extended Luenberger observers [95-98], (ii) Kalman filter/extended Kalman filter observers [99-105], (iii) Sliding mode observer [106-111] and (iv) Artificial intelligence based observers [194]. The SMO based speed sensorless IM drives are presented in [156]. This observer offers good speed tracking performance and load torque disturbance rejections and also insensitive to the parameter variations. However, this observer requires proper gain values to reduce the chattering phenomena. In [109] the comparative study of the Luenberger, EKF and SM observers has been presented.

In MRAS generation of error vector plays a vital role for estimating the rotor speed. Based on the generation of error vector, several MRAS speed estimation methods have been developed, they are back-EMF [112-113], rotor-flux [114-133] and active/reactive power [134-135] based MRAS methods. The rotor-flux based MRAS is the most popular speed estimation method. This method provides accurate speed estimation over a wide speed range. However, this method yields poor performance at very low and zero speed operation due to the presence of integrator in the reference model. In order to overcome with this problem, high-pass filters (HPF) are incorporated after the reference model and before the adjustable model [116]. The back-EMF based MRAS method improves the low speed performance, but it has stability problems at high speeds. Moreover, it suffers from noise and it is more sensitive to the variation of stator resistance [136]. The reactive power based MRAS speed estimation suffers from the inherent instability under the low speed regeneration mode, poor low/zero speed performance and it is sensitive to the variation of rotor resistance.

In [140] initial rotor position estimation method is proposed for the sensorless interior permanent magnet synchronous motor drive using DTFC method. Faiz et al. [141] has investigated on sensorless DTFC of an IM drive with a new switching strategy for mitigating harmonics and it is used in electric vehicle. Maes et al. [142] has investigated on speed sensorless DTFC of IM drives using an adaptive flux observer for estimating the rotor speed and discrete-time DTFC method for reducing stator flux and torque ripples. Youngchang et al. [145] has shown that the speed can be controlled over a wide speed range by using adaptive T1FLC for DTFC of a speed sensorless IM drive. Cristian et al. [171] has proposed a new DTFC method based on SVM for sensorless IM drives. In this method, an improved voltage–current model observer based on MRAS is proposed for rotor speed estimation. The DTFC-SVM of a sensorless IMD is presented using SMC to get the high-performance both steady state as well as in transient conditions [156]. The speed estimation methods are sensitive to the parameter variations. So, parameter estimation is essential to improve the performance of the sensorless IM drive under parameter variations (especially stator and rotor resistance).

1.2.5 Stator and Rotor Resistance Estimation Methods

The stator resistance is an important machine parameter, which needs to be estimated for the proper operation of the sensorless IM drive [193]. Various parameter estimation methods have been proposed in the literature [178-201]. Joong et al. [179] has proposed robust parameter estimation techniques for stator resistance from the steady-state equations of IM and for rotor resistance from the linearly perturbed equations of IM dynamics about the operating point. Tsuji et al. [189] has proposed a stator resistance estimation method in the rotating reference frame. In this method, the error quantity is determined by the difference between the d-axis rotor flux components obtained from the voltage and current models. The stator resistance estimation allows precise control of torque and speed under the low speed region [190-192]. Sayeed et al. [184] has proposed the DTFC of induction machines using T1FLC, which offers a better dynamic response of the IM drive over a wide range of speed operation. Moreover, the performance was improved with fuzzy stator resistance estimation. However, the T1FLC has certain limits due to its single MF with two-dimensional control.

1.3 Scope of Work and Author Contribution

The main objective of this research work is to develop the schemes for DTFC of a speed sensorless IM drive to reduce the ripple contents in stator flux and torque and also speed distortions under various operating conditions. The literature review carried out in the field of inverter-fed IM drive has revealed that the most developments are in the direction of reducing ripple contents in torque and stator flux and also improving the quality of the IM drive output. It is found that extensive efforts are being made to enhance the performance of direct torque and flux controlled IM drive with the speed sensor operation. However, these methods are required rotor speed or position information for accurate speed control of IM drives.

The DTFC of an IMD using linear PI controller is probably fair control method. The stability analysis of this method is observed using root-locus technique with corresponding gain values of the PI controller. However, this method shows considerable ripple contents in stator flux and torque with poor dynamic performance. Moreover, this method requires a precise mathematical model for continuous tuning of PI controller gain values. In order to overcome these drawbacks, the PI controller is replaced by Type-1 fuzzy logic controller (T1FLC). This controller provides quick dynamic response and load torque disturbance rejection. In order to further improve the performance of the IM drive, the T1FLC is replaced by the new Type-2 fuzzy logic controller (T2FLC). It has three-dimensional control and also the advantage of the type-reducer in the defuzzification process to select the appropriate control variable for effectively handling the large footprint of uncertainties. Moreover, this controller provides IM drive performance very close to the actual value performance compared to T1FLC. So, in the present work, an attempt is made in the direction of developing a DTFC of an IMD using T2FLC for getting improved performance.

Recently, speed sensorless IM drives are gaining wide popularity in industrial applications, because it provides a more compact drive with less maintenance, reduced electrical noise, avoidable transducer and the associated cost. Moreover, it is highly suitable for hostile environment. Out of all available methods which are reviewed in section 1.2.4, the MRAS based speed estimation is found to be very attractive. The MRAS based speed estimation methods are classified into three types. Among these, the rotor-flux based MRAS method is the most popular speed estimation method and considerable attempts have been made to improve its performance. Another issue found from the literature is that the performance of the controllers used in the adaptation mechanisms for speed estimation is not precise when operating point changes and also poor load torque disturbance rejection. Despite considerable effort, it is still problematic for MRAS speed estimation to get a satisfactory performance over a wide range of speed operation.

In view of the scope of work revealed by the literature survey made on IM drive, which is presented in section 1.2, an attempt has been made to establish the following contribution in the present investigation. This research work presents entirely new applications of soft-computing techniques (i.e. T1FLC and T2FLC) in the MRAS speed estimation for DTFC of a speed Sensorless IM drive.

- Development of a direct torque and flux controlled IM drive using T2FLC

  The mathematical modelling of T2FLC for DTFC of an IM drive with a speed sensor is developed. In this, the antecedent and consequent parameters of the fuzzy inference system are tuned with the help of experts, which optimally represents the logical/mathematical relationship between the input and output quantities. The proposed method extensively simulated in the MATLAB/SIMULINK environment and simulation results is obtained and compared with the PIC and T1FLC under various operating conditions, such as forward motoring, reversal motoring, changes in speed and loading at various speed operations. The obtained simulation results obtained are verified experimentally using a dSPACE DS-1104 controller board.

- Development of a rotor-flux based MRAS speed estimator for DTFC of a speed sensorless IM drive using T1FLC and T2FLC, respectively.

  The speed of the IM drive is estimated using rotor flux based MRAS. In this MRAS, the Type-1 and Type-2 FLCs are introduced in the adaptation mechanism in place of the fixed gain PI controller with an aim to further enhance the performance of the speed sensorless IM drive. The performance of rotor-flux based MRAS speed estimation using PI, Type-1 and Type-2 FLCs are carried out in the MATLAB/SIMULINK environment and validated with the experimental results.

- Development of DTFC with SVM technique for a speed sensorless IM drive using T1FLC and T2FLCs, respectively.

  Some modifications are proposed to further enhance the performance of DTFC of a speed sensorless IMD using T1FLC and T2FLCs, respectively. The modifications are: the switching table of DTFC method is replaced by the space vector modulation technique and the hysteresis torque and flux comparators are replaced by the T1FLC and T2FLCs, respectively. The objectives of such modifications are to: (i) Improve the performance of the IM drive by reducing the ripple contents in stator flux and torque, (ii) maintain the constant switching frequency and (iii) estimate the accurate rotor speed. The simulation performance of T2FLC is compared with the T1FLC and PI controller and is validated with the experimental results.

- Stator resistance estimation

  Parameter variation is the major problem in speed estimation algorithms, especially under low speed operations. In order to overcome this drawback, parallel rotor speed and stator resistance estimator is developed for DTFC-SVM of a speed sensorless IMD using T1FLC and T2FLC, respectively. An experimental prototype is developed for rotor-flux based MRAS rotor speed and stator resistance estimation using three different control methods. The performance of the proposed methods is extensively simulated and validated with experimental results.

1.4 Thesis Organization

The thesis is organized in the following chapters.

Chapter-1:

This chapter presents the general description of the variable speed drives. An extensive literature review on vector control of IM drives, soft-computing techniques, speed estimation methods, stator and rotor resistance estimation methods are presented. Moreover, the scope of the present work and author contribution followed by the organization of thesis chapters is described.

Chapter-2:

In this chapter, mathematical modelling of the induction motor, speed control techniques (i.e. scalar control and vector control) of IM drive, PI controller design procedure and simulation results are presented.

Chapter-3:

In this chapter, Type-1 and Type-2 FLCs are proposed for DTFC of an IMD. The design procedure of Type-1 and Type-2 FLCs, simulation results and the comparative analysis of PI, Type-1 and Type-2 FLCs are presented.

Chapter-4:

A laboratory experimental prototype system is developed using dSPACE DS-1104 controller board to experimentally validate the simulation results. The simulation results of the previous chapters are experimentally validated under similar conditions.

Chapter-5:

This chapter deals with various speed sensorless techniques for induction motor drive. Also, the modelling of rotor-flux based MRAS speed estimation for DTFC of a speed sensorless IMD using PI, Type-1 and Type-2 FLCs are explained in detail. The performance of the rotor-flux based MRAS speed estimation is extensively simulated in the MATLAB/SIMULINK environment using different controllers and results are presented under various operating conditions over a wide range of speed operation. The obtained simulation results are verified experimentally.

Chapter-6:

In this chapter, some modifications are proposed to further enhance the performance of the DTFC of a speed sensorless IM drive with space vector modulation (DTFC-SVM) technique. The performance of the proposed method is simulated in the MATLAB/SIMULINK environment and experimentally validated by the laboratory developed real-time system.

Chapter-7:

In this chapter, a stator resistance estimation method for rotor-flux based MRAS speed estimator using PI, Type-1 and Type-2 FLCs are presented. The performance of parallel rotor speed and stator resistance estimator is extensively simulated and validated experimentally under low speed operation.

Chapter-8:

The important conclusions of the overall research work are presented in this chapter and the suggestions are also outlined for future work.

Chapter 2

Direct Torque and Flux Control of an Induction Motor Drive

CHAPTER 2: DTFC OF AN INDUCTION MOTOR DRIVE

In this chapter, mathematical modelling of the induction motor and the vector control techniques have been discussed.

This chapter is organized as follows:

- *The basic introduction of the induction motor is presented in section 2.1.*
- *The mathematical modelling of the induction motor is derived in various reference frames and it is simulated in the MATLAB/SIMULINK environment, which is presented in section 2.2.*
- *The principle of field oriented control method and its simulation model using PI controller is presented in section 2.3. Further, direct torque and flux control of an IM drive using PI controller is presented in section 2.4.*
- *Finally, section 2.5 states all concluding remarks.*

2.1 Introduction

The state-space model and equivalent circuits are useful for studying the performance of the machine in the steady-state. This implies that electrical transients are ignored during stator frequency variations and load changes. The dynamic model considers the instantaneous effects of varying voltages/currents, stator frequency and torque disturbances [1-3]. The dynamic model of the induction motor is derived in terms of direct and quadrature axes components. This method is required to obtain the conceptual simplicity with the two sets of the windings, one is on the stator and the other is on the rotor.

The equivalence between the three-phase and two-phase machine models derived from the simple observation and this approach is suitable for extending it to a model of n-phase machine by means of a two-phase machine. The concept of power invariance is introduced, i.e. the power must be equal in the three-phase machine and its equivalent two-phase model. The required transformation in voltages, currents, or flux linkages, is derived in a generalized way. The reference frames are chosen arbitrarily and particular cases such as stationary, rotor, and synchronous reference frames are simple instances of the general case. The state-space model is derived from the dynamic model. The state-space model powerfully evokes the similarity and equivalence between the induction machines and DC machines from the modeling and control point of views [5].

The main objective of this chapter is to present the brief insight into the dynamic modeling of the induction motor and vector control methods such as field-oriented control, direct torque and flux control strategies using PI controller.

2.2 Modelling of Induction Motor

The proper mathematical model is essential for a three-phase induction motor to study and simulate the complete drive system. The space vector based mathematical model of the induction motor is derived and discussed in this subsection. The following assumptions have been considered for the implementation of the induction motor model [1-3, 9]:

i. Each of the stator winding is distributed so as to generate a sinusoidal MMF along the air gap, i.e., space harmonics are negligible.
ii. The slotting in stator and rotor produces negligible variation in respective inductances.
iii. The resistance and reactance of the windings are considered to be constant.
iv. The effects of magnetic circuit saturation, iron losses and anisotropy are neglected.

A set of differential stator and rotor flux linkages and voltage equations are used to describe the mathematical model of an induction motor. The mathematical model of the induction motor is derived in various reference frames and they are presented in detail in Appendix A. The three-phase squirrel cage induction motor voltage variables can be derived using the equivalent circuit is shown in Figure 2.1.

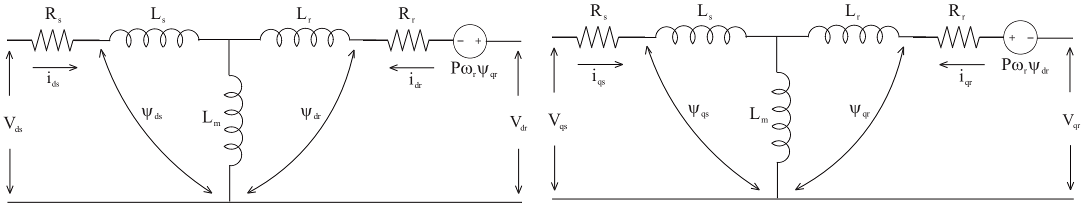

(a) d-axis circuit (b) q-axis circuit

Figure 2.1: Equivalent circuit representation of an IM in stationary (d, q) reference frame

The voltage variables of the IM in a stationary reference frame can be written in matrix form as follows [1-3, 5, 9, 202]:

$$\begin{bmatrix} V_{ds} \\ V_{qs} \\ 0 \\ 0 \end{bmatrix} = \begin{bmatrix} R_s + L_s p & 0 & L_m p & 0 \\ 0 & R_s + L_s p & 0 & L_m p \\ L_m p & \omega_r L_m & R_r + L_r p & \omega_r L_r \\ -\omega_r L_m & L_m p & -\omega_r L_r & R_r + L_r p \end{bmatrix} \begin{bmatrix} i_{ds} \\ i_{qs} \\ i_{dr} \\ i_{qr} \end{bmatrix} \tag{2.1}$$

The developed electromagnetic torque ‘T_e’ in an induction motor can be expressed as:

$$T_e = \frac{3P}{4}\left(\psi_{ds} i_{qs} - \psi_{qs} i_{ds}\right) \tag{2.2}$$

The motor speed is developed according to the equation (2.3) as:

$$T_e = T_L + B\omega_m + J\frac{d\omega_m}{dt} \tag{2.3}$$

The state-space model of the IM can be represented in stationary (d-q) reference frame as:

$$\frac{d}{dt}\begin{bmatrix} i_{ds} \\ i_{qs} \\ \psi_{dr} \\ \psi_{qr} \end{bmatrix} = \begin{bmatrix} -a_1 & 0 & a_2 & a_3\omega_r \\ 0 & -a_1 & -a_3\omega_r & a_2 \\ a_5 & 0 & -a_4 & -\omega_r \\ 0 & a_5 & \omega_r & -a_4 \end{bmatrix} \begin{bmatrix} i_{ds} \\ i_{qs} \\ \psi_{dr} \\ \psi_{qr} \end{bmatrix} + \begin{bmatrix} \frac{1}{\sigma L_s} & 0 \\ 0 & \frac{1}{\sigma L_s} \\ 0 & 0 \\ 0 & 0 \end{bmatrix} \begin{bmatrix} V_{ds} \\ V_{qs} \end{bmatrix} \tag{2.4}$$

where $a_1 = \frac{1}{\sigma L_s}\left(R_s + \frac{L_m^2}{L_r T_r} \right)$, $a_2 = \frac{1}{\sigma L_s}\frac{L_m}{L_r T_r}$, $a_3 = \frac{1}{\sigma L_s}\frac{L_m}{L_r}$, $a_4 = \frac{1}{T_r}$, $a_5 = \frac{L_m}{T_r}$,

$\sigma = 1 - \frac{L_m^2}{L_s L_r} =$ leakage coefficient and $T_r = \frac{L_r}{R_r}$.

The mathematical model of the IM can be represented in stationary (d-q) reference frame using the standard state-space notation as [9, 202]:

$$\dot{X} = AX + BU \tag{2.5}$$

$$Y = CX \tag{2.6}$$

where $A = \begin{bmatrix} -a_1 & 0 & a_2 & a_3\omega_r \\ 0 & -a_1 & -a_3\omega_r & a_2 \\ a_5 & 0 & -a_4 & -\omega_r \\ 0 & a_5 & \omega_r & -a_4 \end{bmatrix}$ $B = \begin{bmatrix} \frac{1}{\sigma L_s} & 0 \\ 0 & \frac{1}{\sigma L_s} \\ 0 & 0 \\ 0 & 0 \end{bmatrix}$ $C = \begin{bmatrix} 1 & 0 \\ 0 & 1 \\ 0 & 0 \\ 0 & 0 \end{bmatrix}^T$ $X = \begin{bmatrix} i_{ds} \\ i_{qs} \\ \psi_{dr} \\ \psi_{qr} \end{bmatrix}$ $U = \begin{bmatrix} V_{ds} \\ V_{qs} \end{bmatrix}$ $Y = \begin{bmatrix} i_{ds} \\ i_{qs} \end{bmatrix}$

where, suffixes *ds, qs, dr,* and *qr* represents the stator and rotor *d-* and *q-* axis quantities fixed on stationary reference frame in all combinations, R_s and R_r are stator and rotor resistances per phase respectively, ψ denotes the flux linkage, P is the number of poles, ω_r represents the rotor speed in rad/sec, 'B' is the viscous friction coefficient, J is the moment of inertia and T_e is the developed electromagnetic torque, T_L is load torque, L_s, L_r represents the stator and rotor self-inductances respectively and L_m represents the mutual inductance.

2.2.1 Scalar control of the IM Drive

The state-space model of the IM referred to a stationary (d-q) reference frame, which is derived in the previous section was implemented in the MATLAB/SIMULINK environment. The MATLAB/SIMULINK function blocks are created and linked using the Graphical User Interface (GUI) which can be edited easily by using menu commands. A set of differential equations of the machine can be modeled by the interconnection of appropriate function block sets, to perform a specific mathematical operation by which the programming efforts are drastically reduced and the debugging of errors is easy.

The generalized dynamic model of three-phase IM is considered for simulation, which is presented in equations from (2.1) to (2.4). The modeling of IM is formulated in various forms of subsystem blocks in SIMULINK as:

- The electrical subsystem to develop three-phase to two-phase (3/2) transformation of voltage and current calculations (Clark transformation).
- The torque subsystem for the development of an electromagnetic torque.
- The flux calculation subsystem to develop the stator and rotor flux quantities.
- The current calculation subsystem to develop the stator and rotor currents.
- The voltage source inverter subsystem for supplying power to the induction motor.

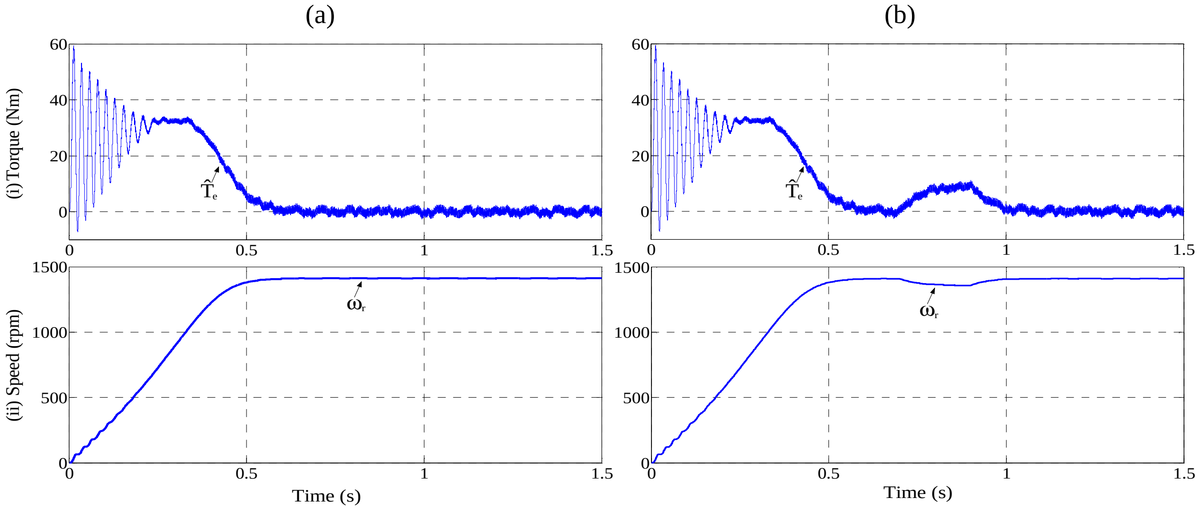

Figure 2.2: Performance of the induction motor drive under: (a) No-load torque (b) Load torque

2.2.2 Simulation Results

The performance of scalar controlled IM drive is simulated at the rated speed of 1410 rpm under no-load torque condition as shown in Figure 2.2 (a). It is observed from the simulation result that the actual speed settled its reference value at 0.62 s. The effect of sudden load torque operation is shown in Figure 2.2 (b). A load torque of 9 Nm is applied at 0.7 s and it is removed at 0.9 s. The sudden application of load torque causes undershoot of around 50 rpm. Similarly, overshoot of 30 rpm when the load torque is suddenly removed. The simulation results are presented trace-wise (from top to bottom) as electromagnetic torque and rotor speed, respectively.

Property of the scalar control of an IM drive:

- This method is simple to implement and widely used in industrial applications.
- The dynamic behavior of scalar control is very poor and sluggish response. Moreover, it is difficult to control the speed under various operating conditions, such as load torque disturbance, sudden changes in speed, etc.

2.3 Field Oriented Control of Induction Motor Drive

The scalar control scheme is simple to implement and it gives good steady-state response. However, the dynamic performance is sluggish and unable to control. This manifests itself in the deviation of air gap flux linkages from their set values. This variation occurs in both phase and magnitude [1-3, 8]. This flux linkage deviation has to be controlled by the frequency and magnitude of the rotor and stator phase currents and their instantaneous phases. However, these control approaches have utilized only the magnitude and frequency of stator phase currents and not their phases. This results in deviation of magnitude and phase of the air gap flux linkages from their set values.

The deviation of the air gap flux linkage affects the electromagnetic torque, which is replicated as rotor speed fluctuations. This is adverse in several high performance applications, such as servos, rolling mills, robotic actuators, process drives, and centrifuges, where fast speed control and high precision is required, which is a difficult task for the IMD with the flux linkage error [3].

In order to overcome the above problem independent control of field flux and torque is required in a similar manner as separately excited direct current (DC) motor, where the magnetic field flux of the motor is controlled by the current flowing in the stator winding, while the torque is controlled directly by the current of the rotor winding. In addition, the DC motor control requires only the armature or field current magnitude control, which provides modest possible control. In contrast, AC machines require a coordinated control of stator current magnitudes, frequencies and their phases, which makes it a complex control.

In the IM, the stator current can be determined along the rotor flux linkages and component along this field producing current, which requires the position of the rotor flux linkage at every instant. The necessity of magnitude control of flux, frequency and flux phasor can be made possible by the inverter control. As this control can be achieved in field coordinates, such a control scheme called field-oriented control (FOC), which is one of the vector control schemes [6]. The field oriented control scheme ensures good and robust control in case of transient as well as steady states.

2.3.1 Principle of Field Oriented Control

The main objective of FOC is to make the squirrel cage induction motor dynamic performance similar manner to that of a separately DC motor, where the torque and flux are controlled independently by assuming flux linkage phasor as a known quantity [6]. The three phase stator currents can be transformed into synchronous reference frame (D^e-Q^e) using the transformation as shown below [202]:

$$\begin{bmatrix} i_{Ds}^{e} \\ i_{Qs}^{e} \end{bmatrix} = \frac{2}{3} \begin{bmatrix} \cos\theta_f & \cos\left(\theta_f - \frac{2\pi}{3}\right) & \cos\left(\theta_f + \frac{2\pi}{3}\right) \\ \sin\theta_f & \sin\left(\theta_f - \frac{2\pi}{3}\right) & \sin\left(\theta_f + \frac{2\pi}{3}\right) \end{bmatrix} \begin{bmatrix} i_{As} \\ i_{Bs} \\ i_{Cs} \end{bmatrix} \tag{2.7}$$

The stator current space vector magnitude and its position can be derived using the equation (2.7) as:

$$i_s = \sqrt{\left(i_{Ds}^{e}\right)^2 + \left(i_{Qs}^{e}\right)^2} \tag{2.8}$$

$$\theta_T = tan^{-1}\left(\frac{i_{Qs}^{e}}{i_{Ds}^{e}}\right) \tag{2.9}$$

The stator current space vector magnitude remains same regardless of the reference frame is chosen. The stator current space vector $\vec{i}_s$ produces the electromagnetic torque T_e and rotor flux ψ_r. The rotor flux producing component of current has to be in phase with ψ_r. The stator current component resolved along ψ_r is a field producing component i_f and the perpendicular component is torque producing component i_T. The rotor flux linkages and electromagnetic torque can be written in terms of these components as follows [3, 202]:

$$\psi_r \propto i_f \tag{2.10}$$

$$T_e \propto i_f \psi_r \propto i_f i_T \tag{2.11}$$

It can be seen from the Figure 2.3 that the i_f and i_T are direct and quadrature axes current components in the rotor flux oriented reference frame. The rotor flux linkage space vector has a speed equal to the sum of the rotor and slip speeds, which is equal to the synchronous speed.

$$\omega_f = \omega_r + \omega_{sl} \tag{2.12}$$

$$\theta_f = \int \left(\omega_r + \omega_{sl}\right) dt \tag{2.13}$$

where, ω_{sl} is slip angle, ω_r is rotor speed and θ_f is field angle.

The field angle calculation is crucial for the implementation of the field oriented control (FOC) control and it is obtained from the rotor and slip speeds.

Depending on the field angle acquisition, the FOC methods are classified into two types: direct field oriented control (DFOC) and indirect field oriented control (IFOC) [3, 6]. In DFOC, the field angle is estimated by using the measured terminal currents and voltages or flux sensing while in IFOC the field angle is obtained by using the measured rotor position and partial estimation with machine parameters. The indirect field oriented control of IMD is widely used in high performance industrial applications due to its simplicity, low cost, fast dynamic response, reliability and eliminates the flux sensor or flux model, but it requires an accurate measurement of shaft position in order to control the accurate location of the rotor flux vector. However, it is very sensitive to the rotor time constant variation which may weaken the performance of IM drive. This control strategy is also referred to as rotor field oriented control.

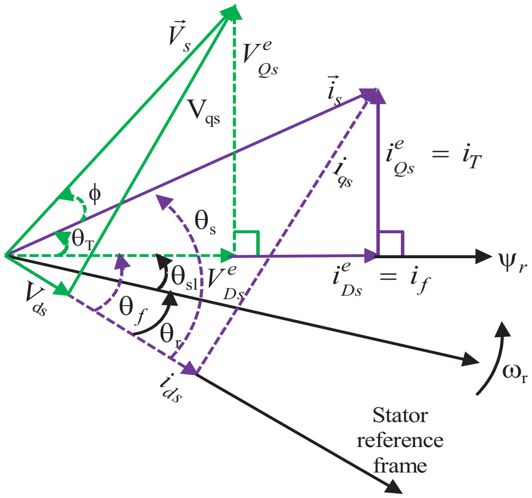

Figure 2.3: Phasor diagram of field oriented control scheme [3]

2.3.2 Indirect Field Oriented Control of IMD

The IFOC scheme can be described by using dynamic model of induction motor in rotor flux oriented reference frame (D^e-Q^e) as [1-3, 9, 202]:

Stator voltage (D^e-*axis*) : $V^e_{Ds} = R_s i^e_{Ds} + \dfrac{d\psi^e_{Ds}}{dt} - \omega_e \psi^e_{Qs}$ (2.14)

Stator voltage (Q^e-*axis*) : $V^e_{Qs} = R_s i^e_{Qs} + \dfrac{d\psi^e_{Qs}}{dt} + \omega_e \psi^e_{Ds}$ (2.15)

Rotor voltage (D^e-*axis*) : $0 = R_r i^e_{Dr} + \dfrac{d\psi^e_{Dr}}{dt} - \omega_{sl} \psi^e_{Qr}$ (2.16)

Rotor voltage (Q^e-*axis*) : $0 = R_r i^e_{Qr} + \dfrac{d\psi^e_{Qr}}{dt} + \omega_{sl} \psi^e_{Dr}$ (2.17)

Resultant flux : $\psi_r = \sqrt{\left(\psi^e_{Dr}\right)^2 + \left(\psi^e_{Qr}\right)^2}$ (2.18)

Electromagnetic torque : $T_e = \dfrac{3P}{4} \dfrac{L_m}{L_r} (\psi^e_{Dr} i^e_{Qs} - \psi^e_{Qr} i^e_{Ds})$ (2.19)

Torque balancing equation : $T_e = T_L + B\omega_m + J\dfrac{d\omega_m}{dt}$ (2.20)

where $\psi^e_{Ds} = i^e_{Ds} L_s + i^e_{Dr} L_m$, $\psi^e_{Qs} = i^e_{Qs} L_s + i^e_{Qr} L_m$, $\psi^e_{Dr} = i^e_{Dr} L_r + i^e_{Ds} L_m$, $\psi^e_{Qr} = i^e_{Qr} L_r + i^e_{Qs} L_m$ and $\omega_{sl} = \omega_e - \omega_r$.

The stator and rotor voltages, the electromagnetic torque equations in the synchronous reference frame can be written in matrix form as follows:

$$\begin{bmatrix} V^e_{Ds} \\ V^e_{Qs} \\ 0 \\ 0 \end{bmatrix} = \begin{bmatrix} R_s + L_s p & -\omega_e L_s & L_m p & -\omega_e L_m \\ \omega_e L_s & R_s + L_s p & \omega_e L_m & L_m p \\ L_m p & -\omega_{sl} L_m & R_r + L_r p & -\omega_{sl} L_r \\ \omega_{sl} L_m & L_m p & \omega_{sl} L_r & R_r + L_r p \end{bmatrix} \begin{bmatrix} i^e_{Ds} \\ i^e_{Qs} \\ i^e_{Dr} \\ i^e_{Qr} \end{bmatrix} \tag{2.21}$$

$$T_e = \frac{3P}{4}\frac{L_m}{L_r}\begin{bmatrix} \psi^e_{Dr} & \psi^e_{Qr} \end{bmatrix}\begin{bmatrix} i^e_{Qs} \\ -i^e_{Ds} \end{bmatrix} \tag{2.22}$$

The rotor flux linkage ‘ ψ_r ’ also known as the rotor flux linkage space vector, is assumed to be on the direct axis to reduce the number of variables in the equation by one, and it also corresponds to the reality that the rotor flux linkage is a single variable. Hence, aligning the d-axis with rotor flux phasor yields [3]:

$$\psi^e_{Qr} = \frac{d\psi^e_{Qr}}{dt} = 0 \tag{2.23}$$

$$\psi_r = \psi^e_{Dr} \tag{2.24}$$

The rotor flux linkage equation (2.24) substituting into the rotor voltage equations (2.16) and (2.17) respectively, we get:

$$0 = R_r i^e_{Dr} + \frac{d\psi_r}{dt} \tag{2.25}$$

$$0 = R_r i^e_{Qr} + \omega_{sl}\psi_r \tag{2.26}$$

The rotor currents in terms of stator quantities can be expressed as:

$$i^e_{Qr} = -i^e_{Qs}\frac{L_m}{L_r} \tag{2.27}$$

$$i^e_{Dr} = \frac{\psi_r}{L_r} - \frac{L_m}{L_r} i^e_{Ds} \tag{2.28}$$

Under steady state condition:

$$p\psi_r = 0 \tag{2.29}$$

By substituting equation (2.29) in equation (2.25), we get:

$$i^e_{Dr} = 0 \tag{2.30}$$

The above rotor current equations (2.27) and (2.28) are substituted into the rotor voltage equations (2.26) and (2.25) respectively, which yields:

$$i_f = \frac{1}{L_m}\left[1 + T_r p\right]\psi_r \tag{2.31}$$

$$\omega_{sl} = k\left[\frac{L_r}{T_r}\right]\left[\frac{T_e}{\psi_r^2}\right] = \left[\frac{L_m}{T_r}\right]\left[\frac{i_T}{\psi_r}\right] \tag{2.32}$$

where, $i_T = i_{Qs}^e$, $i_f = i_{Ds}^e$ and $k = \dfrac{4}{3P}$

The dq-axes currents are relabelled as flux and torque producing components of the stator space vector, respectively. The equation (2.31) represents the field equation in a separately excited DC machine [3]. Likewise, by substituting the rotor flux equation (2.23) into electromagnetic torque equation (2.19), the torque expression can be written as:

$$T_e = \frac{3P}{4}\frac{L_m}{L_r}(\psi_{Dr}^e i_{Qs}^e - \psi_{Qr}^e i_{Ds}^e) = k_T\left(\psi_{Dr}^e i_{Qs}^e\right) = k_T\psi_r i_T \tag{2.33}$$

where k_T is the torque constant and it is given by: $k_T = \dfrac{3P}{4}\dfrac{L_m}{L_r}$

The electrical field angle θ_f can be obtained as the sum of the rotor θ_r and slip θ_{sl} angles and is given by:

$$\theta_f = \theta_r + \theta_{sl} \tag{2.34}$$

The slip angle can be derived by integrating the slip speed as:

$$\theta_{sl} = \int \omega_{sl}\, \mathrm{dt} \tag{2.35}$$

The IFOC scheme is implemented using the above derivations and the phasor diagram of the rotor flux oriented control based IFOC of an IMD is shown in Figure 2.4.

The electromagnetic torque of IFOC scheme which is presented in equation (2.33) is similar to that of the separately excited DC motor, where quadrature current i_{Qs}^e and direct current i_{Ds}^e are similar to that of the armature and field currents respectively. When the IM model is developed in the synchronous reference frame, the sinusoidal current quantities appear as direct current quantities in the steady state. The decoupling torque and flux control are achieved by independently controlling the direct and quadrant axes components of the stator current space vector in the synchronous reference frame, where direct current i_{Ds}^e component controls the stator flux while the quadrature current i_{Qs}^e component is controlling the electromagnetic torque, respectively.

2.3.3 Design of Controllers

The performance of IMD is highly dependent on the design of the speed and current controllers. The speed and current controllers are used in the outer and an inner control loop of IFOC scheme. The outer control loop is used to control the speed of the induction motor while inner control loops are used to control the torque and flux of the IM.

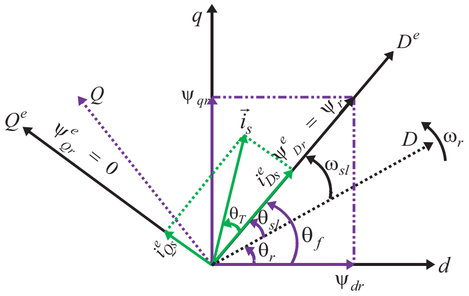

Figure 2.4: Phasor diagram of rotor flux based IFOC [3]

2.3.3.1 Design of PI Current Controllers

The general block diagram of the PI current controller is shown in Figure 2.5. The reference currents are compared with the actual currents and the error currents fed into the PI current controllers. The input and output of the current controllers are error current and reference voltage components which can be expressed as:

$$ei_{Ds} = i^{e*}_{Ds} - i^e_{Ds} \text{ and } ei_{Qs} = i^{e*}_{Qs} - i^e_{Qs} \tag{2.36}$$

$$V^{e^*}_{Ds}(t) = K_p ei_{Ds}(t) + K_i \int ei_{Ds}(t)dt \tag{2.37}$$

$$V^{e^*}_{Qs}(t) = K_p ei_{Qs}(t) + K_i \int ei_{Qs}(t)dt \tag{2.38}$$

where $K_i = K_p / T_i$, $V^{e^*}_{Ds}$ and $V^{e^*}_{Qs}$ are the reference voltage components of the PI current controllers on the D^e and Q^e –axes output.

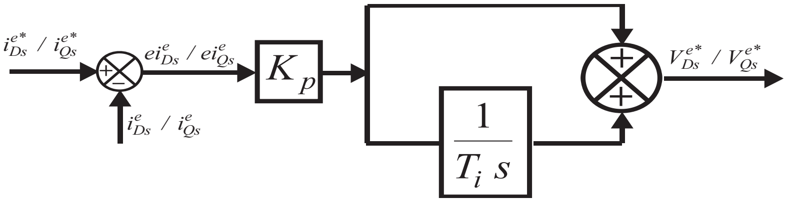

Figure 2.5: Schematic model of PI current controller

The selection of constant gain values of these PI controllers is crucial for the design of the controller in the drive system. An inaccurate selection of gain values may result in undesirable performance and/or unstable response. Therefore, accurate and precise selections of gain values are most important to achieve high performance drive. However, in most cases, these gains are determined by trial and error tuning technique which requires practical experience and may lead to time consumption. Even though, there are numbers of tuning techniques, such as Ziegler-Nichols methods and first order plus time delay method, certain knowledge of process control is required and even that will not ensure the best control performance. On the other hand, the general second order method offers simpler technique and more mathematical formulation approached method [30]. Thus, this method had been applied in getting all the PI values for the analysis.

The direct and quadrature axes stator voltage components in rotor flux oriented reference frame can be derived by substituting equations (2.23) and (2.24) in equation (A.60), as [1-3]:

$$V_{Ds}^{e} = \sigma L_s p i_{Ds}^{e} + R_{sr} i_{Ds}^{e} - \sigma L_s \omega_e i_{Qs}^{e} - \frac{L_m}{L_r T_r} \psi_r \tag{2.39}$$

$$V_{Qs}^{e} = \sigma L_s p i_{Qs}^{e} + R_{sr} i_{Qs}^{e} + \sigma L_s \omega_e i_{Ds}^{e} + \frac{L_m}{L_r} \omega_r \psi_r \tag{2.40}$$

where $R_{sr} = R_s + \frac{L_m^2}{L_r^2} R_r$.

It seems that the direct and quadrature axes voltage equations are coupled with the terms $-\sigma L_s \omega_e i_{Qs}^{e} - \frac{L_m}{L_r T_r} \psi_r$ and $\sigma L_s \omega_e i_{Ds}^{e} + \frac{L_m}{L_r} \omega_r \psi_r$. We can conclude that these terms represent disturbances for the drive, and they can be cancelled if the decoupling method which uses feedback of coupling voltage is employed. In this case, the voltage equations become:

$$V_{Ds}^{e*} = V_{Ds}^{e} - e_{Ds} = \sigma L_s p i_{Ds}^{e} + R_{sr} i_{Ds}^{e} \tag{2.41}$$

$$V_{Qs}^{e*} = V_{Qs}^{e} - e_{Qs} = \sigma L_s p i_{Qs}^{e} + R_{sr} i_{Qs}^{e} \tag{2.42}$$

where $e_{Ds} = -\sigma L_s \omega_e i_{Qs}^{e} - \frac{L_m}{L_r T_r} \psi_r$ and $e_{Qs} = \sigma L_s \omega_e i_{Ds}^{e} + \frac{L_m}{L_r} \omega_r \psi_r$.

The open loop transfer function of current controllers can be derived from equations (2.41) and (2.42) as:

$$\frac{i_{Ds}^{e}}{V_{Ds}^{e*}} = \frac{i_{Qs}^{e}}{V_{Qs}^{e*}} = \frac{K}{Ts+1} \tag{2.43}$$

where $K = \frac{1}{R_{sr}} = 0.1042$, $T = \frac{\sigma L_s}{R_{sr}} = 2.969 \times 10^{-3}$.

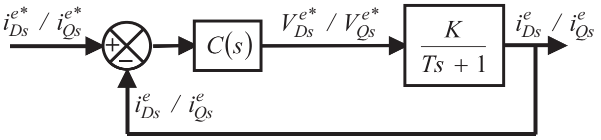

Figure 2.6: Simplified block diagram of flux/torque current loop of IFOC

The block diagram of flux/torque current loop of IFOC with unity feedback is shown in Figure 2.6. The closed-loop characteristic equation of the above system can be written as:

$$s^2 + \frac{KK_p + 1}{T} s + \frac{KK_i}{T} = 0 \tag{2.44}$$

The equation (2.44) is in the form of:

$$s^2 + 2\xi \omega_n s + \omega_n^2 = 0 \tag{2.45}$$

where ξ is damping ratio and ω_n is the natural frequency of the desired closed loop system. By comparing equations (2.44) and (2.45), we get:

$$K_p = \frac{2\xi\omega_n T - 1}{K} \tag{2.46}$$

$$K_i = \frac{T}{K}\omega_n^2 \tag{2.47}$$

For the flux component, by assuming $t_s = 0.015s$ and $\mu_p = 4.33\%$ the values of ξ and ω_n can be calculated as: $\xi = 0.7069$, $\omega_n = 377.2339$.

By substituting ξ and ω_n values in equations (2.46) and (2.47), we get:

$K_{p_{iD}} = 5.5995$ and $T_{i_{iD}} = 0.00138$

For the torque component, by assuming $t_s = 0.02s$ and $\mu_p = 2\%$ the values of ξ and ω_n can be calculated as: $\xi = 0.7797$ and $\omega_n = 256.5089$.

By substituting ξ and ω_n values in equations (2.46) and (2.47), we get:

$K_{p_{iQ}} = 1.8$ and $T_{i_{iQ}} = 0.00096$

2.3.3.2 PI Speed Controller

The PI speed controllers are widely used in high performance industrial applications due to its simplicity and offer zero steady state errors. The general block diagram of the PI speed controller is shown in Figure 2.7. The actual speed is compared with the reference speed and the error speed is processed through the PI speed controller. The PI controller produces the output as a reference torque component. The reference torque component (i_{Qs}^{e}) value is fed to a limiter to give the final value of the reference torque component. The speed error and reference torque component can be expressed as follows:

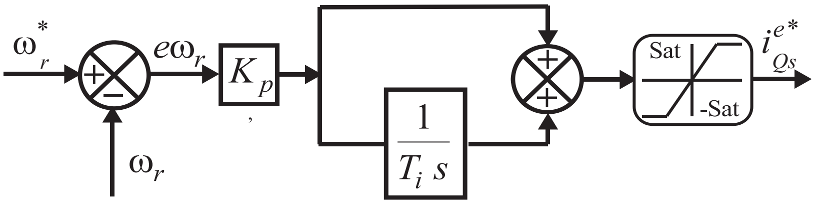

Figure 2.7: Schematic model of PI speed controller

$$e\omega_r = \omega_r^* - \omega_r \tag{2.48}$$

$$i_{Qs}^{e\,*} = K_p e\omega_r(t) + K_i \int e\omega_r(t)\,dt \tag{2.49}$$

where $e\omega_r$ is the error speed, K_p is the proportional gain constant, K_i is the integral gain constant, $i_{Qs}^{e\,*}$ is the reference torque component, ω_r^* and ω_r are the reference speed and actual speed, respectively.

In case of the sudden changes in speed or load torque disturbance, the motor torque may exceed the breakdown torque of the IM which may cause over current and instability. In order to control the torque within the reasonable value, the output of the speed controller is fed to the limiter, which limits the output torque within the desirable range. Ultimately the electromagnetic torque producing component of the current is designed on the basis of reference torque. Therefore, a limiter is mostly desirable after the speed controller in order to keep the operating current of the IMD in the safe zone. This ensures the output current of the inverter remains within the safe limit and thereby providing the feature of an inherent over current protection in the drive.

$$i_{Qs}^{e^*} = \begin{cases} i_{Qs\max}^{e^*} & for\ i_{Qs}^{e^*} \ge i_{Qs\max}^{e^*} \\ -i_{Qs\min}^{e^*} & for\ i_{Qs}^{e^*} \le -i_{Qs\min}^{e^*} \end{cases} \tag{2.50}$$

The block diagram of closed loop speed with unity feedback using a PI controller is shown in Figure 2.8.

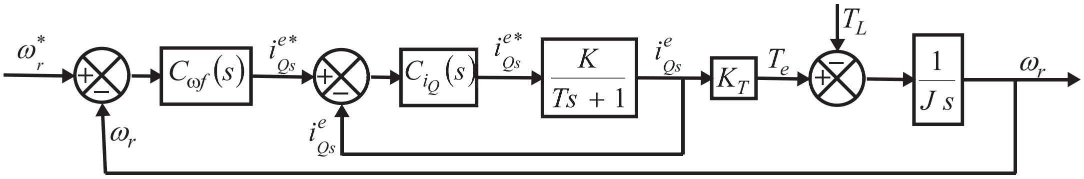

Figure 2.8: The block diagram of closed loop speed with PI controller

The Figure 2.8 is simplified using a block diagram reduction technique by assuming load torque is zero and it is shown in Figure 2.9.

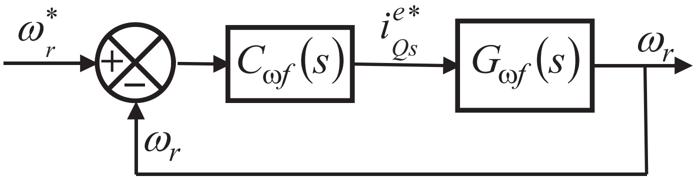

Figure 2.9: Simplified block diagram of closed loop speed with PI controller

From Figure 2.9, the open loop transfer function of the speed controller can be expressed as follows:

$$G_{\omega f}(s) = \frac{A_{\omega f}s + B_{\omega f}}{s^3 + C_{\omega f}s^2 + D_{\omega f}s} \tag{2.51}$$

where $K_T = \frac{3}{2}\frac{P}{2}\frac{L_m}{L_r}\frac{\Psi_r}{J}$, $A_\omega = \frac{KK_TK_{P_{iQ}}}{T}$, $B_\omega = \frac{KK_TK_{i_{iQ}}}{T}$, $C_\omega = \frac{KK_{P_{iQ}}+1}{T}$ and $D_\omega = \frac{KK_{i_{iQ}}}{T}$.

The open loop transfer function of the speed controller is of the third order, so in order to design the PIC the root locus method is considered. The detailed PIC design procedure using the root locus method is given in Appendix B.

Initially, the required settling time and overshoot of the speed control loop is selected, i.e. settling time < 0.3 and overshoot < 2%. By using these time domain specifications a pair of dominant conjugate poles can be calculated as: $\rho_{1,2} = -13.333 \pm j10.707$

By using equation (A.99), $K_{i\omega f}$ can be expressed in terms of $K_{p\omega f}$ as follows:

$$K_{i\omega f} = \alpha_{\omega f} K_{p\omega f} + \beta_{\omega f} \tag{2.52}$$

where $\alpha_{\omega f} = 21.9321$ and $\beta_{\omega f} = -8.8724$

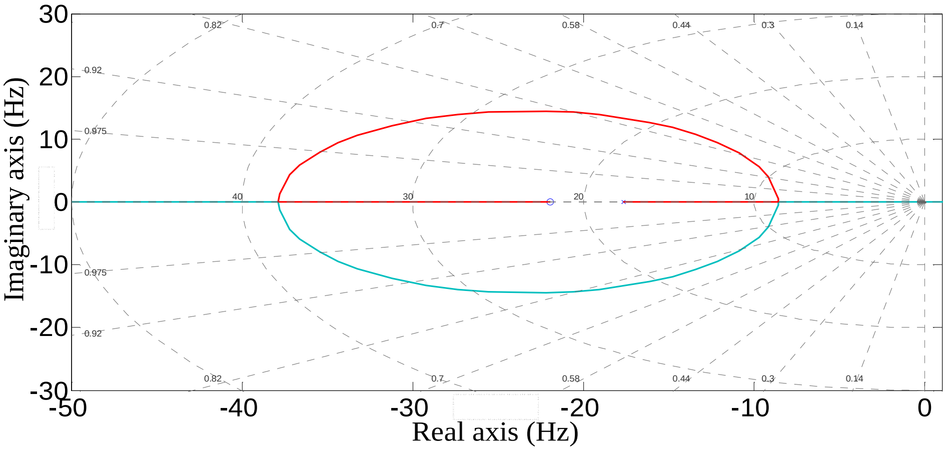

Figure 2.10: Root locus of the closed loop speed control system w.r.t $K_{p\omega f}$

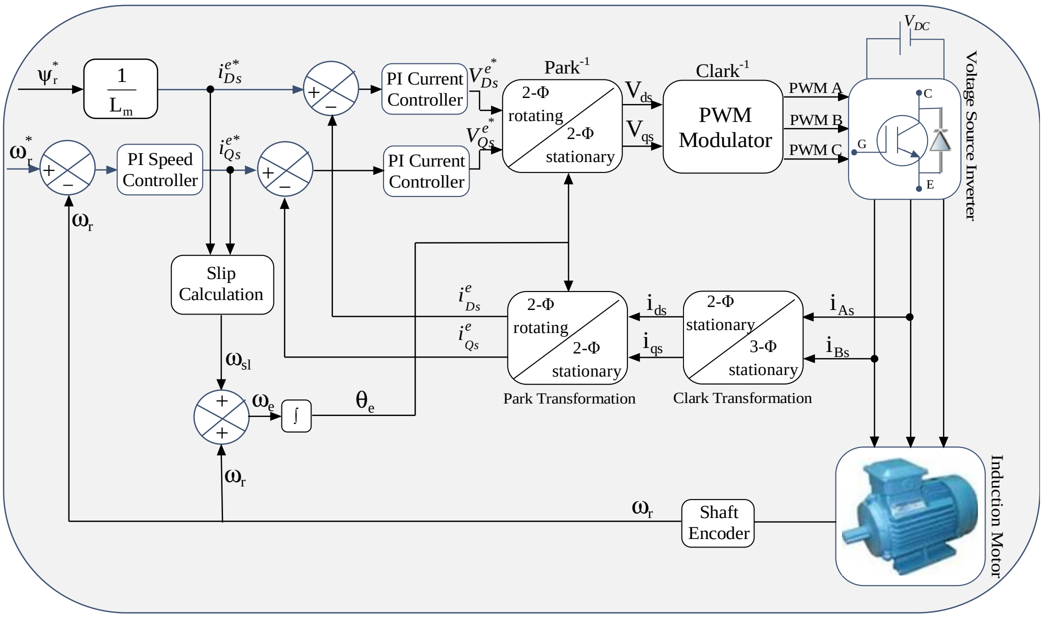

Figure 2.11: Schematic model of indirect field oriented controlled induction motor drive

By substituting $\alpha_{\omega f}$, $\beta_{\omega f}$ values in equation (A.100), we get:

$$1 + K_{p\omega f}\left(\frac{(s+\alpha_{\omega f})(A_{\omega f}s + B_{\omega f})}{s^4 + C_{\omega f}s^3 + D_{\omega f}s^2 + A_{\omega f}\beta_{\omega f}s + B_{\omega f}\beta_{\omega f}}\right) = 0 \tag{2.53}$$

Now draw the root locus of $\dfrac{(s+\alpha_{\omega f})(A_{\omega f}s + B_{\omega f})}{s^4 + C_{\omega f}s^3 + D_{\omega f}s^2 + A_{\omega f}\beta_{\omega f}s + B_{\omega f}\beta_{\omega f}}$.

The interval of $K_{p\omega f}$ for guaranteed dominant pole placement can be obtained from the root locus plot (Figure 2.10) as: $1.75 \leq K_{p\omega f} \leq 7.5$

For getting desired closed loop control performance the PI controller parameters are calculated from the root locus plot (Figure 2.10) as: $K_{p\omega f} = 1.75, T_{i\omega f} = 0.0593$

2.4 Simulation Model of Indirect field Oriented Controlled IM

The schematic model of indirect field oriented controlled IMD is shown in Figure 2.11. The parameter values of an induction motor are given in Appendix C. The mathematical model of IFOC of an IMD is simulated in the MATLAB/SIMULINK environment. The PIC is used in inner and outer control loops (i.e. speed and current controller), whose gain values are presented in Appendix C. In this, the speed controller block is used to control the rotor speed, whereas the current controller blocks are used to control the field and torque components. The synchronously rotating D^e-Q^e axes voltages are converted to stationary d-q axes voltages using field angle. Further, these two-phase stationary voltages are transformed to three-phase voltages. These three-phase voltages are used in the modulation scheme to generate the switching pulses for two-level voltage source inverter and the output of the inverter is fed into IM. The performance of the IFO controlled IMD fed with two-level inverter is simulated and discussed under different operating conditions.

2.4.1 Simulation Results

Initially, the IFOC of IMD is started with a reference speed of 1200 rpm under no-load torque, as the motor starts, the starting torque will be developed to accelerate the machine. Once the speed reaches to reference speed, the developed torque settles at reference torque i.e. zero at no-load operation. The reversal speed of -1200 rpm is applied at a time interval of 1 s shown in Figure 2.12 (a). Furthermore, a load torque of 9 Nm is applied at 0.7 s and it is removed at 0.9 s as shown in Figure 2.12 (b). When a sudden load torque is applied to the motor, undershoot of 20 rpm appears and similarly when the load torque is withdrawn an overshoot of 18 rpm appears for a small interval of time. These results clearly show that the dynamic performance of IFOC scheme is better compared to that of open loop control of IMD.

The properties of the IFOC can be summarized as follows:

- This scheme is based on control philosophy of separately excited DC motor
- The current components i_{Ds}^{e} and i_{Qs}^{e} do not ensure precisely decoupling control of the rotor flux and torque in both dynamic and steady state conditions.
- The flux is asymptotically decoupled with torque, i.e., decoupling is achieved only in the steady state, when the flux remains constant. Coupling is still present when the

flux is weakened in order to operate the motor at higher speed within the input voltage saturation limit.

- This scheme is highly sensitive to the parameters of the rotor time constant. Moreover, the information of rotor position is required.
- This control scheme requires current controllers.

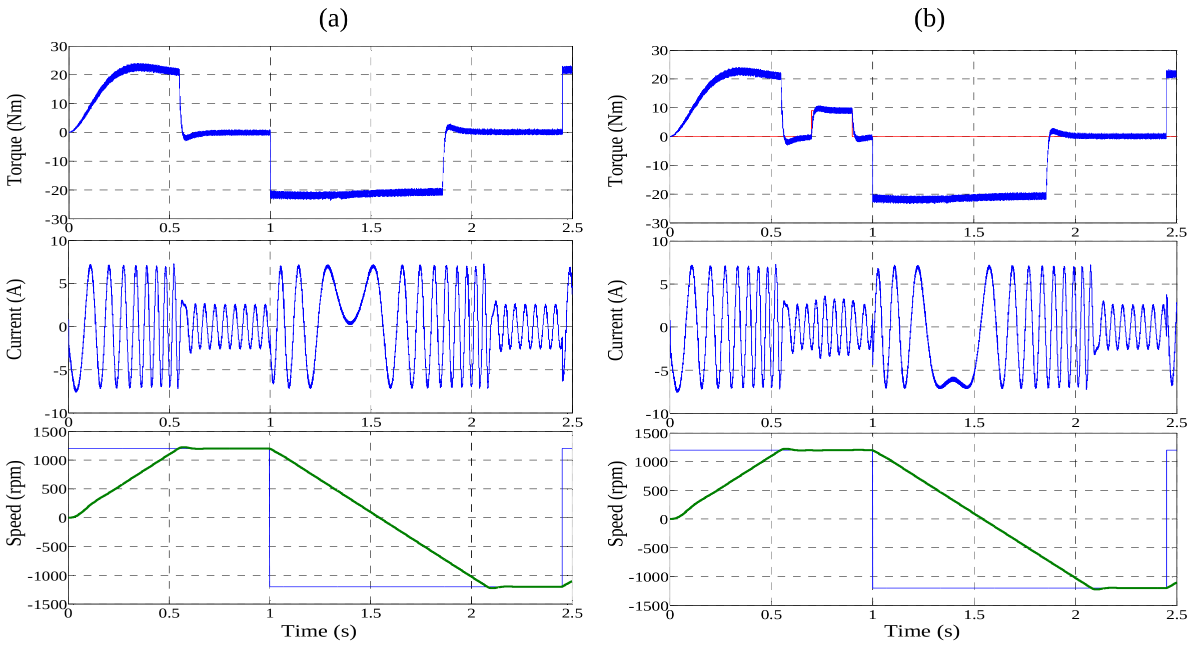
(a)
(b)

Figure 2.12: Simulation responses of indirect field oriented controlled IMD under: (a) No-load torque and (b) Load torque.

The IFOC of IMD has attractive features, however, it suffers from various drawbacks [6, 11-14], which are mentioned in the previous section. In order to overcome these drawbacks, a new control strategy was introduced by I. Takahashi and T. Noguchi in the late 1980’s, i. e. Direct Torque and Flux Control (DTFC) scheme [12, 15].

2.5 Direct Torque and Flux Control of IMD

Over the last two decades, the DTFC has emerged to become one of the alternatives to the FOC scheme. In this scheme, the direct control of torque and stator flux is possible by selecting optimum output voltage vector of the voltage source inverter (VSI). The selection of the most optimum output voltage vector is done in such a way that the control of stator flux and torque are perfectly decoupled [16-21].

2.6 Principle of Direct Torque and Flux Control

The stator flux linkage is given by the integral of the difference between stator voltage and stator voltage drop, which is shown in equation (2.54) as [12]:

$$\vec{\psi}_s = \int \left(\vec{V}_s - \vec{i}_s R_s\right) dt \tag{2.54}$$

If the stator resistance voltage drop is neglected, then the applied voltage is derivative of the stator flux linkage, which is shown in equation (2.55). Hence, in a small period of time the stator flux increment is directly proportional to the applied voltage [12].

$$\vec{V}_s = \frac{d\vec{\psi}_s}{dt} \quad \text{or} \quad \Delta\vec{\psi}_s = \vec{V}_s\,\Delta t \tag{2.55}$$

This means that the applied voltage directly excites the stator flux. The torque expression is given in equation (2.2) can be expressed in the vector form as:

$$\vec{T}_e = \frac{3}{2}\frac{P}{2}\vec{\psi}_s \times \vec{i}_s \tag{2.56}$$

In equation (2.56), $\vec{i}_s$ is to be replaced by the rotor flux $\vec{\psi}_r$. From Figure 2.1, the stator and rotor flux linkage space vectors can be expressed as functions of the stator and rotor current space vectors as:

$$\vec{\psi}_s = L_s\vec{i}_s + L_m\vec{i}_r \tag{2.57}$$

$$\vec{\psi}_r = L_r\vec{i}_r + L_m\vec{i}_s \tag{2.58}$$

By eliminating $\vec{i}_r$ from the equation (2.57), we get:

$$\vec{\psi}_s = \frac{L_m}{L_r}\vec{\psi}_r + \sigma L_s\vec{i}_s \tag{2.59}$$

Equation (2.59) can be rewritten as:

$$\vec{i}_s = \frac{1}{\sigma L_s}\vec{\psi}_s - \frac{L_m}{\sigma L_s L_r}\vec{\psi}_r \tag{2.60}$$

By substituting equation (2.60) in equation (2.56), we get [1, 12]:

$$\vec{T}_e = \frac{3}{2}\frac{P}{2}\frac{L_m}{\sigma L_s L_r}\vec{\psi}_r \times \vec{\psi}_s \tag{2.61}$$

From equation (2.61), the magnitude of torque can be written as [14]:

$$T_e = \frac{3}{2}\frac{P}{2}\frac{L_m}{\sigma L_s L_r}\left|\vec{\psi}_r\right| \cdot \left|\vec{\psi}_s\right| \cdot \sin\gamma \tag{2.62}$$

where γ is the angle between the stator and rotor flux linkage space vectors.

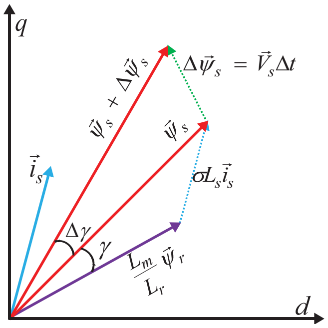

Figure 2.13: Phasor diagram of DTFC strategy in stationary reference frame

In a short period of time (sampling time) the rotor flux is considered as constant due to its large time constant T_r, but the stator flux is changed momentarily by applied voltage $\vec{V}_s$ as shown in Figure 2.13, and the corresponding change in angle γ is $\Delta\gamma$. The incremental torque ΔT_e expression is given as [18]:

$$\Delta T_e = \frac{3}{2}\frac{P}{2}\frac{L_m}{\sigma L_s L_r}\left|\vec{\psi}_r\right| \cdot \left|\vec{\psi}_s + \Delta\vec{\psi}_s\right| \cdot sin\,\Delta\gamma \tag{2.63}$$

If the applied voltage ($\vec{V}_s$) changes, then the stator flux ($\vec{\psi}_s$) will also changes consequently to satisfy the equation (2.55). This ensures that the stator flux space vector moves in the same direction as that of the applied voltage space vector. By selecting the optimum stator voltage space vectors in subsequent intervals of time, it is possible to change the stator flux in the desired way. As explained before the rotor flux is considered as constant in a short period of time (sampling period) but from the equation (2.55) it is clear that by changing the stator voltage vector, one can change the magnitude and direction of the stator flux in each sampling period. Thus, the angle between stator and rotor flux linkages (γ) can be controlled [31]. From equation (2.63) it is clear that by controlling the angle (γ) the torque can also be controlled in each sampling period.

The schematic model of DTF controlled IMD is shown in Figure 2.14. It contains the sub-blocks of stator flux and torque estimator, flux and torque hysteresis controllers, optimum voltage vector selection table to select the appropriate voltage vectors of two-level VSI, respectively. The various sub-blocks which are used in this scheme are described in the following sections.

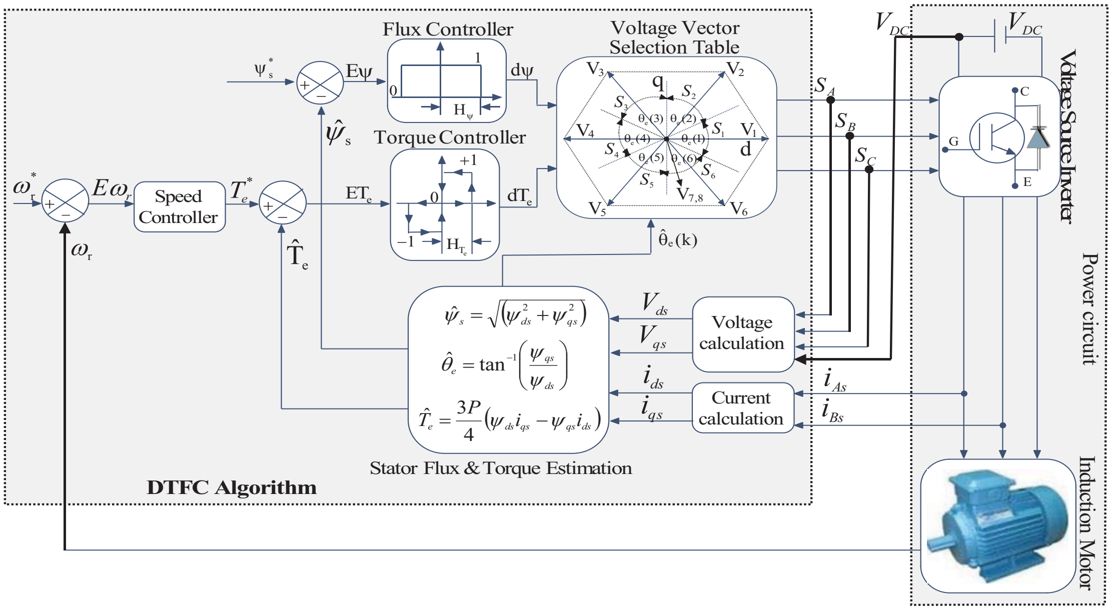

Figure 2.14: Schematic model of direct torque controlled IMD

2.6.1 Stator Flux and Torque Estimation

In DTFC scheme continuous monitoring of electrical torque and stator flux are necessary in order to achieve the high performance drive. Thus, the stator flux linkages can be derived in a stationary reference frame using measured stator current and voltage quantities as follows [1]:

$$\psi_{ds} = \int \left(V_{ds} - i_{ds} R_s \right) dt \tag{2.64}$$

$$\psi_{qs} = \int \left(V_{qs} - i_{qs} R_s \right) dt \tag{2.65}$$

The estimated stator flux can be calculated using the equations (2.64) and (2.65) as:

$$\hat{\psi}_s = \sqrt{\left(\psi_{ds} \right)^2 + \left(\psi_{qs} \right)^2} \tag{2.66}$$

The instantaneous flux position in terms of stator flux linkages is important in torque and flux control. The estimated flux position using stator flux linkages can be expressed as:

$$\hat{\theta}_e = tan^{-1} \left(\frac{\psi_{qs}}{\psi_{ds}} \right) \tag{2.67}$$

The electrical torque can be expressed as a function of the stator flux and current in a stationary reference frame as:

$$\hat{T}_e = \frac{3}{2} \frac{P}{2} \left(\psi_{ds} i_{qs} - \psi_{qs} i_{ds} \right) \tag{2.68}$$

2.6.2 Flux and Torque Hysteresis Controllers

The schematic model of flux hysteresis controller is shown in Figure 2.15**.** The stator flux is estimated from the equation (2.66) and it is compared with the reference stator flux 'ψ_s^*' to generate the error flux $E\psi$, which is fed into the two-level hysteresis flux controller. The error flux can be obtained from the difference between reference flux and estimated flux as:

$$E\psi = \psi_s^* - \hat{\psi}_s \tag{2.69}$$

where ψ_s^* *and* $\hat{\psi}_s$ are reference and estimated stator fluxes respectively, and **'^'** represent the estimated quantity.

The switching logic of the flux hysteresis controller is given in TABLE 2.1. The flux hysteresis controller has two levels of digital output (1 and 0) [1, 12].

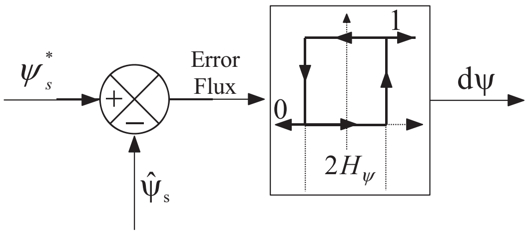

Figure 2.15: Two-level flux hysteresis controller

Table 2.1: Switching logic of flux hysteresis controller

State	Flux Hysteresis ($d\psi$)
$\psi_s^* - \hat{\psi}_s > H_\psi$	1
$\psi_s^* - \hat{\psi}_s < -H_\psi$	0

The schematic model of torque hysteresis controller is shown in Figure 2.16. The electromagnetic torque is estimated from the equation (2.68) and it is compared with the reference torque, which is generated from the speed control loop to generate the error torque 'ET_e', which is fed into the three-level hysteresis torque controller. The error torque can be obtained from the difference between the reference torque and estimated torque as follows:

$$ET_e = T_e^* - \hat{T}_e \tag{2.70}$$

where T_e^* and $\hat{T}_e$ are reference and estimated torques, respectively.

The switching logic of torque hysteresis controller is given in TABLE 2.2. The torque hysteresis controller has three levels of digital output (1, 0, and -1) [1, 12].

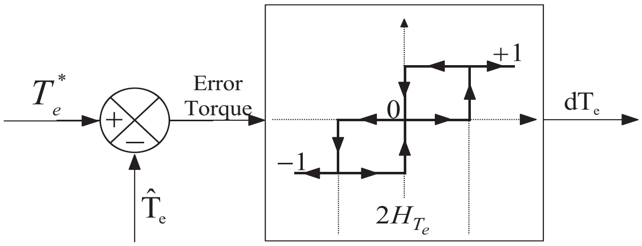

Figure 2.16: Three level torque hysteresis controller

The outputs of flux and torque hysteresis controllers are fed into the optimum voltage vector selection table to select the appropriate switching states of VSI to drive the induction motor. These gives an optimum desired control inputs. The output of switching table will give commands of stator flux and torque needed to be increased or decreased, in order to keep both of them within the pre-fixed hysteresis band limits. If stator flux is needed to be increased, then '$d\Psi=1$' and if the stator flux decrease is required, then '$d\Psi=0$'. Similarly, If the torque is needed to be increased, then '$dT_e=1$', while torque decrease is required, then $dT_e=-1$, and if there is no change in torque is needed, then $dT_e=0$ [1, 12-16].

Table 2.2: Switching logic for torque error

State	Torque Hysteresis (dT_e)
$T_e^* - \hat{T}_e > H_{Te}$	1
$-H_{Te} < \left(T_e^* - \hat{T}_e\right) < H_{Te}$	0
$T_e^* - \hat{T}_e < -H_{Te}$	- 1

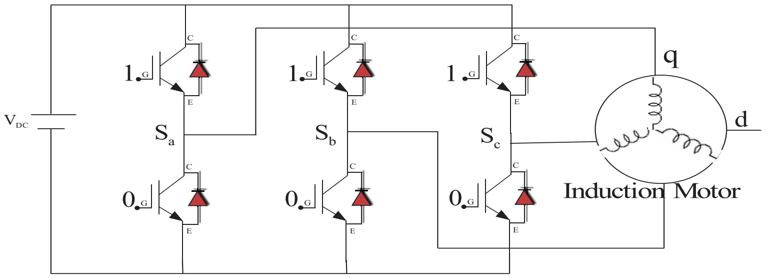

Figure 2.17: Schematic model of two-level voltage source inverter

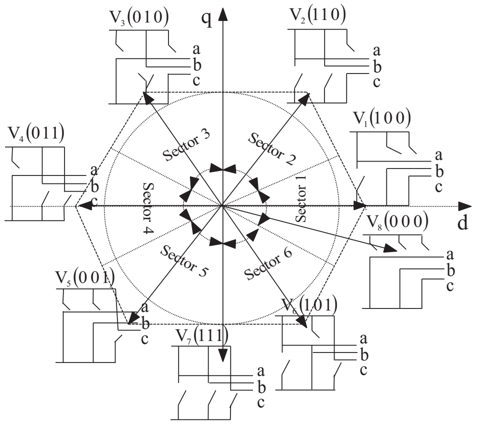

Figure 2.18: Eight possible switching states of the VSI

2.6.3 Two-level Voltage Source Inverter

A two-level VSI which is used in DTFC of IMD is shown in Figure 2.17. According to the combination of the switching states (S_a, S_b, and S_c) of VSI, there are eight possible voltage space vectors, in which six are active voltage space vectors (V_1-V_6) and two are zero voltage space vectors (V_7, V_8). The switching states of each individual voltage space vector are shown in Figure 2.18. When the upper switches are ON, then the switching value is 1 and when the lower switches get ON, then the switching value is 0 [2].

The voltage space vectors of VSI can be expressed as:

$$V_k = \begin{cases} \frac{2}{3} V_{DC} \exp\left[j(k-1)\frac{\pi}{3} \right] & k = 1, 2, \ldots, 6. \\ 0 & k = 7,8. \end{cases} \tag{2.71}$$

2.6.4 Optimum Voltage Vector Selection Table

The selection of switching states based on the position of stator flux vector, and also the requirement of the stator flux and torque, which are needed to be increased or decreased can be described from Figure 2.19. The decoupled control of stator flux and torque is achieved by acting on the radial and tangential components of the stator flux vector as these two (radial and tangential) components are directly proportional to the applied voltage vector. As mentioned earlier, the stator flux space vector moves in the same direction as that of the applied voltage space vector. The tangential component of the voltage space vector will force the stator flux vector to move away from the rotor flux vector, thus increasing the angle γ between them. According to equation (2.63), it is clear that when the angle γ is increased, then the torque will be increased. Hence, the tangential component of stator voltage is responsible for the change in torque whereas the radial component of stator voltage is responsible for the change in stator flux [1, 12].

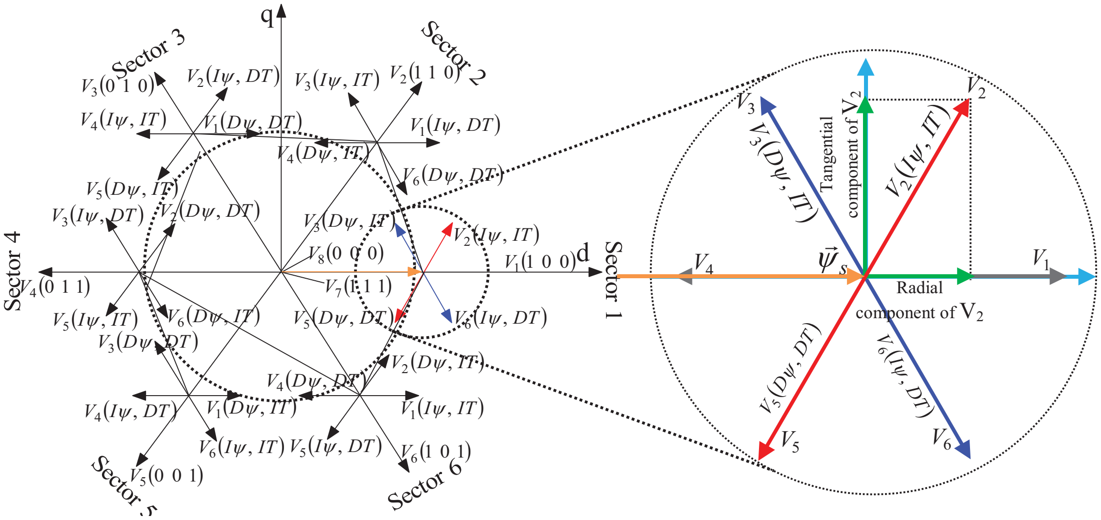

Figure 2.19: The voltage space vector influence on stator flux and torque in six sectors

Table 2.3: Optimum voltage vector selection table

Hysteresis Controller		Sector Selection $\hat{\theta}_e(K)$					
Flux (dψ)	Torque (dT_e)	Sector 1 (330 to 30°)	Sector 2 (30 to 90°)	Sector 3 (90 to 150°)	Sector 4 (150 to 210°)	Sector 5 (210 to 270°)	Sector 6 (270 to 330°)
	1	V_2	V_3	V_4	V_5	V_6	V_1
		110	010	011	001	101	100
1	0	V_7	V_8	V_7	V_8	V_7	V_8
		111	000	111	000	111	000
	-1	V_6	V_1	V_2	V_3	V_4	V_5
		101	100	110	010	011	001
	1	V_3	V_4	V_5	V_6	V_1	V_2
		010	011	001	101	100	110
0	0	V_8	V_7	V_8	V_7	V_8	V_7
		000	111	000	111	000	111
	-1	V_5	V_6	V_1	V_2	V_3	V_4
		001	101	100	110	010	011

In k^{th} (where k=1 to 6) sector voltage vector V_k and its two adjacent voltage vectors will generate positive radial component and the remaining voltage vectors will generate negative radial component. Similarly, the voltage vector starting from V_k the following two voltage vectors in anticlockwise direction will generate positive tangential component, whereas the following two voltage vectors in a clockwise direction will generate negative tangential component. When the zero vectors (V_7, V_8) are selected the torque and flux will remain in the same position [1]. Based on this the optimum voltage vector selections in each sector, which are obtained from the eight possible states of the inverter is summarized in the optimum voltage vector selection Table 2.3. Therefore, the torque can be directly controlled, i.e., increased or decreased almost instantly by moving the stator flux linkage space vector to the required position, being determined by torque demand. This, in turn can be done quickly by selecting the appropriate voltage vector.

2.7 Speed Controller

The performance of the direct torque and flux controlled induction motor drive highly depends on the design of the speed controller.

2.7.1 PI Speed Controller

The PI speed controller has been widely used in industrial control applications due to its simple construction and can provide a satisfactory performance over a wide range of speed operation [10-35]. It also decreases the steady state error and improves the dynamic performance of the system. Therefore, the majority of speed control schemes in the literature for the DTFC of IMD used a simple fixed gain PI controller to acquire the reference torque. The schematic model of PI speed controller is shown in Figure 2.20**.** The reference speed is compared with the actual speed based on equation (2.72) and the error speed is fed into the constant gain PI speed controller to get a reference torque command. The gain values of PI speed controller are given in Appendix C.

$$E\omega_r = \omega_r^* - \omega_r \tag{2.72}$$

$$T_e^* = K_p E\omega_r + K_i \int E\omega_r dt \tag{2.73}$$

where $E\omega_r$ and T_e^* are the error speed and reference torque, respectively.

2.8 Simulation Results

The DTFC of an IMD is mathematically modelled in the MATLAB/SIMULINK environment. The parameters of the squirrel cage IM are illustrated in the Appendix A. The dynamic model of an induction motor referred to a stationary reference frame (d, q-axis) is considered for DTFC scheme, which is derived in section 2.2. The simulated model is then used to verify the performance of the drive using PIC under various operating conditions, such as no-load torque, load torque and speed tracking performances, respectively.

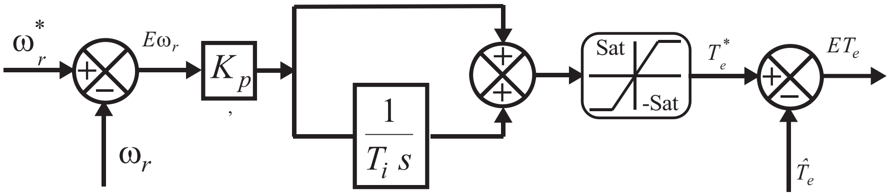

Figure 2.20: Schematic model of PI speed controller

2.8.1 Performance under No-load Torque Condition

Initially, the performance of IM drive is observed under no-load torque operation using PIC shown in Figure 2.21. The presented results of electromagnetic torque, stator flux, reference and actual speeds, stator current, stator flux dq-components in a stationary reference frame and stator flux component in XY-plane are shown in Figure 2.21 (trace-i)-(trace-vi), respectively. When the reference speed of 1200 rpm is applied, the IM develops an electromagnetic torque of 20 Nm with high amplitude of the stator current (±5.4 A) to reach the set reference speed. The IM starts at zero speed and it is settled (i.e. 1200 rpm) at 0.695 s with an overshoot of around 13.5 rpm (shown in zoomed view of Figure 2.21 (iii)). Similarly, the torque and stator currents are settled at the same time as shown in Figure 2.21 (i) and (v), respectively. However, the stator flux ($\hat{\psi}_s$) and stator flux dq-components (i.e. ψ_{ds} and ψ_{qs}) in a stationary reference frame are almost same throughout the operation (i.e. from starting to the steady state) shown in Figure 2.21 (ii) and (iv), respectively. The steady-state performance of the drive is shown in Figure 2.22 (i)-(iv). It is observed that the flux and torque ripple contents are ±0.04 Wb and ±1.75 Nm, respectively.

2.8.2 Performance under Load Torque Condition

The performance of the IMD is observed under sudden load torque operating condition is shown in Figure 2.23 (a)-(b). The sudden load torque of 9 Nm is applied at 1.4 s when IM drive was operating at steady state speed. When the sudden load torque is applied, the IM draws large amplitude of stator current (i.e. ±3.4 A) and undershoot around 1.125% of reference speed is shown in Figure 2.23 (a)-(ii) and (iii), respectively. It is also observed that the recovery time of actual speed under such operating condition is 0.32 s. Similarly, when the load torque is removed, an overshoot around 1.108% of the reference speed appearance shown in Figure 2.23 (vi). The load torque, stator current and error speed are shown in Figure 2.23 (i), (ii) and (iv), respectively.

2.8.3 Tracking Performance of the Speed Commands

Tracking performance of the IM drive is observed through the applications of various sudden changes in step and square speed commands. The simulation results for each case are presented as follows.

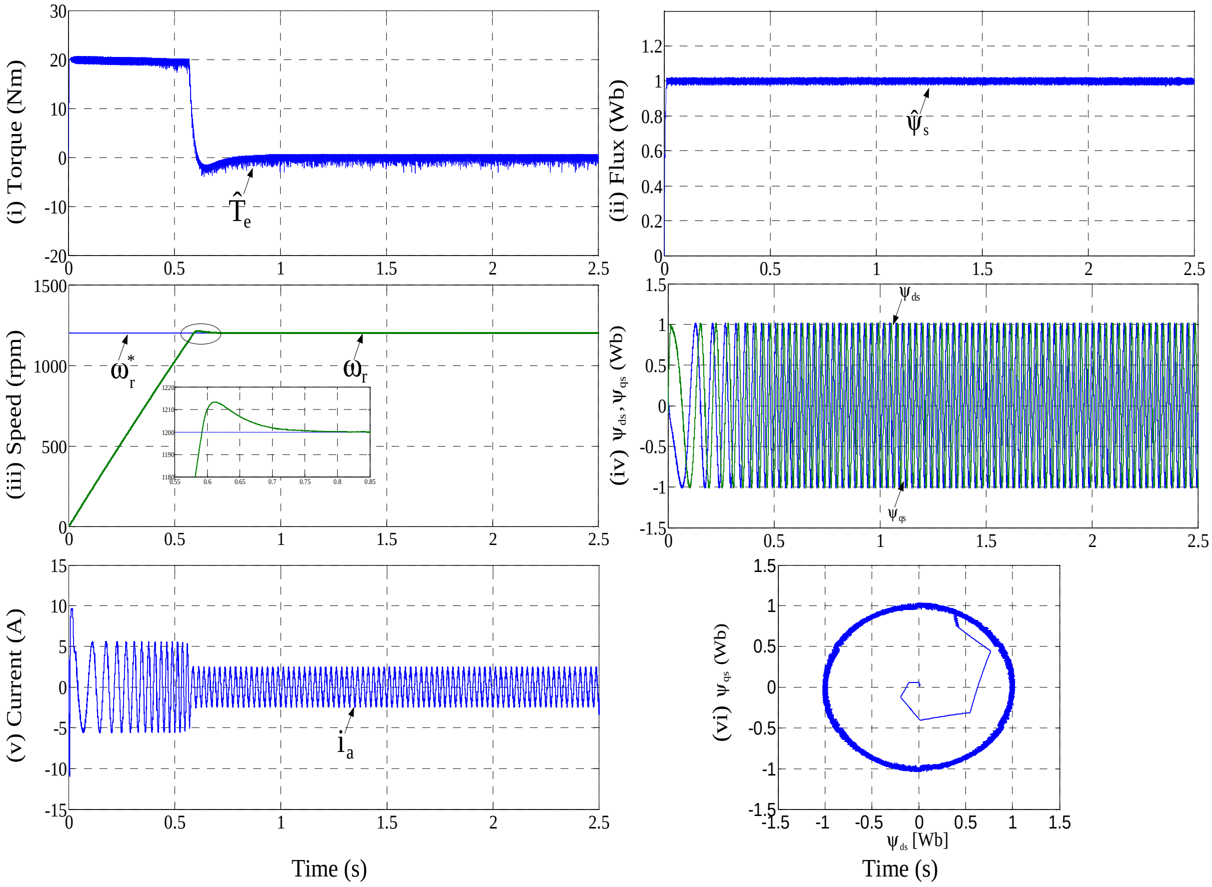

Figure 2.21: Performance of the IMD under no-load torque operating condition: (i) Torque, (ii) stator flux, (iii) speed, (iv) stator flux dq-components in stationary reference frame, (v) stator current and (vi) stator flux plotted in X-Y plane

Performance under reversal speed command:

The performance of the IMD is observed under the reversal speed command shown in Figure 2.24 (a). The reversal speed command from +1200 rpm to -1200 rpm is applied at 2 s. The actual speed reaches its reference speed during reversal speed at 3.17 s. The reference and actual speeds are illustrated in Figure 2.24 (a)-(iii), which reveals that the actual speed tracking the reference speed with an overshoot of around 13.4 rpm. The torque, stator current and stator flux dq-axis components in a stationary reference frame are shown in Figure 2.24 (a)-(i), (ii) and (iv), respectively. The reversal speed transient response of Figure 2.24 (a) is shown in Figure 2.25 (b).

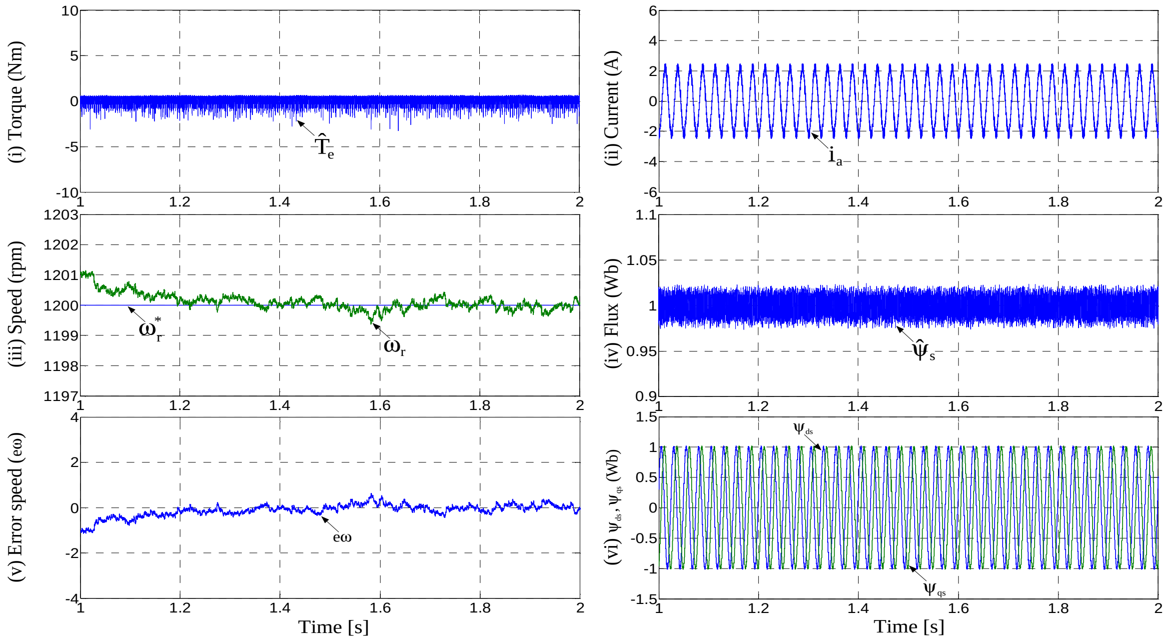

Figure 2.22: Steady-state performance of the IMD under no-load torque operating condition: (i) Torque, (ii) current, (iii) speed, (iv) stator flux, (v) error speed and (vi) stator flux dq-components in stationary reference frame

Performance under step change in speed command:

The performance of the IMD is observed under step changes in speed command is shown in Figure 2.24 (b). The step change in speed command of 300 rpm is applied in four steps (i.e. 600 rpm ⟶ 900 rpm ⟶ 1200 rpm ⟶ 900 rpm ⟶ 600 rpm) at 1.4 s, 2.4 s, 3.6 s, etc. The corresponding reference and actual speed responses under such speed command are shown in Figure 2.24 (b)-(iii). From Figure 2.24 (b)-(iii), it is observed that the actual speed settled the reference speed (from 600 rpm to 900 rpm) in 0.22 s with an overshoot of 1.1%. The torque, current and d and q-axis stator flux components in a stationary reference frame are shown in Figure 2.24 (i), (ii) and (iv), respectively.

(a)

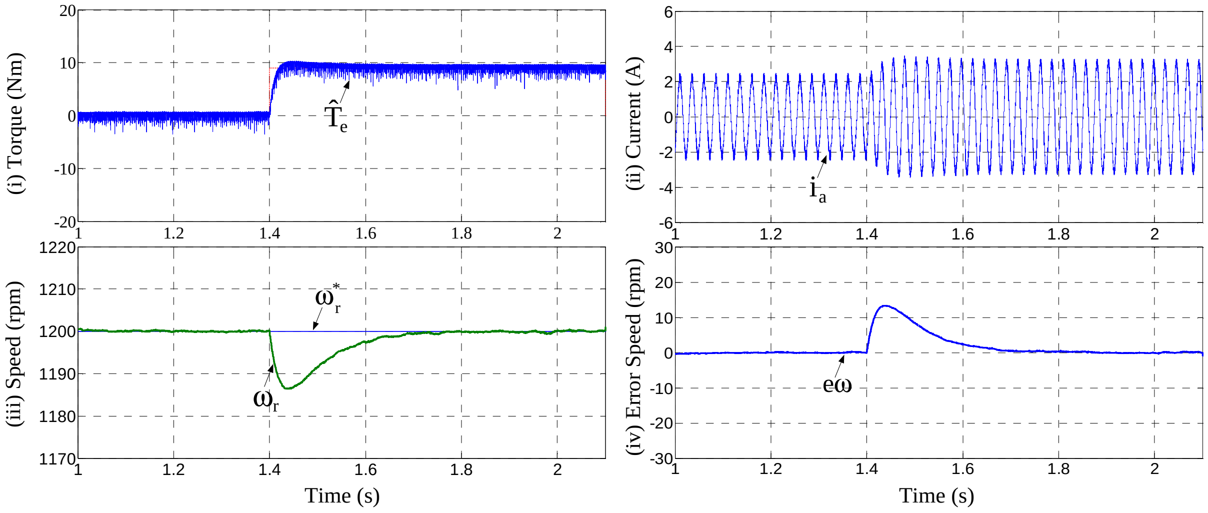

(b)

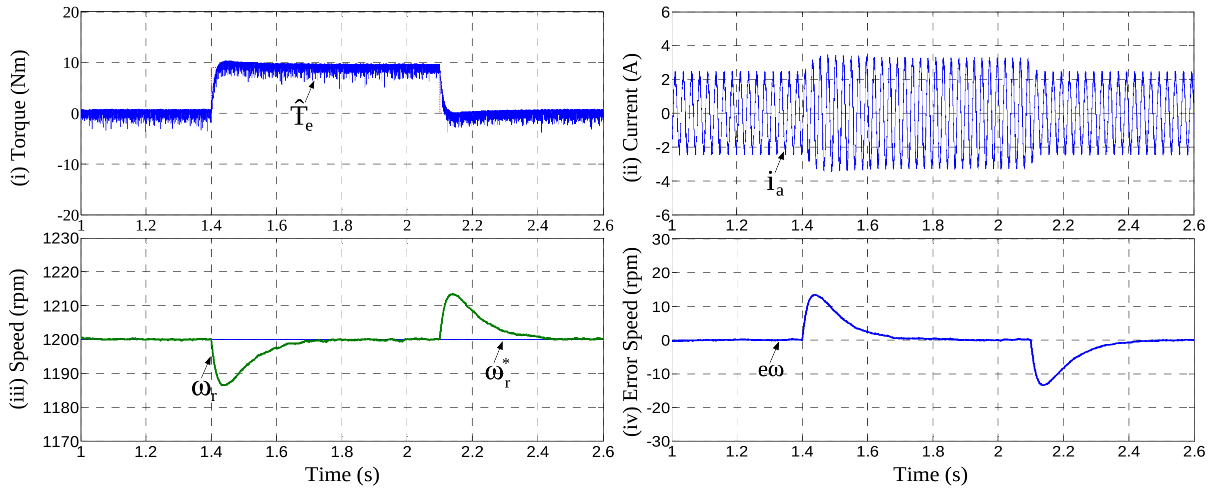

Figure 2.23: Performance of the IMD under load torque: (a) applied and (b) applied and withdrawn: (i) Torque, (ii) stator current, (iii) speed and (iv) error speed

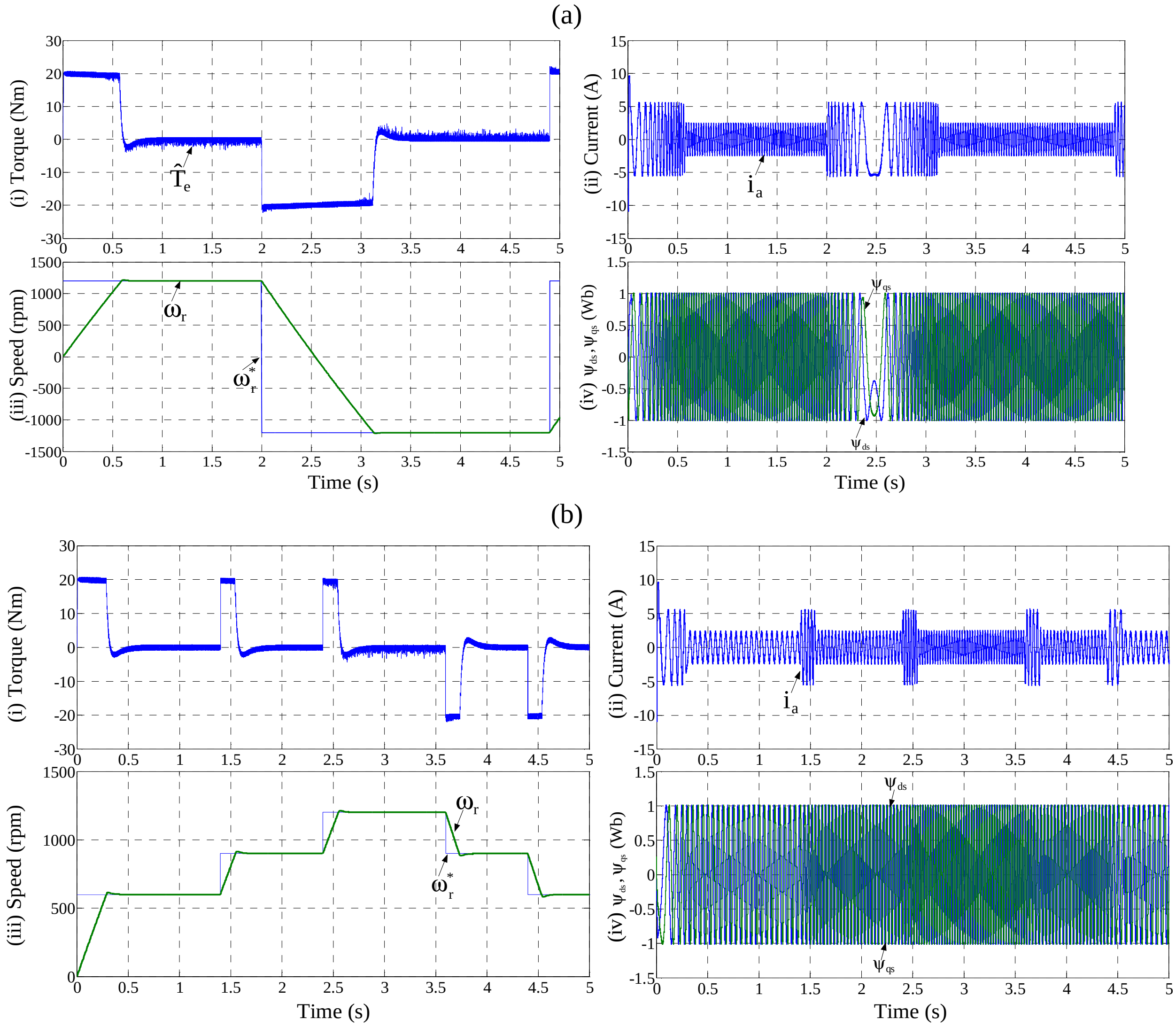

Figure 2.24: Performance of the IMD under the command of: (a) reversal speed and (b) change in speed: (i) torque, (ii) stator current, (iii) speed and (iv) stator flux components

Performance under square speed command:

The performance of the IMD is observed under square speed command is shown in Figure 2.25 (a). The square change in speed command of 600 rpm is applied in four steps (i.e. 1200 rpm ⟶ 600 rpm ⟶ 1200 rpm ⟶ 600 rpm ⟶ 1200 rpm) at 1 s, 2 s, 3 s, etc. The actual speed under such speed command is shown in Figure 2.25 (a)-(ii). From Figure 2.25 (a)-(ii), it is observed that the actual speed settled the reference speed (from 600 to 1200 rpm) in 0.45 s with an overshoot around 1.22% of the reference speed. The electromagnetic torque and stator currents are shown in Figure 2.25 (a)-(i) and (iii), respectively.

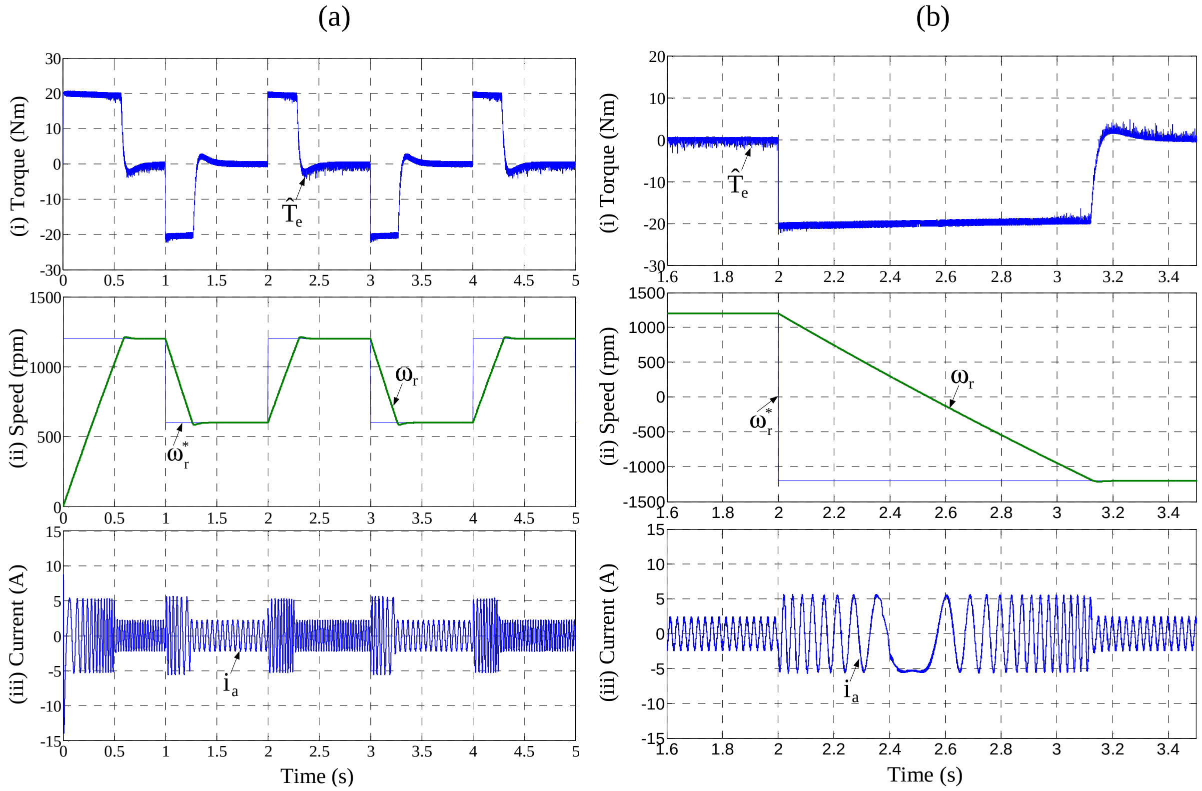
(a) (b)

Figure 2.25 Performance of the IMD under the command of: (a) sudden change in square speed and (b) reversal speed: (i) torque, (ii) speed and (iii) stator current

2.9 Conclusion

This chapter reviews the vector control based induction motor drive. Initially, the mathematical modelling of IM using state space vector theory is presented. It is simulated in the MATLAB/SIMULINK environment using scalar control method. In the scalar control method, the dynamic performance of IM drive is very poor and sluggish. In order to improve the performance, a closed loop control of indirect field oriented control scheme is implemented. However, the IFOC scheme requires coordinate transformations, current controllers and is complex to implement. Therefore, direct torque and flux control scheme is implemented to improve the performance of the IMD. The detailed results of simulation studies using a PI speed controller are presented under various operating conditions, such as no-load, load, sudden change in speed and speed reversal, respectively.

The PI controller offers satisfactory performance over a wide range of ideal operation. However, the PI controller is unable to provide the satisfactory performance under various disturbance conditions, such as the sudden changes in speed and load torque, respectively. Moreover, it requires the precise mathematical model, continuous tuning and accurate gain values to achieve high-performance. In order to overcome these drawbacks, nonlinear speed controllers are highly desirable to improve the performance of the drive and also disturbance rejections. Therefore, Type-1 fuzzy logic control and Type-2 fuzzy logic control based speed controllers are considered for disturbance rejections which are discussed in detail in chapter 3.

Chapter 3

Type-1 and Type-2 Fuzzy Logic Control Based Direct Torque and Flux Control of An Induction Motor Drive

CHAPTER 3: TYPE-1 AND TYPE-2 FUZZY LOGIC CONTROL BASED DIRECT TORQUE AND FLUX CONTROL OF AN INDUCTION MOTOR DRIVE

In the previous chapter, DTFC of an IMD using PIC based speed controller is discussed. The PIC is not an adaptive controller with respect to the various disturbances. It is concluded that under various disturbance conditions, the PIC based speed controller is unable to provide the satisfactory performance. Therefore, in order to improve the drive performance under various disturbance conditions, one has to choose perfect speed controller.

In this chapter, DTFC of an IMD using Type-1 Fuzzy Logic Controller (T1FLC) and Type-2 Fuzzy Logic Controller (T2FLC) based speed controller schemes are proposed to improve the performance of the IMD under various disturbance conditions. Initially, the T1FLC based speed controller is implemented to achieve high performance drive in both dynamic as well as steady-state operating conditions. However, the Type-1 Fuzzy Sets (T1FS) are certain and unable to work effectively when a higher degree of uncertainties present in the system, which can be caused by different load torque disturbances, sudden change in speed and process noise, etc.

In order to overcome the above mentioned drawbacks, T2FLC based speed controller is proposed to handle the higher degree of uncertainties and enhance the drive performance. Moreover, it is robustness to various load torque disturbances. The performance verification through computer simulation of a proposed control scheme is essential prior to its experimental implementation. The detailed performances of both control schemes are carried out in a MATLAB/SIMULINK environment to support the feasibility of proposed controller under various operating conditions, such as no-load, load, and various sudden changes in speed, respectively.

This chapter is organized as follows:

- *The details of T1FLC and T2FLC which includes the type of fuzzy inference system, various methods of defuzzification and design of control rules are presented in section 3.2 and 3.3, respectively.*
- *The simulation results of T1FLC and T2FLC strategies using MATLAB/SIMULINK are presented in sections 3.4.*
- *Finally, the conclusion and remarks are presented in section 3.5.*

3.1 Introduction

The fuzzy logic system (FLS) concept was introduced by Lotfi Zadeh in 1965 to process data and information affected by non-probabilistic uncertainty/imprecision [48]. Soon after, it was proven to be an excellent choice for many control applications, since it mimics human control logic. These were designed to represent mathematically the vagueness and uncertainty of linguistic problems, thereby obtaining formal tools to work with intrinsic imprecision in a different type of problems [49-63]. It is considered as a generalization of the classical set theory. Intelligent systems based on FLC are fundamental tools for nonlinear complex system modelling.

In this thesis, the T1FLC is developed to improve the performance of IMD in dynamic as well as steady-state operating conditions. The T1FLC has an adaptive control approach and gives a robust performance under various disturbance conditions and it can cope with complicated nonlinear systems, which have a large degree of uncertainty. It does not require accurate mathematical modelling and parameters unlike PIC, which makes the T1FLC highly suitable for the drive applications.

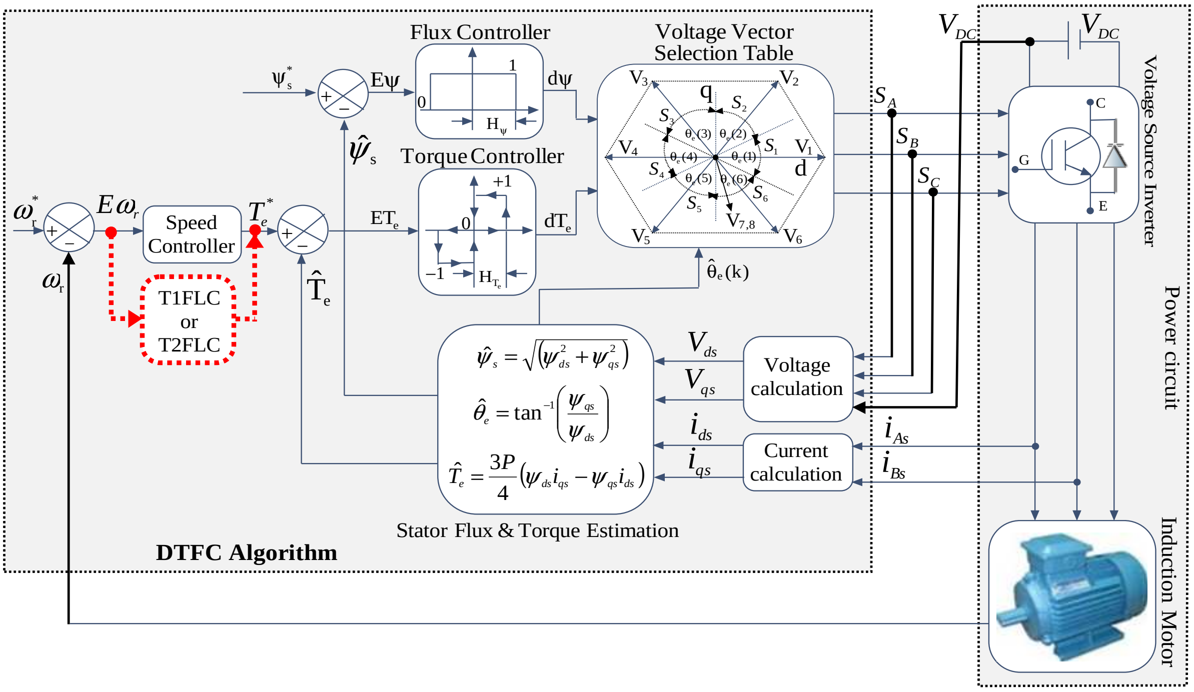

Figure 3.1: Schematic model of DTFC of an IMD using fuzzy logic controller based speed controller

3.2 Type-1 Fuzzy Logic Controller

The DTFC of an IMD is developed using a T1FLC based speed controller shown in Figure 3.1. In this Figure 3.1, the PIC is replaced by T1FLC. From the PIC, the output of the controller can be expressed as [29, 72-73]:

$$T_e^* = K_p E\omega_r + K_i \int E\omega_r dt \tag{3.1}$$

Applying differentiation on both sides of equation (3.1), we get:

$$\frac{dT_e^*}{dt} = K_p \frac{dE\omega_r(t)}{dt} + K_i E\omega_r(t) \tag{3.2}$$

From equation (3.2), it is clear that the rate of change of torque is directly proportional to inputs of the speed controller, i.e., error speed ($E\omega_r$) and change in error speed ($\Delta E\omega_r$). The measured speed (ω_r) is compared with the set reference speed (ω_r^*) and the error speed ($E\omega_r$) signal is processed through a T1FLC, which contributes to zero steady state error in tracking the reference speed signal. The T1FLC has two input variables, error speed ($E\omega_r$), which is derived from the equation (3.3) and the rate of change in error speed ($\Delta E\omega_r$), which is derived from the equation (3.4) as follows [60-62]:

$$E\omega_r(k) = \omega_r^*(k) - \omega_r(k) \tag{3.3}$$

$$\Delta E\omega_r = E\omega_r(K) - E\omega_r(K-1) \tag{3.4}$$

where ω_r and ω_r^* are the actual and reference speeds of the rotor respectively, $E\omega_r(K-1)$ and $E\omega_r(K)$ are previous and present error speeds, respectively. When a change of torque $\Delta T_e^*(k)$ is obtained, then the output of the speed controller is [175-178]:

$$T_e^*(k) = T_e^*(K-1) + \Delta T_e^*(K) \tag{3.5}$$

where $T_e^*(K-1)$ is the previous value of the reference torque from the speed T1FLC.

The T1FLC can be regarded as a mapping set of antecedent Type-1 fuzzy sets (T1FS) into a consequent set. Initially, it is a mapping from $X = X_1,.....,X_n$, where $X_i \subset \Re$, $i = 1,2,...,n$, into $Y_i \subset \Re$. The schematic model of T1FLC is shown in Figure 3.2, it consists of four sub-blocks as follows [48-49, 89-90]:

- Fuzzifier
- Rule Base
- Fuzzy Inference System (FIS)
- Defuzzification

3.2.1 Fuzzification

The fuzzification block is used to convert the crisp inputs $x = (x_1,.....,x_n) \in X$ into different kinds of T1FS.

3.2.2 Rule Base

The rule base is demonstrated in the form of “IF-THEN” which represents expert knowledge. By considering multi-inputs $x_1 \in X_1,...,x_p \in X_p$ and single-output $y \in Y$ FLS, the two kinds of “IF-THEN” expressions can be represented as follows [48, 81]:

$$R^l: \text{IF } x_1 \text{ is } F_1^l \text{ AND } x_2 \text{ is } F_2^l ,\ldots.., x_n \text{ is } F_n^l \text{ THEN } y \text{ is } G^l \qquad l = 1,2,\ldots,M .$$

This rule base represents a Type-1 fuzzy relation between the input space $X_1 \times \ldots . \times X_p$ and the output space Y of the FLS. It is known that a multi-antecedent and single-consequent rule can be considered as a group of multi-input and single-output rules [48].

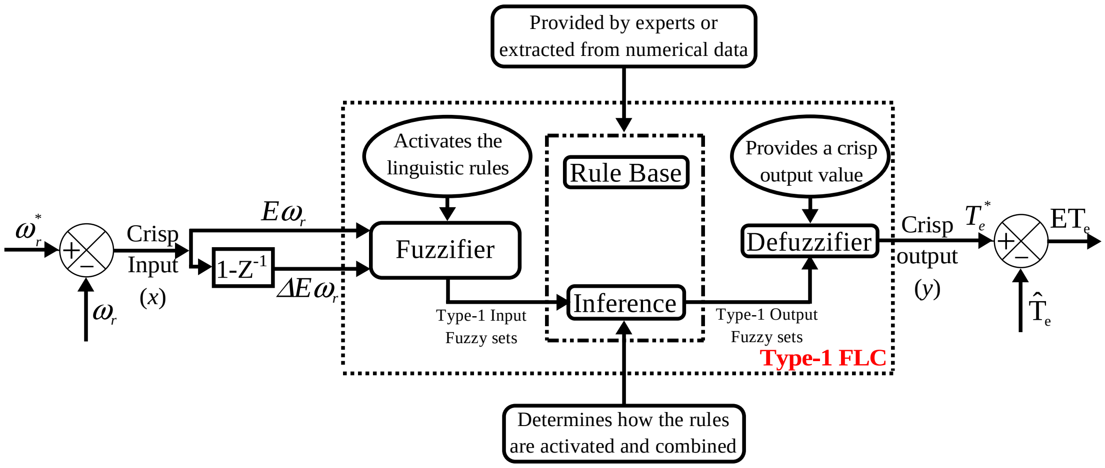

Figure 3.2: Schematic model of Type-1 FLC

3.2.3 Fuzzy Inference Systems

The Type-1 fuzzy inference system (T1FIS) block is used to combine fuzzy IF-THEN rules from the fuzzy rule base into a mapping from the input T1FSs to output T1FSs [48]. The FIS is a famous computing framework based on the concepts of fuzzy reasoning, fuzzy IF-THEN rules and fuzzy set theory [89-90]. It has widely been used in a variety of successful applications till date, such as robotics, expert systems, automatic control of data classifications, target tracking, decision analysis and pattern recognition, etc.

The general construction of a T1FIS contains three blocks; a database, which define the membership functions (MFs) used in the fuzzy rules, a rule base, which contains a rule selections and a reasoning mechanism, which executes the inference method upon the fuzzy rules and given facts to develop a reasonable output [60-62]. The T1FIS takes the input variables either fuzzy singletons or crisp and it produces the fuzzy sets as an output. In some cases, it can have a crisp output where especially the T1FIS is used as a controller. Hence, we require a defuzzification method to convert the fuzzy set into a crisp value. The schematic model of a T1FIS is illustrated in Figure 3.3.

The individual rules are evaluated using Mamdani fuzzy implication schemes. There are two types of implication schemes mainly used for evaluation of rules, such as Mamdani Max-min composition (MMC) and Max-prod composition (MPC) schemes. The differences between these two FIS lie in the consequents of their fuzzy rules, and thus their aggregation and they differ accordingly [48].

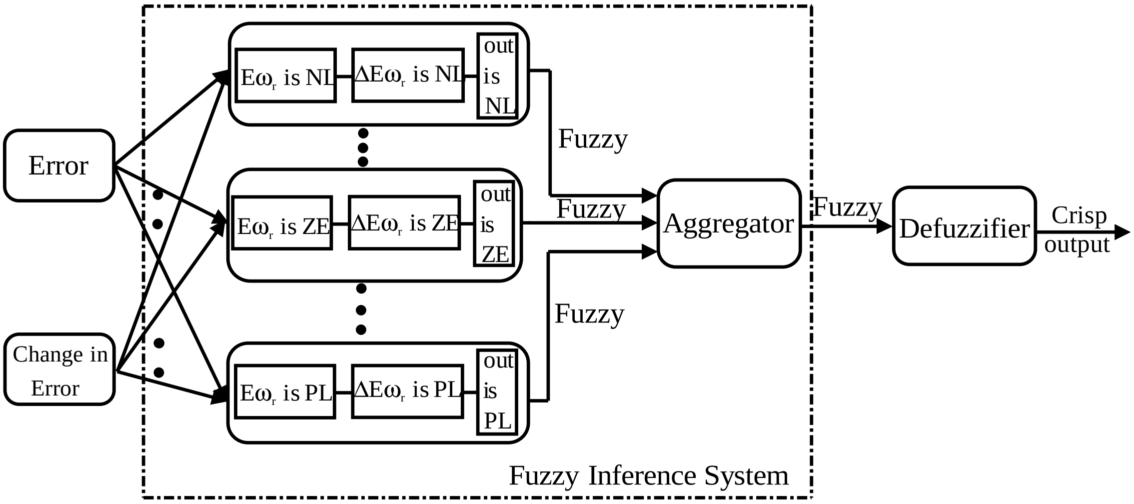

Figure 3.3: Schematic model of T1FIS

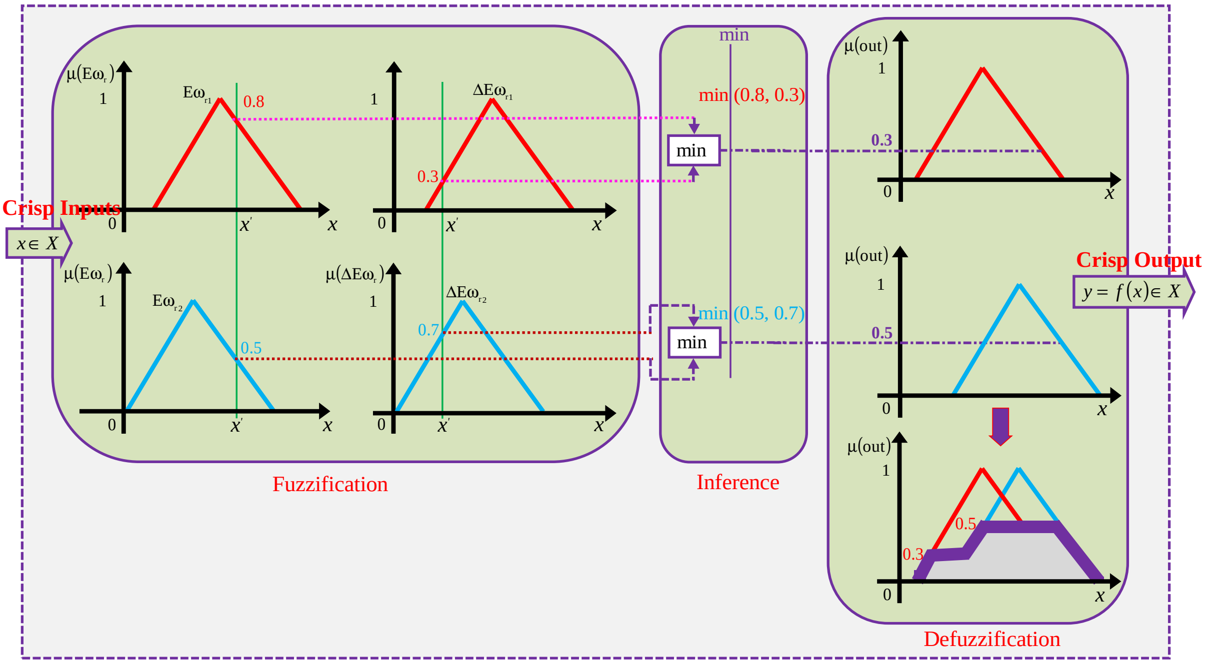

Figure 3.4: The T1FIS using Mamdani max-min composition

3.2.3.1 Mamdani Max-min Composition Scheme

The Mamdani T1FIS using MMC method is illustrated in Figure 3.4. In this Figure 3.4, the aggregation used is Maximum operation and the implication is Minimum operation.

3.2.3.2 Mamdani Max-prod Composition Scheme

The T1FIS using Mamdani MPC scheme is shown in Figure 3.5. In this Figure 3.5, the aggregation used is Maximum operation and the implication is product operation [48].

3.2.4 Defuzzification

The defuzzification block is used to generate the crisp output value from the T1FS that appears at the output of the T1FIS block shown in Figure 3.2.

$$\mu_A(x) = \text{defuzz}(x, mf, Type) \tag{3.6}$$

where, $\text{defuzz}(x, mf, Type)$ provides a defuzzified value of a MF positioned on associated variable value ‘x’ using one of the various defuzzification methods, according to the type of argument.

In the literature, various types of defuzzification methods are presented, such as bisector-of-area, center-of-sum, centroid of area, mean-of-maximum, and height, etc [79-82]. Defuzzification is performed according to the MF of the output variable. For instance, assume that we have the result in Figure 3.4 at the end of the inference. In Figure 3.6, the shaded areas belong to the fuzzy result. The purpose is to obtain a crisp value, represented with a dot in Figure 3.6, from the fuzzy result. Various defuzzification schemes are shown in Figure 3.7. In this control scheme, the centroid or center-of-area (COA) method is chosen for the defuzzification purpose.

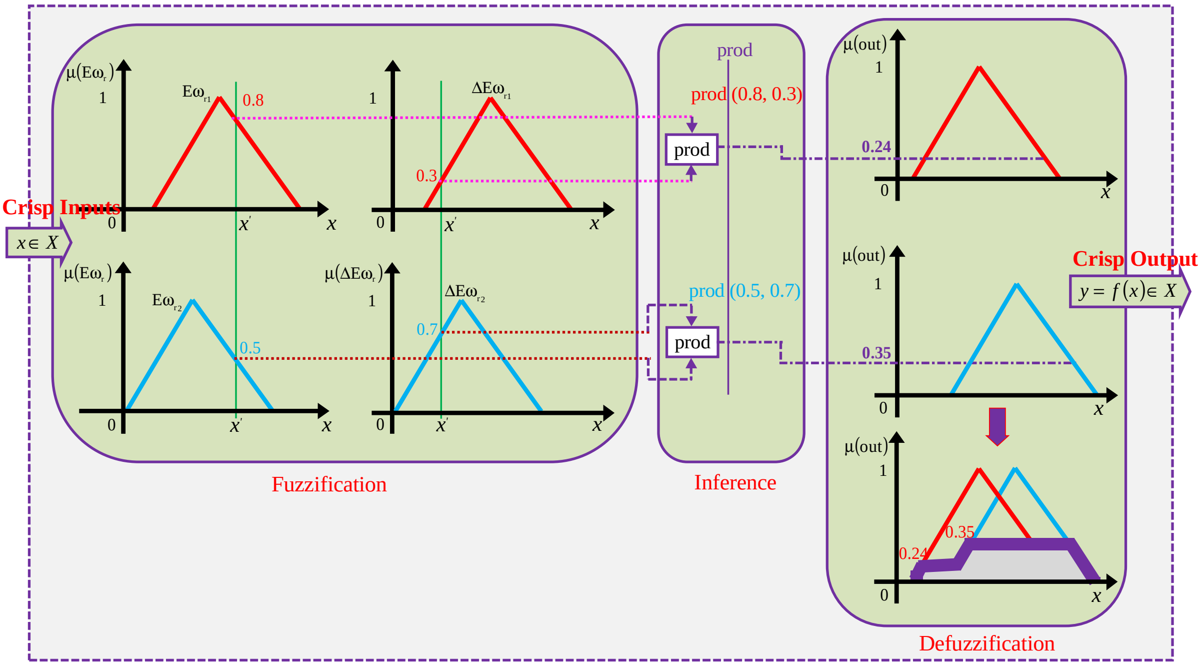

Figure 3.5: The T1FIS using Mamdani max-prod composition

The centroid type defuzzification returns the COA under the curve. The COA can be expressed mathematically as follows [48]:

$$COA = \frac{\int_a^b \mu_A(x)\, x\, dx}{\int_a^b \mu_A(x)\, dx} \tag{3.7}$$

The equation (3.7) can be expressed with a discretized universe of discourse as follows:

$$COA = \frac{\sum_{i=1}^{n} \mu_A(x_i)\, x_i}{\sum_{i=1}^{n} \mu_A(x_i)} \tag{3.8}$$

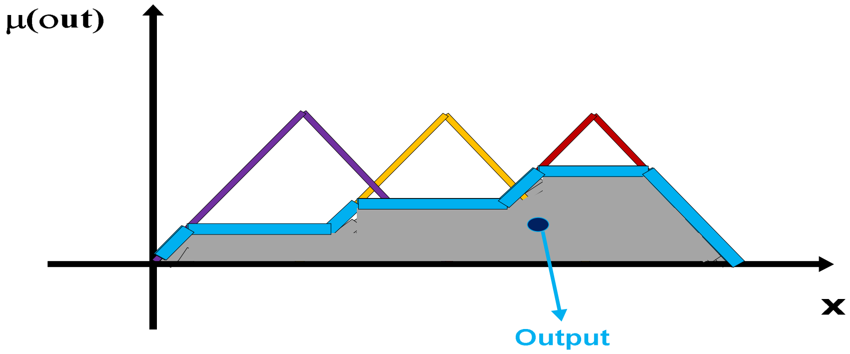

Figure 3.6: Defuzzification

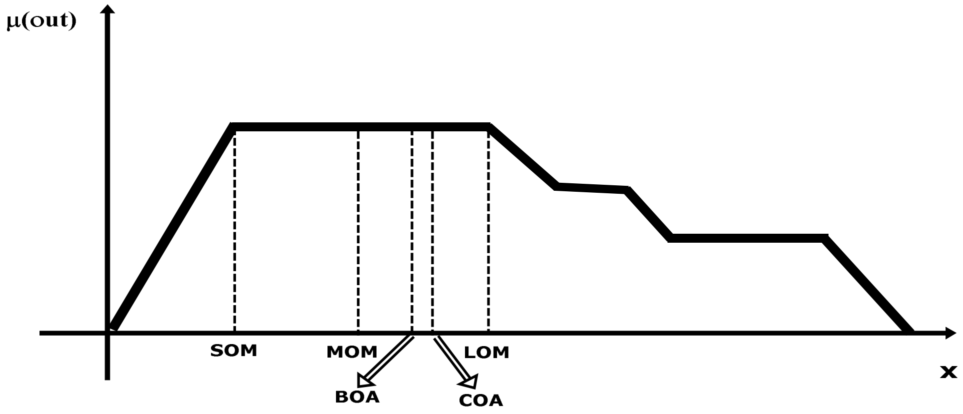

Figure 3.7: Various types of defuzzification schemes

3.2.5 Design of Control Rules

The T1FLC transforms a linguistic control strategy into an automatic control strategy, and fuzzy rules are constructed from an experience database or expert knowledge. In a T1FLC, a rule base is constructed to control the output variable. A fuzzy rule is a simple IF-THEN rule with a condition and a conclusion [48]. The T1FLC rule base design involves defining rules that relate the input variables to the output model properties. Initially, the error speed ‘$E\omega_r$’ and the rate of change in error speed ‘$\Delta E\omega_r$’ has been placed in the input variables of T1FLC [60]. Then the output variable of T1FLC produces the controlled reference torque ‘T_e^*’. The fuzzy rules, for a MISO system with more than one input can be expressed with syntax as:

Rule: IF {error speed ‘$E\omega_r$’ is ‘X’ AND rate of change of error speed ‘$\Delta E\omega_r$’ is Y} THEN {control output ‘T_e^*’ is Z}

where, $\Delta E\omega_r$ and T_e^* are the input/output linguistic or fuzzy variables, whereas X, Y and Z are the input/output linguistic values (NL, NM, etc.).

To convert these numerical variables into linguistic variables, the following seven fuzzy levels or sets are chosen for better control performance as: negative large (NL), negative medium (NM), negative small (NS), zero (ZE), positive small (PS), positive medium (PM) and positive large (PL) and are summarized in Table 3.1.

T1FS are selected based on the speed error. In this thesis, we have considered 7x7 MF. Readers may raise questions like; Why 7x7 MF only, Why not 3x3 or 5x5 MF? While considering 3x3 or 5x5 MF, the actual speed of IM is unable to track the reference speed and produces the error speed due to speed difference. Because of this error speed, the system is unable to produce good performance. So to avoid these difficulties, we have considered 7x7 MF. With the use of 7x7 MF, the actual speed is able to track the reference speed accurately.

3.2.5.1 Triangular Membership Function

In this thesis, we have considered TMF, because it is simple to implement and fast for computation is shown in Figure 3.9 (a), the parameters a, b and c represent the ‘x’ coordinates of the three vertices of $\mu_A(x)$ in a T1FS ‘A’. The triangular curve is a function of a vector *x*, and depends on three scalar parameters *a*, *b*, and *c*, as given by [48]:

$$triangle(x,a,b,c) = \mu_A(x) = \left\{ \begin{matrix} 0 & if\ x \le a \\ \dfrac{x-a}{b-a} & if\ a \le x \le b \\ \dfrac{c-x}{c-b} & if\ b \le x \le c \\ 0 & if\ x \ge c \end{matrix} \right\} \tag{3.9}$$

The equation (3.9) can also be represented using min and max as follows:

$$triangle(x,a,b,c) = \mu_A(x) = max\left(min\left(\frac{x-a}{b-a}, \frac{c-x}{c-b} \right), 0 \right) \tag{3.10}$$

where, a and c are the lower and upper boundaries and the membership grade (MG) is zero, b is the centre and the MG is 1.

3.2.6 Rule Base

The schematic model of T1FLC with rule base is shown in Figure 3.8. The components of the rule base table are determined based on the theory that the large error needs coarse control of the transient state, which requires coarse input/output variables and small error needs fine control in the steady state, which requires fine input/output variables as illustrated in Figure 3.9.

The rule base of a Type-1 FLC is created using 49 rules as follows:

Rule 1: IF $E\omega_r$ is “NL” AND $\Delta E\omega_r$ is “NL” THEN T_e^* is “NL”,

.

Rule 25: IF $E\omega_r$ is “ZE” AND $\Delta E\omega_r$ is “ZE” THEN T_e^* is “ZE”, Rule 49: IF $E\omega_r$ is “PL” AND $\Delta E\omega_r$ is “PL” THEN T_e^* is “PL”.

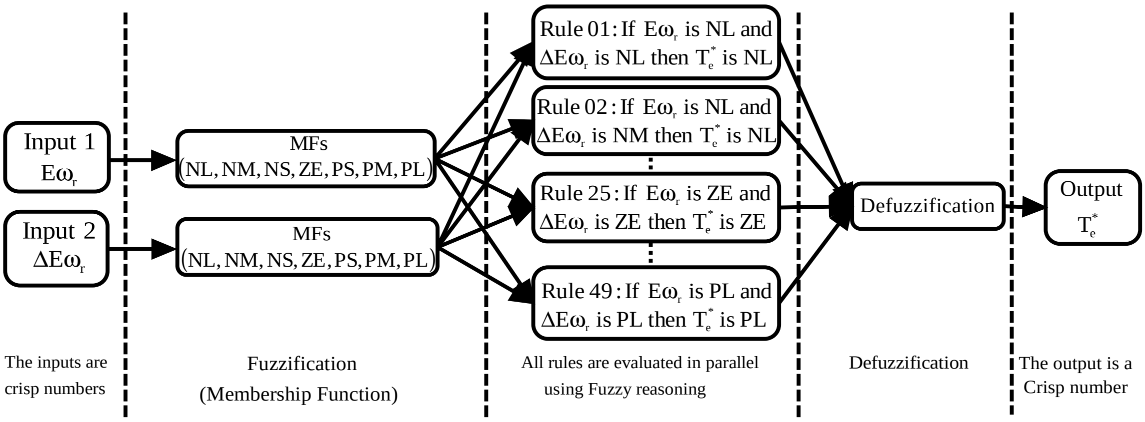

Figure 3.8: Schematic model of T1FLC with rule base

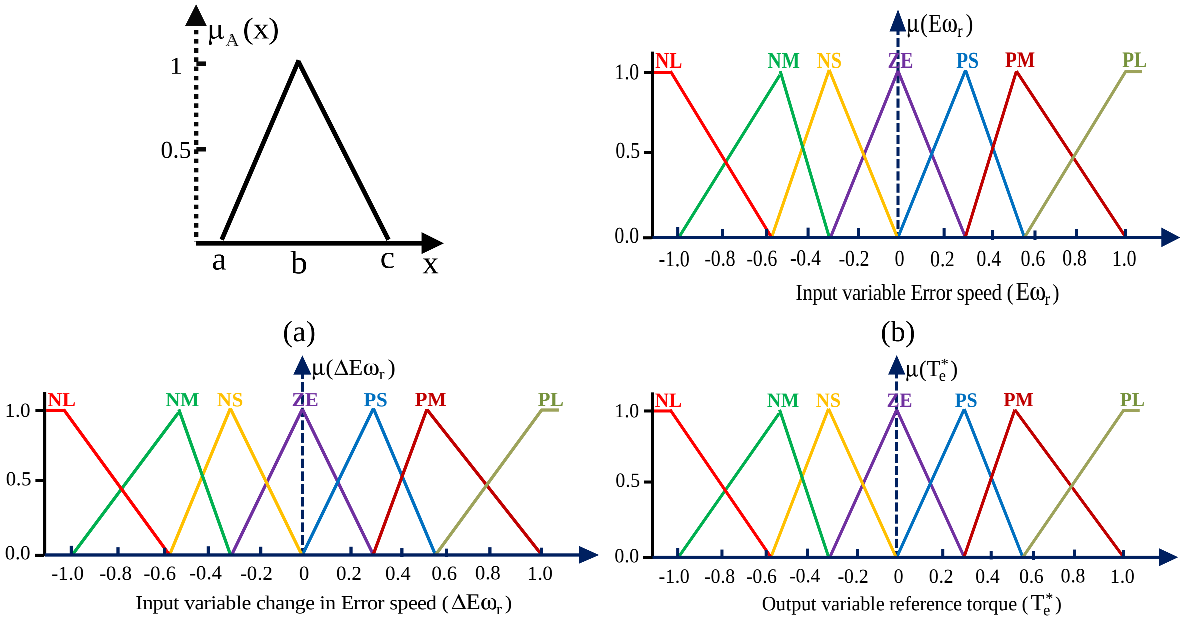

(a) (b)

(c) (d)

Figure 3.9: Membership functions of Type-1 FLC are: (a) Triangular MF, (b) Input variable error speed ‘$E\omega_r$’, (c) change in error speed ‘$\Delta E\omega_r$’ and (d) Output ‘T_e^*’

3.2.7 Construction of Type-1 Fuzzy Inference System

The T1FIS is designed using MATLAB/SIMULINK as illustrated in Figure 3.10. The FIS is characterized as follows:

- Number of input and output variables (2-inputs and 1-output)
- Number of MFs (Seven for each variable)
- Number of rules (49)
- Type of MF (Triangular)
- Fuzzification using continuous universe of discourse
- Type of implication (Mamdani’s max-min operation)

- Type of defuzzification scheme (COA).

TABLE 3.1: FUZZY LOGIC CONTROLLER RULE BASE

Output (T_e^*)		**Change in Error Speed** ($\Delta E\omega_r$)						
		NL	**NM**	**NS**	**ZE**	**PS**	**PM**	**PL**
Error Speed ($E\omega_r$)	**NL**	NL	NL	NL	NL	NM	NS	ZE
	NM	NL	NL	NL	NM	NS	ZE	PS
	NS	NL	NL	NM	NS	ZE	PS	PM
	ZE	NL	NM	NS	ZE	PS	PM	PL
	PS	NM	NS	ZE	PS	PM	PL	PL
	PM	NS	ZE	PS	PM	PL	PL	PL
	PL	ZE	PS	PM	PL	PL	PL	PL

The T1FLC consists of five sub-blocks such as MF editor, FIS editor, Rule editor, Surface viewer and Rule viewer. The FIS editor, MF editor and the rule editor can modify and read the FIS data, but the surface and rule viewer cannot modify in the T1FLC data [48].

The performance of T1FLC is more superior in terms of sensitivity to disturbances, flexibility, various load torque disturbances and noise rejection compared to a PIC. However, the T1FS are certain and does not work effectively when a higher degree of uncertainties are encountered in the system, which can be caused by various load torque disturbances, sudden change in speed, process noise, etc. In such condition the performance of T1FLC can significantly deteriorate. Therefore, a T2FLC based speed controller is proposed to cope with the higher degree of uncertainties and improve the performance under various load torque disturbances and sudden change in speed conditions.

3.3 Introduction to Type-2 FLC

The concept of Type-2 fuzzy sets (T2FS) introduced by Prof. Lofti A. Zadeh in 1975 and is basically “fuzzy- fuzzy” sets where the fuzzy MG (FMG) is a T1FS. The new interval type-2 fuzzy logic (IT2FL) concepts were introduced by Mendel and Liang [80], allowing the characterization of a T2FS with an upper MF and lower MF, each one of these two functions can be represented by a MF of T1FS [78-82, 85, 92].

The T2FS can cope with the uncertainties in a better way by modelling them and reducing their effect on the controller performance. With the development of T2FLC and their capability to directly handle the uncertainties, T2FLC has attracted many researchers in recent years [78-95]. It is an extension of the well-known concept of T1FS. The T2FS are characterized by a three-dimensional (3D) fuzzy MFs i.e., the FMG for each element is also a fuzzy set in the range [0, 1], whereas in case of T1FS the FMG for each element is a crisp value in [0, 1]. The MF of a T2FS is 3D and includes a Footprint of Uncertainty (FOU), which is the new third dimension of T2FS. The FOU offers an extra degree of freedom (DOF) to cope with the uncertainties. This extra DOF is very much useful when the huge value of uncertainties present in the system [83-85].

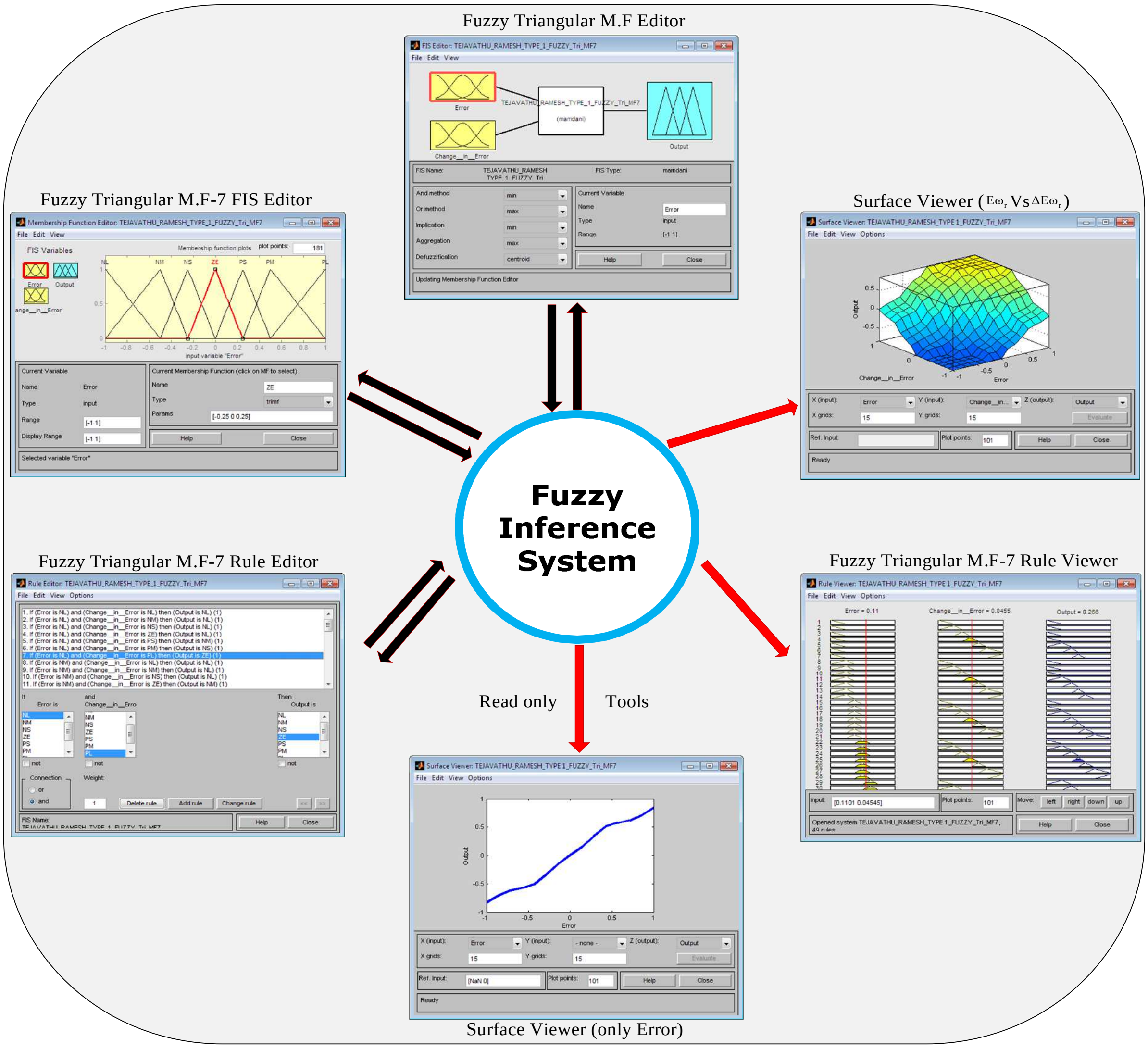

Figure 3.10: Type-1 fuzzy inference system using triangular membership functions

3.3.1 Why Type-2 FLCs?

The T2FLC utilizes an interval T2FSs to represent the inputs/output of the controller. It has several advantages when compared to T1FS [79-92]. As the MFs of a T2FS are fuzzy and contain an FOU, they can model and handle the linguistic and numerical uncertainties associated with the inputs and/or outputs of the FLC. It will result in the reduction of the rule base when compared to T1FS. This is because the uncertainty represented in the FOU of T2FS allows us to cover the same range as T1FS with a smaller number of labels.

The FOU offers an extra DOF which enables the T2FLC to produce outputs that are unable to achieve with the same number of MFs by using T1FLC. Where a T2FS may give rise to an equivalent Type-1 MG that is negative or larger than unity. Each input and/or output will be represented by a large number of T1FS, which are embedded in the T2FS. Further, the T2FLC can be thought of as a collection of many different embedded T1FLC.

3.3.2 The Structure of Type-2 FLC

The schematic model of T2FLC is very much similar to well-known T1FLC as shown in Figure 3.11. The only difference occurs in the output processing block. The output processing block of T1FLC contains only a defuzzifier, whereas the output processing block of T2FLC includes a Type-reducer (TR) [85-88].

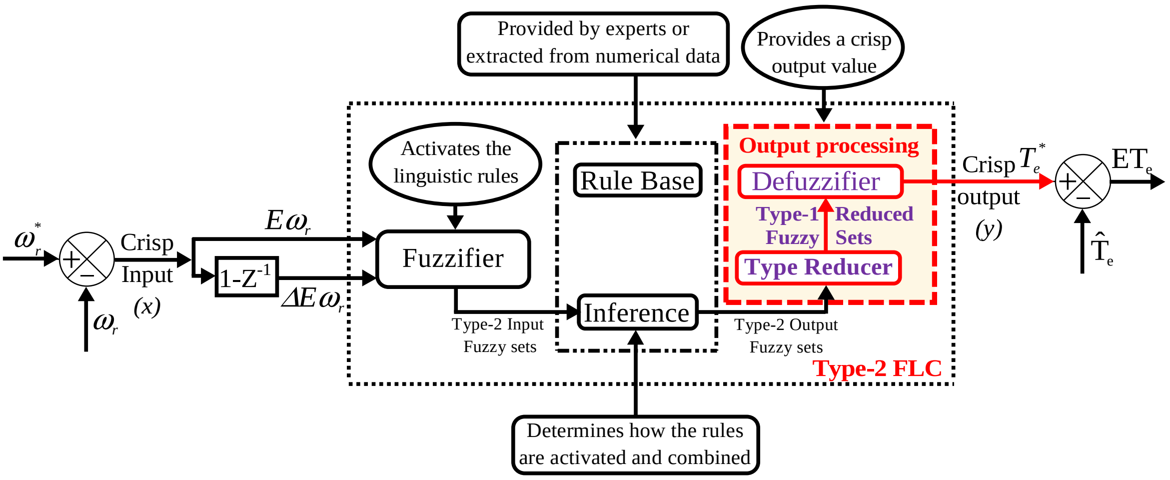

Figure 3.11 The schematic model of Type-2 FLC

FLS is based on the computation with fuzzy sets. While T1FS allows for a fuzzy representation of a term to be made, the fact that the MF of a T1FS is crisp, which means that the degrees of membership (DOM) set are completely crisp – not fuzzy [88, 92]. In a T1FS the MG for each element is a crisp number in the range [0, 1] whereas in a T2FS it is characterized by a 3D MF and an FOU which is shown in Figure 3.12 (a) and Figure 3.12 (b), respectively.

The design configuration of a T2FLC is chosen same as that of a T1FLC. There are two input and one output variables, for each input/output variable has taken the same number of linguistic variables. The operation of a T2FS is identical with the operation of T1FS [89-90]. However, on the interval Type-2 fuzzy system, the fuzzy operation is done at two Type-1 MF which limits the FOU, i.e. lower MF (LMF) and upper MF (UMF) to produce firing strengths. Hence, the MG for each element of this set is a fuzzy set in the range [0, 1]. Operation on IT2FL is shown in Figure 3.14.

A T2FS is bounded from under by the LMF and is bounded from above by the UMF. The area between the LMF and UMF is entitled the FOU. The new third-dimension of T2FS and the FOU gives extra DOF that makes it possible to directly model and handle the uncertainties. Hence, the T2FLC that uses T2FS in either their inputs or outputs have the potential to provide a suitable framework to handle the uncertainties in real world environments. It is worth noting that a T2FS embeds a huge number of T1FS. A T1FS in X is '*A*' and the MG of $x \in X$ in '*A*' is $\mu_A(x)$, which is a crisp number in the range [0, 1] whereas a T2FS in X is $\tilde{A}$ and the MG of $x \in X$ in $\tilde{A}$ is $\mu_{\tilde{A}}(x)$, which is a T1FS in the range [0, 1].

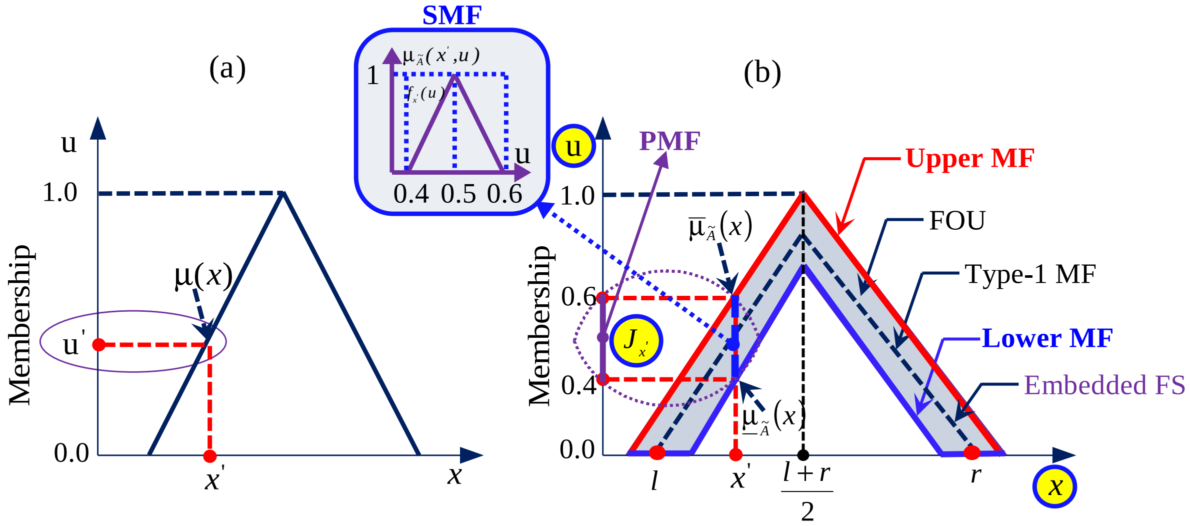

Figure 3.12: Membership functions of: (a) Type-1 FLC and (b) Type-2 FLC

A T2FS is represented by $\tilde{A}$ and it is characterized by a Type-2 MF $\mu_{\tilde{A}}(x,u)$, where $x \in X$ and $u \in J_x \subseteq [0,1]$. In which, $0 \le \mu_{\tilde{A}}(x,u) \le 1$, then the T2FS can be written as follows:

$$\tilde{A} = \big((x,u),\ \mu_{\tilde{A}}(x,u)\big); \quad \forall\, x \in X, \forall\, u \in J_x \subseteq [0,1] \tag{3.11}$$

The equation (3.11) can also be written as follows [80-82, 85-88, 92]:

$$\tilde{A} = \int_{x \in X} \int_{u \in J_x} \mu_{\tilde{A}}(x,u)/(x,u) \qquad J_x \subseteq [0,1] \tag{3.12}$$

where $\iint$ represent union operation over all allowable primary variable (*x*) and secondary variable (*u*). For the discrete universe of discourse the $\int$ is replaced by $\sum$.

At each value of x, say $x = x'$, the two dimensional plane, whose axes are *u* and the $\mu_{\tilde{A}}(x',u)$ is called vertical slice (VS) of $\mu_{\tilde{A}}(x,u)$. Then, a secondary MF (SMF) is a VS of $\mu_{\tilde{A}}(x,u)$, it is $\mu_{\tilde{A}}(x',u)$ for $x' \in X$, $\forall u \in \mathrm{J}_x \subseteq [0,1]$ and is given as follows [82, 87-88]:

$$\mu_{\tilde{A}}(x = x', u) = \mu_{\tilde{A}}(x') = \int_{u \in J_{x'}} f_{x'}(u)/u \qquad J_{x'} \subseteq [0,1] \tag{3.13}$$

The equation (3.12) can be re-written in a VS manner as follows [82, 88-90]:

$$\tilde{A} = \{(x, \mu_{\tilde{A}}(x)) \mid \forall\, x \in X\} \qquad \text{or}$$

$$\tilde{A} = \int_{x \in X} \mu_{\tilde{A}}(x)/x = \int_{x \in X} \left(\int_{u \in J_x} f_x(u)/u \right) \Big/ x \qquad J_x \subseteq [0,1] \tag{3.14}$$

If 'X' and 'J_x' are both discrete then the equation (3.14) can be re-written as follows:

$$\tilde{A} = \sum_{x \in X} \left(\sum_{u \in J_x} f_x(u)/u \right) / x = \tilde{A} = \sum_{i=1}^{N} \left(\sum_{u \in J_{x_i}} f_{x_i}(u)/u \right) / x_i \tag{3.15}$$

$$\tilde{A} = \sum_{K=1}^{M_1} \left(\sum_{u \in J_{x_1}} f_{x_1}(u_{1k})/u_{1k} \right) / x_1 + \ldots\ldots + \sum_{K=N}^{M_N} \left(\sum_{u \in J_{x_N}} f_{x_N}(u_{Nk})/u_{Nk} \right) / x_N \tag{3.16}$$

In equation (3.16), '+' represents the union operation. The discretization along each u_{ik} does not have to be the same, which is why we have shown a different upper sum for each of the bracketed terms [85, 92]. If, however, the discretization along each u_{ik} is the same, then $M_1 = M_2 = \ldots.. = M_N = M$.

Uncertainty in the primary MFs (PMF) of a T2FS $\tilde{A}$ consists of a bounded region that we call the FOU [80-82]. It is the union of all PMF, i.e.,

$$FOU(\tilde{A}) = \bigcup_{x \in X} J_x \tag{3.17}$$

The UMF and LMF are two T1MFs that are bounds for the FOU of a T2FS $\tilde{A}$. The UMF and LMF can be defined as follows [81, 85]:

$$\overline{FOU(\tilde{A})} = \bar{\mu}_{\tilde{A}}(x) \ \forall x \in X \tag{3.18}$$

$$\underline{FOU(\tilde{A})} = \underline{\mu}_{\tilde{A}}(x) \ \forall x \in X \tag{3.19}$$

where $\underline{J}_x = \underline{\mu}_{\tilde{A}}(x)$ and $\bar{J}_x = \bar{\mu}_{\tilde{A}}(x)$ represents the lower and upper bounds on $J_x = \mu_{\tilde{A}}(x)$, respectively.

The equations (3.13) and (3.14) can be re-written in terms of UMF and LMF as follows:

$$\mu_{\tilde{A}}(x) = \int_{u \in [\underline{\mu}_{\tilde{A}}(x), \bar{\mu}_{\tilde{A}}(x)]} f_x(u)/u \tag{3.20}$$

$$\tilde{A} = \mu_{\tilde{A}}(x,u) = \int_{x \in X} \mu_{\tilde{A}}(x)/x = \int_{x \in X} \left(\int_{u \in J_x} f_x(u)/u \right) / x = \int_{x \in X} \left(\int_{u = [\underline{\mu}_{\tilde{A}}(x), \bar{\mu}_{\tilde{A}}(x)]} f_x(u)/u \right) / x \tag{3.21}$$

In the special case when the SMFs are interval T2FS (IT2FS), then the equation (3.21) can be written as follows [81, 85]:

$$\tilde{A} = \int_{x \in X} \left(\int_{u \in J_x} 1/u \right) / x = \int_{x \in X} \left(\int_{u = [\underline{\mu}_{\tilde{A}}(x), \bar{\mu}_{\tilde{A}}(x)]} 1/u \right) / x \tag{3.22}$$

The T2FIS is implemented using MATLAB/SIMULINK with TMF is shown in Figure 3.13. The T2FIS is characterized as follows:

- Number of inputs and output variables - (Two-input and single-output),
- Number of rules - (49 rules),
- Type of MF - (Triangular),

- Number of MFs - (Seven)
- Type of implication - (Mamdani max-min operation)
- Type-reduction - (Center-of-sets)
- Type of defuzzification method - (Centroid-of-area)

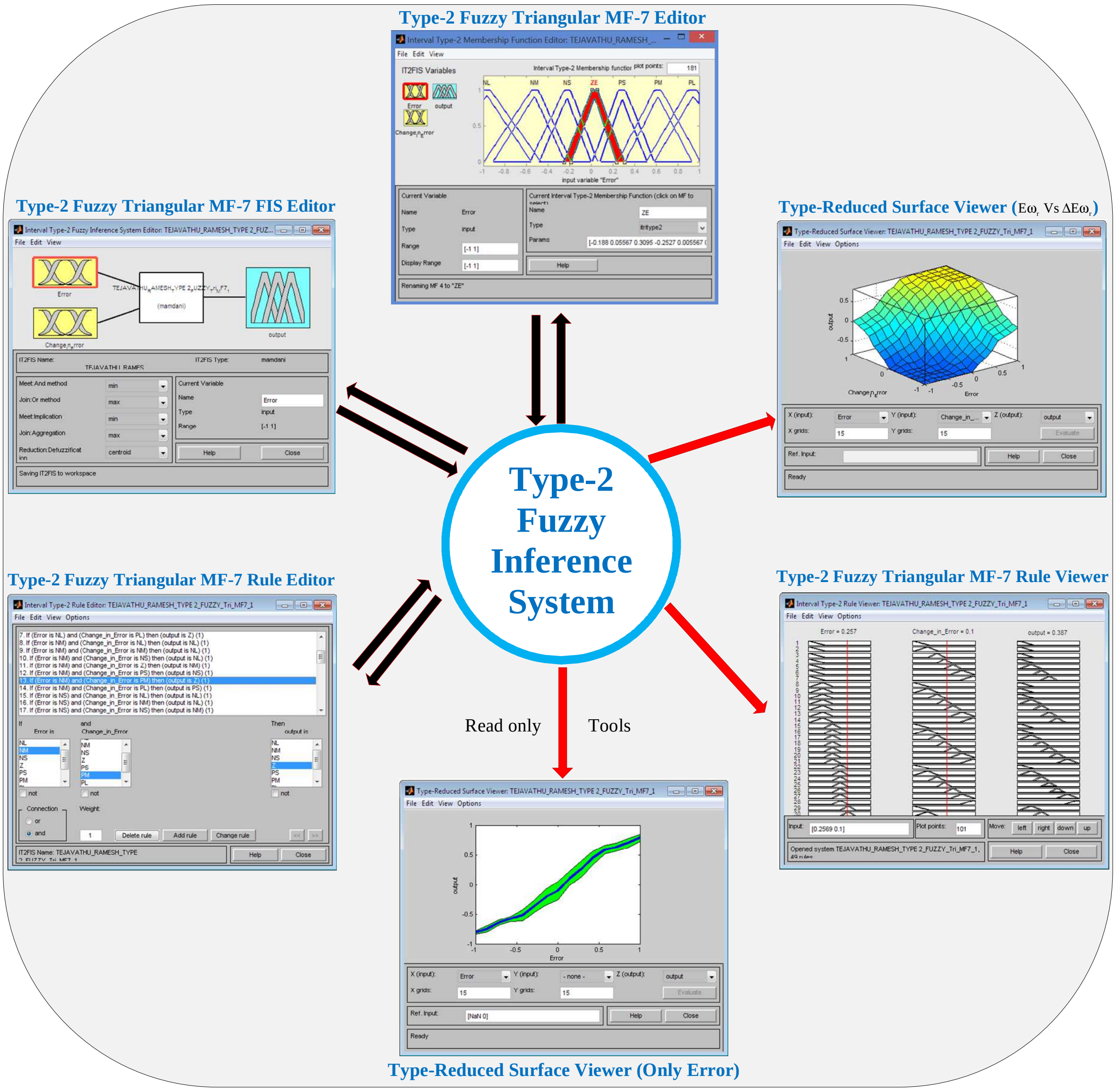

Figure 3.13: Type-2 Fuzzy Inference System with TMF 7x7

The T2FIS Editor handles the high-level issues in the system, such as how many antecedents and consequent variables? What are their names? The T2FIS doesn’t limit the number of inputs [85]. However, the number of inputs may be limited by the available memory of the personal computer. If the number of inputs is too large, or the number of Type-2 MFs (T2MF) is too big, then it may also be difficult to analyse the T2FIS using the other GUI tools. The T2MF Editor is used to define the shapes of all the T2MFs associated with each variable. The Type-2 Rule Editor is for editing the list of rules that defines the behaviour of the system [81].

The Type-2 rule viewer and the surface viewer or TR surface viewer are used for looking at, as opposed to editing the T2FIS. They are strictly read-only tools. The Type-2 rule viewer is a MATLAB/SIMULINK based display of the T2FIS block shown in Figure 3.13. Used as a diagnostic, it can show which rules are active, or how individually T2MF shapes are influencing the results. The surface viewer is used to display the dependency on one of the outputs on any one or two of the inputs, i.e., it generates and plots an output surface map for the system. The Mamdani T2FIS using MMC method is illustrated in Figure 3.14.

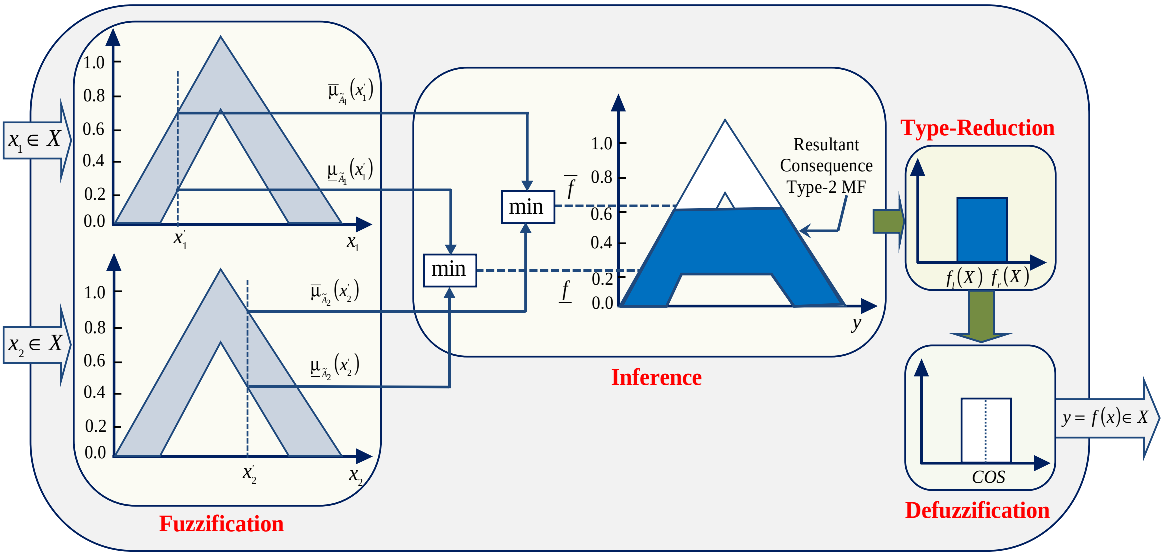

Figure 3.14: The Mamdani T2FIS using MMC

The schematic model of T2FLC is presented in Figure 3.11 consisting of five sub-blocks, such as, fuzzification, FIS, Rule Base, TR and Defuzzification, respectively.

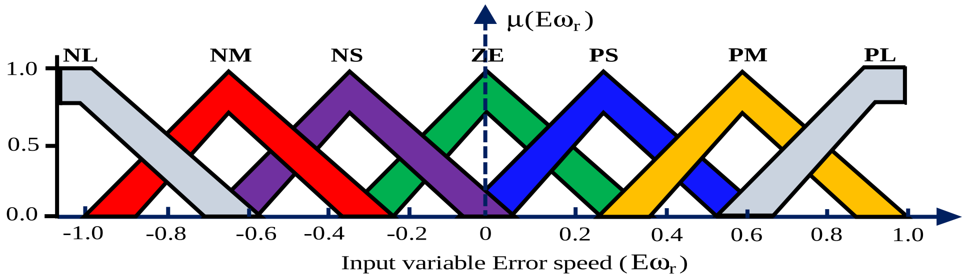

(a): Input variable of error speed ‘ $E\omega_r$ ’

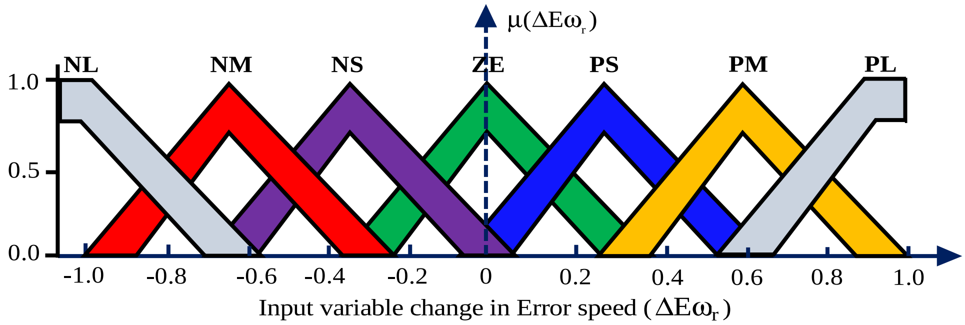

(b): Input variable of change in error speed ‘ $\Delta E\omega_r$ ’

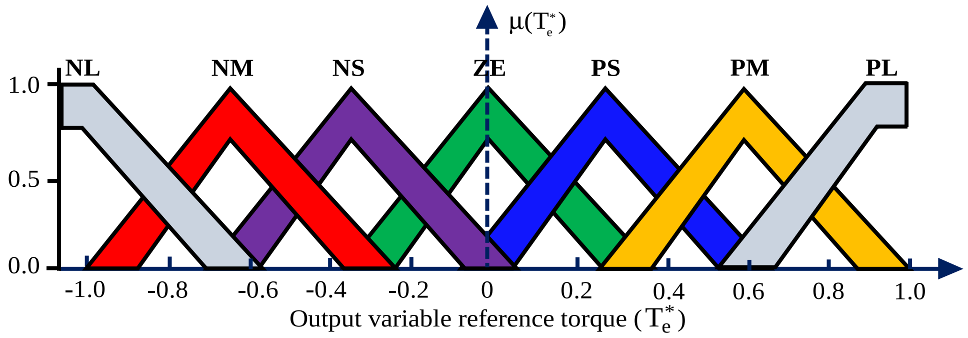

Output variable ‘T_e^*’

Figure 3.15: Membership functions of Type-2 FLC

3.3.2.1 Fuzzifier

The fuzzifier block is used to converts the crisp inputs $\mathrm{x}=(\mathrm{x}_1,\ldots\ldots,\mathrm{x}_n)\in X_1\times\ldots\times X_n\equiv X$ into a T2FS $\tilde{A}_X$ in X [81].

3.3.2.2 Rule Base

The construction of a T2FLC rule will remain exactly same as the T1FLC. The only difference is that the antecedents and consequents will be represented by T2FS. The rule base is expressed with a form of “IF-THEN” which represents expert knowledge. The T2FLC has two inputs and one output variable, which are shown in Figure 3.15, where each input/output variable has seven MFs. Therefore, the total 49 rules are required which are shown in Table 3.1, where each rule has the following form as:

R^l: IF $E\omega_r$ is $\tilde{F}^l_{E\omega r}$ AND $\Delta E\omega_r$ is $\tilde{F}^l_{\Delta E\omega r}$ THEN T_e^* is $\tilde{G}_{Te^*}{}^l$

where, $l=1,2,\ldots,M$, $\tilde{F}^l_{E\omega r}$ and $\tilde{F}^l_{\Delta E\omega r}$ represents the antecedent MFs of 2-inputs (IF-ingredients) and $\tilde{G}_{Te^*}{}^l$ is represent consequent MF (THEN-ingredients) of T2FS.

3.3.2.3 Inference

The inference block is the essential process in FLS. In this block, the rules are combined and the input of T2FS is converted to output T2FS using new operators join $\coprod$ (unions) and meet $\prod$ (intersections), as well as protracted sup-star compositions of type-2 relations. If $\tilde{F}_{E\omega_r}\times\tilde{F}_{\Delta E\omega_r}=\tilde{A}$, then the l^{th} rule in the T2FLC can be re-written as [81, 85]:

$$R^l:\tilde{F}_{E\omega_r}\times\tilde{F}_{\Delta E\omega_r}\to\tilde{G}_{Te^*}{}^l=\tilde{A}\to\tilde{G}_{Te^*}{}^l \tag{3.23}$$

R^l is defined by the MF $\mu_{R^l}(X,y)=\mu_{R^l}\left(E\omega_r,\Delta E\omega_r,\tilde{G}_{Te^*}{}^l\right)$

where

$$\mu_{R^l}(X,y)=\mu_{\tilde{A}\to\tilde{G}_{Te^*}{}^l}(X,y) \tag{3.24}$$

The equation (3.24) can be expressed as follows [81, 85]:

$$\mu_{R^l}(X,y)=\mu_{\tilde{A}\rightarrow\tilde{G}_{Te}^{*l}}(X,y)=\mu_{\tilde{G}_{Te}^{*l}}(T_e^*)\prod\left[\mu_{\tilde{F}E\omega r}(E\omega_r)\prod\mu_{\tilde{F}\Delta E\omega r}(\Delta E\omega_r)\right] \tag{3.25}$$

In general, the 2-dimentional input to R^l is given by the T2FS $\tilde{A}_x$ whose MF is [85]:

$$\mu_{\tilde{A}x}(X)=\mu_{\tilde{X}E\omega r}(E\omega_r)\prod\mu_{\tilde{X}\Delta E\omega r}(\Delta E\omega_r) \tag{3.26}$$

where $\tilde{X}_{E\omega r}$, $\tilde{X}_{\Delta E\omega r}$ are the labels of the fuzzy sets describing the inputs. Each rule R^l defines a T2FS $\tilde{B}^l=\tilde{A}_x\circ R^l$ such that:

$$\mu_{\tilde{B}^l}(y)=\mu_{\tilde{A}_x\circ R^l}(y)=\coprod_{x\in X}\left[\mu_{\tilde{A}_x}(X)\prod\mu_{\tilde{R}^l}(X,y)\right] \quad y=Y \tag{3.27}$$

The equations (3.25) and (3.26) substitute in equation (3.27) we get the inference results of l^{th} fired rule as follows [81, 85]:

$$\mu_{\tilde{B}^l}(y)=\mu_{\tilde{G}_{Te}^{*l}}(T_e^*)\prod\left\{\coprod_{x\in X}\left\{\left[\mu_{\tilde{X}E\omega r}(E\omega_r)\prod\mu_{\tilde{F}^l_{E\omega r}}(E\omega_r)\right]\prod\left[\mu_{\tilde{X}\Delta E\omega r}(\Delta E\omega_r)\prod\mu_{\tilde{F}^l_{\Delta E\omega r}}(\Delta E\omega_r)\right]\right\}\right\} \tag{3.28}$$

where $\mu_{\tilde{X}E\omega r}$, $\mu_{\tilde{X}\Delta E\omega r}$ are the MF of fuzzification.

By using the singleton fuzzification, the l^{th} fired rule values can be simplified as [85]:

$$\mu_{\tilde{B}^l}(y)=\mu_{\tilde{G}_{Te}^{*l}}(T_e^*)\prod\left\{\coprod_{x\in X}\left\{\mu_{\tilde{F}^l_{E\omega r}}(E\omega_{r1})\prod\mu_{\tilde{F}^l_{\Delta E\omega r}}(\Delta E\omega_r)\right\}\right\} \tag{3.29}$$

In this IT2FS, meet under product t-norm is used so the upper and lower firing set is an interval type-1 set, expressed for the l^{th} rule as follows [81, 85]:

$$F^l(X)=\left[\underline{f}^l(X),\overline{f}^l(X)\right]=\left[\underline{f}^l,\overline{f}^l\right] \tag{3.30}$$

where $\overline{f}^l=\overline{\mu}_{\tilde{F}^l_{E\omega r}}(E\omega_r)*\overline{\mu}_{\tilde{F}^l_{\Delta E\omega r}}(\Delta E\omega_r)$, $\underline{f}^l=\underline{\mu}_{\tilde{F}^l_{E\omega r}}(E\omega_r)*\underline{\mu}_{\tilde{F}^l_{\Delta E\omega r}}(\Delta E\omega_r)$, * indicates the product operation, $\underline{\mu}_{\tilde{F}^l_{E\omega r}}$ and $\overline{\mu}_{\tilde{F}^l_{E\omega r}}$ are represents LMF and UMF grades, respectively.

3.3.2.4 Type-reducer

The TR block transforms output T2FS into Type-1 reduced fuzzy sets, which is then transformed into a crisp output through the defuzzifier. There are various schemes for the TR operation in the IT2FS, such as centroid, height, center of sum and center of sets. Among these, the center-of-set (COS) is the most popular TR operation, which can be expressed as:

$$Y_{COS}(X)=[y_l,y_r]=\int_{y^1\in[y_l^1,y_r^1]}\ ,\ldots,\int_{y^M\in[y_l^M,y_r^M]}\int_{f^1\in\left[\overline{f}_l^1,\underline{f}_r^1\right]}\cdots\int_{f^M\in\left[\overline{f}_l^M,\underline{f}_r^M\right]}\left[\frac{\sum_{l=1}^{M}f^l}{\sum_{l=1}^{M}f^l y^l}\right]=T^*_{e\,COS} \tag{3.31}$$

This IT2FS is resolved by its left-most-point (LMP) and right-most-point (RMP), which corresponds to the centroid of the type-2 interval consequent set $\tilde{G}^l$ as [81, 85]:

$$T_e^* = \int_{\theta_1 \in J_{y1}} ,....,\int_{\theta_N \in J_{yN}} \left[\frac{\sum_{l=1}^{M} \theta_l y_l}{\sum_{l=1}^{M} \theta_l} \right] = \left[y_l^l , y_r^l \right] \tag{3.32}$$

where T_e^* is an IT2FS determined by the left-most and right-most end points ($T_{e\ l}^{*l}, T_{e\ r}^{*l}$), which can be derived from the consequent centroid set (y_l^l , y_r^l).

The torque strength $f^l \in F^l = \left(\underline{f}^l , \overline{f}^l \right)$ must be computed or set first before the computation of $C_{\tilde{G}_{Te}^{*l}}$. The LMP $T_{e\ l}^{*l}$ and the RMP $T_{e\ r}^{*l}$ can be expressed as follows:

$$T_{e\ l}^{*l} = y_l^l = \frac{\sum_{l=1}^{M} \left[f_l^{\ l} y_l^{\ l} \right]}{\sum_{i=1}^{M} f_l^{\ l}} \tag{3.33}$$

$$T_{e\ r}^{*l} = y_r^l = \frac{\sum_{l=1}^{l} \left[f_r^{\ l} y_r^{\ i} \right]}{\sum_{l=1}^{M} f_r^{\ l}} \tag{3.34}$$

Computation of $T_{e\ l}^*$ and $T_{e\ r}^*$ is done using Karnik-Mendal algorithm [79, 81-85, 175-178], which is given in Figure 3.16. First, $T_{e\ r}^*$ (or $T_{e\ l}^*$) is arranged in ascending order, then the iterative procedure is shown in Figure 3.16. It briefly states the procedure to compute $T_{e\ r}^*$ and $T_{e\ l}^*$. Let, initially compute the RMP $T_{e\ r}^*$ without loss of generality, assume that y_r^l is arranged in ascending order, i.e., $y_r^1 \le y_r^2 \le y ..... \le y_r^M$. The algorithm for finding crisp output on the right side of T2FS is shown in Figure 3.16. Hence, the value of $T_{e\ r}^*$ can be expressed using Equation (3.34) as:

$$T_{e\ r}^* = T_{e\ r}^* \left(\underline{f}^1 ,....., \underline{f}^R , \overline{f}^{R+1} ,...., \overline{f}^M , y_r^l ,...., y_r^M \right) = \frac{\sum_{l=1}^{R} \underline{f}^l y_r^{\ l} + \sum_{l=R+1}^{M} \overline{f}^l y_r^{\ l}}{\sum_{l=1}^{R} \underline{f}^l + \sum_{l=R+1}^{M} \overline{f}^l} \tag{3.35}$$

The procedure to compute $T_{e\ l}^*$ is similar to that of $T_{e\ r}^*$ as shown in flow chart of Figure 3.16, with slight modifications. In 3rd step of the flowchart, find $L(1 \le L \le M - 1)$ such that $y_l^L \le T_{e\ l}^{*\ '} \le y_l^{L+1}$, and allow $f_l^{\ l} = \overline{f}^l$ for $l \le L$ and $f_l^{\ l} = \underline{f}^l$ for $l > L$. Therefore, $T_{e\ l}^*$ can be expressed using equation (3.33) as follows [79, 85, 178]:

$$T_{e\ l}^* = T_{e\ l}^* \left(\overline{f}^1 ,....., \overline{f}^L , \underline{f}^{L+1} ,...., \underline{f}^M , y_l^l ,...., y_l^M \right) = \frac{\sum_{l=1}^{L} \underline{f}^l y_l^{\ l} + \sum_{l=L+1}^{M} \overline{f}^l y_l^{\ l}}{\sum_{l=1}^{L} \underline{f}^l + \sum_{l=L+1}^{M} \overline{f}^l} \tag{3.36}$$

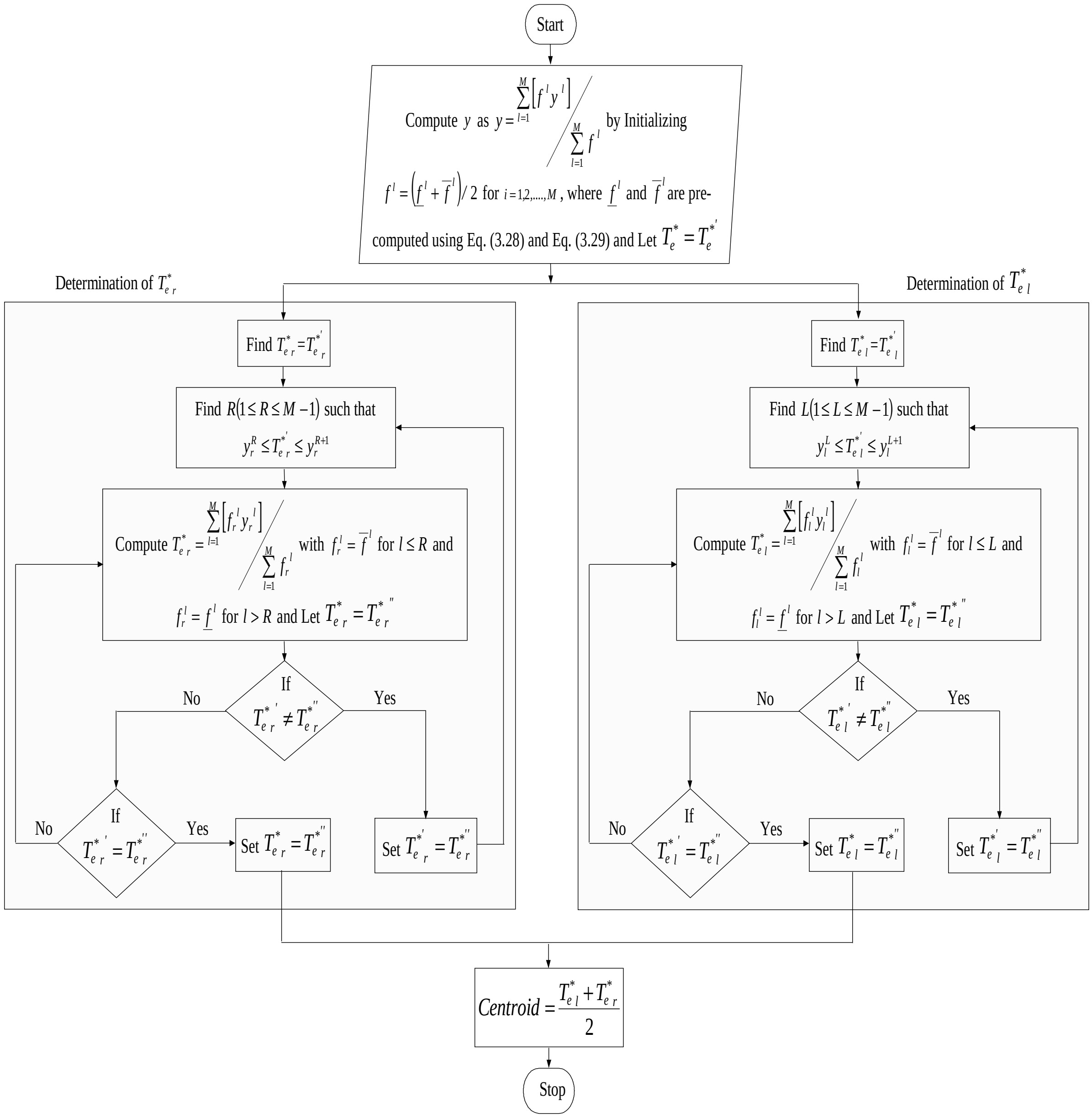

Figure 3.16: The flowchart of T2FLC for finding the crisp value

3.3.2.5 Defuzzification

The TR outputs are given to the input of the defuzzification block. Then the defuzzification block converts the T1FS to crisp output. The defuzzified crisp output is the average value of $T_{e\,r}^*$ and $T_{e\,l}^*$, it is given by:

$$Centroid = y(x) = \frac{T_{e\,l}^* + T_{e\,r}^*}{2} \tag{3.37}$$

3.4 Simulation Results

The proposed DTFC of an IMD using T1FLC and T2FLC based speed controller schemes are simulated in MATLAB/SIMULINK. The SIMULINK model is then used to verify the performance of the drive under various operating conditions, such as under no-load torque, load torque and various sudden changes in speed, respectively.

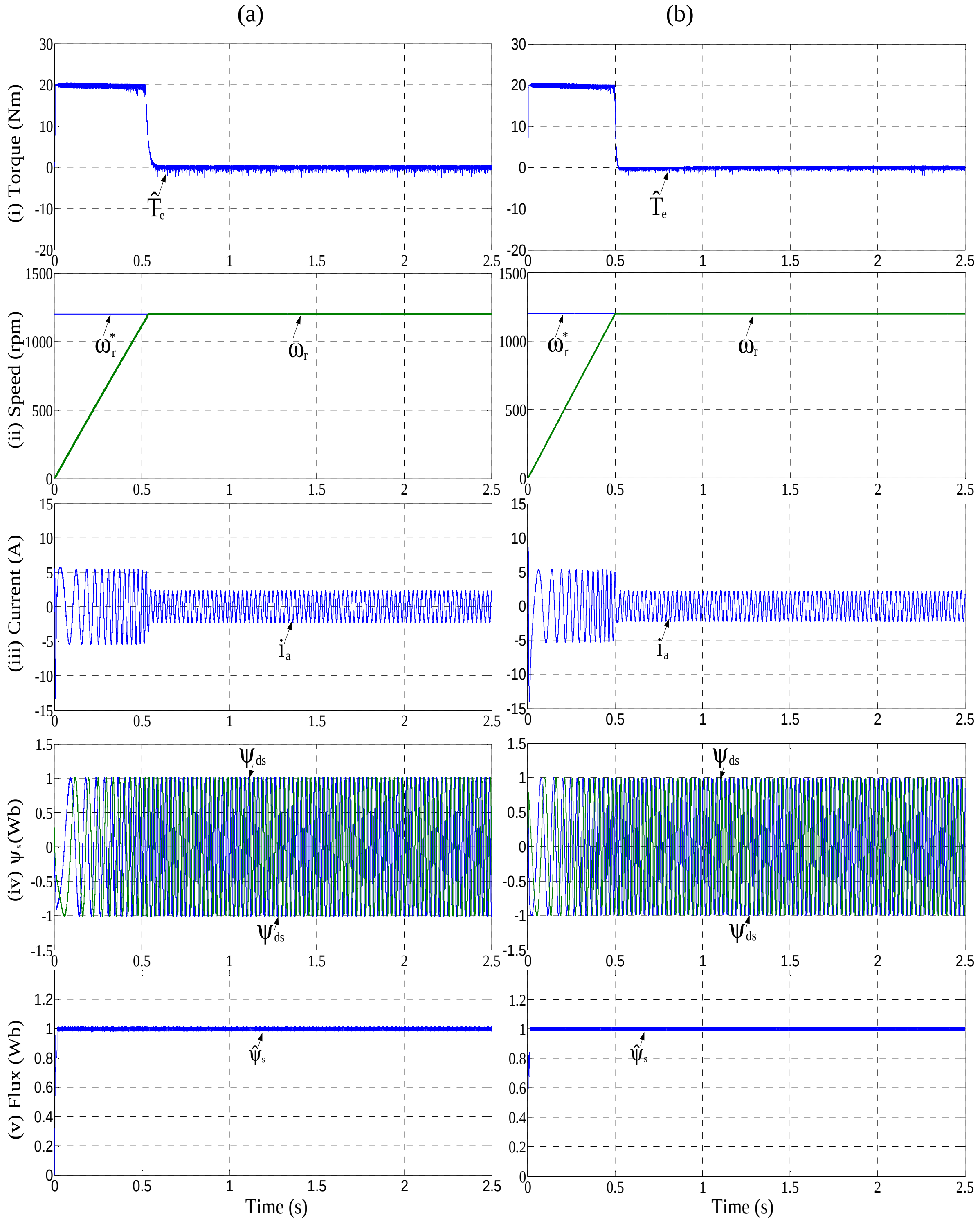

Figure 3.17 Performance of IMD under no-load torque operating condition using: (a) T1FLC and (b) T2FLC: *Traces (from top to bottom):* (i) Torque, (ii) speed, (iii) current, (iv) stator flux dq-components in stationary reference frame and (v) stator flux

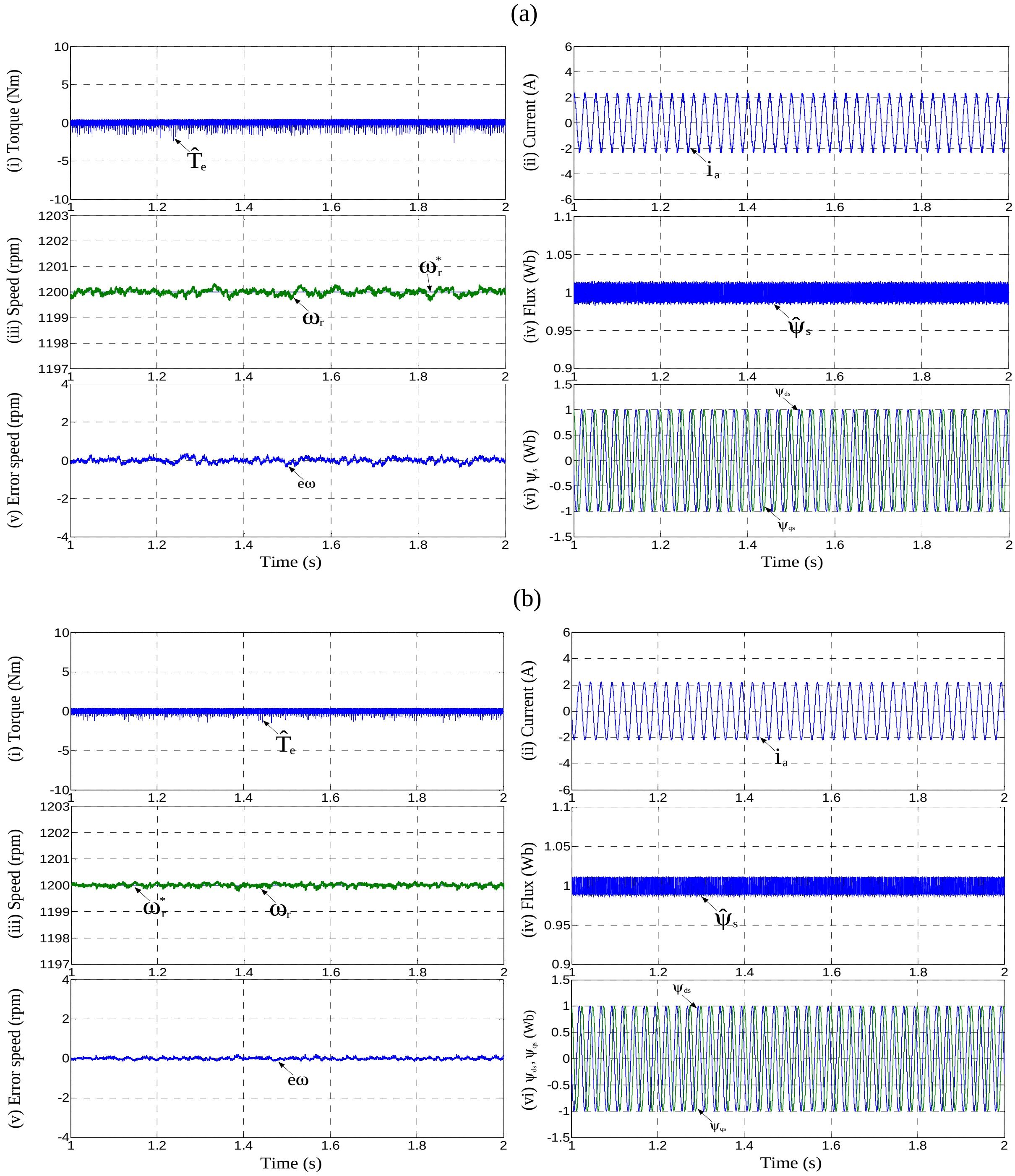

Figure 3.18: Steady-state performance under no-load torque operating condition using: (a) T1FLC and (b) T2FLC: *Traces (from top to bottom):* (i) Torque, (ii) current, (iii) speed, (iv) stator flux, (v) error speed and (vi) stator flux dq-components in stationary reference frame

3.4.1 Performance under Forward Motoring

Initially, the performance of DTFC of an IMD is investigated under no-load torque operation at 1200 rpm using Type-1 and Type-2 FLC schemes are shown in Figure 3.17 (a)-(b). The presented results are electromagnetic torque, reference and actual speeds, stator current, stator flux dq-components in a stationary reference frame and stator flux shown in Figure 3.17 (i)-

(v), respectively. It is observed from the simulation results that the transient response of the IMD using T2FLC scheme shows faster response compared to the T1FLC. It starts at zero speed and reaches the set reference speed ($\omega_r = 1200$ rpm) at 0.537 s with an overshoot of 0.5 rpm using T1FLC, whereas it reaches quickly at 0.498 s using T2FLC scheme.

The steady-state performance of IMD under no-load torque operating condition using T1FLC and T2FLC schemes are shown in Figure 3.18 (a)-(b), respectively. Results show the superiority of the T2FLC over T1FLC schemes.

3.4.2 Loading Performance

The performance of an IMD under the application and rejection of sudden load torque disturbances are observed in the following conditions.

- Loading at 1200 rpm
- Loading and unloading at 1200 rpm
- Loading at different speed commands (i.e. 300 rpm, 600 rpm and 900 rpm)

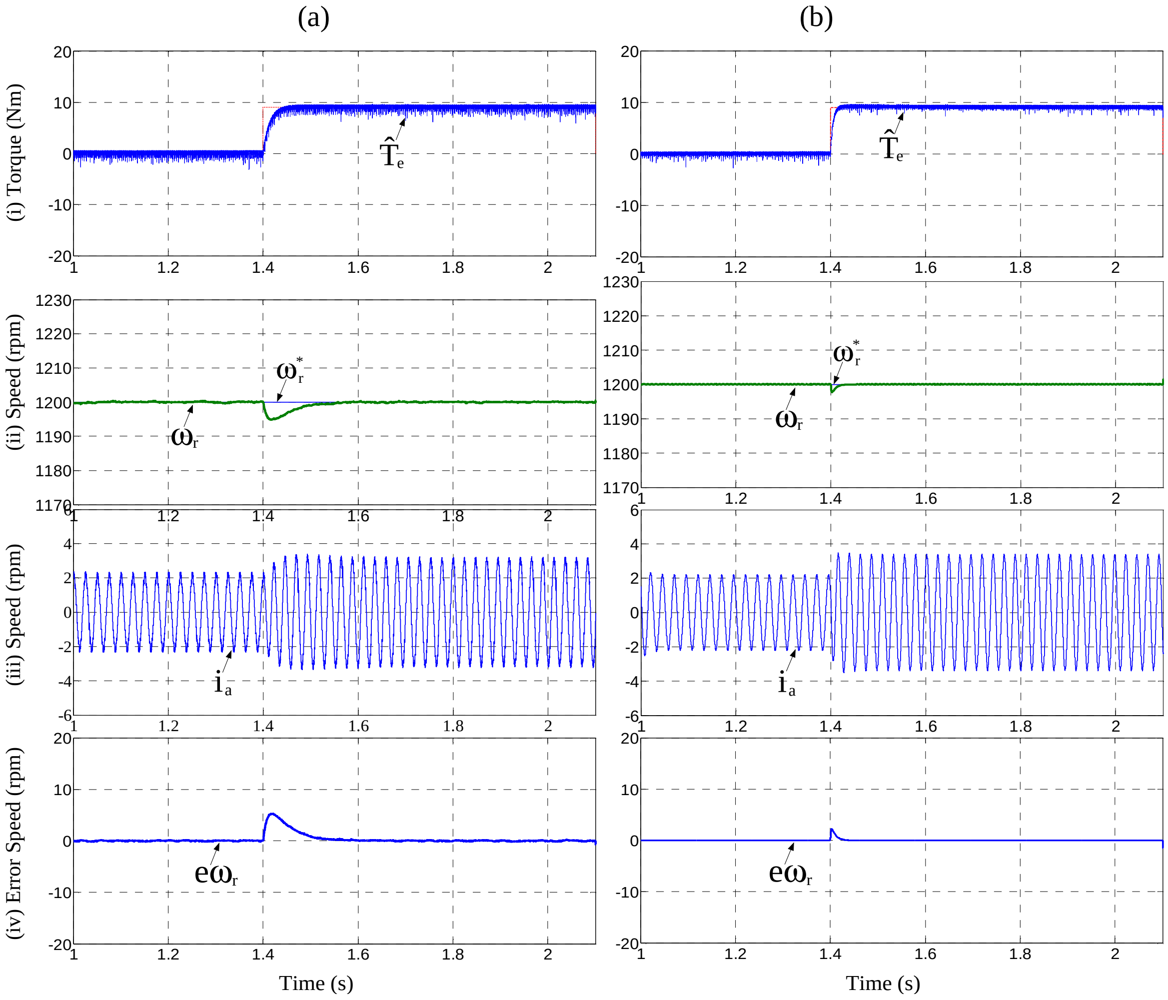

Figure 3.19 Loading performance at 1200 rpm using: (a) T1FLC and (b) T2FLC: *Traces (from top to bottom):* (i) Torque, (ii) speed, (iii) current and (iv) error speed

Loading performance at 1200 rpm

The effect of sudden load torque operation at 1200 rpm using T1FLC and T2FLCs are illustrated in Figure 3.19 (a)-(b). The sudden load torque of 9 Nm is applied at 1.4 s when an induction motor was operating at steady state speed. It is observed from the simulation results that the sudden application of load torque causes undershoot around 5.2 rpm (which is 0.433% of the reference speed) using T1FLC, whereas small undershoot of 2.3 rpm (which is 0.1916% of the reference speed) using T2FLC is observed as shown in Figure 3.19 (ii). It is also observed that the recovery time of actual speed and the ripple contents in torque, error speed and stator currents are less using T2FLC compared to T1FLC are shown in Figure 3.19 (i)-(iv).

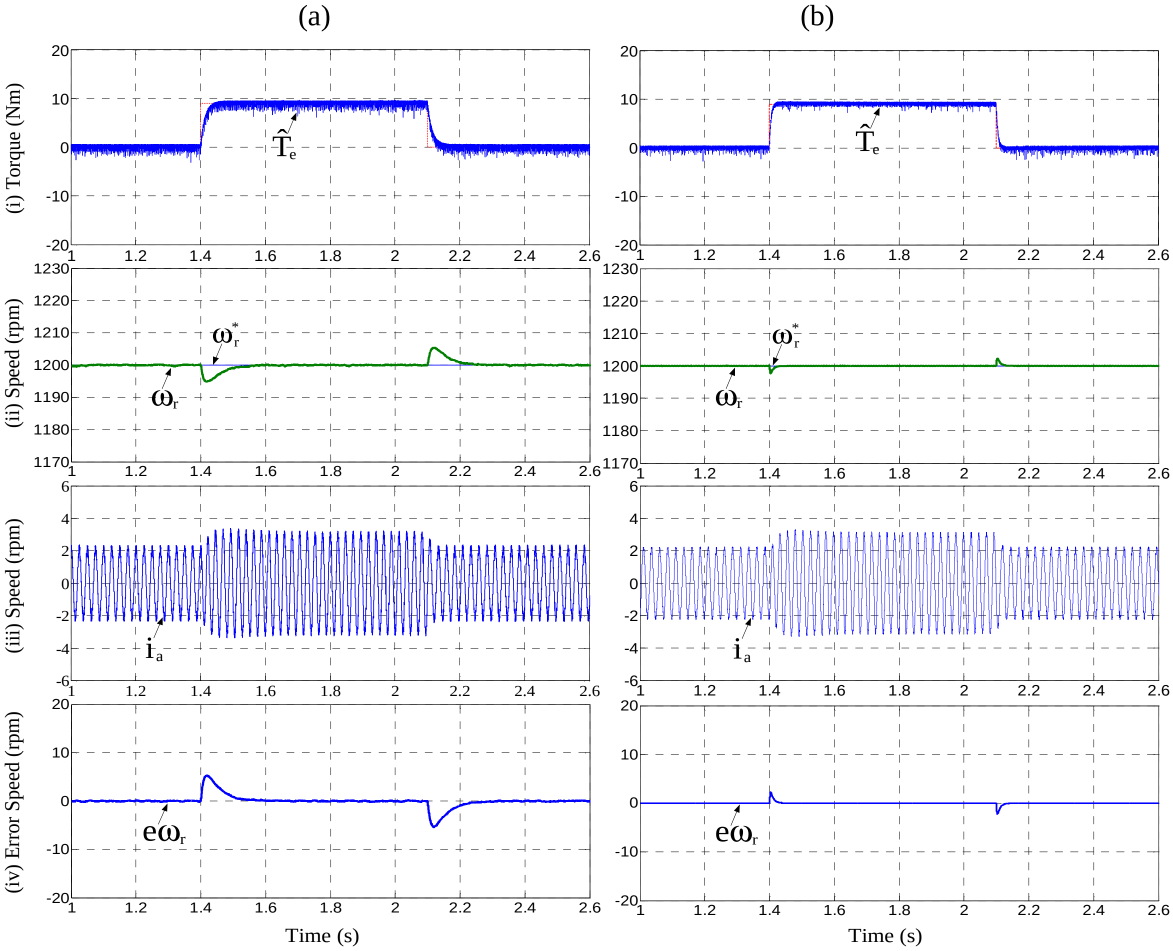

Figure 3.20: Loading and unloading performance at 1200 rpm using: (a) T1FLC and (b) T2FLC: *Traces (from top to bottom):* (i) Torque, (ii) speed, (iii) current and (iv) error speed

Similarly, the load torque is withdrawn at 2.1 s when an induction motor was operating at steady state speed. It is observed from the simulation results that the sudden withdrawn of load torque causes an overshoot of 5.0 rpm and 2.2 rpm using T1FLC and T2FLCs are shown in Figure 3.20 (a)-(b). The torque, reference and actual speeds, stator current and error speed between the reference and actual speed are shown in Figure 3.20 (i)-(iv), respectively.

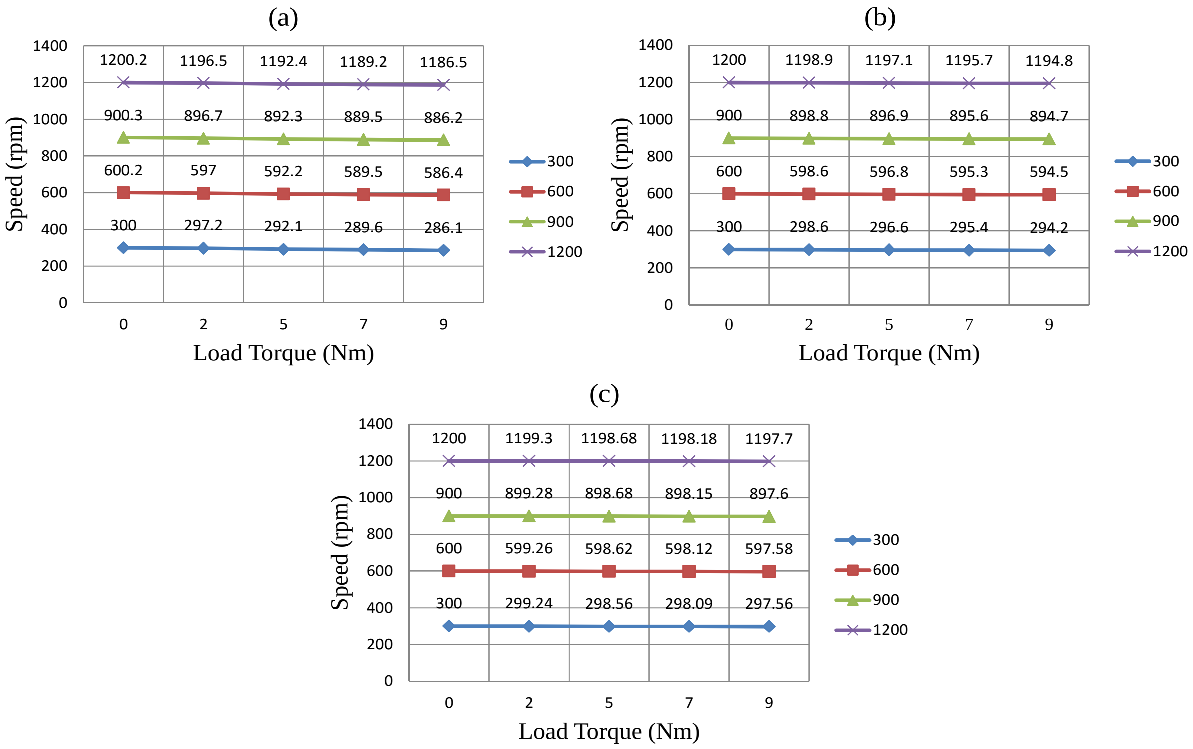

Figure 3.21: Steady-state performance of the actual speed under various load torque conditions at different speed commands using: (a) PIC, (b) T1FLC and (c) T2FLC

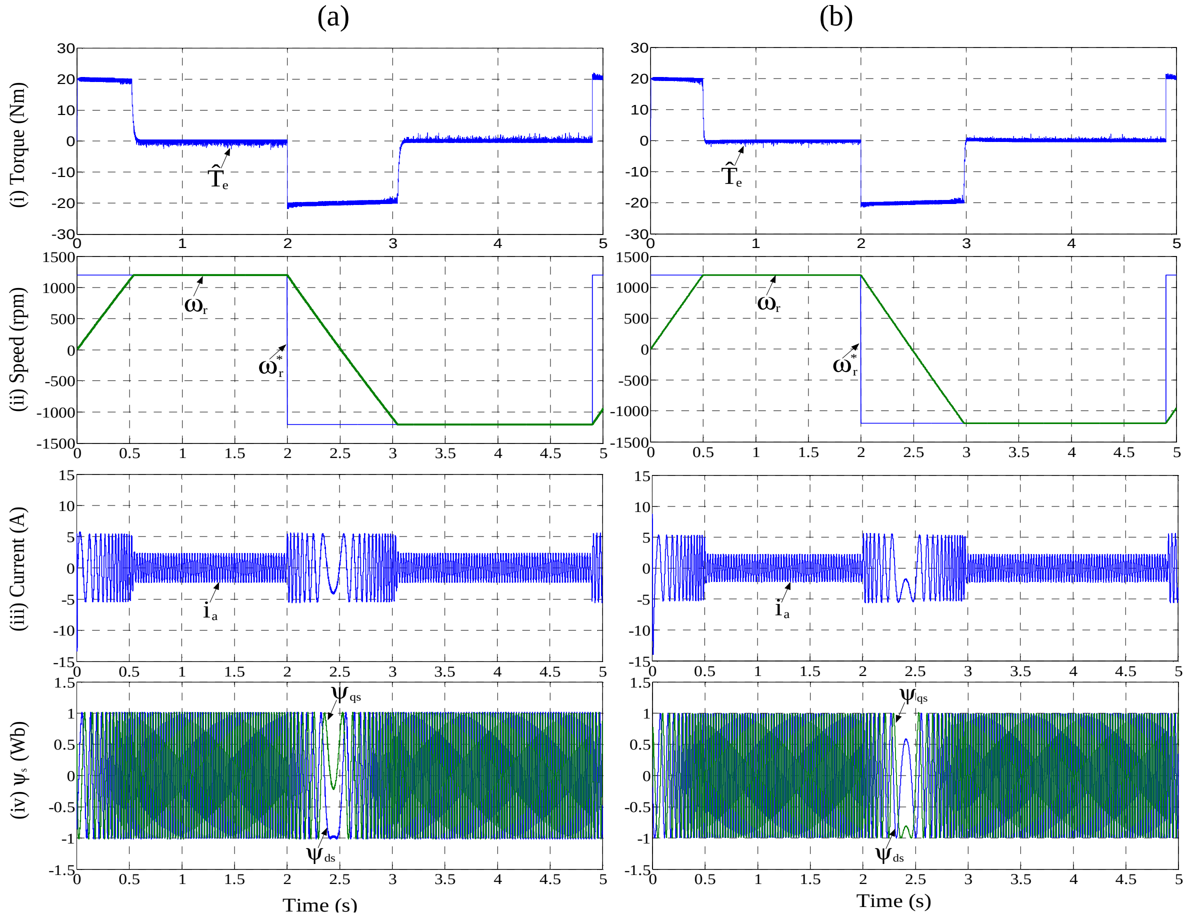

Figure 3.22: Performance of IMD under reversal speed command using: (a) T1FLC and (b) T2FLC: (i) Torque, (ii) speed and (iii) current

The effect of different load conditions is observed under different speed commands using PIC, T1FLC and T2FLCs are illustrated in Figure 3.21(a)-(c). It is observed from the simulation results that the T2FLC shows an improved performance and robustness to various sudden load torque disturbances compared to PIC and T1FLC.

3.4.3 Performance under Reversal Speed Command

The performance of the IMD under the reversal speed in step command is observed using T1FLC and T2FLC as shown in Figure 3.22 (a)-(b). The reversal speed command from +1200 rpm to -1200 rpm is applied at 2 s. The actual speed reaches its reference speed during reversal speed at 3.05 s and 2.93 s using T1FLC and T2FLC, respectively. The reference and actual speeds are illustrated in Figure 3.23 (ii), which reveals that the actual speed tracking the reference speed with small overshoot around 0.7 rpm using T1FLC whereas zero overshoot with quick settling time using T2FLC scheme. The torque, stator current and dq-axes stator flux components in a stationary reference frame are shown in Figure 3.22 (i) and (iii)-(iv) respectively. The reversal speed transient response of Figure 3.22 (a)-(b) is shown in zoomed view in Figure 3.23 (a)-(b).

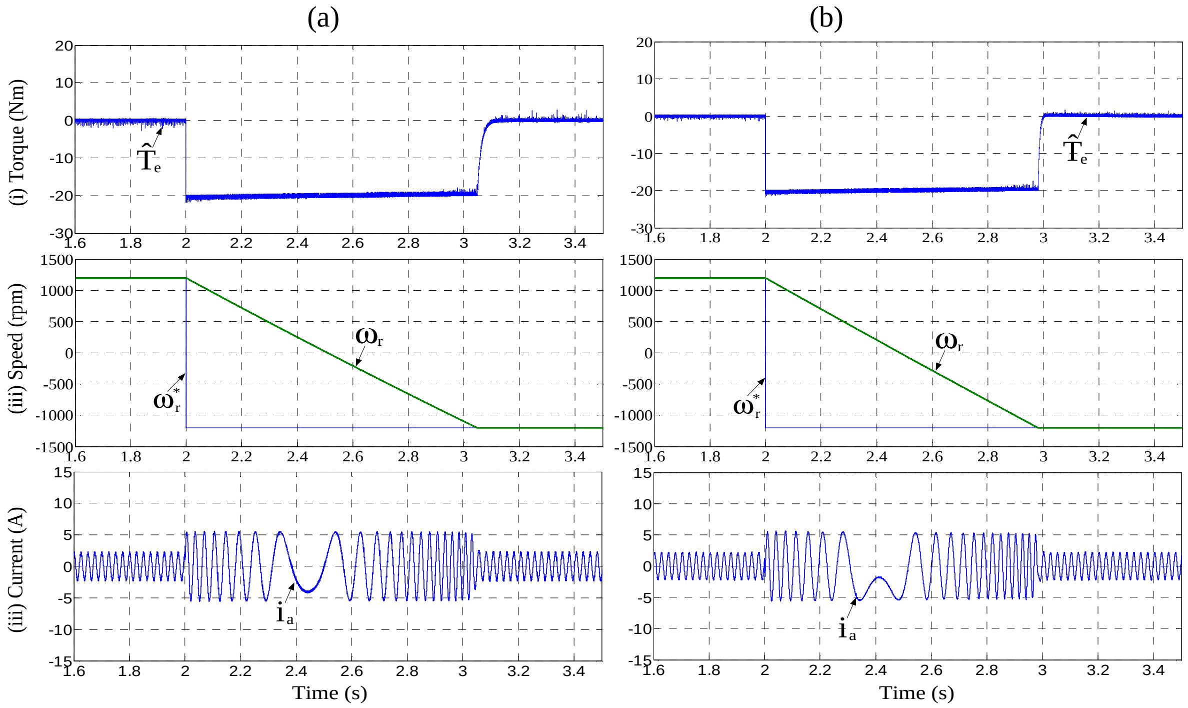

Figure 3.23 Transient performance of IMD under reversal speed command using: (a) T1FLC and (b) T2FLC: (i) Torque, (ii) speed and (iii) current

3.4.4 Tracking Performance of the Speed Commands

Tracking performance of the actual speed is observed through the application of various changes in step and square speed command. The simulation results for each case are presented as follows.

Performance under step change in speed command:

The step change in speed command of 300 rpm is applied in four steps (i.e. 600 rpm ⟶ 900 rpm ⟶ 1200 rpm ⟶ 900 rpm ⟶ 600 rpm) at 1.4 s, 2.4 s, 3.6 s, etc. The corresponding reference and actual speed responses under such speed command is shown in Figure 3.24 (a)-(b). The corresponding actual speed under such speed command is shown in Figure 3.24 (ii). From Figure 3.24 (ii), it is observed that the estimated speed settles the reference speed (from 600 rpm to 900 rpm) in 0.136 s and 0.12 s using T1FLC and T2FLC, respectively. It is also noticed that the speed response does not contain any overshoot using T2FLC whereas small overshoot using T1FLC. The torque, current and dq-axes stator flux components in a stationary reference frame are shown in Figure 3.24 (i), (iii) and (iv), respectively.

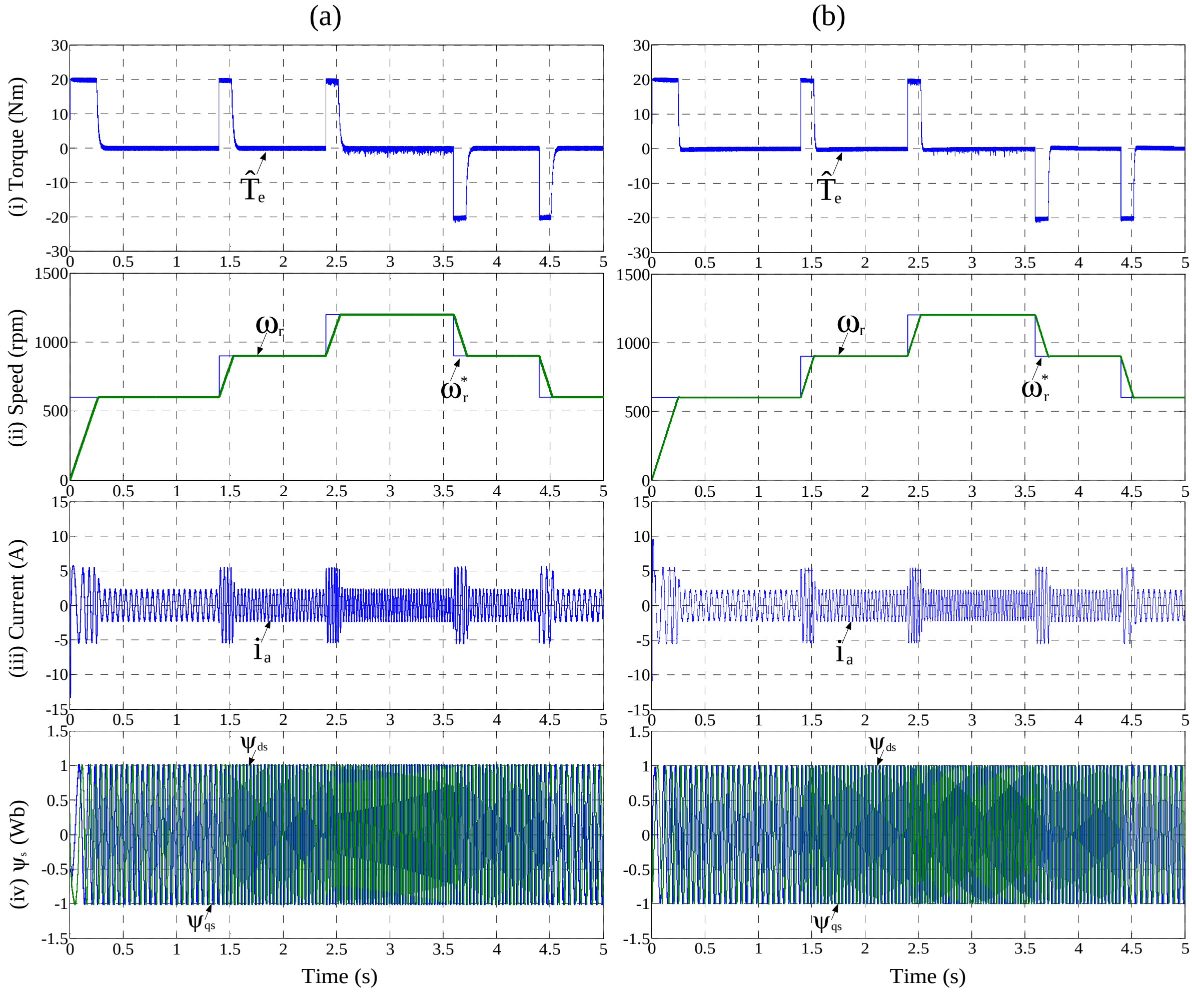

Figure 3.24: Performance under sudden change in step speed command using: (a) T1FLC and (b) T2FLC: (i) Torque, (ii) speed and (iii) current and (iv) d- and q-axis stator flux components

Performance under square speed command:

The performance of the IMD is observed under a square change in speed command using PIC, T1FLC and T2FLCs are shown in Figure 3.25 (a)-(b). The sudden change in speed command of 600 rpm is applied in four steps (i.e. 1200 rpm ⟶ 600 rpm ⟶1200 rpm ⟶ 600 rpm → 1200 rpm) at 1 s, 2 s, 3 s, etc. The reference speed (ω_r^*) and actual speeds (ω_r) are presented in Figure 3.25 (ii), it is observed that under such speed command the estimated speed settles the reference speed (from 600 to 1200 rpm) in 0.282 s and 0.266 s with an overshoot around 0.068% and 0.002% of the reference speed using T1FLC and T2FLC, respectively. The torque and stator current are shown in Figure 3.25 (i) and (iii), respectively. It is noticed that the actual speed accurately tracking the reference speed and settles quickly using T2FLC scheme compared to T1FLC scheme.

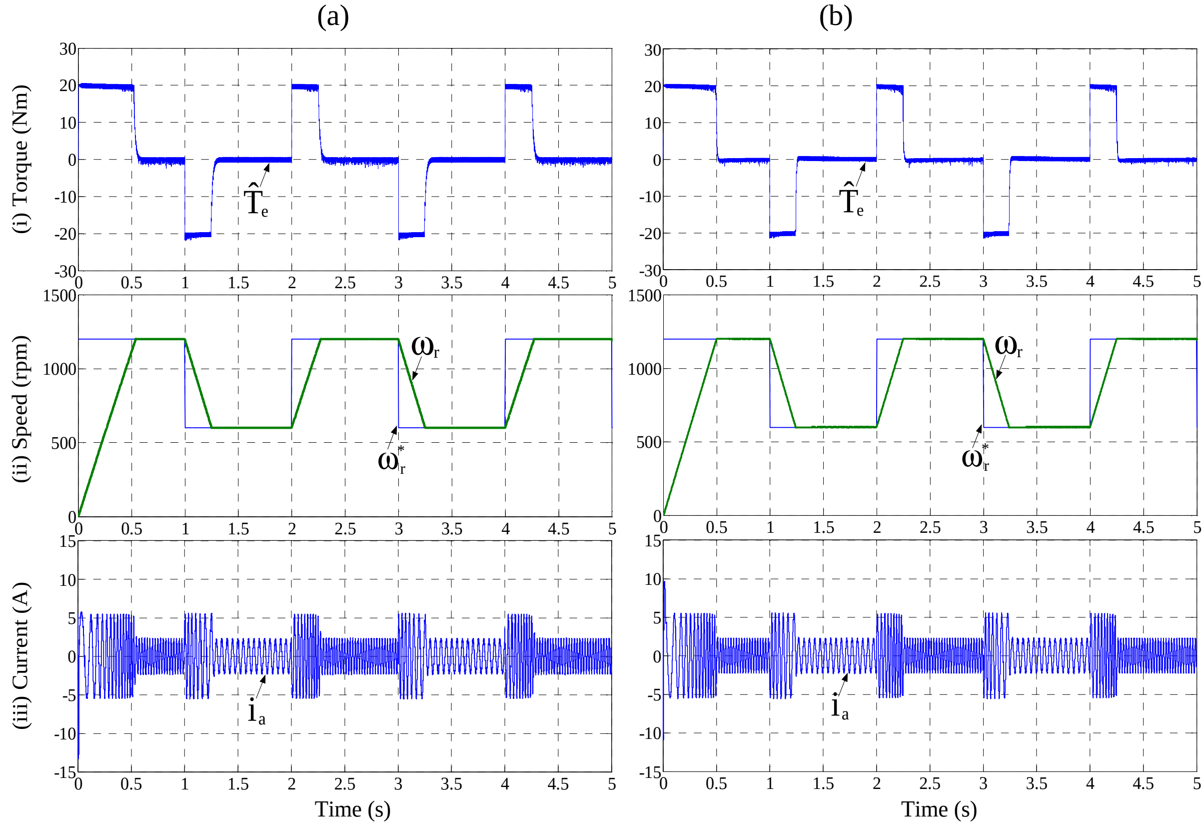

Figure 3.25 Performance under sudden change in square speed command using: (a) T1FLC and (b) T2FLC: (i) Torque, (ii) speed and (iii) current

3.4.5 Performance under Forward Speed with Load Torque Operation

The performance of IMD under forward motoring with load torque is observed using PIC, T1FLC and T2FLCs. A load torque of 9 Nm is applied at starting with a set reference speed of 1200 rpm. It is found that the actual speed reaches the reference speed quickly at 0.925 s using T2FLC, whereas it reaches at 1.504 s using PIC scheme is shown in Figure 3.26 (a)-(c). The performance of IMD is also observed under forward motoring with different load torque conditions at the reference speed of 1200 rpm using three different speed controllers, which are summarized in Table 3.2. From the Table 3.2, the dynamic speed responses of time domain specifications (rise time and settling time) and the bar chart of performance indices (IAE, ISE, ITAE, ISTE and RMSE) are illustrated in Figure 3.27 and Figure 3.28, respectively. From these results, it is found that the T2FLC has superior time domain specifications and performance indices compared to the PIC and T1FLC.

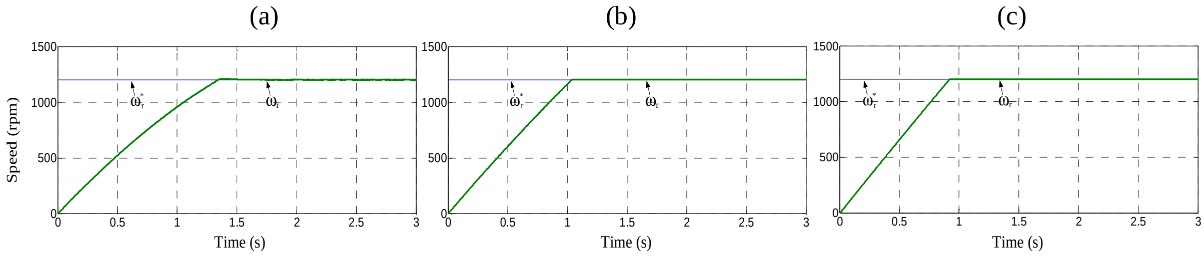

Figure 3.26: Performance under forward motoring with starting load torque of 9 Nm using: (a) PIC, (b) T1FLC and (c) T2FLC

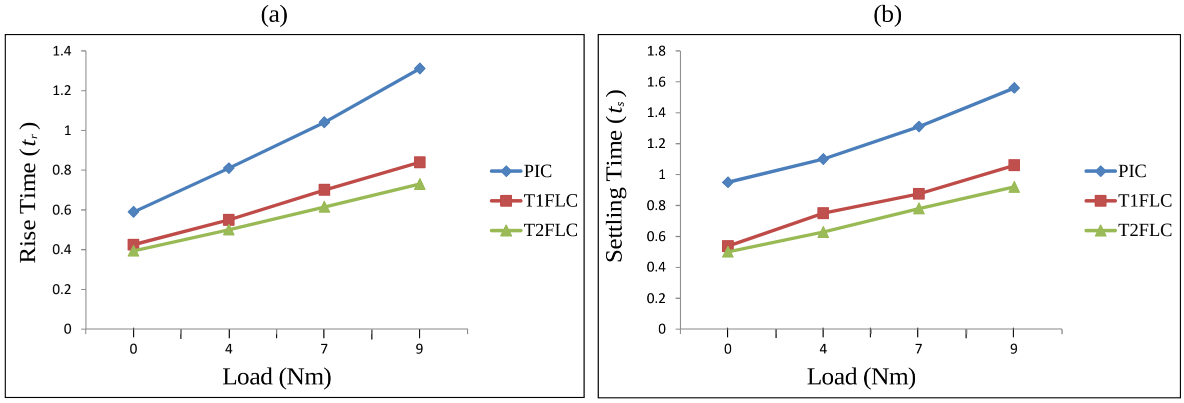

Figure 3.27: Dynamic responses of time domain specifications with different starting load torque conditions using different controller schemes: (a) Rise time (t_r) and (b) settling time (t_s)

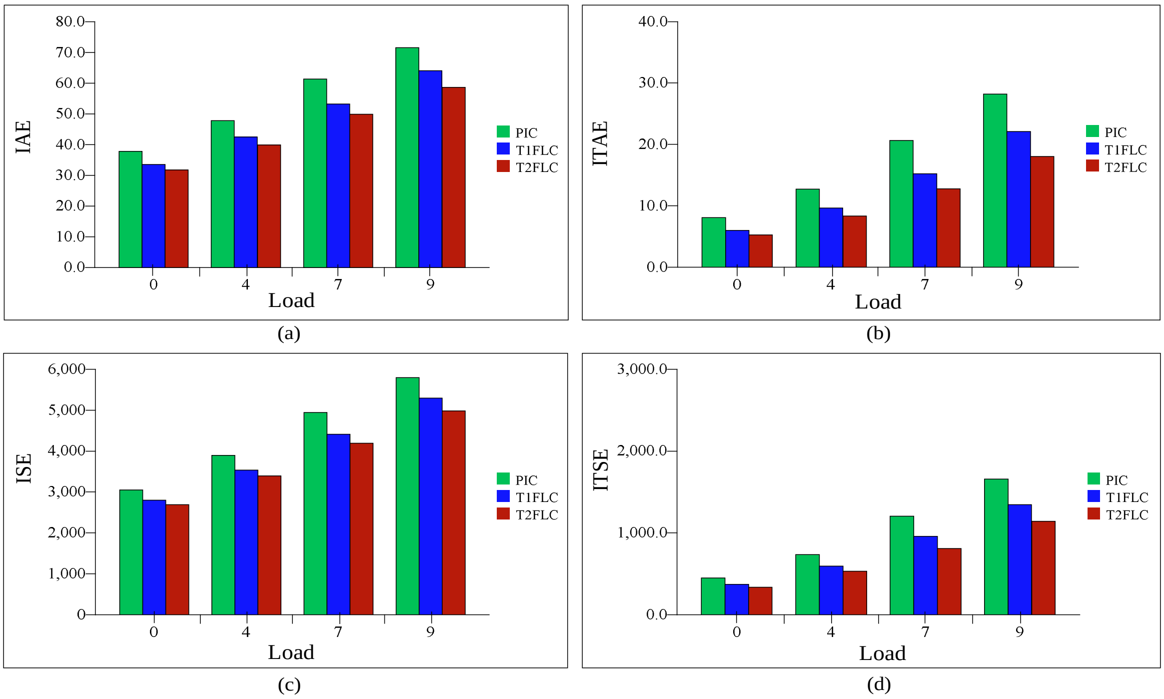

(a) (b)

(c) (d)

Figure 3.28: Bar chart of performance indices under various starting load conditions using different controller schemes are: (a) IAE, (b) ITAE, (c) ISE and (d) ITSE

3.4.6 Performance Indices

In order to give a clear idea of the performance of the three controller schemes, the performance indices (IAE, ITAE, ISE, ISTE and RMSE) are calculated using each control scheme under forward motoring (reference speed of 1200 rpm) with no-load torque operation shown in Figure 3.29. It is found that the T2FLC shows lowest performance indices, because the T2FLC can cope with the uncertainties in a better way by modelling them and reducing their effect on the controller performance compared to PI and Type-1 fuzzy logic controller.

Table 3.2: Performance indices under forward motoring with different starting load torque conditions using three different controller schemes

Starting Load Torque	Controller	Time domine specification			Performance indices					Total Indices
		t_r (s)	M_p (%)	t_s (s)	IAE	ISE	ITAE	ITSE	RMSE	
0	PIC	0.590	1.125	0.695	37.79	3048	8.060	448.80	40.58	3583.23
	T1FLC	0.425	0.079	0.537	33.52	2797	5.990	369.80	38.88	3245.19
	T2FLC	0.394	0.000	0.498	31.80	2706	5.280	336.10	38.25	3117.43
4	PIC	0.810	1.058	1.110	47.85	3896	12.54	736.90	45.89	4739.18
	T1FLC	0.550	0.068	0.790	42.46	3533	9.644	592.90	43.70	4221.70
	T2FLC	0.500	0.000	0.628	39.91	3394	8.324	529.30	42.83	4014.36
7	PIC	1.040	0.894	1.310	61.41	4942	20.65	1205.0	51.75	6280.81
	T1FLC	0.700	0.056	0.875	53.23	4412	15.21	929.10	48.84	5458.38
	T2FLC	0.615	0.000	0.780	49.37	4195	12.75	809.50	47.62	5114.24
9	PIC	1.310	0.816	1.504	78.02	5989	31.38	1796.0	57.89	7952.29
	T1FLC	0.840	0.042	1.060	64.08	5295	22.10	1343.0	53.50	6777.68
	T2FLC	0.760	0.000	0.925	58.70	4982	18.04	1143.0	51.89	6253.63

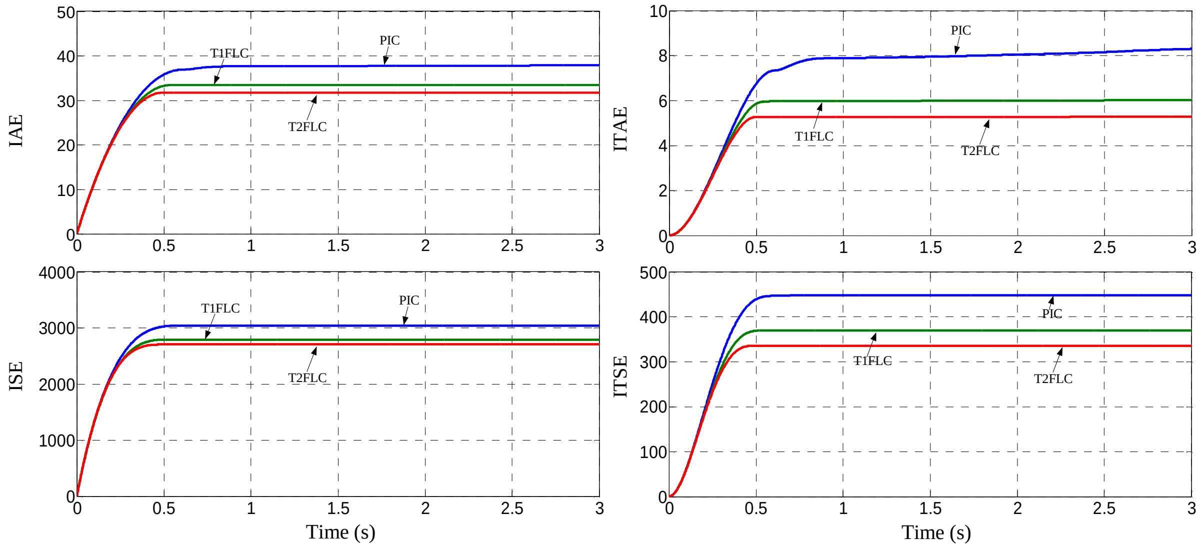

Figure 3.29: Performance indices under forward motoring with no-load torque operation

The performance indices are calculated under sudden load torque operation using three controller schemes. The sudden load torque of 9 Nm is applied at 1.4 s when the IMD is operating at 1200 rpm as shown in Figure 3.30 (a)-(d).

The performance indices under forward motoring (i.e. 1200 rpm) with various starting load torque conditions are observed using three controller schemes, which are illustrated in Table 3.2. It is observed that the PIC shows the highest performance indices whereas lowest performance indices using T2FLC scheme.

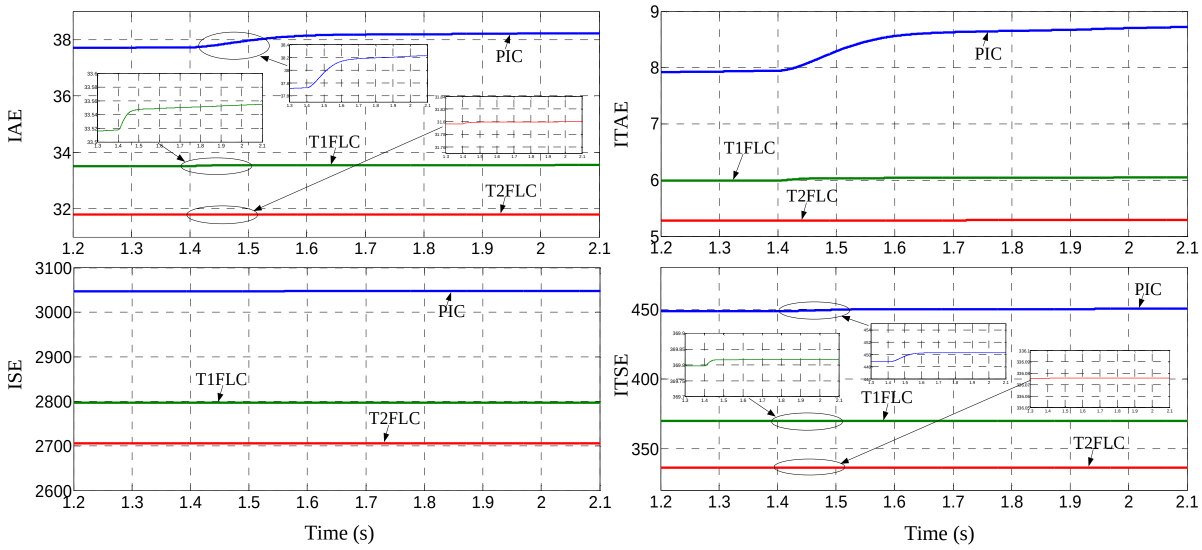

Figure 3.30: Performance indices under forward motoring with sudden load torque operation

3.5 Conclusion

In this chapter, the DTFC of an IMD using Type-1 and Type-2 FLCs has been validated through the simulation (i.e. MATLAB/SIMULINK). The T1FLC provides considerable flux and torque ripples. Moreover, it shows poor load torque disturbance rejection. The T2FLC shows improved performance and also robustness to the sudden changes in speed and load torque disturbances. Finally, in order to give a clear idea of the performance of the three controller schemes, the time domain specifications and parameter indices are calculated for each controller scheme. It is noticed that the T2FLC scheme perform satisfactorily in all speed ranges with the different loading conditions.

The performance evaluation through the simulation and experimental implementation are the two major steps to validate the DTFC of an IMD using Type-1 FLC and Type-2 FLCs, respectively. The primary step has been covered in this chapter. The experimental prototype system is required to perform the second step. Therefore, the development of the experimental prototype system for DTFC of an IMD is presented in the following chapter.

Chapter 4

Development of Experimental System

CHAPTER 4: DEVELOPMENT OF EXPERIMENTAL SYSTEM

An experimental prototype system (EPS) is required for the experimental validation of the different controller schemes developed in this work, such as PIC, Type-1 FLC and Type-2 FLC based speed controller schemes. The EPS has been developed using a 1.5 kW IM, Intelligent Power Module (IPM) based two-level VSI, Digital Signal Processor (DSP) DS1104 dSPACE interfacing controller board and related control circuits. In this chapter system hardware, DSP DS-1104 dSPACE interfacing and experimentation of the laboratory prototype models are described in detail to validate the simulation results presented in the previous chapters. Further, these experimental studies are validated with simulation results using the experimental parameters. A dSPACE DS-1104 controller board is used for the real-time testing and implementation of different control algorithms. Initially, the control algorithm is designed in the MATLAB/SIMULINK software (MATLAB R2009a) and then the real-time workshop of MATLAB is used to generate the optimized C code for real-time testing. The interface between controller board (DS-1104) and MATLAB/SIMULINK allows the control algorithm to run the EPS. The developed EPS includes all the necessary features for the validation/testing of any three-phase AC drives.

This chapter is organized as follows:

- *The introduction of EPS is presented in section 4.1.*
- *The complete details about the development of the EPS using a three-phase two-level VSI module, sensing cards for voltage, current and speed measurements and protection circuits are presented in section 4.2.*
- *The simulation results which are presented in chapter-2 and chapter-3 are validated with the experimental results, which are presented in section 4.3.*
- *The comparison of simulation and experimental results using three controller schemes are presented in section 4.4.*
- *Finally, the conclusion and remarks are presented in section 4.5*

4.1 Introduction

To validate the viability and effectiveness of the PIC, Type-1 and Type-2 FLC based DTFC of an IMD, an EPS is developed in the laboratory. The experimental prototype system is developed using the insulated-gate bipolar transistors (IGBTs) as the switching devices for realizing the inverter based power module. The other hardware components as required for the operation of the experimental setup, such as three-phase IM, voltage sensor, current sensor and speed sensor circuits and protection circuits are developed in the laboratory [203].

A dSPACE DS1104 controller board is used for the real-time simulation and implementation of control algorithms [204]. By using the Real-Time Workshop (RTW) of MATLAB and Real-Time Interface (RTI) feature of dSPACE DS1104, the MATLAB/SIMULINK models of the various controller schemes are implemented. The control algorithm is first designed in the MATLAB/SIMULINK environment and then the RTW of MATLAB generates the optimized C-code for real-time implementation. The interface between MATLAB/Simulink and DSP DS1104 of dSPACE allows the control algorithm to run on the hardware. The master bit I/O is used to generate the required gate pulses and the Analog to Digital Converters (ADCs) are used to interface the sensed voltage, currents, and speed. An optoisolated interface board is also used to isolate the entire DSP master bit I/O. The DTFC of an IMD using PIC, T1FLC, and T2FLC schemes are simulated and verified with the experimental setup using dSPACE DS-1104.

The development of different hardware components are required for the operation of the hardware prototype, which are discussed in the following sections.

4.2 The Development of Experimental Setup

The complete schematic diagram for a realization of the experimental setup (ES) is shown in Figure 4.1. The developed experimental setup consists of the following basic parts.

1. Power circuit (PC)
2. Induction motor and DC machine set
3. Power module (PM)
4. Measurement of various signals
    - The DC-Link voltage of the inverter
    - The DC-link current of the inverter
    - The phase currents of IM
    - The speed of IM
5. Protection circuits
    - Over Voltage (OV)
    - Under Voltage (UV)
    - Over Current (OC)
    - Short Circuit (SC)
6. Optocouplers
7. Development of system software
8. Hardware control

The working stages of each part are described in the following sections.

4.2.1 Power Circuit

A two-level VSI fed IMD has been developed to implement the various control schemes is shown in Figure 4.2. The PC consists of 3-Φ auto-transformer, power module (3-Φ uncontrolled rectifier and inverter module) and the 3-Φ squirrel cage induction motor. A 3-Φ power supply through the 3-Φ auto transformer is supplied to the 3-Φ uncontrolled rectifier, which produces the DC-link voltage. This DC-link voltage is provided to the inverter. Generally, the two-level VSI requires six power semiconductor devices as shown in Figure 4.2. The output of the inverter is then connected to the IM.

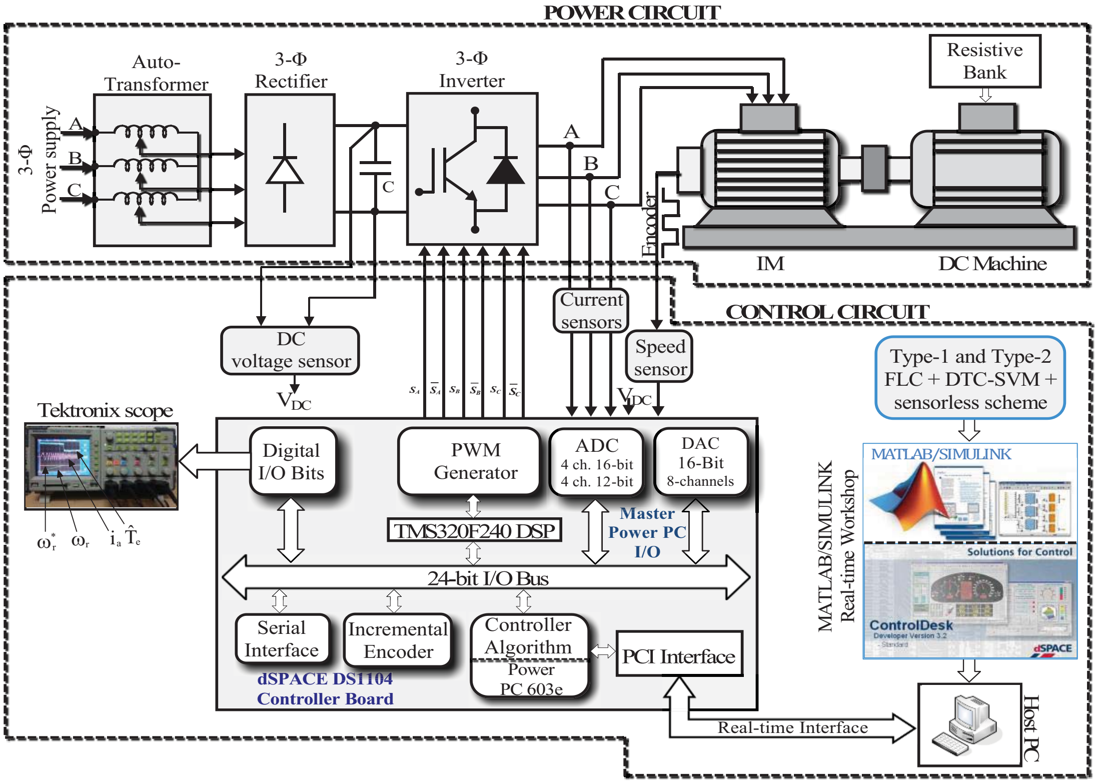

Figure 4.1: Configuration of the experimental setup

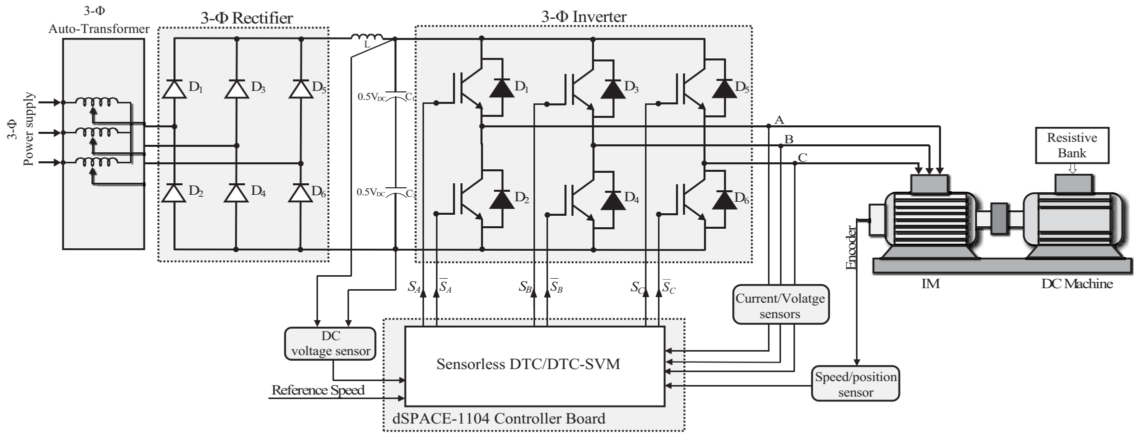

Figure 4.2: Configuration of the power circuit

4.2.2 The Induction Motor

A 1.5 kW, 4-pole star connected three-phase squirrel-cage IM, manufactured by the SIEMENS, is used for experimental validation. The equivalent circuit parameters of the IM were obtained through a set of tests, such as DC, no-load and blocked rotor tests. The magnetizing inductance, core and mechanical losses are calculated using the no-load test, while the stator and rotor leakage inductances and the rotor resistance are calculated using the blocked rotor test. Finally, the stator resistance is calculated using the DC test. The parameter values of IM obtained from the above tests are illustrated in Appendix C.

4.2.3 Power Module

The intelligent power module (IPM-PM25RSB120) is used as a rectifier and inverter [203]. The IPMs are advanced hybrid power devices that combine high speed, low loss IGBTs with optimized gate drive and protection circuitry. The IGBTs based IPMs with a rating of 1200 V /25 A has been used as the switching devices for realizing the two-level VSI. These switching devices are controlled by the DSP DS-1104 dSPACE controller board. The internal diagram of the power module is shown in Figure 4.3.

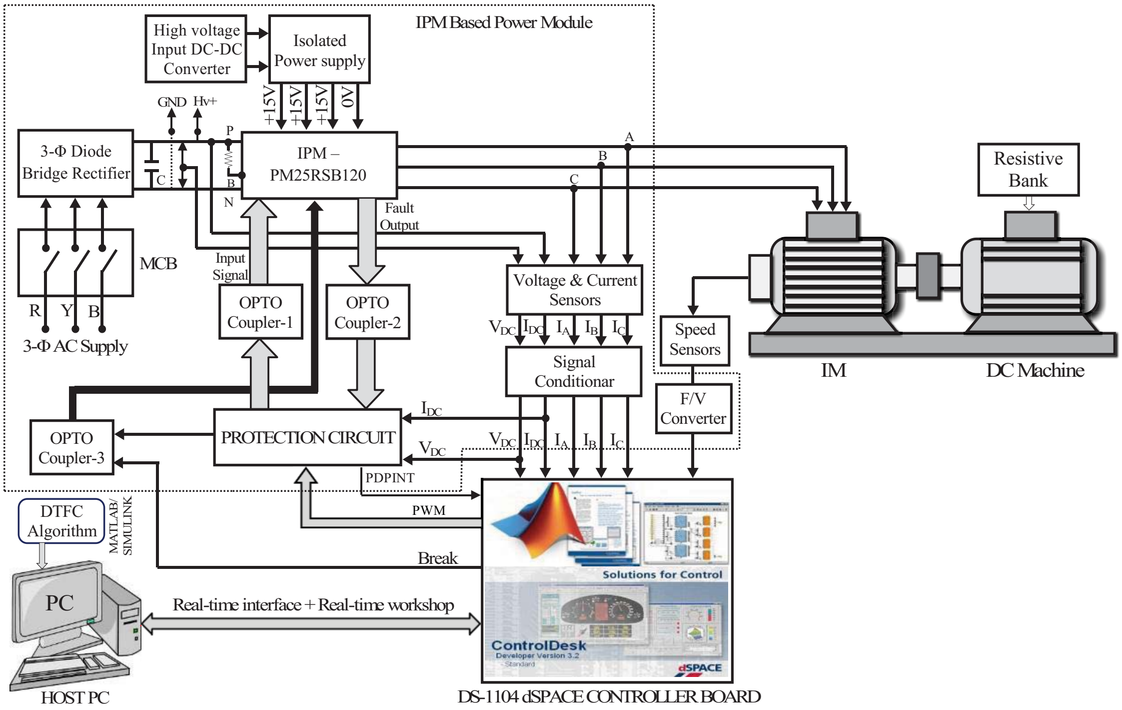

Figure 4.3: Schematic model of IPM based power module

The large effective OC and SC protections are realized through the use of advanced current sense IGBT chips that allow continuous monitoring of power device current. The system reliability is further enhanced by the IPM's integrated OT and UV lockout protection. The IPM has a temperature sensor mounted on the isolating base plate near the IGBT chips.

If the temperature of the base plate exceeds the OT trip level the IPMs internal control circuit will protect the power devices by disabling the gate drive and snubbing the control input signal until the OT condition has diminished [203]. The IPM has been optimized for minimum switching losses in order to meet industry demands for acoustically noiseless inverters with carrier frequencies up to 20 kHz. The built-in gate drive and protection have been carefully designed to minimize the components required for the user supplied interface circuit.

4.2.4 Measurement of Various Signals

For the accurate and reliable operation of the system in a closed loop, the measurement of various signals (voltage, current and speed) and their conditioning is required. The measurement system must fulfill the following requirements:

- High accuracy
- Linearity and fast response
- Galvanic isolation with power circuit

With the availability of isolation amplifiers and Hall-effect current sensors, these requirements are fulfilled to a large extent. In order to implement the control algorithm of DTFC of an IM drive, the following signals are measured:

1. The DC-link voltage
2. The DC-link current
3. The phase currents of the IM
4. Speed of the IM

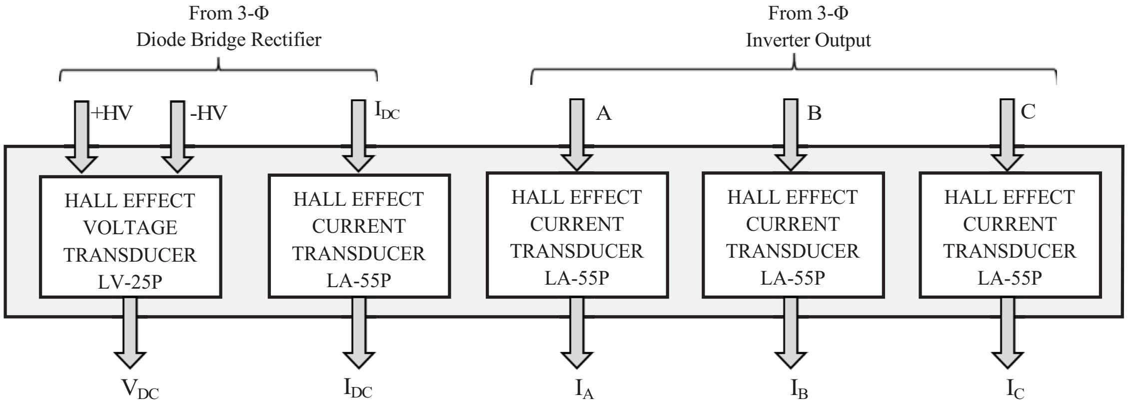

Figure 4.4: Voltage and current sensing cards

The schematic model of various measurement signals is shown in Figure 4.4. The sensor used for voltage and current measurements work on the principle of Hall-effect (HE), hence these sensors are called HE transducer. The IPM output currents and voltage are not directly fed into control circuits. The output of the IPM is very high, but the control circuit operates at low voltage. Therefore, it is essential to convert the IPM output from high voltage to low voltage and voltage transducer sense from high voltage to low voltage, i.e., maximum of 5 V. In order to implement the control algorithm of the IMD in closed loop operation, the following signals have been sensed. The detail information about the voltage, current and speed sensors are described in the following subsections.

4.2.4.1 Current Sensing Card

The schematic model of the current sensing cards is shown in Figure 4.5. The DC link current and line currents of the inverter module are sensed through LEM HE current transducer (LA-55P). The LA-55P is closed loop HE current transducer suitable for measuring current up to 50 A. These current sensors provide the galvanic isolation between the high voltage power circuit and the low voltage control circuit that require a nominal power supply voltage of the range ±12 V to ±15 V. The HE current transducer outputs depend upon transducer primary and secondary winding ratio. The ratio of the number of primary turns to the number of secondary turns for a typical value is 1000:1. A 100 Ω resistor is connected to the M terminal, which converts the current signal into the equivalent voltage signal of 0.1 V/A. The resistance value is chosen in such a way that the voltage across it will not exceed the specification of the ADC. The output of the current / voltage sensor is scaled properly to meet the requirement of the control circuit and it is fed to the dSPACE via its ADC channel for further processing.

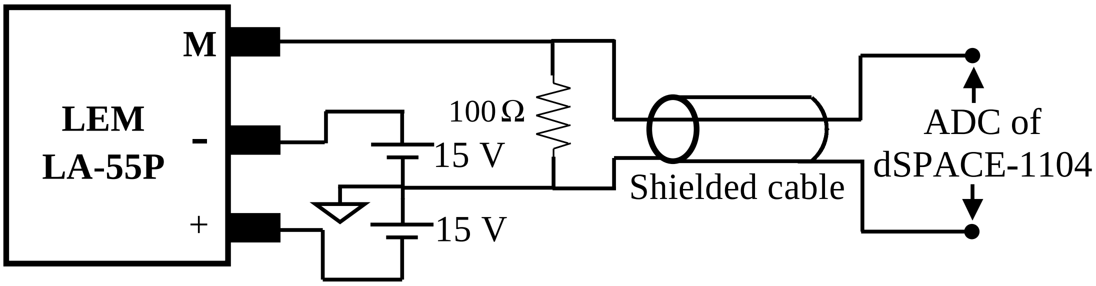

Figure 4.5: Current measurement through LA-55P

4.2.4.2 Voltage Sensing Card

The schematic model of the voltage sensing card is shown in Figure 4.6. The DC-link voltage is sensed through HE voltage transducer using LV-25P. The measurement of DC-link voltage is required for the protection of the IPM from the over and/or under voltages. The HE voltage transducer output depends upon the transducer primary and secondary winding ratio. The principles of the current and voltage transducer are same, but the difference exists in the primary winding of the voltage transducer. A resistor is connected in series with the primary winding of voltage transducer. This resistance can be external or integrated into the transducer construction. The voltage signal is processed through a RC low-pass filter (LPF) before feeding it to the ADC of the dSPACE DS-1104 controller board. The final output is obtained through a unity gain buffer amplifier.

4.2.4.3 Speed Sensing Card

The motor speed is sensed through an incremental encoder (HEDM-5605). An incremental encoder (IE) is mounted on the shaft of the IM. As the disk rotates, it generates two sets of quadrature encoder pulses (QEP), i.e. (QEPA, QEPB) in clockwise and ($\overline{\text{QEPA}}$, $\overline{\text{QEPB}}$) in anticlockwise direction that are shifted 90° out of phase from each other. The encoder also generates the index pulses, i.e. QEPI, $\overline{\text{QEPI}}$, which can be used to indicate an absolute position. The IE generated signals (i.e. QEPA, QEPB, $\overline{\text{QEPA}}$, $\overline{\text{QEPB}}$, QEPI, $\overline{\text{QEPI}}$) are shown in Figure 4.7 (a). The encoder wheel typically makes one revolution for every revolution of the motor. The frequency of the pulses is 512 pulses-per-revolution. Therefore, the frequency of the digital signal coming from the QEPA and QEPB varies proportionally with the velocity of the motor. These signals (i.e. QEPA, QEPB, $\overline{\text{QEPA}}$, $\overline{\text{QEPB}}$, QEPI, $\overline{\text{QEPI}}$) are fed to the capture. The QEP units of the dSPACE controller board through frequency to voltage converter are shown in Figure 4.8. The enhanced QEP module is used for direct interface with a linear or rotary IE to get the position, direction and speed information from a rotating machine. The specification of the IE is shown in Appendix C.

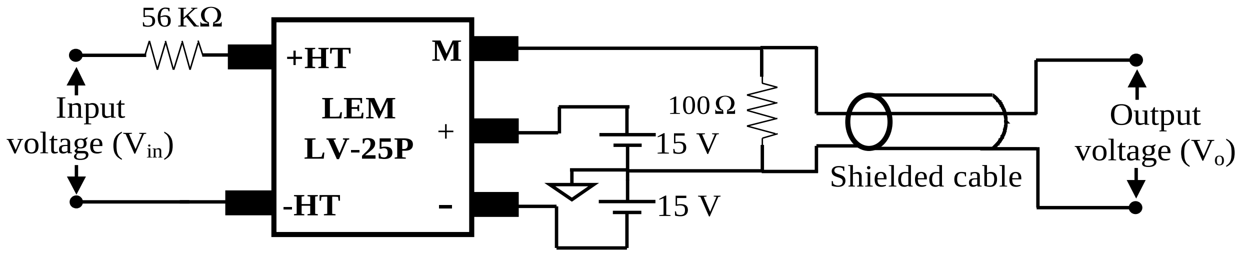

Figure 4.6: Voltage measurement through LV-25P

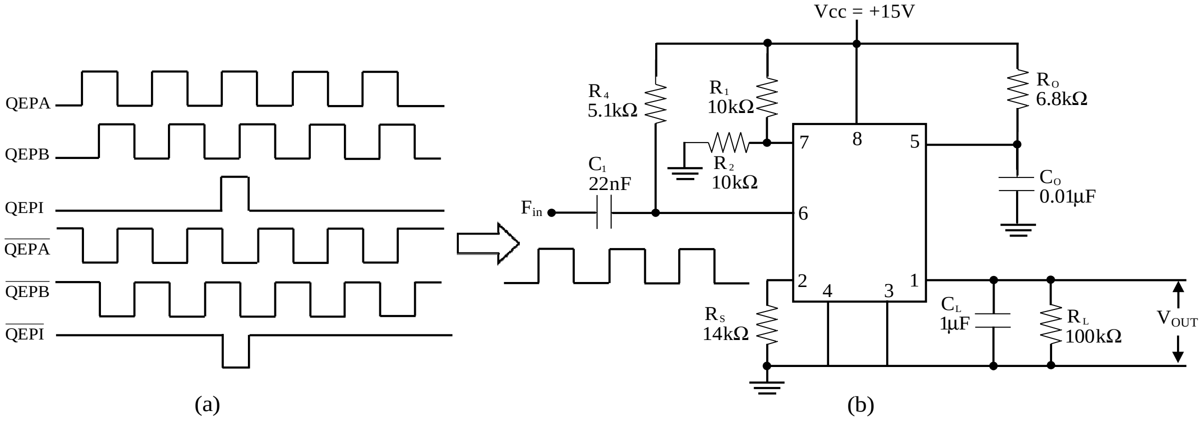

(a) (b)

Figure 4.7: (a) Signals from incremental encoder and (b) Frequency to voltage converter circuit

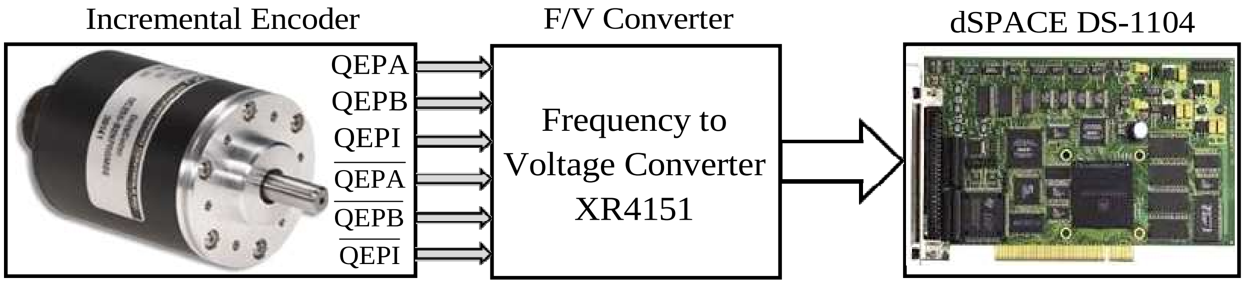

Figure 4.8: Speed sensing with incremental encoder

The square wave of speed sensor output is fed to a frequency to voltage converter circuit as shown in Figure 4.7 (b). The XR4151 can be used as a frequency to voltage converter. The input frequency range is 0 to 10 kHz and corresponding voltage output level is -10 mV to -10 V.

The actual motor speed is measured by a HEDS 5645 incremental encoder attached to the shaft of the induction machine having 512 encoder lines per revolution. The encoder signal interfaces to the dSPACE system via an incremental encoder interface. The rotor speed measurement is to allow DTFC operation with speed sensor and it is employed as a reference for sensorless operation.

4.2.5 Signal Conditioner

The voltage and current signals which are obtained from the voltage and current sensors are processed through the signal conditioner. These signals are properly scaled to meet the requirement of the control circuit and are fed to the dSPACE via its ADC channel for further processing. The schematic model of the current signal processing circuit is shown in Figure 4.9.

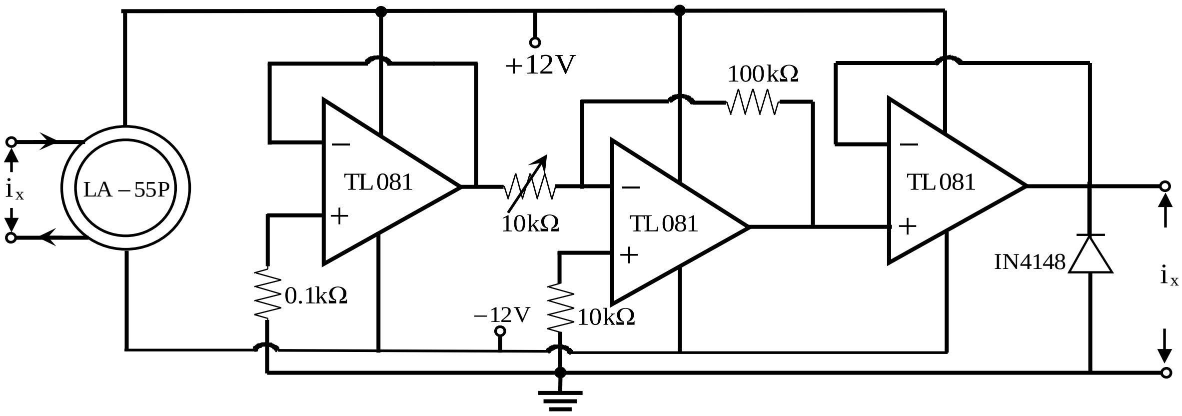

Figure 4.9: Current signals processing circuit, Here X=A, B, C

4.2.6 Protection Circuit

The protection circuit of the complete system is used to prevent from any abnormal electrical conditions, such as UV/OV, OC, OT, SC is essential for the safe operation and also to avoid damage of any switching devices and other components. The various stages of protection circuit are shown in Figure 4.10.

The measured signals from voltage and current sensors (i.e. BLOCK-1) are fed into the signal conditioner (i.e. BLOCK-2) to generate the proper scaled output signals (i.e. voltage/current) and then these signals are fed into the protection circuit (BLOCK-3). It generates the PDPINT signal, which blocks the gate pulses before the driver, whenever OV, UV, SC, OC and OT have occurred in the system.

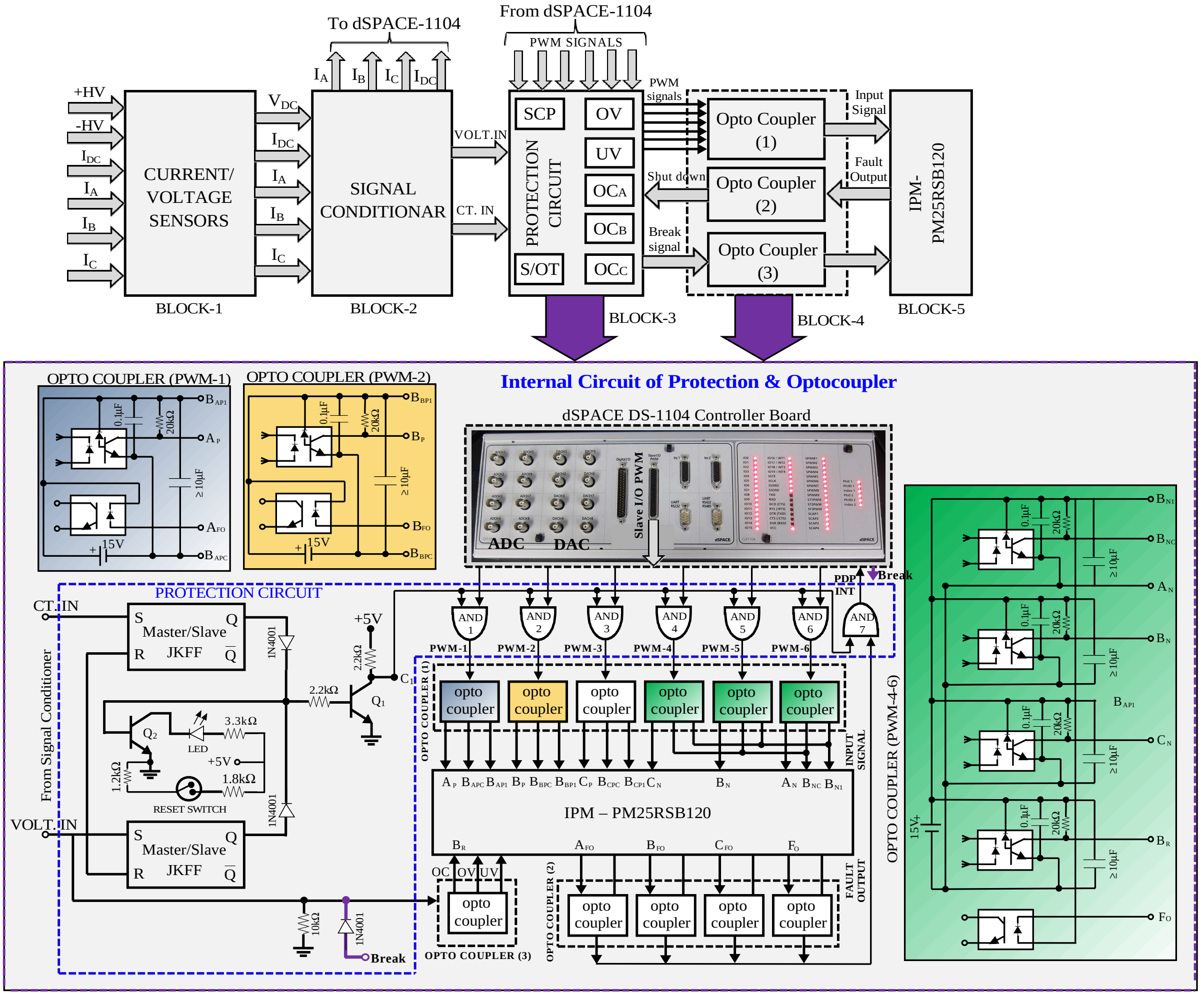

Figure 4.10: Various stages of protection circuit

The schematic diagram of various stages of the protection circuit is shown in Figure 4.10. The current and voltage signals from BLOCK-2 are fed into the input of master / slave JK Flip-Flops (JKFFs). The Master / Slave JKFF output is connected to transistors Q_1 and Q_2. Transistor Q_1 output C_1 terminal is given to the input of AND gates (1-7). The other input of AND gates (1-6) are fed from pulse width modulation (PWM) output of dSPACE DS-1104 controller board. The output of AND gates (1-7) depends upon transistor Q_1 output, then the AND gate’s output is fed into IPM through optocoupler (1). The IPM generates the fault output signals when OC/ OV occur in the system. This signal is fed into optocoupler (2) and its output is ANDed with Q_1 output (C_1) signal. The AND gate (7) output is fed into the input of PDPINT (dSPACE). Under normal condition, the output of PDPINT is high, whereas PDPINT is disabled when OT and OC occurred in the power circuit of the joint to C_1.

Several protection hardware requirements are built in the protection circuit when OV/OC occurs in a power circuit, then the output of dSPACE CT.IN/VOLT.IN is high (i.e. 1). The input of master/slave JKFF J = 1 and its output is Q = 1, $\overline{Q}$ = 0, then the transistors Q_1 and Q_2 conduct and shutdown LED will glow (LED glow to indicate the power circuit affected by the OV / OC) at the same time transistor Q_1 output (C_1 terminal) is 0V. Then the AND gates (1-7) output is low (i.e. 0) and automatically cut the PWM signal to IPM and shut down the IPM. The voltage and current sensor output are fed into the ADC of dSPACE. When the OV /OC is found from the ADC inputs of dSPACE, then cut the PWM signal to protect the circuit and shut down the IPM. The signal conditioner outputs of dSPACE VOLT.IN and break signal from dSPACE, both signals are fed into optocoupler (3). This output fed to the input of IPM module. Both signals are enabled, when OV/OC occurs to the IPM at that time input of IPM B_R signal is enabled after that shut down the IPM unit, which is shown in the internal circuit of Figure 4.10.

4.2.7 Optocouplers

The function of optocoupler is to isolate the control circuit from the power circuit. The Figure 4.10 consists of a three blocks of optocouplers. The PWM signals (i.e. PWM 1 to PWM 6) come from dSPACE DS-1104 controller board are processed through optocoupler (1) to protect the IPM system. The IPM fault output signal is connected to optocoupler (2). The optocoupler (3) is connected between protection circuit and break signal.

4.2.8 System Software

Historically, control software was developed using assembly language. In recent years, the industry began to adopt MATLAB/SIMULINK and Real-Time Workshop (RTW) platform based method, which provides a more systematic way to develop control software. Figure 4.11 shows the Total Development Environment (TDE) of dSPACE and its major component blocks are explained as below:

- MATLAB is widely used as an interactive tool for modelling, analysis and visualization of systems, which itself contains more than 600 mathematical functions and supports additional toolboxes to make it more comprehensive.
- SIMULINK is a MATLAB add-on software that enables block diagram based modelling and analysis of linear, nonlinear, discrete, continuous and hybrid systems.

- RTW is SIMULINK add-on software that enables automatic C or ADA code generation from the SIMULINK model. The generated optimized code can be executed on a personal computer, microcontrollers and signal processors.
- Real-Time Interface (RTI) by add-on software of dSPACE provides block libraries for I/O hardware integration of DS1104 R&D controller and generates optimized code for master and slave processors of the board.
- The dSPACE control desk is a software tool interfacing with real-time experimental setup and provides easy and flexible analysis, visualization, data acquisition and automation of the experimental setup. The major feature of real-time simulation is that the simulation has to be carried out as quickly as the real system would actually run, thus allowing to combine the simulation and the inverter (real plant).

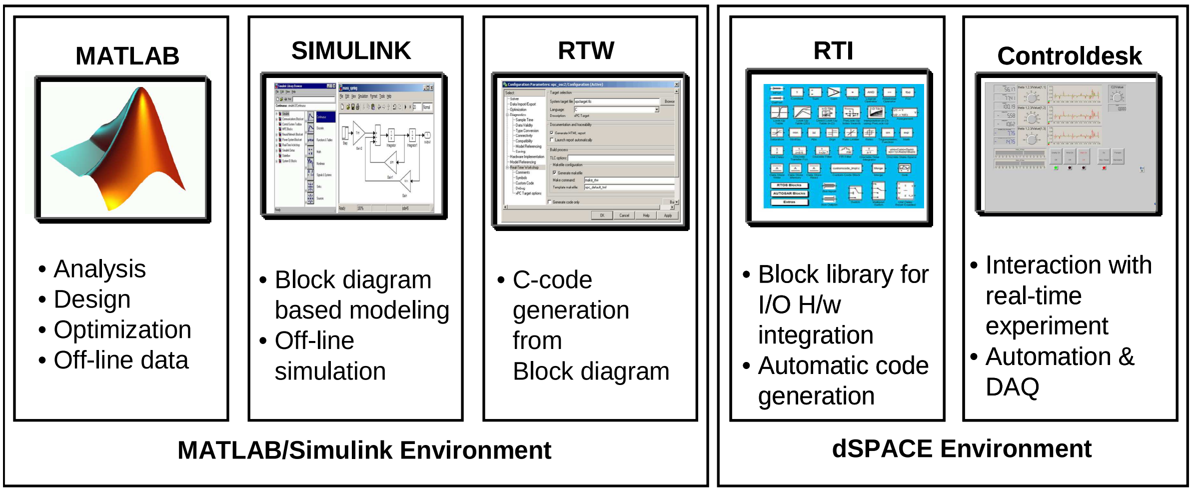

Figure 4.11: Total development environment of dSPACE with MATLAB/SIMULINK

The DSP DS1104 R&D controller board of dSPACE is a standard board that can be plugged into Peripheral Component Interconnect (PCI) slot of a desktop computer. The DS1104 is specially designed for the development of high-speed multivariable digital controllers and real-time simulations for various applications. It is a complete real-time control system based on a 603 PowerPC floating-point processor running at 2.6 GHz. It has 256 MB DDR-400 SDRAM local memory for handling dynamic application data and 128 MB SDR SDRAM global memory for host data exchange. In the board for advanced I/O purposes includes a slave-DSP subsystem based on the TMS320F240 DSP microcontroller. Specific interface connectors and connector panels provide easy access to all input and output signals of the board and help in rapid control prototyping (RCP). Thus, DS1104 R&D controller board is a very good platform for the development of a dSPACE prototype system for cost-sensitive RCP applications. It is used for the real-time simulation and implementation of the control algorithm in real-time. In the real-time simulation, the plant (power circuit of drive) is controlled by the controller (PI processor) that is simulated in real-time. This technique is called rapid prototype control. The major feature of real-time simulation is that the simulation has to be carried out as quickly as the real system would actually run, thus allowing to combine the simulation and the power circuit of the drive [204].

The sensed DC link voltage and three phase currents are fed to the dSPACE board via available ADC channels on its connector panel. In order to add an I/O block (such as ADCs and master bit I/Os in this case) to the Simulink model, the required block is dragged from the dSPACE I/O library and dropped into the Simulink model DTFC of an IMD. In fact, adding a dSPACE I/O block to a Simulink model is almost like adding any Simulink block to the model. In this case, six master bit I/Os configured in the output mode are connected to the model for producing six gating signals to the IGBTs.

The sensed signals are used for processing the designed control algorithm. The vital aspect of real-time implementation is the generation of real-time code of the controller to link the host computer with the hardware. In dSPACE systems, Real-Time Interface (RTI) carries out this linking function. Together with RTW from the Mathworks®, it automatically generates the real-time code from Simulink models and implements this code on the dSPACE real-time hardware. This saves the time and effort considerably as there is no need to manually convert the Simulink model into another language such as ‘C’. RTI carries out the necessary steps by the addition of the required dSPACE blocks (I/O interfaces) to the Simulink model. In other words, RTI is the interface between Simulink and various dSPACE platforms. It is basically the implementation software for single-board hardware and connects the Simulink control models to the I/O of the board. In the present case, the optimized C-code of the Simulink model of the control algorithm is automatically generated by the RTW of MATLAB in conjunction with RTI of dSPACE.

The generated code is then automatically downloaded into the dSPACE hardware where it is implemented in real-time and the gating signals are generated. The gating pulses for the power switches of the converter are issued via the Master-bit I/Os available on the dSPACE board. The DS2201 Connector/LED combo panel provides easy-to-use connections between DS1104 board and the devices to be connected to it. The panel also provides an array of LEDs indicating the states of digital signals (gating pulses). The gating pulses are fed to driver circuits via optocoupler and dead-band circuits. Figure 4.12 shows the schematic diagram of dSPACE-DS1104 board interfaced with the host computer and the real-world plant (power circuit of DTFC). Sensed signals are fed to the ADCs and generated gating pulses are given at Master bit I/Os.

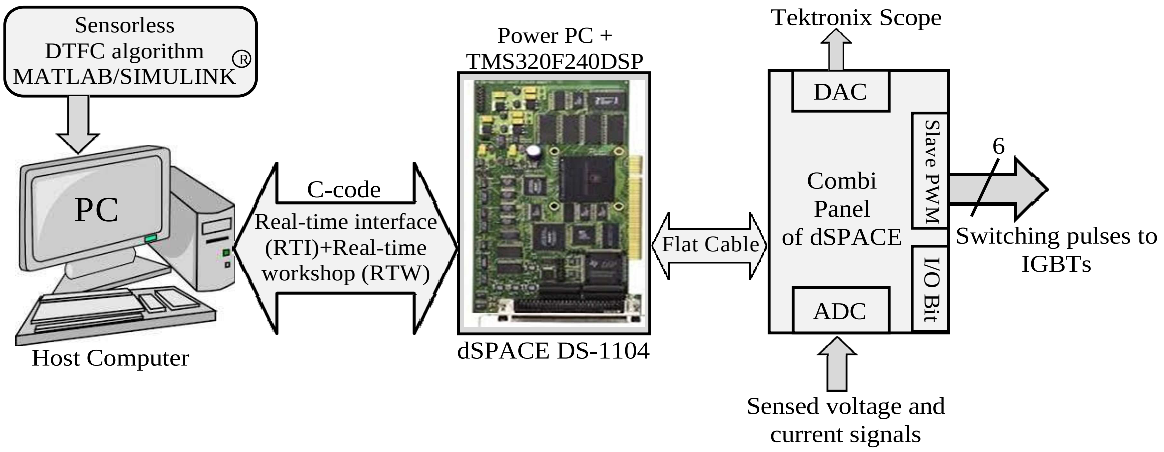

Figure 4.12: Digital signal processor (dSPACE DS-1104) circuit board interfacing

4.2.9 Hardware Control Development

The control algorithm is designed and built in MATLAB/SIMULINK software and the control pulses for 6 IGBTs (Here only 3 firing pulses are generated and remaining 3 are complementary of generated pulses) are generated by real-time simulation using the DSP of dSPACE. The optimized C-code of the SIMULINK model of control algorithm is generated with the help of RTW of MATLAB. The RTW of MATLAB and the RTI of dSPACE result in the real-time simulation of the model. The control pulses are generated at various Master-bit I/Os of the dSPACE, which are interfaced with the IGBT driver circuits through optocoupler and dead-band circuits [204]. This ensures the necessary isolation of the dSPACE hardware from the power circuit that is required for its protection. Figure 4.13 shows the basic schematic diagram of interfacing firing pulses from the dSPACE board to the switching devices of two-level VSI. In this figure, the details of only the phase–*a* cluster of two-level VSI is shown. From Figure 4.13, it can be observed that the following hardware circuits are required for interfacing the two-level VSI with dSPACE board.

1. Isolation circuit
2. Dead-band circuit
3. IGBT driver circuits

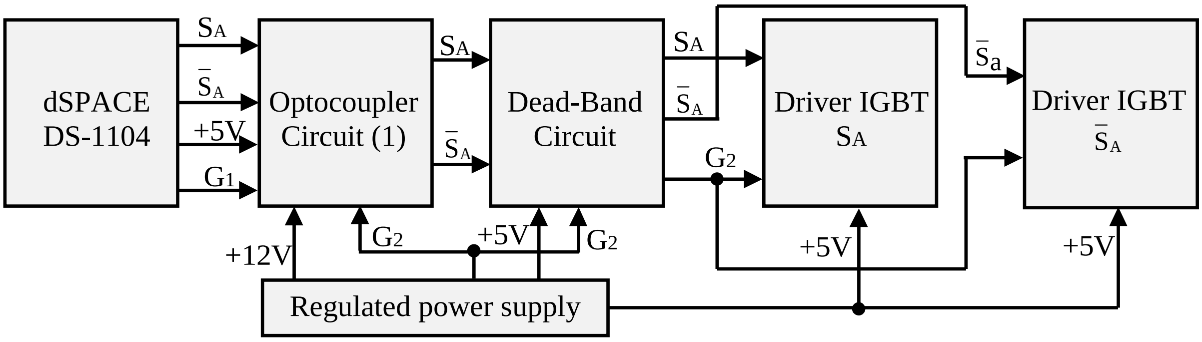

Figure 4.13: Schematic diagram of interfacing firing pulses from dSPACE controller board to switching devices of VSI (phase-A)

4.2.9.1 Optocoupler Circuit

An optocoupler is used for optical isolation of dSPACE hardware (Master-bit I/Os) from direct connection with the power circuit. The optocoupler (6N137) is used for optical isolation.

4.2.9.2 Dead-band Circuit

A dead-band (dead-time or delay) circuit is employed to provide a delay time (of about 5µs) between the switching pulses to two complementary devices connected in the same leg of a VSI. This is required to prevent the short circuit of devices in the same leg due to simultaneous conduction. The delay time between switches of the same leg of VSI is introduced by an *RC* integrator circuit as shown in Figure 4.14.

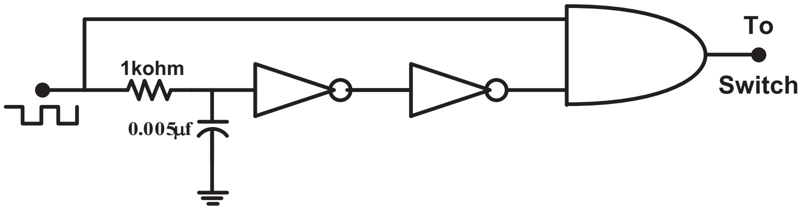

Figure 4.14: Dead-band circuit for each switching device

An identical dead-band circuit is used for each leg of VSI. The different switching signals obtained experimentally for semiconductor devices in the same leg of a two-level VSI are shown in Figure 4.15 with 5 µs delay. In Figure 4.15 the top and bottom signals are for the switches S_A and $\overline{S}_A$ respectively.

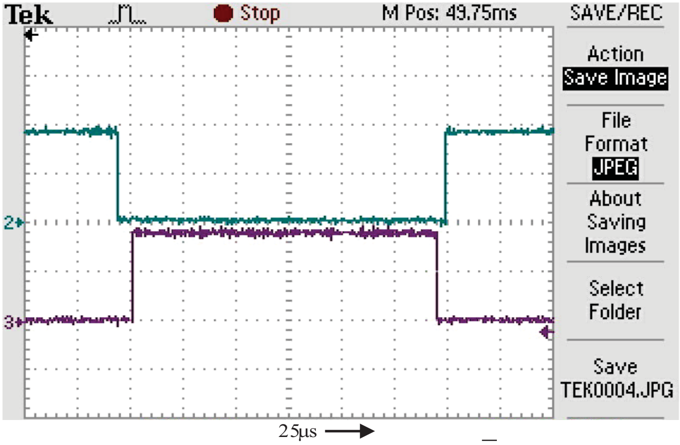

Figure 4.15: Firing signals for the switches S_A and $\overline{S}_A$ with dead-band circuit

4.2.9.3 IGBT Driver Circuits

The IGBT driver circuits are used for pulse amplification and isolation purposes. The IGBT driver circuits not only amplify the pulse signals for driving the devices, but also provide an optical isolation. The driver circuit has special features such as fault protection and protection against the UV lockout.

4.3 Experimental Results

The DTFC of an IMD using PIC, T1FLC and T2FLC are experimentally validated with the laboratory developed EPS and the results are presented here. The EPS is built around a dSPACE DS-1104 controller board. The detailed development of the EPS has been explained in the previous section and the photographic view of the complete experimental prototype is given in Appendix C. The proposed control schemes are tested under various operating conditions, such as forward motoring, reverse motoring, sudden change in step speed and different load torque operations, respectively. Note that the experiments have been performed under the similar conditions for which simulations have been carried out in chapter 2 and 3, respectively. The IM parameters, PIC gain values, switching frequency of the inverter with dead-band and the executed sampling frequency of the DTFC scheme are available in Appendix C. At starting, the reference speed of IM is initiated and the controlling signals are generated through a dSPACE DS-1104 kit and the required DC-link voltage of the inverter is set through a 3-Φ auto-transformer.

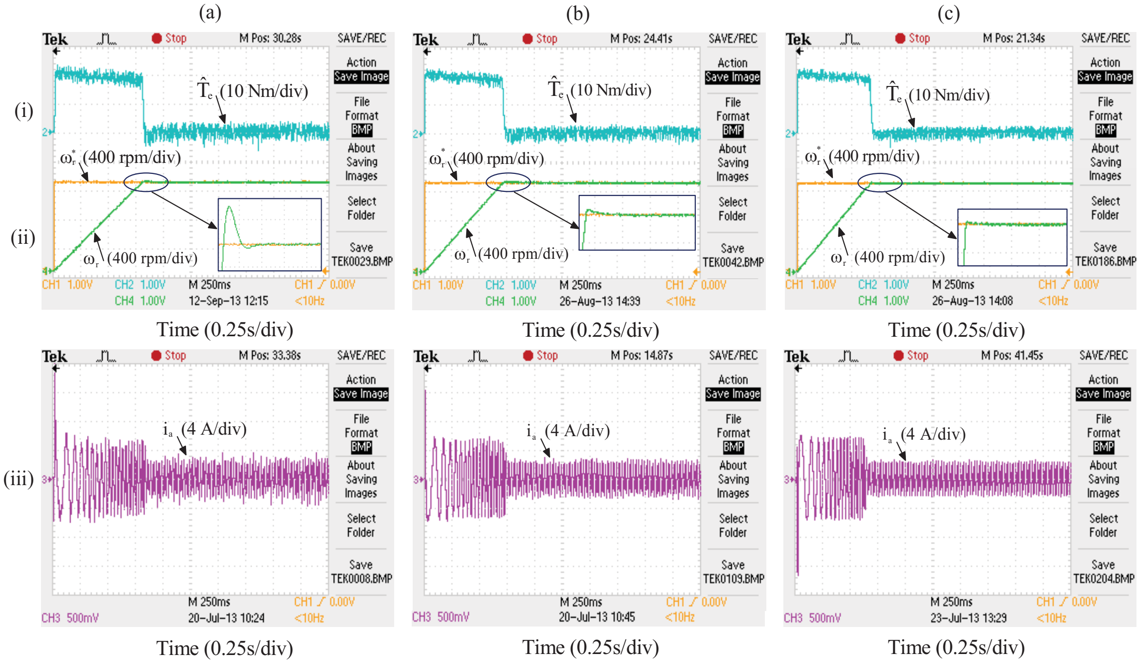

Figure 4.16: Performance of the IM under no-load torque operating condition using: (a) PIC, (b) T1FLC and (c) T2FLC: *Traces (from top to bottom):* (i) Torque, (ii) speed and (iii) stator current

4.3.1 Performance under Forward Motoring

Initially, the performance of the IMD is investigated under no-load torque operation at a reference speed of 1200 rpm using PIC, Type-1 and Type-2 FLC are shown in Figure 4.16 (a)-(c). The presented results are electromagnetic torque ($\hat{T}_e$), reference speed (ω_r^*), actual speed (ω_r) and stator current (i_a) are shown in Figure 4.16 (trace-i)-(trace-iii), respectively.

When the reference speed of 1200 rpm is applied, the IM develops an electromagnetic torque of 20 Nm with high amplitude of the stator current (±5.8 A) to reach the set reference speed. The IM starts at zero speed and it settles (1200 rpm) at 0.82 s, 0.735 s and 0.682 s with an overshoot of around 20 rpm, 2.5 rpm and 0.3 rpm (shown in zoomed view of Figure 4.16 (ii)) using PIC, Type-1 and Type-2 FLC schemes, respectively. Similarly, the stator current and electromagnetic torque is settled at the same time as shown in Figure 4.16 (i)-(iii). However, the stator flux ($\hat{\psi}_s$) and stator flux dq-components (i.e. ψ_{ds} and ψ_{qs}) in a stationary reference frame are almost same from initial state to the steady state is shown in Figure 4.17 (i) and (iii), respectively. The zoomed view of Figure 4.17 (i)-(iii) is presented in Figure 4.17 (iv). It is observed from the experimental results (from Figure 4.17 (i)) that the stator flux ripples are ±0.14 Wb, ±0.10 Wb and ±0.08 Wb using PIC, T1FLC and T2FLC, respectively. From Figure 4.16 (i), it is observed that the ripple content in electromagnetic torque is ±2.3 Nm, ±1.71 Nm and ±1.4 Nm using PIC, T1FLC and T2FLC, respectively.

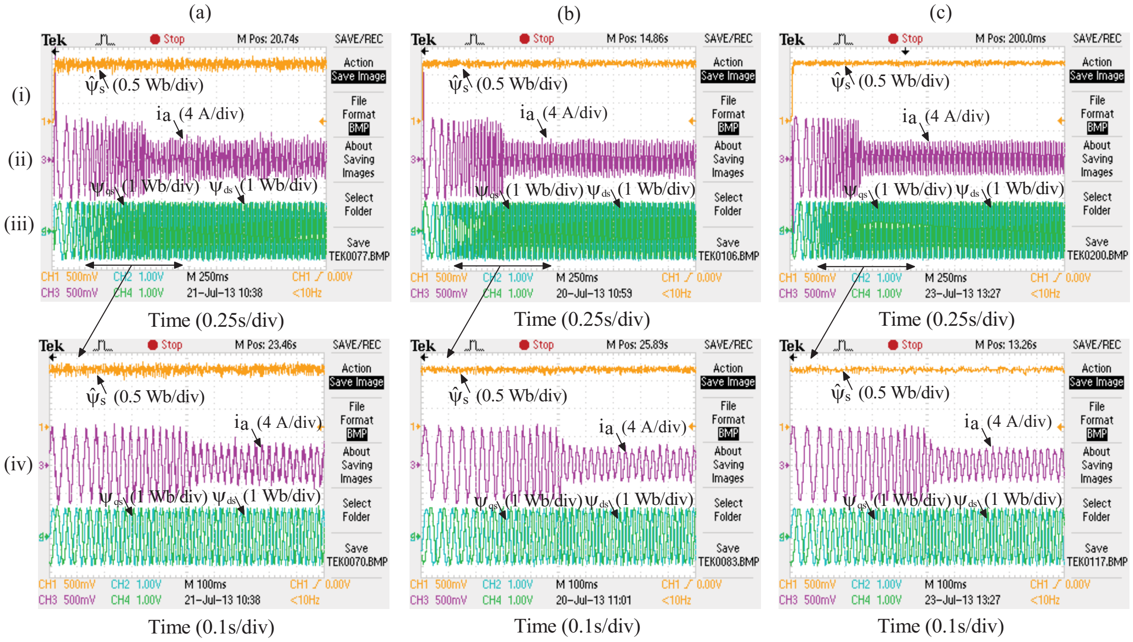

Figure 4.17: Performance of the IM under no-load torque operating condition using: (a) PIC, (b) T1FLC and (c) T2FLC: (i) stator flux, (ii) stator current, (iii) stator flux dq-components in stationary reference frame and (iv) zoomed view of (i-iii)

The steady-state performance of the IMD under no-load torque operating condition using PIC, T1FLC and T2FLC schemes are shown in Figure 4.18 (a)-(c), respectively. Note that the experimental results, which are presented in Figure 4.16, Figure 4.17 and Figure 4.18 (a)-(c) corresponding to the simulation results of the chapter-2 and chapter-3. It is observed that the excellent correlation between the simulation and experimental results. Both simulation and experimental results show the superiority of the T2FLC over T1FLC and PIC schemes.

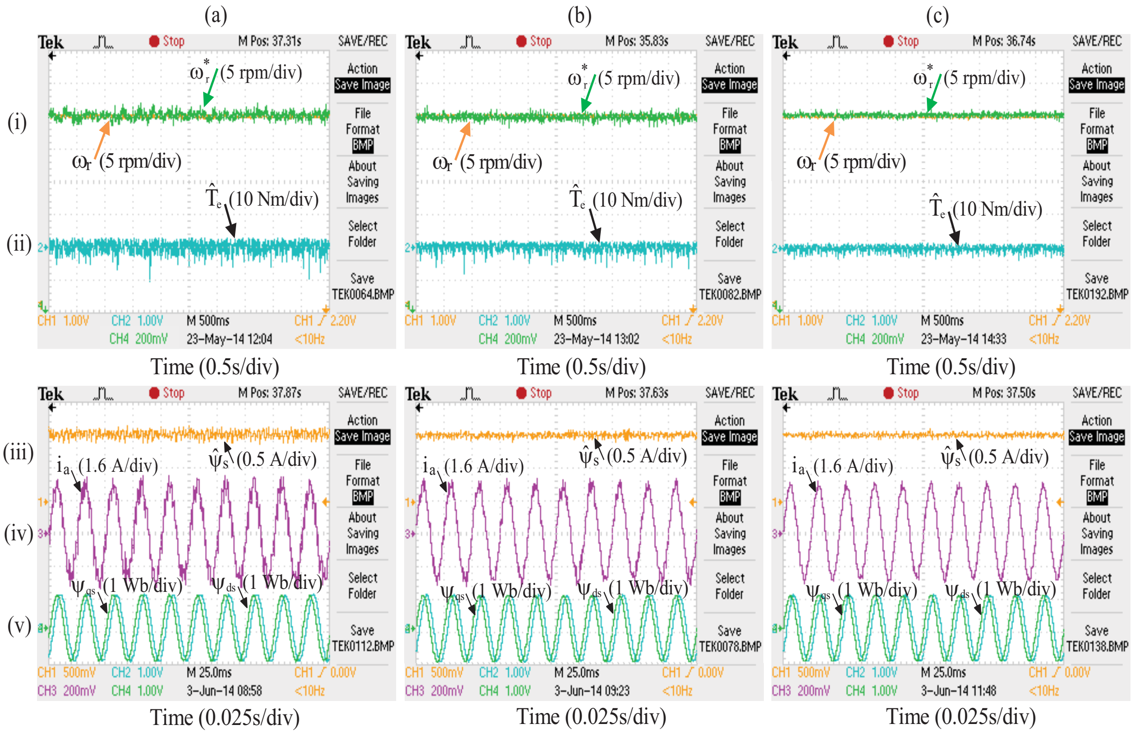

Figure 4.18: Steady-state performance of the IM under no-load torque operating condition using: (a) PIC, (b) T1FLC and (c) T2FLC: (i) speed, (ii) torque, (iii) stator flux, (iv) stator current and (v) stator flux dq-components in stationary reference frame

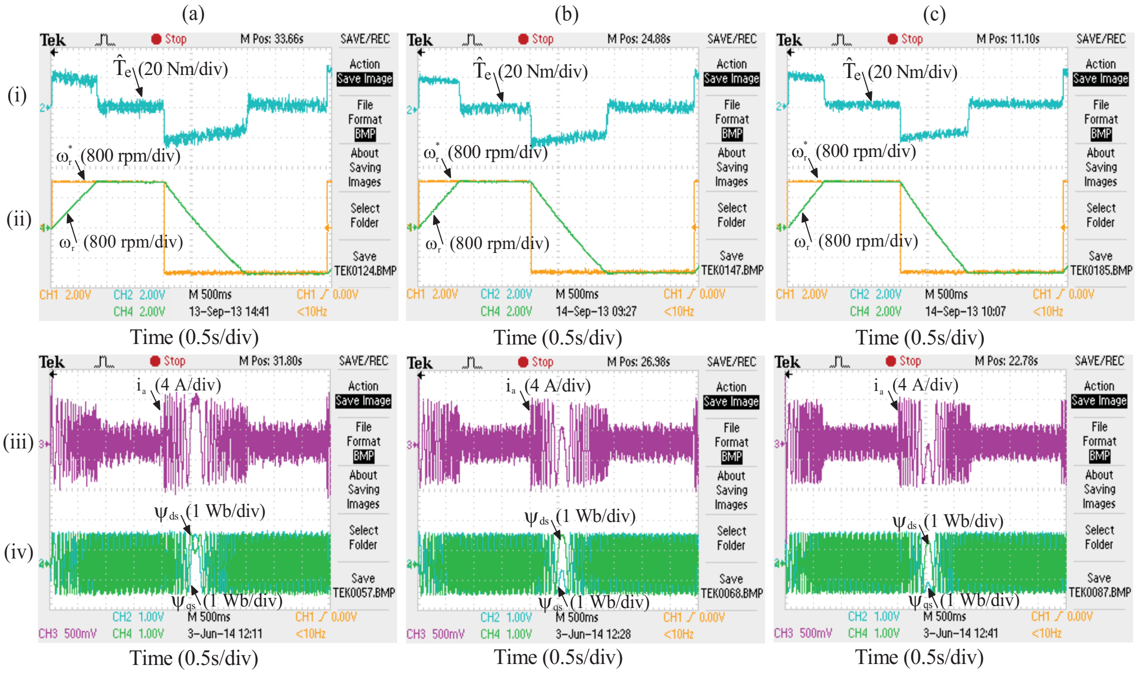

Figure 4.19: Performance of the IM under reversal speed command using: (a) PIC, (b) T1FLC and (c) T2FLC: *Traces (from top to bottom):* (i) Torque, (ii) speed, (iii) stator current and (iv) stator flux dq-components in stationary reference frame

4.3.2 Performance under Reversal Speed Command

The performance of the IMD is observed under reversal speed command at no-load torque using PIC, T1FLC and T2FLC schemes are shown in Figure 4.19 (a)-(c). The reversal speed command from +1200 rpm to -1200 rpm is applied at 2 s. To get the required reference speed of -1200 rpm, a larger amplitude of the stator current (±6 A) and electromagnetic torque of 20 Nm are developed during reversal speed. Moreover, directions of the stator current also get reversed when the speed crosses to zero speed value. The IM is settled to the set reference speed (-1200 rpm) at around 3.5 s, 3.32 s and 3.18 s with an overshoot of around 1.708%, 0.208% and 0.025% of the reference speed using PIC, T1FLC and T2FLC schemes, respectively. Furthermore, the reversal speed is applied from -1200 rpm to +1200 rpm at 4.9 s and the corresponding operation of the IM is shown in Figure 4.19 (ii). It is noticed that the actual speed follows the reference speed. The electromagnetic torque ($\hat{T}_e$), reference speed (ω_r^*), actual speed (ω_r), stator current (i_a) and stator flux dq-components (i.e. ψ_{ds}, ψ_{qs}) in the stationary reference frame are illustrated in Figure 4.19 (i)-(iv), respectively. From Figure 4.19 (iv), it is observed that the magnitude of the stator flux dq-components in the stationary reference frame are maintained almost same magnitude throughout the operation. The transient response during reversal speed using PIC, T1FLC and T2FLC schemes are shown in Figure 4.20 (a)-(c). Note that the experimental results, presented in Figure 4.19 (a)-(c) and Figure 4.20 (a)-(c) are corresponding to the simulation results of chapter-2 and chapter-3.

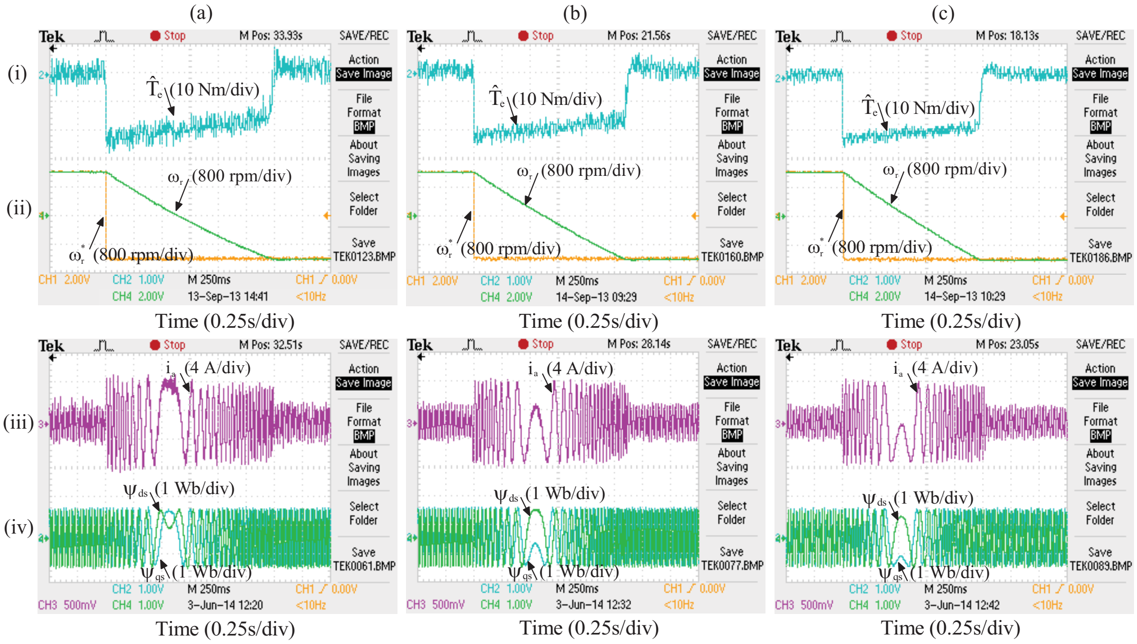

Figure 4.20: Transient performance of the IM under reversal speed command using: (a) PIC, (b) T1FLC and (c) T2FLC: (i) Torque, (ii) speed, (iii) stator current and (iv) stator flux dq-components in stationary reference frame

4.3.3 Tracking Performance of the Speed Commands

Tracking the performance of the actual speed is observed through the applications of various changes in step and square speed commands. The response of the IMD under such speed commands is presented in the following sections.

Performance under sudden change in step speed command:

The performance of the IMD is observed under a sudden change in step speed command using three controller schemes are shown in Figure 4.21 (a)-(c). The sudden change in step speed command of 300 rpm is applied in four steps (i.e. 600 rpm → 900 rpm → 1200 rpm → 900 rpm → 600 rpm) at 1.4 s, 2.4 s, 3.6 s, etc. The corresponding reference and actual speed responses under such speed command are shown in Figure 4.21 (ii). The electromagnetic torque, stator current and stator flux dq-components in a stationary reference frame are shown in Figure 4.21 (i), (iii)-(iv) respectively. From Figure 4.21 (ii), it is observed that the actual speed settled the set reference speed (from 600 rpm to 900 rpm) in 0.3 s, 0.2 s and 0.15 s using PIC, T1FLC and T2FLC schemes, respectively. Moreover, it is also observed that the steady state error between the reference and actual speed is negligible using T2FLC compared to T1FLC and PIC scheme. Note that the experimental results, presented in Figure 4.21 (a)-(c) are corresponding to the simulation results of previous chapters.

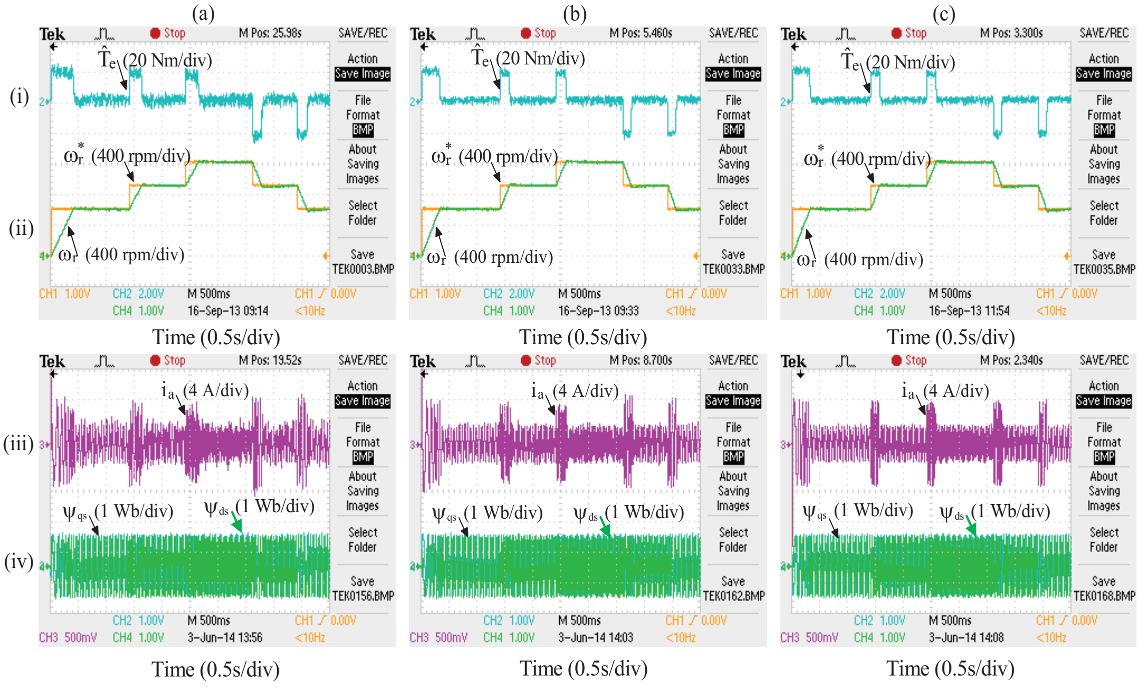

Figure 4.21: Performance of the IM under sudden change in step speed command using: (a) PIC, (b) T1FLC and (c) T2FLC: (i) Torque, (ii) speed, (iii) stator current and (iv) stator flux dq-components in stationary reference frame

Performance under square speed command:

The performance of the IMD is observed under square speed command using PIC, T1FLC and T2FLC schemes are shown in Figure 4.22 (a)-(c). The sudden change in speed command of 600 rpm is applied in four steps (i.e. 1200 rpm → 600 rpm → 1200 rpm → 600 rpm → 1200 rpm) at 1 s, 2 s, 3 s, etc. The reference (ω_r^*) and actual speeds (ω_r) are presented in Figure 4.22 (ii), it is observed that under such speed command the actual speed settled the reference speed (from 600 rpm to 1200 rpm) in 0.52 s, 0.38 s and 0.31 s with an overshoot of around 1.718%, 0.212% and 0.026% of the reference speed using PIC, T1FLC and T2FLC scheme, respectively. The torque, stator current and stator flux dq-components in a stationary reference frame are shown in Figure 4.22 (i), (iii)-(iv), respectively. It is noticed that the actual speed accurately tracking the reference speed and settled quickly using T2FLC scheme compared to T1FLC and PIC scheme. Note that the experimental results, presented in Figure 4.22 (a)-(c) are corresponding to the simulation results of the previous chapters.

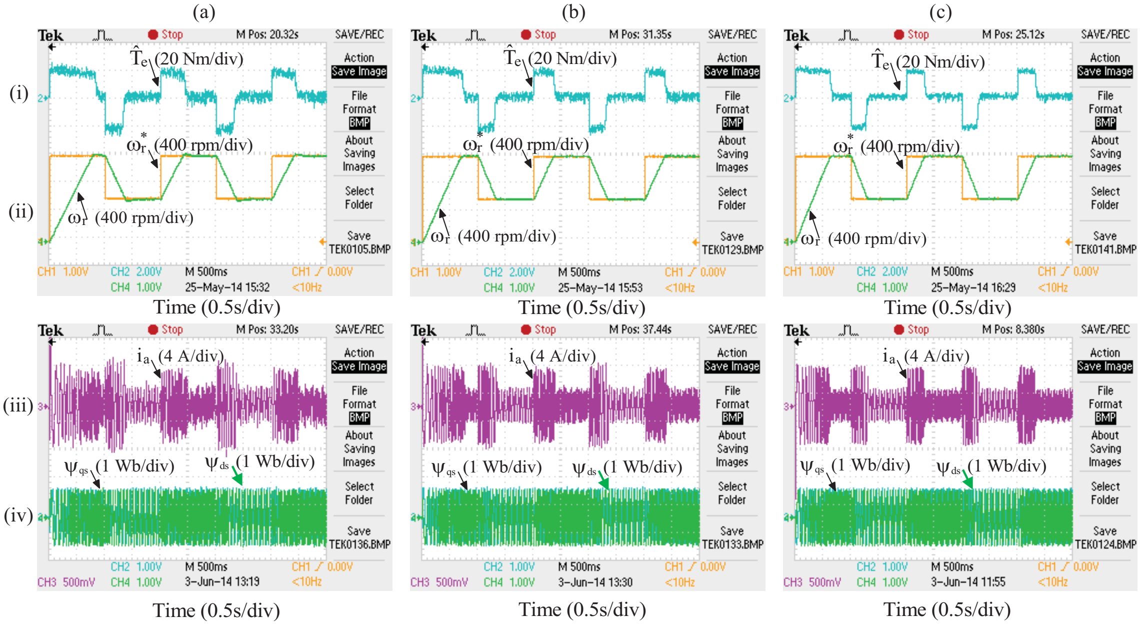

Figure 4.22: Performance of the IM under sudden change in square speed command using: (a) PIC, (b) T1FLC and (c) T2FLC: (i) Torque, (ii) speed, (iii) stator current and (iv) stator flux dq-components in stationary reference frame

4.3.4 Loading Performance

The performance of the IMD is observed under the application and removal of sudden load torques for the following conditions.

- Loading at 1200 rpm
- Loading and unloading at 1200 rpm
- Loading at different speed commands (i.e. 300 rpm, 600 rpm and 900 rpm)

The load torque is applied through the DC machine, which is coupled to the shaft of the IM. The load is modeled through the DC machine supplying a resistive load.

Loading performance at 1200 rpm

The performance of the IMD is observed under sudden load torque operation using PIC, T1FLC and T2FLC schemes are shown in Figure 4.23 (a)-(c). The sudden load torque of 5 Nm is applied at 1.6 s when an IM was operating at steady state speed. The change in load torque has been performed by applying different load resistance at the terminal of the DC generator, which is coupled to the induction motor. When the load torque is applied, the IM draws large amplitude of stator current, i.e. ±4.1 A, ±3.8 A and ±3.6 A using PIC, T1FLC and T2FLC are shown in Figure 4.23 (iii). From Figure 4.23 (i), it is observed that the sudden application of load torque causes an undershoot in actual speed around 1.55%, 0.6584% and 0.35% of the reference speed using PIC, T1FLC and T2FLC schemes, respectively. It is also observed that the recovery time of actual speed under sudden load torque condition is 0.38 s, 0.15 s and 0.05 s using PIC, T1FLC and T2FLC schemes, respectively. From Figure 4.23 (ii), the ripple content in torque is ±2.4 Nm, ±1.85 Nm and ±1.4 Nm using PIC, T1FLC and T2FLC schemes. Hence, the torque and stator current ripple contents using T1FLC scheme are improved by 22.91% and 7.38% over PIC, whereas T2FLC scheme is improved by 24.32% and 5.26% over T1FLC scheme.

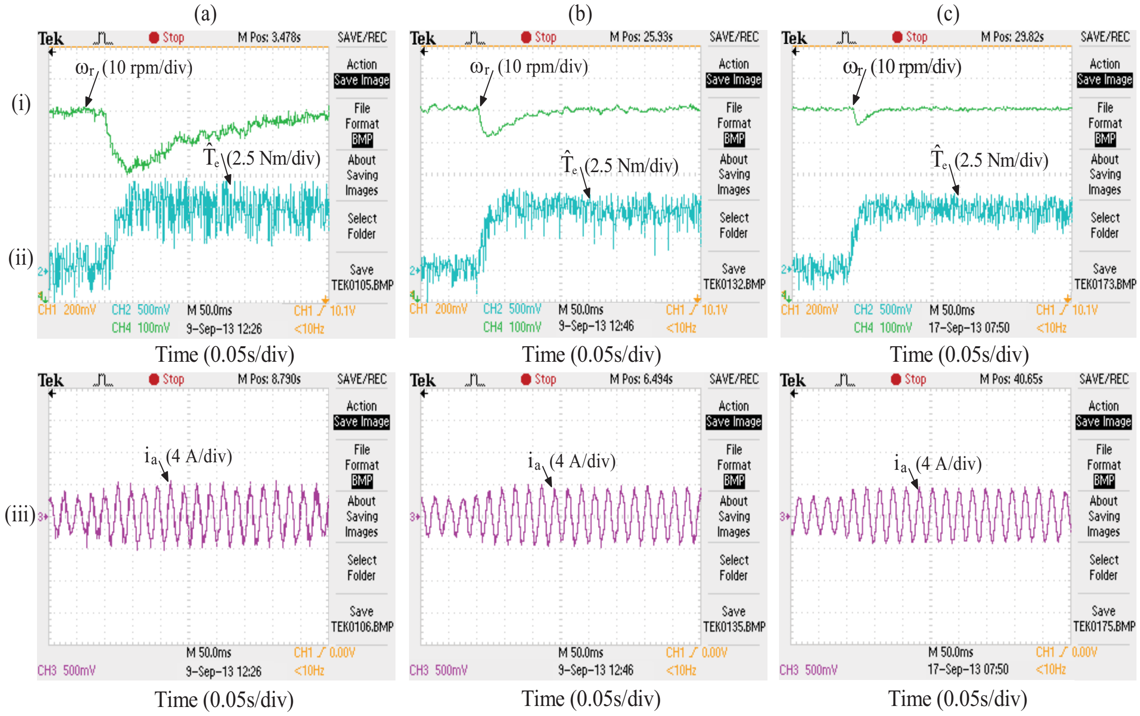

Figure 4.23: Performance of the IM under sudden load torque operation at 1200 rpm using: (a) PIC, (b) T1FLC and (c) T2FLC: (i) speed, (ii) torque and (iii) stator current

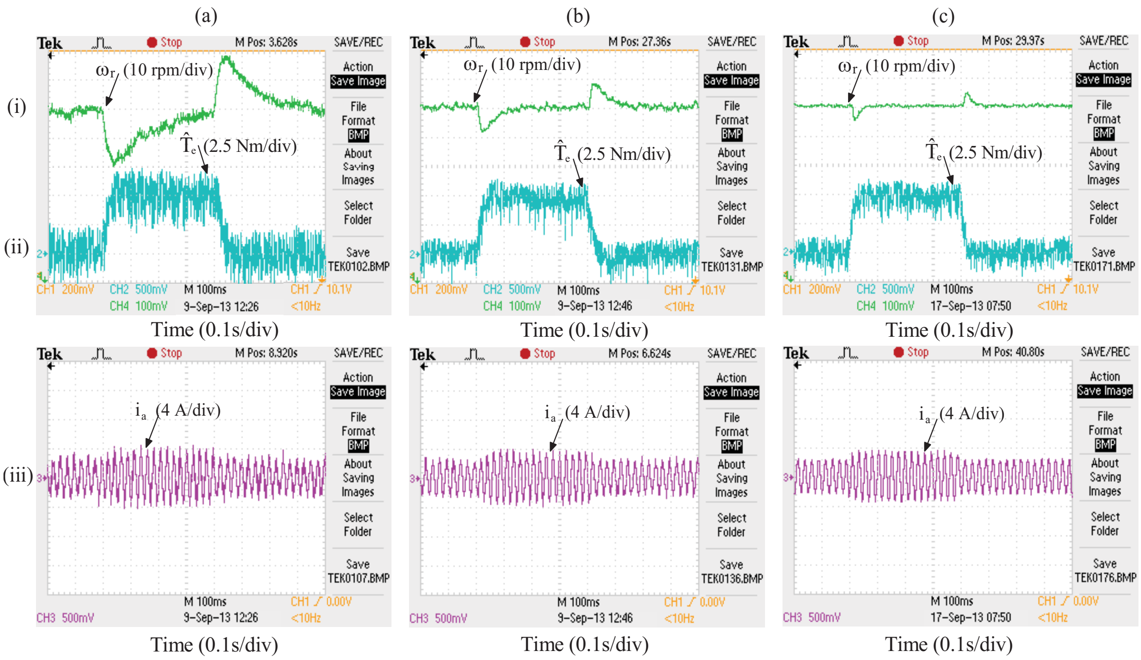

Figure 4.24: Performance of the IM under sudden load and unload torque at 1200 rpm using: (a) PIC, (b) T1FLC and (c) T2FLC: (i) speed, (ii) torque and (iii) stator current

Loading and unloading performance at 1200 rpm

The effect of sudden load and unload torque operation at 1200 rpm using PIC, T1FLC and T2FLC schemes are presented in Figure 4.24 (a)-(c). The sudden load torque of 5 Nm is applied at 1.6 s and it is withdrawn at 2 s when an IM was operating at steady state speed. When the load torque is applied, the effect of load torque is observed in the previous section. Similarly, when the load torque is withdrawn an overshoot around 1.5%, 0.65% and 0.366% of the reference speed appears using PIC, T1FLC and T2FLC, respectively. From Figure 4.24 (i), it is observed that the recovery time of actual speed under sudden load torque condition is 0.35 s, 0.1 s and 0.045 s using PIC, T1FLC and T2FLC, respectively. Hence, the settling time using T1FLC scheme is improved by 71.42% over PIC, whereas T2FLC scheme is improved by 55% over T1FLC scheme. From Figure 4.24 (iii), it is observed that when the load torque is withdrawn the current is dropped to ±2.95 A, ±2.62 A and ±2.4 A using PIC, T1FLC and T2FLC scheme, respectively. The corresponding torque response is presented in Figure 4.24 (ii). The performance of the speed sensorless IM drive is observed under different load torque disturbances at 1200 rpm using three different control schemes, which are illustrated in Table 4.1.

The error speed ($e\omega_r$) between the reference and actual speeds are presented in Figure 4.25 (a)-(c). From Figure 4.25 (i), it is observed that the error speed around 18.6 rpm, 7.8 rpm and 4.2 rpm appears when the sudden load torque disturbance is applied to the IM.

The effect of different load torque condition is observed under different speed commands using PIC, T1FLC and T2FLC are shown in Figure 4.26 (a)-(c). It is observed from the experimental results that the T2FLC shows an improved performance and robustness to various load torque disturbances compared to PIC and T1FLC, respectively.

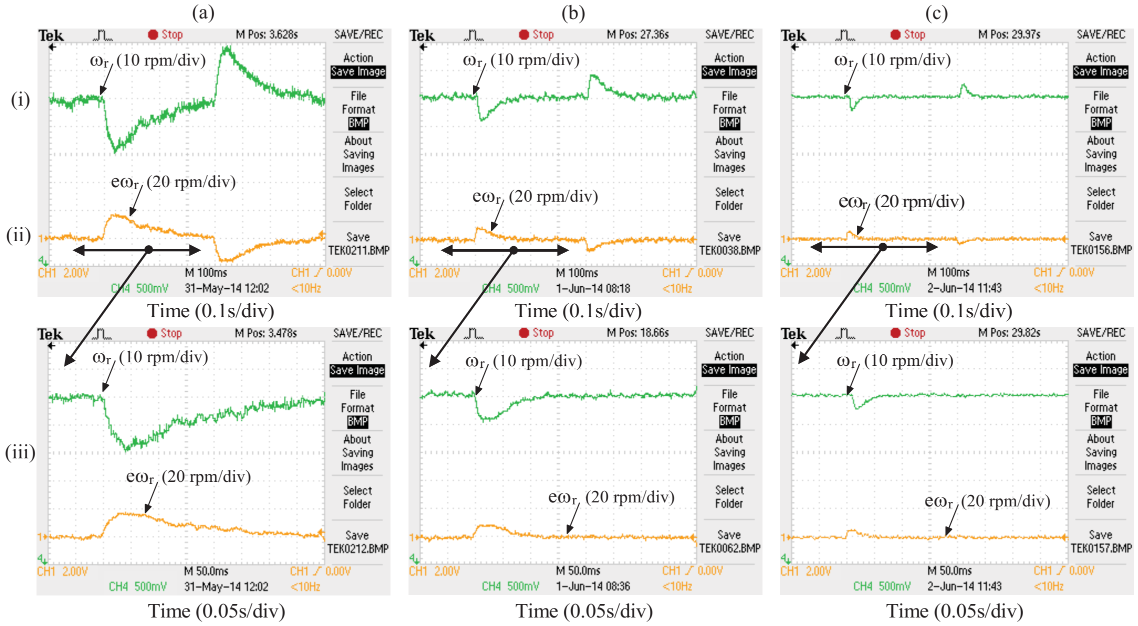

Figure 4.25: Performance of the IM under sudden load and unload torque operation at 1200 rpm using: (a) PIC, (b) T1FLC and (c) T2FLC: (i) speed, (ii) error speed and (iii) zoom of speed and error speed

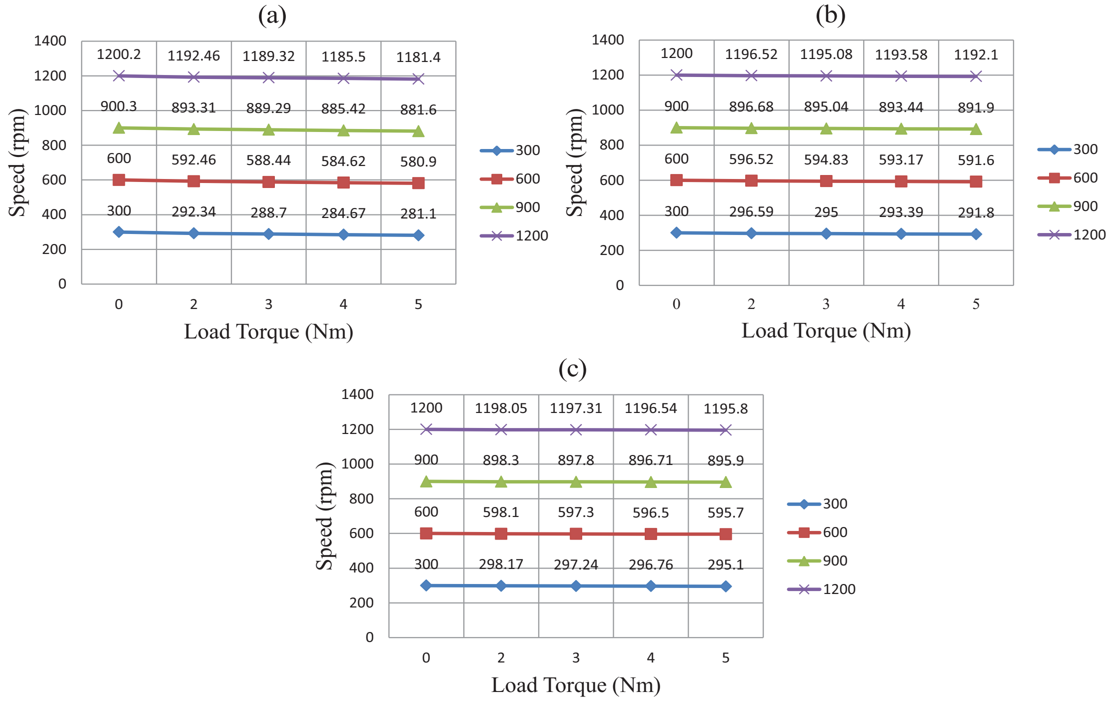

Figure 4.26: Steady-state performance of the actual speed under various load torque conditions at different speed commands using: (a) PIC, (b) T1FLC and (c) T2FLC

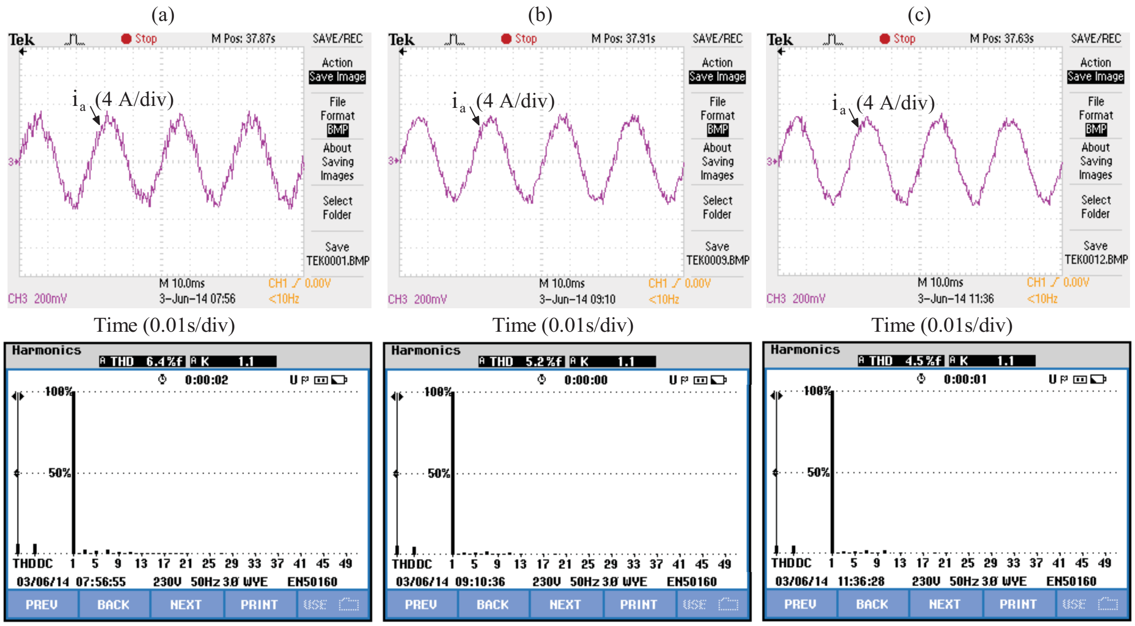

Figure 4.27: THD performance of the stator current using: (a) PIC, (b) T1FLC and (c) T2FLC

The percentage of line current THDs for DTFC of an IMD using PIC, T1FLC and T2FLC scheme under no-load operation is shown in Figure 4.27 (a)-(c). The corresponding values are 6.4, 5.2 and 4.5, respectively. From Figure 4.27, it is observed that the T2FLC offers less current THD compared to T1FLC and PIC scheme.

Table 4.1: Comparison of three controller schemes under different load torque conditions

Load Torque	Controller	Under Load Torque Applied		Under Load Torque Withdrawn	
		Speed Undershoot (rpm)	Recovery Time (s)	Speed Overshoot (rpm)	Recovery Time (s)
2	PIC	7.540	0.271	6.74	0.262
	T1FLC	3.480	0.078	3.39	0.076
	T2FLC	1.950	0.031	1.88	0.030
3	PIC	10.68	0.312	9.62	0.295
	T1FLC	4.920	0.087	4.79	0.084
	T2FLC	2.690	0.035	2.55	0.033
4	PIC	14.50	0.343	14.2	0.314
	T1FLC	6.420	0.098	6.29	0.095
	T2FLC	3.460	0.041	3.57	0.039
5	PIC	18.60	0.380	18.0	0.350
	T1FLC	7.900	0.150	7.80	0.100
	T2FLC	4.200	0.050	4.40	0.045

Table 4.2: Comparison of three controller schemes under various operating conditions

Measured Parameter	Simulation Results					Experimental Results				
	PIC	T1FLC	%T1FLC -IOPI	T2FLC	%T2FLC -IOT1	PIC	T1FLC	%T1FLC -IOPI	T2FLC	%T2FLC -IOT1
$\pm T_{dNLT}$ (Nm)	1.750	1.400	20.00	1.150	17.86	2.30	1.710	25.62	1.400	18.12
$\pm \psi_{dNLT}$ (Wb)	0.040	0.022	45.00	0.012	45.45	0.14	0.100	28.57	0.080	18.13
ω_{cLTA} (rpm)	13.50	5.200	61.51	2.300	55.77	18.6	7.900	57.52	4.200	46.83
ω_{cLTW} (rpm)	13.30	5.000	62.24	2.200	56.00	18.0	7.800	56.66	4.400	43.59
t_{ss} (s)	0.695	0.537	22.73	0.498	7.260	0.82	0.735	10.36	0.682	7.210
t_{sr} (s)	3.170	3.050	3.790	2.930	3.930	3.50	3.320	5.14	3.180	4.210
t_{scss} (s)	0.220	0.136	38.18	0.120	11.64	0.30	0.200	33.33	0.150	25.00
t_{scsqs} (s)	0.450	0.282	37.33	0.266	5.670	0.52	0.380	26.92	0.310	18.42
t_{sLTA} (s)	0.320	0.120	62.50	0.035	70.83	0.38	0.150	60.52	0.050	66.66
t_{sLTW} (s)	0.310	0.100	67.74	0.042	58.00	0.35	0.100	71.42	0.045	55.00
$e\omega_r$ (rpm)	13.50	5.100	61.36	2.200	55.86	18.0	7.800	56.66	4.200	46.15
I_{THD} (%)	3.43	2.98	13.11	2.50	16.10	6.40	5.200	18.75	4.500	13.46

The comparative performance of the IMD using PIC, T1FLC and T2FLC schemes under various operating conditions, such as starting, reversal speed, step change in speed, square change in speed and change in speed during load torque applied and withdrawn are illustrated in Table 4.2 in detail. Where, T_{rNLT}, ψ_{rNLT}, ω_{cLTA}, ω_{cLTW}, t_{ss}, t_{sr}, t_{scss}, t_{scsqs}, t_{sLTA}, t_{sLTW}, $\%I_{THDNLT}$, %T1FLCIOPI and %T2FLCIOT1 represents the no-load torque ripples (Nm), stator flux ripples (Wb), change in speed during load torque applied (rpm), change in speed during load torque withdrawn (rpm), settling time during forward motoring (s), settling time during reversal speed (s), settling time during change in step speed (s), settling time during change in square speed (s), settling time during load torque applied (s), settling time during load torque withdrawn(s), percentage of current THD during no-load torque, percentage of T1FLC improvement over PI controller and percentage of T2FLC improvement over T1FLC, respectively.

4.4 Conclusion

In this chapter, the detailed descriptions of the various components used for the development of the laboratory experimental setup for DTFC of an IMD using two-level VSI are presented. A DSP DS1104 of dSPACE is used for the real-time implementation of various control schemes. The main components of the experimental prototype and software configurations of the EPS have been explained in detail. The developed control scheme and interfacing of the dSPACE DS-1104 between real-time and MATLAB/SIMULINK is described in detail. Also, the control desk features are explained well for conducting the experiment.

The performance of the DTFC of IM drive using proposed schemes has been experimentally validated. It is observed that the experimental results closely follow their simulation counterparts. Initially, the PIC based DTFC of an IM drive is implemented. It is observed that the PIC provides large flux and torque ripples under various operating conditions. Moreover, it has poor dynamic performance and load torque disturbance rejections. In order to improve the dynamic performance of the IMD, the PIC is replaced by T1FLC. The T1FLC provides satisfactory dynamic performance compared to PIC. However, it does not improve the dynamic performance considerably due to certain limits of T1FLC. Furthermore, the PIC is replaced by the proposed T2FLC to get quick dynamic as well as steady-state performance. A rigorous simulation and experimental comparison between the PIC, T1FLC and T2FLC have been carried out under various operating conditions. It is observed that the T2FLC shows improved performance to sudden changes in speed and also robustness to load torque disturbances. Moreover, it is also noticed that the T2FLC perform satisfactorily in all speed ranges with different loading conditions.

The DTFC of an IMD requires the rotor speed information for accurate speed control. However, the use of speed sensor is associated with several drawbacks, such as requirement of shaft extension, reduction of mechanical robustness of the motor, unsuitability for hostile environment, poor signal-transmission, lower reliability, etc. Also, the cost of the speed sensor increases the economy of the drive. In order to overcome these drawbacks, the speed estimation from machine terminal quantities (i.e. voltage and current) is preferred than the speed sensing for high performance industrial applications. Therefore, this aspect will be studied in the following chapter.

Chapter 5

MRAS Speed Estimator for DTFC of A Speed Sensorless IMD

CHAPTER 5: MRAS SPEED ESTIMATOR FOR DTFC OF A SPEED SENSORLESS IMD

The speed sensors used in DTFC of an IMD are for rotor speed/position information. These speed/position sensors have major drawbacks. Therefore, the speed estimation from machine terminal quantities (i.e. current and voltage) is preferred than the speed sensing in various applications. Initially, this chapter presents various types of speed estimation methods, such as signal injection based methods, observer based methods and model reference adaptive system (MRAS) based methods for estimating rotor speed. Among these methods, the MRAS is a simple method with a less computational effort to estimate the rotor speed. Furthermore, in order to improve the performance of the MRAS, its adaptation mechanism is implemented using Type-1 and Type-2 FLCs, which are replaced in place of PIC. Finally, the MRAS speed estimator for DTFC of a sensorless IMD is simulated in the MATLAB/SIMULINK environment under various operating conditions with speed sensor and without any speed sensor. Moreover, the speed estimation algorithm is experimentally validated with laboratory developed EPS using dSPACE DS-1104 controller board and the experimental results are presented under various operating conditions, such as forward motoring, reversal speed, sudden changes in speed, different load torque disturbances, low speed, etc. The development of EPS has been covered in the previous chapter.

This chapter is organized as follows:

- *The various types of speed estimation methods are presented and discussed in detail in section 5.1.*
- *The mathematical modelling of rotor-flux based MRAS (RFMRAS) speed estimation for DTFC of a speed sensorless IM drive and various types of adaptation mechanism schemes are presented in section 5.2.*
- *The RFMRAS speed estimator for DTFC of a speed sensorless IM drive using three different adaptation schemes is simulated in the MATLAB/SIMULINK environment and corresponding results under various operating conditions are presented in section 5.3.*
- *The simulation results are validated with the experimental results, which are presented in section 5.4.*
- *Finally, section 5.5 presents the conclusion and remarks of the system.*

5.1 Introduction

Generally, all the control system design methods for the IMD were developed under the assumption that the rotor speed of the IM is available. In practice, the rotor speed is measured through a speed sensor which is mounted on the shaft of the IM. However, the use of speed sensor is associated with some drawbacks, such as requirement of shaft extension, lower reliability, high cost, increase in size and weight, increase electrical susceptibility, difficulty in mounting in some cases such as motor drives in a harsh environment, etc. In order to overcome these drawbacks, in recent years, the removal of the speed sensors that are measuring mechanical coordinates of the system is one of the main ongoing research and attractive prospect due to the advantages of high reliability, low cost, less maintenance and easy to operation in the harsh environment. The rotor speed is estimated from machine terminal components (i.e. measured voltage and stator currents) [93-145]. The various types of speed estimation methods are presented in Figure 5.1.

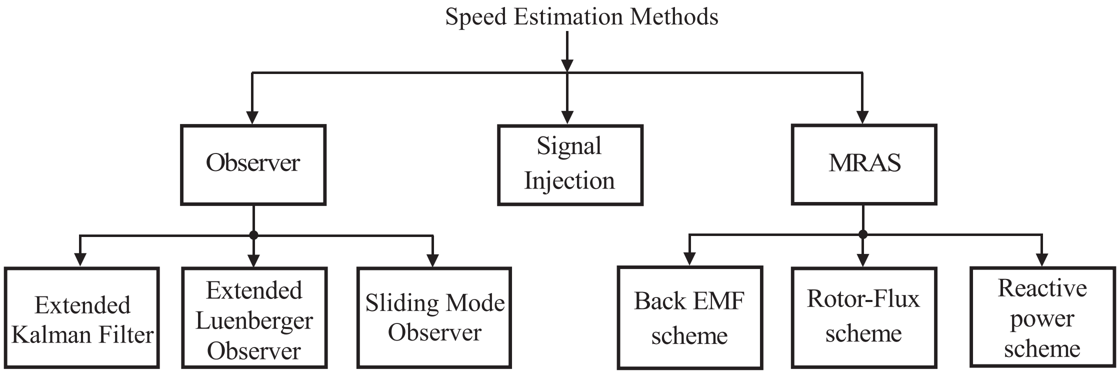

Figure 5.1: Various types of speed estimation methods

In general, an estimator is defined as a dynamic system whose state variables are estimates of another system. The estimators are of two types, open-loop and closed-loop estimators. The difference between these estimators is the correction term in error estimation and is used to adjust the response of the estimator. In open-loop estimators, especially at low speeds, parameter deviations have a significant influence on the performance of the drive in both transient and steady states [3]. In contrast, closed-loop estimators are robust to parameter variations and noise. In closed-loop speed estimators, the accuracy of estimation can be improved. This is achieved by introducing a certain corrective action, based on an error between two conveniently chosen quantities, within the speed estimator.

There are three basic types of closed-loop machine model based speed estimators. The first one is the observer based speed estimator [95-111], which is further classified into three types, such as, Luenberger observer (speed adaptive flux observer) [95-98], Kalman filter observer (KFO) [99-105] and sliding mode observer (SMO) [106-111], respectively. The second one is the signal injection method [94]. The third type of speed estimation relies on MRAS methods [112-146]. The MRAS based speed estimation is the simplest approach and it is analyzed in detail in this chapter. The above mentioned various types of speed estimation methods are discussed in detail in the following subsections.

5.1.1 Observers

An observer can be classified based on the type of representation used for the plant to be observed. If the plant is deterministic, then the observer is a deterministic observer; otherwise it is a stochastic observer. The most commonly used observers are Luenberger and Kalman filter types. The Luenberger observer (LO) is of deterministic type while the Kalman filter (KF) is of stochastic type [3]. The basic LO is applied to a linear, time invariant deterministic system, whereas the extended Luenberger observer (ELO) is applicable to nonlinear time varying deterministic system. The basic KF is applicable to only linear stochastic systems, whereas the extended KF (EKF) can be used for nonlinear systems. The EKF can provide an estimate of the states of a system or estimates of both the states and parameters [109]. Both ELO and EKF are summarized as nonlinear estimators where the former is applicable to deterministic systems and the latter is applicable to stochastic systems.

5.1.1.1 Luenberger Observer (speed adaptive flux observer)

The LO can be used to estimate states which cannot be measured or where the measurements are corrupted by noise. To obtain the full-order nonlinear speed observer, initially the IM model is considered in the stationary reference frame, which can be described as follows [3]:

$$\dot{X} = AX + BV_s \tag{5.1}$$

$$i_s = CX \tag{5.2}$$

The states can be estimated by using equations (5.3a)-(5.3b):

$$\dot{\hat{X}} = \hat{A}X + B\vec{V}_s + G(\vec{i}_s - \hat{\vec{i}}_s) \tag{5.3a}$$

$$\hat{\vec{i}}_s = C\hat{X} \tag{5.3b}$$

where, A is the state matrix of the observer, G is an observer gain matrix, X is state vector, B is a control input matrix, V_s is input vector, C is output matrix and i_s is output vector.

The state matrix of the observer ($\hat{A}$) is a function of the estimated speed ($\hat{\omega}_r$), and in a speed sensorless drive, the rotor speed must be estimated. It is important to note that the estimated speed is considered as a parameter in $\hat{A}$. In equation (5.3a) the observer gain matrix is multiplied by the error vector, where $\vec{i}_s$ and $\hat{\vec{i}}_s$ are the actual and estimated stator current vectors respectively. By using equations (5.3a) and (5.3b) it is possible to implement a speed estimator for SIMD by using MATLAB/SIMULINK environment. The corresponding schematic model of the adaptive state observer is shown in Figure 5.2.

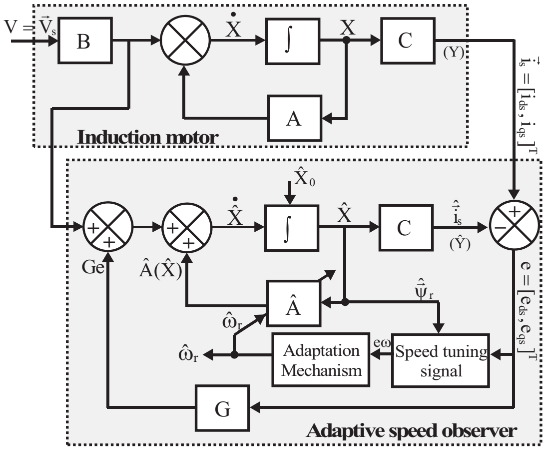

Figure 5.2: Adaptive speed observer (Speed adaptive flux observer)

In Figure 5.2, the estimated rotor flux linkage components and stator current error components are used to obtain the speed tuning signal and this signal is processed through a PI controller to get the estimated speed as:

$$\hat{\omega} = K_p(\hat{\psi}_{qr}e_{ds} - \hat{\psi}_{dr}e_{qs}) + K_i\int(\hat{\psi}_{qr}e_{ds} - \hat{\psi}_{dr}e_{qs})\,dt \tag{5.4}$$

where $e_{ds} = i_{ds} - \hat{i}_{ds}$ and $e_{qs} = i_{qs} - \hat{i}_{qs}$ are the direct and quadrature axis stator current errors respectively.

5.1.1.2 Kalman Filter

In recent years, the EKF algorithm has been used for the rotor speed estimation of the sensorless IM drive. The EKF is basically a full-order stochastic observer for the recursive optimum state estimation of a nonlinear dynamic model in real-time by using signals that are corrupted by noise [92]. The EKF can also be used for unknown parameter estimation (i.e. rotor resistance Rr). The noise sources in EKF take into account of the measurement and modeling inaccuracies [102-105]. Figure 5.3 shows the schematic model of the EKF for speed estimation. The EKF uses the machine model, where estimated speed ($\hat{\omega}_r$) is considered as a parameter as well as a state. However, in the case of LO the estimated speed is considered only as a parameter. The augmented machine model can be given as [3]:

$$\frac{dX}{dt} = AX + BV_s \tag{5.5a}$$

$$i_s = CX \tag{5.5b}$$

where $V_s = \begin{bmatrix} V_{ds} \\ V_{qs} \end{bmatrix}$ $C = \begin{bmatrix} 1 & 0 & 0 & 0 & 0 \\ 0 & 1 & 0 & 0 & 0 \end{bmatrix}$ $i_s = \begin{bmatrix} i_{ds} \\ i_{qs} \end{bmatrix}$

$$X=\begin{bmatrix} i_{ds} \\ i_{qs} \\ \psi_{dr} \\ \psi_{qr} \\ \omega_r \end{bmatrix} \quad A=\begin{bmatrix} -a_1 & 0 & a_2 & a_3\omega_r & 0 \\ 0 & -a_1 & -a_3\omega_r & a_2 & 0 \\ a_5 & 0 & -a_4 & -\omega_r & 0 \\ 0 & a_5 & \omega_r & -a_4 & 0 \\ 0 & 0 & 0 & 0 & 1 \end{bmatrix} \quad B=\begin{bmatrix} \frac{1}{\sigma L_s} & 0 \\ 0 & \frac{1}{\sigma L_s} \\ 0 & 0 \\ 0 & 0 \\ 0 & 0 \end{bmatrix}$$

The equations (5.5a)-(5.5b) can be described in discrete time system as [3]:

$$X(k+1)=AX(k)+BV_s(k) \tag{5.6a}$$

$$i_s(k)=CX(k) \tag{5.6b}$$

The observer described in equations (5.6a)-(5.6b) will be under the influence of two noise sources when applied to a physical system:

1. Process noise - i.e. the thermal noise in a resistor, which is a part of the system.
2. Measurement noise - i.e. quantization noise.

Considering these two noises and whose covariance matrices are Q and R, the above equations (5.6a) and (5.6b) can be rewritten as [3]:

$$X(k+1)=AX(k)+BV_s(k)+V(k) \tag{5.7a}$$

$$i_s(k)=CX(k)+W(k) \tag{5.7b}$$

where $V(k)$ and $W(k)$ are zero-mean white Gaussian noise vectors of $X(k)$ and $i_s(k)$ with covariance Q(k) and R(k), respectively. Both $V(k)$ and $W(k)$ are independent of $X(k)$ and $i_s(k)$, respectively. The statistics of noise and measurements are given three covariance matrices, Q, R and P, where Q is system noise vector covariance matrix (5x5), R is measurement noise vector covariance matrix (2x2) and P is system state vector covariance matrix (5x5).

The sequence of the EKF algorithm implementation is shown in a flowchart Figure 5.4. The EKF is designed in two stages, in the first stage, the states are predicted (x(k+1)) by using a mathematical model and in the second stage, the predicted states are continually corrected by using a feedback correction (eK) scheme. Thus, this scheme uses actual measured states, by adding a term to the predicted states. The additional term contains the weighted difference of measured and estimated output signals ($\mathrm{e}=\mathrm{i_s}-\hat{\mathrm{i}}_\mathrm{s}$). Based on the deviation from the estimated value, the EKF provides an optimum output value at the next input instant. The EKF equation is [3, 92, 101-102]:

$$\dot{\hat{X}}=A\hat{X}+B\vec{V}_s+K(\vec{i}_s-\hat{\vec{i}}_s) \tag{5.8}$$

It can be used for the estimation of the rotor speed of an induction motor and the schematic model of EKF is shown in Figure 5.3. It can be seen that the structure of EKF is similar to that of LO, except that its gain K is designed to minimize the error between the real and estimated state vectors [109].

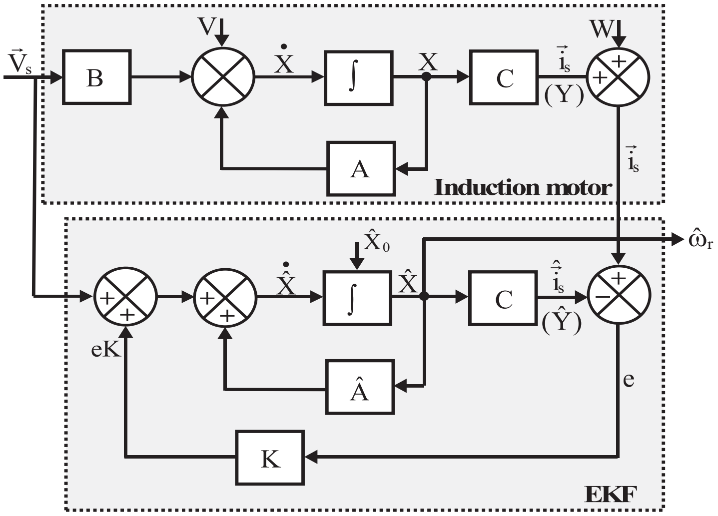

Figure 5.3: Extended Kalman filter based speed estimation

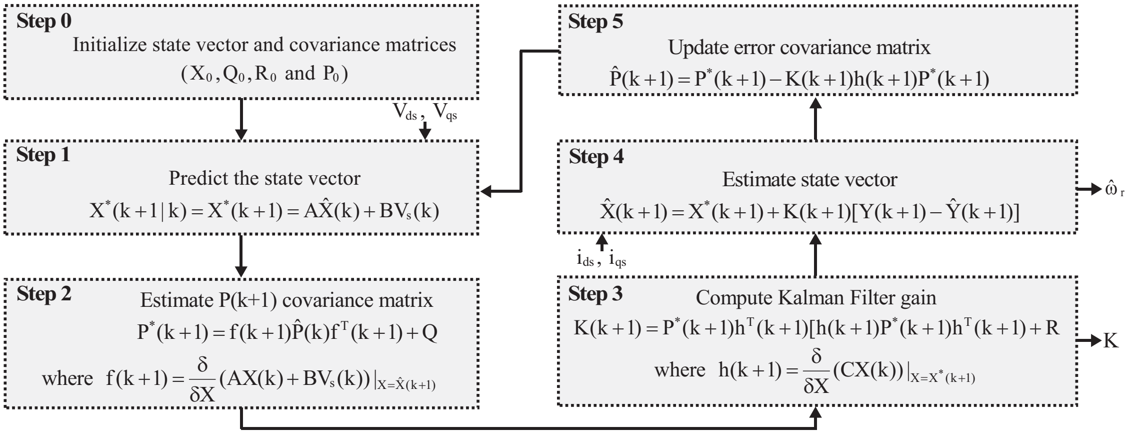

Figure 5.4: Flowchart diagram of EKF algorithm [3]

The main difference between the KF and the LO is that the gains are not fixed in KF whereas in the LO the gains are fixed, but they are computed at every cycle, in function of the level of the noise, the dependence between parameters and the error of the estimation. The KF has a very good immunity to noise, but the main drawback is that the computational complexity of KF is very high, even with powerful DSP, it takes a long time to execute and difficult to apply in real-time, particularly for fast-speed variations. Besides, there is also a parameter variation problem, which makes accuracy poor at low speeds. Moreover, the KF is a bit difficult to tune: there are many gains and parameters which shall be tuned, and it is only effective for a certain level of noise [1, 3, 109].

5.1.1.3 Sliding-Mode Observer

A sliding mode observer (SMO) based sensorless algorithm of the IM is robust to the parameter variation, system disturbance, system order reduction and easy implementation. In general, the sliding mode observer for motor control is implemented through the error between the measured and estimated currents. In an IM, the error between the measured and estimated currents is used to construct sliding mode (SM) surfaces so that after SM, the estimated flux values are driven to converge to real ones exponentially [3, 106-111]. Compared to LO, SMO is different as it employs the sign function of the current error in the feedback correction item, which is expressed in equations (5.9)-(5.10), while LO employs the continuous function. However, chattering phenomena is a severe concern of such observer (i.e. SMO), which may be eliminated by appropriate gain selection [3].

$$\frac{d\hat{X}}{dt} = A\hat{X} + B\vec{V}_s + K\,sgn(\vec{i}_s - \hat{\vec{i}}_s) \tag{5.9}$$

$$\vec{i}_s = C\hat{X} \tag{5.10}$$

where gain *K* is selected so as the observer is stable.

5.1.2 Model Reference Adaptive System

The MRAS is used for rotor speed estimation of speed sensorless IM drive. Among various types of adaptive system configurations, MRAS is important because it leads to relatively easy to implement with high speed adaptation for a wide range of applications. The high performance ability and easy stability analysis of the MRAS make it as one of the major approaches in adaptive control [3, 116]. The advantage of MRAS is to allow an improved noise rejection property which is helpful to obtain unbiased parameter estimation and makes it most popular MRAS scheme. Figure 5.5 shows the basic structure of the MRAS, which mainly consists of three blocks, i.e., reference model (RM), adjustable model (AM) and adaptation mechanism (**AM**). It works on the principle of deriving an error vector using the difference between the outputs of two dynamic models, i.e. the RM and AM. Both the models generate the same quantity, but have different ways (i.e. RM follows $X = f(\vec{V}_s, \vec{i}_s)$ whereas the AM uses $\hat{X} = f(\vec{i}_s, \hat{\omega}_r)$). The error ($\xi_\omega$) between the outputs of these two models are used to drive a suitable **AM** that generates the estimated rotor speed ($\hat{\omega}_r$). The error (ξ_ω) is driven to zero through an **AM**, as a result, the estimated parameter ($\hat{X}$) will converge to its true value (*X*). The reference model is independent of the estimated speed whereas the adjustable model is dependent on the estimated speed. The appropriate **AM** can be derived by using Popov's criterion of hyperstability [114-115]. This results in a stable and quick response system, where the differences between the state-variables of the RM and AM are adapted as a speed tuning signal, which is then fed into a PIC, which outputs the estimated rotor speed.

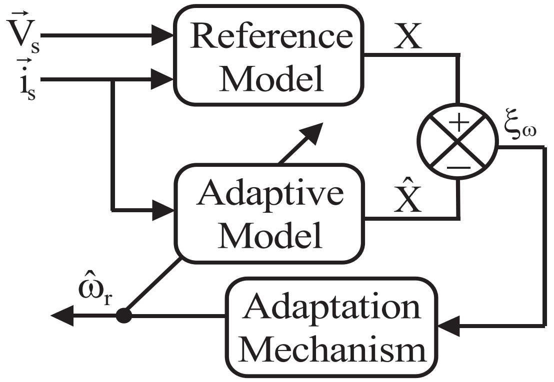

Figure 5.5: The basic schematic model of MRAS speed estimator

In the MRAS speed estimation method, the RM is induction motor itself, and the adjustable model is a suitable equation where the rotor speed is involved. These suitable equations may be function of flux [116-133, 140-146] or back-EMF [112-113] or reactive power [135-139]. The information actuating the adaptation scheme is the difference between the outputs of the reference and the adaptive models. The difference between the output states of the reference model and adaptive model forms error function, depending on this error function various MRAS observers have been classified as:

1. Rotor-flux based MRAS,
2. Back-EMF based MRAS,
3. Reactive power based MRAS.

5.1.2.1 Rotor-Flux Based MRAS

The Rotor-Flux based MRAS (RFMRAS) is the most popular MRAS strategy in adaptive control because of its simplicity. RFMRAS method was first introduced by C. Schauder [116]. The RFMRAS based speed estimator is shown in Figure 5.5, which consists of a RM, an AM and an **AM** which generates the estimated speed. The RM and AM are used to estimate the rotor flux linkages of IM and the **AM** gives the speed tuning signal. The expressions of the rotor flux linkage components in the stationary reference frame can be obtained by using the stator currents and voltages of the IM. The RM calculates the actual rotor flux linkage components (i.e. ψ_{dr}, ψ_{qr}) using the voltage model (VM) according to equation (5.11) and the AM calculates the estimated rotor flux linkages (i.e. $\hat{\psi}_{dr}, \hat{\psi}_{qr}$) using the current model (CM) according to equation (5.12), respectively. The RM is independent of rotor speed whereas the AM is dependent on the rotor speed [3, 116].

$$\psi_{dr} = \frac{L_r}{L_m}\int\left(v_{ds} - \left(R_s + \sigma L_s p\right) i_{ds}\right) dt \tag{5.11a}$$

$$\psi_{qr} = \frac{L_r}{L_m}\int\left(v_{qs} - \left(R_s + \sigma L_s p\right) i_{qs}\right) dt \tag{5.11b}$$

$$\hat{\psi}_{dr} = \int\left(\frac{L_m}{T_r} i_{ds} - \frac{1}{T_r}\hat{\psi}_{dr} - \hat{\omega}_r \hat{\psi}_{qr}\right) dt \tag{5.12a}$$

$$\hat{\psi}_{qr} = \int\left(\frac{L_m}{T_r} i_{qs} - \frac{1}{T_r}\hat{\psi}_{qr} + \hat{\omega}_r \hat{\psi}_{dr}\right) dt \tag{5.12b}$$

where $T_r = {L_r}/{R_r}$, $p = \frac{d}{dt}$, and ‘ ^ ’ indicates estimated signal.

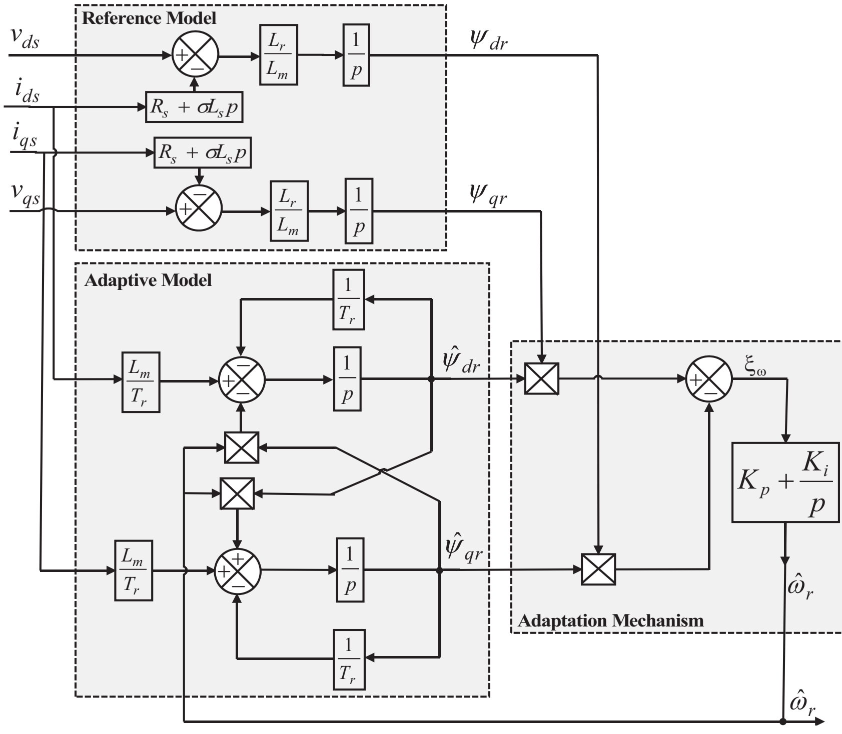

Figure 5.6: Rotor-flux based MRAS speed estimation

The angular difference between the outputs of these two models is used to generate the STS $\xi_\omega = \mathrm{Im}(\vec{\psi}_r \hat{\vec{\psi}}_r^*)$, which is then fed into the **AM**. The **AM** is used to generate the estimated rotor speed ($\hat{\omega}_r$) and it is then fed into AM, which updates the AM by generating the proper rotor speed estimation until error reduced to zero [113, 116, 127-133].

$$\xi_\omega = \mathrm{Im}(\vec{\psi}_r \hat{\vec{\psi}}_r^*) = \hat{\psi}_{dr}\psi_{qr} - \psi_{dr}\hat{\psi}_{qr} \tag{5.13}$$

where ξ_ω indicates the speed tuning signal.

This speed tuning signal is then processed through the PIC to get the estimated speed and it is given by equation (5.14) as:

$$\hat{\omega}_r = \left(K_p + \frac{K_i}{p}\right)\xi_\omega \tag{5.14}$$

The schematic model of RFMRAS speed estimation is implemented using the mathematical expression of Equations (5.15-5.18) as shown in Figure 5.6.

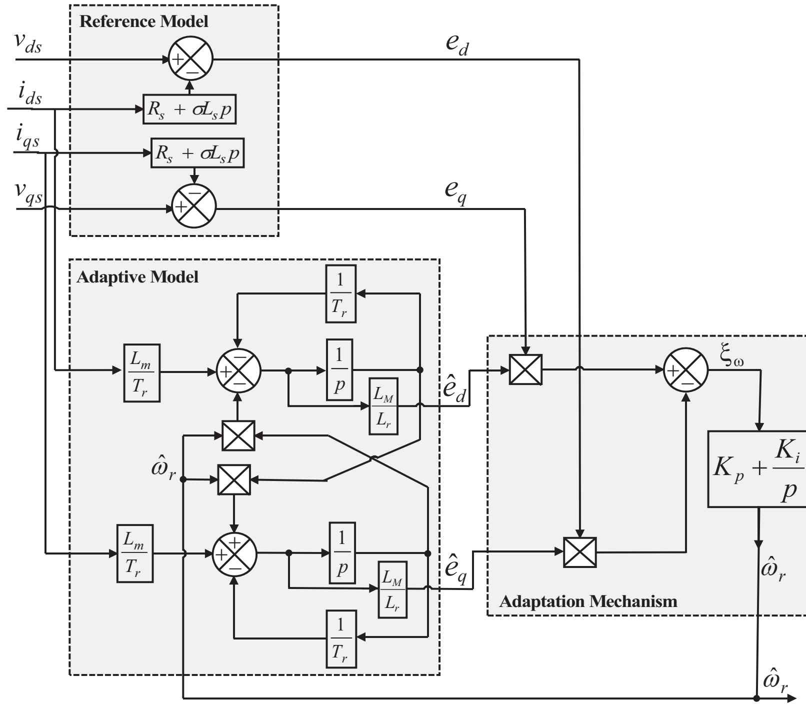

Figure 5.7: The schematic model of back emf based MRAS speed estimator

5.1.2.2 Back-EMF based MRAS

The back EMF based MRAS (BEMFMRAS) scheme was proposed by Peng et al. [112] to provide an enhancement to the RFMRAS scheme. The basic block diagram of BEMFMRAS is shown in Figure 5.7. The advantage of the BEMFMRAS scheme is that it does not require any integration in its RM. The RFMRAS uses rotor flux linkages as the RM and AM, whereas the BEMFMRAS uses the induced back EMFs.

The expressions of RM and AM for estimating rotor speed are [3, 112]:

$$e_d = \frac{L_m}{L_r}\frac{d\psi_{dr}}{dt} = V_{ds} - (R_s + L_s p) i_{ds} \tag{5.15a}$$

$$e_q = \frac{L_m}{L_r}\frac{d\psi_{qr}}{dt} = V_{qs} - (R_s + L_s p) i_{qs} \tag{5.15b}$$

$$\hat{e}_d = \frac{L_m}{L_r}\frac{d\hat{\psi}_{dr}}{dt} = \frac{L_m}{L_r}\left(\frac{L_m}{T_r} i_{ds} - \frac{\psi_{dr}}{T_r} - \omega_r \psi_{qr}\right) \tag{5.16a}$$

$$\hat{e}_q = \frac{L_m}{L_r}\frac{d\hat{\psi}_{qr}}{dt} = \frac{L_m}{L_r}\left(\frac{L_m}{T_r} i_{qs} - \frac{\psi_{qr}}{T_r} + \omega_r \psi_{dr}\right) \tag{5.16b}$$

The **AM** for BEMFMRAS scheme can be derived similarly to the RFMRAS as follows:

$$\xi_\omega = Im(\vec{e}\hat{\vec{e}}^{*}) = \hat{e}_d e_q - e_d \hat{e}_q \tag{5.17}$$

$$\hat{\omega}_r = \left(K_p + \frac{K_i}{p} \right) \xi_\omega \tag{5.18}$$

This scheme avoids the use of an integrator in the reference model (which is common for RFMRAS) and has neither drift nor initial condition problems. However, the reference model is highly sensitive to the stator resistance variations and may have stability problems at a low stator frequency. Moreover, it shows low noise immunity due to stator current differentiation and poor dynamic performance at the low stator frequency compared to RFMRAS [3, 127-129].

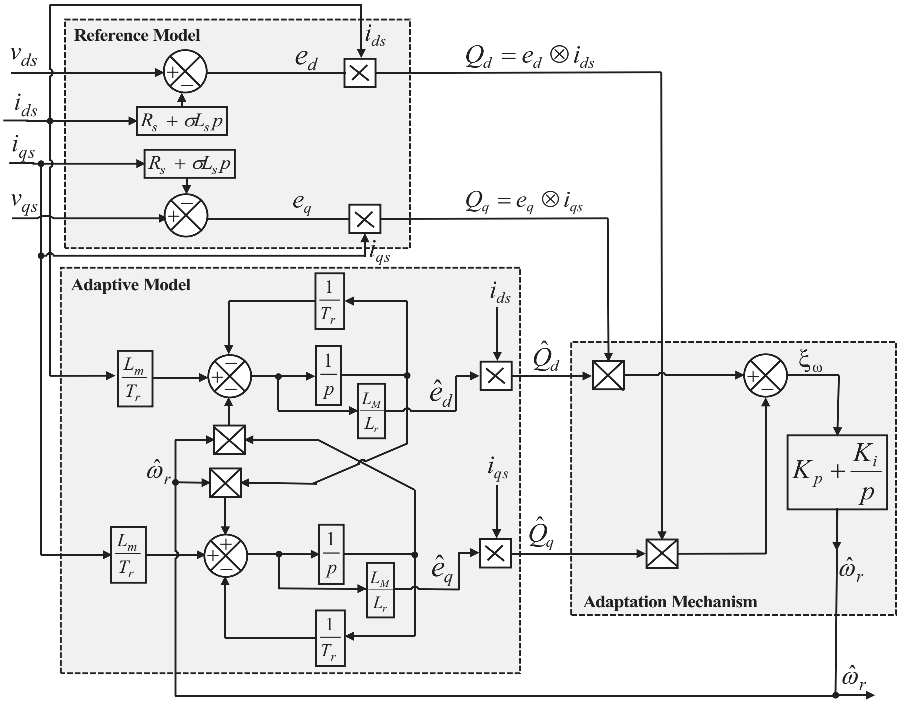

Figure 5.8: Reactive power based MRAS speed estimator

5.1.2.3 Reactive Power based MRAS

In this method, the STS is deliberately chosen to be $\mathrm{Im}(\Delta\vec{e}\vec{i}_s^{\,*}) = \vec{i}_s \otimes \Delta\vec{e}$, where $\Delta\vec{e} = \vec{e} - \hat{\vec{e}}$ and $\vec{e}$, $\hat{\vec{e}}$ are the space vectors of the BEMFMRAS in RM and AM respectively. This method is called the reactive power based MRAS (RPMRAS). This method was proposed by Maiti et al. [136] to estimate the rotor speed without stator resistance sensitivity, as shown in Figure 5.8. As stator resistance varies with the temperature, its variation affects the performance and the stability of the rotor flux, back-EMF based MRAS speed estimators, especially more at low speeds.

The expressions of RM and AM power components for estimating rotor speed are [136]:

$$Q_d = i_{ds} \otimes e_d = i_{ds} \otimes (V_{ds} - L_s p i_{ds}) \tag{5.19a}$$

$$Q_q = i_{qs} \otimes e_q = i_{qs} \otimes (V_{qs} - L_s p i_{qs}) \tag{5.19b}$$

$$\hat{Q}_d = i_{ds} \otimes \hat{e}_d = i_{ds} \otimes \frac{L_m}{L_r}\left(\frac{L_m}{T_r} i_{ds} - \frac{\psi_{dr}}{T_r} - \omega_r \otimes \psi_{qr}\right) \tag{5.20a}$$

$$\hat{Q}_q = i_{qs} \otimes \hat{e}_q = i_{qs} \otimes \frac{L_m}{L_r}\left(\frac{L_m}{T_r} i_{qs} - \frac{\psi_{dr}}{T_r} + \omega_r \otimes \psi_{dr}\right) \tag{5.20b}$$

The **AM** for BEMFMRAS scheme can be derived similarly to rotor-flux based MRAS as follows [3, 135-139]:

$$\xi_e = \mathrm{Im}(\Delta\vec{e}\,\vec{i}_s^{\,*}) = \vec{i}_s \otimes \Delta\vec{e} = Q_q\hat{Q}_d - Q_d\hat{Q}_q \tag{5.21}$$

$$\hat{\omega}_r = \left(K_p + \frac{K_i}{p}\right)\xi_e \tag{5.22}$$

The RPMRAS offers robustness against stator resistance variation and also avoids integrator. However, this method exhibits an unstable system when operating in the regeneration mode. The noise sensitivity is high due to the presence of stator current differentiation. The AM requires flux computation through CM. Therefore, the estimator is highly dependent on the variation of the rotor time constant.

The various types of speed estimation methods for sensorless drives are presented. The KF methods are not widely employed because of its complexity and large computational burden, SMO schemes require the prior knowledge of an upper bound for the system uncertainties, it needs to be determined precisely as this is employed in the switching gain calculation. The control effort required for precise upper bound determination is high, which is undesirable in a practice. Therefore, among these sensorless speed estimation techniques MRAS speed estimation offer simple implementation and require less computational effort compared to other methods. The MRAS schemes are classified as RF, BEMF and RP based MRAS schemes depending on the error vector. The BEMFMRAS method is having stability problems at low stator frequencies and shows low noise immunity due to stator current differentiation and the RPMRAS has an instability problem during the regenerative mode. Moreover, BEMF and RP quantities vanish at low and zero speed. Therefore, the simplicity of RFMRAS speed observer makes it most popular speed estimation method and it is considered in this thesis work.

5.2 Rotor-Flux based MRAS Speed Estimator

The schematic model of the RFMRAS speed estimator for DTFC of a speed sensorless IM drive is shown in Figure 5.9. The speed of the IMD can be estimated by using the RFMRAS speed estimator scheme, which is developed using the voltage model (VM) as a RM and the current model (CM) as an AM. The RM is independent of rotor speed whereas the AM is dependent on the rotor speed [116]. The outputs of these two models are used to generate the STS, which is fed into the **AM**. The **AM** is used to generate the estimated rotor speed and then it is fed into AM, which updates the AM by producing the proper rotor speed estimation until error reduced to zero. The process of updating AM is made to continue till the error signal between RM and AM tends to be zero and the estimated speed is accurately tracking the reference speed.

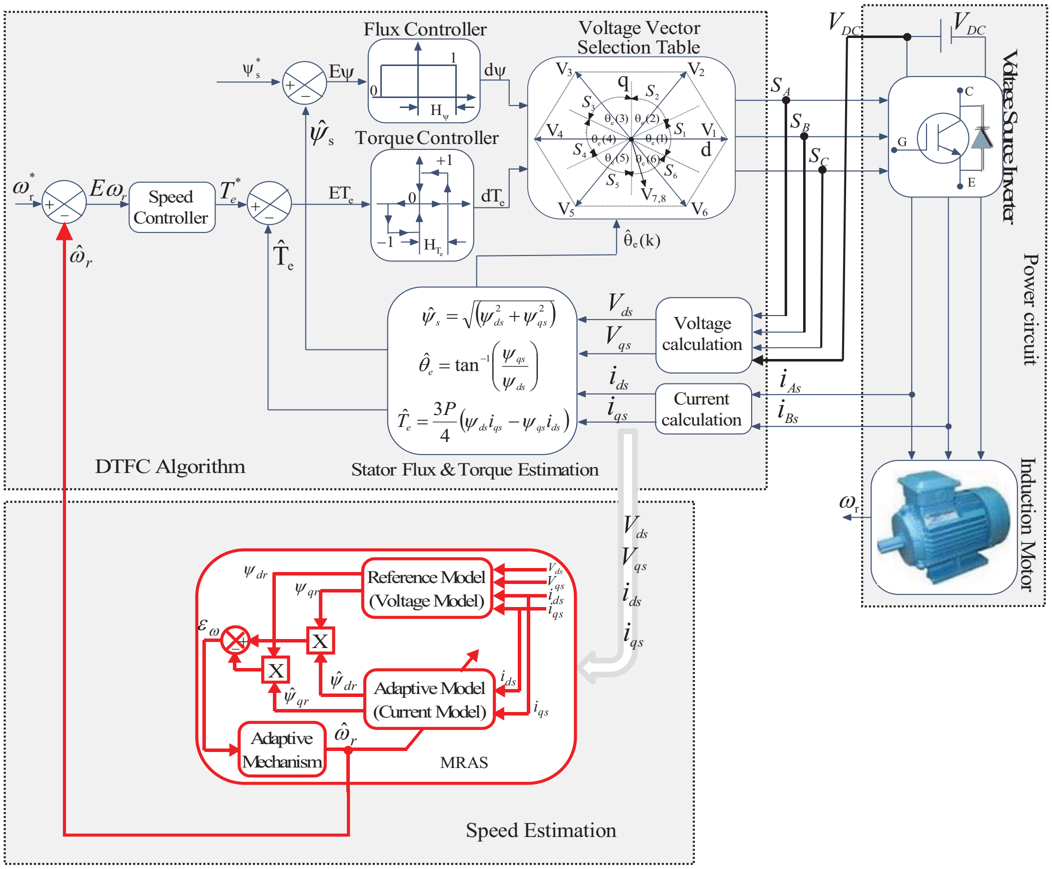

Figure 5.9: Schematic model of RFMRAS speed estimator for DTFC of a speed sensorless IM drive

The mathematical modelling of RFMRAS speed estimation for a speed sensorless IM drive is derived using its dq-model. The stator and rotor voltage equations of the IM from equations (2.43) can be written in the stationary reference frame dq-coordinates as [3]:

$$V_{ds} = R_s i_{ds} + p\psi_{ds} \tag{5.23}$$

$$V_{qs} = R_s i_{qs} + p\psi_{qs} \tag{5.24}$$

$$0 = R_r i_{dr} + p\psi_{dr} + \omega_r \psi_{qr} \tag{5.25}$$

$$0 = R_r i_{qr} + p\psi_{qr} - \omega_r \psi_{dr} \tag{5.26}$$

where

$$\psi_{ds} = L_s i_{ds} + L_m i_{dr} \tag{5.27}$$

$$\psi_{qs} = L_s i_{qs} + L_m i_{qr} \tag{5.28}$$

$$\psi_{dr} = L_r i_{dr} + L_m i_{ds} \tag{5.29}$$

$$\psi_{qr} = L_r i_{qr} + L_m i_{qs} \tag{5.30}$$

Reference Model:

Solving the equation (5.27) in terms of rotor current and substituting it in (5.29) yields:

$$\psi_{dr} = \frac{L_r}{L_m}(\psi_{ds} - L_s i_{ds}) + L_m i_{ds} \tag{5.31}$$

Simplifying the above equation (5.31) and applying derivative yields:

$$p\psi_{dr} = \frac{L_r}{L_m}(p\psi_{ds} - \sigma L_s p i_{ds}) \tag{5.32}$$

Simplifying the equation (5.24) in terms of stator flux component and substituting it in equation (5.32), which yields d-axis rotor flux linkage of the RM as:

$$p\psi_{dr} = \frac{L_r}{L_m}(V_{ds} - R_s i_{ds} - \sigma L_s p i_{ds}) \tag{5.33}$$

Similarly, the q-axis rotor flux linkage of the RM as:

$$p\psi_{qr} = \frac{L_r}{L_m}(V_{qs} - R_s i_{qs} - \sigma L_s p i_{qs}) \tag{5.34}$$

Adaptive Model:

Solving the d-axis rotor current from the equation (5.29) and substituting it in equation (5.25), we get:

$$p\psi_{dr} = \left(\frac{L_m}{T_r} i_{ds} - \frac{1}{T_r}\psi_{dr} - \omega_r \psi_{qr}\right) \tag{5.35}$$

Solving the equation (5.35) results in expression for d-axis AM rotor flux as:

$$p\hat{\psi}_{dr} = \left(\frac{L_m}{T_r} i_{ds} - \frac{1}{T_r}\hat{\psi}_{dr} - \hat{\omega}_r \hat{\psi}_{qr}\right) \tag{5.36}$$

Similarly, the q-axis AM rotor flux as:

$$p\hat{\psi}_{qr} = \left(\frac{L_m}{T_r} i_{qs} - \frac{1}{T_r}\hat{\psi}_{qr} + \hat{\omega}_r \hat{\psi}_{dr}\right) \tag{5.37}$$

The RM and AM equations of dq-axes rotor flux components, i.e. equation (5.33)-(5.34) and (5.36)-(5.37) are used for generating the speed tuning signal (ξ_ω), which is then fed into the **AM** to generate the estimated speed.

Adaptation Mechanism:

The **AM** plays a crucial role in the dynamics and stability of the MRAS. The **AM** can be derived in two ways: (i) approach based on Popov's Hyperstability theory and (ii) Lyapunov's method. Here, Popov's Hyperstability theory is considered for designing the **AM**. The Hyperstability theory mainly deals with the stability properties of the feedback control system, which is shown in Figure 5.10.

Figure 5.10 consists of two blocks: they are linear time-invariant block and nonlinear time-varying block. According to Hyperstability theory, the nonlinear and time varying feedback system is asymptotically stable, i.e. $\underset{t\to\infty}{Lim}\,\xi = 0$, if the following two conditions hold.

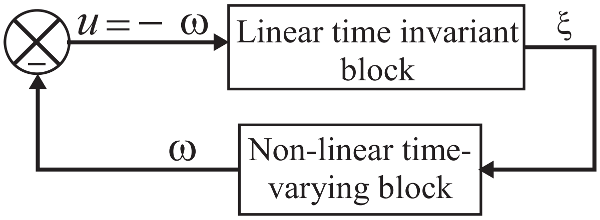

Figure 5.10: Nonlinear and time-varying feedback system.

Condition I: the input ξ and the output ω of the non-linear time-varying block satisfy the Popov's integral inequality [114-115]:

$$\int_0^{t_1} \xi^T \omega dt \geq -\gamma^2 \quad \text{for all } t_1 \geq 0 \tag{5.38}$$

where γ is an arbitrary finite constant.

Condition II: The transfer function matrix $[F(s)]$ of the linear time-invariant block is strictly positive and real, i.e. $[F(j\omega) + F^T(-j\omega)]$ is a strictly positive definite Hermitian matrix.

Initially, for the purpose of designing **AM** the error (ξ) between the output of RM and AM is treated as a state variable [114].

$$\xi_d = \psi_{dr} - \hat{\psi}_{dr} \tag{5.39a}$$

$$\xi_q = \psi_{qr} - \hat{\psi}_{qr} \tag{5.39b}$$

From the above equation the error vector can be defined as:

$$[\xi] = [\xi_d \quad \xi_q]^T \tag{5.40}$$

In general ω_r is variable, but for the derivation of the adaptation mechanism it is valid to initially consider the rotor speed as a constant parameter of the reference model.

By using the equations (5.33), (5.34), (5.36), (5.37) and (5.39), the state equations of the linear time-invariant block can be derived as:

$$p\xi_d = -\frac{1}{T_r}\xi_d - \omega_r\xi_q - \left(\omega_r - \hat{\omega}_r\right)\hat{\psi}_{qr}$$

$$p\xi_q = \omega_r\xi_d - \frac{1}{T_r}\xi_q + \left(\omega_r - \hat{\omega}_r\right)\hat{\psi}_{dr} \tag{5.41}$$

The above equation (5.41) can be represented in the matrix form as:

$$p\begin{bmatrix}\xi_d \\ \xi_q\end{bmatrix} = \begin{bmatrix} -\frac{1}{T_r} & -\omega_r \\ \omega_r & -\frac{1}{T_r}\end{bmatrix}\begin{bmatrix}\xi_d \\ \xi_q\end{bmatrix} - \begin{bmatrix}\hat{\psi}_{qr} \\ -\hat{\psi}_{dr}\end{bmatrix}\left(\omega_r - \hat{\omega}_r\right) \tag{5.42}$$

The above equation (5.42) can be represented as [116, 114, 128]:

$$p[\xi] = [A][\xi] - [W] \tag{5.43}$$

where $[A] = \begin{bmatrix} -\frac{1}{T_r} & -\omega_r \\ \omega_r & -\frac{1}{T_r}\end{bmatrix}$ and $[W] = \begin{bmatrix}\hat{\psi}_{qr} \\ -\hat{\psi}_{dr}\end{bmatrix}\left(\omega_r - \hat{\omega}_r\right)$.

According to the general structure of the adaptation law, $\hat{\omega}_r$ can be expressed as [114]:

$$\hat{\omega}_r = \Phi_2\left([\xi]\right) + \int_0^t \Phi_1\left([\xi]\right)d\tau \tag{5.44}$$

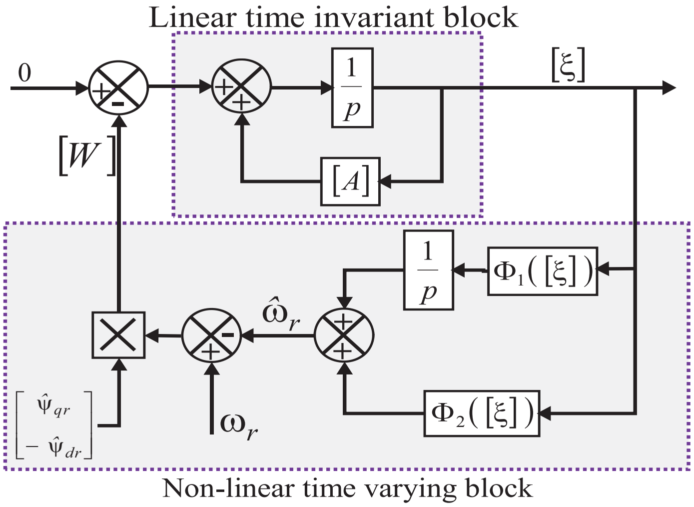

Figure 5.11: Equivalent model of the rotor flux-based MRAS

Using the equations (5.43) and (5.44), the MRAS represents as a nonlinear feedback system and it is shown in Figure 5.11.

By substituting the components of $[\xi]$ and $[W]$ in equation (5.38), we get Popov's criterion for the present system as follows [114]:

$$\int_0^t [\xi_d \quad \xi_q] \begin{bmatrix} \hat{\psi}_{qr} \\ -\hat{\psi}_{dr} \end{bmatrix} (\omega_r - \hat{\omega}_r)\, dt \geq -\gamma^2 \quad \text{for all } t_1 \geq 0 \tag{5.45}$$

The equation (5.45) can be rewritten as:

$$\int_0^t [\xi_d \hat{\psi}_{qr} - \hat{\psi}_{dr} \xi_q](\omega_r - \hat{\omega}_r)\, dt \geq -\gamma^2 \quad \text{for all } t_1 \geq 0 \tag{5.46}$$

By substituting the equation (5.44) in equation (5.46), we get:

$$\int_0^t [\xi_d \hat{\psi}_{qr} - \hat{\psi}_{dr} \xi_q] \left(\omega_r - \Phi_2([\xi]) - \int_0^t \Phi_1([\xi])\, d\tau \right) dt \geq -\gamma^2 \quad \text{for all } t_1 \geq 0 \tag{5.47}$$

The above inequality can be solved by using the following well-known relation:

$$\int_0^{t_1} k.(p.f(t)).f(t) dt \geq -\frac{1}{2} k.f(0)^2 \qquad \text{for all } k \geq 0 \tag{5.48}$$

By using equation (5.48), it can be shown that equation (5.47) is satisfied by the following functions [114]:

$$\Phi_1 = K_2(\xi_q \hat{\psi}_{dr} - \xi_d \hat{\psi}_{qr}) = K_i(\psi_{qr} \hat{\psi}_{dr} - \psi_{dr} \hat{\psi}_{dr})$$

$$\Phi_2 = K_1(\xi_q \hat{\psi}_{dr} - \xi_d \hat{\psi}_{qr}) = K_p(\psi_{qr} \hat{\psi}_{dr} - \psi_{dr} \hat{\psi}_{dr}) \tag{5.49}$$

where Φ_1 and Φ_2 are the integral and proportional parts of the adaptation law respectively.

The speed tuning signal (STS) can be obtained from the equation (5.49) as follows:

$$\xi_\omega = \psi_{qr} \hat{\psi}_{dr} - \psi_{dr} \hat{\psi}_{dr} \tag{5.50}$$

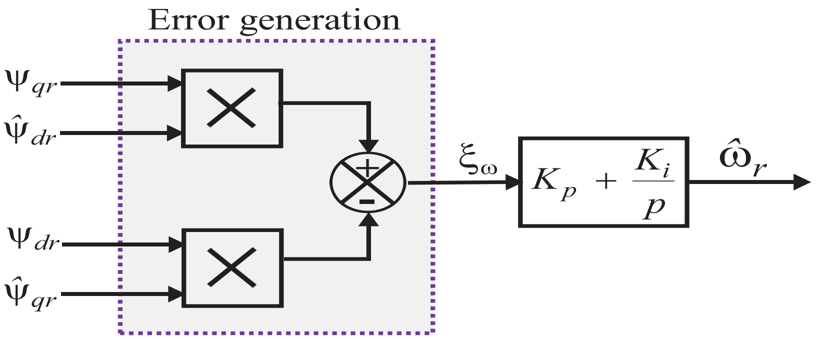

Figure 5.12: Adaptation mechanism for MRAS observer

The speed tuning signal is processed through the PIC, it generates the estimated rotor speed by minimizing the speed tuning signal which is shown in the Figure 5.12 and the estimated rotor speed can be expressed as:

$$\hat{\omega}_r = \left(K_p + \frac{K_i}{p}\right)\xi_\omega \tag{5.51}$$

The speed tuning error signal is fed into PIC and it generates the estimated rotor speed, this estimated speed is used to adjust the AM until the satisfactory performance achieved. Since, the RFMRAS scheme is a closed-loop system, the accuracy of the system can be enhanced. However, the use of integrator in the RM may create the initial value and DC drift problems during experimental implementation. Therefore, in order to mitigate these problems, a low-pass filter (LPF) with low cutoff frequency (i.e. typically 1Hz) can be used in place of RM integrator [3, 116]. In order to adjust the rotor flux linkage outputs of AM with the rotor flux linkage outputs of RM, a high pass filter (HPF) is placed in front of the original AM, which is shown in Figure 5.13.

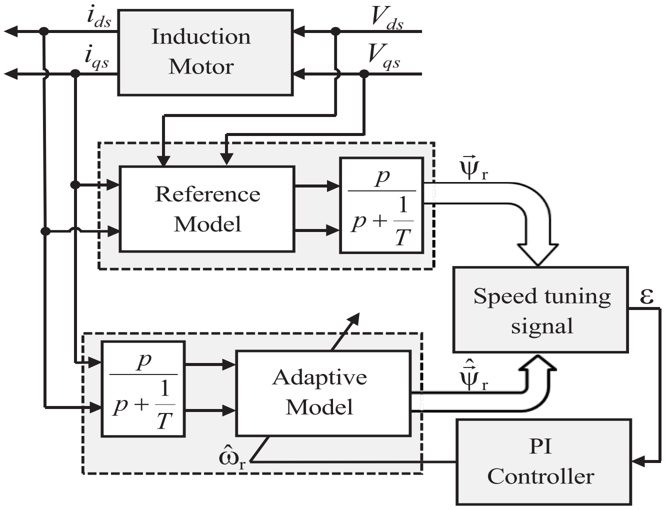

Figure 5.13: Schematic model of RFMRAS speed estimator using PIC based adaptation mechanism

5.2.1 PIC based MRAS Speed Estimator

The schematic model of the RFMRAS speed estimator using PIC based adaptation mechanism scheme is shown in Figure 5.13. The speed tuning signal (ξ_ω) is fed into the PIC, which estimates the rotor speed and then the estimated rotor speed is fed back into AM. The PIC based **AM** offers satisfactory performance over a wide range of operation and it is widely used in industrial control system applications. The linear PIC were used in adaptation scheme for the majority of MRAS speed observer to estimate the rotor speed. However, the PIC may not be able to provide the satisfactory performance under a sudden change in speed, load torque disturbance conditions, low speed commands due to continuous variation in machine parameters and the operating conditions in addition to the nonlinearities present in the inverter. Moreover, it requires a precise mathematical model, continuous tuning and accurate gain values (K_p and K_i) to achieve high performance drive [127-129, 132-133].

Therefore, in order to overcome with the above drawbacks, the adaptive control based adaptation mechanisms are highly desirable.

The PIC in the adaptation mechanism is replaced with artificial intelligence techniques, such as Type-1 FLC and Type-2 FLC to improve the performance of the sensorless drive under a wide range of speed operations.

5.2.2 Type-1 Fuzzy Logic Controller based MRAS Speed Estimator

In this section, the PIC based adaptation mechanism is replaced by T1FLC. The T1FLC can handle complicated nonlinear systems and it does not require precise mathematical modelling and gain values unlike constant gain PIC, which makes the controller highly suitable for a speed sensorless drive. The schematic model of the MRAS speed estimator using T1FLC based adaptation mechanism is shown in Figure 5.14.

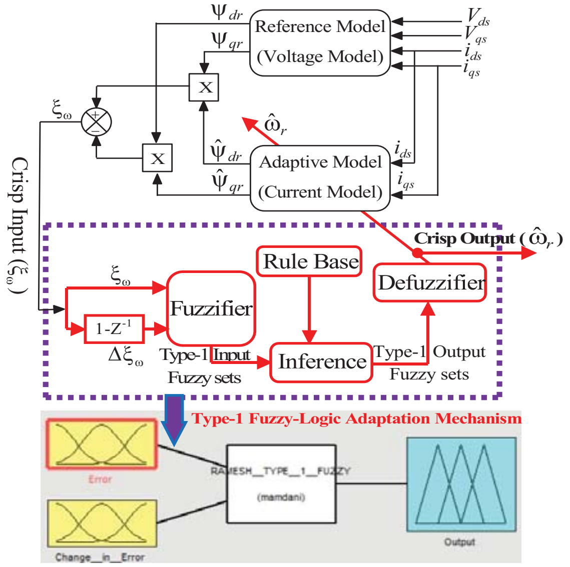

Figure 5.14: Schematic model of T1FLC based MRAS speed estimator

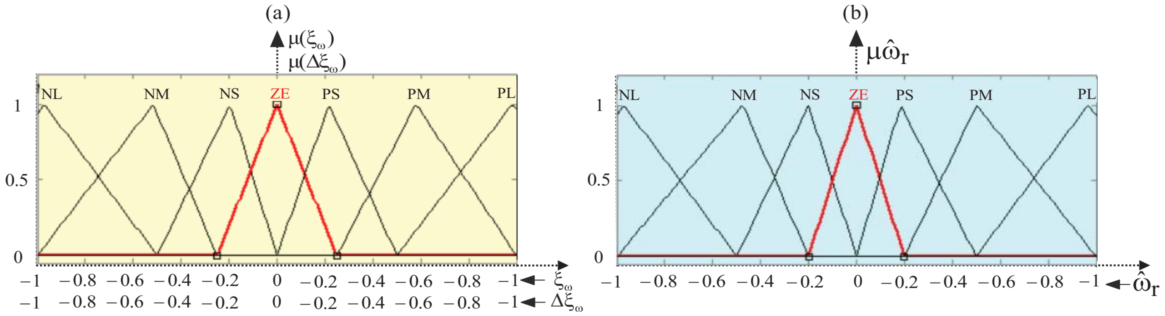

Figure 5.15: Type-1 FLC: (a) Input MFs (ξ_ω and $\Delta\xi_\omega$) and (b) output MF of $\hat{\omega}_r$

Similar to the PIC, the speed tuning signal ξ_ω is fed into T1FLC to determine the rotor speed estimation. The input variables of T1FLC are speed tuning signal 'ξ_ω' (i.e. equation

5.50) and rate of change in speed tuning error signal ‘ $\Delta\xi_\omega$ ’ (i.e. equation 5.52) and the output variable is estimated rotor speed ‘ $\hat{\omega}_r$ ’, which are shown in Figure 5.15.

$$\Delta\xi_\omega(k) = \xi_\omega(k) - \xi_\omega(k-1) \tag{5.52}$$

where, $\xi_\omega(k)$ and $\xi_\omega(k-1)$ are the present and the previous values of the STSs, respectively.

The Mamdani type and triangular MFs (i.e. 7MFs) are considered for both input and output variables and therefore, the total number of possible rules should be 49 as illustrated in Table 5.1, in which each rule base has the following form as [48-49]:

$$R^l : \text{IF } \xi_\omega \text{ is } F^l_{\xi_\omega} \text{ AND } \Delta\xi_\omega \text{ is } F^l_{\Delta\xi_\omega} \text{ THEN } \hat{\omega}_r \text{ is } G_{\hat{\omega}_r}{}^l$$

where, $l = 1,2,...,M$, $F^l_{\xi_\omega}$ and $F^l_{\Delta\xi_\omega}$ represent the antecedent MFs of fuzzy sets (IF-ingredients) and $G_{\hat{\omega}_r}{}^l$ represents consequent MF (THEN-ingredients) respectively.

In this control scheme, the centroid method is considered for the defuzzification purpose. The centroid of the estimated speed $\hat{\omega}_{Cr}$ (found from the crisp output of T1FLC) is estimated for the overall MF and which can be expressed as follows [177]:

$$\hat{\omega}_{rC} = \frac{\sum_{k=0}^{n} \mu_A(\hat{\omega}_{rCk})\,\hat{\omega}_{rCk}}{\sum_{k=1}^{n} \mu_A(\hat{\omega}_{rCk})} \tag{5.53}$$

where, $\mu_A(\hat{\omega}_{rCk})$ and $\hat{\omega}_{rCk}$ are overall output MF and crisp output quantity of adaptation mechanism and k=1, 2, …, n number of samples of the aggregated output MF.

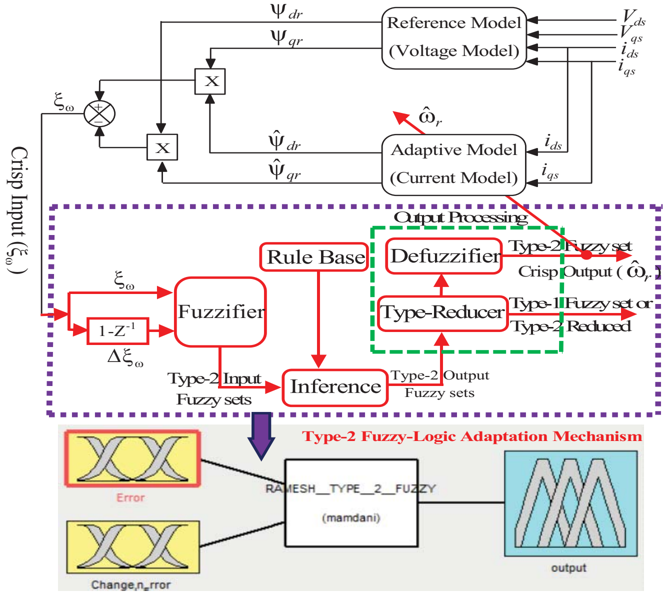

Figure 5.16: Schematic model of T2FLC based MRAS speed estimator

5.2.3 Type-2 Fuzzy Logic Controller based MRAS Speed Estimator

The schematic model of T2FLC based MRAS speed estimator is shown in Figure 5.16. The T1FLC based adaptation mechanism is replaced by T2FLC to further enhance the dynamic as well as the steady state performance of the speed sensorless IM drive. The input and output triangular MFs of T2FLC is illustrated in Figure 5.17. Here, the number of inputs (i.e. $\xi_\omega(k)$ and $\xi_\omega(k-1)$) and the output ($\hat{\omega}_r$) MFs are considered to remain same as that of the T1FLC to show the improvement of T2FLC over T1FLC, which are shown in Figure 5.17 (a) and Figure 5.17 (b), respectively. Moreover, the corresponding number of rules for T2FLC is also same as that of T1FLC, which is illustrated in Table 5.1.

The rule base of T2FLC is framed using IF and THEN form as follows [85, 81]:

$$R^l: \text{IF } \xi_\omega \text{ is } \tilde{F}^l_{\xi_\omega} \text{ AND } \Delta\xi_\omega \text{ is } \tilde{F}^l_{\Delta\xi_\omega} \text{ THEN } \hat{\omega}_r \text{ is } (y^l_l, y^l_r)$$

where, $l = 1,2,...,M$, $\tilde{F}^l_{\xi_\omega}$ and $\tilde{F}^l_{\Delta\xi_\omega}$ represents the antecedent MFs of 2-inputs (IF-ingredients) and (y^l_l, y^l_r) are represent left and right consequent MF (THEN-ingredients) of T2FS.

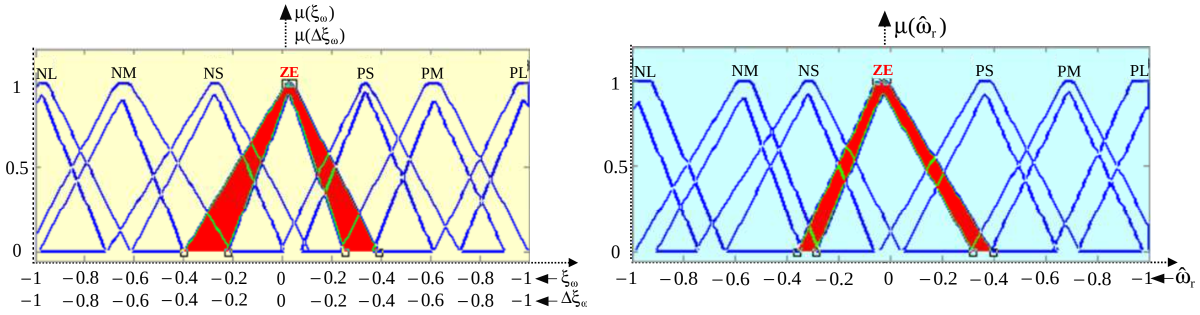

Figure 5.17: Type-2 FLC: (a) Input MFs (ξ_ω and $\Delta\xi_\omega$) and (b) output MF of $\hat{\omega}_r$

Table 5.1: Rule base of fuzzy logic controller

Output ($\hat{\omega}_r$)		**Change in Error Speed** ($\Delta\xi_\omega$)						
		NL	**NM**	**NS**	**ZE**	**PS**	**PM**	**PL**
Error Speed (ξ_ω)	**NL**	NL	NL	NL	NL	NM	NS	ZE
	NM	NL	NL	NL	NM	NS	ZE	PS
	NS	NL	NL	NM	NS	ZE	PS	PM
	ZE	NL	NM	NS	ZE	PS	PM	PL
	PS	NM	NS	ZE	PS	PM	PL	PL
	PM	NS	ZE	PS	PM	PL	PL	PL
	PL	ZE	PS	PM	PL	PL	PL	PL

5.2.3.1 Design of Type-2 FLC Rule Base

The type-2 fuzzy sets of l^{th} rule can be obtained as [81-85]:

$$F^l(X)=\left[\underline{f}^l(X),\overline{f}^l(X)\right]=\left[\underline{f}^l,\overline{f}^l\right] \tag{5.54}$$

where $\overline{f}^l=\overline{\mu}_{\tilde{F}^l_{\xi\omega}}(\xi_\omega)*\overline{\mu}_{\tilde{F}^l_{\Delta\xi\omega}}(\Delta\xi_\omega)$ and $\underline{f}^l=\underline{\mu}_{\tilde{F}^l_{\xi\omega}}(\xi_\omega)*\underline{\mu}_{\tilde{F}^l_{\Delta\xi\omega}}(\Delta\xi_\omega)$, '*' indicates the product operation, $\underline{\mu}_{\tilde{F}^l_{\xi\omega}}$ and $\overline{\mu}_{\tilde{F}^l_{\xi\omega}}$ represents LMF and UMF grades, respectively.

Type-reducer:

The type-reducer block transforms a T2FS output of T2FIS into Type-1 reduced a fuzzy set, which is then transformed into a crisp output through the defuzzifier. The COS is considered for TR operation. A singleton fuzzification with minimum t-norm is used and the output can be expressed as [85, 177-178]:

$$\hat{\omega}_{rCOS}=\int_{f_l\in J_{y1}},....,\int_{f_N\in J_{yN}}\left[\frac{\sum_{l=1}^{M} f_l y_l}{\sum_{l=1}^{M} f_l}\right]=\left[y_l^l,y_r^l\right]=\left[\hat{\omega}_{rl},\hat{\omega}_{rr}\right] \tag{5.55}$$

where $\hat{\omega}_{rCOS}$ is an IT2FS determined by the left-most and right-most end points ($\hat{\omega}_{rl},\hat{\omega}_{rr}$), which can be derived from the consequent centroid set (y_l^l,y_r^l) and the estimated speed strength $\underline{f}^l\in F^l=\left(\underline{f}^l,\overline{f}^l\right)$ must be computed or set first before the computation of $\hat{\omega}_{rCOS}$ [79].

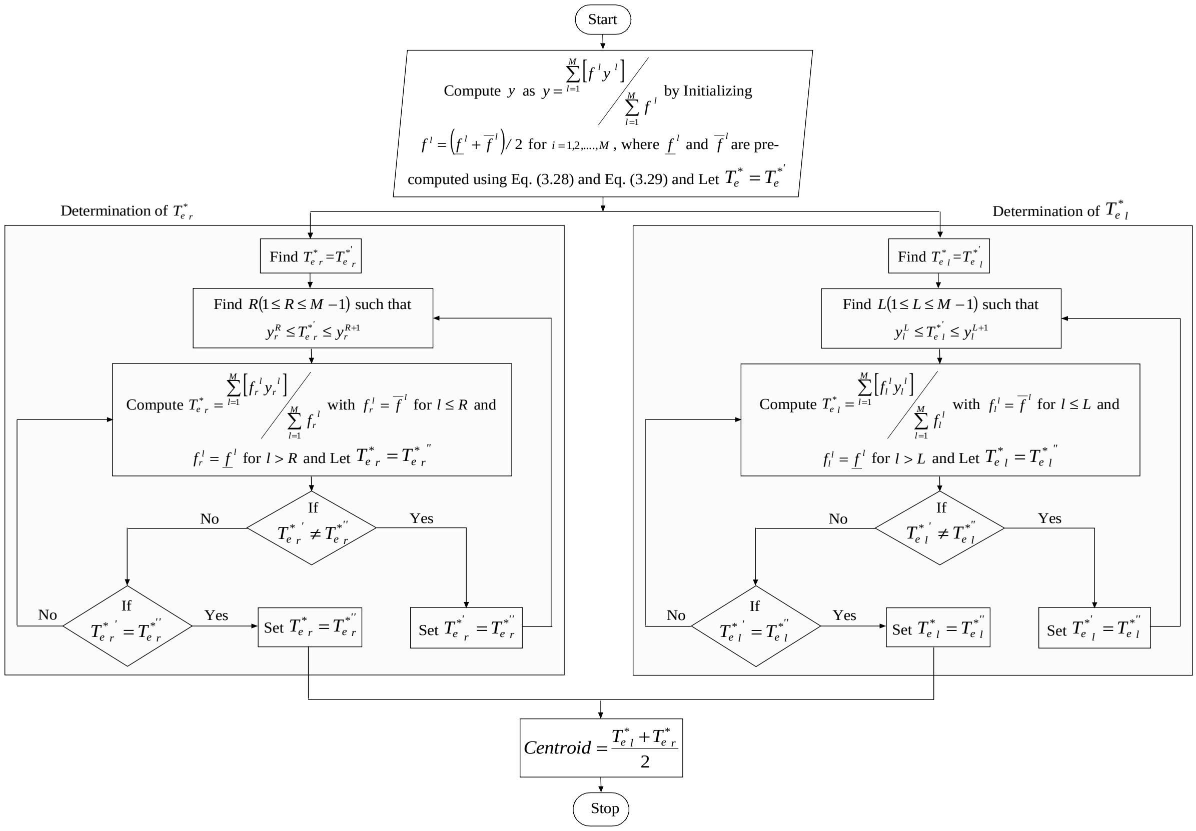

Figure 5.18: The flowchart of T2FLC for finding the crisp value of the estimated speed

The LMP ($\hat{\omega}_{r_l}$) and RMP ($\hat{\omega}_{r_r}$) can be expressed as follows [80, 178]:

$$\hat{\omega}_{r_l} = y_l^l = \frac{\sum_{l=1}^{M}\left[f_l^{\,l} y_l^{\,l}\right]}{\sum_{i=1}^{M} f_l^{\,l}} \tag{5.56}$$

$$\hat{\omega}_{r_r} = y_r^l = \frac{\sum_{l=1}^{l}\left[f_r^{\,l} y_r^{\,l}\right]}{\sum_{l=1}^{M} f_r^{\,l}} \tag{3.33}$$

Computation of $\hat{\omega}_{r_l}$ and $\hat{\omega}_{r_r}$ is done using Karnik-Mendal algorithm [79], which is given in Figure 5.18. The procedure to compute the RMP ($\hat{\omega}_{r_l}$) and LMP ($\hat{\omega}_{r_r}$) is considered similar to that of used for computing $T_{e_l}^*$ and $T_{e_r}^*$, respectively.

Defuzzification:

The type-reducer output is fed into the defuzzification block. Then the defuzzification block converts from the T1FS to crisp output. The defuzzified crisp output is the average value of $\hat{\omega}_{rr}$ and $\hat{\omega}_{rl}$, it is given by:

$$Centroid = y(x) = \frac{\hat{\omega}_{rl} + \hat{\omega}_{rr}}{2} \tag{5.57}$$

5.3 Simulation Results

The RFMRAS speed estimator for sensorless IMD (Figure 5.9) is mathematically modelled in the MATLAB/SIMULINK environment using PIC, T1FLC and T2FLC schemes, respectively. The Simulink model is then used to verify the performance of the DTFC of an IMD under various operating conditions, such as no-load torque, load torque, sudden changes in speed and low speed, respectively.

5.3.1 Performance under Forward Motoring

Initially, the performance of the sensorless IMD is simulated under no-load torque operation at 1200 rpm using three adaptation schemes and it is shown in Figure 5.19 (a)-(c). The reference speed (ω_r^*), actual speed (ω_r) and estimated speed ($\hat{\omega}_r$) under such command is shown in Figure 5.19 trace-(ii). The electromagnetic torque, stator current, stator flux dq-components in a stationary reference frame (i.e. ψ_{ds} , ψ_{qs}) and stator flux are shown in Figure 5.19 (i), (iii)-(v), respectively. It is observed that the IM drive starts at zero speed and reaches the set reference speed ($\omega_r = 1200$ rpm) at 0.69 s with an overshoot of 13.9 rpm using PIC, whereas it reaches the set reference speed quickly at 0.496 s with zero overshoot using

T2FLC, respectively. It is observed from the simulation results that the transient response of the IM drive using T2FLC is faster compared to the PIC and T1FLC, respectively.

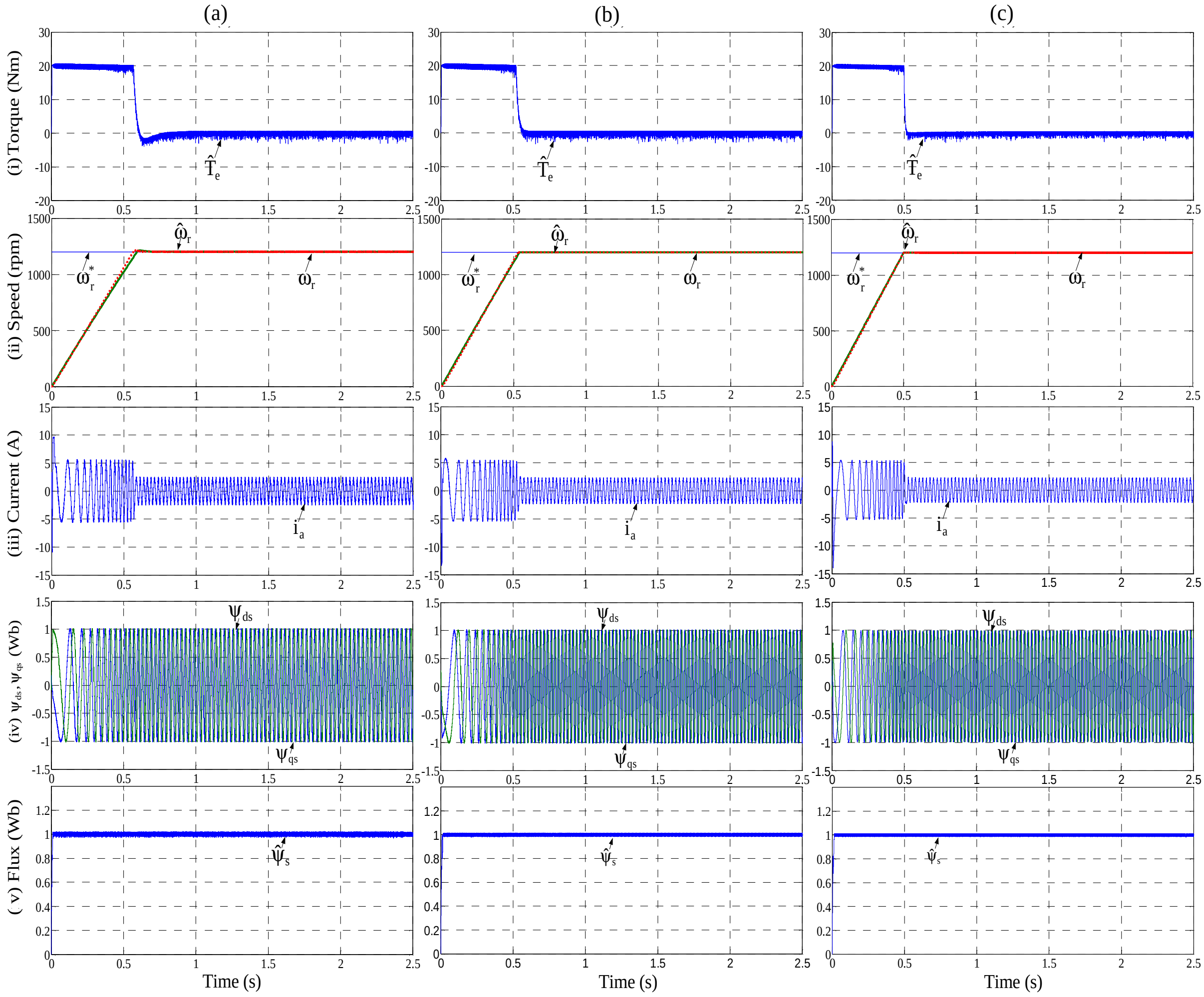

Figure 5.19: Performance under no-load torque operating condition using: (a) PIC, (b) T1FLC and (c) T2FLC: *Traces (from top to bottom):* (i) Torque, (ii) speed, (iii) stator current, (iv) stator flux dq-components in stationary reference frame and (v) stator flux

5.3.2 Loading Performance

The performance of the sensorless IMD is observed under the application and removal of sudden load torque disturbances in the following conditions.

- Loading at 1200 rpm,
- Loading and unloading at 1200 rpm,
- Loading at different speed commands (i.e. 300 rpm, 600 rpm and 900 rpm).

Loading performance at 1200 rpm

The effect of sudden load torque operation is observed at 1200 rpm using PIC, T1FLC and T2FLC shown in Figure 5.20 (a)-(c). The sudden load torque of 9 Nm is applied at 1.4 s when the induction motor is operating at steady state speed. It is observed that the sudden application of load torque causes an undershoot around 1.083%, 0.45% and 0.166% of the reference speed using PIC, T1FLC and T2FLC as shown in Figure 5.20 (ii). It is also observed that the recovery time of the estimated speed under such command is 0.298 s, 0.11 s and 0.04 s using PIC, T1FLC and T2FLC schemes, respectively. Moreover, slight error speed, ripple contents in torque and stator currents are less using T2FLC compared to T1FLC and PIC, which are shown in Figure 5.20 (i), (iii)-(iv), respectively. Similarly, when the load torque is removed (i.e. at 2.1 s), an overshoot around 1.125%, 0.43%, 0.166% of the reference speed appears using PIC, T1FLC and T2FLC as shown in Figure 5.21 (ii). The torque, reference speed, estimated and actual speeds, stator current and the error speed between the estimated and actual speeds are shown in Figure 5.21 (i)-(iv), respectively.

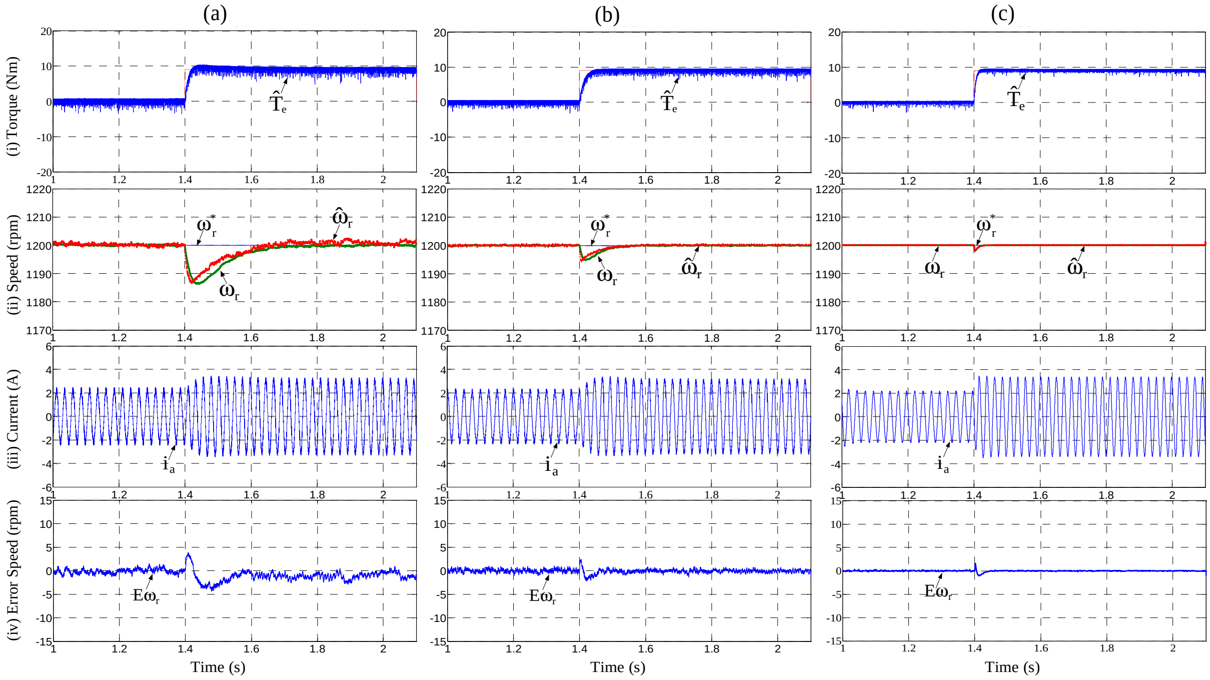

Figure 5.20 Loading performance at 1200 rpm using: (a) PIC, (b) T1FLC and (c) T2FLC: *Traces (from top to bottom):* (i) Torque, (ii) speed, (iii) stator current and (iv) error speed

The effect of different load torque conditions is observed under different speed commands using PIC, T1FLC and T2FLC schemes, which are illustrated in Figure 3.21(a)-(c). It is observed that the T2FLC shows an excellent performance and robustness to various load torque disturbances compared to PIC and T1FLC, respectively.

5.3.3 Performance under Reversal Speed Command

The performance of the sensorless drive is observed under the reversal speed command using PIC, T1FLC and T2FLC shown in Figure 5.23 (a)-(c). The reversal speed command from +1200 rpm to -1200 rpm is applied at 2 s. The estimated speed reaches its reference speed during reversal speed at 3.16 s, 3.04 s and 2.93 s using PIC, T1FLC and T2FLC, respectively. The reference, actual and estimated speeds are shown in Figure 5.23 (ii), which reveals that the estimated speed tracking the reference speed with an overshoot of 13.8 rpm, 0.8 rpm and 0 rpm of the reference speed using PIC, T1FLC and T2FLC schemes, respectively. The torque, stator current and stator flux dq-axis components in a stationary reference frame are shown in Figure 5.23 (i), (iii)-(iv), respectively. The transient response of reversal speed is shown in Figure 5.24 (a)-(c).

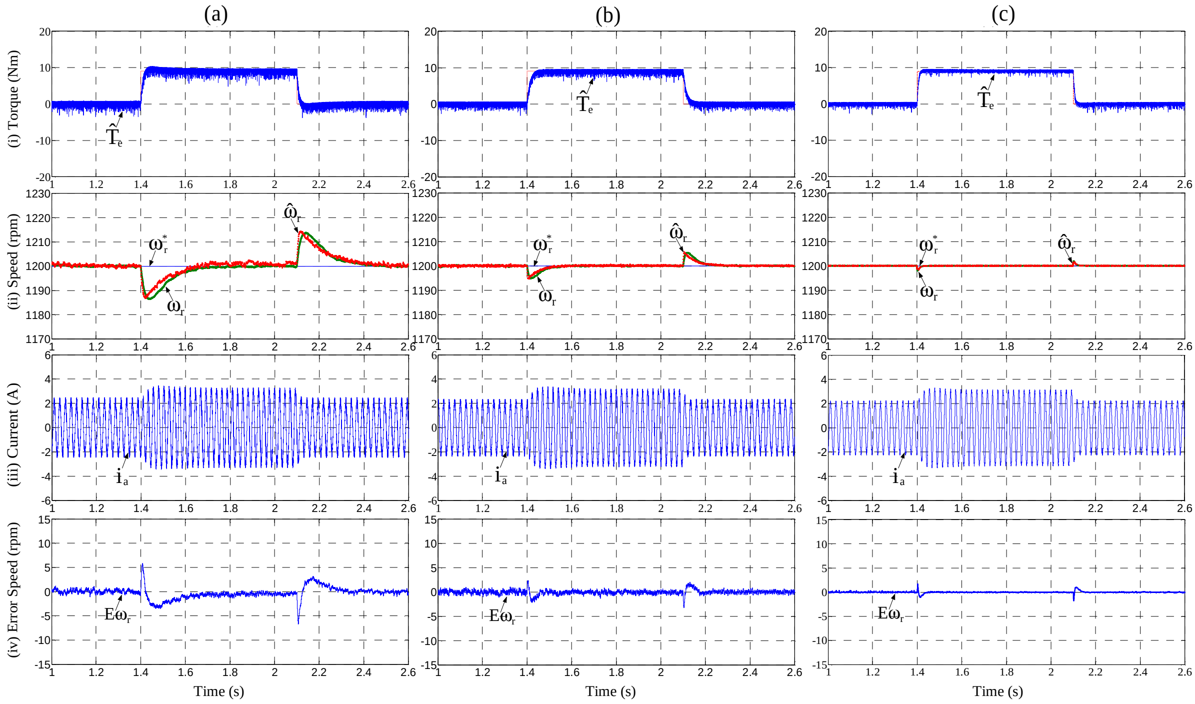

Figure 5.21: Loading and unloading performance at 1200 rpm using: (a) PIC, (b) T1FLC and (c) T2FLC: *Traces (from top to bottom):* (i) Torque, (ii) speed, (iii) stator current and (iv) error speed

5.3.4 Tracking Performance of the Speed Commands

Tracking performance of the sensorless IM drive is observed through the applications of various changes in speed, such as step and square speed commands, respectively. The simulation results for each case are presented as follows.

Performance under step change in speed command:

The performance of the sensorless IMD is observed under a sudden change in step speed command using three controller schemes are shown in Figure 5.25 (a)-(c). The sudden change in step speed command of 300 rpm is applied in four steps (i.e. 600 rpm → 900 rpm → 1200 rpm → 900 rpm → 600 rpm) at 1.4 s, 2.4 s, 3.6 s, etc. The corresponding reference and actual speed responses under such speed commands are shown in Figure 5.25 (ii). The electromagnetic torque, stator current and stator flux dq-components in a stationary reference frame are shown in Figure 5.25 (i), (iii)-(iv) respectively. From Figure 5.25 (ii), it is observed that the estimated speed settles at the reference speed (from 600 rpm to 900 rpm) in 0.22 s, 0.136 s and 0.12 s using PIC, T1FLC and T2FLC, respectively. Moreover, it is also observed that the error between the estimated and actual speed is negligible using T2FLC compared to T1FLC and PIC.

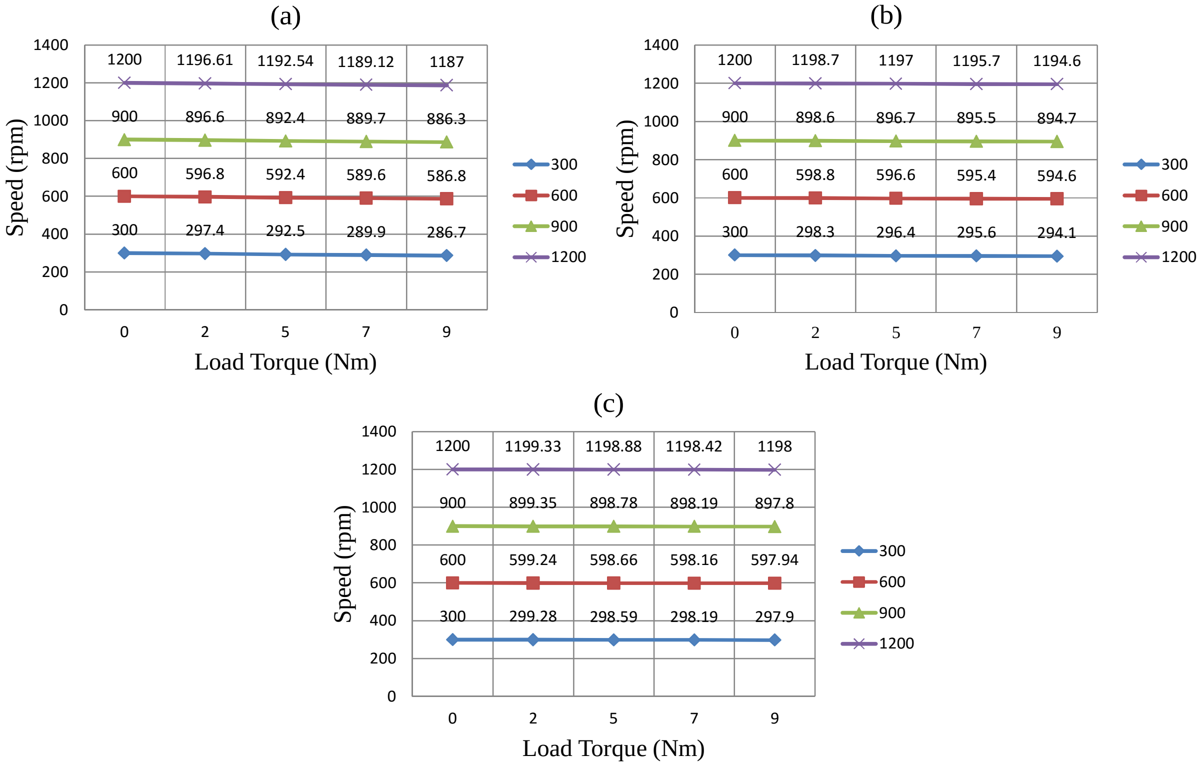

Figure 5.22: Steady-state performance of the estimated speed under various load conditions at different speed commands using: (a) PIC, (b) T1FLC and (c) T2FLC

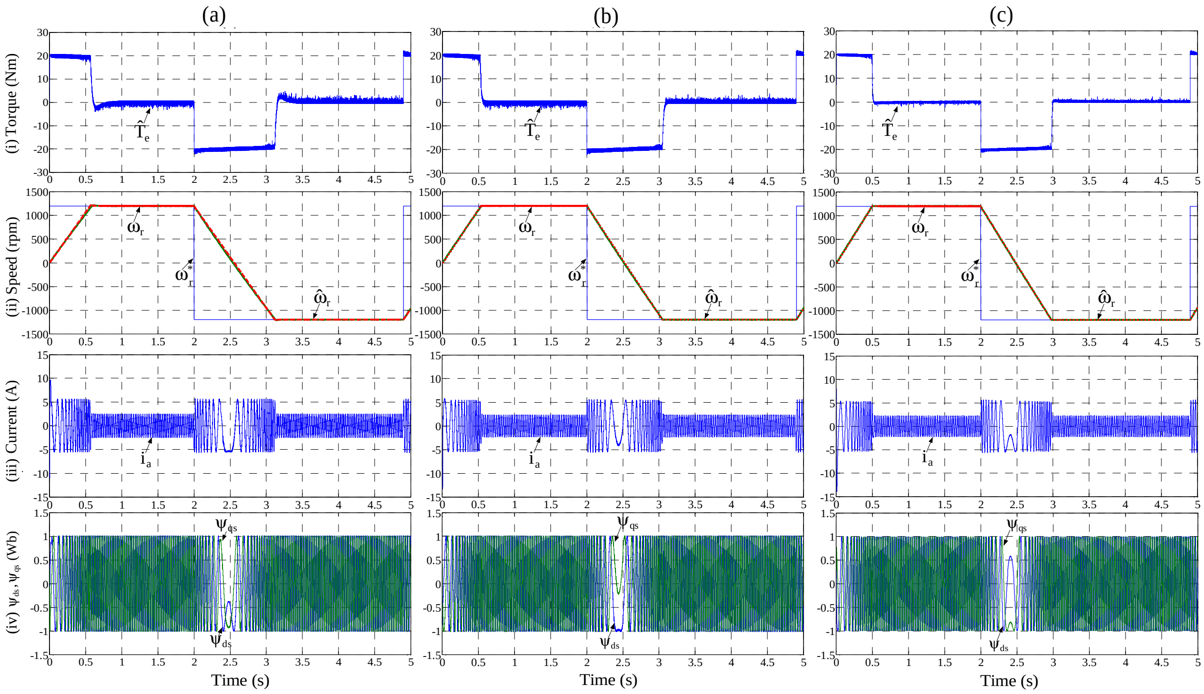

Figure 5.23: Performance under reversal speed command using: (a) PIC, (b) T1FLC and (c) T2FLC: (i) Torque, (ii) speed (iii) stator current and (iv) stator flux dq-components

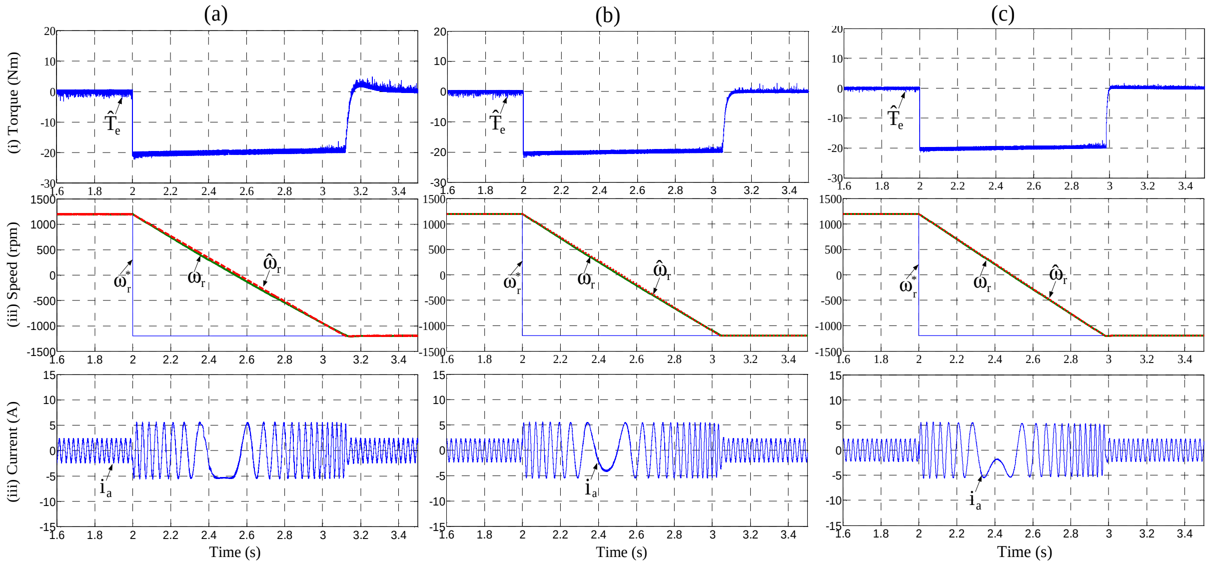

Figure 5.24: Transient performance under reversal speed command using: (a) PIC, (b) T1FLC and (c) T2FLC: (i) Torque, (ii) speed and (iii) stator current

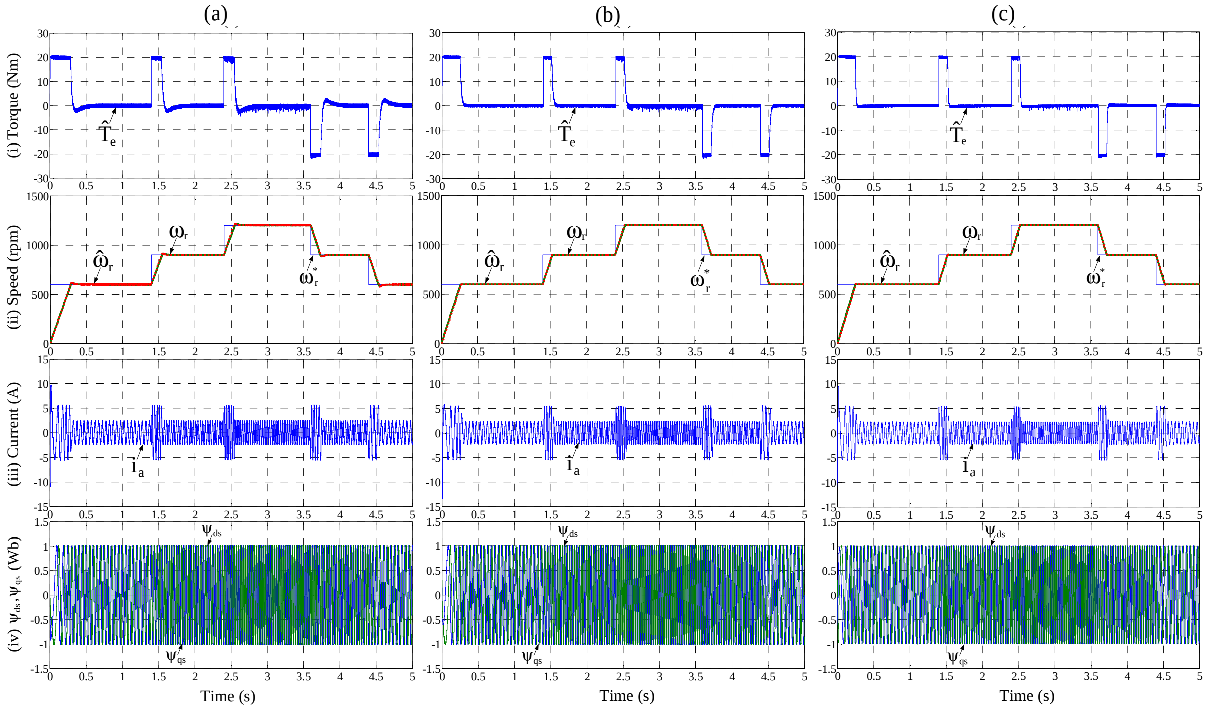

Figure 5.25: Performance under a step change in speed command using: (a) PIC, (b) T1FLC and (c) T2FLC: (i) Torque, (ii) speed and (iii) stator current and (iv) stator flux components

Performance under square change in speed command:

The performance of the sensorless IMD is observed under a square change in speed command using PIC, T1FLC and T2FLC as shown in Figure 5.26 (a)-(c). The sudden change in speed command of 600 rpm is applied in four steps (i.e. 1200 rpm ⟶ 600 rpm ⟶ 1200 rpm ⟶ 600 rpm ⟶1200 rpm) at 1 s, 2 s, 3 s, etc. The reference (ω_r^*), actual speed (ω_r) and estimated speed ($\hat{\omega}_r$) are presented in Figure 5.26 (ii), it is observed that under such speed command the estimated speed settles at the reference speed (from 600 to 1200 rpm) in 0.442 s, 0.28 s and 0.262 s with an overshoot around 1.14%, 0.067% and 0.002% of the reference speed using PIC, T1FLC and T2FLC scheme, respectively. The torque and stator current are shown in Figure 5.26 (i) and (iii), respectively. It is noticed that the estimated speed accurately tracking the reference speed and settles quickly using T2FLC compared to T1FLC and PIC.

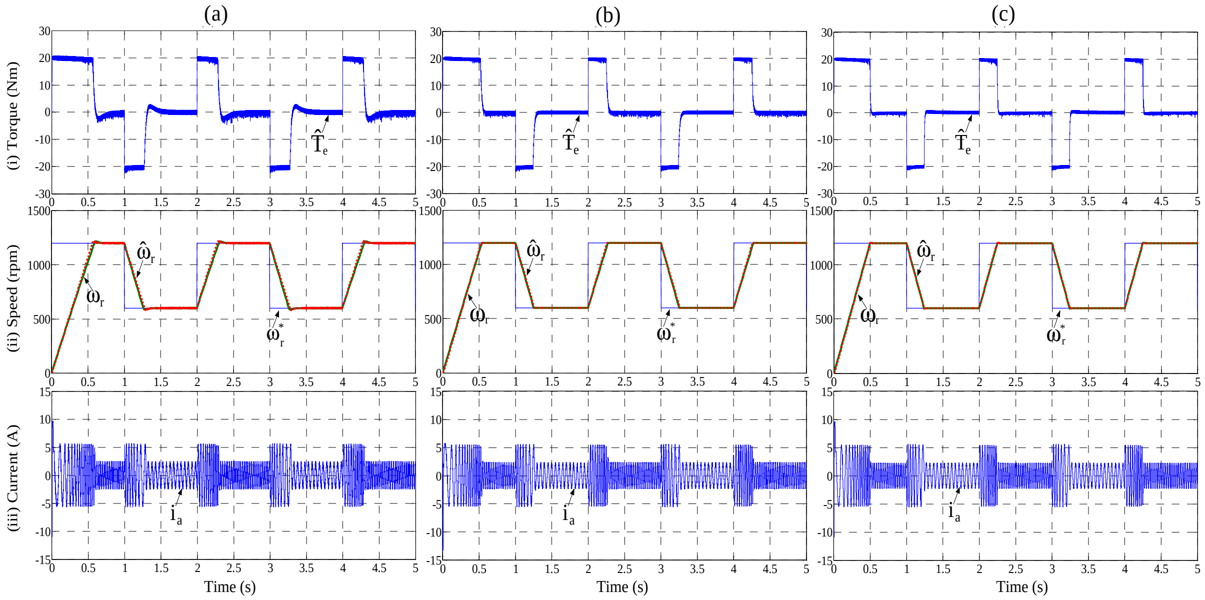

Figure 5.26: Performance under square change in speed command using: (a) PIC, (b) T1FLC and (c) T2FLC: (i) Torque, (ii) speed and (iii) stator current

Table 5.2: Performance indices under forward motoring with different starting load torque conditions using three different controller schemes

Starting Load Torque	Controller	Time domine specification			Performance indices					Total Indices
		t_r (s)	M_p (%)	t_s (s)	IAE	ISE	ITAE	ITSE	RMSE	
0	PIC	0.583	1.158	0.690	37.49	3042	8.040	447.40	40.18	3575.11
	T1FLC	0.425	0.080	0.531	33.12	2796	5.950	369.60	38.48	3243.15
	T2FLC	0.394	0.000	0.496	31.75	2705	5.272	335.90	38.15	3116.07
4	PIC	0.781	1.062	1.092	47.14	3892	12.17	735.80	45.21	4732.32
	T1FLC	0.550	0.066	0.790	42.41	3532	9.617	592.75	43.52	4220.29
	T2FLC	0.500	0.000	0.628	39.89	3393	8.312	529.05	42.62	4012.87
7	PIC	1.004	0.898	1.296	60.75	4939	20.05	1202.5	51.28	6273.58
	T1FLC	0.700	0.054	0.875	53.02	4411	15.04	928.20	48.54	5455.80
	T2FLC	0.615	0.000	0.780	49.25	4194	12.52	808.70	47.27	5111.74
9	PIC	1.294	0.825	1.465	77.69	5981	30.56	1791.5	56.34	7937.09
	T1FLC	0.840	0.041	1.060	63.72	5293	21.80	1341.5	53.20	6773.22
	T2FLC	0.762	0.000	0.920	58.30	4981	17.89	1141.5	51.18	6249.87

5.3.5 Performance under Forward Motoring with Load Torque Operation

The performance of the speed sensorless IM drive is observed under forward motoring with different load torque at starting using PIC, T1FLC and T2FLC, respectively. A load torque of 9 Nm is applied at starting with the reference speed of 1200 rpm. It is found that the estimated speed reaches the reference speed quickly at 0.92 s using T2FLC, whereas it is reached at 1.465 s using PIC scheme is illustrated in Table 5.2.

5.3.6 Performance Indices

In order to give a clear idea of the performance of the three controller schemes, the performance indices (IAE, ITAE, ISE, ISTE and RMSE) are calculated using each control scheme under forward motoring (i.e. reference speed of 1200 rpm) with no-load torque and load torque operation is illustrated in Table 5.2. From the Table 5.2, it is found that the T2FLC has superior time domain specifications and performance indices, because the T2FLC can cope with the uncertainties in a better way by modelling them and reducing their effect on the controller performance compared to PI and Type-1 fuzzy logic controller. The T2FLC is able to perform effectively when various disturbances occur in the system like; sudden changes in speed or load torques as it has advantages of both type-2 fuzzy sets and type-1 fuzzy sets (i. e. type-2 reducer set) compared to the PIC and T1FLC.

5.4 Experimental Results

The performance of the speed sensorless IM drive using PIC, T1FLC and T2FLC is experimentally validated with the laboratory developed EPS and the results are presented. The EPS is built around a dSPACE DS-1104 controller board. The detailed development of the EPS has been explained in the chapter-4. The proposed control schemes are tested under various operating conditions, such as forward motoring, reversal speed, sudden change in speed and load torque operations, respectively. Note that the experiments have been performed under the same operating conditions in which simulations have been carried out in the section 5.3.

5.4.1 Performance under Forward Motoring

Initially, the performance of the speed sensorless IM drive is investigated under no-load torque operation at a reference speed of 1200 rpm using PIC, T1FLC and T2FLC as shown in Figure 5.27 (a)-(c). The reference speed (ω_r^*), actual speed (ω_r) and estimated speed ($\hat{\omega}_r$) are shown in Figure 5.27 (ii). The actual speed is measured through the incremental encoder. The measured speed is used only for checking the tracking performance of the estimated speed not for any computation purposes. The IM starts at zero speed and settles (1200 rpm) at 0.81

s, 0.726 s and 0.678 s with an overshoot of around 20 rpm, 2.5 rpm and 0.3 rpm using PIC, Type-1 and Type-2 FLCs, respectively. The electromagnetic torque and stator current are shown in Figure 5.27 (i) and (iii), respectively. From Figure 5.27 (i), it is observed that the ripple content in electromagnetic torque is ±2.41 Nm, ±1.74 Nm and ±1.41 Nm using PIC, T1FLC and T2FLC, respectively. The steady-state performance of the speed sensorless IM drive is shown in Figure 5.28 (a)-(c). Note that the experimental results, which are presented in Figure 5.28 (a)-(c) and Figure 5.28 (a)-(c) corresponding to the simulation result of the Figure 5.19 (a)-(c). The results reveal an excellent correlation between the simulation and experimental results. Both simulation and experimental results show the superiority of the T2FLC compared to the T1FLC and PIC.

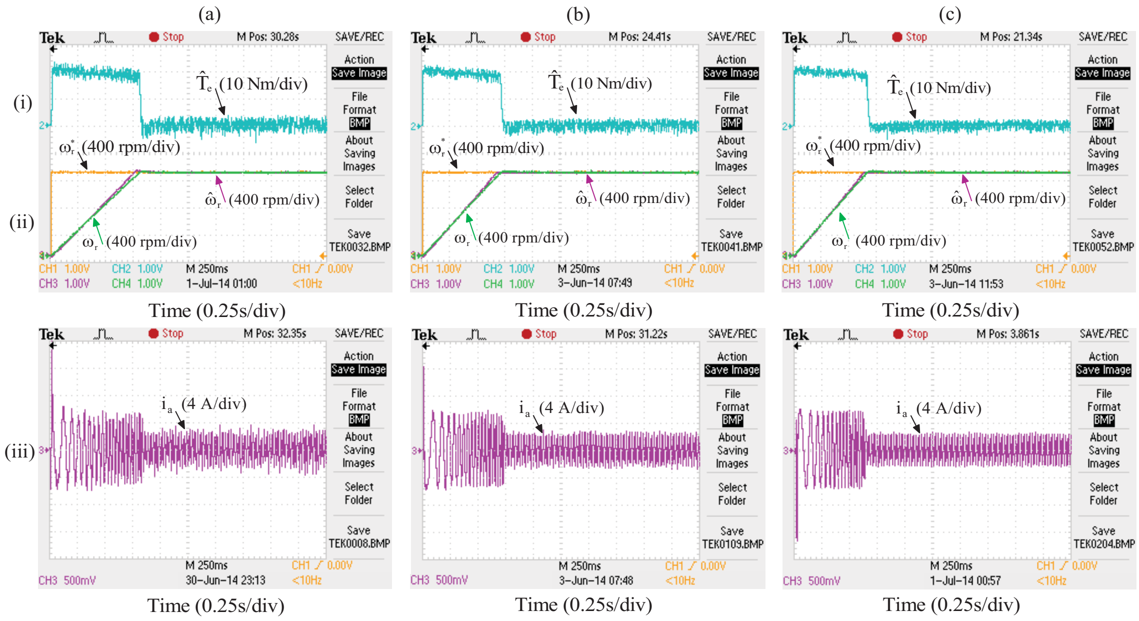

Figure 5.27: Performance under no-load torque operating condition using: (a) PIC, (b) T1FLC and (c) T2FLC: *Traces (from top to bottom):* (i) Torque, (ii) speed and (iii) stator current

5.4.2 Performance under Reversal Speed Command

The performance of the speed sensorless IM drive is observed under the reversal speed command using PIC, T1FLC and T2FLC as shown in Figure 5.29 (a)-(c). The reversal speed command from +1200 rpm to -1200 rpm is applied at 2 s. Furthermore, the direction of the speed is changed from -1200 rpm to +1200 rpm at 4.9 s and the corresponding responses are shown in Figure 5.29 (ii). From Figure 5.29 (ii), it is noticed that the estimated speed settles the set reference speed (i.e. -1200 rpm) at around 3.5 s, 3.31 s and 3.18 s with an overshoot around 1.712%, 0.21% and 0.025% of the reference speed using PIC, T1FLC and T2FLC, respectively. The electromagnetic torque, stator current and stator flux dq-components in the stationary reference frame are illustrated in Figure 5.29 (i), (iii)-(iv), respectively. From

Figure 5.29 (iv), it is observed that the magnitude of the stator flux dq-components are maintained almost same magnitude throughout the operation. The transient response during reversal speed command using PIC, T1FLC and T2FLC is shown in Figure 5.30 (a)-(c). Note that the experimental results, presented in Figure 5.29 (a)-(c) and Figure 5.30 (a)-(c) are corresponding to the simulation results of Figure 5.23 (a)-(c) and Figure 5.24 (a)-(c), respectively.

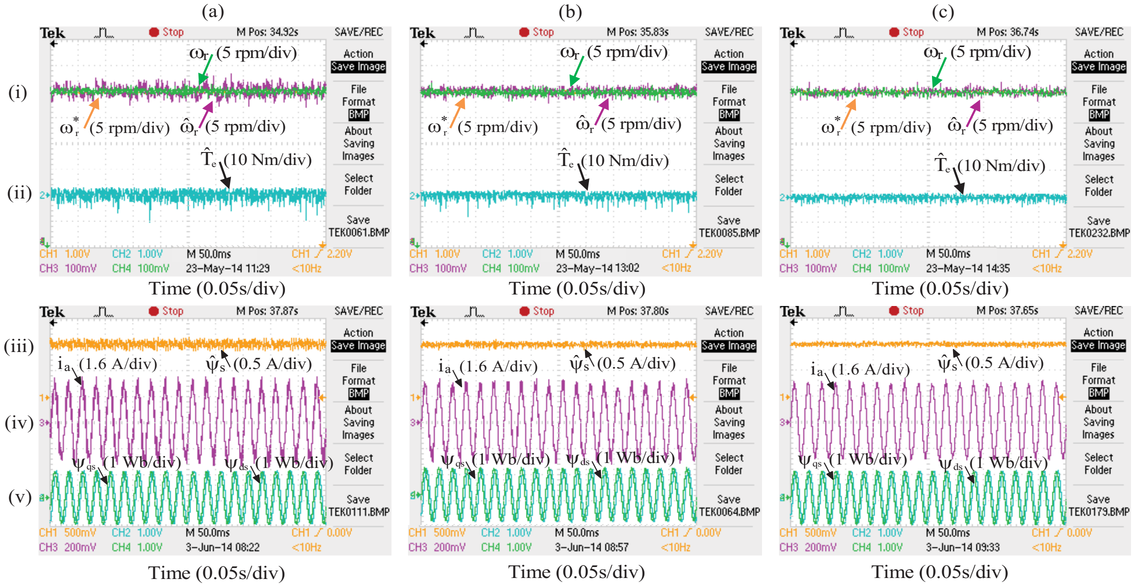

Figure 5.28: Steady-state performance under no-load torque operating condition using: (a) PIC, (b) T1FLC and (c) T2FLC: (i) speed, (ii) torque, (iii) stator flux, (iv) stator current and (v) stator flux dq-components in a stationary reference frame

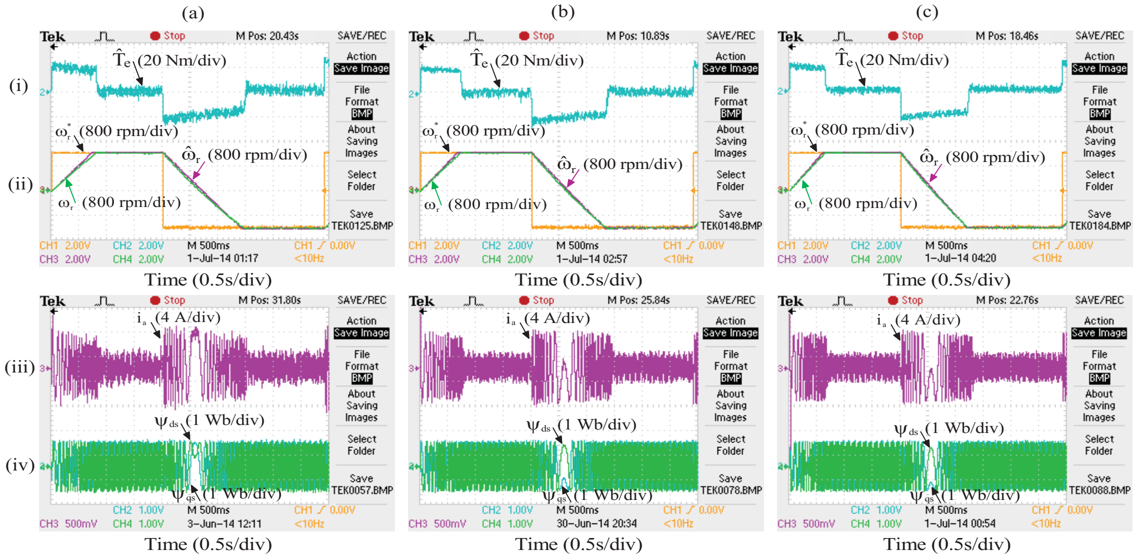

Figure 5.29: Performance under reversal speed command using: (a) PIC, (b) T1FLC and (c) T2FLC: *Traces (from top to bottom):* (i) Torque, (ii) speed, (iii) stator current and (iv) stator flux dq-components in a stationary reference frame

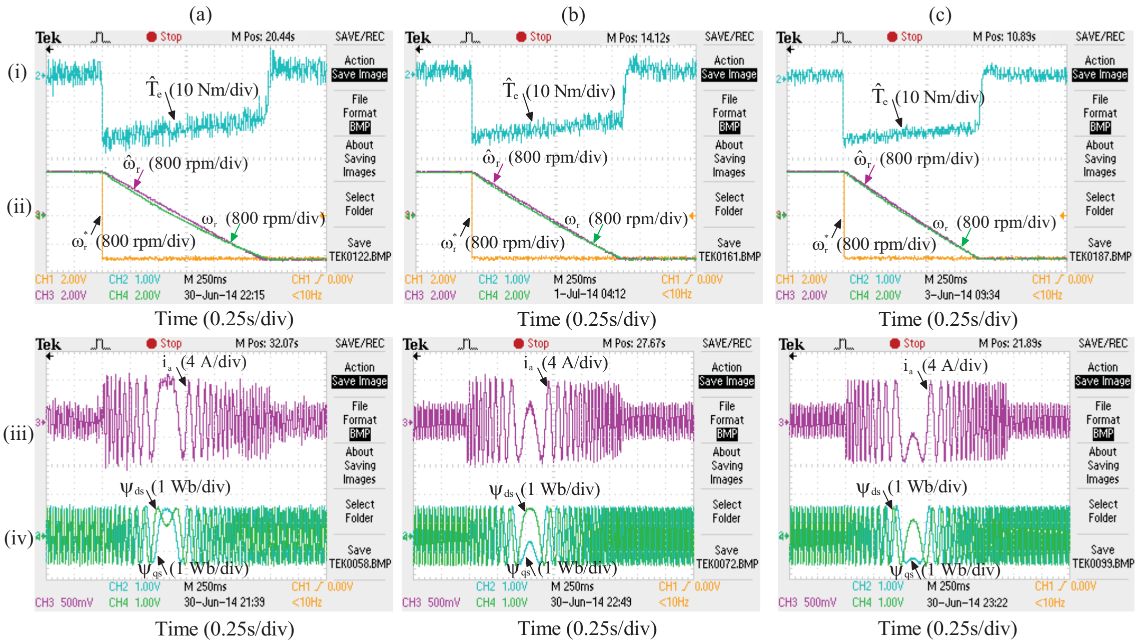

Figure 5.30: Transient performance under the reversal speed command using: (a) PIC, (b) T1FLC and (c) T2FLC: (i) Torque, (ii) speed, (iii) stator current and (iv) stator flux dq-components in the stationary reference frame

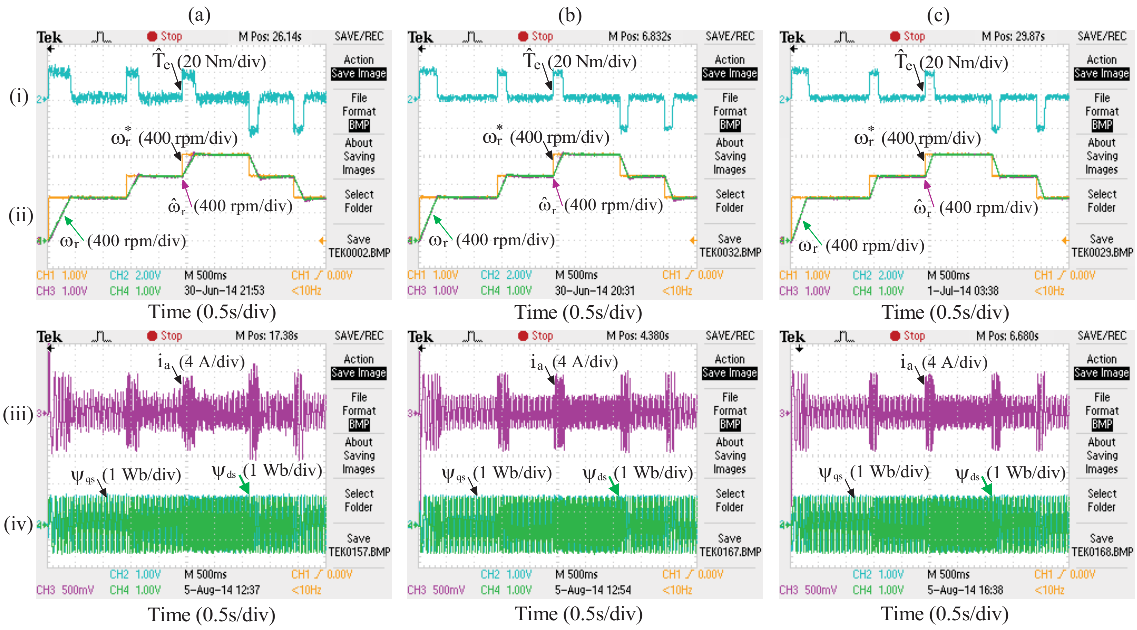

Figure 5.31: Performance under a step change in speed command using: (a) PIC, (b) T1FLC and (c) T2FLC: (i) Torque, (ii) speed, (iii) stator current and (iv) stator flux dq-components in the stationary reference frame

5.4.3 Tracking Performance of Various Speed Commands

The tracking performance of the estimated speed is observed through the applications of various speed commands, such as step and square changes in speed command respectively.

The performance of the speed sensorless IMD under such speed commands are presented in the following sections.

Performance under step change in speed command:

The performance of the speed sensorless IM drive is observed under a step changes in speed command using three different controllers are shown in Figure 5.31 (a)-(c). The step change in speed command of 300 rpm is applied in four steps (i.e. 600 rpm→900 rpm→1200 rpm →900 rpm→600 rpm) at 1.4 s, 2.4 s, 3.6 s, etc. The corresponding reference, actual and estimated speed responses under such speed commands are shown in Figure 5.31 (ii). From Figure 5.31 (ii), it is observed that the estimated speed settles (from 600 rpm to 900 rpm) in 0.29 s, 0.2 s and 0.15 s using PIC, T1FLC and T2FLC, respectively. Moreover, it is also observed that the steady state error between the actual and estimated speed is negligible using T2FLC compared to T1FLC and PIC. The electromagnetic torque, stator current and stator flux dq-components in a stationary reference frame are shown in Figure 5.31 (i), (iii)-(iv), respectively. Note that the experimental results, presented in Figure 5.31 (a)-(c) are corresponding to the simulation results of Figure 5.25 (a)-(c).

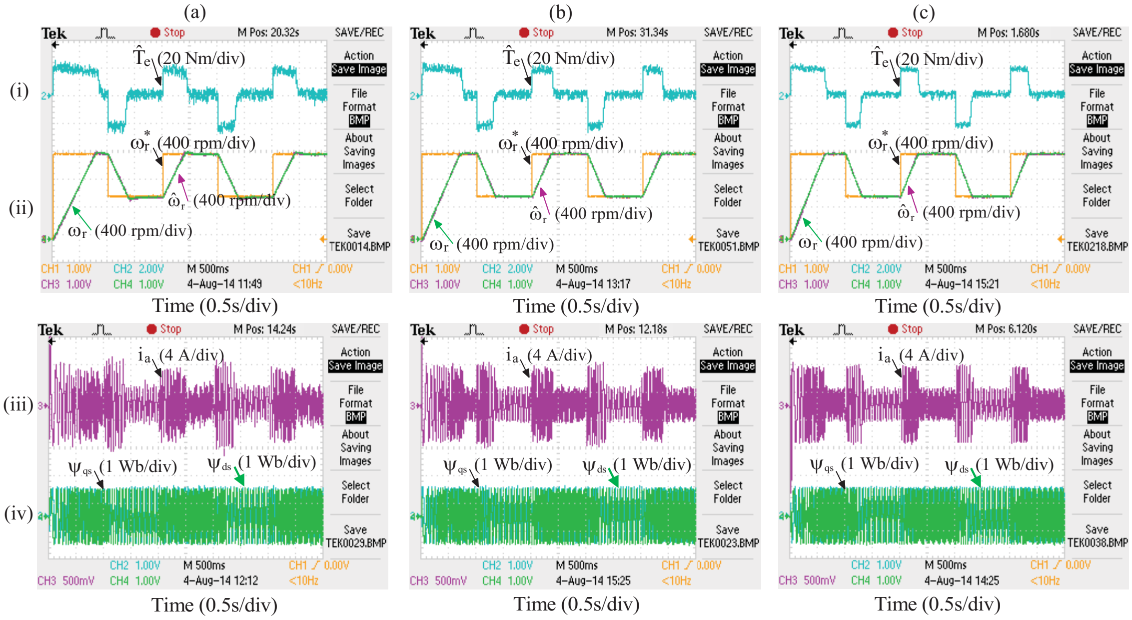

Figure 5.32: Performance under square change in speed command using: (a) PIC, (b) T1FLC and (c) T2FLC: (i) Torque, (ii) speed, (iii) stator current and (iv) stator flux dq-components in the stationary reference frame

Performance under square change in speed command:

The performance of the speed sensorless IM drive is observed under square changes in speed command using PIC, T1FLC and T2FLC as shown in Figure 5.32 (a)-(c). The square change in speed command of 600 rpm is applied in four steps (i.e. 1200 rpm→ 600 rpm →1200 rpm → 600 rpm → 1200 rpm) at 1 s, 2 s, 3 s, etc. The reference speed, actual and estimated speeds are shown in Figure 5.32 (ii), it is observed that under such speed command the estimated speed settles at the set reference speed (from 600 to 1200 rpm) in 0.51 s, 0.376 s and 0.31 s with an overshoot of around 1.708%, 0.211% and 0.026% of the reference speed using PIC, T1FLC and T2FLC, respectively. The torque, stator current and stator flux are shown in Figure 5.32 (i), (iii)-(iv), respectively. It is noticed that the estimated speed accurately tracks the reference speed and also settles quickly using T2FLC compared to T1FLC and PIC. Note that the experimental results, presented in Figure 5.32 (a)-(c) are corresponding to the simulation results of the Figure 5.26 (a)-(c).

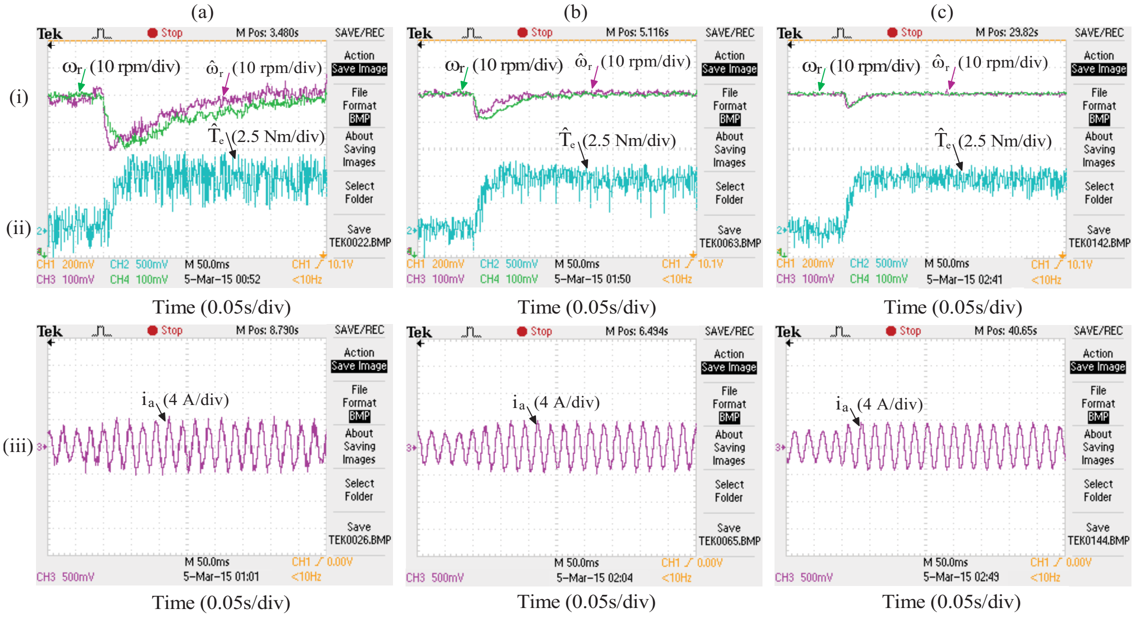

Figure 5.33: Performance under sudden load torque operation at 1200 rpm using: (a) PIC, (b) T1FLC and (c) T2FLC: (i) speed, (ii) torque and (iii) stator current

5.4.4 Loading Performance

The performance of the speed sensorless IM drive is observed under the application and rejection of sudden load torques for the following conditions:

- Loading at 1200 rpm
- Loading and unloading at 1200 rpm
- Loading at different speed commands (i.e. 300 rpm, 600 rpm and 900 rpm)

Loading performance at 1200 rpm

The performance of the sensorless IM drive is observed under sudden load torque operation using PIC, T1FLC and T2FLC as shown in Figure 5.33 (a)-(c). The sudden load torque of 5

Nm is applied at 1.4 s when IM is operating at steady state speed (i.e. 1200 rpm). When the sudden load torque is applied, the IM draws large amplitude of stator current, i.e. ±4.14 A, ±3.83 A and ±3.61 A using PIC, T1FLC and T2FLC is shown in Figure 5.33 (iii). From Figure 5.33 (i), it is observed that the sudden application of load torque causes an undershoot in estimated speed around 1.566%, 0.734% and 0.35% of the reference speed using PIC, T1FLC and T2FLC, respectively. It is also observed that the recovery time of the estimated speed under sudden load torque operation is 0.31 s, 0.11 s and 0.05 s using PIC, T1FLC and T2FLC, respectively. From Figure 5.33 (ii), it is observed that the ripple content in torque is ±2.45 Nm, ±1.84 Nm and ±1.41 Nm using PIC, T1FLC and T2FLC, respectively. Hence, the torque and stator current ripple contents using T1FLC are reduced by around 24.89% and 7.49% over PIC, whereas T2FLC is reduced by 23.36% and 5.745% over T1FLC.

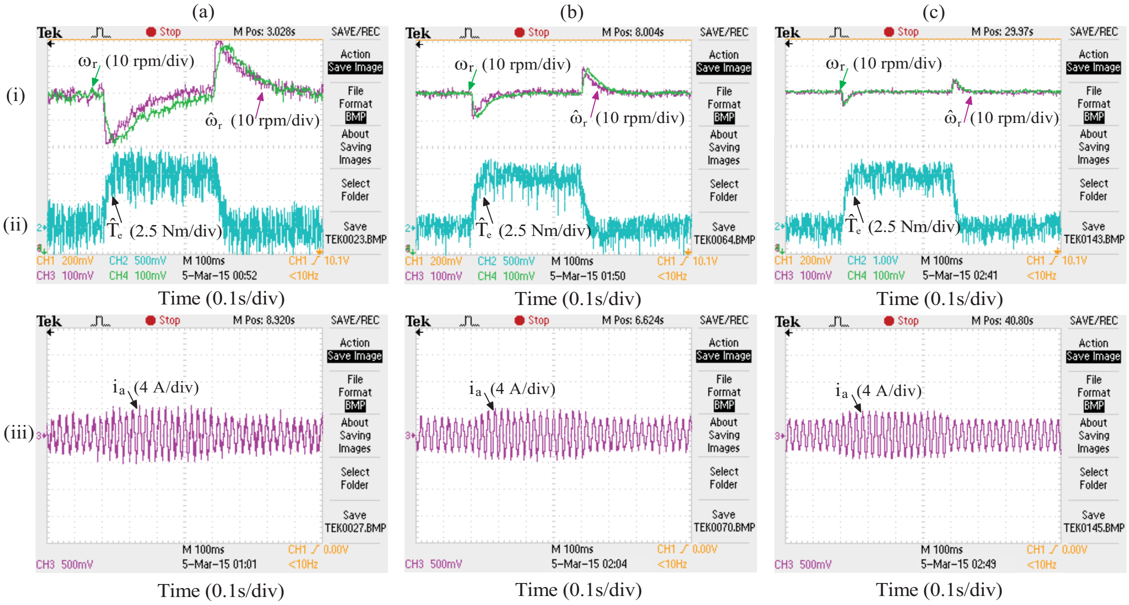

Figure 5.34: Performance under loading and unloading torque at 1200 rpm using: (a) PIC, (b) T1FLC and (c) T2FLC: (i) speed, (ii) torque and (iii) stator current

Loading and unloading performance at 1200 rpm

The effects of sudden load and unload torque operation is observed under steady-state speed (i.e.1200 rpm) using PIC, T1FLC and T2FLC are shown in Figure 5.34 (a)-(c). The sudden load torque of 5 Nm is applied at 1.4 s and is withdrawn at 1.8 s when an IM was operating at steady-state speed. When the load torque is applied, the effect of load torque is observed in the previous section. Similarly, when the load torque is withdrawn, an overshoot appears in the estimated speed around 1.55%, 0.7167% and 0.3% of the reference speed using PIC, T1FLC and T2FLC are shown in Figure 5.34 (i). It is also observed that the recovery time of the estimated speed under sudden load torque condition is 0.32 s, 0.1 s and 0.05 s using PIC, T1FLC and T2FLC, respectively. The T2FLC scheme shows faster response compared to the PIC and T1FLC schemes. Hence, the settling time using T1FLC is improved by 75% over PIC, whereas using T2FLC is improved by 50% over T1FLC. From Figure 5.34 (iii), it is observed that when the load torque is withdrawn the current drops down to ±2.97 A, ±2.64 A and ±2.45 A using PIC, T1FLC and T2FLC, respectively. The torque responses under such commands are presented in Figure 5.34 (ii). The performance of the sensorless drive is also observed under various load torque disturbances at steady-state speed using three control schemes are illustrated in Table 5.3.

The speed errors under load torque disturbance condition using three different control schemes are shown in Figure 5.35 (a)-(c). The actual speed error ($e\omega_r = \omega_r^* - \omega_r$) and the estimated speed error ($E\omega_r = \omega_r - \hat{\omega}_r$) are shown in Figure 5.35 (ii) and (iii), respectively. From Figure 5.35 (ii), it is observed that the estimated speed error appears around 11.8 rpm, 6.8 rpm and 2.1 rpm when sudden load torque is applied and is withdrawn.

Table 5.3: Comparison of three control schemes under different load torque conditions at 1200 rpm

Load Torque	Controller	Under Load Torque Applied		Under Load Torque Withdrawn	
		Speed Undershoot (rpm)	Recovery Time (s)	Speed Overshoot (rpm)	Recovery Time (s)
2	PIC	7.83	0.252	7.49	0.248
	T1FLC	3.88	0.078	3.83	0.071
	T2FLC	1.97	0.030	1.86	0.029
3	PIC	10.8	0.267	10.2	0.271
	T1FLC	5.31	0.081	5.28	0.078
	T2FLC	2.71	0.035	2.54	0.033
4	PIC	14.6	0.289	14.3	0.295
	T1FLC	6.89	0.095	6.54	0.087
	T2FLC	3.52	0.041	3.28	0.040
5	PIC	18.8	0.310	18.6	0.320
	T1FLC	8.80	0.110	8.60	0.100
	T2FLC	4.20	0.050	3.90	0.050

The effect of different load torque conditions is observed under different speed commands using PIC, T1FLC and T2FLC are shown in Figure 5.36 (a)-(c). It is observed from the experimental results that the T2FLC shows an improved performance and robustness to various load torque disturbances compared to PIC and T1FLC, respectively.

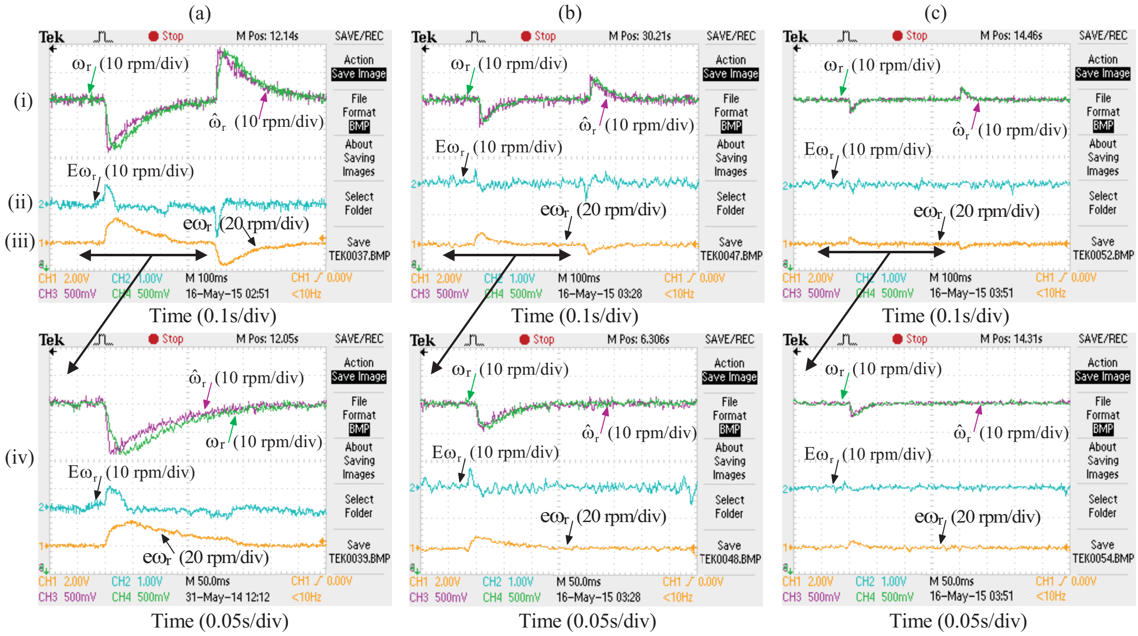

Figure 5.35: Performance under load torque operation at 1200 rpm using: (a) PIC, (b) T1FLC and (c) T2FLC: (i) speed, (ii) error speed, (iii) actual error speed and (iv) zoom of speed and error speeds

5.4.5 Performance under Low Speed Operation

The tracking performance of the sensorless IMD is observed under very low speed operation, such as step-up (i.e. acceleration mode) and step-down (i.e. deceleration mode) speeds from 0 rpm to 100 rpm and 100 rpm to 0 rpm, respectively.

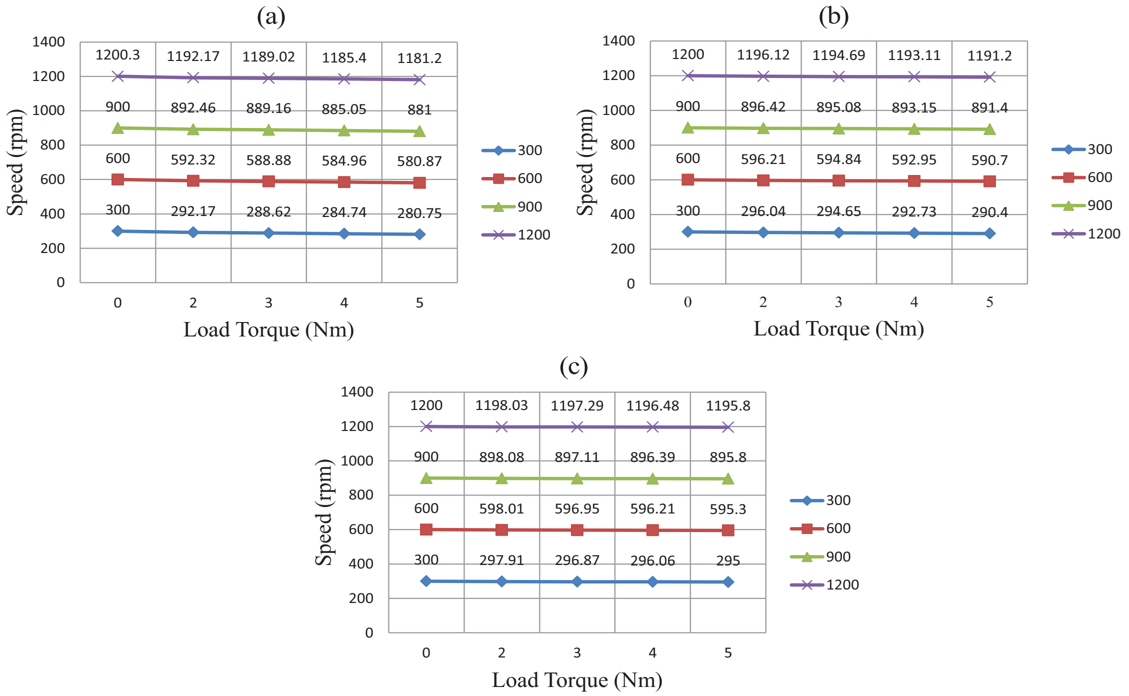

Figure 5.36: Steady-state performance of the estimated speed under various load torque conditions at different speed commands using: (a) PIC, (b) T1FLC and (c) T2FLC

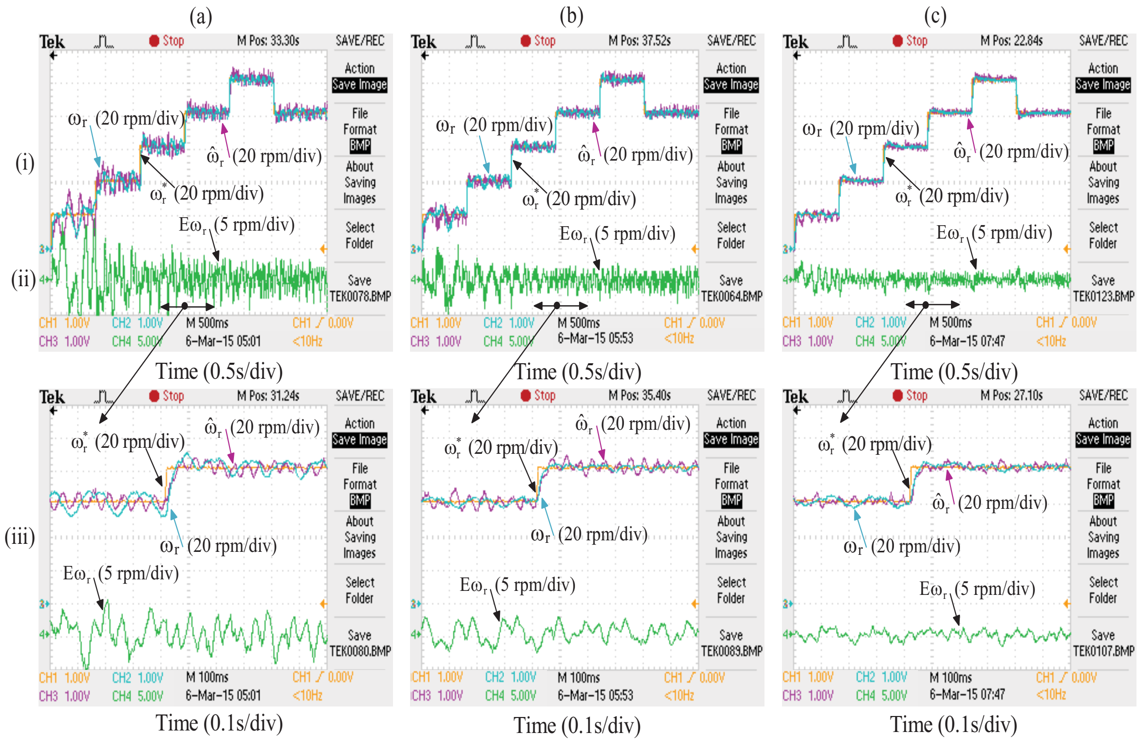

Figure 5.37: Performance of the sensorless IMD under low speed operation using: (a) PIC, (b) T1FLC and (c) T2FLC: (i) speed and (ii) error speed and (iii) zoomed view of (i)-(ii)

Step-up speed from 0 rpm to 100 rpm in a series of five 20 rpm steps:

The step change in speed command from 0 to 100 rpm is applied in a series of five 20 rpm steps using three control schemes are shown in Figure 5.37 (a)-(c). The step change in speed command of 20 rpm is applied in six steps (i.e. 0 rpm→20 rpm→40 rpm→60 rpm→80 rpm →100 rpm→80 rpm) at a time interval of 0.8 s (i.e. 0.8 s→1.6 s→ etc). The reference speed, actual and estimated speeds are available in Figure 5.37 (i) and the estimated speed error is shown in Figure 5.37 (ii). Unstable operation is observed with high disturbances at a speed of 20 rpm using PIC, while stable operation with fewer disturbances obtained using T2FLC, respectively. The zoomed view of Figure 5.37 (i)-(ii) is presented in Figure 5.37 (iii).

Similarly, the step change in speed command from 100 rpm to 0 rpm is applied in a series of five 20 rpm steps using three different controllers are shown in Figure 5.38 (a)-(c). It is observed that under low speed operation the T2FLC shows better performance with less steady-state errors compared to the PIC and T1FLC. The percentage of line current THDs using PIC, T1FLC and T2FLC under no-load torque is shown in Figure 5.39 (a)-(c). The corresponding values are 6.5, 5.3 and 4.6, respectively. From Figure 5.39, it is observed that the T2FLC offers less current THD compared to T1FLC and PIC.

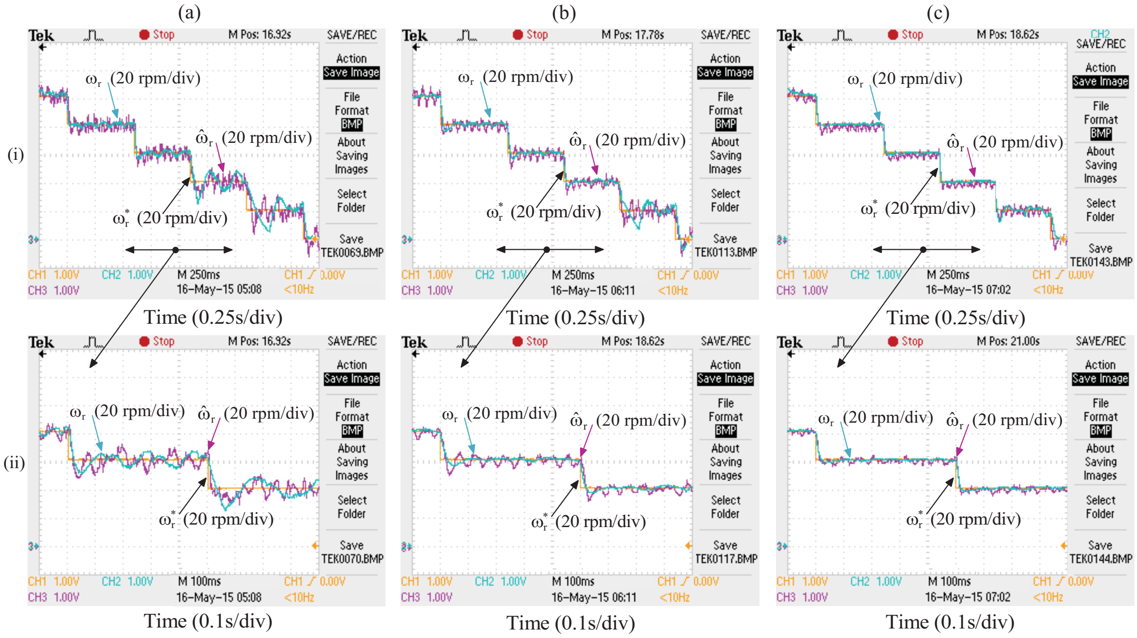

Figure 5.38: Performance of the sensorless IMD under the deceleration command at 1200 rpm using: (a) PIC, (b) T1FLC and (c) T2FLC: (i) speed and (ii) error speed

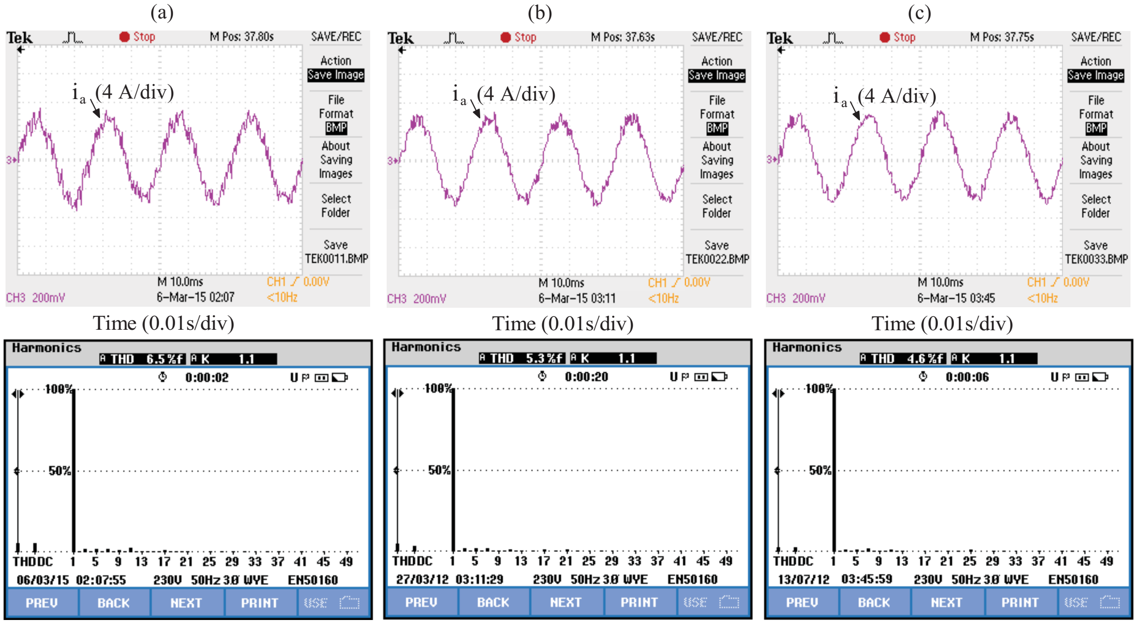

Figure 5.39: THD performance of the stator current using: (a) PIC, (b) T1FLC and (c) T2FLC.

The comparative analysis of the speed sensorless IM drive using PIC, T1FLC and T2FLC under various operating conditions, such as, forward motoring, reversal speed, step change in speed, square change in speed and change in speed during load torque applied and is withdrawn are illustrated in Table 5.4 in detail. Where, T_{rNLT}, ψ_{rNLT}, ω_{cLTA}, ω_{cLTW}, t_{ss}, t_{sr}, t_{scss}, t_{scsqs}, t_{sLTA}, t_{sLTW}, $\%I_{\mathrm{THD}}$, %T1FLCIOPI and %T2FLCIOT1 represents the no-load torque ripples (Nm), stator flux ripples (Wb), change in speed during load torque applied (rpm), change in speed during load torque withdrawn (rpm), settling time during starting (s), settling time during reversal speed (s), settling time during change in step speed (s), settling time during change in speed during square change in speed (s), settling time during load torque applied (s), settling time during load torque withdrawn (s), percentage of stator current THD, percentage of T1FLC improvement over PI controller and percentage of T2FLC improvement over T1FLC, respectively.

Table 5.4: Comparison of three different controllers under various operating conditions

Measured Parameter	Simulation Results					Experimental Results				
	PIC	T1FLC	%T1FLC -IOPI	T2FLC	%T2FLC -IOT1	PIC	T1FLC	%T1FLC -IOT1	T2FLC	%T2FLC -IOT1
$\pm T_{dNLT}$ (Nm)	1.780	1.420	20.22	1.150	19.01	2.41	1.740	27.801	1.410	18.965
$\pm \psi_{dNLT}$ (Wb)	0.042	0.022	47.62	0.012	45.45	0.14	0.100	28.571	0.080	20.000
ω_{cLTA} (rpm)	13.00	5.400	58.46	2.000	62.96	18.8	8.800	53.191	4.20	52.272
ω_{cLTW} (rpm)	13.50	5.100	62.22	2.000	60.78	18.6	8.600	53.763	3.600	58.139
t_{ss} (s)	0.690	0.531	23.04	0.496	6.591	0.81	0.726	10.370	0.678	6.6115
t_{sr} (s)	3.160	3.040	3.797	2.930	3.618	3.50	3.310	5.4285	3.180	3.9274
t_{scss} (s)	0.220	0.136	38.18	0.120	11.76	0.29	0.200	32.659	0.150	25.000
t_{scsqs} (s)	0.442	0.280	36.65	0.262	6.428	0.51	0.376	26.562	0.310	17.553
t_{sLTA} (s)	0.298	0.110	63.08	0.040	63.63	0.31	0.110	64.516	0.050	54.545
t_{sLTW} (s)	0.310	0.096	64.51	0.032	66.66	0.32	0.100	68.750	0.050	50.000
$e\omega_r$ (rpm)	13.30	5.200	60.90	2.000	61.53	17.6	8.100	53.977	3.800	53.086
$E\omega_r$ (rpm)	5.200	2.300	55.76	1.050	54.34	8.50	6.200	27.058	2.500	59.677
I_{THD} (%)	3.520	3.080	12.50	2.610	15.25	6.50	5.300	18.460	4.600	13.200

5.5 Conclusion

In this chapter, RFMRAS speed estimator for DTFC of a sensorless IMD using PIC, T1FLC and T2FLC is presented. Initially, PIC based MRAS speed estimator is implemented. This scheme shows significant ripples in torque, flux, speed and stator current and also takes a large time to reach the steady-state under load torque disturbances. In order to improve the performance of the sensorless drive, PIC is replaced by T1FLC. It shows improved performance compared to PIC. However, the MFs of T1FSs are two-dimensional and unable to provide satisfactory performance when various disturbances occur in the system and produces ripple content in torque, rotor speed and stator currents. Therefore, T2FLC is implemented. It shows improved dynamic as well as steady-state performance and also robust to various load torque disturbances and sudden change in speed conditions. A detailed simulation and experimental comparison of the three adaptation schemes have been carried out in a speed sensorless mode of operation under no-load, load, various changes in speed and low speed operating conditions, respectively. The simulation and experimental system verification confirm that the T2FLC shows better dynamic as well as steady-state performance and is capable of sudden change in speed and robustness to load torque disturbance rejection. Moreover, it is also noticed that the T2FLC performs satisfactorily in all speed ranges with different loading conditions compared to T1FLC and PIC, respectively.

The DTFC of a sensorless IMD offers satisfactory performance over a wide range of operation and also simple to implement. However, it requires flux hysteresis and torque hysteresis comparators. The use of flux and torque hysteresis comparators causes a variable switching frequency and produces high ripple contents. Therefore, these aspects will be studied in the next chapter.

Chapter 6

MRAS Speed Estimator for DTFC-SVM of A Speed Sensorless IMD

CHAPTER 6: MRAS SPEED ESTIMATOR FOR DTFC-SVM OF A SPEED SENSORLESS IMD

The DTFC of a speed sensorless IM drive is developed using switching table, flux and torque hysteresis controllers to get a quick dynamic response. The torque and flux are controlled independently using hysteresis controllers. However, the hysteresis controller provides considerable torque and flux ripples with variable switching frequency. In order to overcome these drawbacks, DTFC with space vector modulation (DTFC-SVM) technique is implemented for a speed sensorless IMD employing PIC, T1FLC and T2FLC schemes, respectively. Initially, the PIC based DTFC-SVM of a speed sensorless IM drive is implemented. It gives considerable flux and torque ripples with poor dynamic and tracking the performance of the sensorless IMD. In order to enhance the dynamic and tracking the performance of the sensorless drive, the PI controllers (i.e. Speed, torque, flux and adaptation) are replaced by T1FLCs. However, the T1FLC unable to cope with the large footprint of uncertainty because of single MFs and two-dimensional (2-D) control and also lack of type-reduction. Therefore, Type-2 FLC is proposed to further enhance the dynamic and tracking performance of the speed sensorless IMD. The T2FLC consists of 3-D control with type-reduction in defuzzification process to effectively deal with the large uncertain data (i.e. larger footprint of data) than T1FLC. Additionally, Mamdani and Centroid method with simple IF and THEN rules are used in both control schemes (i.e. T1FLC and T2FLC). Finally, the RFMRAS speed estimator for DTFC-SVM of the sensorless IMD is simulated in the MATLAB/SIMULINK environment under various operating conditions with speed sensor and speed sensorless. Moreover, the speed estimation algorithm is experimentally validated with laboratory developed EPS using dSPACE DS-1104 controller board and the experimental results are presented under various operating conditions, such as forward motoring, reversal speed, sudden change in speed, load torque, low speed, etc.

This chapter is organized as follows:

- *Various types of DTFC-SVM methods are presented and are discussed in detail in section 6.1.*
- *The mathematical modeling of space vector modulation is presented in section 6.2.*
- *Various types of speed, torque, flux and adaptation control schemes for DTFC-SVM of a speed sensorless IMD (SSIMD) are presented in section 6.3.*
- *The RFMRAS speed estimator for DTFC of a SSIMD using three different control schemes are simulated in the MATLAB/SIMULINK environment and corresponding simulation results under various operating conditions are presented in section 6.4.*

- *The simulation results are validated with the experimental results, which are presented in section 6.5.*
- *Finally, section 6.6 presents the conclusion and remarks of the system.*

6.1 Introduction

The main disadvantages of the switching table-based DTFC (ST-DTFC) schemes are: variable switching frequency, high switching losses, torque and current distortion caused by sector changes, starting and low speed operation problems and high sampling frequency, which is required for digital implementation of hysteresis controllers. In order to overcome these drawbacks, Habetler [152] introduced the concept of direct torque and flux control with space vector modulation (DTFC-SVM) for electrical machines. The basic concept of SVM strategy is the adjustment of stator flux speed by zero voltage vector insertion for controlling the generated torque. The ST-DTFC algorithm is based on the instantaneous values and directly calculated the switching pulses for the VSI. The control algorithm in DTFC-SVM method is based on average values, whereas the switching pulses for the VSI are calculated by SVM [6, 153-155]. This is the main difference between ST-DFTC and DTFC-SVM control methods. Basically, in DTFC-SVM the controller calculates the required stator voltage vector, averaged over a sampling period and then it is realized by SVM technique. Depending on the generation of reference stator voltage vector, the DTFC-SVM strategies have been classified into various types, such as, DTFC-SVM scheme with closed-loop flux control [6], DTFC-SVM scheme with closed-loop torque control, DTFC-SVM scheme with closed-loop torque and flux control operating in polar coordinates, DTFC-SVM scheme with closed-loop torque and flux control operating in stator flux coordinates [161]. The brief description of each control strategy is presented in the following subsections.

6.1.1 DTFC-SVM Scheme with Closed-loop Flux Control

The torque of IM increases linearly with the slip frequency under constant rotor flux operating mode, and the maximum torque is limited only by the maximum current of the inverter [6, 161-165]. Therefore, in order to increase the torque overload capability of a DTFC-SVM scheme, the rotor flux instead of stator flux magnitude should be regulated and it is shown in Figure 6.1.

For a given command of rotor flux $\vec{\psi}_r^*$ and torque T_e^*, the stator flux components $\psi_{Ds}^{e*}, \psi_{Qs}^{e*}$ in the rotor flux coordinates can be calculated according to the following equations:

$$\psi_{Ds}^{e*} = \frac{L_s}{L_m}\left(\vec{\psi}_r^* + T_r \sigma \, p\vec{\psi}_r^*\right) \tag{6.1a}$$

$$\psi_{Qs}^{e*} = \frac{4}{3P}\frac{L_r}{L_m}\sigma L_s \frac{T_e^*}{\psi_r^*} \tag{6.1b}$$

The appropriate stator voltage vector $\vec{V}_s^*$ is calculated from the equation (6.2), which is applied to the IM in the next sampling period according to the following equation [164]:

$$\vec{V}_s^* = \frac{\Delta\vec{\psi}_s}{T_s} + R_s\,\vec{i}_s \tag{6.2}$$

The main drawback of this scheme is that it requires both stator and rotor flux estimations. Therefore, in order to estimate stator and rotor fluxes all the motor parameters are necessary. Moreover, it is very sensitive to motor parameter variations.

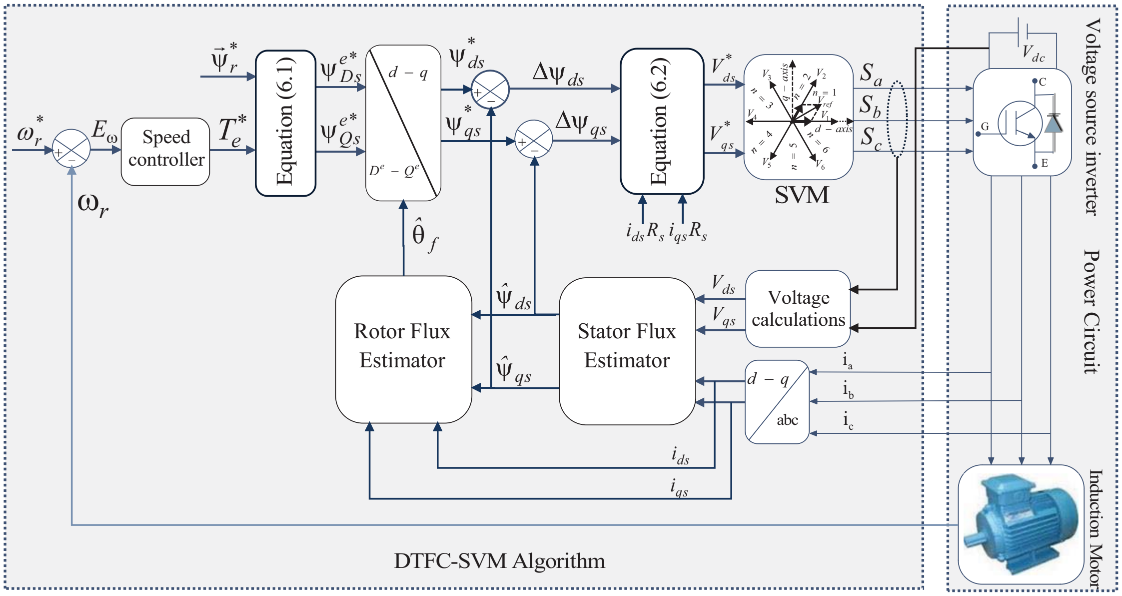

Figure 6.1: The schematic model of DTFC-SVM scheme with closed-loop flux control

6.1.2 DTFC-SVM Scheme with Closed-loop Torque Control

In this scheme, the basic working principle is similar to that of the ST-DTFC, i.e. the appropriate stator voltage vector, which is applied to the IM in the next sampling period is obtained by working on the angle between stator and rotor flux linkages (load angle) [155]. The control scheme which is shown in Figure 6.2 is originally proposed for the permanent magnet synchronous motors (PMSM). However, the basics of DTFC are identical for both PMSM and IM, so the same control scheme can be applied for the IM.

The torque controller will generate the load angle $\Delta\gamma$, which is used for calculating the reference stator flux linkage $\vec{\psi}_s^*$ and it is represented in equation (6.3) as [155]:

$$\vec{\psi}_s^* = \left|\vec{\psi}_s^*\right| \cdot e^{j\left(\hat{\theta}_e + \Delta\gamma\right)} \tag{6.3}$$

The reference stator voltage vector $\vec{V}_s^*$, which is applied to the IM in the next sampling period can be calculated using the equation (6.2).

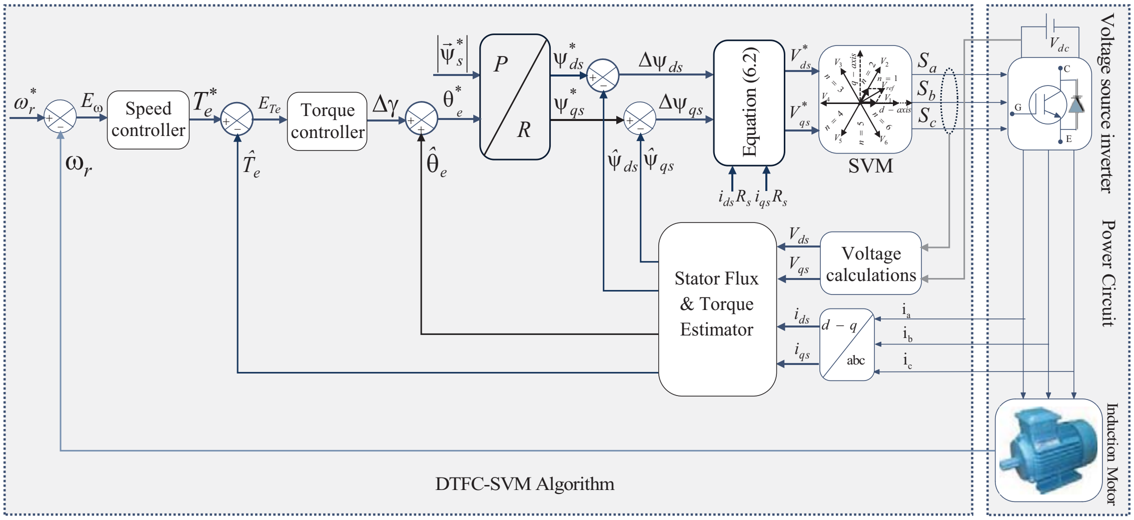

Figure 6.2: The schematic model of DTFC-SVM scheme with closed-loop torque control

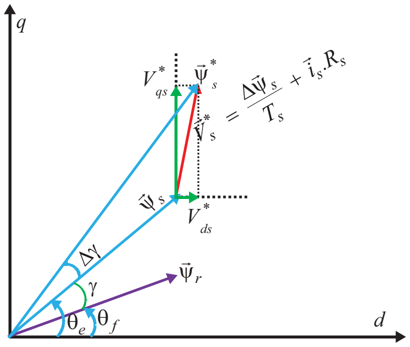

Figure 6.3: vector diagram of DTFC-SVM

The realization of reference stator voltage vector $\vec{V}_s^*$ using the voltage drop across the stator winding resistance R_s and the incremental stator flux linkage $\Delta\vec{\psi}_s$ is shown in Figure 6.3. In this scheme, the stator flux is operated in open-loop, so if any disturbance occurs, it takes large time to settle.

6.1.3 DTFC-SVM Scheme with Closed-loop Torque and Flux Control Operating in Polar Coordinates

In this scheme both the stator flux and torque are controlled in closed-loop, so this scheme provides slightly a superior control performance than that of the previous schemes and the schematic model of this scheme is shown in Figure 6.4.

The incremental stator flux linkage $\Delta\vec{\psi}_s$ can be calculated using the outputs of stator flux and torque controllers, i.e. K_ψ and $\Delta\gamma$ as follows [165-166]:

$$\Delta\vec{\psi}_s(k) = \vec{\psi}_s(k) - \vec{\psi}_s(k-1)$$

$$\Delta\vec{\psi}_s(k) = \left\{ \left[1 + k_\psi(k)\right] \cdot e^{j\Delta\gamma(k)} - 1 \right\} \cdot \vec{\psi}_s(k-1) \tag{6.4}$$

where $e^{j\Delta\gamma(k)} \cong 1 + j\Delta\gamma(k)$.

The equation (6.4) can be approximated as:

$$\Delta\vec{\psi}_s(k) = \left\{ k_\psi(k) + j\Delta\gamma(k) \right\} \cdot \vec{\psi}_s(k-1) \tag{6.5}$$

The reference stator voltage vector $\vec{V}_s^*$, which is applied to the IM in the next sampling period can be calculated as similar to the previous method. To enhance the dynamic performance of the torque control, the load angle increment is composed of two parts, i.e. the dynamic part delivered by the torque controller and the static part generated by the feed-forward loop.

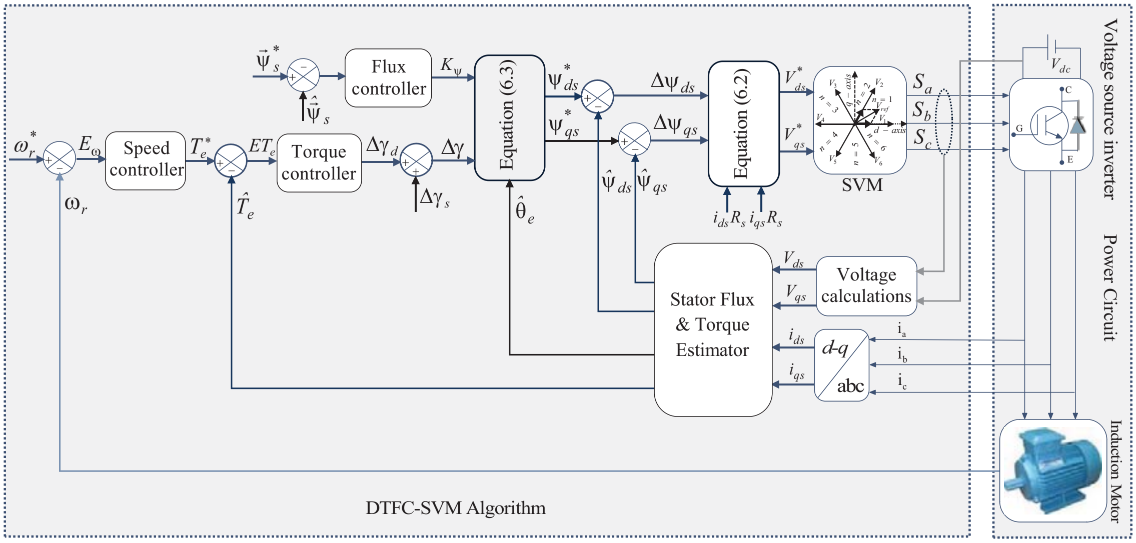

Figure 6.4: The schematic model of DTFC-SVM scheme with closed-loop torque and flux control operating in polar coordinates

6.1.4 DTFC-SVM Scheme with Closed-loop Torque and Flux Control Operating in Stator Flux Oriented Coordinates

The schematic model of the DTFC-SVM scheme with closed-loop torque and flux control operating in stator flux oriented coordinates and the vector diagram are shown in Figure 6.5 and Figure 6.6, respectively.

In this scheme, the outputs of the flux and torque controllers are interpreted as the direct and quadrature axis components of the reference stator voltage vector $\vec{V}_s^{e*}$ in stator flux oriented coordinate system. These stator voltage vector components are transformed into the stationary reference frame (d-q), and these transformed reference voltages are fed to the SVM block [156, 171-172, 176].

In the first three DTFC-SVM schemes, the reference stator voltage vector is manipulated using equation (6.2) and this expression is very sensitive to disturbances because of the derivative term. Consequently, if any disturbance occurs in the feedback signal, then the system may not be stable because of the differentiation algorithm.

In the fourth scheme, the torque and stator flux are controlled in closed loop and the structure of this scheme is simple compared to previous schemes. Moreover, this scheme doesn't have any derivative terms. Therefore, this scheme is considered for experimental realization.

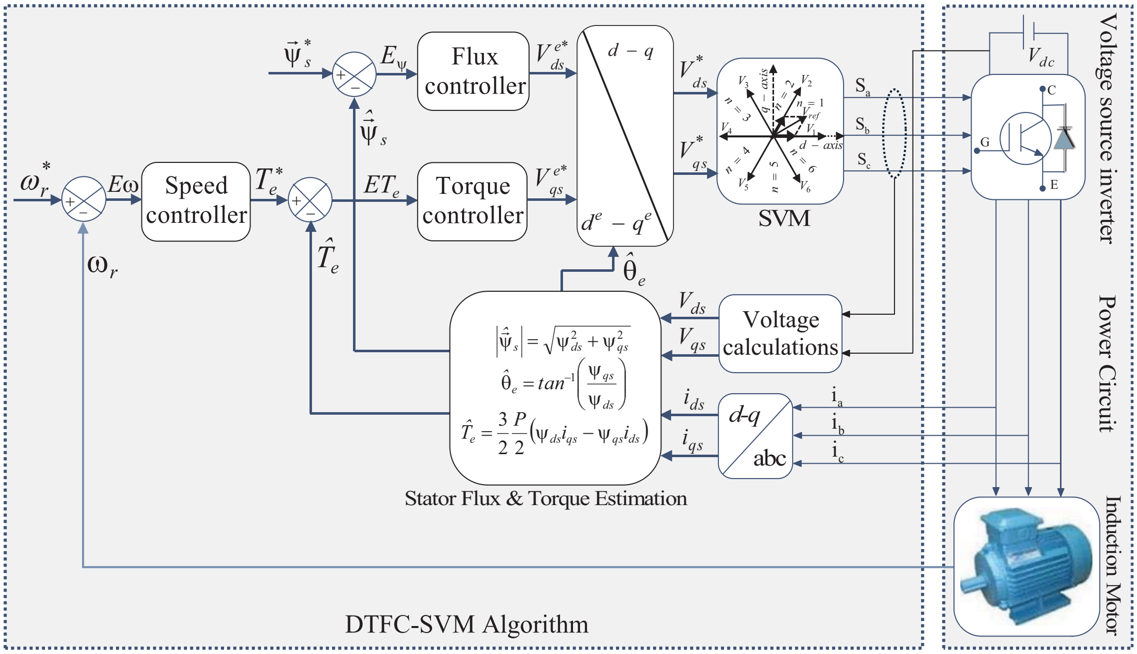

Figure 6.5: The schematic model of DTFC-SVM scheme with closed-loop torque and flux control operating in stator flux oriented coordinates

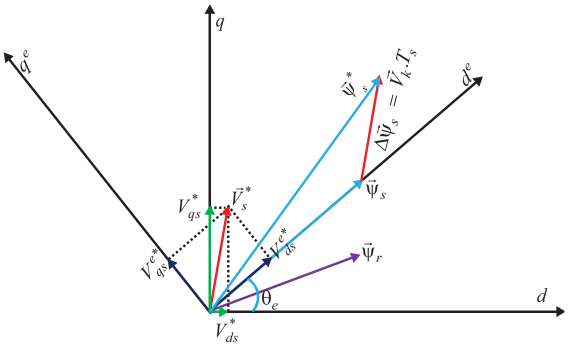

Figure 6.6: vector diagram of DTFC-SVM with closed-loop torque and flux control operating in stator flux oriented coordinates

6.2 Space Vector Modulation

Since IM drives become an industry standard, they require a magnificent switching algorithm. Among all the switching algorithms, the space vector modulation (SVM) is most suitable for two-level VSI, as it offers a great flexibility in optimizing switching pattern and it is suitable for digital implementation. This section discusses the principle of SVM and its implementation. The schematic model of two-level VSI is shown in Figure 4.2, depending on the switching state, eight combinations of switching states are possible. Out of which, two are null states (V_0 and V_7) that produce a zero inverter output voltage (i.e. line/phase voltages for the corresponding switching states). The other six active states (i.e. V_1 toV_6) produces a voltage vector of the same magnitude 0.667 V_{dc} and have been divided by a constant phase displacement of 60° in a space vector plane as shown in Figure 6.7. The tips of these vectors form a regular hexagon. The defined area enclosed by two adjacent vectors, within the hexagon is known as a sector. Thus, there are six sectors numbered 1 to 6 as shown in Figure 6.7. The vectors having zero magnitude are referred to as zero-switching state vectors [176-178]. They assume a position at the origin in the d-q reference plane. These combinations form a discrete set of space vectors. The different combinations of switching states and the corresponding space vectors are illustrated in Table 6.1.

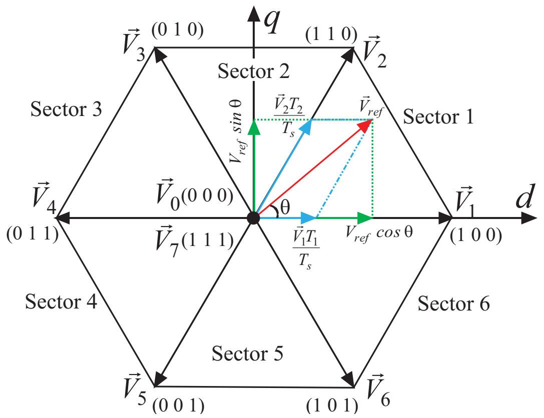

Figure 6.7: Space vector representation for two-level VSI

The DTFC-SVM algorithm estimates the reference voltage vector ($\vec{V}_{ref}$), which is applied to the IM in the next sampling period and it is fed into the SVM block. The SVM generates the appropriate gate pulses for realizing the reference voltage vector ($\vec{V}_{ref}$) by assuming reference voltage vector as constant till the next sampling period (T_s) and these gate pulses are fed to the two-level VSI [161-162].

The estimated reference voltage vector ($\vec{V}_{ref}$) has fallen into one of the six sectors of the space vector diagram (i.e. Figure 6.7) and it is obtained by applying the two neighboring active vectors and zero vectors. The zero vectors are used for changing the amplitude of the reference voltage vector, while the active vectors are used to change the position of the reference voltage vector. Usually, the neighboring active vectors are selected for realizing the reference voltage vector to reduce the torque ripple.

Table 6.1: Switching states and the corresponding space vectors

Space vector		Switching state combination	Vector definition
Zero vector	$\vec{V}_0$	0 0 0	$\vec{V}_0 = 0$
	$\vec{V}_7$	1 1 1	$\vec{V}_0 = 0$
Active vector	$\vec{V}_1$	1 0 0	$\vec{V}_1 = \frac{2}{3} V_{dc} \cdot e^{j0}$
	$\vec{V}_2$	1 1 0	$\vec{V}_2 = \frac{2}{3} V_{dc} \cdot e^{j\frac{\pi}{3}}$
	$\vec{V}_3$	0 1 0	$\vec{V}_3 = \frac{2}{3} V_{dc} \cdot e^{j\frac{2\pi}{3}}$
	$\vec{V}_4$	0 1 1	$\vec{V}_4 = \frac{2}{3} V_{dc} \cdot e^{j\frac{3\pi}{3}}$
	$\vec{V}_5$	0 0 1	$\vec{V}_5 = \frac{2}{3} V_{dc} \cdot e^{j\frac{4\pi}{3}}$
	$\vec{V}_6$	1 0 1	$\vec{V}_6 = \frac{2}{3} V_{dc} \cdot e^{j\frac{5\pi}{3}}$

In SVM, the volt-second balancing principle is used to calculate the dwell times for realizing the gate pulses. As mentioned earlier, the dwell times are calculated under the assumption that; the sampling period (T_s) is sufficiently small such that the reference voltage vector can be considered as constant during sampling period (T_s).

Dwell-time calculations:

In a particular sampling period (T_s) assume that the reference voltage vector is settled in sector 1, and it is shown in Figure 6.7. From Figure 6.7, it is clear that the reference voltage vector ($\vec{V}_{ref}$) can be synthesized by $\vec{V}_1$, $\vec{V}_2$ and $\vec{V}_0$. The volt-second balancing equation can be written as [171, 176-178]:

$$\vec{V}_{ref} \cdot T_s = \vec{V}_1 \cdot T_1 + \vec{V}_2 \cdot T_2 + \vec{V}_0 \cdot T_0 \tag{6.6}$$

$$T_s = T_1 + T_2 + T_0 \tag{6.7}$$

where T_1, T_2 and T_0 are the dwell times for the vectors $\vec{V}_1, \vec{V}_2$ and $\vec{V}_0$ respectively, and the space vectors $\vec{V}_{ref}$, $\vec{V}_1$, $\vec{V}_2$ and $\vec{V}_0$ can be expressed as [153]:

$$\vec{V}_{ref} = V_{ref}\left(cos\,\theta + j\,sin\,\theta\right),\ \vec{V}_1 = \frac{2}{3} V_{dc}\,,\ \vec{V}_2 = \frac{2}{3} V_{dc}\left(cos\frac{\pi}{3} + j\,sin\frac{\pi}{3}\right) \text{ and } \vec{V}_0 = 0 \tag{6.8}$$

By substituting equation (6.8) in (6.6) and separating the real and imaginary parts, we get:

$$V_{ref}\, cos\,\theta \cdot T_s = \frac{2}{3} V_{dc} \cdot T_1 + \frac{1}{3} V_{dc} \cdot T_2 \tag{6.9}$$

$$V_{ref}\, sin\,\theta \cdot T_s = \frac{1}{\sqrt{3}} V_{dc} \cdot T_2 \tag{6.10}$$

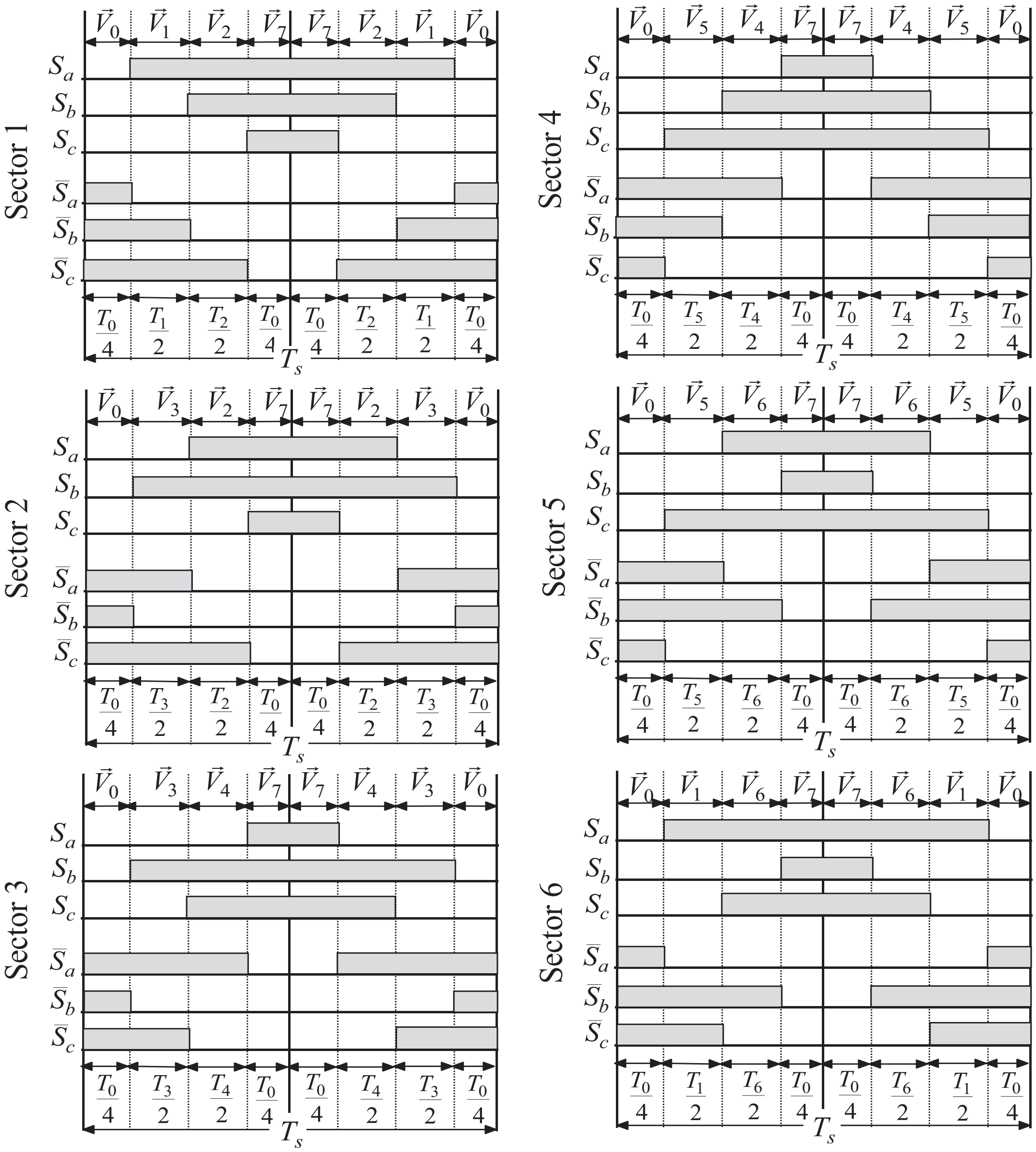

Figure 6.8: Typical seven-segment switching pattern of the VSI in all the six sectors

By solving equations (6.7), (6.9) and (6.10), the dwell times in sector-1 can be written as:

$$T_1 = \sqrt{3}\,\frac{V_{ref}}{V_{dc}} \cdot T_s \cdot sin\left(\frac{\pi}{3} - \theta\right), \qquad \forall\, \theta \in \left[0, \frac{\pi}{3}\right) \tag{6.11}$$

$$T_2 = \sqrt{3}\,\frac{V_{ref}}{V_{dc}} \cdot T_s \cdot sin\,\theta\,, \qquad \forall\, \theta \in \left[0, \frac{\pi}{3}\right) \tag{6.12}$$

$$T_0 = T_s - T_1 - T_2 \tag{6.13}$$

Note that even though the above dwell times are calculated when the reference voltage vector $\vec{V}_{ref}$ is in sector 1, they can also be used when $\vec{V}_{ref}$ is in other sectors by making a small modification in the actual angular displacement (θ). The modified angular displacement (θ') can be written as:

$$\theta' = \theta - (k-1)\frac{\pi}{3}, \qquad \forall\, \theta' \in \left[0,\ \frac{\pi}{3}\right) \tag{6.14}$$

where k is the sector number (i.e. $k=1,2,\ldots,6$).

In the process of obtaining the switching pulses, the space vectors are selected and their dwell times are calculated, the next step is to arrange them in a proper switching sequence. The way the space vectors are selected and arranged in the sequence has a great influence on the output voltage harmonic profile and also on the inverter switching losses.

In order to reduce the inverter switching losses and compress the output voltage harmonic profile, while arranging the switching sequence the following conditions need to be satisfied:

- In one sampling period (T_s) all three phases are switched.
- In one sampling period (T_s) the transitions in a switch are as minimum as possible, while moving one switching state to another switching state.
- Minimum or zero transitions in a switch are required, while moving reference voltage vector $\vec{V}_{ref}$ from one sector to another sector.

By considering the above conditions, a typical seven-segment switching pattern of the VSI in all the six sectors is generated and it is shown in Figure 6.8.

6.3 DTFC-SVM of a Speed Sensorless IMD

The schematic model of DTFC-SVM of a speed sensorless IM drive is shown in Figure 6.9. The DTFC-SVM of a sensorless IMD is implemented using three different control approaches (i.e. PIC, T1FLC and T2FLC), such as:

1. PIC based DTFC-SVM of a speed sensorless IMD
2. T1FLC based DTFC-SVM of a speed sensorless IMD
3. T2FLC based DTFC-SVM of a speed sensorless IMD

These three control approaches are described in the following subsections.

6.3.1 PIC based DTFC-SVM of a Speed Sensorless IMD

The PI controllers (PICs) are used in DTFC-SVM of a speed sensorless IMD as shown in Figure 6.9. In this method, four PICs are used, such as speed PI controller (SPIC), torque PI controller (TPIC), flux PI controller (FPIC) and adaptation PI controller (APIC), respectively. A root locus analysis is used for tuning the flux, torque and speed controllers. The complete design procedure and gain values of flux, torque and speed PICs are presented in Appendix B.

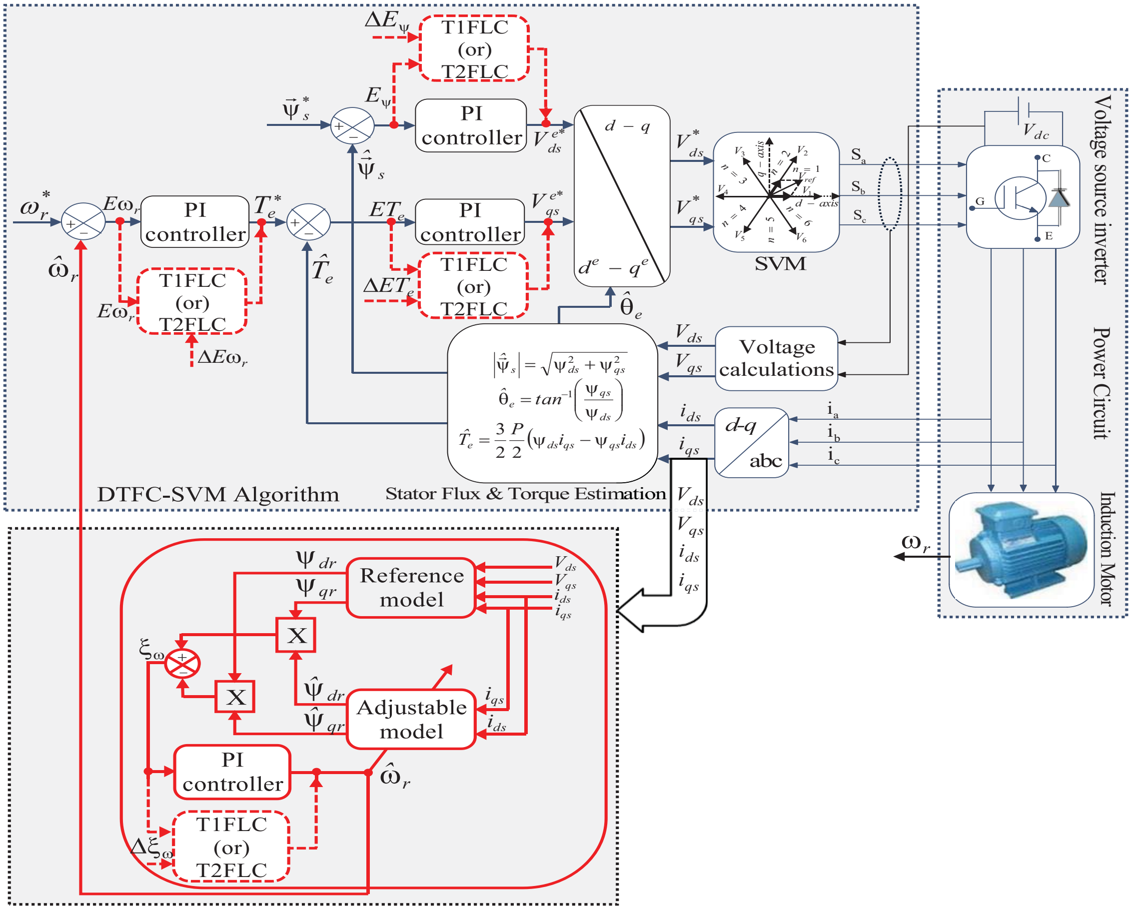

Figure 6.9: Schematic model of DTFC-SVM for a sensorless IMD using PIC (thick line) and T1FLC or T2FLC (dotted one)

6.3.2 T1FLC based DTFC-SVM of a Speed Sensorless IMD

The schematic model of T1FLC based DTFC-SVM of a speed sensorless IMD is shown in Figure 6.9 (shown by dotted line). In this Figure 6.9, the PICs (i.e. speed, torque, flux and adaptation) are replaced by T1FLCs to enhance the performance of the sensorless drive. From the SPIC, the output of the controller can be expressed as:

$$T_e^* = K_p E\omega_r + K_i \int E\omega_r dt \tag{6.15}$$

Applying differentiation on both sides of the equation (6.15), we get:

$$\frac{dT_e^*}{dt} = K_p \frac{dE\omega_r(t)}{dt} + K_i E\omega_r(t) \tag{6.16}$$

From equation (6.16), it is clear that the rate of change of torque is directly proportional to the inputs of speed control, i.e., error speed ($E\omega_r$) and change of error speed ($\Delta E\omega_r$). The design procedure for T1FLC based speed controller (ST1FLC) remains the same, which is explained in the section 3.2.

Similarly, the TPIC, FPIC and APICs are replaced by torque T1FLC (TT1FLC), flux T1FLC (FT1FLC) and adaptation T1FLC (AT1FLC), respectively. The same numbers of triangular MFs (i.e. seven) are used in both inputs (i.e. error and change in error) and output variable with the same number of rules (i.e. 49), which are illustrated in Table 6.2 and Table 6.3, respectively. The input variables of TT1FLC are torque error ‘ ET_e ’ and rate of change in torque error ‘ ΔET_e ’ and the output variable is a component of the reference stator voltage in stator flux oriented coordinate system ‘ V_{qs}^{e*} ’ as shown in Figure 6.10 (a). Similarly, the input variables of FT1FLC are flux error ‘ E_ψ ’ and rate of change of flux error ‘ ΔE_ψ ’ and the output variable is components of the reference stator voltage in stator flux oriented coordinate system ‘ V_{ds}^{e*} ’ as shown Figure 6.10 (b).

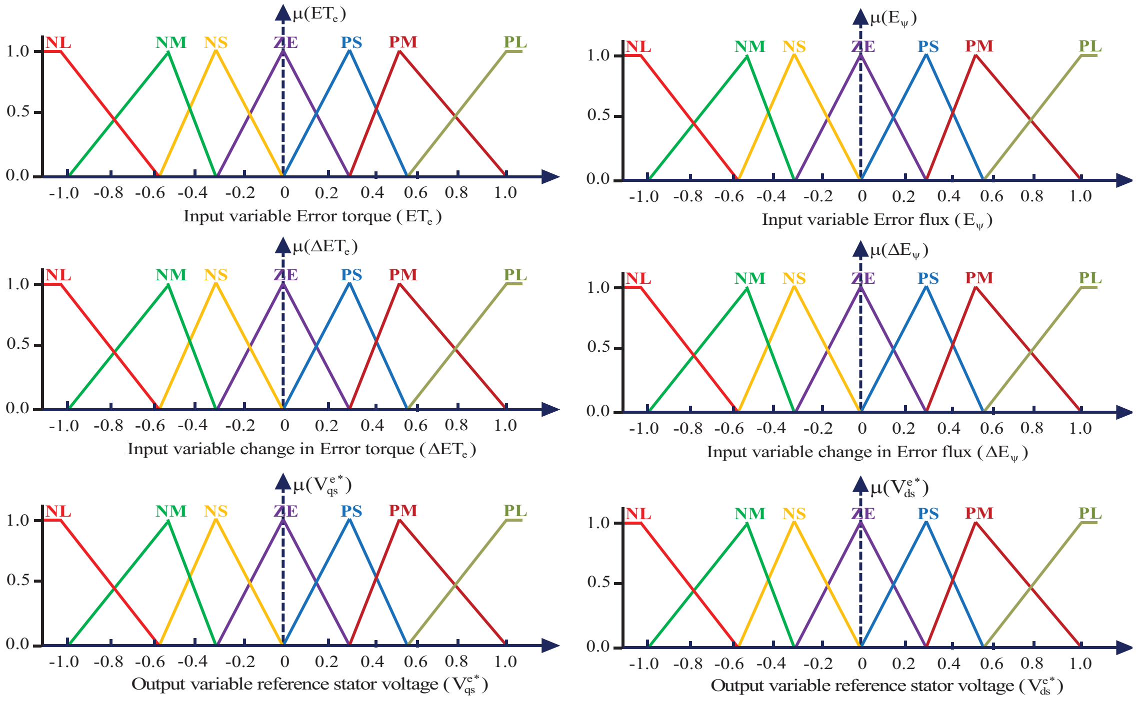

(a) Torque Type-1 FLC (b) Flux Type-1 FLC

Figure 6.10: Membership functions of Type-1 fuzzy logic controllers

In this control scheme, the centroid method is considered for the defuzzification purpose. The centroid of components of the reference stator voltages (found from the crisp output of T1FLC) are estimated for the overall MFs and which can be expressed as follows:

$$V_{qsC}^{e*} = \frac{\sum_{k=0}^{n} \mu_A(V_{qsCk}^{e*})\, V_{qs\,Ck}^{e*}}{\sum_{k=1}^{n} \mu_A(V_{qs\,Ck}^{e*})} \tag{6.17}$$

$$V_{ds\,C}^{e*} = \frac{\sum_{k=0}^{n} \mu_A(V_{ds\,Ck}^{e*})\, V_{dsCk}^{e*}}{\sum_{k=1}^{n} \mu_A(V_{dsCk}^{e*})} \tag{6.18}$$

where, $\mu_A(V_{qsCk}^{e*})$, V_{qsCk}^{e*}, $\mu_A(V_{dsCk}^{e*})$ and V_{dsCk}^{e*} are overall output MFs and crisp output quantity of torque and flux controllers and $k = 1, 2, \ldots, n$ number of samples of the aggregated output MF.

In adaptation control scheme, the adaptation PIC (APIC) is replaced by T1FLC. The design procedure for adaptation T1FLC (AT1FLC) remains the same, which is explained in the section 5.2.2.

Table 6.2: Rule base of TT1FLC and TT2FLC

Output (V_{qs}^{e*})		**Change in Error Torque** (ΔET_e)						
		NL	**NM**	**NS**	**ZE**	**PS**	**PM**	**PL**
Error Torque (ET_e)	**NL**	NL	NL	NL	NL	NM	NS	ZE
	NM	NL	NL	NL	NM	NS	ZE	PS
	NS	NL	NL	NM	NS	ZE	PS	PM
	ZE	NL	NM	NS	ZE	PS	PM	PL
	PS	NM	NS	ZE	PS	PM	PL	PL
	PM	NS	ZE	PS	PM	PL	PL	PL
	PL	ZE	PS	PM	PL	PL	PL	PL

6.3.3 T2FLC based DTFC-SVM of a Speed Sensorless IMD

The schematic model of T2FLC based DTFC-SVM of a sensorless IMD is shown in Figure 6.9 (shown by dotted line). In this Figure 6.9, the PICs (i.e. TPIC, FPIC, SPIC and APIC) are replaced by T2FLCs (i.e. TT2FLC, FT2FLC, ST2FLC and AT2FLC) to further enhance the performance of the sensorless drive. The TT2FLC and FT2FLC inputs (error and change in error) and output MFs remain same as that of the TT1FLC and FT1FLC, which are shown in Figure 6.11 (a) and Figure 6.11 (b), respectively. Moreover, the corresponding number of rules for TT2FLC and FT2FLCs are also same as that of the TT1FLC and FT1FLC, which are illustrated in Table 6.2 and Table 6.3, respectively. The rules are framed using IF and THEN method. The design procedure of ST2FLC and AT2FLCs remains the same, which are explained in the section 3.3 and section 5.2.3, respectively.

Table 6.3: Rule base of FT1FLC and FT2FLC

Output (V_{ds}^{e*})		**Change in Error Flux** (ΔE_ψ)						
		NL	**NM**	**NS**	**ZE**	**PS**	**PM**	**PL**
Error Flux (E_ψ)	**NL**	NL	NL	NL	NL	NM	NS	ZE
	NM	NL	NL	NL	NM	NS	ZE	PS
	NS	NL	NL	NM	NS	ZE	PS	PM
	ZE	NL	NM	NS	ZE	PS	PM	PL
	PS	NM	NS	ZE	PS	PM	PL	PL
	PM	NS	ZE	PS	PM	PL	PL	PL
	PL	ZE	PS	PM	PL	PL	PL	PL

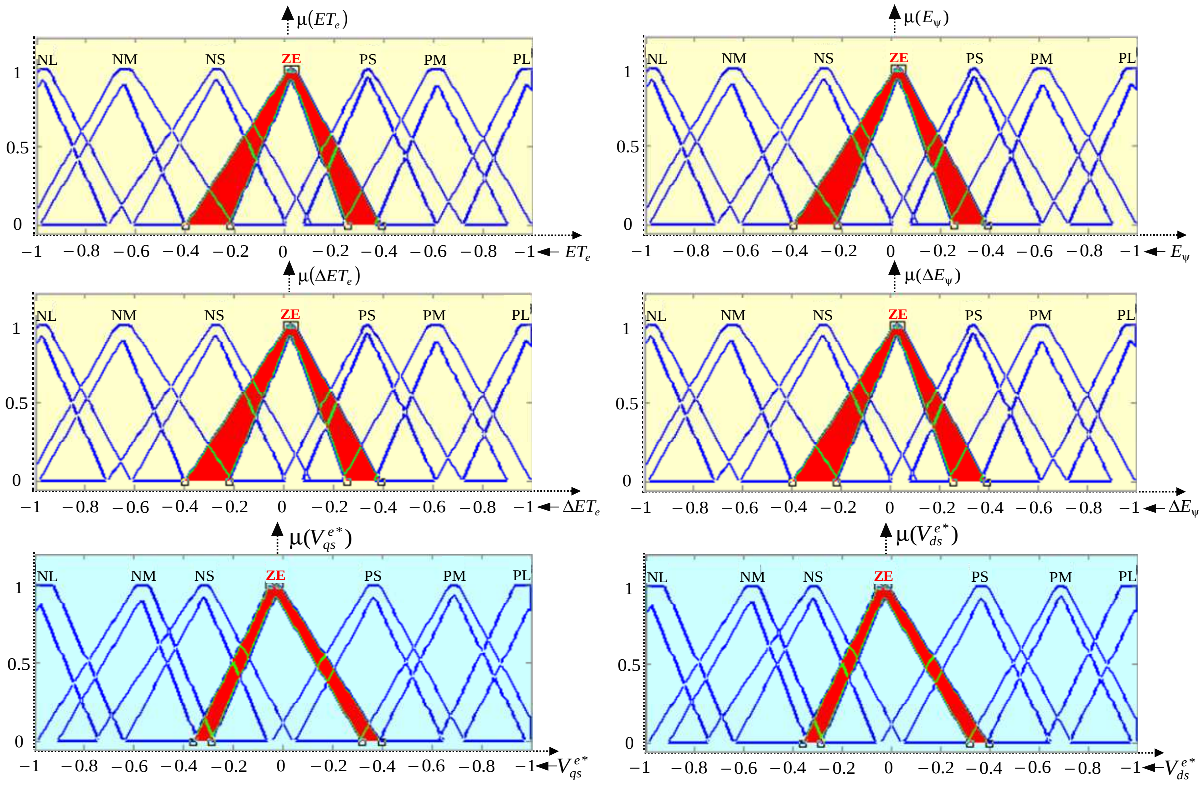

(a) Torque Type-2 FLC (b) Flux Type-2 FLC

Figure 6.11: Membership functions of Type-2 fuzzy logic controllers

6.3.3.1 Design of FT2FLC Rule Base

The type-2 fuzzy sets of l^{th} rule can be obtained as [85]:

$$F^l(X) = \left[\underline{f}^l(X), \overline{f}^l(X)\right] = \left[\underline{f}^l, \overline{f}^l\right] \tag{6.19}$$

Where, $\overline{f}^{l} = \overline{\mu}_{\tilde{F}^{l}_{E_\psi}}\left(E_\psi\right) * \overline{\mu}_{\tilde{F}^{l}_{\Delta E_\psi}}\left(\Delta E_\psi\right)$, $\underline{f}^{l} = \underline{\mu}_{\tilde{F}^{l}_{E_\psi}}\left(E_\psi\right) * \underline{\mu}_{\tilde{F}^{l}_{\Delta E_\psi}}\left(\Delta E_\psi\right)$, * indicates the product operation, $\underline{\mu}_{\tilde{F}^{l}_{E_\psi}}$ and $\overline{\mu}_{\tilde{F}^{l}_{E_\psi}}$ represents the LMF and UMF grades, respectively.

Type-reducer:

The type-reducer block transforms a T2FS output of T2FIS into Type-1 reduced fuzzy sets, which are then transformed into a crisp output through the defuzzifier. The COS is considered for type-reducer operation. A singleton fuzzification with minimum t-norm is used and the output can be expressed as [172-174]:

$$V^{e*}_{ds_{COS}} = \int_{f1 \in J_{y1}} ,....., \int_{fN \in J_{yN}} \left[\frac{\sum_{l=1}^{M} f_l y_l}{\sum_{l=1}^{M} f_l} \right] = \left[y^l_l , y^l_r \right] = \left[V^{e*}_{ds_l} , V^{e*}_{ds_r} \right] \tag{6.20}$$

where $V^{e*}_{ds_{COS}}$ is an IT2FS determined by the LMP and RMP ($V^{e*}_{ds_l}, V^{e*}_{ds_r}$), which can be derived from the consequent centroid set (y^l_l, y^l_r) and the reference stator voltage (V^{e*}_{ds}) strength $\underline{f}^l \in F^l = (\underline{f}^l, \overline{f}^l)$ must be computed or set first before the computation of $V^{e*}_{ds_{COS}}$.

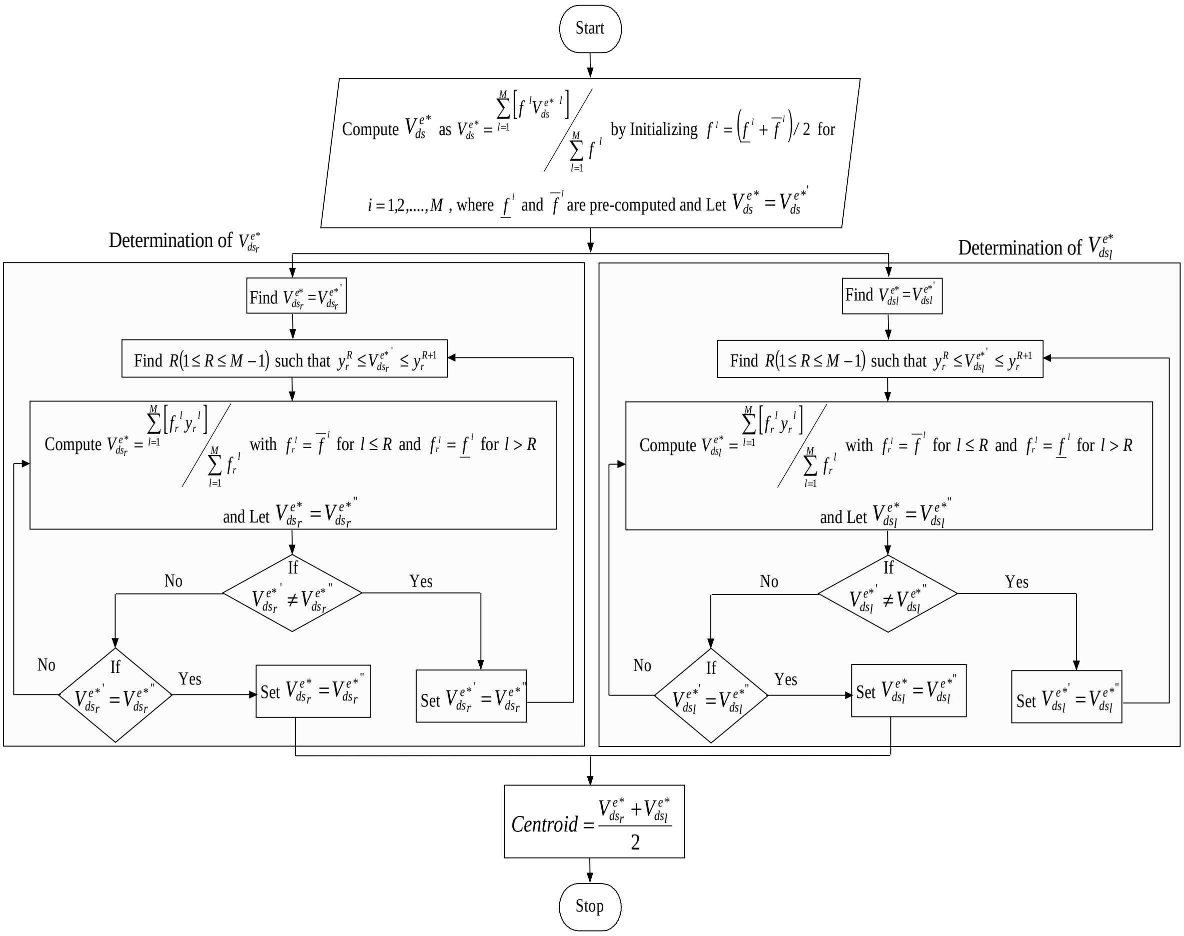

Figure 6.12: The flowchart of T2FLC for finding the crisp value of the estimated speed

The LMP ($V_{ds_l}^{e*}$) and RMP ($V_{ds_r}^{e*}$) can be expressed as follows:

$$V_{ds_l}^{e*} = y_l^l = \frac{\sum_{l=1}^{M}\left[f_l^{\,l} y_l^{\,l}\right]}{\sum_{i=1}^{M} f_l^{\,l}} \tag{6.21}$$

$$V_{ds_r}^{e*} = y_r^l = \frac{\sum_{l=1}^{l}\left[f_r^{\,l} y_r^{\,l}\right]}{\sum_{l=1}^{M} f_r^{\,l}} \tag{6.22}$$

Computation of LMP ($V_{ds_l}^{e*}$) and RMP ($V_{ds_r}^{e*}$) is done using Karnik-Mendal algorithm [79], which is given in Figure 6.12. The procedure to compute the RMP ($V_{ds_r}^{e*}$) and LMP ($V_{ds_l}^{e*}$) is considered similar to that of used for computing $T_{e\ l}^{*}$ and $T_{e\ r}^{*}$ (which are presented in the section-3.3), respectively.

Centroid of FT2FLC:

The type-reducer output is fed into the centroid type defuzzification block. Then the defuzzification block converts from the T1FS to crisp output. The defuzzified crisp output is the average value of $V_{ds_r}^{e*}$ and $V_{ds_l}^{e*}$, it is given by:

$$Centroid = y(x) = \frac{V_{ds_l}^{e*} + V_{ds_r}^{e*}}{2} \tag{6.23}$$

Similarly, the design procedure for TT2FLC is same as FT2FLC. The defuzzified crisp output is the average value of $V_{qs_r}^{e*}$ and $V_{qs_l}^{e*}$, it is given by:

$$Centroid = y(x) = \frac{V_{qs_l}^{e*} + V_{qs_r}^{e*}}{2} \tag{6.24}$$

The speed of the IMD is estimated as close as to the actual speed of the IM using T2FLC compared to T1FLC and PIC schemes, which leads to enhance the dynamic performance of the sensorless IMD with T2FLCs compared to T1FLC and PICs, respectively. The detailed performance of the sensorless IM drive using three different control schemes will be studied in simulation and experimental results with discussion in the following sections.

6.4 Simulation Results

The RFMRAS speed estimator for DTFC-SVM of a sensorless IMD (Figure 6.9) is mathematically modelled in the MATLAB/SIMULINK environment using PIC, T1FLC and T2FLC schemes, respectively. The Simulink model is then used to verify the performance of the DTFC-SVM of a sensorless IMD under various operating conditions, such as, under no-load torque, load torque, sudden changes in speed and low speed, respectively.

6.4.1 Performance under Forward Motoring

Initially, the performance of the sensorless drive is simulated under no-load torque operation at 1200 rpm using three control schemes are shown in Figure 6.13 (a)-(c). The reference speed (ω_r^*), actual speed (ω_r) and estimated speed ($\hat{\omega}_r$) under such command is shown in Figure 6.13 trace-(ii). The torque, stator current, stator flux dq-components in a stationary reference frame (i.e. ψ_{ds}, ψ_{qs}) and stator flux are shown in Figure 6.13 (i), (iii)-(v), respectively. It is observed that the IMD starts at zero speed and reaches the set reference speed (i.e. 1200 rpm) at 0.65 s with an overshoot of 12.5 rpm using PIC, whereas it reaches quickly at 0.489 s with zero overshoot using T2FLC scheme, respectively. It is observed from the simulation results that the transient response of the IMD using T2FLC scheme shows faster compared to the PIC and T1FLCs, respectively.

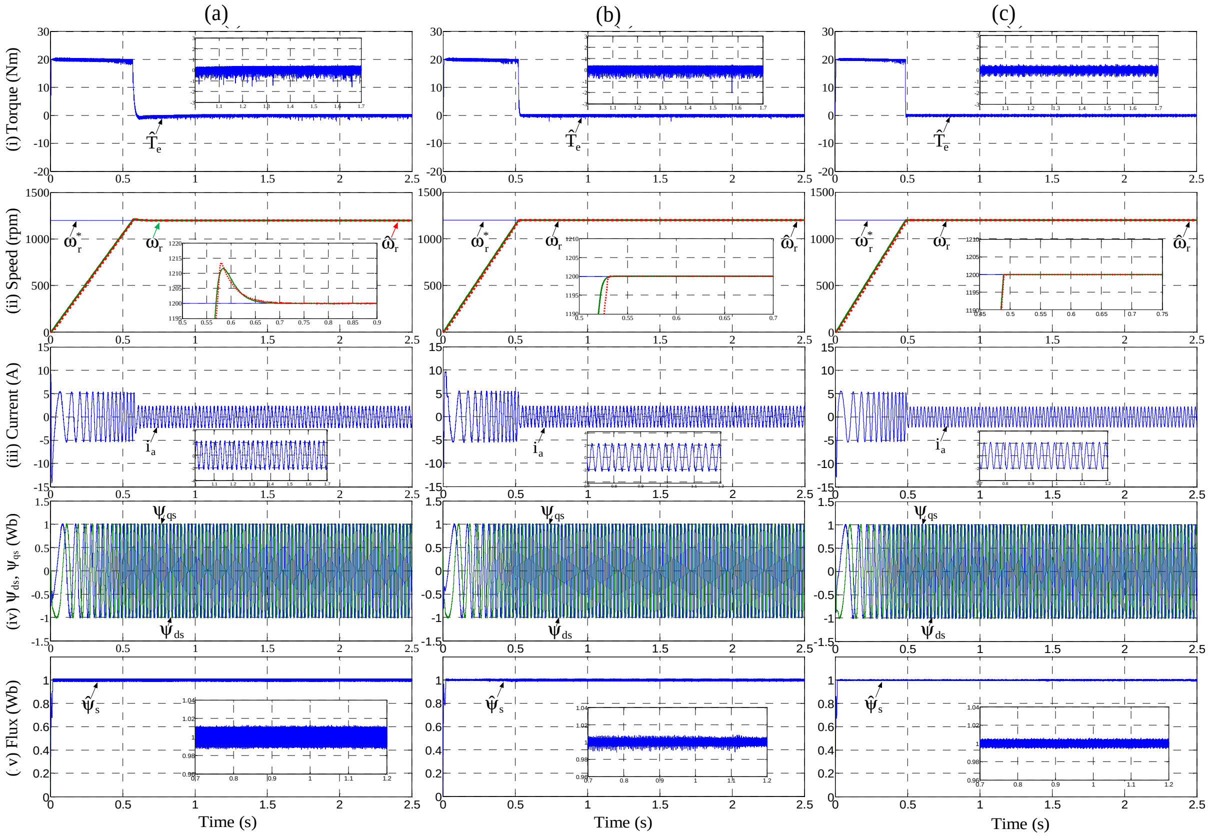

Figure 6.13: Performance under no-load torque operating condition using: (a) PIC, (b) T1FLC and (c) T2FLC: *Traces (from top to bottom):* (i) Torque, (ii) speed, (iii) stator current, (iv) stator flux dq-components in stationary reference frame and (v) stator flux

6.4.2 Loading Performance

The sudden load torque of 9 Nm is applied at 1.4 s when the induction motor is operating at steady state speed as shown in Figure 6.14 (a)-(c). It is observed that the sudden application of load torque causes an undershoot of around 1.0%, 0.4% and 0.166% of the reference speed using PIC, T1FLC and T2FLC schemes as shown in Figure 6.14 (ii). It is also observed that the recovery time of the estimated speed under such commands is 0.23 s, 0.05 s and 0.03 s using PIC, T1FLC and T2FLC schemes, respectively. Moreover, the ripple contents of the torque, stator currents and error speed are less using T2FLC compared to T1FLC and PIC, which are shown in Figure 6.14 (i), (iii)-(iv), respectively. Similarly, when the load torque is removed (i.e. at 2.1 s), an overshoot around 0.958%, 0.366% and 0.175% of the reference speed appears using PIC, T1FLC and T2FLC schemes are shown in Figure 6.15 (ii). The torque, reference speed, estimated and actual speed, stator current and the error speed between the estimated and actual speed are shown in Figure 6.15 (i)-(iv), respectively.

The effect of different load torque conditions is observed under different speed commands using PIC, T1FLC and T2FLC schemes, which are illustrated in Figure 6.16 (a)-(c). It is observed that the T2FLC shows an excellent performance and robustness to various load torque disturbances compared to PIC and T1FLC, respectively.

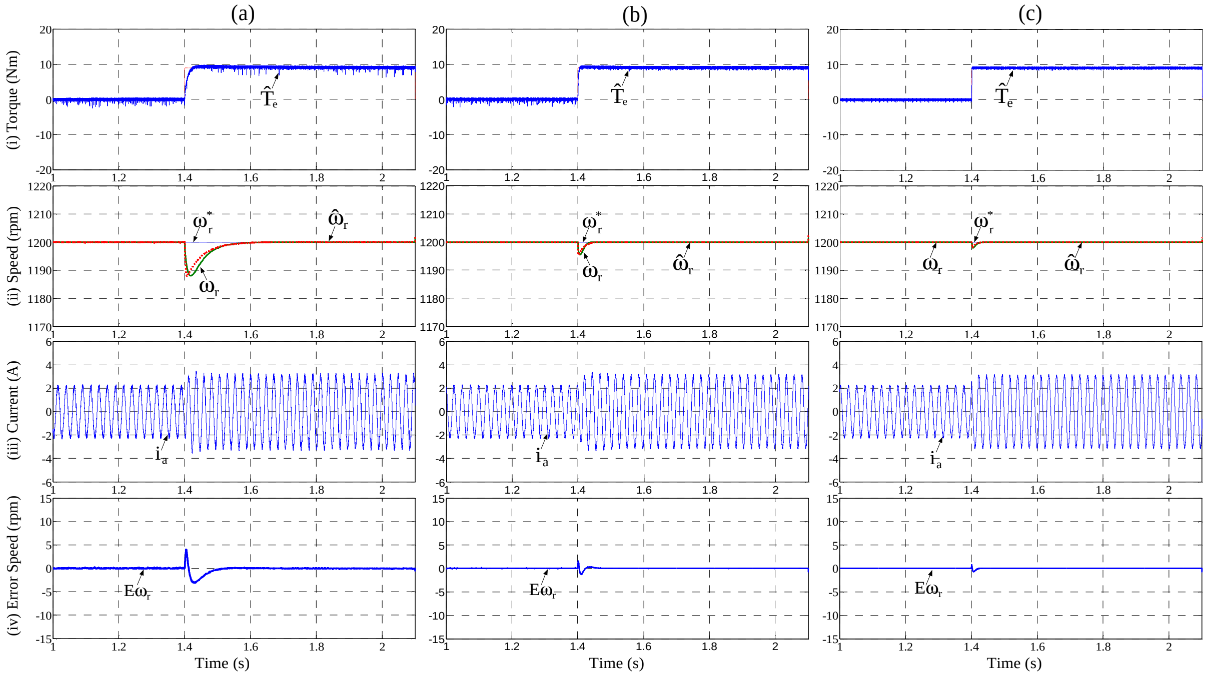

Figure 6.14: Loading performance at 1200 rpm using: (a) PIC, (b) T1FLC and (c) T2FLC: *Traces (from top to bottom):* (i) Torque, (ii) speed, (iii) stator current and (iv) error speed

6.4.3 Performance under Reversal Speed Command

The reversal speed command from +1200 rpm to -1200 rpm is applied at 2 s as shown in Figure 6.17 (a)-(c). The estimated speed reaches its reference speed during reversal speed at 3.16 s, 3.04 s and 2.92 s using PIC, T1FLC and T2FLC schemes, respectively. The reference speed, actual and estimated speeds are shown in Figure 6.17 (ii), which reveals that the estimated speed tracks the reference speed with an overshoot of 12 rpm, 0.5 rpm and 0 rpm of the reference speed using PIC, T1FLC and T2FLC schemes, respectively. The torque, stator current and stator flux dq-axis components are shown in Figure 6.17 (i), (iii)-(iv), respectively. The transient response of reversal speed is shown in Figure 6.18 (a)-(c).

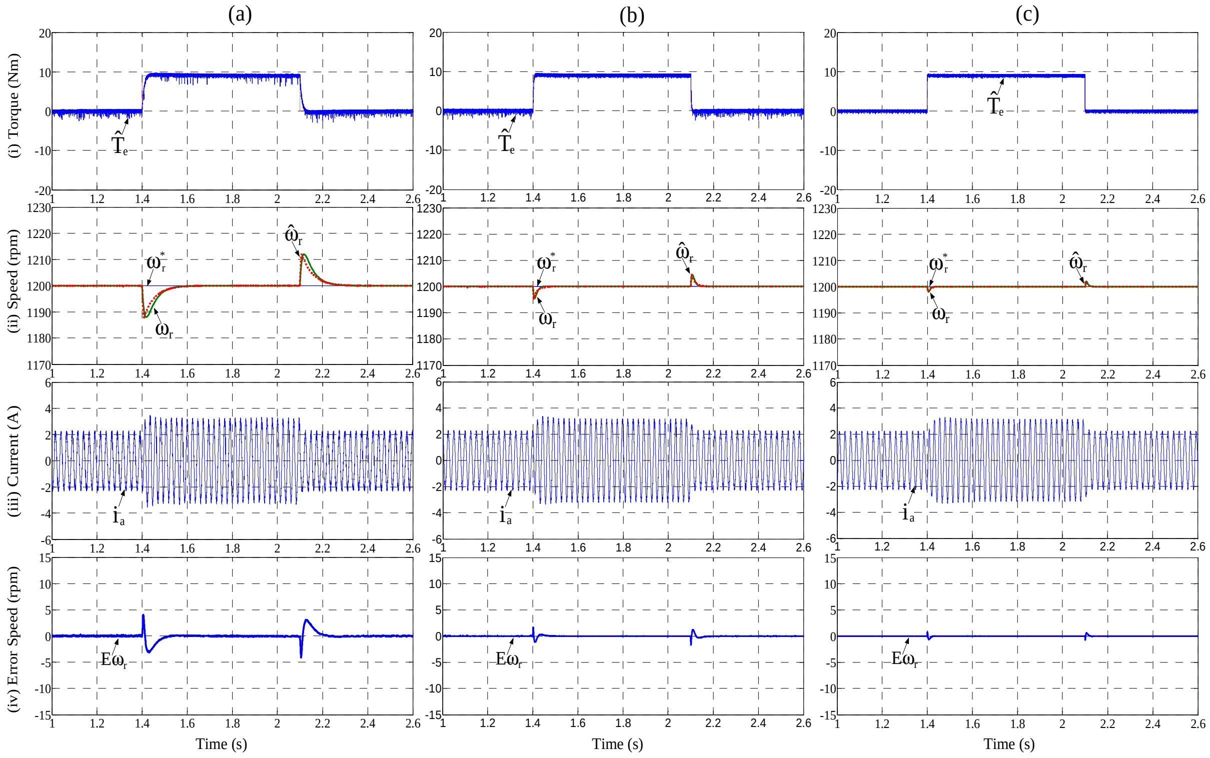

Figure 6.15: Loading and unloading performance at 1200 rpm using: (a) PIC, (b) T1FLC and (c) T2FLC: *Traces (from top to bottom):* (i) Torque, (ii) speed, (iii) stator current and (iv) error speed

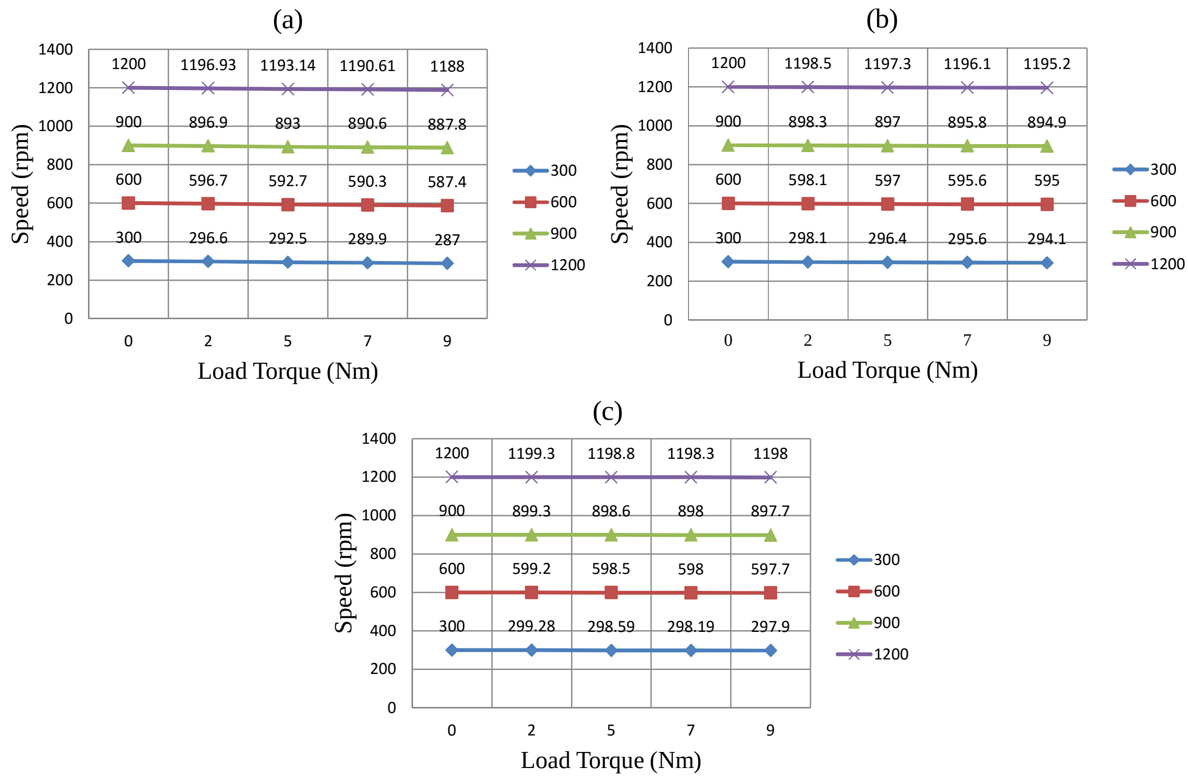

Figure 6.16: Steady-state performance of the estimated speed under various sudden load torque conditions at different speed commands using: (a) PIC, (b) T1FLC and (c) T2FLC

6.4.4 Tracking Performance of the Speed Commands

Tracking performance of the sensorless drive is observed under a sudden change in step speed command is shown in Figure 6.19 (a)-(c). The sudden change in step speed command of 300 rpm is applied in four steps (i.e. 600 rpm → 900 rpm → 1200 rpm → 900 rpm → 600 rpm) at 1.4 s, 2.4 s, 3.6 s, etc. The corresponding reference and actual speed responses under such speed commands are shown in Figure 6.19 (ii). The torque, stator current and stator flux dq-components are shown in Figure 6.19 (i), (iii)-(iv) respectively. From Figure 6.19 (ii), it is observed that the estimated speed settled the reference speed (i.e. from 600 to 900 rpm) in 0.22 s, 0.136 s and 0.12 s using PIC, T1FLC and T2FLC schemes, respectively. Moreover, it is also observed that the error between the estimated and actual speed is negligible using T2FLC compared to T1FLC and PIC scheme.

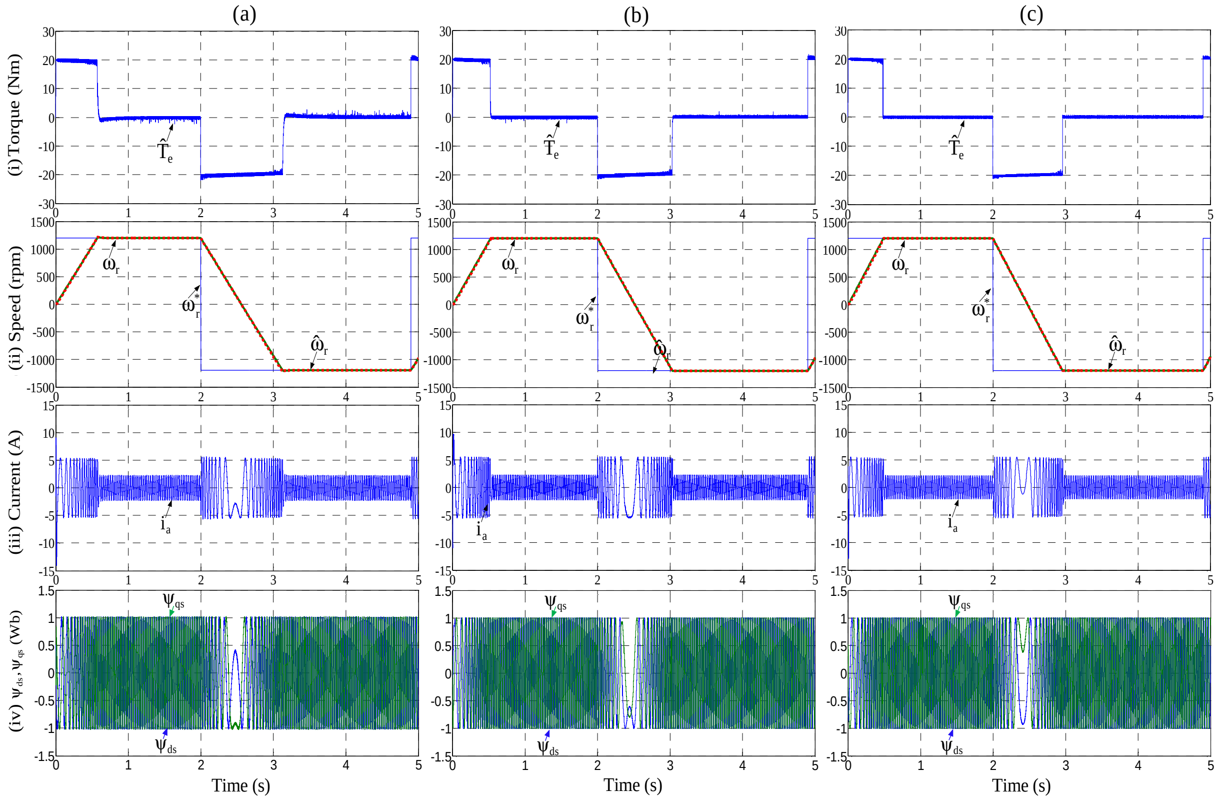

Figure 6.17: Performance under reversal speed command using: (a) PIC, (b) T1FLC and (c) T2FLC: (i) Torque, (ii) speed (iii) stator current and (iv) stator flux components

Performance under square change in speed command:

The sudden change in speed command of 600 rpm is applied in four steps (i.e. 1200 rpm →600 rpm→1200 rpm →600 rpm→1200 rpm) at 1 s, 2 s, 3 s and 4 s is shown in Figure 6.20 (a)-(c). The reference speed (ω_r^*), actual speed (ω_r) and estimated speed ($\hat{\omega}_r$) are presented in Figure 6.20 (ii), it is observed that under such speed command the estimated speed settled the reference speed (i.e. from 600 rpm to 1200 rpm) in 0.442 s, 0.28 s and 0.26 s with an overshoot of around 0.958%, 0.0366%, 0.0% of the reference speed using PIC, T1FLC and T2FLC scheme, respectively. The torque and stator current are shown in Figure 6.20 (i) and (iii), respectively. It is noticed that the estimated speed accurately tracking the reference speed and settles quickly using T2FLC compared to T1FLC and PICs.

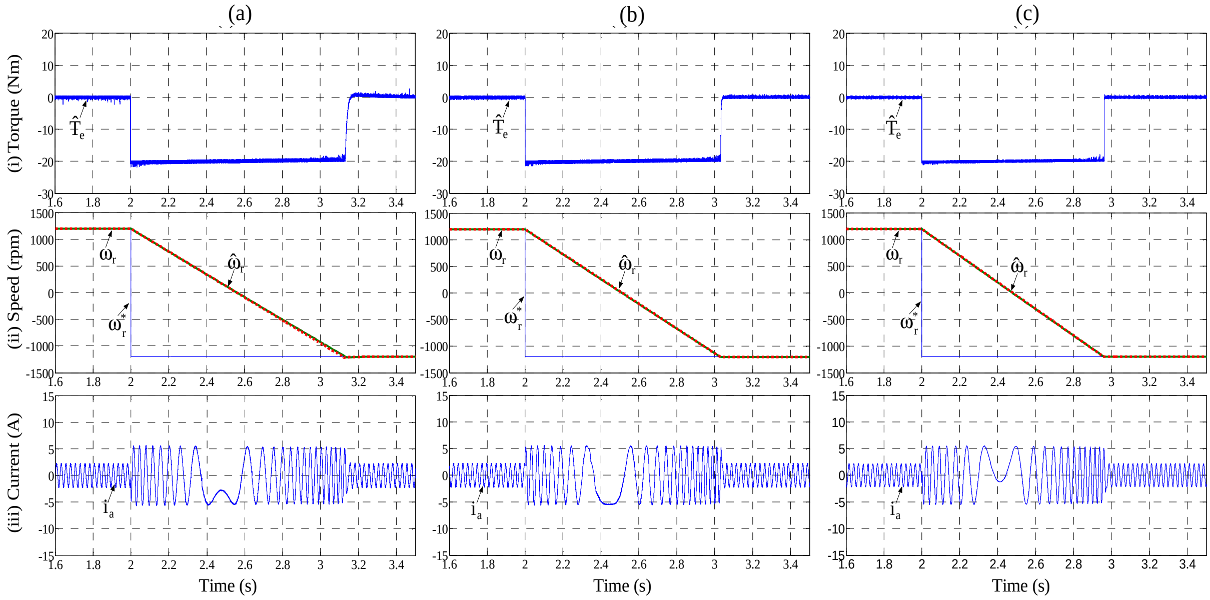

Figure 6.18: Transient performance under reversal speed command using: (a) PIC, (b) T1FLC and (c) T2FLC: (i) Torque, (ii) speed and (iii) stator current

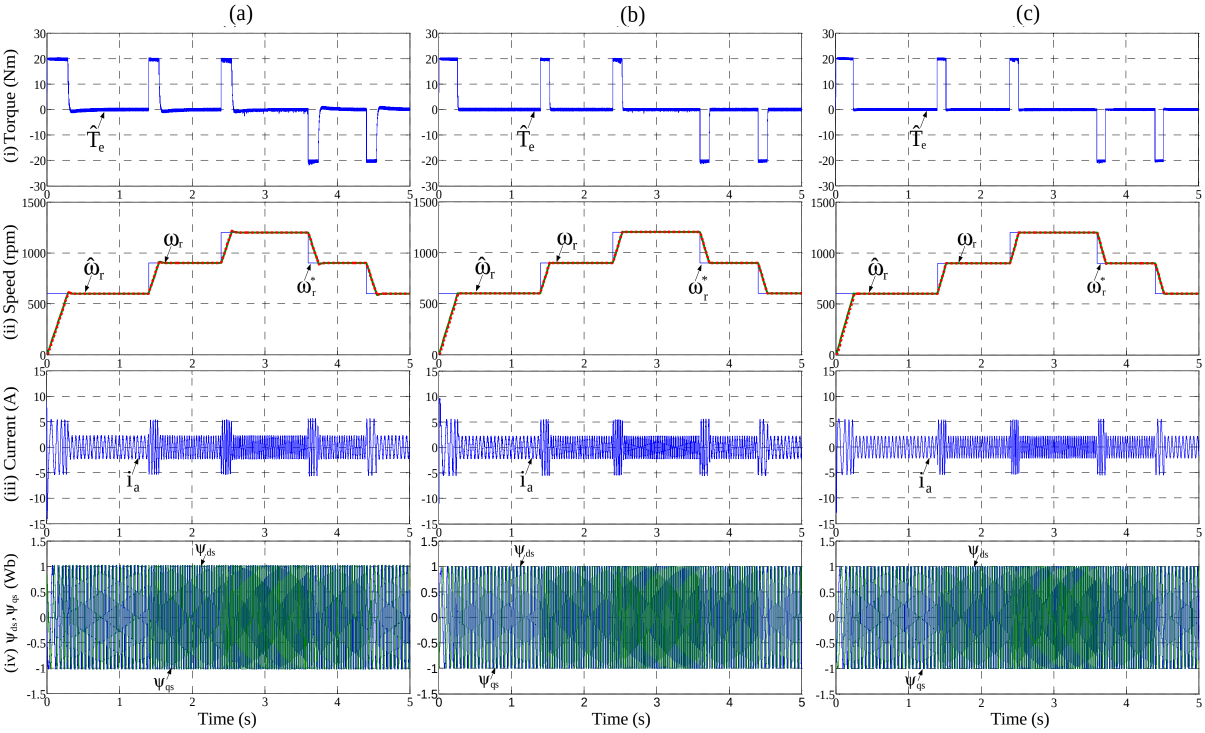

Figure 6.19: Performance under a step change in speed command using: (a) PIC, (b) T1FLC and (c) T2FLC: (i) Torque, (ii) speed and (iii) stator current and (iv) stator flux components

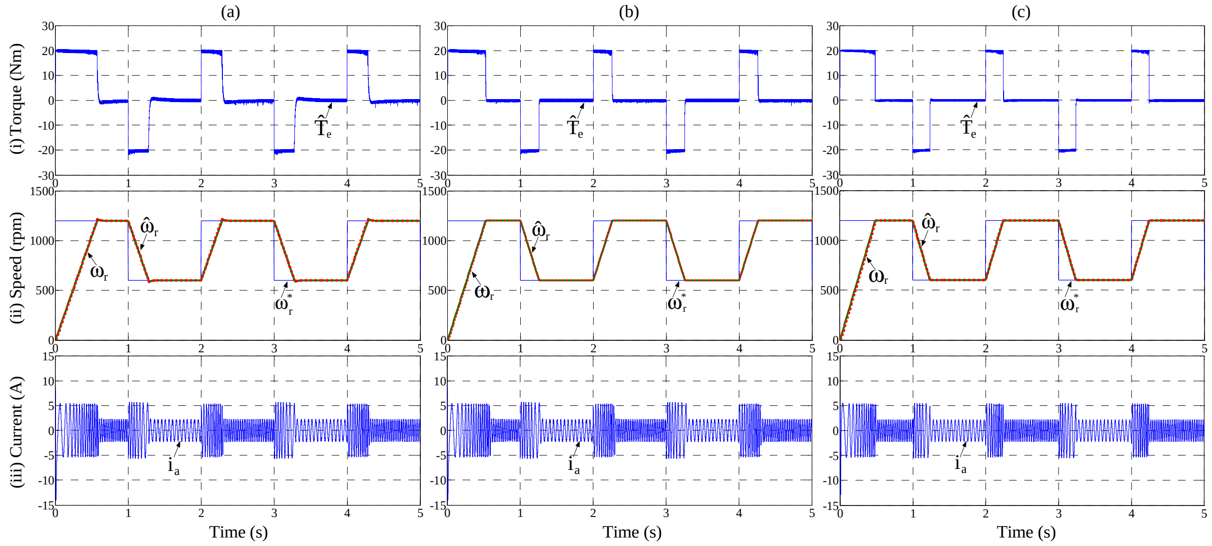

Figure 6.20: Performance under square change in speed command using: (a) PIC, (b) T1FLC and (c) T2FLC: (i) Torque, (ii) speed and (iii) current

Table 6.4: Performance indices under forward motoring with different starting load torque conditions using three different controller schemes

Starting Load Torque	Controller	Time domine specification			Performance indices					Total indices
		t_r (s)	M_p (%)	t_s (s)	IAE	ISE	ITAE	ITSE	RMSE	
0	PIC	0.579	1.041	0.650	34.18	3021	7.810	441.32	38.63	3542.94
	T1FLC	0.410	0.070	0.520	31.21	2788	5.230	361.40	33.89	3219.73
	T2FLC	0.385	0.000	0.489	27.85	2697	4.964	329.84	30.64	3090.29
4	PIC	0.763	0.958	1.012	43.78	3881	11.04	728.62	43.54	4707.98
	T1FLC	0.528	0.062	0.785	39.38	3523	8.517	580.65	40.93	4192.47
	T2FLC	0.481	0.000	0.617	35.53	3362	7.182	516.12	36.46	3957.29
7	PIC	0.995	0.891	1.278	54.88	4912	18.11	1185.9	49.24	6220.13
	T1FLC	0.683	0.051	0.867	50.28	4397	12.91	908.16	44.32	5412.67
	T2FLC	0.609	0.000	0.764	44.37	4149	10.08	789.65	41.15	5034.25
9	PIC	1.217	0.788	1.414	71.24	5951	27.86	1768.3	54.33	7872.73
	T1FLC	0.829	0.030	1.002	59.14	5248	18.07	1315.6	49.68	6690.49
	T2FLC	0.746	0.000	0.908	51.19	4935	13.34	1105.2	47.38	6152.11

6.4.5 Performance Indices

In order to give a clear idea of the performance of three different controller schemes, the performance indices (IAE, ITAE, ISE, ISTE and RMSE) are calculated using each control scheme under forward motoring (i.e. reference speed of 1200 rpm) with no-load torque and load torque operation, which are illustrated in Table 6.4. It is observed that the PIC shows the highest performance indices whereas lowest performance indices observed using T2FLC scheme.

6.5 Experimental Results

The performance of the DTFC-SVM of a sensorless IMD using PIC, T1FLC and T2FLC schemes are experimentally validated by the laboratory developed EPS and the results are presented under various operating conditions, such as forward motoring, reversal speed, sudden change in speed and load torque operations, respectively. Note that the experiments have been performed under the same operating conditions in which simulations have been carried out in the previous section 6.4.

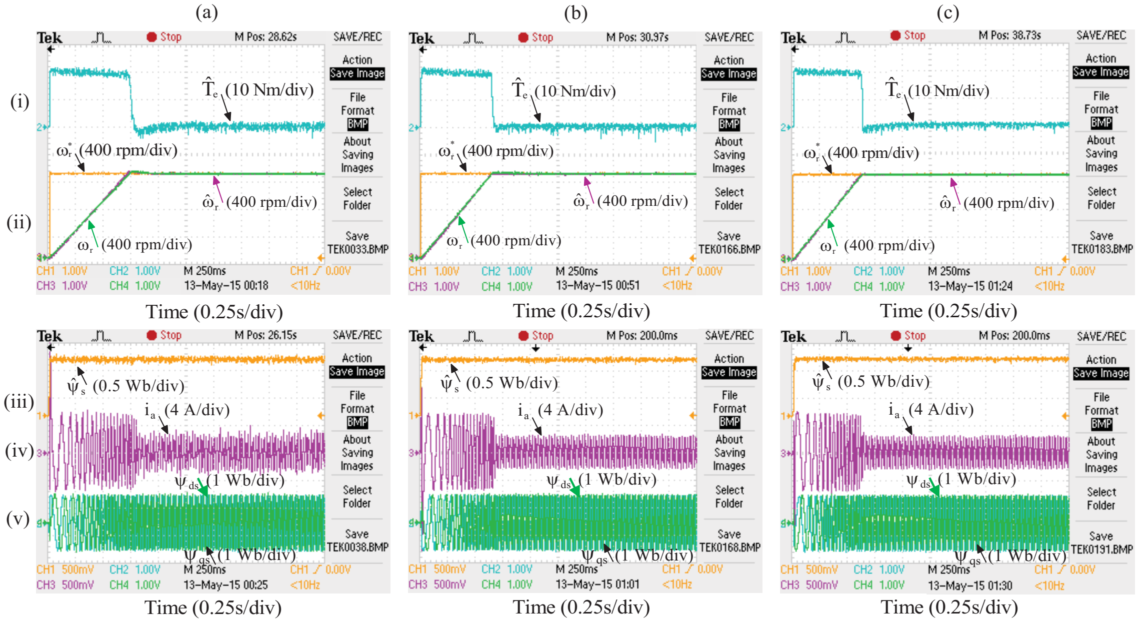

Figure 6.21: Performance under no-load torque operating condition using: (a) PIC, (b) T1FLC and (c) T2FLC: *Traces (from top to bottom):* (i) Torque, (ii) speed, (iii) stator flux, (iv) stator current and (v) stator flux components

6.5.1 Performance under Forward Motoring

Initially, the performance of the sensorless IMD is investigated under no-load torque operation at a reference speed of 1200 rpm using PIC, T1FLC and T2FLC schemes are shown in Figure 6.21 (a)-(c). The reference speed (ω_r^*), actual speed (ω_r) and estimated speed ($\hat{\omega}_r$) are shown in Figure 6.21 (ii). The actual speed is measured through the incremental encoder. The actual speed is used to check for only the tracking performance of the estimated speed not for any computation purposes. The IM starts at zero speed and settled (1200 rpm) at 0.81 s, 0.71 s and 0.658 s with an overshoot of around 19.5 rpm, 2.2 rpm and 0 rpm using PIC, Type-1 and Type-2 FLC schemes, respectively. The electromagnetic torque and stator current are shown in Figure 6.21 (i) and (iv), respectively. From Figure 6.21 (i), it is observed that the ripple content in electromagnetic torque is ±1.4 Nm, ±1.02 Nm and ±0.76 Nm using PIC, T1FLC and T2FLC schemes, respectively. The steady-state performance of the sensorless drive is shown in Figure 6.22 (a)-(c). Note that the experimental results, which are presented in Figure 6.21 (a)-(c) and Figure 6.22 (a)-(c) corresponding to the simulation result of the Figure 6.13 (a)-(c). The results reveal an excellent correlation between the simulation and experimental results. Both simulation and experimental results show the superiority of the T2FLC over T1FLC and PIC, respectively.

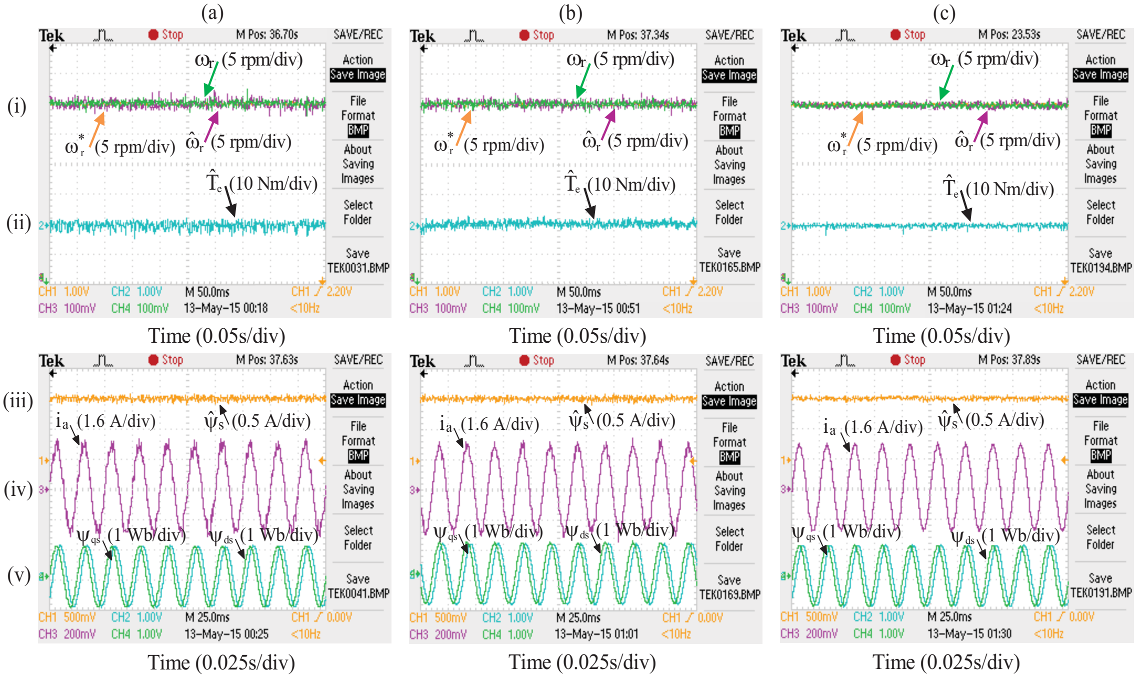

Figure 6.22: Steady-state performance under no-load torque operating condition using: (a) PIC, (b) T1FLC and (c) T2FLC: (i) speed, (ii) torque, (iii) stator flux, (iv) stator current and (v) stator flux dq-components in a stationary reference frame

6.5.2 Performance under Reversal Speed Command

The reversal speed command from +1200 rpm to -1200 rpm is applied at 2 s. Further, the direction of the speed is changed from -1200 rpm to +1200 rpm at 4.9 s and the corresponding responses are shown in Figure 6.23 (a)-(c). From Figure 6.23 (ii), it is noticed that the estimated speed settles the set reference speed (i.e.-1200 rpm) at around 3.46 s, 3.28 s and 3.13 s with an overshoot around 1.625%, 0.183% and 0.0% of the reference speed using PIC, T1FLC and T2FLC schemes, respectively. The torque, stator current and stator flux dq-components are shown in Figure 6.23 (i), (iii)-(iv), respectively. The transient response during reversal speed using PIC, T1FLC and T2FLC schemes are shown in Figure 6.24 (a)-(c). Note that the experimental results, presented in Figure 6.23 (a)-(c) and Figure 6.24 (a)-(c) are corresponding to the simulation results of Figure 6.17 (a)-(c) and Figure 6.18 (a)-(c), respectively.

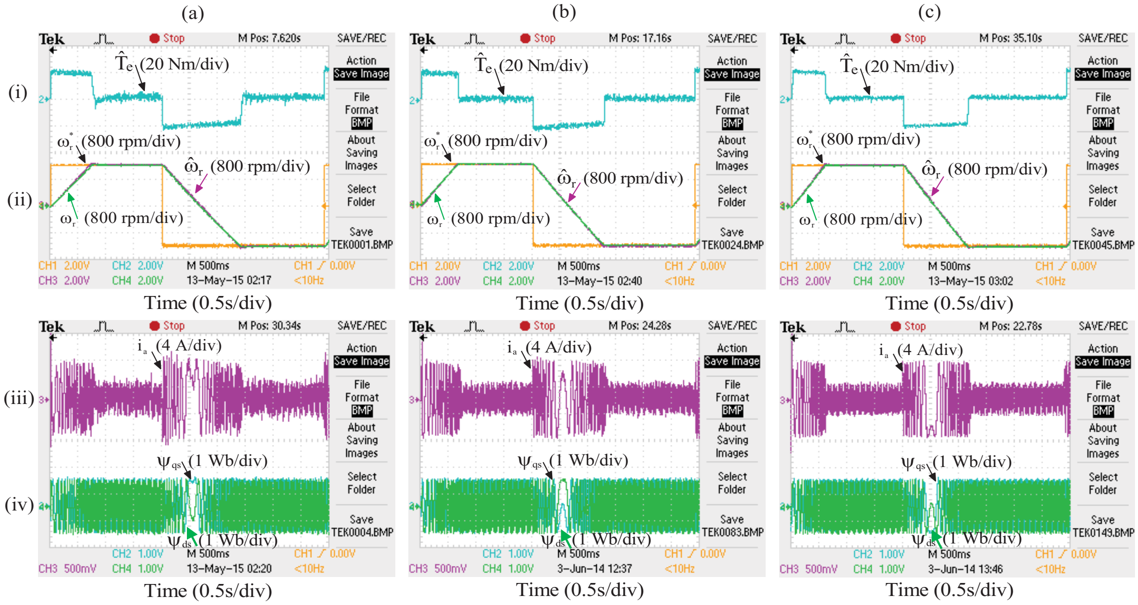

Figure 6.23: Performance under reversal speed command using: (a) PIC, (b) T1FLC and (c) T2FLC: (i) Torque, (ii) speed, (iii) stator current and (iv) stator flux dq-components

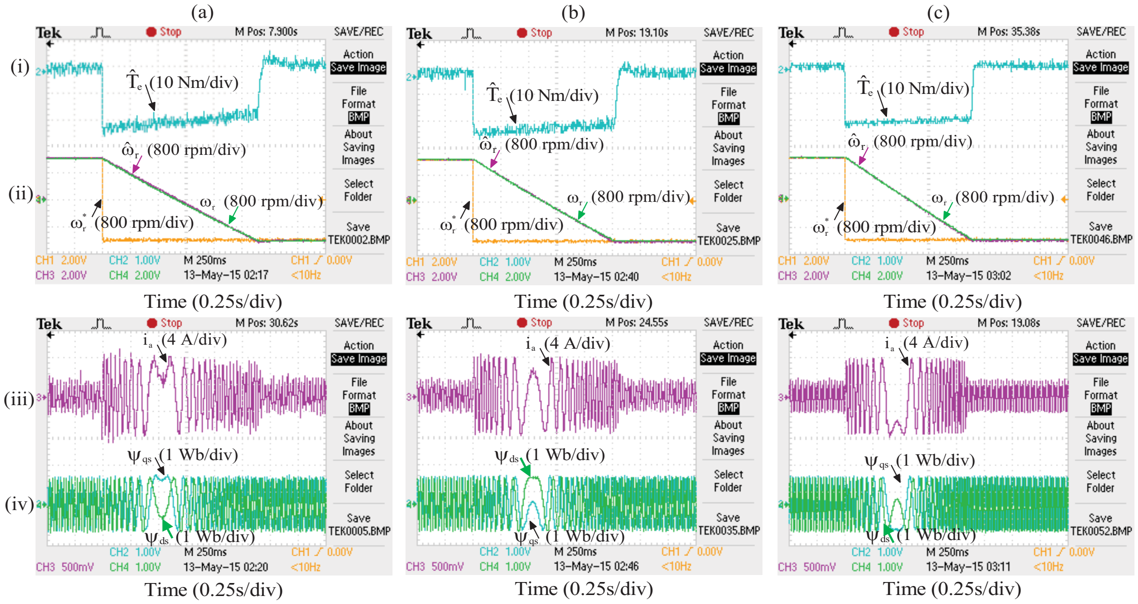

Figure 6.24: Transient performance under the reversal speed command using: (a) PIC, (b) T1FLC and (c) T2FLC: (i) Torque, (ii) speed, (iii) stator current and (iv) stator flux dq-components

6.5.3 Tracking Performance of Various Speed Commands

Tracking performance of the estimated speed is observed under the step and square change in speed commands. The performance of the speed sensorless IMD under such speed commands are presented in the following sections.

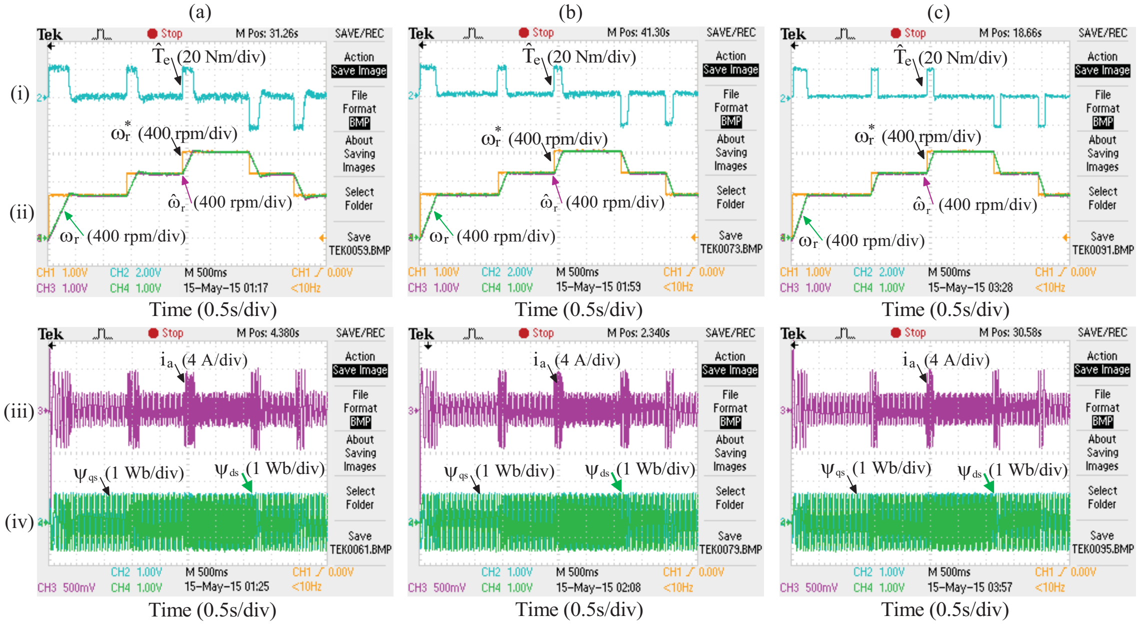

Figure 6.25: Performance under a step change in speed command using: (a) PIC, (b) T1FLC and (c) T2FLC: (i) Torque, (ii) speed, (iii) stator current and (iv) stator flux dq-components in the stationary reference frame

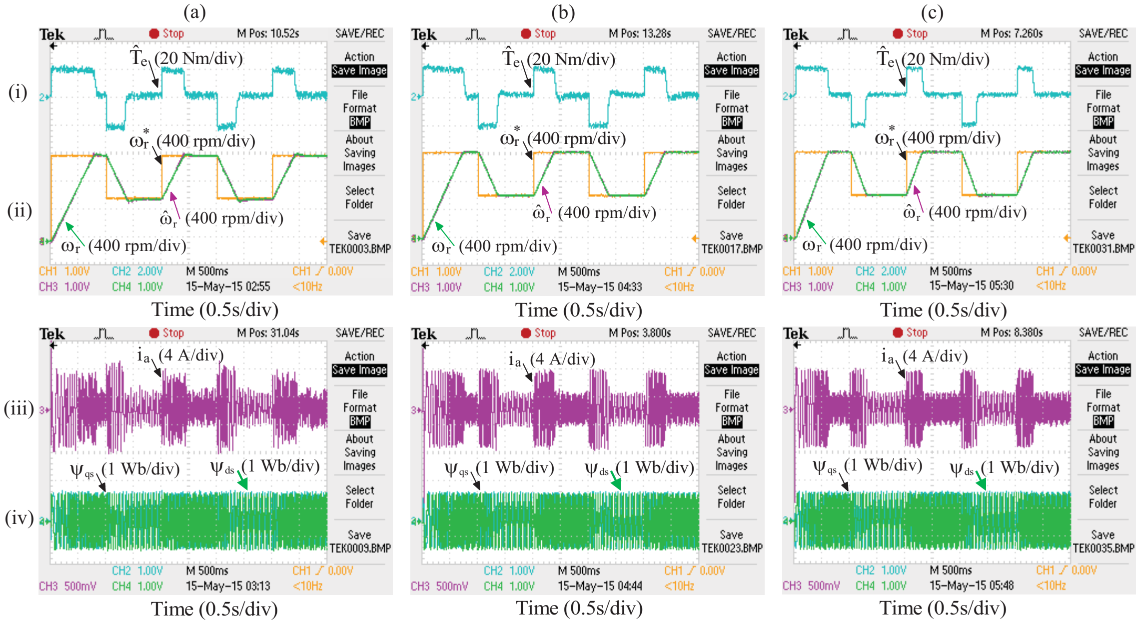

Figure 6.26: Performance under square change in speed command using: (a) PIC, (b) T1FLC and (c) T2FLC: (i) Torque, (ii) speed, (iii) stator current and (iv) stator flux dq-components

Performance under step change in speed command:

The step change in speed command of 300 rpm is applied in four steps (i.e. 600 rpm → 900 rpm → 1200 rpm → 900 rpm → 600 rpm) at 1.4 s, 2.4 s, 3.6 s, etc. The corresponding reference speed, actual and estimated speed responses under such speed commands are shown in Figure 6.25 (a)-(c). From Figure 6.25 (ii), it is observed that the estimated is speed settled (i.e. from 600 to 900 rpm) in 0.29 s, 0.2 s and 0.148 s using PIC, T1FLC and T2FLC schemes, respectively. Moreover, it is also observed that the steady state error between the actual and estimated speed is negligible using T2FLC compared to T1FLC and PIC scheme. The torque, stator current and stator flux dq-components are shown in Figure 6.25 (i), (iii)-(iv), respectively. Note that the experimental results, presented in Figure 6.25 (a)-(c) are corresponding to the simulation results of Figure 6.19 (a)-(c).

Performance under square change in speed command:

The square change in speed command of 600 rpm is applied in four steps (i.e. 1200 rpm → 600 rpm → 1200 rpm → 600 rpm → 1200 rpm) at 1 s, 2 s, 3 s, etc. The corresponding responses are shown in Figure 6.26 (a)-(c). The reference speed, actual and estimated speeds are presented in Figure 6.26 (ii), it is observed that under such speed command the estimated speed settles the set reference speed (i.e. from 600 rpm to 1200 rpm) in 0.51 s, 0.376 s and 0.305 s with an overshoot of around 1.625%, 0.183% and 0.0% of the reference speed using PIC, T1FLC and T2FLC scheme, respectively. The torque, stator current and stator flux dq-components are shown in Figure 6.26 (i), (iii)-(iv), respectively. It is noticed that the estimated speed accurately tracks the reference speed and also settles quickly using T2FLC scheme compared to T1FLC and PIC scheme, respectively. Note that the experimental results, presented in Figure 6.26 (a)-(c) are corresponding to the simulation results of the Figure 6.20 (a)-(c).

6.5.4 Loading Performance

The sudden load torque of 5 Nm is applied at 1.4 s when IM is operating at steady state speed (i.e. 1200 rpm) as shown in Figure 6.27 (a)-(c). When the sudden load torque is applied, the IM draws large amplitude of stator current, i.e. ±4.0 A, ±3.81 A and ±3.6 A using PIC, T1FLC and T2FLC schemes as shown in Figure 6.27 (iii). From Figure 6.27 (i), it is observed that the sudden application of load torque causes an undershoot in estimated speed around 1.416%, 0.667% and 0.33% of the reference speed using PIC, T1FLC and T2FLC schemes, respectively. It is also observed that the recovery time of the estimated speed under sudden load torque operation is 0.3 s, 0.1 s and 0.05 s using PIC, T1FLC and T2FLC schemes, respectively. From Figure 6.27 (ii), it is observed that the ripple content in torque is ±1.63 Nm, ±1.12 Nm and ±0.79 Nm using PIC, T1FLC and T2FLC schemes. Hence, the torque and stator current ripple contents using T1FLC scheme are enhanced by around 31.28% and 4.75% over PIC, whereas T2FLC scheme is improved by 29.46% and 5.51% over T1FLC scheme.

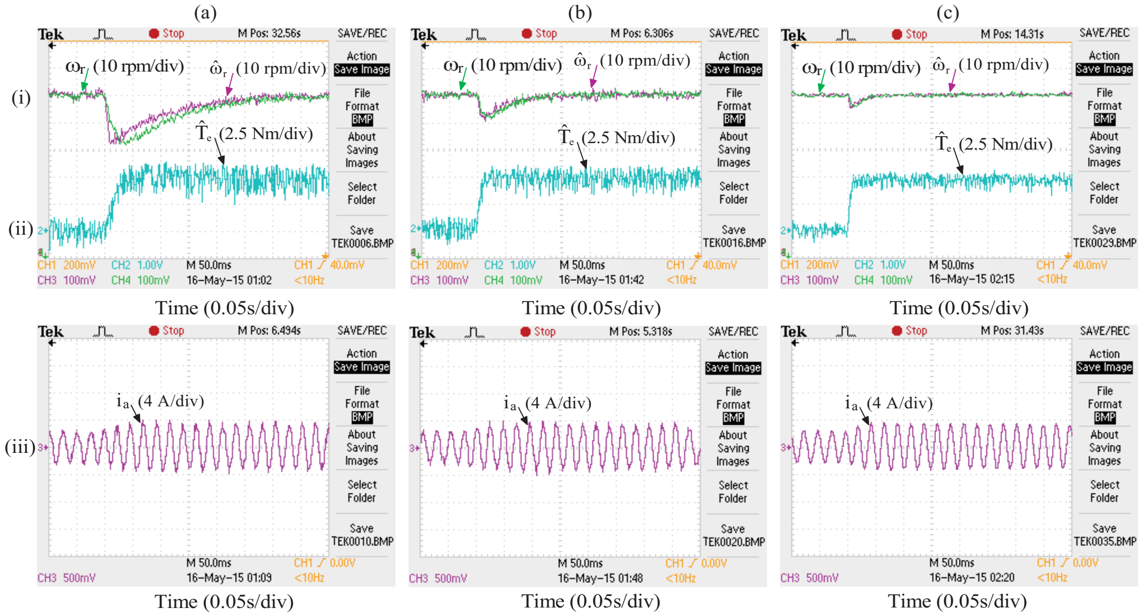

Figure 6.27: Performance under sudden load torque operation at 1200 rpm using: (a) PIC, (b) T1FLC and (c) T2FLC: (i) speed, (ii) torque and (iii) stator current

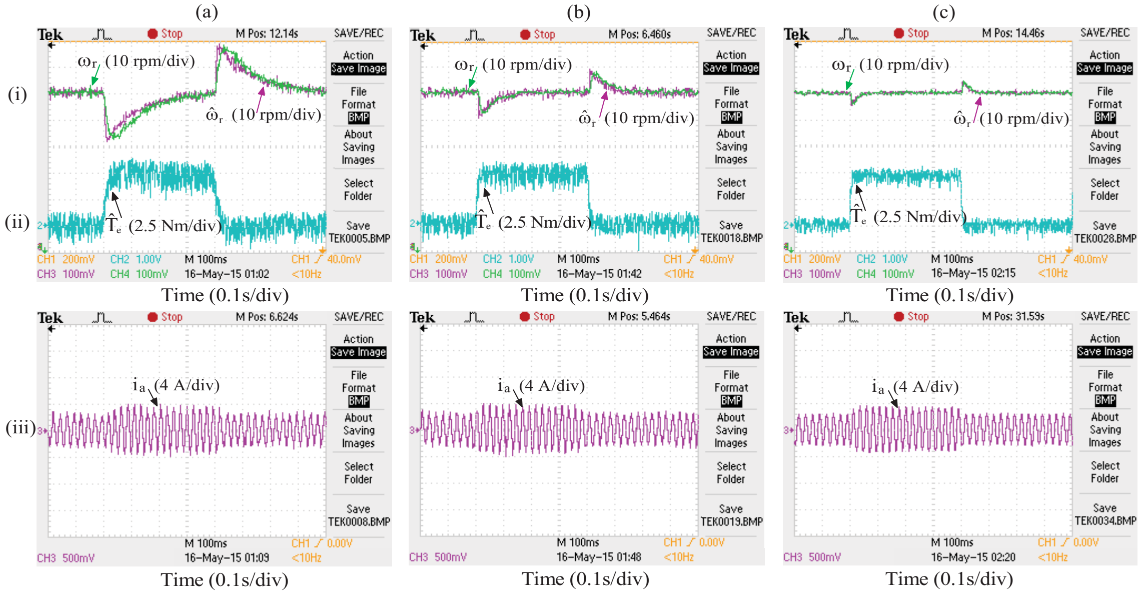

Figure 6.28: Performance under loading and unloading torque at 1200 rpm using: (a) PIC, (b) T1FLC and (c) T2FLC: (i) speed, (ii) torque and (iii) stator current

The sudden load torque of 5 Nm is withdrawn at 1.8 s as shown in Figure 6.28 (a)-(c). When the load torque is withdrawn, an overshoot appears in the estimated speed around 1.46%, 0.7% and 0.33% of the reference speed using PIC, T1FLC and T2FLC schemes is shown in Figure 6.28 (i). It is also observed that the recovery time of the estimated speed under sudden load torque condition is 0.3 s, 0.11 s and 0.045 s using PIC, T1FLC and T2FLC schemes, respectively. The T2FLC scheme shows faster dynamic response compared to the PIC and T1FLC schemes. Hence, the settling time using T1FLC scheme is improved by

63.33% over PIC, whereas T2FLC scheme is improved by 59% over T1FLC scheme. From Figure 6.28 (iii), it is observed that when the load torque is withdrawn the current drops down to ±2.85 A, ±2.6 A and ±2.4 A using PIC, T1FLC and T2FLC scheme, respectively. The torque responses under such commands are presented in Figure 6.28 (ii). The performance of the sensorless drive is also observed under various load torque disturbances at a steady-state speed of 1200 rpm using PIC, T1FLC and T2FLC schemes, which are illustrated in Table 6.5.

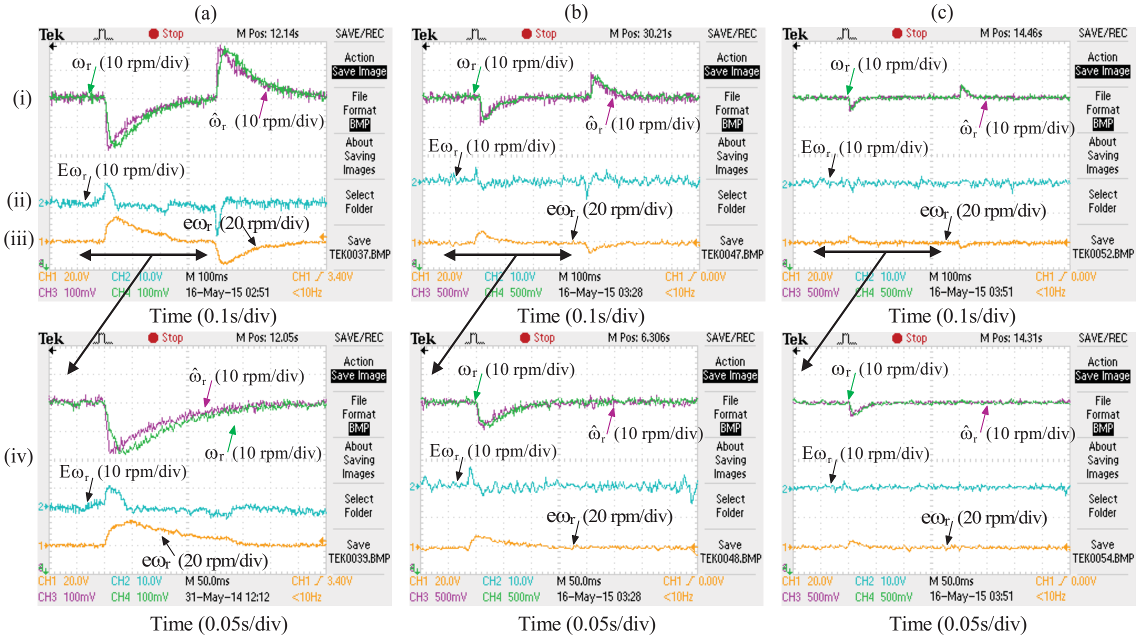

Figure 6.29: Performance under load torque operation at 1200 rpm using: (a) PIC, (b) T1FLC and (c) T2FLC: (i) speed, (ii) error speed, (iii) actual error speed and (iv) zoom of speed and error speeds

Table 6.5: Comparison of three control schemes under different load torque conditions at 1200 rpm

Load Torque	Controller	Under Load Torque Applied		Under Load Torque Withdrawn	
		Speed Undershoot (rpm)	Recovery Time (s)	Speed Overshoot (rpm)	Recovery Time (s)
2	PIC	6.22	0.202	5.89	0.208
	T1FLC	3.18	0.069	3.13	0.074
	T2FLC	1.65	0.030	1.76	0.029
3	PIC	9.52	0.229	9.38	0.236
	T1FLC	4.62	0.078	4.95	0.089
	T2FLC	2.34	0.034	2.34	0.031
4	PIC	13.4	0.246	13.2	0.278
	T1FLC	6.18	0.094	6.11	0.106
	T2FLC	3.18	0.041	3.18	0.038
5	PIC	17.1	0.280	16.8	0.300
	T1FLC	7.46	0.090	7.45	0.140
	T2FLC	3.80	0.040	3.82	0.042

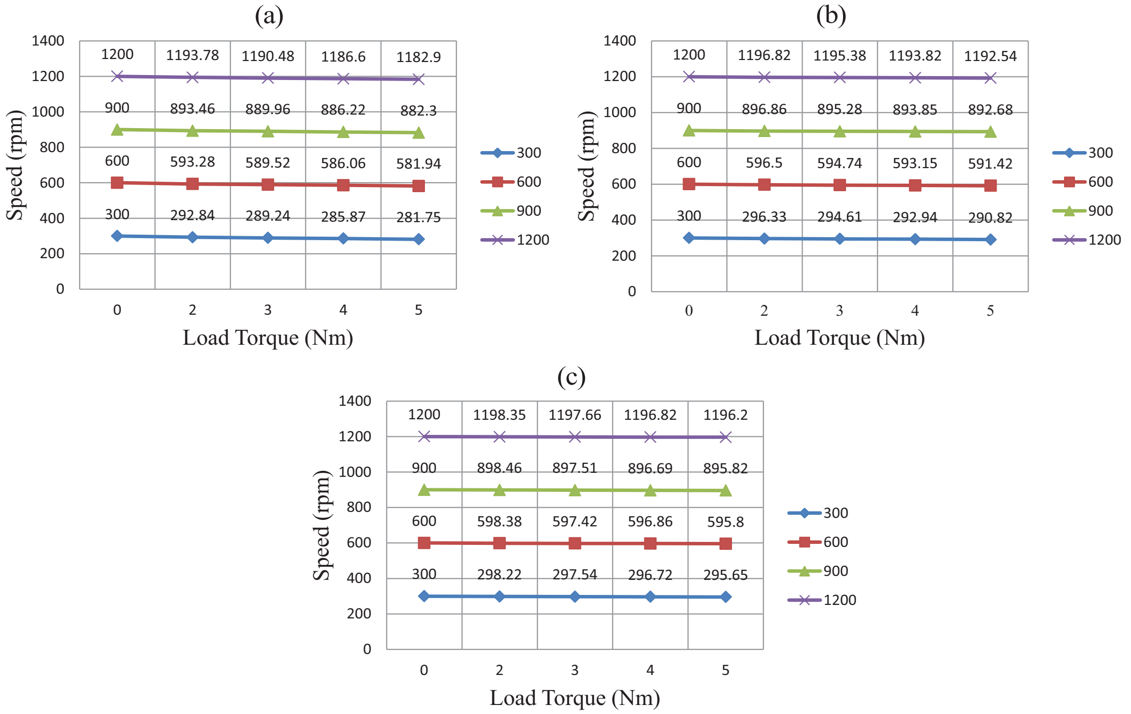

Figure 6.30: Steady-state performance of the estimated speed under various load torque conditions at different speed commands using: (a) PIC, (b) T1FLC and (c) T2FLC

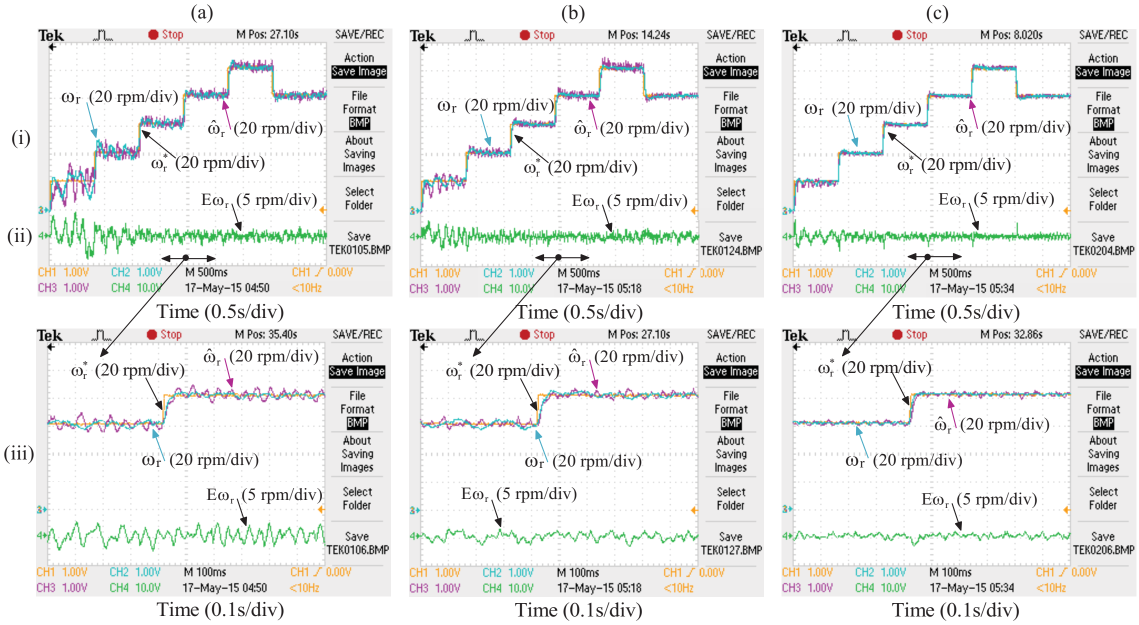

Figure 6.31: Performance of the sensorless IMD under the step change in acceleration speed command using: (a) PIC, (b) T1FLC and (c) T2FLC: (i) speed and (ii) error speed and (iii) zoom of speed and error speed

The speed errors under load torque disturbance condition using three control schemes are presented in Figure 6.29 (a)-(c). The estimated speed error ($E\omega_r = \omega_r - \hat{\omega}_r$) and the actual speed error ($e\omega_r = \omega_r^* - \omega_r$) are shown in Figure 6.29 (ii) and (iii), respectively. From Figure

6.29 (ii), it is observed that the estimated speed error appears around 7.8 rpm, 4.51 rpm and 2.4 rpm of the reference speed, when sudden load torque is applied and it is withdrawn.

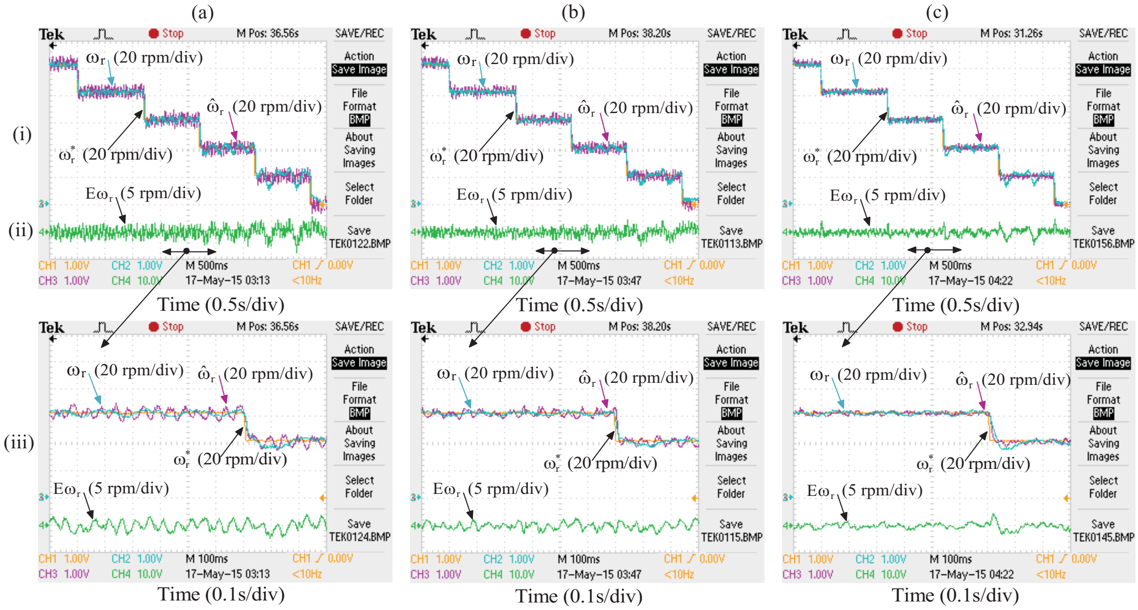

Figure 6.32: Performance of the sensorless IMD under the step change in deceleration speed command using: (a) PIC, (b) T1FLC and (c) T2FLC: (i) speed, (ii) error speed and (iii) zoomed view

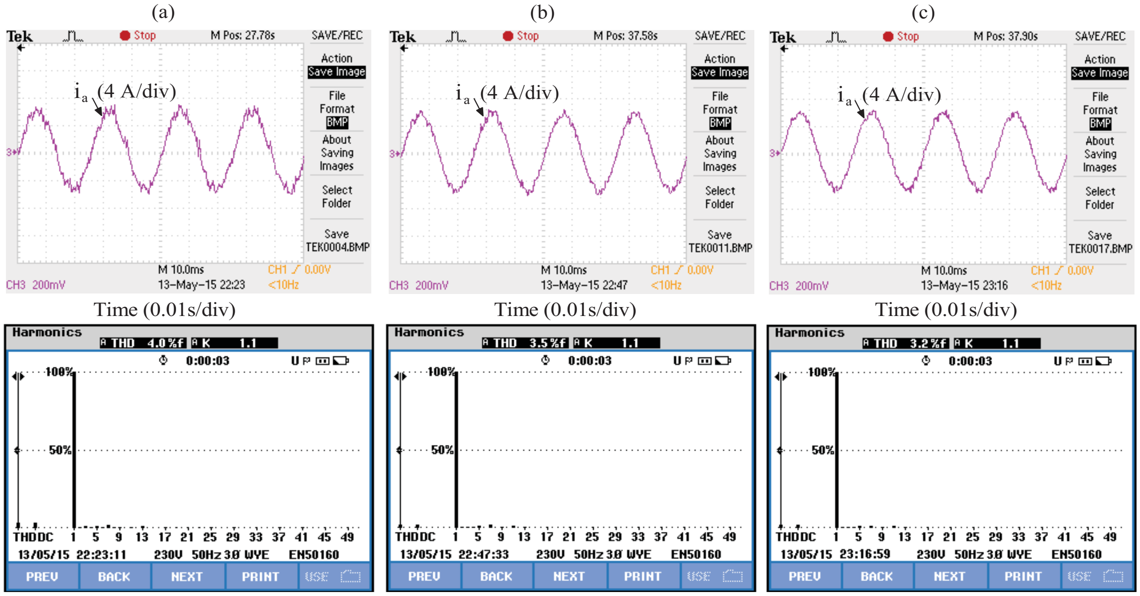

Figure 6.33: THD performance of the stator current using: (a) PIC, (b) T1FLC and (c) T2FLC.

The effect of different load torque conditions is observed under different speed commands using PIC, T1FLC and T2FLC schemes are illustrated in Figure 6.30 (a)-(c). It is observed from the experimental results that the T2FLC scheme shows an excellent performance and robustness to various load torque disturbances compared to PIC and T1FLC scheme, respectively.

6.5.5 Performance under Low Speed Operation

Tracking performance of the sensorless IMD is observed under very low speed operation, such as step-up (i.e. acceleration mode) and step-down (i.e. deceleration mode) speeds from 0 rpm to 100 rpm and 100 rpm to 0 rpm, respectively.

Step-up speed from 0 rpm to 100 rpm in a series of five 20 rpm steps:

The change in speed command from 0 rpm to 100 rpm is applied in a series of five 20 rpm steps using three control schemes are shown in Figure 6.31 (a)-(c). The step change in speed command of 20 rpm is applied in six steps (i.e. 0 rpm→20 rpm→40 rpm→60 rpm→80 rpm →100 rpm→80 rpm) at a time interval of 0.8 s (i.e. 0.8 s→1.6 s→ etc). The reference, actual and estimated speeds are available in Figure 6.31 (i) and the estimated speed error is shown in Figure 6.31 (ii). Unstable operation is observed with high disturbances at a speed of 20 rpm using PIC scheme, while stable operation with fewer disturbances obtained using T2FLC scheme, respectively. The zoomed view of Figure 6.31 (i)-(ii) is presented in Figure 6.31 (iii).

Table 6.6: Comparison of three control schemes under various operating conditions

Measured Parameter	Simulation Results					Experimental Results				
	PIC	T1FL-C	%T1FL-CIOPI	T2FLC	%T2FL-CIOT1	PIC	T1FLC	%T1FL-CIOT1	T2FL-C	%T2FL-CIOT1
± T_{dNLT} (Nm)	0.925	0.615	33.51	0.405	34.14	1.40	1.02	27.14	0.76	25.49
± ψ_{dNLT} (Wb)	0.015	0.010	33.33	0.006	40.00	0.10	0.07	30.00	0.06	14.28
ω_{cLTA} (%)	12.00	4.800	60.00	2.000	58.33	17.1	7.46	56.37	3.82	49.06
ω_{cLTW} (%)	11.50	4.400	61.73	2.100	52.27	16.8	7.45	55.65	3.82	48.72
t_{ss} (s)	0.650	0.520	19.69	0.489	5.961	0.81	0.710	12.34	0.658	7.324
t_{sr} (s)	3.160	3.040	3.797	2.920	3.948	3.46	3.28	5.202	3.130	4.573
t_{scss} (s)	0.220	0.136	38.18	0.120	11.76	0.29	0.200	32.65	0.148	26.00
t_{scsqs} (s)	0.442	0.280	36.65	0.260	7.143	0.51	0.376	26.56	0.305	18.88
t_{sLTA} (s)	0.230	0.05	78.26	0.030	40.00	0.28	0.090	67.85	0.04	55.55
t_{sLTW} (s)	0.220	0.06	72.72	0.031	48.33	0.31	0.14	54.83	0.042	70.00
$e\omega_r$ (rpm)	12.00	4.80	60.00	2.000	58.33	17.1	7.45	56.37	3.82	49.06
$E\omega_r$ (rpm)	4.100	1.90	53.65	0.850	55.26	7.80	4.51	42.17	2.40	46.78
I_{THD} (%)	3.200	2.82	11.87	2.540	9.929	4.00	3.50	12.50	3.20	8.571

Similarly, the sudden change in speed command from 100 rpm to 0 rpm is applied in a series of five 20 rpm steps using three control schemes are shown in Figure 6.32 (a)-(c). It is observed that under low speed operation the T2FLC scheme shows better performance with less steady-state errors compared to the PIC and T1FLC. The percentage of line current THDs for DTFC-SVM of a sensorless IMD using PIC, T1FLC and T2FLC under no-load operation is shown in Figure 6.33 (a)-(c). The corresponding values are 4.0, 3.5 and 3.2, respectively. From Figure 6.33, it is observed that the T2FLC offers less current THD compared to T1FLC and PIC, respectively.

The comparative performance of the sensorless IMD using PIC, T1FLC and T2FLC under various operating conditions, such as, at starting, reversal speed, step change in speed, square change in speed and change in speed during load torque applied and is withdrawn are illustrated in Table 6.6 in detail. Where, T_{rNLT}, ψ_{rNLT}, ω_{cLTA}, ω_{cLTW}, t_{ss}, t_{sr}, t_{scss}, t_{scsqs}, t_{sLTA}, t_{sLTW}, $\%I_{THD}$, %T1FLCIOPI and %T2FLCIOT1 represent the no-load torque ripples (Nm), stator flux ripples (Wb), change in speed during load torque applied (rpm), change in speed during load torque withdrawn (rpm), settling time during starting (s), settling time during reversal speed (s), settling time during change in step speed (s), settling time during change in speed during square change in speed (s), settling time during load torque applied (s), settling time during load torque withdrawn (s), percentage of stator current THD, percentage of T1FLC improvement over PI controller and percentage of T2FLC improvement over T1FLC, respectively.

6.6 Conclusion

In this chapter, DTFC-SVM of a sensorless IMD using PIC, T1FLC and T2FLC are presented. Initially, PIC based DTFC-SVM of a SSIMD is implemented. This scheme shows significant ripples in torque, flux, speed and stator current and also takes a long time to reach the steady-state under load torque disturbances. In order to enhance the performance of the sensorless drive, PICs are replaced by T1FLCs. It shows better performance compared to PIC scheme. Furthermore, T1FLCs are replaced by T2FLCs to further enhance the performance of the sensorless drive. It shows improved dynamic as well as steady-state performance and also robust to various load torque disturbances and sudden change in speed conditions. A detailed simulation and experimental comparison of the three control schemes has been carried out in a speed sensor and speed sensorless mode of operation under no-load, load, various changes in speed and low speed operating conditions, respectively. The simulation and experimental system verification confirm that the T2FLC scheme shows better dynamic as well as steady-state performance and is capable of sudden change in speed and robustness to load torque disturbance rejection. Moreover, it is also noticed that the T2FLC perform satisfactorily in all speed ranges with different loading conditions compared to T1FLC and PICs, respectively.

The DTFC-SVM of a sensorless IMD offers satisfactory performance over a wide range of operation and also simple to implement. However, the machine parameter variation (i.e. stator resistance Rs) with temperature is a major problem in rotor-flux based MRAS speed estimation over a wide range of speed operation. Therefore, these aspects will be studied in the next chapter.

Chapter 7

Stator Resistance Estimation

CHAPTER 7: STATOR RESISTANCE ESTIMATION

The parameter sensitivity with the temperature variation is the major issue of a rotor-flux based MRAS (RFMRAS) speed estimation technique, especially at low speed operation. Therefore, in order to overcome this issue, a parallel RFMRAS rotor speed and stator resistance estimation for DTFC-SVM of speed sensorless IMD is proposed to enhance the performance of the speed sensorless drive under parameter variations at low speed operation. In the proposed scheme, the PIC is replaced by T1FLC to enhance the performance of the sensorless drive. Furthermore, the T1FLC is replaced by Type-2 FLC to enhance the performance of the speed sensorless IM drive under parameter variation (i.e. stator resistance). Finally, the proposed schemes are simulated in the MATLAB/SIMULINK environment under low speed operation with speed sensor and speed sensorless modes. Moreover, the proposed schemes are experimentally validated by the laboratory developed EPS using dSPACE DS-1104 controller board and the experimental results are presented.

This chapter is organized as follows:

- *The detail of stator resistance sensitivity is presented in section 7.1.*
- *The mathematical modeling of a parallel RFMRAS rotor speed and stator resistance estimation is presented in section 7.2.*
- *The proposed schemes are simulated in the MATLAB/SIMULINK environment and the corresponding results under various operating conditions with speed sensor and speed sensorless are presented in section 7.3.*
- *The simulation results are validated with the experimental results, which are presented in section 7.4.*
- *Finally, section 7.5 presents the conclusion of the system.*

7.1 Introduction

The estimation of rotor speed using the RFMRAS is based on the machine model, it is sensitive to the variation of machine parameters (i.e. stator and rotor resistances). The variation of the stator and rotor resistances with temperature is the major issue at low speed operation [179-183]. These variations affect the performance of the speed sensorless IM drive at low speed operation. The fundamental component of the stator voltage is low during the rotor flux estimation, so, the stator resistance (R_s) drop becomes more analogous to the applied voltage as stator resistance varies with temperature in the voltage model (VM). In the current model (CM), the rotor resistance (R_r) also affect the performance of the sensorless IM drive under low speed operations along with stator resistance [190-201]. However, variations are very slow so that it can be considered as a constant parameter (rotor resistance). The accurate measurement of the stator resistance R_s is essential for proper operation of a sensorless drive in the low speed region, since any discrepancy between the value used within speed observer and actual resistance may lead to a considerable speed estimation error [190-191, 197]. Therefore, continuous adaptation of the stator resistance is highly essential to maintain stable operation under low speed operating conditions.

7.2 Parallel Rotor Speed and Stator Resistance Estimation

The schematic model of parallel RFMRAS rotor speed and stator resistance estimation for DTFC-SVM of speed sensorless IM drive is shown in Figure 7.1. It is an extension of the RFMRAS speed estimator for DTFC-SVM of a speed sensorless IM drive. In this scheme, the stator resistance estimation is developed in conjunction with the rotor speed estimation as shown in Figure 7.1.

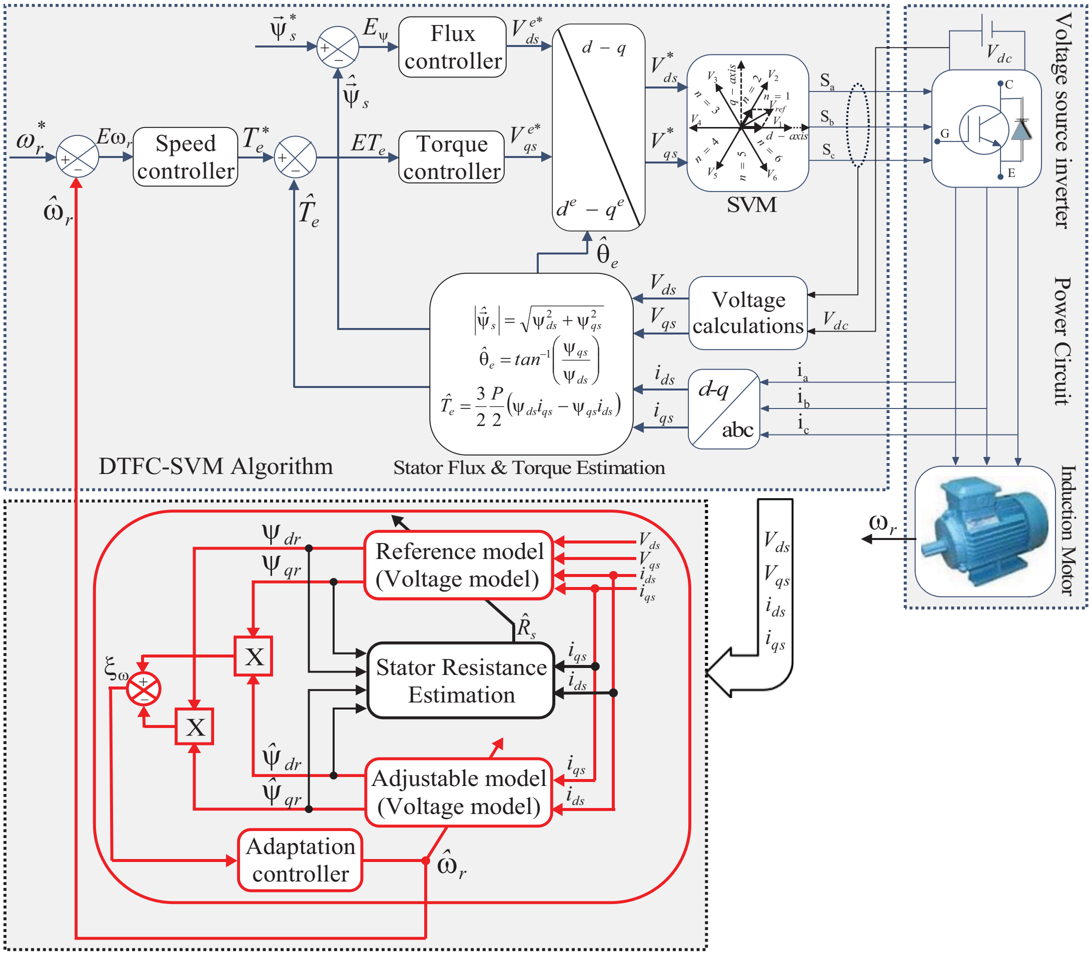

Figure 7.1: Schematic model of parallel RFMRAS rotor speed and stator resistance estimation for DTFC-SVM of speed sensorless IMD

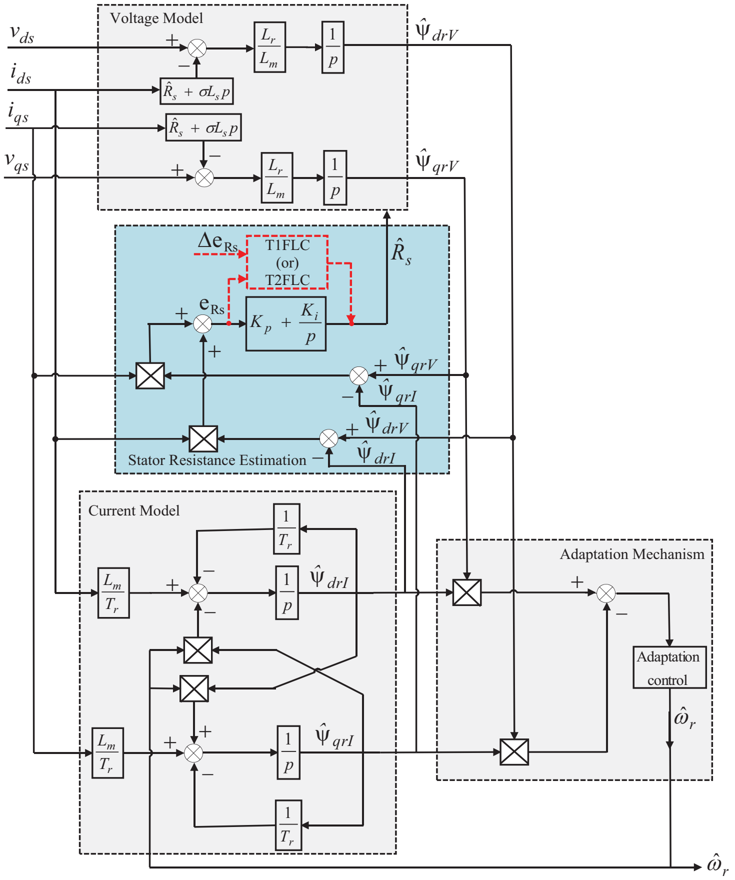

Figure 7.2: Internal model of parallel rotor speed and stator resistance estimation

The stator resistance estimation block is used to estimate the accurate value of rotor speed under very low speed operations by suppressing the effect of change in stator resistance. The RM/VM is implemented using measured stator voltage and current quantities, whereas AM/CM is implemented using measured stator current and estimated rotor speed quantities [190]. These two models are used to estimate the rotor flux linkage. In this scheme, the VM and CM are exactly same as in the RFMRAS speed estimation, which is explained in section 5.2. The internal schematic model of the stator resistance estimator is shown in Figure 7.2.

The equations (5.33) and (5.34) can be rewritten as [114, 191]:

$$\psi_{drV} = \frac{L_r}{L_m}\int (V_{ds} - \left(R_s + \sigma L_s p\right) i_{ds})dt \tag{7.1}$$

$$\psi_{qrV} = \frac{L_r}{L_m}\int (V_{qs} - \left(R_s + \sigma L_s p\right) i_{qs})dt \tag{7.2}$$

$$\vec{\psi}_{rV} = \psi_{drV} + j\psi_{qrV} \tag{7.3}$$

The equations (5.36) and (5.37) can be rewritten as:

$$\psi_{drI} = \int\left(\frac{L_m}{T_r} i_{ds} - \frac{1}{T_r}\psi_{drI} - \hat{\omega}_r \psi_{qrI}\right)dt \tag{7.4}$$

$$\psi_{qrI} = \int\left(\frac{L_m}{T_r} i_{qs} - \frac{1}{T_r}\psi_{qrI} + \hat{\omega}_r \psi_{drI}\right)dt \tag{7.5}$$

$$\vec{\psi}_{rI} = \psi_{drI} + j\psi_{qrI} \tag{7.6}$$

where $\vec{\psi}_{rV}$ and $\vec{\psi}_{rI}$ are outputs of the VM and CMs.

In order to make the system asymptotically stable, the parallel rotor speed and stator resistance are estimated using the concept of Hyperstability theory [116, 190-191]. Similar to the speed estimation (which is presented in section 5.2), the differences between the state-variables of the RM and AM are adapted as a resistance tuning signal, which is then fed into a PIC and it produces the estimated stator resistance. For the purpose of deriving an **AM** it is valid to initially treat rotor speed as a constant parameter, since it changes slowly compared to the change in rotor flux. The stator resistance of the motor varies with temperature, but variations are slow so that it can be treated as a constant parameter, too [190].

Initially, for the purpose of designing **AM** the error equations $\left(\vec{\varepsilon}_V \ and\, \vec{\varepsilon}_I\right)$ are treated as state variables of the linear model and these are represented by the following equations [191].

$$p\vec{\varepsilon}_V = -\frac{L_r}{L_m}\left(R_s - \hat{R}_s\right)\cdot \vec{i}_s \tag{7.7}$$

$$\vec{\varepsilon}_V = \vec{\psi}_{rV} - \hat{\vec{\psi}}_{rV} = \varepsilon_{dV} + j\varepsilon_{qV} \tag{7.8}$$

$$p\vec{\varepsilon}_I = -\frac{1}{T_r}\vec{\varepsilon}_I + j\omega_r\vec{\varepsilon}_I + j\left(\omega_r - \hat{\omega}_r\right)\cdot \hat{\vec{\psi}}_{rI} \tag{7.9}$$

$$\vec{\varepsilon}_I = \vec{\psi}_{rI} - \hat{\vec{\psi}}_{rI} = \varepsilon_{dI} + j\varepsilon_{qI} \tag{7.10}$$

By separating the real and imaginary parts from the equations (7.9) and (7.7) and representing in matrix form, we get [190-191]:

$$p\begin{bmatrix} \varepsilon_{dI} \\ \varepsilon_{qI} \\ \varepsilon_{dV} \\ \varepsilon_{qV} \end{bmatrix} = \begin{bmatrix} -\frac{1}{T_r} & -\omega_r & 0 & 0 \\ \omega_r & -\frac{1}{T_r} & 0 & 0 \\ 0 & 0 & 0 & 0 \\ 0 & 0 & 0 & 0 \end{bmatrix}\begin{bmatrix} \varepsilon_{dI} \\ \varepsilon_{qI} \\ \varepsilon_{dV} \\ \varepsilon_{qV} \end{bmatrix} - \begin{bmatrix} 0 & \Delta\omega & 0 & 0 \\ -\Delta\omega & 0 & 0 & 0 \\ 0 & 0 & \frac{L_r}{L_m}\Delta R_s & 0 \\ 0 & 0 & 0 & \frac{L_r}{L_m}\Delta R_s \end{bmatrix}\begin{bmatrix} \hat{\psi}_{drI} \\ \hat{\psi}_{qrI} \\ i_{ds} \\ i_{qs} \end{bmatrix} \tag{7.11}$$

where $\Delta\omega = \omega_r - \hat{\omega}_r$ and $\Delta R_s = R_s - \hat{R}_s$

The above equation can be represented as follows:

$$p[\varepsilon] = [A][\varepsilon] - [W] \tag{7.12}$$

where $[\varepsilon]^T = \left[\varepsilon_{dI} \quad \varepsilon_{qI} \quad \varepsilon_{dV} \quad \varepsilon_{qV}\right] = \left[\vec{\varepsilon}_I^T \quad \vec{\varepsilon}_V^T\right]$, $\hat{\vec{\psi}}_{rI} = [\hat{\psi}_{drI} \quad \hat{\psi}_{qrI}]^T$, $\vec{i}_s = [i_{ds} \quad i_{qs}]^T$

$$[W]=\left[\begin{array}{c|c} -\Delta\omega\begin{bmatrix}0 & -1\\ 1 & 0\end{bmatrix} & \begin{matrix}0 & 0\\ 0 & 0\end{matrix} \\ \cdots\cdots\cdots\ \cdots\cdots\cdots & \cdots\cdots\cdots\ \cdots\cdots \\ \begin{matrix}0 & 0\\ 0 & 0\end{matrix} & \frac{L_r}{L_m}\Delta R_s\begin{bmatrix}1 & 0\\ 0 & 1\end{bmatrix}\end{array}\right]\begin{bmatrix}\hat{\psi}_{drI}\\ \hat{\psi}_{qrI}\\ i_{ds}\\ i_{qs}\end{bmatrix}=\left[\begin{array}{c|c} -\Delta\omega J & 0\\ \cdots\ \cdots\cdots\cdots & \cdots\cdots\ \cdots\cdots \\ 0 & \frac{L_r}{L_m}\Delta R_s I\end{array}\right]\begin{bmatrix}\hat{\vec{\psi}}_{rI}\\ \vec{i}_s\end{bmatrix},$$

$$[A]=\begin{bmatrix}-\frac{1}{T_r} & -\omega_r & 0 & 0\\ \omega_r & -\frac{1}{T_r} & 0 & 0\\ 0 & 0 & 0 & 0\\ 0 & 0 & 0 & 0\end{bmatrix},\ J=\begin{bmatrix}0 & -1\\ 1 & 0\end{bmatrix},\ 0=\begin{bmatrix}0 & 0\\ 0 & 0\end{bmatrix}\text{ and } I=\begin{bmatrix}1 & 0\\ 0 & 1\end{bmatrix}.$$

By substituting $[\varepsilon]$ and $[W]$ in equation (5.38), we get Popov's criterion for the present system as follows [114, 191]:

$$S=\int_0^t\left[\vec{\varepsilon}_I^T\ \ \vec{\varepsilon}_V^T\right]\left[\begin{array}{c|c} -\Delta\omega J & 0\\ \cdots\ \cdots\cdots\cdots & \cdots\cdots\ \cdots\cdots \\ 0 & \frac{L_r}{L_m}\Delta R_s I\end{array}\right]\begin{bmatrix}\hat{\vec{\psi}}_{rI}\\ \vec{i}_s\end{bmatrix}dt\geq-\gamma^2\quad\forall\ t_1\geq 0 \tag{7.13}$$

The equation (7.13) can be rewritten as:

$$S=-\int_0^t\Delta\omega(\vec{\varepsilon}_I^T\cdot J\cdot\hat{\vec{\psi}}_{rI})dt+\frac{L_r}{L_m}\int_0^t\Delta R_s(\vec{\varepsilon}_V^T\cdot\vec{i}_s)\,dt\geq-\gamma^2\qquad\forall\ t_1\geq 0 \tag{7.14}$$

$$S=S_1+\frac{L_r}{L_m}S_2\geq-\gamma^2\qquad\forall\ t_1\geq 0 \tag{7.15}$$

The validity of equation (7.15) can be verified by means of inequalities (7.16) and (7.17) with adaptive mechanisms are given in (7.18), (7.19) for rotor speed estimation and stator resistance identification, respectively [114, 191]:

$$S_1=-\int_0^t\Delta\omega\left(\vec{\varepsilon}_I^T\cdot J\cdot\hat{\vec{\psi}}_{rI}\right)dt\geq-\gamma_1^2\qquad\forall\ t_1\ \geq\ 0 \tag{7.16}$$

$$S_2=\int_0^t\Delta R_s\left(\vec{\varepsilon}_V^T\cdot\vec{i}_s\right)dt\geq-\gamma_2^2\qquad\forall\ t_1\ \geq\ 0 \tag{7.17}$$

$$\hat{\omega}_r=\left(K_{p\omega}+\frac{K_{I\omega}}{p}\right)\left(\vec{\varepsilon}_I^T\cdot J\cdot\hat{\vec{\psi}}_{rI}\right)=\left(K_{p\omega}+\frac{K_{I\omega}}{p}\right)e_{\omega} \tag{7.18}$$

$$\hat{R}_s=\left(K_{pR_s}+\frac{K_{IR_s}}{p}\right)\left(-\vec{\varepsilon}_V^T\cdot\vec{i}_s\right)=\left(K_{pR_s}+\frac{K_{IR_s}}{p}\right)e_{R_s} \tag{7.19}$$

where $K_{p\omega}, K_{I\omega}, K_{pR_s}$ and K_{IR_s} are PIC parameters of rotor speed and stator resistance adaptation mechanisms, respectively.

In order to calculate the error quantity for rotor speed estimation, the output of the voltage model is taken as equal to the true rotor flux linkage space vector i.e. $\vec{\psi}_{rI} \equiv \hat{\vec{\psi}}_{rV}$

By substituting the above relation in equation (7.10), we get:

$$\vec{\varepsilon}_I = \hat{\vec{\psi}}_{rV} - \hat{\vec{\psi}}_{rI} \tag{7.20}$$

By using equations (7.18) and (7.20) the error quantity for speed estimation can be derived as:

$$e_{\omega} = \vec{\varepsilon}_I^{\,T} \cdot J \cdot \hat{\vec{\psi}}_{rI} == \hat{\psi}_{drI}\hat{\psi}_{qrV} - \hat{\psi}_{drV}\hat{\psi}_{qrI} \tag{7.21}$$

In order to calculate the error quantity for stator resistance estimation, the output of the current model is taken as equal to the true rotor flux linkage space vector i.e. $\vec{\psi}_{rV} \equiv \hat{\vec{\psi}}_{rI}$

By substituting the above relation in equation (7.8), we get:

$$\vec{\varepsilon}_V = \hat{\vec{\psi}}_{rI} - \hat{\vec{\psi}}_{rV} \tag{7.22}$$

By using equations (7.19) and (7.22), the error quantity for stator resistance estimation can be derived as:

$$e_{R_s} = -\vec{\varepsilon}_V^{\,T} \cdot \vec{i}_s = i_{ds}\left(\hat{\psi}_{drV} - \hat{\psi}_{drI}\right) + i_{qs}\left(\hat{\psi}_{qrV} - \hat{\psi}_{qrI}\right) \tag{7.23}$$

The error quantities are processed through the PIC of stator resistance estimator, it generates the estimated stator resistance quantities by minimizing the error quantities. However, the constant gain PIC may not provide satisfactory performance under variation of the stator resistance. Therefore, the T1FLC and T2FLC based stator resistance estimation approach are proposed.

7.2.1 Fuzzy Logic Controller based Stator Resistance Estimator

In this method, the PIC of the stator resistance estimator is replaced by the T1FLC to enhance the performance of the estimator with high accuracy and it is relatively robust to parameter variations even at low stator frequencies [192-194]. The T1FLC based stator resistance estimator is shown in Figure 7.2 (shown by the dotted red line).

From the PIC based stator resistance estimator, the output of the controller can be expressed as:

$$\hat{R}_s = K_p e_{R_s} + K_i \int e_{R_s}\, dt \tag{7.24}$$

Applying differentiation on both sides of the equation (7.24), we get:

$$\frac{d\hat{R}_s}{dt} = K_p \frac{de_{R_s}(t)}{dt} + K_i e_{R_s}(t) \tag{7.25}$$

From equation (7.25), it is clear that the change of the resistance is directly proportional to the inputs of resistance control, i.e., error resistance (e_{R_s}) and change of the error resistance (Δe_{R_s}). The design procedure for the T1FLC based resistance controller is similar to the speed estimation, which is explained in the section 5.2.2. The same numbers of triangular based MFs are used in both the inputs (i.e. error and change in error) and the output variable with the same number of rules (i.e. 49), which is illustrated in Table 7.1. The input variables of T1FLC based stator resistance estimator are error resistance ‘ e_{R_s} ’ and rate of change in error resistance ‘ Δe_{R_s} ’ and the output variable is the estimated stator resistance ‘ $\hat{R}_s$ ’ as shown in Figure 7.3 (a).

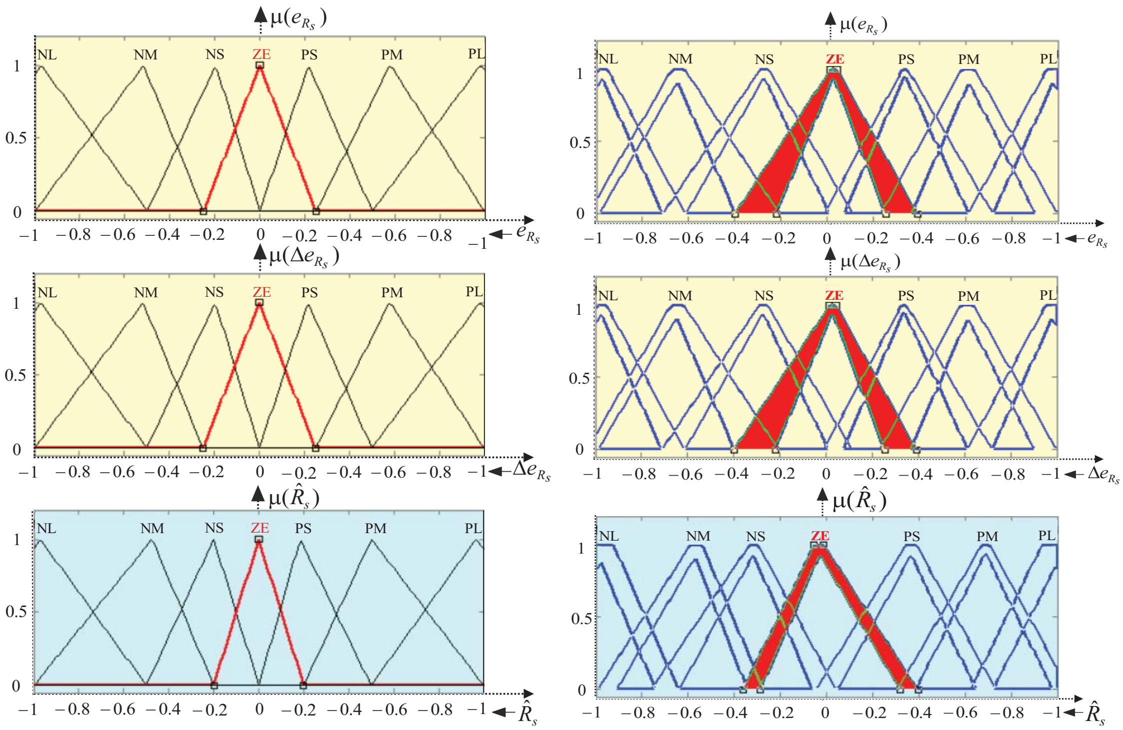
(a)

(b)

Figure 7.3: MFs of FLC based stator resistance estimation: (a) T1FLC and (b) T2FLC

Further, the PIC is replaced by T2FLC to further enhance the performance of the sensorless drive under stator resistance variations. The schematic model of T2FLC based stator resistance estimator is shown in Figure 7.2 (shown by the dotted red line). The input and output triangular MFs of T2FLC are illustrated in Figure 7.3 (b). Here, the number of inputs (i.e. e_{R_s} and Δe_{R_s}) and output ($\hat{R}_s$) MFs are considered remain same as that of the T1FLC to show the improvement of T2FLC over T1FLC. Moreover, the corresponding number of rules for T2FLC is also same as that of T1FLC, which is illustrated in Table 7.1.

Table 7.1: Rule base of T1FLC and T2FLC based stator resistance estimation

Output ($\hat{R}_s$)		**Change in Error Torque** (e_{Rs})						
		NL	**NM**	**NS**	**ZE**	**PS**	**PM**	**PL**
Error Torque (Δe_{Rs})	**NL**	NL	NL	NL	NL	NM	NS	ZE
	NM	NL	NL	NL	NM	NS	ZE	PS
	NS	NL	NL	NM	NS	ZE	PS	PM
	ZE	NL	NM	NS	ZE	PS	PM	PL
	PS	NM	NS	ZE	PS	PM	PL	PL
	PM	NS	ZE	PS	PM	PL	PL	PL
	PL	ZE	PS	PM	PL	PL	PL	PL

7.3 Simulation Results

The parallel RFMRAS rotor speed and stator resistance estimation for DTFC-SVM of a sensorless IM drive (Figure 7.1) is mathematically modelled in the MATLAB/SIMULINK environment using PIC, T1FLC and T2FLC schemes, respectively. Then the simulink model is used to verify the performance of the sensorless IMD under low speed operation with parameter variation. The schematic model is similar to the RFMRAS speed estimator but the stator resistance in the RM is replaced with estimated stator resistance. The rotor flux components of RM are now less sensitive to stator resistance variation. The variation of stator resistance affects the performance of the sensorless drive at low speed operations.

7.3.1 Performance under Parameter Variation

Initially, the performance of the speed sensorless IM drive is simulated under stator resistance variation without parameter estimation (i.e. stator resistance) is shown in Figure 7.4 (a)-(c). The stator resistance (R_s) is increased to 40% of rated value (i.e. R_s to 1.4 R_s) at 1.5 s is shown in Figure 7.4 (ii). The RFMRAS speed estimator is sensitive to the variation of stator resistance. The reference speed (ω_r^*), actual speed (ω_r) and estimated speed ($\hat{\omega}_r$) under such command is shown in Figure 7.4 (i). From Figure 7.4 (i), it is observed that the sudden application of stator resistance variation diverges the estimated speed from the reference speed by around 70 rpm, 50 rpm and 40 rpm using PIC, T1FLC and T2FLC schemes, respectively.

The performance of the speed sensorless drive is observed with stator resistance estimation under low speed (i.e. 100 rpm) operation using three control schemes are shown in Figure 7.5 (a)-(c). The reference speed, actual and estimated speed is shown in Figure 7.5 (i). The actual and estimated stator resistances are shown in Figure 7.5 (ii). Similarly, the performance of the sensorless IM drive is observed under step changes in speed command from 40 rpm to 100 rpm in a series of three 20 rpm steps using three control schemes, which are shown in Figure 7.6 (a)-(c). The step changes in speed command of 20 rpm are applied in three steps (i.e. 40 rpm → 60 rpm → 80 rpm → 100 rpm) at a time interval of 0.8 s (i.e. 2.4 s → 3.2 s → 4 s). The reference speed, actual and estimated speeds are shown in Figure 7.6 (i). The actual resistance and estimated resistance under such commands are shown in Figure 7.6 (ii). It is observed that the estimated speed accurately tracks the reference speed with a slight disturbance in stator resistance estimation using T2FLC while large disturbances observed using PIC and T1FLC schemes.

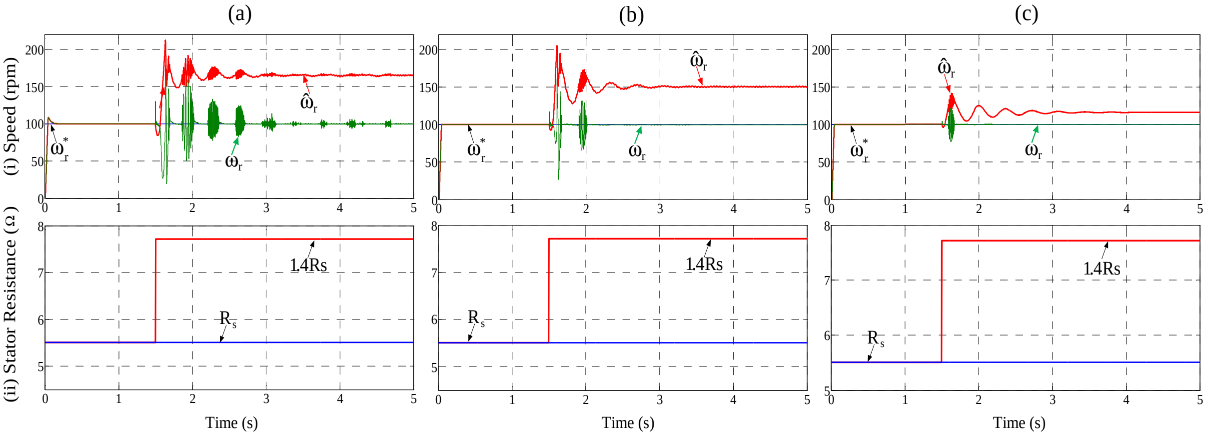

Figure 7.4: Performance under stator resistance variation without stator resistance estimation using: (a) PIC, (b) T1FLC and (c) T2FLC: (i) speed and (ii) stator resistance variation

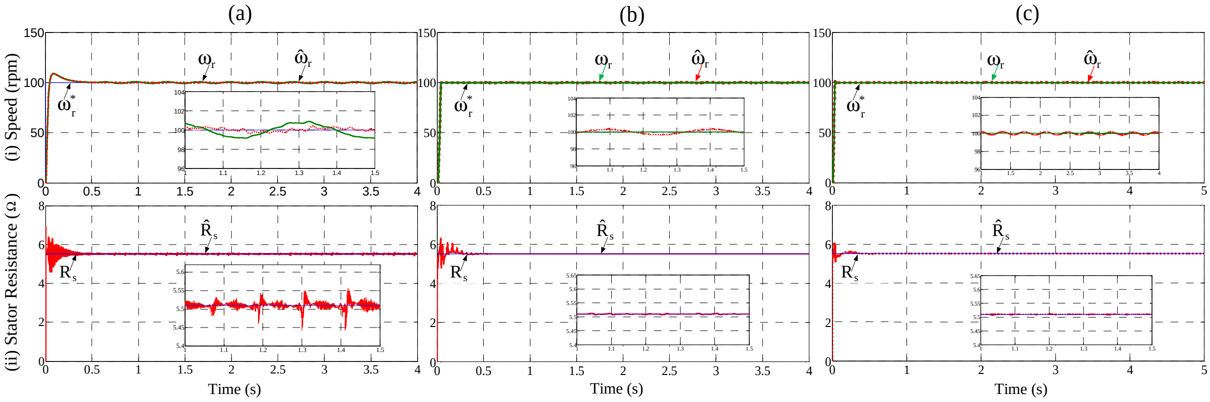

Figure 7.5: Performance with stator resistance estimation using: (a) PIC, (b) T1FLC and (c) T2FLC: (i) speed and (ii) stator resistance

The performance of the speed sensorless IM drive is observed under stator resistance estimation with the variation of stator resistance is shown in Figure 7.7 (a)-(c). A sudden step variation of stator resistance around 40% (i.e. 1.4 R_s) is applied at 1.5 s. The reference speed, actual and estimated speed is shown in Figure 7.7 (i). From Figure 7.7 (i), it is observed that the estimated speed closely follows the reference speed with slight disturbances using T2FLC scheme while large disturbances observed using the PIC scheme. Moreover, the performance of the T2FLC scheme reflects the variation in stator resistance by compensating the variation quickly compared to the PIC and T1FLC schemes.

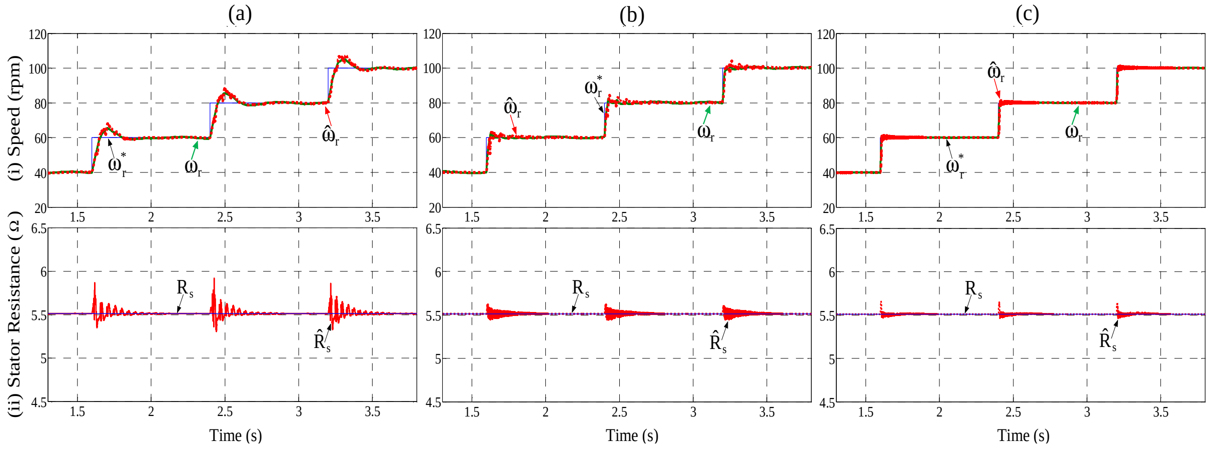

Figure 7.6: Performance under accelerating speed command with stator resistance estimation using: (a) PIC, (b) T1FLC and (c) T2FLC: (i) speed and (ii) stator resistance

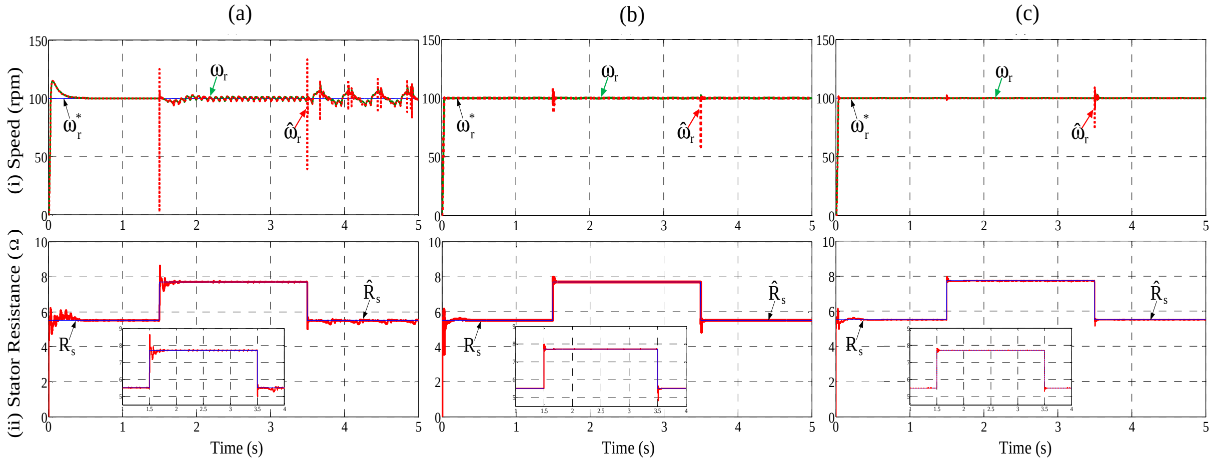

Figure 7.7: Performance under step variation of stator resistance with stator resistance estimation using: (a) PIC, (b) T1FLC and (c) T2FLC: (i) speed and (ii) stator resistance

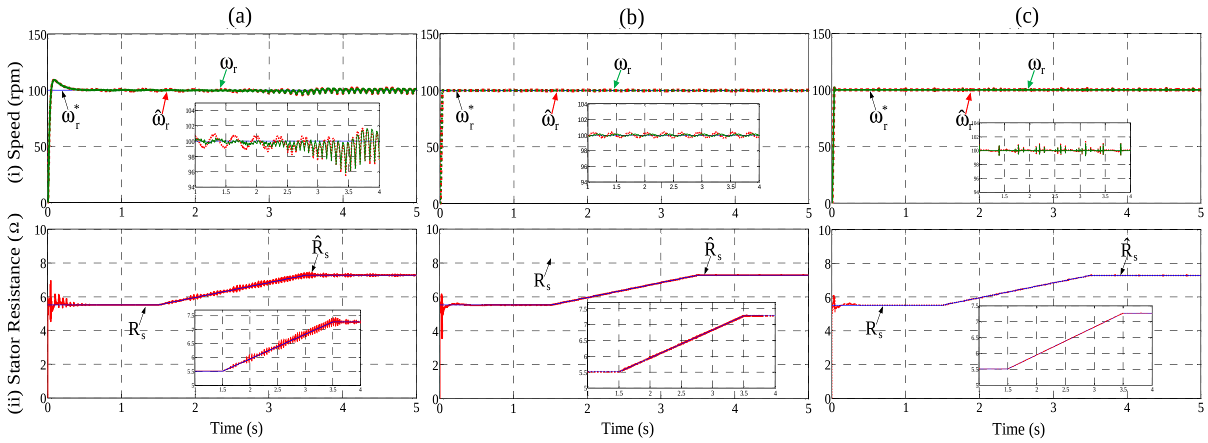

Figure 7.8: Performance under ramp variation of stator resistance with stator resistance estimation using: (a) PIC, (b) T1FLC and (c) T2FLC: (i) speed and (ii) stator resistance

The performance of the speed sensorless IMD is observed under ramp variation of stator resistance is shown in Figure 7.8 (a)-(b). The stator resistance is changed from R_s to $1.32\,R_s$ during 2seconds is shown in Figure 7.8 (ii). The reference speed, actual and estimated speed is shown in Figure 7.8 (i). It is observed that the variation of stator resistance does not affect the estimated speed using T2FLC while some deviations between the reference and estimated speed under stator resistance variation using PIC and T1FLC schemes.

7.4 Experimental Results

The performance of the parallel RFMRAS rotor speed and stator resistance estimation for DTFC-SVM of a speed sensorless IMD using PIC, T1FLC and T2FLC schemes are experimentally validated by the laboratory developed EPS. The experimental results are presented under the operating conditions of low and step changes in speed (both in acceleration and deceleration speed) without the stator resistance variation. The performance of the speed sensorless IM drive under stator resistance variation can be observed by connecting an external resistance R_{sx} in series with the stator winding for all phases.

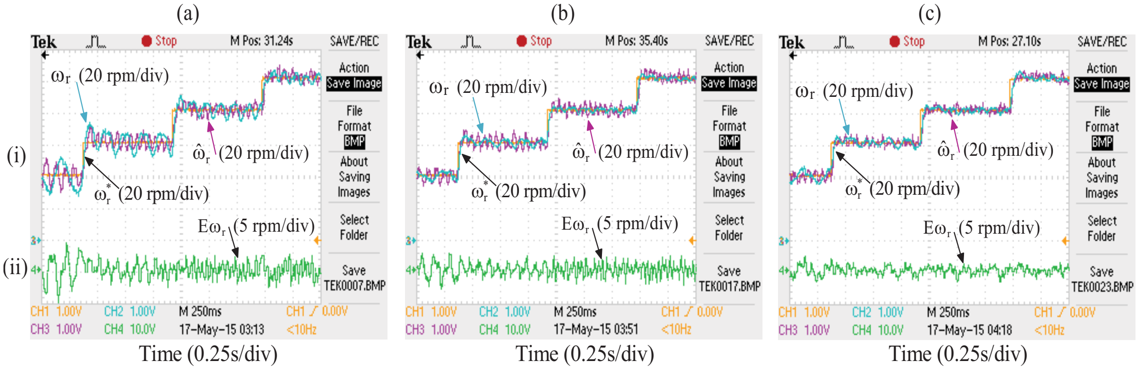

Figure 7.9: Performance under acceleration speed command using: (a) PIC, (b) T1FLC and (c) T2FLC: (i) speed and (ii) error speed

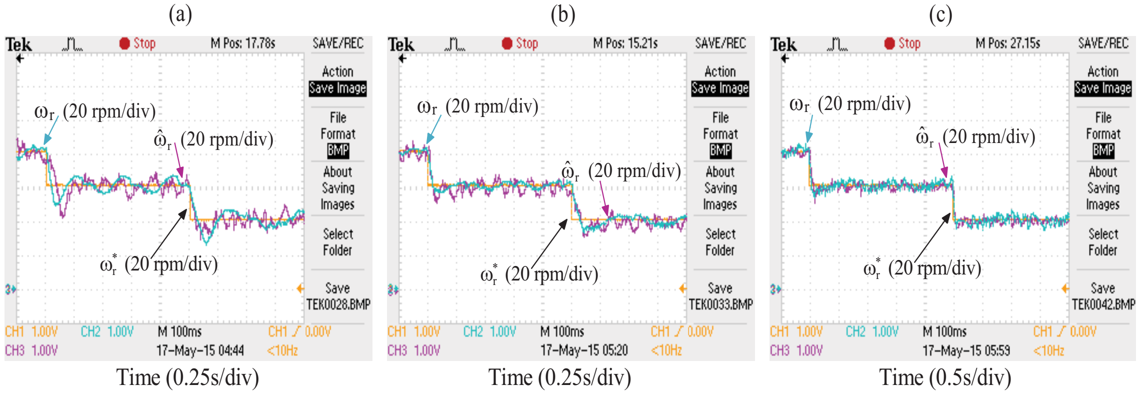

Figure 7.10: Performance under deceleration speed command using: (a) PIC, (b) T1FLC and (c) T2FLC: speed

The stator resistance is estimated under step changes in speed command (i.e Acceleration) using three control schemes are shown in Figure 7.9 (a)-(c). The step changes in speed command of 20 rpm are applied in three steps (i.e. 40 rpm → 60 rpm → 80 rpm → 100 rpm) at a time interval of 0.8 s (i.e. 2.4 s→ 3.2 s→ 4 s). The reference speed, actual and estimated speeds are shown in Figure 7.9 (i) and the estimated speed error is shown in Figure 7.9 (ii). Similarly, step changes in speed command (i.e. deceleration speed) is applied in a series of two 20 rpm steps are shown in Figure 7.10 (a)-(c). It is observed from the simulation and experimental results that the T2FLC shows an improved performance and also insensitive to the variation of stator resistance compared to PIC and T1FLC schemes.

7.5 Conclusion

In this chapter, parallel RFMRAS rotor speed and stator resistance estimation for DTFC-SVM of a speed sensorless IMD using PIC, T1FLC and T2FLC schemes are presented. The PIC based stator resistance estimation shows sensitive to the variation of stator resistance and provides large disturbances in estimated speed. The T1FLC based stator resistance estimation shows improved performance and robustness to stator resistance variation compared to the PIC. The T2FLC based stator resistance estimation shows further improved performance compared to the T1FLC. The simulation and experimental results reveal that the T2FLC based stator resistance estimator provides better speed estimation with less settling time and quick error compensation when there is a change in the stator resistance compared to the PIC and T1FLC schemes.

Chapter 8

Conclusions and Future Scope

CHAPTER 8: CONCLUSIONS AND FUTURE SCOPE

The research work developed in this thesis has focused on the application of soft-computing techniques (i.e. Type-1 and Type-2 fuzzy logic controllers) for DTFC of a speed sensorless IM drive. The main objective was to investigate different control approaches (i.e. PIC, T1FLC and T2FLCs) to enhance the performance of the IM drive fed by two-level voltage source inverter with speed sensor and speed sensorless operation. The proposed Type-1 and Type-2 fuzzy logic controllers for DTFC of a speed sensorless IM drive have been developed and experimentally validated using dSPACE DS-1104 control board as a suitable means of producing a satisfactory performance over a wide range of speed operation. This chapter summarizes the investigations and findings of the research, presents conclusions and a direction for possible future work.

8.1 Conclusion

The mathematical modelling of the IM is presented in chapter-2. Subsequently, the various speed control methods of IM are presented. i.e., scalar control, indirect field oriented control (IFOC) and direct torque and flux control (DTFC). The scalar control is simple to implement and also that provides satisfactory steady-state performance. However, the dynamic behavior is very poor and has sluggish response. In order to overcome these problems, the IFOC method is implemented. This method provides the satisfactory dynamic and steady-state performance compared to scalar control. However, this method is highly sensitive to the parameters of the rotor time constant. Moreover, it requires the coordination transformations and current controllers. Therefore, in order overcome these drawbacks the DTFC method is implemented to enhance the performance of the IM drive. The modelling of this method was done on the basis of the literature review, MATLAB simulation and investigation on experimental. The DTFC of IM drive is implemented using a fixed gain PI controller (PIC).

The performance of the DTFC of an IMD is largely influenced by the PIC which is used in the speed controller for generating reference torque command. The PIC offers satisfactory dynamic as well as steady-state performance over a wide range of ideal operation. However, it requires a precise mathematical model, continuous tuning and accurate gain values. Tuning of gain values for the electric drive controller is a complex due to the nonlinearity of the machines, power converter and controller. Because of this, the PIC produces considerable torque and stator flux ripples. Moreover, the PIC is poor in load torque disturbance rejection and changes in speed. Therefore, it is felt that the control techniques should be intelligent to increase the effectiveness of control performance. An intelligent control system is expected to possess inbuilt adaptation or learning and decision making capabilities and hence it is able to meet desired performance over a wide range of speed operation as well as better load torque disturbance rejection and also uncertainty in the operating parameters. This is the motivation to further investigate the DTFC of IM drive over a wide range of speed operation and load torque disturbances using soft-computing techniques (i.e. Type-1 and Type-2 fuzzy logic controllers), which are presented in chapter-3. Initially, the PIC is replaced by Type-1 fuzzy logic controller (T1FLC) to improve the performance of the IM drive under load torque disturbances and changes in speed command. The T1FLC is implemented using Mamdani type and centroid method with simple IF and THEN rules without the requirement of large complex mathematical equations. Moreover, the T1FLC effectively handles the nonlinear system based on decision taken by the expertise via pre-learned algorithm compared to the PIC. Further, the T1FLC is replaced by Type-2 fuzzy logic controller (T2FLC) to enhance the performance of the IM drive. The T2FLC effectively handles the large footprint of uncertainties compared to the T1FLC due to the availability of three-dimensional control with type-reduction in the defuzzification process. The salient features of T1FLC and T2FLC schemes are reported in Chapter-3 as:

- The ripple contents in stator flux and torque of the IMD using T1FLC is considerably improved. Moreover, the settling time and speed drops under various load torque disturbances are improved by around 61% compared to PIC.
- Similarly, the ripple contents in stator flux and torque of the IMD using T2FLC is considerably improved over T1FLC. Moreover, the settling time and speed drops under various load torque disturbances are improved by around 56% compared to T1FLC.

A comparative simulated performance of the DTFC of an IMD using PIC, T1FLC and T2FLC is presented under various operating conditions, such as no-load torque, load torque, step changes in speed and various speed tracking conditions. An experimental prototype is developed in the laboratory using dSPACE DS-1104 controller board and intelligent power module PEC16DSMO1 to examine the performance of the IM drive under similar rating and the parameters of the IM as used in the MATLAB/SIMULINK, which are presented in Chapter-4. The Simulation results are validated with the experimental results under the same operating conditions as presented in chapter-2 and chapter-3. It is observed from the simulation and experimental results that the DTFC of an IMD using T2FLC scheme provides fewer ripple contents in stator flux and torque, less current THD. Moreover, it significantly improved the speed drops and settling time under load torque disturbances.

A speed sensor is often used in DTFC of an IM drive for speed measurement in a closed-loop operation. However, the use of speed sensor may affect the reliability, difficult to install in a hostile environment, increases the cost and connections of the drive system. Therefore, speed sensorless control techniques are shown to provide great advantages over speed sensor drive systems. The speed of the IM drive can be estimated using rotor-flux based model reference adaptive system (RFMRAS) method. The mathematical modelling of the RFMRAS is presented in chapter-5. The RFMRAS have been formulated using the machine dynamic equations, which are originally introduced by Schauder. A suitable adaptation mechanism (**AM**) for rotor speed estimation is derived based on Popov’s Hyperstability theory.

The performance of the speed sensorless IM drive depends on the type of adaptation mechanism is used in RFMRAS speed estimation. Initially, the PIC based **AM** is used in RFMRAS speed estimator, which is derived using the Popov’s Hyperstability theory by minimizing the speed tuning signal. The PIC based adaptation scheme provides satisfactory performance. However, it requires continuous tuning and accurate gain values. Therefore, the T1FLC and T2FLC schemes are proposed, which are used in place of PIC to enhance the performance of the speed sensorless IM drive by minimizing the speed tuning signal. The proposed adaptation schemes are validated with extensive simulation (i.e. MATLAB/SIMULINK) and experimental results. The simulation and experimental results confirm that the T2FLC based RFMRAS speed estimator shows the better transient performance as well as load torque disturbance rejections compared to the T1FLC and PIC. Excellent correlation between the simulation and experimental results confirms that the usefulness of the proposed control schemes.

The main problem associated with the DTFC method is that variable switching frequency and considerable torque and flux ripples due to the use of torque and flux hysteresis controllers. These drawbacks can be overcome with the direct torque and flux control by applying space vector modulation (DTFC-SVM) technique, which is presented in chapter-6. The DTFC-SVM technique is based on the analysis of stator equations like in DTFC method, consequently control algorithm is not sensitive to rotor parameter changes. Therefore, the DTFC-SVM method with closed-loop flux and torque control in stator flux coordinates have been considered for speed sensorless IM drives. The performance of DTFC-SVM of a speed sensorless IM drive is largely influenced by speed, flux, torque, adaptation control schemes in use. Initially, the PIC is used in these controllers due to its simplicity. These PI controllers are designed using root-locus method, which are presented in Appendix B. In order to improve the performance of speed sensorless IM drive, the PICs are replaced by T1FLC in speed, flux, torque and adaptation controllers. Further, the T2FLC is proposed to enhance the performance of the sensorless drive over a wide range of speed operating regions. The simulation results of DTFC-SVM of a speed sensorless IM drive is also validated with the experimental results under same parameters and operating condition as used in the MATLAB/SIMULINK. It is concluded that the T2FLC based DTFC-SVM of a speed sensorless IMD provides fewer flux ripples and torque distortions, quick dynamic response, less speed drops and quick settling time under load torque disturbances compared to T1FLC and PI controllers.

Sensitivity to the variation of the machine parameter (i.e. stator resistance) is very important for speed sensorless IM drives. The precise value of stator resistance is very important for accurate speed estimation of a speed sensorless IM drive under low speed operation. Any mismatch between the actual stator resistance and the value used in speed estimation lead to a speed estimation error. The variation of stator resistance under low speed operation can be minimized by online stator resistance estimation. The performance enhancement of the RFMRAS speed estimation at low speed regions with parallel rotor speed and stator resistance estimation for DTFC-SVM of a speed sensorless IM drive using PIC, T1FLC and T2FLC approaches have been discussed in chapter-7. Experimental results were carried out to investigate the performance of the proposed schemes in speed sensorless operation with stator resistance estimation. The simulation and experimental results show the improved low speed performance using T2FLC based stator resistance estimation scheme compared to the T1FLC and PI controllers.

In conclusion, the Type-2 fuzzy logic controller and DTFC-SVM method with closed loop flux and torque control in stator flux coordinates has shown great capabilities to significantly improve the performance of speed sensorless IM drives using the RFMRAS speed estimator over a wide range of speed.

8.2 Scope for Future Work

While the thesis brings the work to a successful concluding stage, as per the objectives set for the investigations. The significant conclusions have been listed in this chapter and also given rise to the interesting and useful following aspects, which may be taken for further study of inverter fed sensorless drives.

1. It could be interesting to explore the possibility of carrying the investigation on multilevel inverter fed sensorless IM drive to improve the flux and torque ripples further.
2. The proposed T2FLC based DTFC with SVM can be extended to overmodulation region and hybrid space vector modulation as well.

3. The proposed T2FLC based DTFC-SVM scheme with closed loop flux and torque may be extended to other sensorless drives. For example, permanent magnet synchronous motor and doubly fed induction motor drives.
4. The Type-2 Neuro-fuzzy controller can be used instead of T2FLC to further enhance the controller performance for speed sensorless drives.
5. The performance of the speed sensorless IM drive may be further improved by replacing the neural network (NN) flux observer in place of voltage model. The basic configuration of the NN based MRAS speed estimator is shown in Figure 8.1.

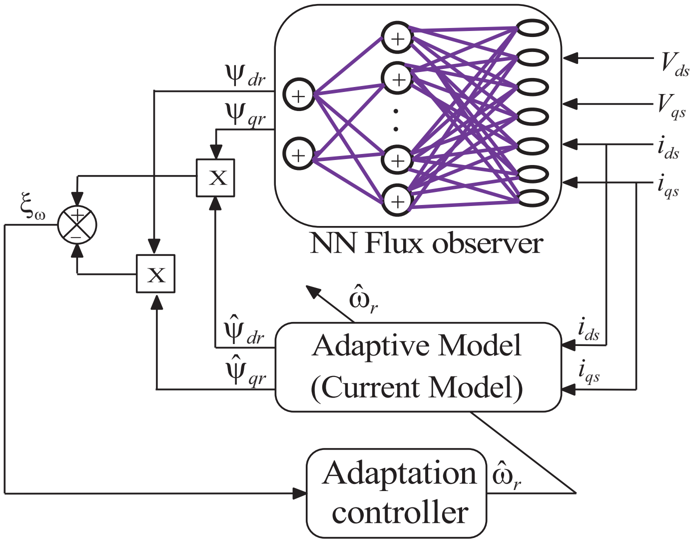

Figure 8.1: Neural network based MRAS speed observer

Bibliography

[1] B. K. Bose. *Modern Power Electronics and AC Drives*. Prentice Hall, Upper Saddle River, 2002.

[2] I. Boldea and S. A. Nasar. *Electric Drives*, 2nd ed. CRC Press, 2006.

[3] P. Vas. *Sensorless Vector and Direct Torque Control*.OXFORD UNIVERSITY PRESS, 1998.

[4] S. P. Singh, B. Singh, M. P. Jain. Comparative study on the performance of a commercially designed induction generator with induction motors operating as self-excited induction generators. *IEE Proce. on Generation, Trans. and Distribution*, 140(5):374-380, Sep. 1993.

[5] W. Lehonhard.*Control of Electrical Drives*. Springer, Berlin, 1996.

[6] G. Buja, M. P. Kazmierkowski. Direct torque control of PWM inverter-fed AC motors-a survey. *IEEE Transactions on Industrial Electronics*, 51(4):744-757, Aug. 2004.

[7] M. G. Alfredo, T. A. Lipo, Donald W. Novotny. A New Induction Motor V/f Control Method Capable of High-Performance Regulation at Low Speeds. *IEEE Trans. on Ind. Appl.*, 34(4):813-821, Aug. 1998.

[8] F. Blaschke. The principle of field orientation as applied to the new transvector closed-loop control system for rotating field machines. *Siemens review*, 34(5):217-220, 1972.

[9] R. Krishnan. *Electric motor drives: modeling, analysis, and control*. Prentice Hall, 2001.

[10] A. B. Plunkett. Direct Flux and Torque Regulation in a PWM Inverter-Induction Motor Drive. *IEEE Transactions on Industry Applications*, 13(2):139-146, March 1977.

[11] M. Depenbrock. Direct Self-Control (DSC) of Inverter-Fed Induction Machine. *IEEE Transactions on Power Electronics*, 3(4):420-429, October 1988.

[12] I. Takahashi, Y. Ohmori. High-performance direct torque control of an induction motor. *IEEE Transactions on Industry Applications*, 25(2):257-264, Mar. 1989.

[13] T. G. Habetler, F. Profumo, M. Pastorelli. Direct torque control of induction machines over a wide speed range. *In proce. of IEEE Conf. on Industry Applications*, 1:600-606, Oct. 1992.

[14] M. P. Kazmierkowski, A. B. Kasprowicz. Improved Direct Torque and Flux Vector Control of PWM Inverter-Fed Induction Motor Drives. *IEEE Trans. on Industrial Elect.*, 42(4):344-350, Aug. 1995.

[15] T. Noguchi, M. Yamamoto, S. Kondo, I. Takahashi. Enlarging switching frequency in direct torque-controlled inverter by means of dithering. *IEEE Transactions on Industry Applications*. 35(6):1358-66, Nov. 1999.

[16] G. Buja. A new control strategy of the induction motor drives: The direct flux and torque control. *In proce. of IEEE Conf. on IEEE Industry Electronics Newslett.*, 45:14–16, Dec. 1998.

[17] D. Casadei, G. Serra, A. Tani. The Use of Matrix Converters in Direct Torque Control of Induction Machines. *IEEE Transactions on Industry Electronics*, 48(6):1057-1064, Dec. 2001.

[18] D. Casadei, F. Profumo, G. Serra, A. Tani. FOC and DTC: Two viable schemes for induction motors torque control. *IEEE Trans. on Power Electron.*, 17(5):779–787, Sept. 2002.

[20] J. H. Ryu, K. W. Lee, J. S. Lee. A Unified Flux and Torque Control Method for DTC-Based Induction-Motor Drives. *IEEE Trans. on Power Electron.*, 21(1):234-242, Jan. 2006.

[21] H. Abdelhakim, M. H. Benbouzid, D. Diallo, R. Abdessemed, J.Ghouili, K. Srairi.A Loss-Minimization DTC Scheme for EV Induction Motors. *IEEE Trans. on Vehicular Technology*, 56(1):81-88, Jan. 2007.

[22] D. Telford, M. Dunnigan, B. W. Williams. A novel torque ripple reduction strategy for direct torque control of the induction motor. *IEEE Trans. on Industrial Electronics*, 48(4):867-70, 2001.

[23] V. Lokesh and R. K. Saket. Power estimation of MWW based generation system using SEIG. *In prof. of IEEE student conf. on Electrical, Electronics and Computer Science*, pp:1-4, 2012..

[24] J. S. Shakya, G. Singh, and R. K. Saket. Performance evaluation of seig for variable speed wind energy conversion system. *International Journal of Research and Reviews in Applied Sciences*, 24(1): 31, July 2015..

[25] Z. Leonowicz, A. Lempart. Assessing the benefits and risks of application of inverter drives in industry. *In Proceedings of IEEE International Conference on Environment and Electrical Engineering*, pp. 144-148, May 2012.

[26] B. Hamane, M. L. Doumbia, M. Bouhamida, A. Draou, H. Chaoui, and M. Benghanem. Comparative study of PI, RST, sliding mode and fuzzy supervisory controllers for DFIG based wind energy conversion system. *International Journal of Renewable Energy Research*. 5(4):1174-85, Dec. 2015.

[27] A. M. Sylla and M. L. Doumbia. Maximum power control of grid-connected DFIG-based wind systems. *In Proc. of IEEE conf. on Electrical Power and Energy,* pp. 267-273, Oct. 2012.

[28] S. Madishetti, G. Bhuvaneswari, B. Singh. Improved power quality converter for direct torque control-based induction motor drives. *IET Power Electronics*, 6(2):276-286, Feb. 2013.

[29] N. VenkataramanaNaik, S. P. Singh. Improved dynamic performance of direct torque control at low speed over a scalar control. *In proceeding of IEEE annual India Conf.,* pp:1-5, Dec. 2013.

[30] H. H. N. Talib, I. Zulkifilie, A. R. Nasrudin, and A. S. A. Hasim. Comparison analysis of indirect FOC induction motor drive using PI, anti-windup and pre filter schemes. *International Journal of Power Electronics and Drive Sys.*, 5(2): 219-227, Jan. 2014.

[31] V. Lokesh, R. K. Saket, and S Eslamian. Power estimation and reliability evaluation of municipal waste water and self-excited induction generator-based micro hydropower generation system. *International Journal of Hydrology Science and Technology*, 3(2):176-191, Jan. 2013.

[32] C. M. F. S. Reza, M. D. Islam, S. Mekhilef. A review of reliable and energy efficient direct torque controlled induction motor drives. *Renewable and Sust. Energy Reviews*, 37:919-932, sep.2014.

[33] S. S. Gupta, K. Mukherjee, T. K. Bhattacharya, A. K. Chattopadhyay. Performance of an SCR-inverter-based commutatorless series motor with load commutation and unaided start-up capability. *IEEE Transactions on Industry Applications*, 36(4):1151-1157, July 2000.

[34] K. Mukherjee, S. S. Gupta, T. K. Bhattacharya and A. K. Chattopadhyay. Simplified steady-state model of an SCR-inverter-based load-commutated commutatorless series motor. *IEEE Transactions on Energy Conversion*, 17(2):197-202, June 2002.

[35] S. S. Gupta, K. Mukherjee, T. K. Bhattacharya, A. K. Chattopadhyay and S. N. Bhadra. A simplified analytical averaged model of a thyristorized commutator less series motor. *IEEE Transactions on Industry Applications*, 42(6):1508-1515, Nov. 2006.

[36] W. Oh, Y. Kim, C. Kim, T. Kwon, H. Kim. Speed control of induction motor using genetic algorithm based fuzzy controller. *In Proceedings of the IECON*, 2:625–629, 1999.

[37] F. Lin, H. Shieh, K. Shyu, P. Huang. Online gain tuning IP controller using real coded genetic algorithm, *Journal of Electric Power Syst. Res*. 72:157–169, 2004.

[38] F. Lin, W. Chou, P. Huang. Adaptive sliding mode controller based on real time genetic algorithm for induction motor servo drive, *IEE Proc. Electr. Power Appl*. 150:1–13, 2003.

[39] A. A. Naassani, M. Eric, J. P. Louis. Synthesis of Direct Torque and Rotor Flux Control Algorithms by Means of Sliding-Mode Theory. *IEEE Trans. on Ind. Electron.,* 52(3):785-799, Jun. 2005.

[40] O. Barambones, A. J. Garrido, and F. J. Maseda. Integral sliding-mode controller for induction motor based on field-oriented control theory. *IET Control Theory Applications,* 1(3):786–794, May 2007.

[41] T. Geyer, G. Papafotiou, and M. Morari. Model predictive direct torque control—Part I: Concept, algorithm, and analysis. *IEEE Trans. Ind. Electron.*, 56(6);1894–1905, Jun. 2009.

[42] G. Papafotiou, J. Kley, K. G. Papadopoulos, P. Bohren, and M. Morari. Model predictive direct torque control—Part II: Implementation and experimental evaluation. *IEEE Trans. Ind. Electron.*, 56(6):1906–1915, Jun. 2009.

[43] J. Beerten, J. Verveckken, and J. Driesen. Predictive direct torque control for flux and torque ripple reduction. *IEEE Trans. on Ind. Electron.*, 57(1):404–412, Jan. 2010.

[44] P. Vas, *Artificial-Intelligence-Based Electrical Machines and Drives*, Oxford University Press, New York, USA, 1999.

[45] Z. Ibrahim, E. Levi. A comparative analysis of fuzzy logic and PI speed control in high performance ac drives using experimental approach. *IEEE Trans. on Industrial Appl*. 38:1210–1218, 2002.

[46] M. A. Denai, S. A. Attia. Intelligent control of an induction motor. *Electric Power Compon. Syst.,* 30(4):409–427, Apr. 2002.

[47] J. W. Finch, D. Giaouris. Controlled AC electrical drives. *IEEE Transactions on Industrial Electronics*, 55(2):481–491, Feb. 2008.

[48] L. Zadeh. Fuzzy sets. *Information and Control.* 8:338-353, 1965.

[49] T. Takagi, M. Sugeno. Fuzzy identification of systems and its application to modeling and control. *IEEE Transactions on Sys. Man and Cybernetics,*15:116–132, Jan. 1985.

[50] S. A. Mir, D. S. Zinger, M. E. Elbuluk. Fuzzy Controller for Inverter Fed Induction Machines. *IEEE Transactions on Industrial Applications*, 30(1):78-84, Jan. 1994.

[51] I. G. Bird, H. Zelaya De La Parra. Fuzzy logic torque ripple reduction for DTC based AC drives. *Electronic Letters,* 33(17):1501-1502, Aug. 1997.

[52] P. Vas. *Artificial Intelligence Based Electrical Machines and Drives Application of fuzzy, Neural, Fuzzy Neural, and Genetic Algorithm based Techniques*. Oxford university press, New Yark, pp: 173-234, April 1999.

[53] K. H. Chao, and C. M. Liaw. Fuzzy robust speed controller for detuned field oriented induction motor drives. *IEE Proceedings On Electric Power Applications*, 147(1):27-36, Jan. 2000.

[54] L. Arias, E. Romeral, Aldabas, M. G. Jaync. Improving Direct Torque Control by means of Fuzzy Logic. *Electronic Letters,* 37(1):69-71, Jan. 2001.

[55] M. N. Uddin, T. S. Radwan, M. Azizur Rahman. Performances of fuzzy logic-based indirect vector control for induction motor drive. *IEEE Trans. on Industrial Appl.*, 38(5):1219-1225, Sept. 2002.

[56] L. Mokrani, R. Abdessemed. A fuzzy self-tuning PI controller for speed control of induction motor drive. *In Proc. of the IEEE Conference on Control Applications*, 2:785–790, Jun. 2003.

[57] Y. S. Lai, J. C. Lin. New Hybrid Fuzzy Controller for Direct Torque Control Induction Motor Drives. *IEEE Transactions on Power Electron.*, 18(5):1211-1219, Sept. 2003.

[58] L. Romeral, A. Arias, E. Aldabas, M. G. Jayne. Novel Direct Torque Control Scheme with Fuzzy Adaptive Torque-Ripple Reduction. *IEEE Trans. on Industrial Electron.*, 50(3):487-492, Jun. 2003.

[59] S. M. Gadoue, D. Giaouris, J.W. Finch. Tuning of PI speed controller in DTC of induction motor based on genetic algorithms and fuzzy logic schemes. *In Proceedings of the 5th International Conference on Technology and Automation*, pp:85–90, 2005.

[60] S. M. Gadoue, D. Giaouris, J. W. Finch. Artificial intelligence-based speed control of DTC induction motor drives-A comparative study. *Electric Power Systems Research*, 79(1):210-219, Jan. 2009.

[61] B. Sahu, K. B. Mohanty, S. Pati. A comparative study on fuzzy and PI speed controllers for field-oriented induction motor drive. *In Proceedings of the International Symposium Modern Electric Power Systems*, pp:1-7, 2010.

[62] M. Nasir Uddin, M. Hafeez. FLC-Based DTC Scheme to Improve the Dynamic performance of an IM Drive. *IEEE Transactions on Industrial Applications*, 48(2):823-831, Mar. 2012.

[63] K. Mohanraj, S. Paramasivam, S. S. Dash, A. F. Zobaa. Open and Short Circuit Diagnosis of a VSI Fed Three Phase Induction Motor Drive Using Fuzzy Logic Technique. *International Review on Modelling and Simulations*. 6(6):1858-64, Dec. 2013.

[64] F. Barrero, A. Gonzalez, A. Torralba, E. Galvan, L.G. Franquelo. Speed control of induction motors using a novel fuzzy sliding mode structure. *IEEE Trans. on Fuzzy Syst.*, 10(3):375–383, Jun. 2002.

[65] A. Hazzab, I. K. Bousserhane, M. Kamli. Design of fuzzy sliding mode controller by genetic algorithms for induction machine speed control. *Int. J. Emerging Electric Power Syst.,* 1(2):1016–1027, Dec. 2004.

[66] L. A. Cabrera, M. E. Elbuluk, and D. S. Zinger. Learning Techniques to Train Neural Networks as a State Selector for Inverter-Fed Induction Machines Using Direct Torque Control. *IEEE Trans. on Power Electron.*, 12(5):788-799, Sept. 1997.

[67] M. S. Ballal, H. M. Suryawanshi, M. K. Mishra. Detection of incipient faults in induction motors using FIS, ANN and ANFIS techniques. *Journal of Power Electr.*, 8(2):181-191, 2008.

[68] P. Janik, Z. Leonowicz, J. Rezmer, S. Chistan, D. Schulz. Advanced Signal Processing Methods for Evaluation of Harmonic Distortion Caused by DFIG Wind Generator. *In Proceedings of the Power Systems Computation Conference*, pp:1-6, Jul. 2008.

[69] A. Zobaa, B. Reljin. Neural network applications in electrical engineering. *Neurocomputing*. 70(16):2613-4, Oct. 2007.

[70] M. N. Uddin, H. Wen. Development of a self-tuned neuro-fuzzy controller for induction motor drives. *In Proceedings of the Industry Applications Conference IAS annual meeting,* 43(4):2630–2636, Jul. 2007.

[71] A. Bechouche, H. Sediki, D. O. Abdeslam, S. Haddad. Identification of induction motor at standstill using artificial neural network. *In Proceedings of IEEE Annual Conference on Industrial Electronics Society*, pp:2908-2913, Nov. 2010.

[72] N. Venkataramana Naik and S. P. Singh. A NF based direct torque control of induction motor drive using BCSVM. *In proc. of IEEE India Intern. Conference on Power Electronics*, 2014.

[73] N. Venkataramana Naik, J. Thankachan, and S. P. Singh. A Neuro-Fuzzy Direct Torque Control Using Bus-Clamped Space Vector Modulation. *IETE Technical Review*, pp:1-13, 2015.

[74] D. Flieller, N. K. Nguyen, P. Wira, G. Sturtzer, D. O. Abdeslam and J. Merckle. A self-learning solution for torque ripple reduction for nonsinusoidal permanent-magnet motor drives based on artificial neural networks. *IEEE Trans. on Industrial Electronics*, 61(2):655-66, Feb. 2014.

[75] J. S. Roger Jang. ANFIS: Adaptive-Network-Based Fuzzy Inference System. *IEEE Transactions on Sys. Man and Cyber net*, 23(3):665-85, May 1993.

[76] P. Z. Grabowski, M. P. Kazmierkowski, B. K. Bose and F. Blaabjerg. A Simple Direct-Torque Neuro-Fuzzy Control of PWM-Inverter-Fed Induction Motor Drive. *IEEE Trans. on Ind. Electron.*, 47(4):863-870, Aug. 2000.

[77] F. J. Lin and R. J. Wai. Adaptive fuzzy neural network control for IM spindle motor drive. *IEEE Transactions on Energy Conn,* 17(4):507-513, Dec. 2002.

[78] H. Chaoui, B. Hamane, and M. L. Doumbia. Adaptive Control of Venturini Modulation Based Matrix Converters Using Interval Type-2 Fuzzy Sets. *Journal of Control, Automation and Electrical Systems*, *27*(2):132-143, Apr. 2016.

[79] N. N. Karnik, J. M. Mendel, and Q. Liang. Type-2 fuzzy logic systems. *IEEE Transactions on Fuzzy Systems*, 7:643-658, Sept. 1999.

[80] Q. Liang and J. M. Mendel. Interval type-2 fuzzy logic systems: Theory and design. *IEEE Transactions on Fuzzy Systems,* 8(5):535-550, Oct. 2000.

[81] J. M. Mendel. *Uncertain rule-based fuzzy logic systems: Introduction and new directions*. Prentice Hall PTR, Upper Saddle River, 2001.

[82] J. M. Mendel and R. I. B. John. Type-2 fuzzy sets made simple. *IEEE Transactions on Fuzzy Systems*,10(2):117-227, Apr. 2002.

[83] P. Z. Lin, C. F. Hsu, and T. T. Lee. Type-2 Fuzzy Controller Design using a sliding mode approach for application to DC-DC Converters. *In IEE Proceedings on Electric Power Applications,* 152(6):1482-1488, Nov. 2005.

[84] S. Barkati, E. M. Berkouk, and M. S. Boucherit. Application of type-2 fuzzy logic controller to an induction motor drive with seven-level diode-clamped inverter and controlled in feed. *Springer-Verlag on Electrical Engg.*, 90(5):347-359, May 2008.

[85] O. Castillo and P. Melin. Recent advances in interval Type-2 fuzzy systems. *Springer Science and Business Media*, Apr. 2012.

[86] S. Rafa, A. Larabi, L. Barazane, M. Manceur, N. Essounbouli, A. Hamzaoui. Implementation of a new fuzzy vector control of induction motor. *ISA transactions*, 53(3):744-754, May 2014.

[87] D. Wu and J. M. Mendel. On the continuity of type-1 and interval type-2 fuzzy logic systems. *IEEE Transactions on Fuzzy Systems*, 19(1):179-192, Feb. 2011.

[88] D. Wu. Approaches for reducing the computational cost of interval type-2 fuzzy logic systems: overview and comparisons. *IEEE Transactions on Fuzzy Systems*, 21(1):80-99, Feb. 2013.

[89] M. Suresh and A. K. Panda. Types-1 and -2 fuzzy logic controllers-based shunt active filter Id-Iq control strategy with different fuzzy membership functions for power quality improvement using RTDS hardware. *IET Power Electronics*, 6(4):818-833, Apr. 2013.

[90] M. Suresh and A. K. Panda. Performance analysis and real-time implementation of shunt active filter Id-Iq control strategy with type-1 and type-2 FLC triangular MF. *International Transactions on Electrical Energy Systems*, *24*(3), 347-362, Mar. 2014.

[91] H. K. Lam, L. Hongyi, C. Deters, E. L. Secco, H. A. Wurdemann, and K. Althoefer. Control Design for Interval Type-2 Fuzzy Systems Under Imperfect Premise Matching. *IEEE Trans. on Ind. Electron.,* 61(2):956–968, Feb. 2014.

[92] P. Melin and O. Castillo. A review on type-2 fuzzy logic applications in clustering, classification and pattern recognition. *Applied Soft Computing*, 21:568-577, Aug. 2014.

[93] C. Lascu, I. Boldea and F. Blaabjerg. Very-low-speed variable-structure control of sensorless induction machine drives without signal injection. *IEEE Trans. On Ind. Applicat.*, 41(2):591–598, Mar. 2005.

[94] J. Holtz. Sensorless control of induction machines—with or without signal injection. *IEEE Transactions on Industrial Electronics*, 53(1):7-30, Feb. 2006.

[95] F. Cupertino, A. Lattanzi, L. Salvatore and S. Stasi. Induction motor control in the low-speed range using ekf- and lkf-based algorithms. *In proceeding of IEEE-ISIE*, 3:1244–1249, 1999.

[96] T. S. Kwon, M. H. Shin, and D. S. Hyun. Speed sensorless stator flux-oriented control of induction motor in the field weakening region using luenberger observer. *IEEE Transactions on Power Electronics*, 20(4):864–869, Jul. 2005.

[97] L. Kyo-Beum and F. Blaabjerg. Reduced-order extended luenberger observer based sensorless vector control driven by matrix converter with nonlinearity compensation. *IEEE Transactions on Industrial Electronics*, 53(1):66-75, Feb. 2006.

[98] P. Vaclavek and P. Blaha. Lyapunov-function-based flux and speed observer for ac induction motor sensorless control and parameters estimation. *IEEE Transaction on Industrial Electronics*, 53(1):138–145, February 2006.

[99] K. L. Shi, T. F. Chan, Y. K. Wong, and S. L. Ho. Speed estimation of an induction motor drive using an optimized extended kalman filter. *IEEE Trans. Industrial Electron*., 49(1):124–133, Feb. 2002.

[100] M. Sirovy, Z. Peroutka, J. Molnar, J. Michalik, M. Byrtus, P. Wikstroem. Sophisticated software for design and optimization of VSDs for high-power pumps: Variable speed drive with frequency converter. *In Proc. of Int. Conf. on Power Elect. and Motion Control*, pp. 1-6, 2010.

[101] M. Barut, S. Bogosyan, and M. Gokasan. Speed-sensorless estimation for induction motors using extended kalman filters. *IEEE Trans. on Indus. Electronics*, 54(1):272–280, Feb. 2007.

[102] M. Barut, S. Bogosyan, and M. Gokasan. Experimental Evaluation of Braided EKF for Sensorless Control of Induction Motors. *IEEE Trans. on Industrial Electronics*, 55(2):620-632, Feb. 2008.

[103] M. Jannati, T. Sutikno, N. R. N Idris, and M. J. A. Aziz. High Performance Speed Control of Single-Phase Induction Motors Using Switching Forward and Backward EKF Strategy. *International Journal of Power Electronics and Drive Systems,* 7(1), Mar. 2016.

[104] I. M. Alsofyani, N. R. N Idris, Y. A Alamri, T. Sutikno. Comparison of Estimated Torques Using Low Pass Filter and Extended Kalman Filter for IM Drives at Low Speed. *International Journal of Power Electronics and Drive Systems*, 6(1):92-99, Mar. 2015.

[105] I. M. Alsofyani and N. R. N. Idris. Simple Flux Regulation for Improving State Estimation at Very Low and Zero Speed of a Speed Sensorless Direct Torque Control of an Induction Motor. *IEEE Transactions on Power Electronics,* 31(4):3027-3035, Apr. 2016.

[106] A. Rojko and K. Jezernik. Speed-sensorless sliding-mode torque control of an induction motor. *IEEE Transaction on Industrial Electronics*, 49(1):87–75, Feb. 2002.

[107] C. Lascu and G. D. Andreescu. Sliding-mode observer and improved integrator with dc-offset compensation for flux estimation in sensorless-controlled induction motors. IEEE *Transaction on Industrial Electronics*, 53(3):785–794, June 2006.

[108] M. Comanescu and L. Xu. Sliding-mode mras speed estimators for sensorless vector control of induction machine. *IEEE Transaction on Industrial Electronics*, 53(1):146–153, Feb. 2006.

[109] Y. Zhang, Z. Zhao, T. Lu, L. Yuan, W. Xu, and J. Zhu. A comparative study of Luenberger observer, sliding mode observer and extended Kalman filter for sensorless vector control of induction motor drives. *In IEEE Energy Conver. Congress and Exp.*, pp:2466-2473, Sep. 2009.

[110] Y. H. Park, K. H. Park, S. C. Baek, and Y. A. Kwon. Sliding mode observer with parameter estimation for sensorless induction motor. *In Proc.. of IEEE TENCON*, pp:37-41, Nov. 2010.

[111] M. Jannati, A. Monadi, N. R. N. Idris and M.J.A. Aziz. Speed Sensorless Vector Control of Unbalanced Three-Phase Induction Motor with Adaptive Sliding Mode Control. *International Journal of Power Electronics and Drive Systems*, 4(3):406-418, Sep. 2014.

[112] F. Z. Peng, T. Fukao. Robust speed identification for speed-sensorless vector control of induction motors. *IEEE Transactions on Industry Applications*, 30(5):1234-40, Sep. 1994.

[113] M. Rashed and A. F. Stronach. A stable back-emf mras-based sensorless low speed induction motor drive insensitive to stator resistance variation. *IEE Proceeding of Electric Power Applications*, 151(6):685–693, Nov. 2004.

[114] Y. D. Landau, *Adaptive Control: The Model Reference Approach*. Marcel Dekker, New York, 1979.

[115] Y. D. Landau. Adaptive control: The model reference approach. *IEEE Transactions on Systems, Man and Cybernetics*, 1:169-170, 1984.

[116] C. Schauder. Adaptive speed identification for vector control of induction motors without rotational transducers. *IEEE Transactions on Industry Applications*, 28(5):1054-1061, 1992.

[117] G. Buja and R. Menis. Accuracy of the speed estimation in the sensorless induction motor drives based on the mras technique. *Conf. Rec. of IEEE-OPTIM*, 2: 407 – 414, 1998.

[118] P. Vas, A. F. Stronach, M. Rashed, and M. Neuroth. Implementation of ANN-based sensorless induction motor drives. *In Proc. of Inter. Conf. on Elect. Machines & Drives,* pp:329-333, 1999.

[119] M. C. Ta, T. Uchida, and Y. Hori. MRAS based speed sensorless control for induction motor drives using instantaneous reactive power. *In Proceeding of IEEE-IECON*, 2:1417–1422, 2001.

[120] J. Holtz and Q. Juntao. Drift and parameter compensated flux estimator for persistent zero-stator-frequency operation of sensorless-controlled induction motors. *IEEE Transactions on Industry Applications*, 39(4):1052-1060, Jul. 2003.

[121] V. M. Leppanen and J. Luomi. Speed-sensorless induction Machine control for zero speed and frequency. *IEEE Transactions on Industrial Electronics*, 51(5):400-405, Nov. 2002.

[122] H. Chien-Feng, H. Rong-Bin, and L. Chang-Huan. Stability analysis and PI controller tuning for a speed-sensorless vector-controlled induction motor drive. *In Prof. of Annual Conference of IEEE Industrial Electronics Society*, 1:877-882, Nov. 2004.

[123] M. Cirrincione and M. Pucci. An MRAS-based sensorless high-performance induction motor drive with a predictive adaptive model. *IEEE Transactions on Industrial Electronics,* 52(2):532-551, April 2005.

[124] M. Comanescu and L. Xu. Sliding mode MRAS speed estimators for sensorless vector control of induction machine. *IEEE Trans. on Industrial Electronics,* 53(1):146-153, February 2006.

[125] L. M. Grzesiak and M. P. Kazmierkowski. Improving flux and speed estimators for sensorless ac drives. *IEEE Magazine on Industrial Electronics*, 1(3):8–19, 2007.

[126] F. Misoc, M. M. Morcos, J. Lookadoo. Effect of DC–DC converter topologies and operation on the electrical performance of fuel cells. *Electric Power Components and Systems*, 38(7): 851–861, August 2010.

[127] S. M. Gadoue, D. Giaouris, and J. W. Finch. Sensorless Control of Induction Motor Drives at Very Low and Zero Speeds Using Neural Network Flux Observers. *IEEE Transactions on Industrial Electronics*, 56(8):3029-3039, Aug. 2009.

[128] S. M. Gadoue. Artificial intelligence applied to speed sensorless induction motor drives. *NEWCASTLE UNIVERSITY*, 2009.

[129] S. M. Gadoue, D. Giaouris, and J. W. Finch. MRAS Sensorless Vector Control of an Induction Motor Using New Sliding-Mode and Fuzzy-Logic Adaptation Mechanisms. *IEEE Transactions on Energy Conversion,* 25(2):394-402, Jun. 2010.

[130] A. B. Nanda, T. K. Bhattacharya. Stator flux based speed sensorless control of single phase induction motor drives. *In Proc. of IEEE Inter. Conf. on Energy, Automation, and Signal*, pp:1-6, Dec. 2011.

[131] Y. C. Luo and W. X. Chen. Sensorless stator field orientation controlled induction motor drive with a fuzzy speed controller. *Computers and Mathematics with Applications*, 64(5):1206-1216, Sep. 2012.

[132] D. Giribabu, S. P.Srivastava and M. K. Pathak. Rotor Flux Based MRAS for Three Level Inverter fed Induction Motor Drive Using Fuzzy Logic Controller. *Int. J. Power Electronics*, 4(5):463-478, Jan. 2012.

[133] D. Giribabu, S. P. Srivastava and M. K. Pathak. Rotor Flux Based MRAS for Sensorless Operation of Three Level Inverter fed Induction Motor. *In Proc. of IEEE Students' Conference on Electrical, Electronics and Computer Science*, pp:1-4, March 2012.

[134] H. M. Kojabadi. Active power and MRAS based rotor resistance identification of an IM drive. *Simulation Modelling Practice and Theory*, 17(2):376-389, Feb. 2009.

[135] S. Maiti and C. Chakraborty. Mras-based speed estimation techniques for vector controlled double-inverter-fed slip-ring induction motor drive. *In proc. of 34th Annual IEEE Conference on Industrial Electronics*, pp:1275-1280, Nov, 2008.

[136] S. Maiti, C. Chakraborty, and S. Sengupta. Simulation studies on mrac-based speed estimation technique for the vector controlled permanent magnet synchronous motor drive. *Simulation Modelling Practice and Theory*, 2008.

[137] S. Maiti, V. Verma, C. Chakraborty, and Y. Hori. An Adaptive Speed Sensorless Induction Motor Drive With Artificial Neural Network for Stability Enhancement. *IEEE Transactions on Industrial Informatics*, 8(4):757-766, Nov. 2012.

[139] V. Verma, C. Chakraborty, and Y. Hori. Speed Sensor less Vector Controlled Induction Motor Drive Using Single Current Sensor. *IEEE Transactions on Energy Conv.,* 28:938-950, 2013.

[140] M. F. Rahman, L. Zhong, M. E. Haque, and M. A. Rahman. A direct torque controlled interior permanent magnet synchronous motor drive without a speed sensor. *IEEE Trans. on Energy Conversion*, 18(1):17–22, Mar. 2003.

[141] J. Faiz, M. B. Sharifian, A. Keyhani, A. B. Proca. Sensorless direct torque control of induction motors used in electric vehicle. *IEEE Trans. on Energy Conversion*, 18(1):1-10, Mar. 2003.

[142] J. Maes and J. A. Melkebeek. Speed-sensorless direct torque control of induction motors using an adaptive flux observer. *IEEE Transactions on Ind. Appl*., 36(3):778–785, May 2000.

[143] M. Hajian, J. Soltani, G. A. Markadeh, S. M. Hosseinnia. Adaptive nonlinear direct torque control of sensorless IM drives with efficiency optimization. *IEEE Trans. Ind. Electron.*, 57(3):975-985, Mar. 2010.

[144] A. Lesan, Y. Eshag, M. L. Doumbia, and P Sicard. Methodology and experimental set-up for DSP-based sensorless PWM speed estimation of induction machine. *In Proc. of 38th Annual Conference on IEEE Industrial Electronics Society*, pp. 3699-3704. Oct. 2012.

[145] Y. Zhang, J. Zhu, Z. Zhao, W. Xu, and D. G. Dorrell. An Improved Direct Torque Control for Three-Level Inverter-Fed Induction Motor Sensorless Drive. *IEEE Trans. on Power Electron*., 27(3):1502-1513, Mar. 2012.

[146] J.K Kang and S.K Sul. New direct torque control of induction motor for minimum torque ripple and constant switching frequency. *IEEE Trans. on Industry Appl.*, 35(5):1076-1082, Sep. 1999.

[147] N. R. N. Idris and A. H. M. Yatim. Direct torque control of induction machines with constant switching frequency and reduced torque ripple. *IEEE Transactions on Industrial Electronics,* 51(4):758-767, Aug. 2004.

[148] C. L. Toh, N. R. N. Idris, and A. H. M. Yatim. Constant and High Switching Frequency Torque Controller for DTC Drives. *IEEE Power Electron. Letters,* 3(2):76-80, Jun. 2005.

[149] R. Abdelli, D. Rekioua, T. Rekioua. Performances improvements and torque ripple minimization for VSI fed induction machine with direct control torque. *ISA Transactions*, 50(2):213-219, Apr. 2011.

[150] A. Jidin, N. R. N. Idris, A. H. Yatim, M. E. Elbuluk, T. Sutikno. A wide-speed high torque capability utilizing overmodulation strategy in DTC of induction machines with constant switching frequency controller. *IEEE Trans. on Power Electr.,* 27(5):2566-2575, May 2012.

[151] T. G. Habetler and D. D. Divan. Control strategies for direct torque control using discrete pulse modulation. *IEEE Transaction on Industrial Applications*, 27(5):893–901, Sept. 1991.

[152] T. G. Habetler, F. Profumo, M. Pastorelli, and L. M. Tolbert. Direct Torque Control of Induction Machines Using Space Vector Modulation. *IEEE Trans. on Industrial Appl*, 28(5):1045-1050, Sept. 1992.

[153] D. Casadei, G. Serra, and K. Tani. Implementation of a direct control algorithm for induction motors based on discrete space vector modulation. *IEEE Transactions on Power Electronics,* 15(4):769-777, July 2000.

[154] Y. S. Lai and J. H. Chen. A New Approach to Direct Torque Control of Induction Motor Drives for Constant Inverter Switching Frequency and Torque Ripple Reduction. *IEEE Trans. on Energy Con.*, 16(3):220-227, Sept. 2001.

[155] J. Rodriguez, J. Pontt, C. Silva, R. Huerta, and H. Miranda. Simple direct torque control of induction machine using space vector modulation. *Electron. Letters,* 40(7):412-413, Apr. 2004.

[156] C. Lascu, I. Boldea, and F. Blaabjerg. Direct Torque Control of Sensor less Induction Motor Drives: A Sliding-Mode Approach. *IEEE Trans. on Ind. Appl.*, 40(2):170- 177, Mar. 2004.

[157] C. Lascu, I. Boldea, F. Blaabjerg. Variable-Structure Direct Torque Control—A Class of Fast and Robust Controllers for Induction Machine Drives. *IEEE Trans. on Ind. Electron.*, 51(4):785-792, Aug. 2004.

[158] Y. Kumsuwan, P. Suttichai, H. A. Toliyat. Modified direct torque control method for induction motor drives based on amplitude and angle control of stator flux. *Electric power systems research*, 78(10):1712-1718, Oct. 2008.

[159] A. Y. Lesan, M. L. Doumbia, P. Sicard. Comparative study of speed estimation techniques for sensorless vector control of induction machine. *In Proc. of 38th Annual Conference on IEEE Industrial Electronics Society*, pp. 4298-4303, Oct. 2012.

[160] M. Zelechowski, M. P. Kazmierkowski, and F. Blaabjerg. Controller design for direct torque controlled space vector modulated (DTC-SVM) induction motor drives. *In Proceedings of the IEEE International Symposium on Industrial Electronics,* 3:951-956, 2005.

[161] M. Zelechowski. *Space vector modulated direct torque controlled inverter-fed induction motor drive*. Warszaw University of Technology, 2005.

[162] M. Jasinski, M. P. Kazmierkowski, and M. Zelechowski. Direct Power and Torque Control Scheme for Space Vector Modulated AC/DC/AC Converter-Fed Induction Motor. *Recent Developments of Electrical Drives*. Springer Netherlands, pp:261-274, 2006.

[163] J. Michalik, J. Molnar, Z. Peroutka. Space vector modulated four-quadrant active current-source rectifier with DFT based power factor control for DC motor drive. *In Proceedings of IEEE Annual Conference on Industrial Electronics Society*, pp. 1813-1819. Oct. 2014.

[164] Z. Zhang, R. Tang, B. Bai and D. Xie. Novel Direct Torque Control Based on Space Vector Modulation with Adaptive Stator Flux Observer for Induction Motors. *IEEE Trans. on Magnetics,* 46(8):3133-3136, Aug. 2010.

[165] T. Vinay Kumar, and S. Srinivasa Rao. Switching state algorithm for space vector pulse width modulation (SVPWM). *In proc. of Mediterranean Conference and Exhibition on Power Generation, Transmission, Distribution and Energy Conversion*, pp:185-185, Nov. 2010

[166] T. V. Kumar, and S. Srinivasa Rao. Reduction of torque ripple in direct torque control of induction motor using constant switching frequency operation. *In Proc. of Mediterranean Conf. and Exhibition on Power Generation, Trans., Distri. and Energy Conver.*, pp:1-6, Nov. 2010.

[167] D. Stando, M. P. Kazmierkowski. Novel Speed Sensorless DTC-SVM Scheme for Induction Motor Drives. *In Proc. of Intern. Conf. on Compa. and Power Electr.,* pp:225-230, Jun. 2013.

[168] Y. Pan, Y. Zhang, Z. Wang. A novel variable domain adaptive fuzzy control of direct torque control for induction motor based on space vector control. *In Proc. of International Conference on Fuzzy Systems and Knowledge Discovery*, 2:639-643. Aug 2010.

[169] U. V. Patil, H. M. Suryawanshi, and M. M. Renge. Closed-loop hybrid direct torque control for medium voltage induction motor drive for performance improvement. *IET Power Electronics*, 7(1):31-40, Jan. 2014.

[170] T. Vinay Kumar and S. Srinivasa Rao. Hardware Implementation of Direct Load Angle Controlled Induction Motor Drive. *Electric Power Components and Systems*, 42(14):1505-1516, Oct. 2014.

[171] C. Lascu, I. Boldea, and F. Blaabjerg. A Modified Direct Torque Control for Induction Motor Sensor less Drive. *IEEE Transactions on Industry Applications*, 36(1):122-130, Jan. 2000.

[172] D. Casadei, G. Serra, A. Tani, L. Zarri, and F. Profumo. Performance analysis of a speed sensor less induction motor drive based on a constant switching-frequency DTC scheme. *IEEE Trans. on Industrial Appl.,* 39(2):476–484, Mar. 2003.

[173] T. Vinay Kumar, and S. Srinivasa Rao. Sensorless SVM-DTC method for induction motor drives based on amplitude and angle decoupled control of stator flux. *International Conference on Power, Control and Embedded Systems*, pp:1-6, Nov. 2010.

[174] H. Yu, Z. Chen. Three-Phase Induction Motor DTC-SVPWM Scheme with Self-tuning PI-Type Fuzzy Controller. *Intern. Jour. of Comp. and Commun. Engg.*, 4(3):204-212, May 2015.

[175] N. Venkataramana Naik, and S. P. Singh. A novel type-2 fuzzy logic control of induction motor drive using space vector PWM. *In Proc. of IEEE India Conference,* pp:1142-1147, Dec. 2012.

[176] N. Venkataramana Naik, and S. P. Singh. Improved torque and flux performance of type-2 fuzzy-based direct torque control induction motor using space vector pulse-width modulation. *Electric Power Components and Systems*, 42(6):658-669, Apr. 2014.

[177] N. Venkataramana Naik and S. P. Singh. A Comparative Analytical Performance of F2DTC and PIDTC of Induction Motor Using DSPACE-1104. *IEEE Transactions on Industrial Electronics,* 62(12):7350-7359, Dec. 2015.

[178] N. Venkataramana Naik, A. Panda and S. P. Singh. A Three-Level Fuzzy-2 DTC of Induction Motor Drive Using SVPWM. *IEEE Transactions on Industrial Electronics,* 99:1-10, 2015.

[179] I. J. Ha, and S. H. Lee. An online identification method for both stator-and rotor resistances of induction motors without rotational transducers. *IEEE Transactions on Industrial Electronics*, 47(4):842-853, Aug. 2000.

[180] B. K. Bose, N. R. Patel, and K. Rajashekara. A neuro-fuzzy-based on-line efficiency optimization control of a stator flux-oriented direct vector-controlled induction motor drive. *IEEE Transactions on Industrial Electronics*, 44(2):270-273, Apr. 1997.

[181] L. A. Cabrera, M. E. Elbuluk, and I. Husain. Tuning the stator resistance of induction motors using artificial neural network. *IEEE Trans. on Power Electronics*, 12(5):779-787, Sep. 1997.

[182] T. G. Habetler, F. Profumo, G. Griva, M. Pastorelli and A. Bettini. Stator resistance tuning in a stator-flux field-oriented drive using an instantaneous hybrid flux estimator. *IEEE Transactions on Power Electronics*, 13(1):125-133, Jan. 1998.

[183] B. K. Bose and N. R. Patel. Quasi-fuzzy estimation of stator resistance of induction motor. *IEEE Transactions on Power Electronics*, 13(3):401-409, May 1998.

[184] S. Mir, M. E. Elbuluk, and D. S. Zinger. PI and fuzzy estimators for tuning the stator resistance in direct torque control of induction machines. *IEEE Transactions on Power Electronics*, 13(2):279-287, Mar. 1998.

[185] H. Jun, B. R. Duggal and M. Vilathgamuwa. A MRAS-based Speed sensorless field oriented control of induction motor with on-line stator resistance tuning. *In International Conference on Power Electronic Drives and Energy Systems for Industrial Growth*, 1:38-43, Dec. 1998.

[186] K. Akatsu and A. Kawamura. Sensorless very low-speed and zero-speed estimations with online rotor resistance estimation of induction motor without signal injection. *IEEE Transactions on Industry Applications*, 36(3):764-771, May 2000.

[187] R. Marino, S. Peresada, and P. Tomei. On-line stator and rotor resistance estimation for induction motors. *IEEE Transactions on Control Systems Technology*, 8(3):570-579, May 2000.

[188] B. Karanayil, M. F. Rahman, and C. Grantham. PI and fuzzy estimators for on-line tracking of rotor resistance of indirect vector controlled induction motor drive. *In IEEE International Electric Machines and Drives Conference*, pp:820-825, 2001.

[189] M. Tsuji, S. Chen, K. Izumi, E. Yamada. A sensorless vector control system for induction motors using q-axis flux with stator resistance identification. *IEEE Transactions on Industrial Electronics*, 48(1):185-94, Feb. 2001.

[190] V. Vasic and S. Vukosavic. Robust MRAS-Based algorithm for stator resistance and rotor speed identification. *IEEE Power Engineering +Review,* 21(11):39-41, November 2001.

[191] V. Vasic, S. N. Vukosavic, and E. Levi. A stator resistance estimation scheme for speed sensorless rotor flux oriented induction motor drives. *IEEE Transactions on Energy Conversion*, 18(4):476-483, Dec. 2003.

[192] M. Rashed, F. Stronach, and P. Vas. A new stable mras-based speed and stator resistance estimators for sensorless vector control induction motor drive at low speeds. *In Proc. of IEEE IAS Annual Meeting*, 2:1181–1188, Oct. 2003.

[193] H. A. Toliyat, E. Levi, and M. Raina. A review of RFO induction motor parameter estimation techniques. *IEEE Transactions on Energy Conversion*, 18:271–283, Jun. 2003.

[194] B. Karanayil, M. F. Rahman, and C. Grantham. Stator and rotor resistance observers for induction motor drive using fuzzy logic and artificial neural networks. *IEEE Transactions on Energy Conversion*, 20(4):771-780, Dec. 2005.

[195] T. Bhattacharya and L. Umanand. Improved flux estimation and stator-resistance adaptation scheme for sensorless control of induction motor. *IEEE Proc. of Electric Power Application*, 153(6):911–920, Nov. 2006.

[196] B. Karanayil, M. F. Rahman, and C. Grantham. Online Stator and rotor resistance estimation scheme using artificial neural networks for vector controlled speed sensorless induction motor drives. *IEEE Transactions on Industrial Electronics,* 54(1):167-176, Feb. 2007.

[197] S. Maiti, C. Chakraborty, Y. Hori, and M. C. Ta. Model reference adaptive controller-based rotor resistance and speed estimation techniques for vector controlled induction motor drive utilizing reactive power. *IEEE Trans. on Industrial Electr.*, 55(2):594-601, Feb. 2008.

[198] I. Vicente, A. Endemano, X. Garin, and M. Brown. Comparative study of stabilising methods for adaptive speed sensorless full-order observers with stator resistance estimation. *IET Control Theory and Applications*, 4(6):993-1004, Jun. 2010.

[199] A. Bechouche, H. Sediki, D. O. Abdeslam, S. Haddad. A novel method for identifying parameters of induction motors at standstill using ADALINE. *IEEE Transactions on Energy Conversion*, 27(1):105-116, Mar. 2012.

[200] H. Sediki, A. Bechouche, D. O. Abdeslam, S. Haddad. ADALINE approach for induction motor mechanical parameters identification. *Mathematics and Computers in Simulation*, 90:86-97, Apr. 2013.

[201] K. B. Lee, J. H. Song, I. Choy, J. Y. Yoo. Improvement of low-speed operation performance of DTC for three-level inverter-fed induction motors. *IEEE Transactions on Industrial Electronics*, 48(5):1006-1014, Oct. 2001.

[202] P. C. Krause, O. Wasynczuk, S. D. Sudhoff. *Analysis of Electric Machinery and Drive Systems*. IEEE Press, 2002.

[203] *Intelligent Power Module* (PEC16DSM01), User Manual, Version 2.0.

[204] *dSPACE 1104 User's Guide*, Release 7.2, dSPACE GmbH.

[205] Q. G. Wang, Z. Zhang, K. J. Astrom, and L. S. Chek. Guaranteed dominant pole placement with PID controllers. *Journal of Process Control*, 19(2):349-352, Feb. 2009.

Appendix A

A.1 Machine Modelling

The voltage equations that describe the performance of the IM were developed in chapter 2. Where some of the machine inductances are functions of the rotor speed (ω_r), whereupon the coefficients of the differential equations (voltage equations) that describe the behavior of IM are time varying except when the rotor is stalled. The same effect is obtained by projecting the time varying machine variables into a reference frame which is rotating at an angular speed of rotor speed (ω_r). This frame of reference is called as Rotor (*D-Q*) reference frame.

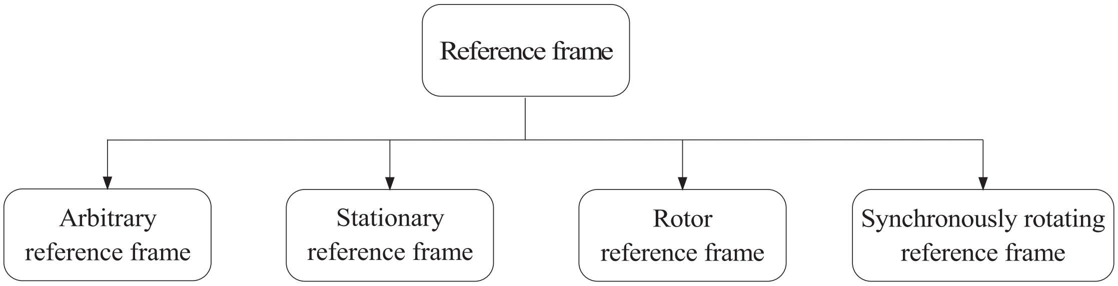

Figure A. 1: Different types of reference frames

The different types of the reference frames, which are used in the analysis of electric machines are illustrated in Figure A. 1.

Arbitrary reference frame: The reference frame which rotates at an angular speed of arbitrary speed (ω_a) is called as arbitrary (d^a - q^a) reference frame.

Stationary reference frame: The reference frame which is fixed on the stator is called as stationary (*d-q*) reference frame.

Synchronously rotating reference frame: The reference frame which rotates at an angular speed of synchronous speed (ω_e) is called as a synchronously rotating reference frame.

A.2 Circuit Model of Induction Motor

The generalized equations describing the behavior of an induction machine under transient and steady state conditions are established by considering it as an elementary ‘P’ pole idealized machine. The effect of the number of poles is taken into account by multiplying the expression of torque by number of pole-pairs.

An ideal three-phase induction motor can be schematically represented in Figure A. 2, where it is regarded as a group of linear coupled circuits. Distributed stator and rotor windings are shown by concentrated coils. The magnetic axes of the individual stator and rotor phases also marked. The connections and current conventions for the stator phases and the angular relationship of various axes are shown in Figure A. 3. The axis of a rotor phase is displaced by an angle θ_r from the axis of the corresponding stator phase. As the rotor rotates at ω_r rad/s, the angle θ_r varies with the time and is given by:

$$\theta_r = \omega_r t \tag{A.1}$$

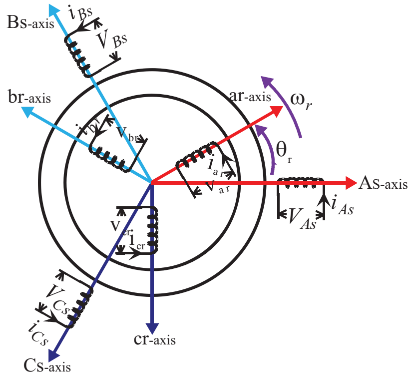

Figure A. 2: Idealized three-phase induction motor

If ω_e is the synchronous speed in electrical rad/sec, then slip is given by:

$$S = \frac{\omega_e - \omega_r}{\omega_e} \tag{A.2}$$

The $d^e - q^e$ reference frame is considered to be rotating synchronously with respect to the stator. Thus, considering the d^e-axis to be coincident with phase 'As' axis of the stator at t = 0, it will advance by an angle θ_e such that:

$$\theta_e = \omega_e t \tag{A.3}$$

The angle between d^e-axis and the rotor phase 'ar' axis is given as $\delta = \theta_e - \theta_r$.

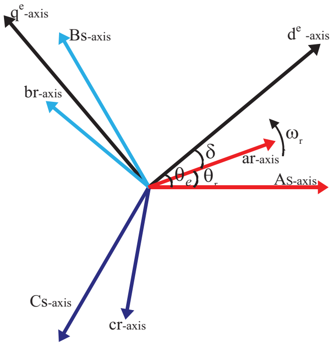

Figure A. 3: Axes of two pole three-phase Induction motor

A.3 Space Vector Representation

The mathematical model of the three-phase induction motor is derived using the equivalent circuit. A symmetric three-phase machine is represented by phase quantities, such as current, voltage and flux linkages. However, the three-phase machine can be described using space vectors such as stator current, voltage and flux space vectors in the stationary reference frame ($d-q$)fixed to stator may be defined as:

$$\vec{V}_s = \frac{2}{3}\left[V_{As} + aV_{Bs} + a^2 V_{Cs}\right] \tag{A.4}$$

$$\vec{i}_s = \frac{2}{3}\left[i_{As} + ai_{Bs} + a^2 i_{Cs}\right] \tag{A.5}$$

$$\vec{\psi}_s = \frac{2}{3}\left[\psi_{As} + a\psi_{Bs} + a^2\psi_{Cs}\right] \tag{A.6}$$

Similarly, the space vectors of the rotor voltage, current and flux in the rotor reference frame (D-Q) may be defined as:

$$\vec{V}_r^r = \frac{2}{3}\left[V_{ar} + aV_{br} + a^2 V_{cr}\right] \tag{A.7}$$

$$\vec{i}_r^r = \frac{2}{3}\left[i_{ar} + ai_{br} + a^2 i_{cr}\right] \tag{A.8}$$

$$\vec{\psi}_r^r = \frac{2}{3}\left[\psi_{ar} + a\psi_{br} + a^2\psi_{cr}\right] \tag{A.9}$$

where $a = e^{j\frac{2\pi}{3}} = -\frac{1}{2} + j\frac{\sqrt{3}}{2}$ and $a^2 = e^{j\frac{4\pi}{3}} = -\frac{1}{2} - j\frac{\sqrt{3}}{2}$

$1, a, a^2$ are the complex unity vectors, V_{As}, V_{Bs} and V_{Cs} are the three-phase stator voltages which are phase shifted by 120^0 from each other.

The three-phase stator voltage space vector is shown in Figure A. 4.

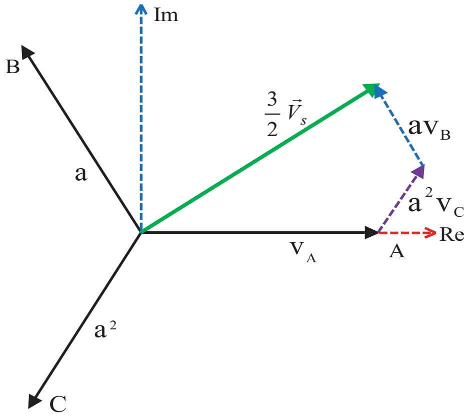

Figure A. 4: Construction of space vector for three phase voltage variable

Using the coupled circuit approach and motor notation, the voltage equations of the magnetically coupled stator and rotor circuits can be written as:

$$V_{ABCs} = R_s i_{ABCs} + \frac{d\psi_{ABCs}}{dt} \tag{A.10}$$

Similarly, the rotor voltage equations are:

$$V_{abcr} = R_r i_{abcr} + \frac{d\psi_{abcr}}{dt} \tag{A.11}$$

In a magnetic linear system, the flux linkages can be expressed as:

$$\begin{bmatrix} \psi_{abcs} \\ \psi_{abcr} \end{bmatrix} = \begin{bmatrix} L_s & L_{sr} \\ (L_{sr})^T & L_r \end{bmatrix} \begin{bmatrix} i_{abcs} \\ i_{abcr} \end{bmatrix} \tag{A.12}$$

The winding inductances are derived as:

$$\boldsymbol{L_s} = \begin{bmatrix} L_{ls} + L_{ms} & -\frac{1}{2}L_{ms} & -\frac{1}{2}L_{ms} \\ -\frac{1}{2}L_{ms} & L_{ls} + L_{ms} & -\frac{1}{2}L_{ms} \\ -\frac{1}{2}L_{ms} & -\frac{1}{2}L_{ms} & L_{ls} + L_{ms} \end{bmatrix} \text{and } \boldsymbol{L_r} = \begin{bmatrix} L_{lr} + L_{mr} & -\frac{1}{2}L_{mr} & -\frac{1}{2}L_{mr} \\ -\frac{1}{2}L_{mr} & L_{lr} + L_{mr} & -\frac{1}{2}L_{mr} \\ -\frac{1}{2}L_{mr} & -\frac{1}{2}L_{mr} & L_{lr} + L_{mr} \end{bmatrix}$$

$$\boldsymbol{L_{sr}} = L_{sr} \begin{bmatrix} cos\,\theta_r & cos\left(\theta_r + \frac{2\pi}{3}\right) & cos\left(\theta_r - \frac{2\pi}{3}\right) \\ cos\left(\theta_r - \frac{2\pi}{3}\right) & cos\,\theta_r & cos\left(\theta_r + \frac{2\pi}{3}\right) \\ cos\left(\theta_r + \frac{2\pi}{3}\right) & cos\left(\theta_r - \frac{2\pi}{3}\right) & cos\,\theta_r \end{bmatrix} \tag{A.13}$$

where L_{ls}, L_{ms}, L_{lr} and L_{mr} are leakage and magnetizing inductances of the stator, rotor windings and L_{sr} is the amplitude of mutual inductance between stator and rotor windings.

The stator voltage space vector in a stationary reference frame can be generated by substituting the three-phase stator voltage equation (A.10) into equation (A.4) as we get:

$$\vec{V}_s = \frac{2}{3}\left[R_s i_{As} + \frac{d\psi_{As}}{dt} + a\left(R_s i_{Bs} + \frac{d\psi_{Bs}}{dt} \right) + a^2\left(R_s i_{Cs} + \frac{d\psi_{Cs}}{dt} \right) \right] \tag{A.14}$$

$$\vec{V}_s = \left[\frac{2}{3}\left(i_{As} + a i_{Bs} + a^2 i_{Cs}\right) R_s + \frac{2}{3}\frac{d}{dt}\left(\psi_{As} + a\psi_{Bs} + a^2\psi_{Cs}\right) \right] \tag{A.15}$$

The stator voltage space vector can be simplified as:

$$\vec{V}_s = \left[R_s \vec{i}_s + \frac{d\vec{\psi}_s}{dt} \right] \tag{A.16}$$

Similarly, the rotor voltage space vector in the rotor reference frame can be generated by substituting the three phase rotor voltage equation (A.11) into the equation (A.7) as we get:

$$\vec{V}_r^{\,r} = \frac{2}{3}\left[R_r i_{ar} + \frac{d\psi_{ar}}{dt} + a\left(R_r i_{br} + \frac{d\psi_{br}}{dt} \right) + a^2\left(R_r i_{cr} + \frac{d\psi_{cr}}{dt} \right) \right] \tag{A.17}$$

$$\vec{V}_r^{\,r} = \left[\frac{2}{3}\left(i_{ar} + a i_{br} + a^2 i_{cr}\right) R_s + \frac{2}{3}\frac{d}{dt}\left(\psi_{ar} + a\psi_{br} + a^2\psi_{cr}\right) \right] \tag{A.18}$$

The rotor voltage space vector in the rotor reference frame can be simplified as:

$$\vec{V}_r^r = \left[R_r \vec{i}_r^r + \frac{d\vec{\psi}_r^r}{dt} \right] \tag{A.19}$$

A.6 Three-Phase to Two-Phase Transformation (Clarke Transformation)

The dynamic performance of a three-phase induction machine is somewhat complex due to the three-phase rotor moves with respect to the stator as shown in Figure A. 5 (a). In order to reduce the complexity and obtain the constant coefficients in the differential equations, the three-phase components are transformed into two-phase axes components are shown in Figure A. 5 (b).

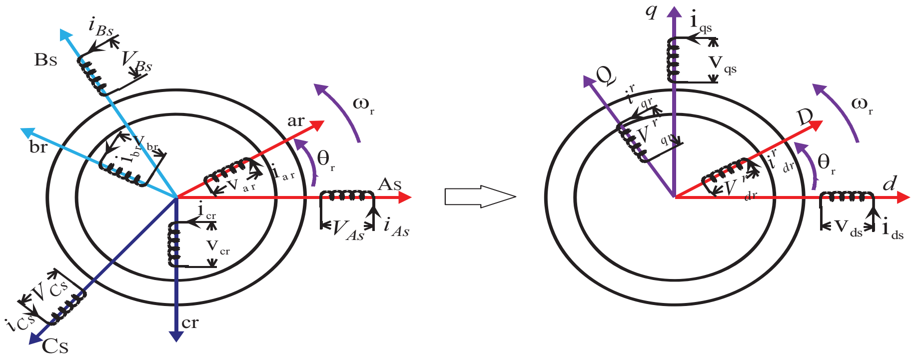

(a) (b)

Figure A. 5: Equivalence of induction motor stator and rotor windings in: (a) three-phase quantities and (b) two-phase quantities

A dynamic model for the three-phase induction machine can be derived from the three-phase to two-phase axis transformation. The equivalence is based on the equality of the MMF produced in the two-phase and three-phase windings and equal current magnitudes. The *d* and *q* axis MMF are found by resolving the MMF of the three-phases along the *d* and *q* axes. The three-phase machine variables can be represented as a space vector expressed on a two orthogonal (*d*-*q*) axis, as shown in Figure A. 6.

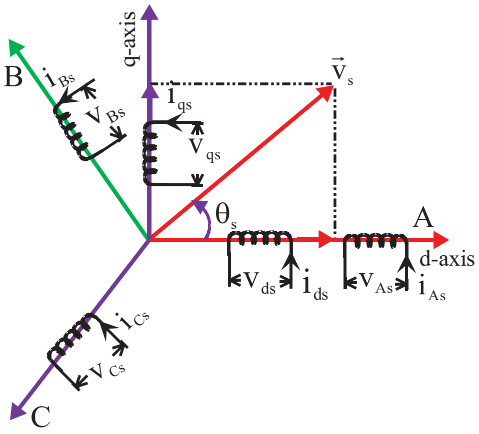

Figure A. 6: Two axis components of stator voltage space vector

The equation (A.4) is resolved into its real and imaginary parts producing the dq-axes components of the stator voltage space vector in the stator reference frame as:

$$V_{ds} = \frac{2}{3}V_{As} - \frac{1}{3}V_{Bs} - \frac{1}{3}V_{Cs} \tag{A.20}$$

$$V_{qs} = \frac{1}{\sqrt{3}}V_{Bs} - \frac{1}{\sqrt{3}}V_{Cs} \tag{A.21}$$

where V_{ds} and V_{qs} are the actual stator voltages that flows in the stator *d*, *q*-axis windings.

The stator voltage space vector can be described in the complex form as:

$$\vec{V}_s = V_{ds} + jV_{qs} = \left|\vec{V}_s\right| e^{j\theta_s} \tag{A.22}$$

The three-phase to two-phase transformation can be written in a matrix form as:

$$\begin{bmatrix} V_{ds} \\ V_{qs} \end{bmatrix} = \begin{bmatrix} \frac{2}{3} & -\frac{1}{3} & -\frac{1}{3} \\ 0 & \frac{1}{\sqrt{3}} & -\frac{1}{\sqrt{3}} \end{bmatrix} \begin{bmatrix} V_{As} \\ V_{Bs} \\ V_{Cs} \end{bmatrix} \tag{A.23}$$

The expression (A.23) can be inverse transformed from two phase (*dq*-axis) into three-phase (*ABC*-axis) is written in matrix form as:

$$\begin{bmatrix} V_{As} \\ V_{Bs} \\ V_{Cs} \end{bmatrix} = \begin{bmatrix} 1 & 0 \\ -\frac{1}{2} & \frac{\sqrt{3}}{2} \\ -\frac{1}{2} & -\frac{\sqrt{3}}{2} \end{bmatrix} \begin{bmatrix} V_{ds} \\ V_{qs} \end{bmatrix} \tag{A.24}$$

A.5 PARK Transformation (dq to $d^e q^e$-axes)

The two-phase stator *d-q* axes stationary reference frames are required to transform into two-phase synchronously rotating reference frame d^e-q^e axes for indirect field oriented control scheme implementation. Figure A. 7 shows the synchronously rotating reference frame d^e-q^e axes, which rotate at synchronous speed ω_e with respect to stator *d-q* axes and θ_e is the stator flux position.

The stator voltages on the *d-q* axis can be converted into the d^e-q^e frame as follows:

$$\vec{V}_s^e = V_{ds}^e + jV_{qs}^e = \vec{V}_s\, e^{-j\theta_e} = \left(V_{ds} + jV_{qs}\right)e^{-j\theta_e} \tag{A.25}$$

where subscript '*s*' stands for the stator quantities and the superscript *e* stands for the synchronous reference frame.

The equation (A.25) can be written in matrix form as:

$$\begin{bmatrix} V_{ds}^e \\ V_{qs}^e \end{bmatrix} = \begin{bmatrix} \cos\theta_e & \sin\theta_e \\ -\sin\theta_e & \cos\theta_e \end{bmatrix} \begin{bmatrix} V_{ds} \\ V_{qs} \end{bmatrix} \tag{A.26}$$

Again, the synchronous (d^e-q^e) frame matrix expression (A.26) resolving into a stationary (d-q) reference frame is given by:

$$\begin{bmatrix} V_{ds} \\ V_{qs} \end{bmatrix} = \begin{bmatrix} \cos\theta_e & -\sin\theta_e \\ \sin\theta_e & \cos\theta_e \end{bmatrix} \begin{bmatrix} V_{ds}^e \\ V_{qs}^e \end{bmatrix} \tag{A.27}$$

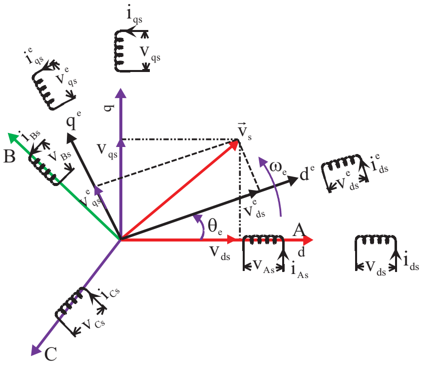

Figure A. 7: Stator voltage space vector component in stationary (d-q) and synchronous (d^e-q^e) reference frame

Similarly, the stator current and flux space vectors expressed in the stationary reference frame as follows:

$$\vec{i}_s = \frac{2}{3}\left[i_{As} + a i_{Bs} + a^2 i_{Cs}\right] = i_{ds} + j i_{qs} \tag{A.28}$$

$$\vec{\psi}_s = \frac{2}{3}\left[\psi_{As} + a\psi_{Bs} + a^2\psi_{Cs}\right] = \psi_{ds} + j\psi_{qs} \tag{A.29}$$

The rotor voltage space vector in a reference frame fixed on the rotor can be expressed in a similar way of stator voltage space vector fixed on the stator reference frame as follows:

$$\vec{V}_r^r = \frac{2}{3}\left[V_{ar} + aV_{br} + a^2 V_{cr}\right] \tag{A.30}$$

$$\vec{V}_r^r = V_{Dr}^r + jV_{Qr}^r = \left|\vec{V}_r^r\right| e^{j\theta_r} \tag{A.31}$$

where V_{Dr}^r and V_{Qr}^r are the direct and quadrature axis rotor voltage components in the rotor reference frame which are quadrature in space and θ_r is the rotor position.

A.6 Dynamic Modelling of Induction Motor in Arbitrary Reference Frame

The reference frames are like observer platforms, in which each of the platforms gives a unique view of the system at hand as well as dramatic simplifications of the system equations. The mathematical model of the IM can be expressed in different types of reference frames. Instead of giving the transformations for each and every particular reference frame, it is advantageous to derive the general transformation for any arbitrary rotating reference frame. Thus, any particular reference frame equations can be derived from the generalized reference model by substituting the appropriate frame speed (ω) and position (θ) in it.

The three-phase IM under consideration is assumed to have a symmetrical air gap. The dq-reference frames are usually selected on the basis of computational reduction. The two commonly used reference frames in the analysis of the IM are the stationary and synchronously rotating frames. In the stationary reference frame, the dq-variables of the machine are in the same frame as those normally used for the supply network. In the synchronously rotating reference frame, the direct and quadrature axis variables are DC quantities in steady state. Here, firstly the equations of the IM, in arbitrary reference frame ($d^a - q^a$) which is rotating at an angular speed ω_a, will be derived. The IM in the stationary reference frame can be obtained by setting $\omega_a = 0$, whereas the synchronously rotating reference frame can be obtained by setting $\omega_a = \omega_e$.

The space vectors of stator and rotor quantities in the arbitrary reference frame can be written as:

$$\left.\begin{aligned}\vec{V}_s^a &= V_{ds}^a + j\,V_{qs}^a\\ \vec{i}_s^{\,a} &= i_{ds}^a + j\,i_{qs}^a\\ \vec{\psi}_s^a &= \psi_{ds}^a + j\,\psi_{qs}^a\end{aligned}\right\}\tag{A.32}$$

$$\left.\begin{aligned}\vec{V}_r^a &= V_{dr}^a + j\,V_{qr}^a\\ \vec{i}_r^{\,a} &= i_{dr}^a + j\,i_{qr}^a\\ \vec{\psi}_r^a &= \psi_{dr}^a + j\,\psi_{qr}^a\end{aligned}\right\}\tag{A.33}$$

where superscript '*a*' represents the arbitrary reference frame, subscripts '*r*' and '*s*' represents the stator and rotor quantities, respectively and subscripts '*d*' and '*q*' represents a direct and quadrature axis components.

Using the frame transformation the stator quantities in the stator reference frame and the rotor quantities in the rotor reference frame can be written as:

$$\left.\begin{aligned}\vec{V}_s &= \vec{V}_s^a \cdot e^{j\theta_a}\\ \vec{i}_s &= \vec{i}_s^{\,a} \cdot e^{j\theta_a}\\ \vec{\psi}_s &= \vec{\psi}_s^a \cdot e^{j\theta_a}\end{aligned}\right\}\tag{A.34}$$

$$\left.\begin{aligned}\vec{V}_r^r &= \vec{V}_r^a \cdot e^{j(\theta_a-\theta_r)}\\ \vec{i}_r^{\,r} &= \vec{i}_r^{\,a} \cdot e^{j(\theta_a-\theta_r)}\\ \vec{\psi}_r^r &= \vec{\psi}_r^a \cdot e^{j(\theta_a-\theta_r)}\end{aligned}\right\}\tag{A.35}$$

where θ_a is the angular displacement of the arbitrary reference frame and angular speed of the arbitrary reference frame can be written as:

$$\omega_a = \frac{d\theta_a}{dt}\tag{A.36}$$

Substituting the equation (A.34) into equation (A.16) gives the stator voltage in the arbitrary reference frame as:

$$\vec{V}_s^a \cdot e^{j\theta_a} = R_s \vec{i}_s^a \cdot e^{j\theta_a} + \frac{d}{dt}\left(\vec{\psi}_s^a \cdot e^{j\theta_a}\right)$$

$$\vec{V}_s^a \cdot e^{j\theta_a} = R_s \vec{i}_s^a \cdot e^{j\theta_a} + e^{j\theta_a}\frac{d}{dt}\left(\vec{\psi}_s^a\right) + \vec{\psi}_s^a \cdot e^{j\theta_a} \cdot j\frac{d\theta_a}{dt} \tag{A.37}$$

The equation (A.37) can be further simplified as:

$$\vec{V}_s^a = R_s \vec{i}_s^a + p\vec{\psi}_s^a + j\omega_a \vec{\psi}_s^a \tag{A.38}$$

Similarly, substituting the equation (A.35) into equation (A.19) gives the rotor voltage in the arbitrary reference frame as:

$$\vec{V}_r^a \cdot e^{j(\theta_a - \theta_r)} = R_r \vec{i}_r^a \cdot e^{j(\theta_a - \theta_r)} + \frac{d}{dt}\left(\vec{\psi}_r^a \cdot e^{j(\theta_a - \theta_r)}\right)$$

$$\vec{V}_r^a e^{j(\theta_a - \theta_r)} = R_r \vec{i}_r^a e^{j(\theta_a - \theta_r)} + e^{j(\theta_a - \theta_r)}\frac{d}{dt}\left(\vec{\psi}_r^a\right) + \vec{\psi}_r^a e^{j(\theta_a - \theta_r)} j\frac{d}{dt}\left(\theta_a - \theta_r\right) \tag{A.39}$$

The equation (A.39) can be further simplified as:

$$\vec{V}_r^a = R_r \vec{i}_r^a + p\vec{\psi}_r^a + j\omega_{am} \vec{\psi}_r^a \tag{A.40}$$

Similarly, the stator and rotor flux linkages in the arbitrary reference frame can be written as:

$$\vec{\psi}_s^a = L_s \vec{i}_s^a + L_m \vec{i}_r^a \tag{A.41}$$

$$\vec{\psi}_r^a = L_r \vec{i}_r^a + L_m \vec{i}_s^a \tag{A.42}$$

The developed electromagnetic torque 'T_e' of an induction motor is given by:

$$T_e = \frac{3}{2}\frac{P}{2}\left(\psi_{ds}^a \cdot i_{qs}^a - \psi_{qs}^a \cdot i_{ds}^a\right) \tag{A.43}$$

The torque balancing mechanical equation is given by:

$$T_e = T_L + B\omega_m + Jp\omega_m \tag{A.44}$$

where $\omega_{am} = \omega_a - \omega_r$, p is differential operator $\frac{d}{dt}$, P is the number of poles, j is complex operator, J is moment of inertia and B is viscous friction coefficient.

By substituting the equation (A.41) in equation (A.38) we will get:

$$\vec{V}_s^a = \left[\left(R_s + L_s p\right) + j\omega_a L_s\right]\vec{i}_s^a + \left[L_m p + j\omega_a L_m\right]\vec{i}_r^a \tag{A.45}$$

By substituting equation (A.42) in equation (A.40) we will get:

$$\vec{V}_r^a = \left[L_m p + j\omega_{am} L_m\right]\vec{i}_s^a + \left[\left(R_r + L_r p\right) + j\omega_{am} L_r\right]\vec{i}_r^a \tag{A.46}$$

As we know that the rotor coils of the induction motor are short circuited, so $V_{dr}^a = V_{qr}^a = 0$.

By separating real and imaginary parts from the equations (A.45) and (A.46) we will get the voltage equations of IM in arbitrary reference frame and they can be arranged in matrix form as follows:

$$\begin{bmatrix} V_{ds}^{a} \\ V_{qs}^{a} \\ 0 \\ 0 \end{bmatrix} = \begin{bmatrix} R_s + L_s p & -\omega_a L_s & L_m p & -\omega_a L_m \\ \omega_a L_s & R_s + L_s p & \omega_a L_m & L_m p \\ L_m p & -\omega_{am} L_m & R_r + L_r p & -\omega_{am} L_r \\ \omega_{am} L_m & L_m p & \omega_{am} L_r & R_r + L_r p \end{bmatrix} \begin{bmatrix} i_{ds}^{a} \\ i_{qs}^{a} \\ i_{dr}^{a} \\ i_{qr}^{a} \end{bmatrix} \tag{A.47}$$

From the equation (A.42), we can get the rotor current in the arbitrary reference frame as:

$$\vec{i}_r^{\,a} = \frac{1}{L_r}\left(\vec{\psi}_r^{\,a} - L_m \vec{i}_s^{\,a}\right) \tag{A.48}$$

The rotor current $\vec{i}_r^{\,a}$ is substituting into the rotor voltage equation (A.40), we get:

$$p\vec{\psi}_r^{\,a} = \frac{L_m R_r}{L_r}\vec{i}_s^{\,a} - \left(\frac{R_r}{L_r} + j\omega_{am}\right)\vec{\psi}_r^{\,a} \tag{A.49}$$

The rotor current $\vec{i}_r^{\,a}$ is substituting into the equation (A.45), we get:

$$\vec{V}_s^{\,a} = \left[\left(R_s + L_s p\right) + j\omega_a L_s - \frac{L_m}{L_r}\left(L_m p + j\omega_a L_m\right)\right]\vec{i}_s^{\,a} + j\omega_a \frac{L_m}{L_r}\vec{\psi}_r^{\,a} + \frac{L_m}{L_r} p\vec{\psi}_r^{\,a} \tag{A.50}$$

By substituting equation (A.49) in equation (A.50) and solve for $p\vec{i}_s^{\,a}$, we get:

$$p\vec{i}_s^{\,a} = \frac{1}{\sigma L_s}\left\{\vec{V}_s^{\,a} - \left(R_s + \frac{L_m^2}{L_r T_r} + j\sigma L_s \omega_a\right)\vec{i}_s^{\,a} + \left(\frac{L_m}{L_r T_r} - j\omega_r \frac{L_m}{L_r}\right)\vec{\psi}_r^{\,a}\right\} \tag{A.51}$$

where $\sigma = 1 - \frac{L_m^2}{L_s L_r} =$ leakage coefficient and $T_r = \frac{L_r}{R_r}$

By separating and equating real and imaginary parts on both sides of equations (A.51) and (A.49) respectively, we get

$$p i_{ds}^{a} = -\frac{R_s + \frac{L_m^2}{L_r T_r}}{\sigma L_s} i_{ds}^{a} + \omega_a i_{qs}^{a} + \frac{L_m}{\sigma L_s L_r T_r}\psi_{dr}^{a} + \frac{L_m}{\sigma L_s L_r}\omega_r \psi_{qr}^{a} + \frac{V_{ds}^{a}}{\sigma L_s} \tag{A.52}$$

$$p i_{qs}^{a} = -\omega_a i_{ds}^{a} - \frac{R_s + \frac{L_m^2}{L_r T_r}}{\sigma L_s} i_{qs}^{a} - \frac{L_m}{\sigma L_s L_r}\omega_r \psi_{dr}^{a} + \frac{L_m}{\sigma L_s L_r T_r}\psi_{qr}^{a} + \frac{V_{qs}^{a}}{\sigma L_s} \tag{A.53}$$

$$p\psi_{dr}^{a} = \frac{L_m}{T_r} i_{ds}^{a} - \frac{1}{T_r}\psi_{dr}^{a} + \omega_{am}\psi_{qr}^{a} \tag{A.54}$$

$$p\psi_{qr}^{a} = \frac{L_m}{T_r} i_{qs}^{a} - \omega_{am}\psi_{dr}^{a} - \frac{1}{T_r}\psi_{qr}^{a} \tag{A.55}$$

By arranging the equations (A.52-A.55) together in matrix form for getting the state-space model of the induction motor in the arbitrary reference frame in terms of stator current components (i_{ds}, i_{qs}) and rotor flux components (ψ_{dr}, ψ_{qr}) as state variables, we get:

$$\frac{d}{dt}\begin{bmatrix} i_{ds}^a \\ i_{qs}^a \\ \psi_{dr}^a \\ \psi_{qr}^a \end{bmatrix} = \begin{bmatrix} -a_1 & \omega_a & a_2 & a_3\omega_r \\ -\omega_a & -a_1 & -a_3\omega_r & a_2 \\ a_5 & 0 & -a_4 & \omega_{am} \\ 0 & a_5 & -\omega_{am} & -a_4 \end{bmatrix}\begin{bmatrix} i_{ds}^a \\ i_{qs}^a \\ \psi_{dr}^a \\ \psi_{qr}^a \end{bmatrix} + \begin{bmatrix} \frac{1}{\sigma L_s} & 0 \\ 0 & \frac{1}{\sigma L_s} \\ 0 & 0 \\ 0 & 0 \end{bmatrix}\begin{bmatrix} V_{ds}^a \\ V_{qs}^a \end{bmatrix} \tag{A.56}$$

where $a_1 = \frac{1}{\sigma L_s}\left(R_s + \frac{L_m^2}{L_r T_r}\right), a_2 = \frac{1}{\sigma L_s}\frac{L_m}{L_r T_r}, a_3 = \frac{1}{\sigma L_s}\frac{L_m}{L_r}$, $a_4 = \frac{1}{T_r}$, and $a_5 = \frac{L_m}{T_r}$.

The IM mathematical model can be represented in the arbitrary reference frame using the state-space standard notation as:

$$\dot{X} = AX + BU \tag{A.57}$$

$$Y = CX \tag{A.58}$$

where,

$$A = \begin{bmatrix} -a_1 & \omega_a & a_2 & a_3\omega_r \\ -\omega_a & -a_1 & -a_3\omega_r & a_2 \\ a_5 & 0 & -a_4 & \omega_{am} \\ 0 & a_5 & -\omega_{am} & -a_4 \end{bmatrix}, B = \begin{bmatrix} \frac{1}{\sigma L_s} & 0 \\ 0 & \frac{1}{\sigma L_s} \\ 0 & 0 \\ 0 & 0 \end{bmatrix}, C = \begin{bmatrix} 1 & 0 \\ 0 & 1 \\ 0 & 0 \\ 0 & 0 \end{bmatrix}^T, X = \begin{bmatrix} i_{ds}^a \\ i_{qs}^a \\ \psi_{dr}^a \\ \psi_{qr}^a \end{bmatrix}, U = \begin{bmatrix} V_{ds}^a \\ V_{qs}^a \end{bmatrix}, Y = \begin{bmatrix} i_{ds}^a \\ i_{qs}^a \end{bmatrix}$$

A.7 Synchronous Reference Frame

The induction motor model in the synchronous reference frame can be obtained from the arbitrary reference frame equations (A.47) and (A.56) by substituting $\omega_a = \omega_e$. These equations can be written in matrix form as follows:

$$\begin{bmatrix} V_{ds}^e \\ V_{qs}^e \\ 0 \\ 0 \end{bmatrix} = \begin{bmatrix} R_s + L_s p & -\omega_e L_s & L_m p & -\omega_e L_m \\ \omega_e L_s & R_s + L_s p & \omega_e L_m & L_m p \\ L_m p & -\omega_{sl} L_m & R_r + L_r p & -\omega_{sl} L_r \\ \omega_{sl} L_m & L_m p & \omega_{sl} L_r & R_r + L_r p \end{bmatrix}\begin{bmatrix} i_{ds}^e \\ i_{qs}^e \\ i_{dr}^e \\ i_{qr}^e \end{bmatrix} \tag{A.59}$$

The state space model of IM in the synchronous reference frame can be expressed as follows:

$$\frac{d}{dt}\begin{bmatrix} i_{ds}^e \\ i_{qs}^e \\ \psi_{dr}^e \\ \psi_{qr}^e \end{bmatrix} = \begin{bmatrix} -a_1 & \omega_e & a_2 & a_3\omega_r \\ -\omega_e & -a_1 & -a_3\omega_r & a_2 \\ a_5 & 0 & -a_4 & \omega_{sl} \\ 0 & a_5 & -\omega_{sl} & -a_4 \end{bmatrix}\begin{bmatrix} i_{ds}^e \\ i_{qs}^e \\ \psi_{dr}^e \\ \psi_{qr}^e \end{bmatrix} + \begin{bmatrix} \frac{1}{\sigma L_s} & 0 \\ 0 & \frac{1}{\sigma L_s} \\ 0 & 0 \\ 0 & 0 \end{bmatrix}\begin{bmatrix} V_{ds}^e \\ V_{qs}^e \end{bmatrix} \tag{A.60}$$

where $\omega_{sl} = \omega_e - \omega_r$

A.8 Stationary Reference Frame

The induction motor model in the stationary reference frame can be obtained from the arbitrary reference frame equations (A.47) and (A.56) by substituting $\omega_a = 0$. The voltage equations of IM in a stationary reference frame can be written in matrix form as follows:

$$\begin{bmatrix} V_{ds} \\ V_{qs} \\ 0 \\ 0 \end{bmatrix} = \begin{bmatrix} R_s + L_s p & 0 & L_m p & 0 \\ 0 & R_s + L_s p & 0 & L_m p \\ L_m p & \omega_r L_m & R_r + L_r p & \omega_r L_r \\ -\omega_r L_m & L_m p & -\omega_r L_r & R_r + L_r p \end{bmatrix} \begin{bmatrix} i_{ds} \\ i_{qs} \\ i_{dr} \\ i_{qr} \end{bmatrix} \tag{A.61}$$

The state space model of IM in a stationary reference frame can be expressed as follows:

$$\frac{d}{dt} \begin{bmatrix} i_{ds} \\ i_{qs} \\ \psi_{dr} \\ \psi_{qr} \end{bmatrix} = \begin{bmatrix} -a_1 & 0 & a_2 & a_3 \omega_r \\ 0 & -a_1 & -a_3 \omega_r & a_2 \\ a_5 & 0 & -a_4 & -\omega_r \\ 0 & a_5 & \omega_r & -a_4 \end{bmatrix} \begin{bmatrix} i_{ds} \\ i_{qs} \\ \psi_{dr} \\ \psi_{qr} \end{bmatrix} + \begin{bmatrix} \frac{1}{\sigma L_s} & 0 \\ 0 & \frac{1}{\sigma L_s} \\ 0 & 0 \\ 0 & 0 \end{bmatrix} \begin{bmatrix} V_{ds} \\ V_{qs} \end{bmatrix} \tag{A.62}$$

A.9 Rotor Reference Frame

The speed of the rotor reference frame is $\omega_a = \omega_r$ and angular position is $\theta_a = \theta_r$. The induction motor model in the rotor reference frame is obtained from the arbitrary reference frame equations (A.47) and (A.56) with $\omega_a = \omega_r$. The superscript *m* denotes a rotor reference frame, the voltage equations of IM in the rotor reference frame can be written in matrix form as follows:

$$\begin{bmatrix} V_{ds}^r \\ V_{qs}^r \\ 0 \\ 0 \end{bmatrix} = \begin{bmatrix} R_s + L_s p & -\omega_r L_s & L_m p & -\omega_r L_m \\ \omega_r L_s & R_s + L_s p & \omega_r L_m & L_m p \\ L_m p & 0 & R_r + L_r p & 0 \\ 0 & L_m p & 0 & R_r + L_r p \end{bmatrix} \begin{bmatrix} i_{ds}^r \\ i_{qs}^r \\ i_{dr}^r \\ i_{qr}^r \end{bmatrix} \tag{A.63}$$

The state space model of IM in the rotor reference frame can be expressed as follows:

$$\frac{d}{dt} \begin{bmatrix} i_{ds}^r \\ i_{qs}^r \\ \psi_{dr}^r \\ \psi_{qr}^r \end{bmatrix} = \begin{bmatrix} -a_1 & \omega_r & a_2 & a_3 \omega_r \\ -\omega_r & -a_1 & -a_3 \omega_r & a_2 \\ a_5 & 0 & -a_4 & 0 \\ 0 & a_5 & 0 & -a_4 \end{bmatrix} \begin{bmatrix} i_{ds}^r \\ i_{qs}^r \\ \psi_{dr}^r \\ \psi_{qr}^r \end{bmatrix} + \begin{bmatrix} \frac{1}{\sigma L_s} & 0 \\ 0 & \frac{1}{\sigma L_s} \\ 0 & 0 \\ 0 & 0 \end{bmatrix} \begin{bmatrix} V_{ds}^r \\ V_{qs}^r \end{bmatrix} \tag{A.64}$$

Appendix B

B.1 Controller Design for DTC-SVM Method with Closed-loop Torque and Flux Control in Stator Flux Coordinates

The controller design as well as the stability analysis of DTC-SVM with closed loop torque and flux control in stator flux coordinates requires the transfer function of the machine model in stator flux coordinate system. The mathematical model of IM equations in the stator flux coordinate system (i.e. synchronous reference frame system) can be derived by substituting $\omega_a = \omega_e$ in equations (A.38) and (A.40-A.44), as:

$$\vec{V}_s^e = R_s \vec{i}_s^{\,e} + p\vec{\psi}_s^e + j\omega_e \vec{\psi}_s^e \tag{A.65}$$

$$\vec{V}_r^e = R_r \vec{i}_r^{\,e} + p\vec{\psi}_r^e + j\omega_{sl} \vec{\psi}_r^e \tag{A.66}$$

$$\vec{\psi}_s^e = L_s \vec{i}_s^{\,e} + L_m \vec{i}_r^{\,e} \tag{A.67}$$

$$\vec{\psi}_r^e = L_r \vec{i}_r^{\,e} + L_m \vec{i}_s^{\,e} \tag{A.68}$$

$$T_e = \frac{3}{2}\frac{P}{2}\left(\psi_{ds}^e \cdot i_{qs}^e - \psi_{qs}^e \cdot i_{ds}^e\right) \tag{A.69}$$

$$T_e = T_L + B\omega_m + Jp\omega_m \tag{A.70}$$

where $\omega_{sl} = \omega_e - \omega_r$

As we know that the rotor coils of the induction motor are short circuited, so $\vec{V}_r^e = 0$ and at the same time in a stator flux oriented coordinate system the quadrature axis component of the stator flux (ψ_{qs}^e) is zero.

By substituting $\psi_{qs}^e = 0$ and $\vec{V}_r^e = 0$ in equations (A.32) and (A.33) respectively, the space vectors of stator and rotor quantities in the stator flux oriented reference frame can be written as:

$$\left.\begin{aligned} \vec{V}_s^e &= V_{ds}^e + j\,V_{qs}^e \\ \vec{i}_s^{\,e} &= i_{ds}^e + j\,i_{qs}^e \\ \vec{\psi}_s^e &= \psi_{ds}^e = \psi_s^e \end{aligned}\right\} \tag{A.71}$$

$$\left.\begin{aligned} \vec{V}_r^e &= 0 \\ \vec{i}_r^{\,e} &= i_{dr}^e + j\,i_{qr}^e \\ \vec{\psi}_r^e &= \psi_{dr}^e + j\,\psi_{qr}^e \end{aligned}\right\} \tag{A.72}$$

By substituting $\vec{V}_r^e = 0$ and $\psi_{qs}^e = 0$ in equations (A.66) and (A.69) respectively, the rotor voltage and electrical torque can be rewritten as:

$$0 = R_r \vec{i}_r^{\,e} + p\vec{\psi}_r^e + j\omega_{sl} \vec{\psi}_r^e \tag{A.73}$$

$$T_e = \frac{3}{2}\frac{P}{2}\psi_s^e \cdot i_{qs}^e \tag{A.74}$$

The equation (A.67) can be rearranged as:

$$\vec{i}_r^{\,e} = \frac{1}{L_m}\left(\psi_s^e - L_s \vec{i}_s^{\,e}\right) \tag{A.75}$$

By substituting equation (A.75) in equation (A.68), we get:

$$\vec{\psi}_r^e = \frac{L_r}{L_m}\psi_s^e - \frac{\sigma L_s L_r}{L_m}\vec{i}_s^{\,e} \tag{A.76}$$

By substituting equations (A.75) and (A.76) in equation (A.73), we get:

$$\left(R_r + L_r p + j\omega_{sl} L_r\right)\psi_s^e = \left(R_r L_s + \sigma L_s L_r p + j\omega_{sl}\sigma L_s L_r\right)\vec{i}_s^{\,e} \tag{A.77}$$

By equating real and imaginary parts on both sides of equations (A.65) and (A.77) respectively, we get:

$$V_{ds}^e = R_s i_{ds}^e + p\psi_s^e \tag{A.78}$$

$$V_{qs}^e = R_s i_{qs}^e + \omega_e \psi_s^e \tag{A.79}$$

$$\left(R_r + L_r p\right)\psi_s^e = \left(R_r L_s + \sigma L_s L_r p\right) i_{ds}^e - \left(\omega_{sl}\sigma L_s L_r\right) i_{qs}^e \tag{A.80}$$

$$L_r \omega_e \psi_s^e - L_r \omega_r \psi_s^e = \left(\omega_{sl}\sigma L_s L_r\right) i_{ds}^e + \left(R_r L_s + \sigma L_s L_r p\right) i_{qs}^e \tag{A.81}$$

B.2 Flux Control Loop

The equation (A.78) can be rewritten as:

$$i_{ds}^e = \frac{1}{R_s}\left(V_{ds}^e - p\psi_s^e\right) \tag{A.82}$$

By substituting equation (A.82) in equation (A.80), we get:

$$\left(R_r L_s + \sigma L_s L_r p\right)V_{ds}^e = \left(R_r R_s + p\left(R_s L_r + R_r L_s\right) + \sigma L_s L_r p^2\right)\psi_s^e + \left(\omega_{sl}\sigma L_s L_r R_s\right) i_{qs}^e \tag{A.83}$$

Under the assumption that the last term in the equation (A.83) is very small:

$$\left(\omega_{sl}\sigma L_s L_r R_s\right) i_{qs}^e \approx 0 \tag{A.84}$$

Equation (A.83) can be rewritten as:

$$\left(R_r L_s + \sigma L_s L_r p\right)V_{ds}^e = \left(R_r R_s + p\left(R_s L_r + R_r L_s\right) + \sigma L_s L_r p^2\right)\psi_s^e \tag{A.85}$$

The open loop transfer function of the flux control loop (Figure B. 1) can be obtained from equation (A.85) as:

$$\frac{\psi_s^e}{V_{ds}^e} = \frac{s + A_\psi}{s^2 + B_\psi s + C_\psi} \tag{A.86}$$

where $A_\psi = \dfrac{R_r}{\sigma L_r}$, $B_\psi = \dfrac{R_s L_r + R_r L_s}{\sigma L_s L_r}$, and $C_\psi = \dfrac{R_s R_r}{\sigma L_s L_r}$.

B.3 Torque Control Loop

The equation (A.79) can be rewritten as:

$$\omega_e \psi_s^e = V_{qs}^e - R_s i_{qs}^e \tag{A.87}$$

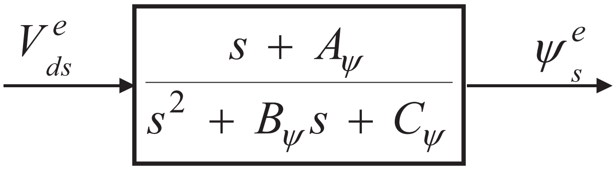

Figure B. 1: Open loop transfer function of flux control loop

By substituting equation (A.87) in equation (A.81), we get:

$$\left(R_s L_r + R_r L_s + \sigma L_s L_r p\right) i_{qs}^e = L_r V_{qs}^e - L_r \omega_e \psi_s^e - \left(\omega_{sl} \sigma L_s L_r\right) i_{ds}^e \tag{A.88}$$

Under the assumption that the last term in the equation (A.88) is very small:

$$\left(\omega_{sl} \sigma L_s L_r\right) i_{ds}^e \approx 0 \tag{A.89}$$

Equation (A.88) can be rewritten as:

$$\left(R_s L_r + R_r L_s + \sigma L_s L_r p\right) i_{qs}^e = L_r V_{qs}^e - L_r \omega_e \psi_s^e \tag{A.90}$$

Differentiating equation (A.90) by assuming ψ_s^e as constant, we get:

$$\left(\left(R_s L_r + R_r L_s\right) p + \sigma L_s L_r p^2\right) i_{qs}^e = L_r p V_{qs}^e - L_r \psi_s^e p \omega_e \tag{A.91}$$

By assuming viscous friction coefficient (B) as zero and the IM is working under no-load condition, the equations (A.70) and (A.74) respectively can be written as:

$$p \omega_e = \frac{P}{2J} T_e \tag{A.92}$$

$$i_{qs}^e = \frac{T_e}{\frac{3}{2}\frac{P}{2}\psi_s^e} \tag{A.93}$$

By substituting equations (A.92) and (A.93) in equation (A.91), we get:

$$\left(\left(R_s L_r + R_r L_s\right) p + \sigma L_s L_r p^2\right) T_e = \frac{3}{2}\frac{P}{2} \psi_s^e L_r p V_{qs}^e - \frac{3}{2J}\left(\frac{P}{2}\right)^2 L_r \left(\psi_s^e\right)^2 T_e \tag{A.94}$$

The open loop transfer function of the torque control loop (Figure B. 2) can be obtained from equation (A.94) as:

$$G_T(s) = \frac{T_e}{V_{qs}^e} = \frac{A_T s}{s^2 + B_T s + C_T} \tag{A.95}$$

where $A_T = \frac{3}{2}\frac{P}{2}\frac{\psi_s^e}{\sigma L_s}$, $B_T = \frac{R_s L_r + R_r L_s}{\sigma L_s L_r}$ and $C_T = \frac{3}{2}\left(\frac{P}{2}\right)^2 \frac{\left(\psi_s^e\right)^2}{\sigma L_s J}$.

B.4 Design of PI Controller using Root-Locus Technique

The transfer function of the PI controller is given as follows:

$$C(s)=\frac{V(s)}{E(s)}=K_p+\frac{K_i}{s}=K_p\left(1+\frac{1}{T_i\,s}\right) \tag{A.96}$$

where K_p is the controller proportional gain, K_i is controller integral gain, T_i is controller integrating time and $K_i=\frac{K_p}{T_i}$.

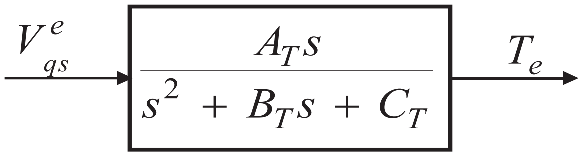

Figure B. 2: Open loop transfer function of torque control loop

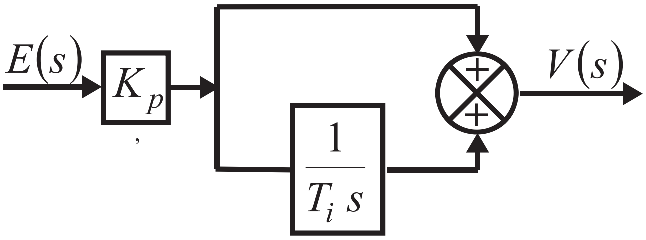

Figure B. 3: Block diagram of PI Controller

The general block diagram of the PI controller, which is used in the MATLAB/Simulink model of the DTFC-SVM scheme is shown in Figure B. 3. The Root Locus Method is used for tuning the gain values of the flux, torque and speed PI controllers. A root locus plot is a complete description of the system with respect to a specific parameter (K_p) of the design.

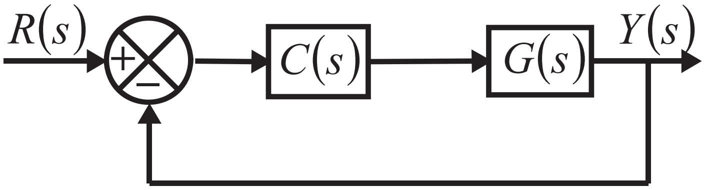

Figure B. 4: Generalized feedback control system

The generalized feedback control system with plant transfer function $G(s)$ and controller transfer function $C(s)$ is shown in Figure B. 4. The closed-loop characteristic equation of the above system can be written as:

$$1+C(s)\cdot G(s)=0 \tag{A.97}$$

In the root-locus method, we can predefine the closed loop control performance in terms of settling time and damping or overshoot. In this method the requirements (in terms of settling time and overshoot) of the closed loop control performance in the time domain are converted into a pair of conjugate poles: $\rho_{1,2} = -a \pm jb$. In order to achieve this predefined closed loop control performance, the dominance of $\rho_{1,2}$ is required. The dominance of $\rho_{1,2}$ requires that the real part of any of other poles must be lesser than m times $-a$ and there are no zero's nearby [205]. Thus, we want all other poles to be located at the left of the line $s = -ma$, and also for getting required overshoot they must be within $\pm\theta = cos^{-1}(damping \;\; factor)$, i.e., the desired (hatched) region of Figure B. 5.

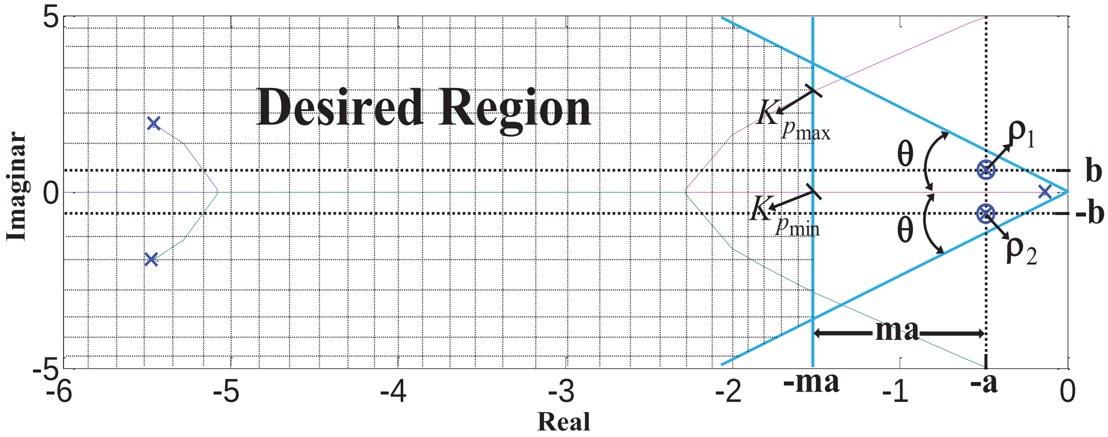

Figure B. 5: Desired (hatched) region of other closed loop poles

The main purpose of the root locus method is to find the PI parameters such that all the closed loop poles lie in the desired region except the dominant poles, $\rho_{1,2}$.

The general design procedure of PI controller parameters using the root-locus method is described in 5 simple steps, which are explained as follows [205]:

Step 1. Find out the desired pair of conjugate poles.

Step 2. Find out K_i in terms of K_p.

For getting K_i in terms of K_p substitute $\rho_1 = -a + jb$ in equation (A.97), we get:

$$K_p + \frac{K_i}{-a + jb} = \frac{-1}{G(\rho_1)} \tag{A.98}$$

By equating real parts on both sides of the equation (A.98), we get:

$$K_i = \alpha K_p + \beta \tag{A.99}$$

where $\alpha = \frac{a^2 + b^2}{a}$ and $\beta = -\frac{a^2 + b^2}{a}\left\{Re\left(\frac{-1}{G(\rho_1)}\right)\right\}$.

Step 3. Draw the root locus of the closed loop system with respect to K_p.

The closed-loop characteristic equation of the generalized control system can be written by substituting equations (A.96) and (A.99) in equation (A.97), as follows:

$$1 + K_p\left(\frac{(s + \alpha)\cdot G(s)}{s + (\beta\, G(s))}\right) = 0 \tag{A.100}$$

Now draw the root locus of $\frac{(s + \alpha)\cdot G(s)}{s + (\beta\, G(s))}$.

Step 4. Determine the interval of K_p i.e. $[K_{p\,\min}, K_{p\,\max}]$ for guaranteed dominant pole placement from the root locus.

Step 5. Choose K_p and K_i accordingly.

B.5 Design of Flux PI Controller

The block diagram of the unity feedback flux control loop with PI controller is shown in Figure B. 6. Using the IM parameters given in Appendix C the open loop flux transfer function (Equation A.86) can be expressed as follows:

$$G_\psi(s) = \frac{s + A_\psi}{s^2 + B_\psi s + C_\psi} \tag{A.101}$$

where $A_\psi = \frac{R_r}{\sigma\, L_r} = 158.22$, $B_\psi = \frac{R_s L_r + R_r L_s}{\sigma L_s\, L_r} = 351.52$, and $C_\psi = \frac{R_s R_r}{\sigma L_s\, L_r} 2844.36$.

The transfer function of the flux PI controller (Equation A.96) can be expressed as follows:

$$C_\psi(s) = K_{p\psi} + \frac{K_{i\psi}}{s} \tag{A.102}$$

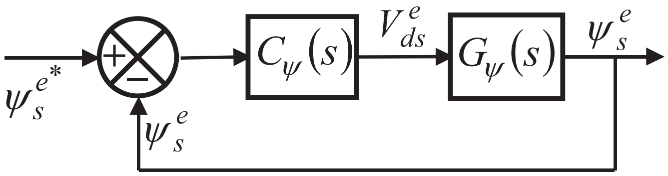

Figure B. 6: Flux control loop with PI controller

Initially, the required settling time and overshoot of the flux control loop are set as follows: settling time < 0.003 and overshoot < 4.33%. By using these time domain specifications a pair of dominant conjugate poles can be calculated as: $\rho_{1,2} = -1333.33 \pm j333.53$

By using equation (A.99), $K_{i\psi}$ can be expressed in terms of $K_{p\psi}$ as follows:

$$K_{i\psi} = \alpha_\psi K_{p\psi} + \beta_\psi \tag{A.103}$$

where $\alpha_\psi = 1416.76$ and $\beta_\psi = -1584203$.

By substituting α_ψ , β_ψ values in equation (A.100), we get:

$$1 + K_{p\psi}\left(\frac{\left(s + \alpha_\psi\right)\cdot\left(s + A_\psi\right)}{s^3 + B_\psi s^2 + \left(C_\psi + \beta_\psi\right)s + \beta_\psi A_\psi}\right) = 0 \tag{A.104}$$

Now draw the root locus of $\frac{\left(s + \alpha_\psi\right)\cdot\left(s + A_\psi\right)}{s^3 + B_\psi s^2 + \left(C_\psi + \beta_\psi\right)s + \beta_\psi A_\psi}$.

The interval of $K_{p\psi}$ for guaranteed dominant pole placement can be obtained from the root locus plot as: $K_{p\psi} \geq 1963$

For getting desired closed loop control performance, the PI controller parameters are calculated from the root locus plot as: $K_{p\psi} = 2660$, $T_{i\psi} = 0.00122$. For these parameters the root loci of the closed loop flux is obtained and it is shown in Figure B. 7.

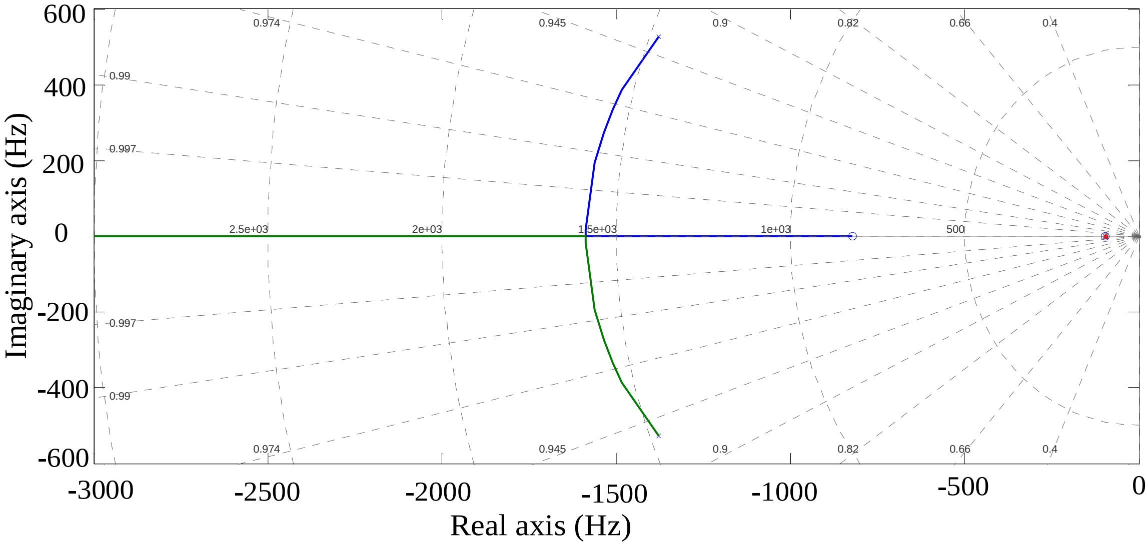

Figure B. 7: Root loci of the closed loop flux control system

B.6 Design of Torque PI Controller

The block diagram of the unity feedback torque control loop with PI controller is shown in Figure B. 8. Using the IM parameters given in Appendix C, the open loop torque transfer function (Equation A.95) can be expressed as follows:

$$G_T(s) = \frac{A_T s}{s^2 + B_T s + C_T} \tag{A.105}$$

where $A_T = \frac{3}{2}\frac{P}{2}\frac{\psi_s^e}{\sigma L_s} = 105.25$, $B_T = \frac{R_s L_r + R_r L_s}{\sigma L_s L_r} = 351.52$, and $C_T = \frac{3}{2}\left(\frac{P}{2}\right)^2\frac{\left(\psi_s^e\right)^2}{\sigma L_s J} = 2365.09$.

The transfer function of the torque PI controller (Equation A.96) can be expressed as follows:

$$C_T(s) = K_{pT} + \frac{K_{iT}}{s} \tag{A.106}$$

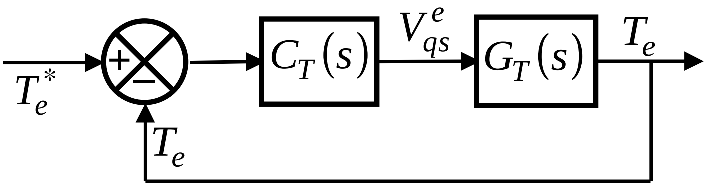

Figure B. 8: Torque control loop with PI controller

Initially, the required settling time and overshoot of the torque control loop are set as follows: settling time < 0.0015 and overshoot < 2%. By using these time domain specifications a pair of dominant conjugate poles can be calculated as: $\rho_{1,2} = -2666.67 \pm j535.38$

By using equation (A.99), K_{iT} can be expressed in terms of K_{pT} as follows:

$$K_{iT} = \alpha_T K_{pT} + \beta_T \tag{A.107}$$

where $\alpha_T = 2774.15$ and $\beta_T = -61046.47$

By substituting α_T , β_T values in equation (A.100), we get:

$$1 + K_{pT}\left(\frac{A_T(s + \alpha_T)}{s^2 + B_T s + (C_T + A_T\beta_T)}\right) = 0 \tag{A.108}$$

Now draw the root locus of $\dfrac{A_T(s + \alpha_T)}{s^2 + B_T s + (C_T + A_T\beta_T)}$.

The interval of K_{pT} for guaranteed dominant pole placement can be obtained from the root locus plot as: $K_{pT} \geq 39$.

For getting desired closed loop control performance the PI controller parameters are calculated from the root locus plot as: $K_{pT} = 49.3$, $T_{iT} = 0.0006511$. For these parameters the root loci of the closed loop torque is obtained and it is shown in Figure B. 9.

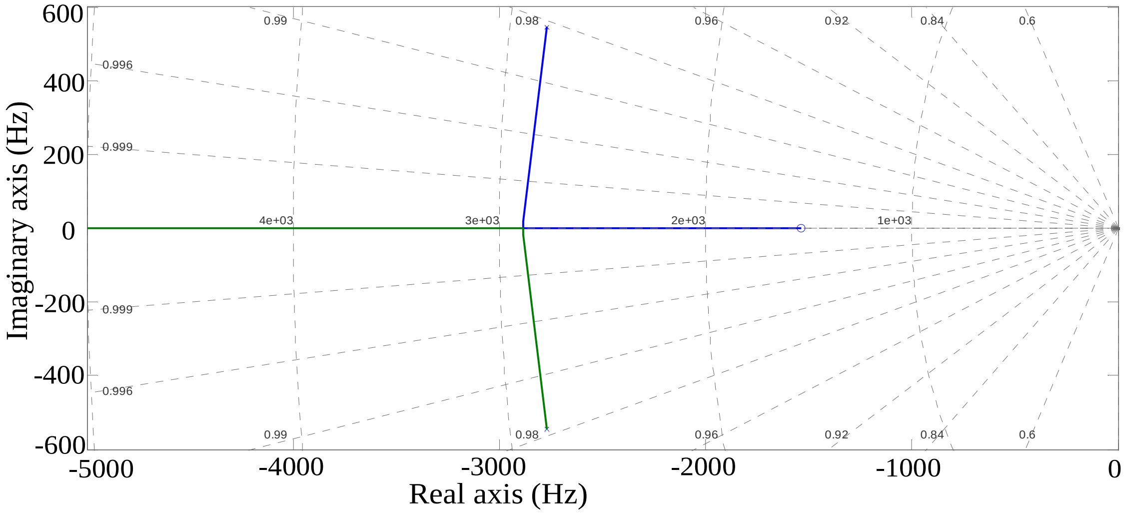

Figure B. 9: Root loci of the closed loop torque control system

B.7 Design of Speed PI Controller

The block diagram of the generalized unity feedback speed control loop with PI controller is shown in Figure B. 10. Where $G_{To}(s)$ is the closed loop transfer function of the Torque control loop with PI controller and it is expressed as:

$$G_{T0}(s) = \frac{A_T K_{pT} s + A_T K_{iT}}{s^2 + (A_T K_{pT} + B_T)s + (A_T K_{iT} + C_T)} \tag{A.109}$$

The transfer function of the speed PI controller (Equation A.96) can be expressed as follows:

$$C_\omega(s) = K_{p\omega} + \frac{K_{i\omega}}{s} \tag{A.110}$$

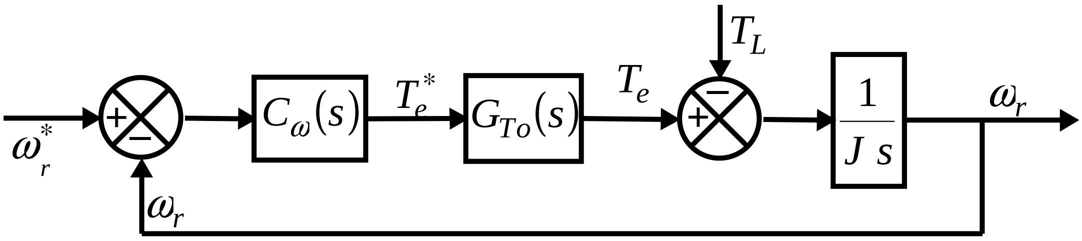

Figure B. 10: Generalized block diagram of the speed control loop

By assuming $T_L = 0$ the block diagram of the speed control loop with PI controller is shown in Figure B. 11.

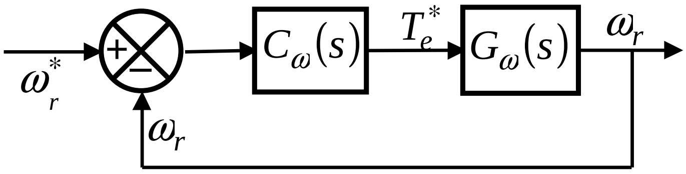

Figure B. 11: Speed control loop with PI controller

In Figure B. 11 the open loop speed transfer function can be expressed as follows:

$$G_\omega(s) = \frac{A_\omega s + B_\omega}{s^3 + C_\omega s^2 + D_\omega s} \tag{A.111}$$

where $A_\omega = \frac{A_T K_{pT}}{J}$, $B_\omega = \frac{A_T K_{iT}}{J}$, $C_\omega = A_T K_{pT} + \mathrm{B_T}$, and $D_\omega = A_T K_{iT} + \mathrm{C_T}$.

Initially, the required settling time and overshoot of the speed control loop are set as follows: settling time < 0.3 and overshoot < 2%. By using these time domain specifications a pair of dominant conjugate poles can be calculated as: $\rho_{1,2} = -13.333 \pm j10.707$

By using equation (A.99), $K_{i\omega}$ can be expressed in terms of $K_{p\omega}$ as follows:

$$K_{i\omega} = \alpha_\omega K_{p\omega} + \beta_\omega \tag{A.112}$$

where $\alpha_\omega = 21.9321$ and $\beta_\omega = -26.026$

By substituting α_ω, β_ω values in equation (A.100), we get:

$$1 + K_{p\omega}\left(\frac{(s + \alpha_\omega)(A_\omega s + B_\omega)}{s^4 + C_\omega s^3 + D_\omega s^2 + A_\omega \beta_\omega s + B_\omega \beta_\omega}\right) = 0 \tag{A.113}$$

Now draw the root locus of $\dfrac{(s + \alpha_\omega)(A_\omega s + B_\omega)}{s^4 + C_\omega s^3 + D_\omega s^2 + A_\omega \beta_\omega s + B_\omega \beta_\omega}$.

The interval of $K_{p\omega}$ for guaranteed dominant pole placement can be obtained from the root locus plot (Figure B. 13) as: $K_{p\omega} \geq 2.14$

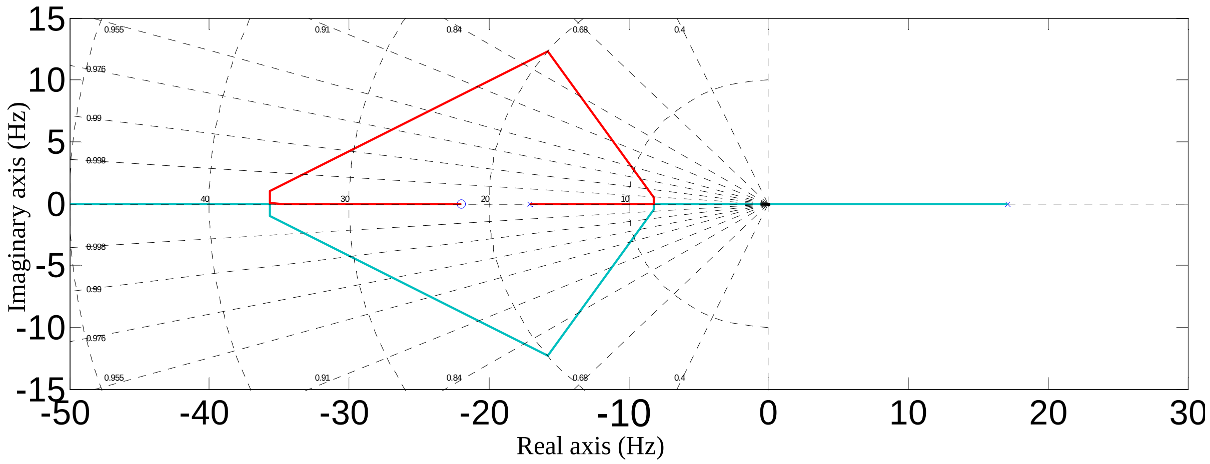

Figure B. 12: Root locus of the closed loop speed control system w.r.t $K_{p\omega}$

For getting desired closed loop control performance the PI controller parameters are calculated from the root locus plot (Figure B. 12) as: $K_{p\omega} = 6.34, T_{i\omega} = 0.0561$. For these parameters the root loci of the closed loop speed is obtained and it is shown in Figure B. 13.

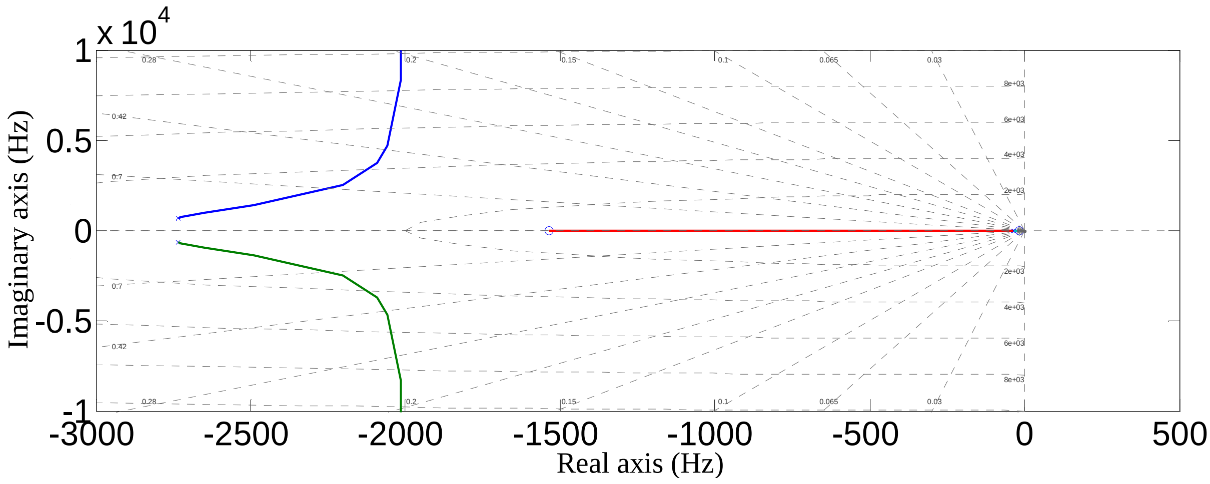

Figure B. 13: Root locus of the closed loop speed control system

Appendix C

C.1 Rating and Specifications

TABLE C.1 PARAMETERS AND RATINGS OF INDUCTION MOTOR

Parameters	Nominal values
Stator resistance (R_s)	5.5 Ω
Rotor resistance (R_r)	4.51 Ω
Mutual inductance (L_m)	0.2919 H
Stator self inductance (L_s)	0.3065 H
Rotor self inductance (L_r)	0.3065 H
Inertia (J)	0.089 kg.m^2
Rated supply voltage ($V_{L\text{-}L}$)	440 V (L-L)
Rated speed (W_r)	1410 rpm
Number of poles (P)	4
Rated power (P_r)	1.5 kW
Sampling time (Ts)	50 µs

TABLE C.2 SPECIFICATIONS OF THE INTELLIGENT POWER MODULE

Parameters	Nominal values
Three-phase supply	460 V
DC Link voltage	750 V_{DC}
Diodes	1200 V/60 A
IGBT	1200 V/25 A
Dead time	5 µs
Switching frequency	20 kHz
Max. output voltage of fault terminal	3.3 V
Max. value of speed terminal	2.6 V
Break pulse amplitude	5 V
The Max. Amplitude of PWM1 to PWM6	5 V
Fault output current (I_{FO})	20 mA
Fault output voltage (V_{FO})	20 V

TABLE C.4 SPECIFICATION OF THE VOLTAGE SENSOR (LV-25P)

Parameters	Nominal values
Primary nominal r.m.s current (I_{PN})	10 mA
Secondary nominal r.m.s current (I_{SN})	25 mA
Conversion ratio (K)	2500:1000
Supply voltage (V_s)	±12V-15 V
Response time @ 90% of V_{PN} (t_r)	40 µs

TABLE C.3 SPECIFICATION OF THE CURRENT SENSOR (LA-55P)

Parameters	Nominal values
Primary nominal r.m.s current (I_{PN})	50 A
Secondary nominal r.m.s current (I_{SN})	50 mA
Conversion ratio (K)	1:1000
Supply voltage (V_s)	±12 V-15 V
Frequency bandwidth (*f*)	DC-200 kHz
Reaction time @ 10% of I_{PN}	<500 µs
Response time @ 10% of I_{PN} (t_r)	<1 µs

TABLE C.5 SPECIFICATION OF THE SPEED SENSOR

Parameters	Nominal values
Supply voltage	4.5 V-5.5 V
Supply current	50-70 mA
Output pulse amplitude	512 Pulse per revolution

C.2 PI Controller gain values

TABLE C.6 GAIN VALUES OF PI SPEED CONTROLLER

Gain	Value
Proportional ($K_{p\omega}$)	6.34
Integral ($T_{i\omega}$)	0.0561

TABLE C.7 GAIN VALUES OF PI TORQUE CONTROLLER

Gain	Value
Proportional (K_{pT})	49.3
Integral (T_{iT})	0.00065

TABLE C.8 GAIN VALUES OF PI FLUX CONTROLLER

Gain	Value
Proportional ($K_{p\psi}$)	2660
Integral ($T_{i\psi}$)	0.00122

TABLE C.9 GAIN VALUES OF PI ADAPTATION CONTROLLER

Gain	Value
Proportional (K_{pA})	582
Integral (T_{iA})	0.12

TABLE C.10 GAIN VALUES OF PI RESISTANCE CONTROLLER

Gain	Value
Proportional (K_{pR_s})	26.7
Integral (T_{iR_s})	0.0013

C.3 PI Photographic view of the experimental prototype

The prototype has been fabricated for testing the high performance DTFC of speed sensorless IM drive. The photographic view of the complete experimental setup is shown in Figure C.1.

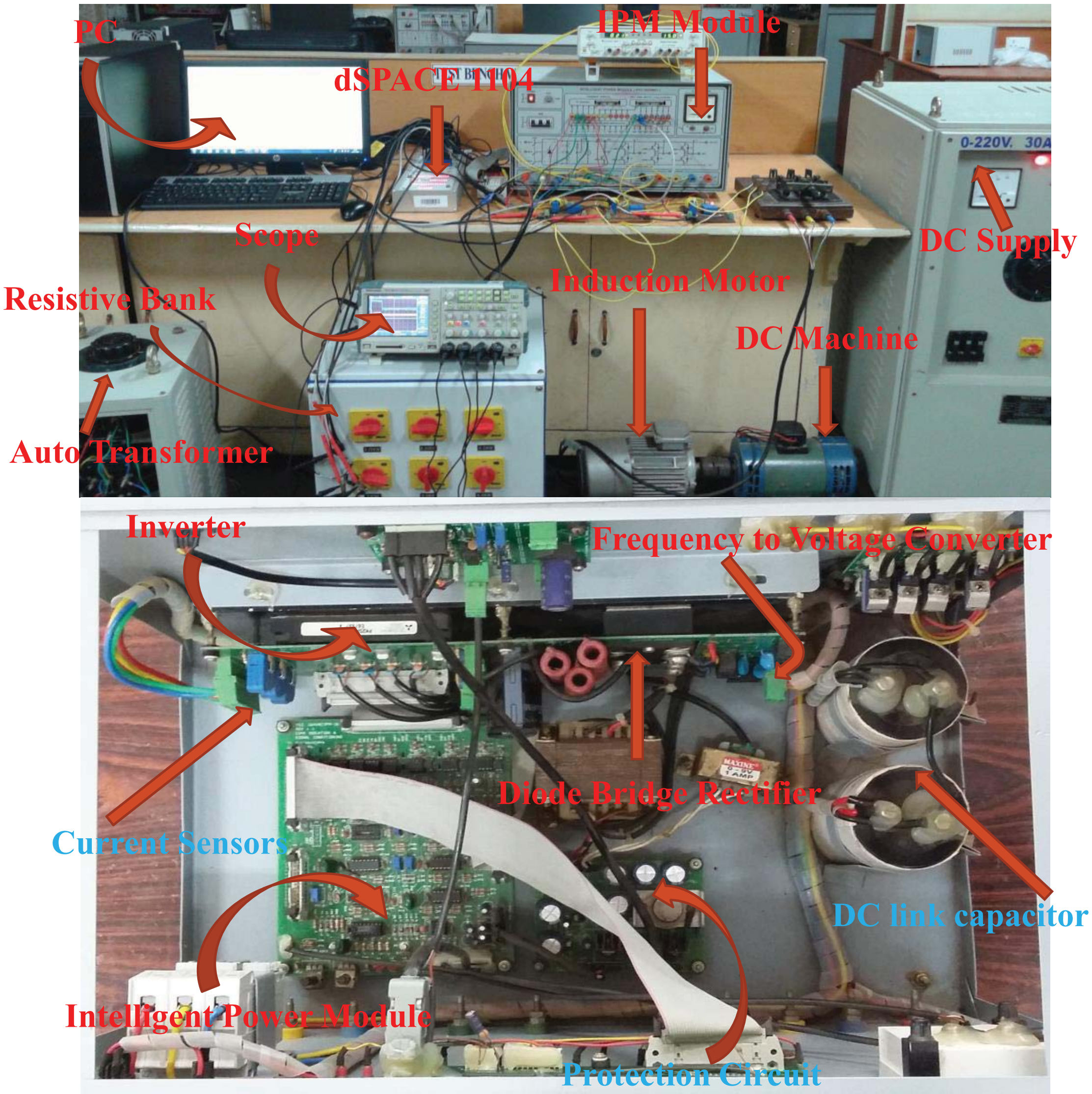

Figure C.1: Photographic view of the complete experimental setup

Dissemination

Journals

[1] A. K. Panda, Tejavathu Ramesh and S. Shiva Kumar. Rotor-flux based MRAS speed estimator for DTFC-SVM of a speed sensorless induction motor drive using Type-1 and Type-2 fuzzy logic controllers over a wide-range of speed operation. *International Transactions on Electrical Energy Systems,* DOI: 10.1002/etep.2181, December 2015.

[2] Tejavathu Ramesh, A. K. Panda and S. Shiva Kumar. Type-2 fuzzy logic control based MRAS speed estimator for speed sensorless direct torque and flux control of an induction motor drive. *ISA Transactions*, Elsevier, vol. 57, pp. 262–275, April 2015.

[3] Tejavathu Ramesh, A. K. Panda and S. Shiva Kumar. MRAS speed estimator based on Type-1 and Type-2 fuzzy logic controller for the speed sensorless DTFC-SVPWM of an Induction Motor Drive. *Journal of Power Electronics*, vol.15, no. 3, pp: 730-740, May 2015.

[4] A. K. Panda, Tejavathu Ramesh, and S. Shiva Kumar. High-performance direct torque and flux control of an induction motor drive using sliding-mode and fuzzy logic speed controllers. *International Journal of Power Electronics,* vol. 6, no.2, pp: 147-178, January 2014.

[5] Tejavathu Ramesh, A. K. Panda, and S. Shiva Kumar. Fuzzy logic and sliding-mode speed control based direct torque and flux control scheme to improve the performance of an induction motor drive. *International Journal on Electrical Engineering and Informatics*, vol. 6, no.1, pp: 155, March 2014.

[6] Tejavathu Ramesh, A. K. Panda, and S. Shiva Kumar. Type-1 and Type-2 fuzzy logic and sliding-mode based speed control of direct torque and flux control induction motor drives–a comparative study. *International Journal of Emerging Electric Power Systems*, vol. 14, no. 5, pp: 385-400, August 2013.

[7] Tejavathu Ramesh and A. K. Panda. High Performance Direct torque and flux control of induction motor drive using fuzzy logic based speed controller. *International Review of Electrical Engg.*, Vol. 8, Issue 2, pp. 696-710, May 2013.

Conferences

[1] Tejavathu Ramesh, A. K. Panda, and S. Shiva Kumar. Type-1 and Type-2 fuzzy logic speed controller based high performance direct torque and flux controlled induction motor drive. *In Proc. of Annual IEEE India Conference*, pp. 1-6, Dec. 2013.

[2] Tejavathu Ramesh, A. K. Panda, and S. Shiva Kumar. Sliding-mode and fuzzy logic control based MRAS speed estimators for sensorless direct torque and flux control of an induction motor drive. *In Proc. of Annual IEEE India Conf.*, pp. 1-6, Dec. 2013.

[3] Tejavathu Ramesh and A. K. Panda. High performance direct torque and flux control of induction motor drive using fuzzy logic based speed controller. *In Proc. of IEEE Intern. Conf. on Circuits, Power and Computing Tech.*, pp: 213-218, Sep. 2013.

[4] Tejavathu Ramesh and A. K. Panda. Artificial intelligence based high performance direct torque and flux control of induction motor drive. *In Proc. of IEEE International Conf. on Circuits, Power and Computing Technologies,* pp: 225-230, Sep. 2013.

[5] Tejavathu Ramesh, A. K. Panda, and S. Shiva Kumar. Fuzzy logic and sliding-mode based speed control of direct torque and flux control scheme to improve the performance of an induction motor drive. *In Proc. of International Conference on Computer Applications in Electrical Engineering Recent Advances*, pp. 1-6, 2013.

[6] Tejavathu Ramesh and A. K. Panda. High performance direct torque and flux control of induction motor drive using fuzzy logic based speed controller. *In Proc. of National Conf. on Power Electronics Sys. & Applications*, pp. 67-83, March 2013.

[7] Tejavathu Ramesh and A.K. Panda. Direct flux and torque control of three phase induction motor drive using PI and fuzzy logic controllers for speed regulator and low torque ripple. *In Proc. of IEEE Students Conference on Engineering and Systems*, pp: 1-6, 2012.